Applied Petroleum Geomechanics

Jon Jincai Zhang

APPLIED PETROLEUM GEOMECHANICS

JON JINCAI ZHANG

Gulf Professional Publishing
An imprint of Elsevier

Gulf Professional Publishing is an imprint of Elsevier
50 Hampshire Street, 5th Floor, Cambridge, MA 02139, United States
The Boulevard, Langford Lane, Kidlington, Oxford, OX5 1GB, United Kingdom

Notices
Knowledge and best practice in this field are constantly changing. As new research and experience broaden our understanding, changes in research methods, professional practices, or medical treatment may become necessary.

Practitioners and researchers must always rely on their own experience and knowledge in evaluating and using any information, methods, compounds, or experiments described herein. In using such information or methods they should be mindful of their own safety and the safety of others, including parties for whom they have a professional responsibility.

To the fullest extent of the law, neither the Publisher nor the authors, contributors, or editors, assume any liability for any injury and/or damage to persons or property as a matter of products liability, negligence or otherwise, or from any use or operation of any methods, products, instructions, or ideas contained in the material herein.

Library of Congress Cataloging-in-Publication Data
A catalog record for this book is available from the Library of Congress

British Library Cataloguing-in-Publication Data
A catalogue record for this book is available from the British Library

ISBN: 978-0-12-814814-3

Publisher: Brian Romer
Senior Acquisition Editor: Katie Hammon
Editorial Project Manager: Lindsay Lawrence
Production Project Manager: Anitha Sivaraj
Cover Designer: Mark Rogers

Typeset by TNQ Technologies

To my family.

About the author

Dr. Jon Jincai Zhang is a geomechanics expert. He currently is a Geoscience and Petrophysical Advisor with a major operator, Sinopec, in Houston, USA. Previously, he worked for 5 years as a Senior Geophysical Adviser at Hess Corporation for worldwide projects in pore-pressure prediction, geomechanics, and hydraulic fracturing. Before this, he had worked for 5 years as a Staff Petrophysical Engineer at Shell Exploration and Production Company based in Houston for pore-pressure prediction and geomechanics projects mainly in North and South Americas. He also had several years of experience in consulting, JIPs, and management at Halliburton, USA, (KSI) as the Geomechanics Manager. His early career started as an engineer and then a senior engineer in rock mechanics at China Coal Research Institute in Beijing. He has been an adjunct professor at North China Institute of Science and Technology. He has authored or coauthored more than 100 research papers and three books.

He graduated in 1984 from the Hebei University of Engineering and then pursued graduate study at China University of Geosciences and China Coal Research Institute from 1984 to 1987. He holds a Ph.D. in petroleum and geological engineering from the University of Oklahoma. He has been an Associate Editor of Journal of Petroleum Science and Engineering since 2010 and has been serving on the Publications Committee of American Rock Mechanics Association since 2010. Dr. Zhang also served on the SPE Special Series Committee of the Journal of Petroleum Technology from 2010 to 2012 and has been an Administrative Chairperson for SPE Geomechanics Technical Section since 2018.

Foreword

In the past, projects involving "rock engineering" were designed using classical continuum mechanics "closed-form" solutions. By presenting such solutions in terms of dimensionless parameters, the consequences of their variations from the initial assumptions provided the engineer with valuable practical insights. Such an approach is still used in most cases where only limited pertinent laboratory and/or field data are known.

In the last quarter century, rock mechanics/geomechanics has become increasingly concerning with energy-related issues, mainly, the extraction of hydrocarbons and, more recently, a renewal interest in hot-dry rock geothermal reservoirs. Practical examples can be found in the US Proceedings published yearly by ARMA in which the number of papers somewhat reflects the health of a particular discipline. An often main remaining issue is that rock formations have been subject, over geological times, to complex, ill-defined, and often unknown histories of loading and deformations; hence, variability and heterogeneity are inherent features of most locations. In addition, as deeper horizons and more complex geometries are contemplated, unusual stress and temperature conditions are encountered, combined with the presence of natural deformable fractures have led to the development of more sophisticated numerical approaches. In unconventional petroleum resources, combining horizontal drilling technology with multiple parallel stimulations by hydraulic fractures has recently resulted in unexpected substantial recoverable reserves. This contributed to the United States recently becoming a net exporter of hydrocarbons.

As technologies advance in the energy industries, geomechanics finds more applications and has become an important knowledge to guide exploration and production activities. For me, Dr. Jincai Zhang's book offers the advantage of first assembling some basic concepts an engineer could be confronted with and require a rapid solution owing to time constraints. This book provides and facilitates such approaches by combining theoretical fundamentals with practical examples. Another valuable information contained in this book is the shared data provided via detailed examples of worked-out solutions. Wherever possible, the author has been willing to share empirical relationships, derived from vast worldwide experience.

The first few chapters mostly review fundamental continuum mechanics parameters with comments on their determinations as well as limitations. After discussing more detailed failure criteria, the reader is exposed to the fundamental concepts of fracture mechanics before diving into the subject of in situ stresses. Different techniques of in situ stress measurements are critically reviewed, including a very detailed pore pressure and fracture gradient prediction. The chapter on borehole stability is nicely introduced by the previous chapter covering wellbore strengthening. Finally, the last two chapters summarize part of our understanding as well as remaining challenges of hydraulic fracturing and sanding.

Jincai Zhang's book nicely fills a gap existing between fundamentals and complex references. As such, I highly recommend it be used for senior and graduate students. I also believe it should be part of important reference book for practicing engineers.

Jean-Claude Roegiers, Ph.D.
ARMA Fellow
Professor Emeritus
McCasland Chair
The University of Oklahoma

Preface

Although I took the course of Rock Mechanics (fundamentals of Geomechanics) when I was an undergraduate, I did not really enjoy Rock Mechanics until I was a Ph.D. student at the University of Oklahoma. This was thanks to a very prestigious professor, Dr. J.-C. Roegiers, who taught us Rock Mechanics. What attracted me to his class was not only his fascinating teaching, but his humor and his unique tradition. That is, after the end of course he invited his students to an all-you-can-drink bar: drinking Rolling Rock, and forgetting about Mechanics; for a stressful student, this was a big relaxation and enjoyment. After I took his three courses, I found Rock Mechanics was a huge enjoyment, because it could explain mechanisms in many difficult engineering problems. This led me to choose Petroleum Geomechanics as my dissertation topic!

After I finished my Ph.D., I joined the research team of Dr. Hartmut Spetzler, a very kind and knowledgeable professor, who once built and tested the first polyaxial compression apparatus for rocks in the United States. After 3 years of academic experience in his Colorado lab (certainly including field tests in Arizona summers), I went back to the industry to pursue my career in applying geomechanics to solve practical problems encountered in the petroleum industry.

Conventional oil and gas reserves are becoming more difficult to be found. Consequently, exploration and production have to go much deeper into ultra-deepwater and ultra-deep formations, drill through long sections of salt formations and complicated geological structures, access extremely low permeable reservoirs (shale oil and shale gas, geothermal), and produce in much more difficult formations. To successfully access these formations, geomechanics plays a more important role, finds more applications, and has become a key knowledge to guide exploration and production activities. The applications include better understanding rock mechanical properties and behaviors, estimating in situ stresses and pore pressures, analyzing drilling mechanics, ensuring wellbore stability, and well integrity, stimulating tight rocks (e.g., hydraulic fracturing), and mitigating sand production and casing failures.

This book, Applied Petroleum Geomechanics, as the title suggests, aims to apply geomechanics principles, theory, and knowledge to the petroleum industry for solving practical problems. It provides a basis of geomechanics

and rock mechanics knowledge, gives detailed applications of geomechanics in the petroleum and related industries (e.g., other energy industries and geological engineering), and provides a quick reference and guide in geomechanics for engineers and geologists.

This book consists of 12 chapters. In Chapter 1 basic rock mechanics concepts are introduced. Stress—strain governing equations are given for both elastic and poroelastic rocks with consideration of thermal and anisotropic effects. The in situ stress equations accounting for anisotropy effect are derived.

Chapters 2 and 3 discuss rock physical and mechanical properties and rock failure criteria. The anisotropy, stress-dependent behaviors, and fluid impacts on rock properties are discussed. Empirical equations and new correlations for obtaining rock properties are examined for both conventional and unconventional reservoirs. Laboratory test methods and rock failure criteria are discussed to reveal rock failure mechanisms.

Chapter 4 overviews basic rock fracture mechanics. Stress distributions around the fracture tips in three fracture modes are introduced. Sneddon's solutions of fracture widths are examined, which can be applied to hydraulic fracturing modeling and wellbore strengthening design.

In Chapters 5 and 6, measurements and interpretations of horizontal stresses are discussed. Integrated methods for calculating overburden stress and the minimum and maximum horizontal stresses are examined in different faulting stress regimes. Poisson's ratio—dependent stress polygons are applied to constrain in situ stresses.

Chapters 7 and 8 cover pore pressure generation mechanisms and overpressure behaviors. Pore pressure predictions in hydraulically connected formations and in shales are systematically examined. Resistivity, sonic, porosity, and d-exponent methods are modified using depth-dependent normal compaction trends for easy applications. Methods and procedures of real-time pore pressure detection are also presented.

In Chapter 9, fracture gradient prediction methods in sedimentary rocks and salt are overviewed. Case applications are examined to illustrate how to apply those methods. For depleted reservoirs, wellbore strengthening techniques can be used to increase formation fracture gradient and reduce mud losses in drilling operations. Semianalytical solutions for calculating the fracture width are presented with consideration of in situ stress anisotropy.

Chapter 10 covers borehole failure types, wellbore stresses, and wellbore stability. Elastic and poroelastic solutions are discussed for determining the required mud weight for borehole stability. Impacts of bedding planes, rock

anisotropy, and salt body are also considered in wellbore solutions to improve borehole stability modeling.

Chapters 11 and 12 emphasize reservoir geomechanics and its applications in hydraulic fracturing and sanding prediction. Effects of in situ stresses, shear stresses, and depletion on hydraulic fracture initiation, propagation, and containment are investigated. Relationships of perforation orientation, stress and strength, and sanding potentials are analyzed to provide optimal perforation and drawdown for mitigating sand production.

In the acknowledgments, I am grateful to my many current and former colleagues, industry colleagues, and friends for their support, collaboration, and discussions over the years. I am especially indebted to Dr. J.-C. Roegiers for his inspirations, insights, and collaboration.

I would like to thank Ms. Katie Hammon, Elsevier Acquisition Manager, who several years ago encouraged me to write a book to share my industry experience in applied geomechanics. My sincere thanks goes to Ms. Lindsay Lawrence, Elsevier Editorial Project Manager, for her help and encouragement during the book writing. I want to thank Ms. Swapna Praveen at Elsevier for helping me to obtain permissions on the figures cited in this book. I would also like to thank Elsevier Production Project Manager Ms. Anitha Sivaraj for her hard work for this book.

I wish to express my sincere gratitude to the reviewers below for their time and effort spent in reviewing the manuscript:

Ms. Shuling Li, at BP USA, reviewed Chapters 1 to 12;

Dr. Chong Zhou, at Petronas, reviewed Chapters 2, 3, 5, 10;

Dr. Yanhui Han, at Aramco Services, reviewed Chapters 6 and 12;

Dr. Jiajia Gao, at NUS, reviewed some poroelastic equations.

Jon Jincai Zhang

March 2019

CHAPTER 1

Stresses and strains

Contents

Abstract

Basic rock mechanics concepts are introduced, including stresses and strains, normal and shear stresses, total and effective stresses, displacement and deformation, and normal and shear strains. The 2-D and 3-D Mohr circle representations of stresses are described, which can be used to interpret mechanical behaviors of rocks under stresses and depletion. Stress–strain governing equations are given for both elastic and poroelastic rocks with thermal effects. Rock anisotropic behaviors are investigated, and the constitutive equations for transversely isotropic and orthotropic rocks are presented. Considerations of anisotropy and poroelasticity play a very important role in understanding mechanical behaviors of rocks, particularly in shale oil and gas formations in which anisotropy and pore pressure are dominant characteristics. In situ stress equations accounting for anisotropy effects are also derived.

Applied Petroleum Geomechanics
ISBN 978-0-12-814814-3
https://doi.org/10.1016/B978-0-12-814814-3.00001-0

Keywords: Anisotropy of rock; Constitutive equation; Effective stress; Mohr's circle; Stress and strain.

1.1 Stresses

1.1.1 Normal and shear stresses

The stress is equal to the force divided by the area. On a real or imaginary plane through a rock, there can be normal force (ΔN) and shear force (ΔS), as shown in Fig. 1.1. The forces induce normal and shear stresses in the rock. It should be noted that a solid can sustain a shear force and shear stress, whereas a liquid or gas cannot (Hudson and Harrison, 1997). A liquid or gas contains a pressure, i.e., a force per unit area, which acts equally in all directions and hence is a scalar quantity. However, stresses in rocks normally are not equal in different directions, and they are vectors.

The normal (shear) stress is the normal (shear) force per unit area as shown in Fig. 1.1A. The normal and shear forces and normal and shear stress components are shown in Fig. 1.1B. The normal stress is perpendicular to each of the planes, but the shear stress is parallel to each of the planes as shown in Fig. 1.1B. The normal and shear stresses can be mathematically defined as follows when the size of the small area is reduced to zero:

$$\text{normal stress, } \sigma_n = \lim \frac{\Delta N}{\Delta A} (\Delta A \to 0) \tag{1.1}$$

$$\text{shear stress, } \tau = \lim \frac{\Delta S}{\Delta A} (\Delta A \to 0) \tag{1.2}$$

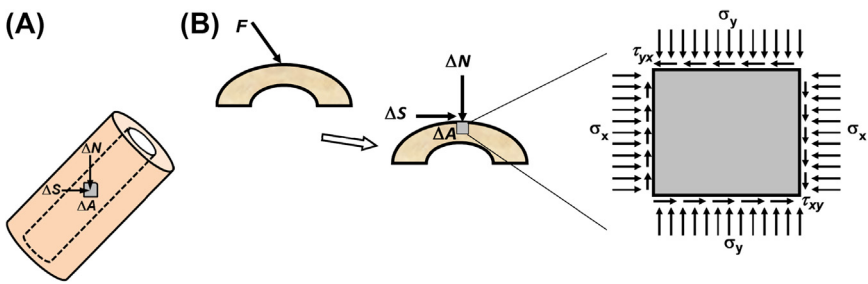

Figure 1.1 (A) Normal force (ΔN) and shear force (ΔS) and their acting area (ΔA). (B) Normal stress (σ) and shear stress (τ) induced by normal and shear forces plotted in a two-dimensional small element.

1.1.2 Stress components

If an infinitesimal cube is cut within the rock, it will have normal and shear stresses acting on each plane of the cube. The compressive normal stress is positive, and the tensile normal stress is treated as negative in rock mechanics sign convention. Each normal stress is perpendicular to each of the planes, as shown in Fig. 1.2. However, the case of the shear stresses is not so direct because the resulting shear stresses on any face will not generally be aligned with these axes. The shear stress on any face in Fig. 1.2 has two perpendicular components that are aligned with the two axes parallel to the edges of the face. Therefore, there are nine stress components comprising three normal components and six shear components acting on a cubic element. The stress tensor can be expressed as follows:

$$\boldsymbol{\sigma} = \begin{bmatrix} \sigma_x & \tau_{xy} & \tau_{xz} \\ \tau_{yx} & \sigma_y & \tau_{yz} \\ \tau_{zx} & \tau_{zy} & \sigma_z \end{bmatrix} \tag{1.3}$$

By considering equilibrium of moments around the x, y, and z axes, the shear stresses have the following relations:

$$\tau_{xy} = \tau_{yx}, \quad \tau_{yz} = \tau_{zy}, \quad \tau_{xz} = \tau_{zx} \tag{1.4}$$

Therefore, the state of stress at a point is defined completely by six independent components. These are three normal stress components (σ_x, σ_y, σ_z) and three shear stress components (τ_{xy}, τ_{yz}, τ_{zx}).

1.1.3 Stresses in an inclined plane

The principal stresses in two dimensions are very useful because many engineering problems of practical interest are effectively two-dimensional, such as the borehole problem during drilling operations, which can be

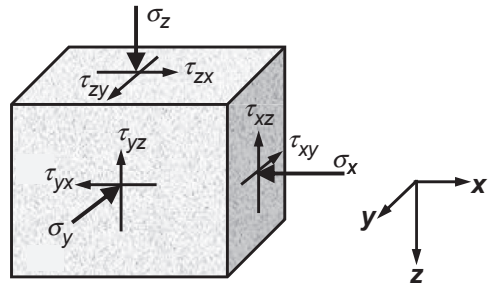

Figure 1.2 Normal and shear stress components on an infinitesimal cube in the rock.

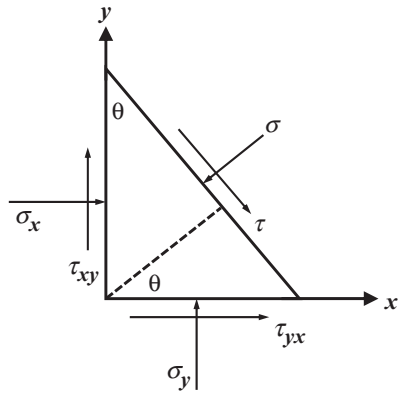

Figure 1.3 Force equilibrium on a small triangle element, assuming that all the stress components are positive.

simplified as the state of plane strain. Consider a two-dimensional small triangular element of the rock in which the normal stresses σ_x and σ_y and shear stress τ_{xy} act in the xy-plane. The normal (σ) and shear (τ) stresses at a surface oriented normal to a general direction θ in the xy-plane (Fig. 1.3) can be calculated as follows:

$$\begin{aligned}\sigma &= \frac{\sigma_x + \sigma_y}{2} + \frac{\sigma_x - \sigma_y}{2}\cos 2\theta + \tau_{xy}\sin 2\theta \\ \tau &= \frac{\sigma_y - \sigma_x}{2}\sin 2\theta + \tau_{xy}\cos 2\theta\end{aligned} \tag{1.5}$$

By proper choice of θ, it is possible to obtain $\tau = 0$. From Eq. (1.5) this happens when:

$$\tan 2\theta = \frac{2\tau_{xy}}{\sigma_x - \sigma_y} \tag{1.6}$$

Eq. (1.6) has two solutions, θ_1 and θ_2. The two solutions correspond to two directions for which the shear stress τ vanishes. These two directions are named the principal axes of stress. The corresponding normal stresses, σ_1 and σ_3, are the principal stresses, and they are found by introducing Eq. (1.6) into the first equation of Eq. (1.5):

$$\begin{aligned}\sigma_1 &= \frac{\sigma_x + \sigma_y}{2} + \sqrt{\tau_{xy}^2 + \frac{(\sigma_x - \sigma_y)^2}{4}} \\ \sigma_3 &= \frac{\sigma_x + \sigma_y}{2} - \sqrt{\tau_{xy}^2 + \frac{(\sigma_x - \sigma_y)^2}{4}}\end{aligned} \tag{1.7}$$

Thus, in the direction θ_1, which identifies a principal axis, the normal stress is σ_1 and the shear stress is zero. In the direction θ_2, which identifies the other principal axis, the normal stress is σ_3 and the shear stress is also zero. The principal axes are mutually orthogonal. The equations for calculating principal stresses in three dimensions can be found in rock mechanics textbooks (e.g., Jeager et al., 2007). All unsupported excavation surfaces (including wellbores) are principal stress planes (Hudson and Harrison, 1997). This is because all unsupported excavation surfaces have no shear stresses acting on them and are therefore principal stress planes.

1.1.4 Principal stresses

It is possible to show that there is one set of axes with respect to which all shear stresses are zero, and the three normal stresses have their extreme values, as shown in Fig. 1.4. These three mutually perpendicular planes are called principal planes, and the three normal stresses acting on these planes are the principal stresses. It is convenient to specify the stress state using these principal stresses because they provide direct information on the maximum and minimum values of the normal stress components (Hudson and Harrison, 1997). The values σ_1, σ_2, and σ_3 in Fig. 1.4 are the principal stresses, and $\sigma_1 > \sigma_2 > \sigma_3$, which are three principal stress components. Therefore, the principal stress tensor can be expressed as follows:

$$\boldsymbol{\sigma} = \begin{bmatrix} \sigma_1 & 0 & 0 \\ 0 & \sigma_2 & 0 \\ 0 & 0 & \sigma_3 \end{bmatrix} \tag{1.8}$$

1.1.5 Effective stresses

The effect of pore pressure on the mechanical properties of saturated rocks has been extensively investigated by using the concept of the effective stress that

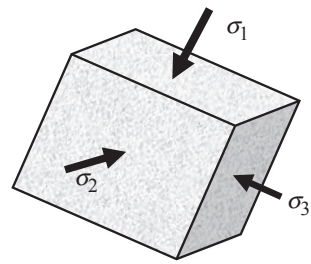

Figure 1.4 Principal stress components in the principal planes.

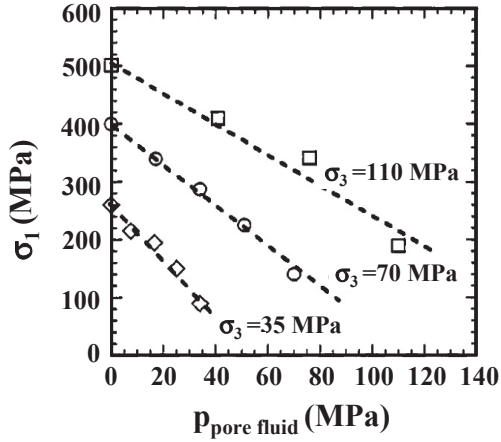

Figure 1.5 Stresses at failure (σ_1 or rock strength) in a Darley Dale sandstone as a function of pore pressure for different confining stresses (σ_3). *(Based on the data of Murrell, S.A.F., 1965. The effect of triaxial stress systems on the strength of rocks at atmospheric temperatures. Geophys. J. R. Astronom. Soc. 10, 231–281.)*

Terzaghi proposed. A set of data that illustrates the effective stress principle of brittle failure is that of Murrell (1965), who conducted standard triaxial compression tests on a Darley Dale sandstone, at different values of pore pressures. The Darley Dale sandstone was a poorly graded feldspathic sandstone with 21% porosity. In each test, the pore pressure and the confining stress were held constant, while the axial stress was increased until failure occurred. Based on the data presented by Murrell (1965), a figure was plotted to show the pore pressure effect on rock failure, as shown in Fig. 1.5 (Jeager and Cook, 1979). It indicates that the rock strength reduces markedly as the fluid pore pressure in the rock increases. Therefore, in porous rocks (most subsurface formations), the effective stresses should be considered in geomechanical analysis. Effective stress is the applied stress, or total stress, minus the product of fluid pressure (the pore pressure) and effective stress coefficient. In one-dimensional case, it can be expressed as:

$$\sigma' = \sigma - \alpha p_p \tag{1.9}$$

where σ and σ' are the total and effective stresses, respectively; p_p is the pore pressure; α is Biot's coefficient (Biot, 1941), which can be obtained from the following equation:

$$\alpha = 1 - K_{\text{dry}}/K_m \tag{1.10}$$

where K_{dry} is the bulk modulus of the dry porous rock; K_m is the bulk modulus of the matrix mineral in the rock; α is restricted to the range of $\phi < \alpha \leq 1$ (ϕ is porosity). In Terzaghi's effective stress law, $\alpha = 1$.

In the three-dimensional condition the relation between changes in total stress (σ_{ij}) and effective stress (σ'_{ij}) can be expressed in the following equation (Biot, 1941):

$$\sigma'_{ij} = \sigma_{ij} - \alpha p_p \delta_{ij} \tag{1.11}$$

where σ_{ij} is the index notation of the total stress tensor, as shown in Eq. (1.3); δ_{ij} is Kronecker's delta, $\delta_{ij} = 1$, when $i = j$; and $\delta_{ij} = 0$, when $i \neq j$.

1.1.6 In situ stresses, far-field and near-field stresses

In situ stress state is the original stress status in the rock before excavations or other perturbations. In situ stresses are also called far-field stresses. For example, the stress state before a borehole is drilled shown in Fig. 1.6 is the in situ stress state (Zhang, 2013). As a first approximation, one can assume that the three principal stresses of a natural in situ stress field are acting vertically (one component, σ_V) and horizontally (two components, σ_H and σ_h). More details about in situ stresses can be found in Chapters 5 and 6.

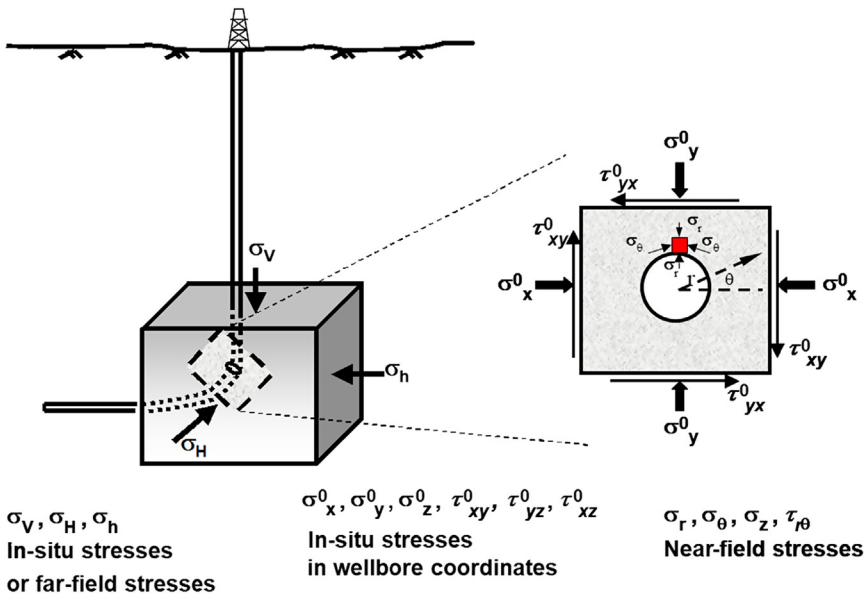

Figure 1.6 Schematic representation of in situ stresses (far-field stresses) and near-field stresses (2-D case) in a borehole.

The near-field stresses are the stress redistributions of the in situ stresses caused by current excavations, such as the stresses near the borehole wall in Fig. 1.6.

1.2 Mohr's circle representation of stresses

1.2.1 Mohr's circles for two-dimensional stresses

Mohr's circle or the Mohr diagram is a useful tool to represent the stress state and rock failure. The Mohr circle can be used to determine graphically the stress components acting on a rotated coordinate system, i.e., acting on a differently oriented plane passing through a particular point (e.g., the point P in Fig. 1.7A). When the principal stresses (σ_1, σ_3) are available, a two-dimensional Mohr's circle can be illustrated in Fig. 1.7A; notice that the stresses plotted in x-axis are the principal stresses. The diameter of the circle is $\sigma_1 - \sigma_3$ and the center is at $((\sigma_1 + \sigma_3)/2,0)$. The normal stress σ and shear stress τ at each point on the circle represent a state of stress on a plane whose normal direction is inclined at θ to σ_1 (i.e., θ is the angle between the inclined plane and the direction of σ_3), as shown in Fig. 1.7B. From the Mohr circle diagram, the normal and shear stresses at each point (e.g., the point P) or in each inclined plane can be easily obtained, i.e.,

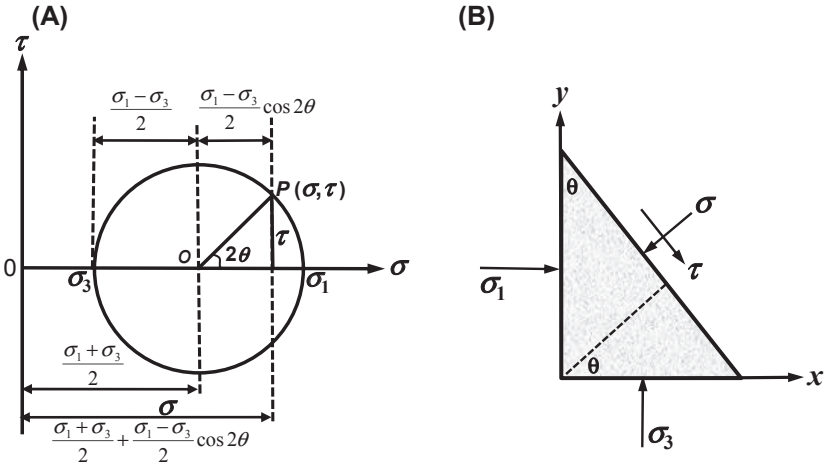

Figure 1.7 (A) Mohr's circle diagram for a two-dimensional state of stresses (principal stresses σ_1 and σ_3). (B) Shear and normal stresses on a plane exerted by the far-field principal stresses (σ_1 and σ_3) (corresponding to the stress state at the point P).

$$\sigma = \frac{\sigma_1 + \sigma_3}{2} + \frac{\sigma_1 - \sigma_3}{2}\cos 2\theta$$
$$\tau = \frac{\sigma_1 - \sigma_3}{2}\sin 2\theta \tag{1.12}$$

Eqs. (1.12) and (1.5) are also very useful for analyzing stress states in fractures. The maximum shear stress can be obtained from Eq. (1.12) when $2\theta = 90$ degrees, that is,

$$\tau_{max} = \frac{\sigma_1 - \sigma_3}{2} \tag{1.13}$$

1.2.2 Mohr's circles for three-dimensional stresses

To construct Mohr's circles for a three-dimensional case of stresses at a point, the values of the principal stresses (σ_1, σ_2, σ_3) and their principal directions (n_1, n_2, n_3) must be first evaluated. When the principal stresses are available, the three-dimensional Mohr's circles can be plotted (Parry, 2004), as illustrated in Fig. 1.8. All admissible stress points (σ, τ) lie on the three circles or within the shaded area enclosed by them, as shown in Fig. 1.8B, and each of those points (such as the point P) represents a state of stress on a plane (e.g., a weak plane or a fault plane) in the cube in Fig. 1.8A. Three-dimensional Mohr's circles combined with shear failure

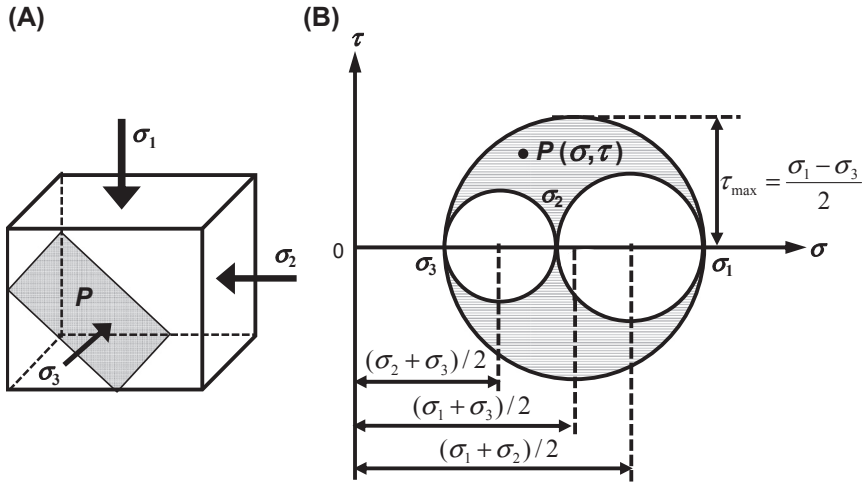

Figure 1.8 (A) Principal stresses and (B) a plane in a cube represented by Mohr's circles in a three-dimensional stress state. The *dashed vertical lines* point to the centers of the three circles.

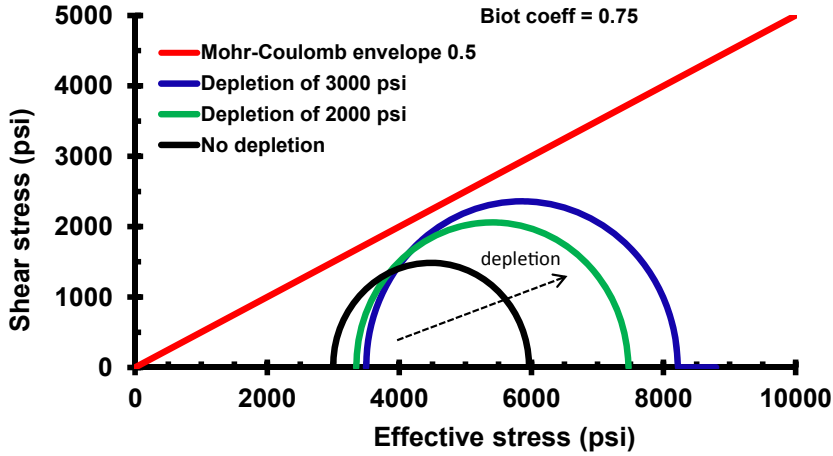

Figure 1.9 2-D Mohr's circle diagram showing the stress changes before (left circle) and after depletion of 2000 psi (middle) and 3000 psi (right) in the Middle Bakken reservoir at the depth of 11,087 ft with the Mohr–Coulomb shear failure envelope in a fractured formation.

envelopes can be used to analyze normal and shear stresses in fault planes for assessment of shear failures and fault reactivations (Barton et al., 1995). The maximum shear stress is the same to the one obtained from Eq. (1.13).

For fluid-saturated porous rocks, the effective stresses should be used for constructing the Mohr circles, i.e., replacing the total stresses (σ, σ_1, σ_2, σ_3) by effective stresses (σ', σ'_1, σ'_2, σ'_3), respectively. Fig. 1.9 shows the relationship of the in situ effective stresses and shear failure envelope for different degrees of depletion in the Bakken shale oil play (Dohmen et al., 2017). Reservoir depletion (decrease of pore pressure) causes the size of Mohr's circle to increase, and this may induce the reservoir rocks approaching shear failures.

1.3 Strains

In elasticity theory of solid mechanics, infinitesimal strain is assumed for solid deformation. The infinitesimal strain theory, or small deformation theory, is a mathematical approach to the description of the deformation of a solid body in which the displacements are assumed to be much smaller than any relevant dimension of the body; therefore, its geometry and the constitutive properties of the material at each point of space can be assumed to be unchanged by the deformation. Strain is a description of deformation

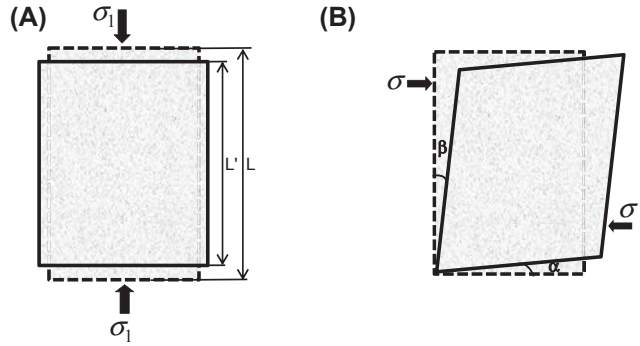

Figure 1.10 Illustration of normal and shear strains. σ_1, σ are the applied stresses; L, L' are the original and the deformed lengths, respectively; α, β are the angles after deformations.

in terms of relative displacement of particles in the body. Strain is defined as deformation of a solid due to stress. It is a relative change in shape or size of an object due to externally applied stresses (forces), and it is dimensionless and has no unit. There are two types of strains: normal and shear strains. Normal strain describes the relative size change; it is elongation or contraction of a line segment. Contractile normal strain is taken as positive in rock mechanics sign convention. If a rock sample in a typical uniaxial compression test is loaded in the axial direction, then displacements (contraction and elongation) are formed in axial and lateral directions. The strain in axial direction is equal to the relative displacement (the length change) divided by the original length of the rock sample, as shown in Fig. 1.10A, i.e.,

$$\varepsilon = \frac{L - L'}{L} \tag{1.14}$$

Engineering shear strain is defined as the change in angle between two line segments originally perpendicular, as illustrated in Fig. 1.10B, i.e.,

$$\gamma = \alpha + \beta \tag{1.15}$$

In a three-dimensional domain, the normal strains can be written in the following forms:

$$\varepsilon_x = \frac{\partial u_x}{\partial x}, \quad \varepsilon_y = \frac{\partial u_y}{\partial y}, \quad \varepsilon_z = \frac{\partial u_z}{\partial z} \tag{1.16}$$

where ε_x, ε_y, ε_z are the normal strains in x, y, and z directions, respectively; u_x, u_y, u_z are the displacements in x, y, and z directions, respectively.

The shear strains can be expressed as follows:

$$\begin{aligned}\gamma_{xy} &= \gamma_{yx} = \frac{\partial u_x}{\partial y} + \frac{\partial u_y}{\partial x},\\ \gamma_{yz} &= \gamma_{zy} = \frac{\partial u_y}{\partial z} + \frac{\partial u_z}{\partial y},\\ \gamma_{zx} &= \gamma_{xz} = \frac{\partial u_z}{\partial x} + \frac{\partial u_x}{\partial z}\end{aligned} \tag{1.17}$$

where γ_{xy}, γ_{yz}, γ_{zx} are the engineering shear strains in x, y, and z directions, respectively; and $\gamma_{xy} = \gamma_{yx} = 2\varepsilon_{xy} = 2\varepsilon_{yx}$; $\gamma_{yz} = \gamma_{zy} = 2\varepsilon_{yz} = 2\varepsilon_{zy}$; $\gamma_{zx} = \gamma_{xz} = 2\varepsilon_{zx} = 2\varepsilon_{xz}$

The tensorial normal and shear strain components of the infinitesimal strain tensor can be expressed in the following matrix forms:

$$\boldsymbol{\varepsilon} = \begin{bmatrix} \varepsilon_{xx} & \varepsilon_{xy} & \varepsilon_{xz} \\ \varepsilon_{yx} & \varepsilon_{yy} & \varepsilon_{yz} \\ \varepsilon_{zx} & \varepsilon_{zy} & \varepsilon_{zz} \end{bmatrix} = \begin{bmatrix} \varepsilon_x & \gamma_{xy}/2 & \gamma_{xz}/2 \\ \gamma_{yx}/2 & \varepsilon_y & \gamma_{yz}/2 \\ \gamma_{zx}/2 & \gamma_{zy}/2 & \varepsilon_z \end{bmatrix} \tag{1.18}$$

Note that this matrix is symmetrical and hence has six independent components.

1.4 Stress–strain relations in isotropic rocks

1.4.1 Stress–strain relations for different rocks

Rocks behave mechanically different under compression tests, and different models can be used to describe the stress–stain behaviors. Fig. 1.11 illustrates some typical models to describe stress–strain constitutive relationships. The commonly used model assumes that the rock has a linear elastic stress–strain relationship in which elasticity can be applied, as shown in Fig. 1.11A. The stress and strain in uniaxial compression in Fig. 1.11A follows a linear relationship, and rock failure happens when the stress reaches the rock strength. This behavior is mainly for brittle rocks.

Fig. 1.11B illustrates the elastic perfectly plastic behavior, i.e., the rock has the elastic behavior before the stress reaches the peak strength. After reaching the peak strength, a constant stress state is kept (residual strength is the same as the peak strength, i.e., no stress drop), but straining continues,

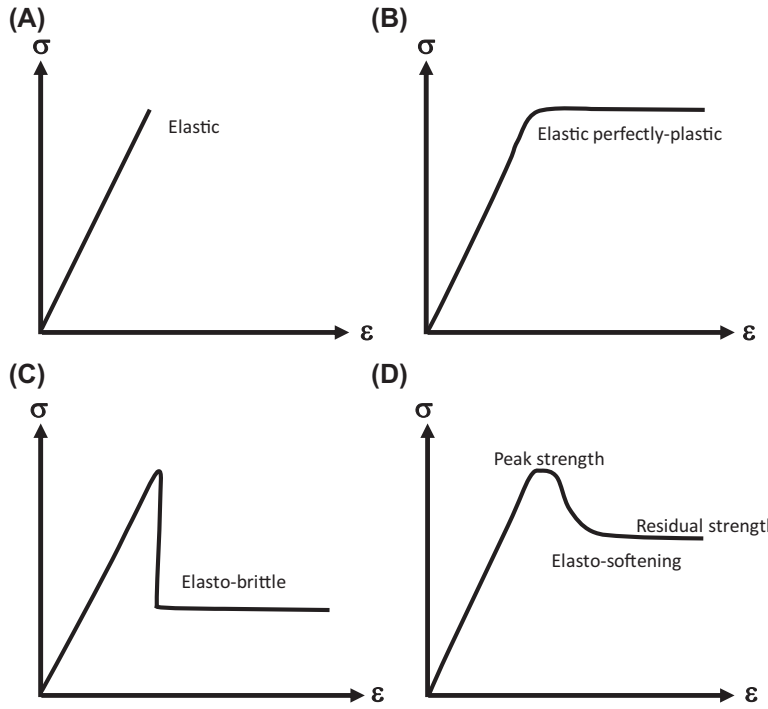

Figure 1.11 Stress–strain relationships and models: (A) linear elastic rocks; (B) elastic perfectly plastic rocks: ductile rocks; (C) elasto-brittle: brittle rocks; (D) elasto-plastic: strain-softening rocks. In each plot, the maximum value of the stress is the rock strength.

and the rock is in creep state. This behavior is for very ductile rocks or for a rock under the triaxial test with a very high confining stress. Fig. 1.11C shows elasto-brittle deformation normally for very brittle rocks. In this case the rock has a very low residual strength after the stress reaching the peak strength. Fig. 1.11D displays the elasto-plastic strain-softening model normally for brittle rocks, and it has a higher residual strength than that in the elasto-brittle case. There are also other models used to describe rock deformations, such as nonlinear, elasto-plastic strain-hardening models.

1.4.2 Isotropic dry rocks

For a linear elastic material (as shown in Fig. 1.11A) or for a rock in the elastic deformation stage, the one-dimensional stress and strain have a linear relationship, i.e.,

$$\sigma_x = E\varepsilon_x \tag{1.19}$$

For linear elastic isotropic dry materials, the stress and strain follow Hooke's law, which can be expressed as follows in the three-dimensional condition:

$$\begin{aligned}
\varepsilon_x &= \frac{1}{E}[\sigma_x - \nu(\sigma_y + \sigma_z)] \\
\varepsilon_y &= \frac{1}{E}[\sigma_y - \nu(\sigma_x + \sigma_z)] \\
\varepsilon_z &= \frac{1}{E}[\sigma_z - \nu(\sigma_x + \sigma_y)] \\
\varepsilon_{xy} &= \frac{1}{2G}\tau_{xy} \\
\varepsilon_{xz} &= \frac{1}{2G}\tau_{xz} \\
\varepsilon_{yz} &= \frac{1}{2G}\tau_{yz}
\end{aligned} \tag{1.20}$$

where σ and τ are the normal and shear stresses, respectively; ε_{xy}, ε_{xz}, ε_{yz} are the shear strains; ν is Poisson's ratio; E and G are Young's and shear moduli, respectively.

When any two of the moduli of E, G, ν, λ, and K are defined, the remaining ones are fixed by certain relations. Some useful relations are listed in Table 1.1.

A very useful stress–strain state is the uniaxial strain condition, where the lateral strains are constrained (i.e., $\varepsilon_x = \varepsilon_y = 0$), and only the vertical

Table 1.1 Relations to convert elastic moduli and Poisson's ratio.

***E*, Young's modulus**	***K*, bulk modulus**	**λ, Lamé constant**
$E = 3K\,(1-2\nu)$	$K = \lambda\dfrac{1+\nu}{3\nu}$	$\dfrac{\lambda}{G} = \dfrac{2\nu}{1-2\nu}$
$E = 2G\,(1+\nu)$	$K = \dfrac{2}{3}G\dfrac{1+\nu}{1-2\nu}$	$\dfrac{\lambda}{\lambda+G} = 2\nu$
$E = \dfrac{9KG}{3K+G}$	$K = \lambda + \dfrac{2}{3}G$	$\dfrac{G}{\lambda+G} = 1-2\nu$
$E = G\dfrac{3\lambda+2G}{\lambda+G}$	$K = \dfrac{GE}{9G-3E}$	$\dfrac{\lambda+2G}{\lambda+G} = 2(1-\nu)$
$E = \dfrac{\lambda}{\nu}(1+\nu)(1-2\nu)$	$G = \dfrac{E}{2(1+\nu)}$	$\dfrac{3\lambda+2G}{\lambda+G} = 2(1+\nu)$

deformation is allowed. In this case, the relationship of three principal stresses can be obtained from Eq. (1.20) by substituting $\varepsilon_x = \varepsilon_y = 0$:

$$\sigma_x = \sigma_y = \frac{\nu}{1-\nu}\sigma_z \tag{1.21}$$

If σ_x, σ_y, and σ_z represent three in situ stresses in the subsurface, then the in situ stresses in the uniaxial strain condition have the following relation:

$$\sigma_h = \sigma_H = \frac{\nu}{1-\nu}\sigma_V \tag{1.22}$$

where σ_h, σ_H, and σ_V are the minimum and maximum horizontal, and vertical stresses, respectively.

1.4.3 Isotropic thermal rocks

Stress–strain relations for isotropic, linear elastic dry materials with consideration of thermal effect can be written as shown below (Bower, 2010):

$$\begin{bmatrix} \varepsilon_x \\ \varepsilon_y \\ \varepsilon_z \\ 2\varepsilon_{yz} \\ 2\varepsilon_{xz} \\ 2\varepsilon_{xy} \end{bmatrix} = \frac{1}{E}\begin{bmatrix} 1 & -\nu & -\nu & 0 & 0 & 0 \\ -\nu & 1 & -\nu & 0 & 0 & 0 \\ -\nu & -\nu & 1 & 0 & 0 & 0 \\ 0 & 0 & 0 & 2(1+\nu) & 0 & 0 \\ 0 & 0 & 0 & 0 & 2(1+\nu) & 0 \\ 0 & 0 & 0 & 0 & 0 & 2(1+\nu) \end{bmatrix}\begin{bmatrix} \sigma_x \\ \sigma_y \\ \sigma_z \\ \tau_{yz} \\ \tau_{xz} \\ \tau_{xy} \end{bmatrix} - \alpha_T \Delta T \begin{bmatrix} 1 \\ 1 \\ 1 \\ 0 \\ 0 \\ 0 \end{bmatrix} \tag{1.23}$$

where, σ_x, σ_y, σ_z are the normal stresses; τ_{xy}, τ_{yz}, τ_{xz} are the shear stresses; α_T is the thermal expansion coefficient; ΔT is the increase in temperature of the rock. Notice that this equation uses the rock mechanics sign convention (compressive normal stress and contractile normal strain are taken as positive; the same convention is used in the following equations). In solid mechanics sign convention, the last term in Eq. (1.23) has an opposite sign.

The inverse relationship can be expressed as:

$$\begin{bmatrix}\sigma_x\\ \sigma_y\\ \sigma_z\\ \tau_{yz}\\ \tau_{xz}\\ \tau_{xy}\end{bmatrix} = \frac{E}{(1+\nu)(1-2\nu)}\begin{bmatrix} 1-\nu & \nu & \nu & 0 & 0 & 0\\ \nu & 1-\nu & \nu & 0 & 0 & 0\\ -\nu & \nu & 1-\nu & 0 & 0 & 0\\ 0 & 0 & 0 & \frac{1-2\nu}{2} & 0 & 0\\ 0 & 0 & 0 & 0 & \frac{1-2\nu}{2} & 0\\ 0 & 0 & 0 & 0 & 0 & \frac{1-2\nu}{2}\end{bmatrix} \times \begin{bmatrix}\varepsilon_x\\ \varepsilon_y\\ \varepsilon_z\\ 2\varepsilon_{yz}\\ 2\varepsilon_{xz}\\ 2\varepsilon_{xy}\end{bmatrix} + \frac{E\alpha_T\Delta T}{1-2\nu}\begin{bmatrix}1\\1\\1\\0\\0\\0\end{bmatrix} \tag{1.24}$$

This expression can be written in a much more convenient form using index notation (Bower, 2010):

$$\varepsilon_{ij} = \frac{1+\nu}{E}\sigma_{ij} - \frac{\nu}{E}\sigma_{kk}\delta_{ij} - \alpha_T\Delta T\delta_{ij} \tag{1.25}$$

where, δ_{ij} is the Kronecker delta function; if $i = j$, $\delta_{ij} = 1$; otherwise, $\delta_{ij} = 0$.

The inverse relation is:

$$\sigma_{ij} = \frac{E}{1+\nu}\left[\varepsilon_{ij} + \frac{\nu}{1-2\nu}\varepsilon_{kk}\delta_{ij}\right] + \frac{E\alpha_T\Delta T}{1-2\nu}\delta_{ij} \tag{1.26}$$

The stress–strain relations are often expressed using the elastic modulus tensor C_{ijkl} or the elastic compliance tensor S_{ijkl} as follows:

$$\sigma_{ij} = C_{ijkl}(\varepsilon_{kl} + \alpha_T\Delta T\delta_{kl}) \tag{1.27}$$

$$\varepsilon_{ij} = S_{ijkl}\sigma_{kl} - \alpha_T\Delta T\delta_{ij} \tag{1.28}$$

1.4.4 Plane stress and plane strain in isotropic thermal rocks

1.4.4.1 Plane stress state

Plane stress and plane strain states can simplify 3-D stress–strain relations into the corresponding 2-D forms. For a plane stress (biaxial stress) deformation state, it has $\sigma_z = \tau_{yz} = \tau_{zx} = 0$; therefore, substituting this condition into Eq. (1.23) the strain–stress relations have the following forms:

$$\begin{aligned}
\varepsilon_x &= \frac{1}{E}(\sigma_x - \nu\sigma_y) - \alpha_T \Delta T \\
\varepsilon_y &= \frac{1}{E}(\sigma_y - \nu\sigma_x) - \alpha_T \Delta T \\
\varepsilon_z &= -\frac{\nu}{E}(\sigma_x + \sigma_y) - \alpha_T \Delta T \\
\varepsilon_{xy} &= \frac{1}{2G}\tau_{xy}
\end{aligned} \tag{1.29}$$

and from Eq. (1.24) stress–strain relations can be expressed as follows:

$$\begin{aligned}
\sigma_x &= \frac{E}{1-\nu^2}(\varepsilon_x + \nu\varepsilon_y) + \frac{E\alpha_T \Delta T}{1-\nu} \\
\sigma_y &= \frac{E}{1-\nu^2}(\varepsilon_y + \nu\varepsilon_x) + \frac{E\alpha_T \Delta T}{1-\nu} \\
\tau_{xy} &= 2G\varepsilon_{xy}
\end{aligned} \tag{1.30}$$

This case occurs when a thin plate is stressed in its own plane. It also occurs in the analysis at any free surface, if the x- and y-axes are taken in the surface (Jeager and Cook, 1979).

1.4.4.2 Plane strain state

For a plane strain (biaxial strain) deformation state, $\varepsilon_z = \varepsilon_{yz} = \varepsilon_{zx} = 0$; substituting this relation into Eq. (1.23) the strain–stress relations can be expressed as follows:

$$\begin{aligned}
\varepsilon_x &= \frac{1+\nu}{E}[(1-\nu)\sigma_x - \nu\sigma_y] - (1+\nu)\alpha_T \Delta T \\
\varepsilon_y &= \frac{1+\nu}{E}[(1-\nu)\sigma_y - \nu\sigma_x] - (1+\nu)\alpha_T \Delta T \\
\varepsilon_{xy} &= \frac{1}{2G}\tau_{xy}
\end{aligned} \tag{1.31}$$

and from Eq. (1.24) the stress–strain relations are as follows:

$$\begin{aligned}
\sigma_x &= \frac{E}{(1+\nu)(1-2\nu)}[(1-\nu)\varepsilon_x + \nu\varepsilon_y] + \frac{E\alpha_T\Delta T}{(1-2\nu)} \\
\sigma_y &= \frac{E}{(1+\nu)(1-2\nu)}[(1-\nu)\varepsilon_y + \nu\varepsilon_x] + \frac{E\alpha_T\Delta T}{(1-2\nu)} \\
\sigma_z &= \nu(\sigma_x + \sigma_y) + E\alpha_T\Delta T \\
\sigma_z &= \frac{E\nu(\varepsilon_x + \varepsilon_y)}{(1+\nu)(1-2\nu)} + \frac{E\alpha_T\Delta T}{(1-2\nu)} \\
\tau_{xy} &= 2G\varepsilon_{xy}
\end{aligned} \tag{1.32}$$

if the thermal effect is not considered, then $\sigma_z = \nu(\sigma_x+\sigma_y)$.

Plane strain state is often applicable to very long or thick structures, where the length of the structure is much greater than the other two dimensions (e.g., Zhang et al., 2018). It is applicable to boreholes, hydraulic fractures, and two-dimensional openings. For instance, Fig. 1.12 shows a classic hydraulic fracture model (the PKN model), where the fracture is very long in y-direction. The PKN model assumes a plane strain deformation in the vertical plane, i.e., each vertical cross section acts independently; i.e., the

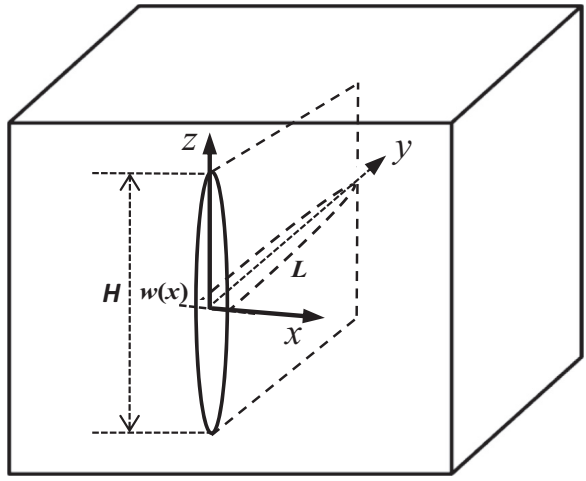

Figure 1.12 Plane strain wellbore model of the PKN fracture for simplifying the 3-D problem.

fracture height is fixed and independent to the fracture length growth (or length ≫ height).

1.4.5 Isotropic porous rocks

For the fluid-saturated rocks, the effect of pore pressure and Biot's coefficient (α) needs to be considered. Poroelasticity can be applied to consider this effect (Detournay and Cheng, 1993). In porous rocks, the strain and stress relations previously introduced should consider the effective stresses instead of the total stresses (i.e., replacing each total stress σ by effective stress σ' using $\sigma' = \sigma - \alpha p_p$). For instance, the strain and stress relations in isotropic porous rocks can be expressed as follows by replacing the total stresses in Eq. (1.20) by the corresponding effective stresses (Eq. 1.9):

$$\begin{aligned}
\varepsilon_x &= \frac{1}{E}[\sigma_x - \nu(\sigma_y + \sigma_z) - \alpha(1-2\nu)p_p] \\
\varepsilon_y &= \frac{1}{E}[\sigma_y - \nu(\sigma_x + \sigma_z) - \alpha(1-2\nu)p_p] \\
\varepsilon_z &= \frac{1}{E}[\sigma_z - \nu(\sigma_x + \sigma_y) - \alpha(1-2\nu)p_p] \\
\varepsilon_{xy} &= \frac{1}{2G}\tau_{xy} \\
\varepsilon_{xz} &= \frac{1}{2G}\tau_{xz} \\
\varepsilon_{yz} &= \frac{1}{2G}\tau_{yz}
\end{aligned} \tag{1.33}$$

The in situ stresses in the uniaxial strain condition (refer to Eq. 1.22) with consideration of pore pressures can be solved from Eq. (1.33), assuming $\varepsilon_x = \varepsilon_y = 0$, $\sigma_x = \sigma_h$, $\sigma_y = \sigma_H$, and $\sigma_z = \sigma_V$, i.e.,

$$\sigma_h = \sigma_H = \frac{\nu}{1-\nu}(\sigma_V - \alpha p) + \alpha p_p \tag{1.34}$$

1.5 Stress–strain relations in anisotropic elastic rocks

Most rocks are anisotropic materials and have a characteristic orientation. For example, in a shale formation, the clay minerals are oriented in the

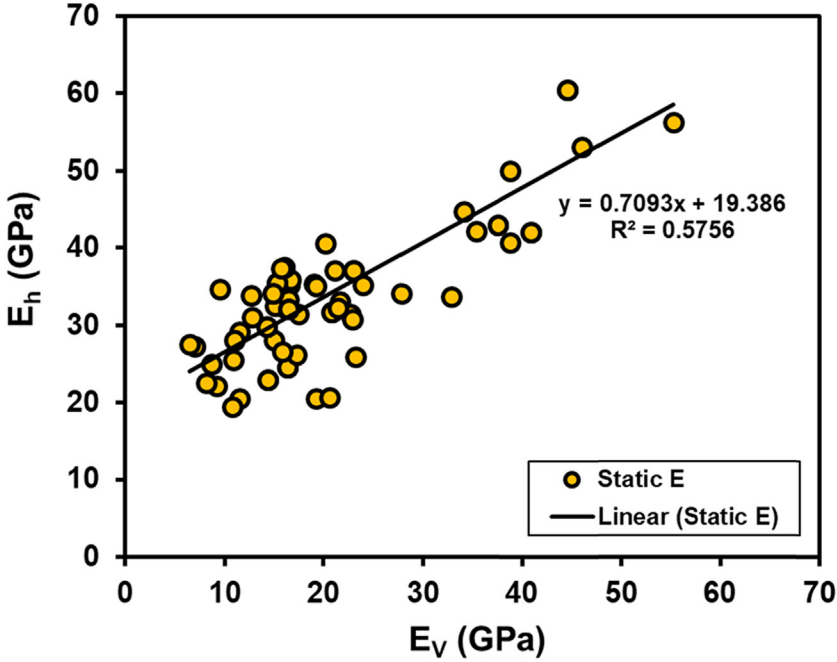

Figure 1.13 Lab experimental results of horizontal and vertical Young's moduli in the Haynesville and Bossier shales.

bedding direction. The shale will be stiffer if it is loaded parallel to the bedding direction than that loaded perpendicular to the same direction. For instance, uniaxial compression tests in shale core samples were performed with weak plane laminations orientated different angles to the loading direction, the anisotropic strength ratio (the ratio of the maximum to the minimum compressive strengths) could be > 3. The anisotropic ratios in Young's moduli of the loading parallel to the bedding direction to the loading perpendicular to the bedding direction are also very different. For example, the compression test results in core samples show that the ratios of the horizontal to vertical Young's moduli vary from 1 to 4.2 in the Haynesville and Bossier shale gas formations (Fig. 1.13).

To model anisotropic elastic media, stress–strain relation with thermal effect can be written in a more compact matrix form to account for the anisotropy (Bower, 2010):

$$\boldsymbol{\sigma} = \mathbf{C}(\boldsymbol{\varepsilon} + \boldsymbol{\alpha}_T \Delta \mathbf{T}) \tag{1.35}$$

$$\text{where } \boldsymbol{\sigma} = \begin{bmatrix} \sigma_{11} \\ \sigma_{22} \\ \sigma_{33} \\ \sigma_{23} \\ \sigma_{13} \\ \sigma_{12} \end{bmatrix}, \mathbf{C} = \begin{bmatrix} c_{11} & c_{12} & c_{13} & c_{14} & c_{15} & c_{16} \\ c_{12} & c_{22} & c_{23} & c_{24} & c_{25} & c_{26} \\ c_{13} & c_{23} & c_{33} & c_{34} & c_{35} & c_{36} \\ c_{14} & c_{24} & c_{34} & c_{44} & c_{45} & c_{46} \\ c_{15} & c_{25} & c_{35} & c_{45} & c_{55} & c_{56} \\ c_{16} & c_{26} & c_{36} & c_{46} & c_{56} & c_{66} \end{bmatrix}, \boldsymbol{\varepsilon} = \begin{bmatrix} \varepsilon_{11} \\ \varepsilon_{22} \\ \varepsilon_{33} \\ 2\varepsilon_{23} \\ 2\varepsilon_{13} \\ 2\varepsilon_{12} \end{bmatrix},$$

$$\boldsymbol{\alpha}_{\mathbf{T}} = \begin{bmatrix} \alpha_{T11} \\ \alpha_{T22} \\ \alpha_{T33} \\ 2\alpha_{T23} \\ 2\alpha_{T13} \\ 2\alpha_{T12} \end{bmatrix};$$

$c_{11} \equiv C_{1111}, c_{12} \equiv C_{1122} = C_{2211}$, etc. are the elastic stiffnesses of the rock.

The inverse of Eq. (1.35) has the following form:

$$\boldsymbol{\varepsilon} = \mathbf{S}\boldsymbol{\sigma} - \boldsymbol{\alpha}_{\mathbf{T}}\Delta\mathbf{T} \tag{1.36}$$

$$\text{where } \mathbf{S} = \begin{bmatrix} s_{11} & s_{12} & s_{13} & s_{14} & s_{15} & s_{16} \\ s_{12} & s_{22} & s_{23} & s_{24} & s_{25} & s_{26} \\ s_{13} & s_{23} & s_{33} & s_{34} & s_{35} & s_{36} \\ s_{14} & s_{24} & s_{34} & s_{44} & s_{45} & s_{46} \\ s_{15} & s_{25} & s_{35} & s_{45} & s_{55} & s_{56} \\ s_{16} & s_{26} & s_{36} & s_{46} & s_{56} & s_{66} \end{bmatrix};$$

$s_{11} \equiv S_{1111}, s_{12} \equiv S_{1122} = S_{2211}$, etc. are the elastic compliances of the rock, and $\mathbf{S} = \mathbf{C}^{-1}$.

In an anisotropic rock, each matrix of **C** and **S** has 21 independent elastic components. Therefore, if an anisotropic rock contains no symmetry planes, then 21 elastic stiffnesses (C_{ij}) are required to completely describe the rock properties. It is difficult to obtain those stiffnesses. However, for most practical cases a simplified model can be adopted, and anisotropic rocks are often modeled as orthotropic or transversely isotropic (TI) media in a coordinate system attached to their apparent structures or directions of symmetry.

1.5.1 Orthotropic elastic rocks

Orthotropy (orthorhombic symmetry) is a simplification of the anisotropy. An orthotropic rock has three mutually perpendicular symmetry planes at each point in the rock, and these planes have the same orientation throughout the rock (Amadei et al., 1987; Amadei, 1996). This type of rock has nine independent material constants. For a rock that is orthotropic in a local 1, 2, 3 Cartesian coordinate system attached to clearly defined planes of anisotropy (refer to Fig. 1.14), the elastic compliance matrix can be expressed as follows:

$$\mathbf{S} = \begin{bmatrix} 1/E_1 & -\nu_{21}/E_2 & -\nu_{31}/E_3 & 0 & 0 & 0 \\ -\nu_{12}/E_1 & 1/E_2 & -\nu_{32}/E_3 & 0 & 0 & 0 \\ -\nu_{13}/E_1 & -\nu_{23}/E_2 & 1/E_3 & 0 & 0 & 0 \\ 0 & 0 & 0 & 1/G_{23} & 0 & 0 \\ 0 & 0 & 0 & 0 & 1/G_{13} & 0 \\ 0 & 0 & 0 & 0 & 0 & 1/G_{12} \end{bmatrix} \tag{1.37}$$

where E_1, E_2, and E_3 are Young's moduli in the 1, 2, and 3 directions, respectively; G_{12}, G_{13}, and G_{23} are the shear moduli in planes parallel to the 12, 13, and 23 planes, respectively; ν_{ij} ($i, j = 1, 2, 3$) are Poisson's ratios that characterize the normal strains in the symmetry directions j when a stress is applied in the symmetry directions i. Because of symmetry of the compliance matrix, Poisson's ratios ν_{ij} and ν_{ji} are such that $\nu_{ij}/E_i = \nu_{ji}/E_j$ (Amadei, 1996).

For the orthotropic rock the thermal expansion coefficient tensor has the following form:

$$\boldsymbol{\alpha} = \begin{bmatrix} \alpha_{T1} & 0 & 0 \\ 0 & \alpha_{T2} & 0 \\ 0 & 0 & \alpha_{T3} \end{bmatrix} \tag{1.38}$$

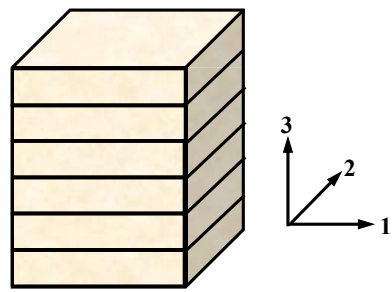

Figure 1.14 An orthotropic rock (a layered rock formation) with three planes of symmetry normal to the axes (the 1, 2, 3 directions).

1.5.2 Transversely isotropic elastic rocks

A TI model is a simplification of orthotropy. It is azimuthally symmetric about a single axis. Examples of TI materials are layered rocks or isotropic rocks with a single set of oriented fractures. There are five independent stiffness coefficients required to completely describe the elastic properties (Havens, 2012). If rock properties are uniform horizontally within a layer, but vary vertically from layer to layer, then the formations can be treated as vertical transverse isotropy (VTI). The vertical axis (axis 3 as shown in Fig. 1.14) is the axis of rotational symmetry, which is perpendicular to the symmetric isotropic plane (the horizontal plane). Because the rock has isotropic properties in the horizontal plane, the plane is the plane of transverse isotropy. Transverse isotropy requires that $c_{22} = c_{11}$, $c_{23} = c_{13}$, $c_{55} = c_{44}$, so that the stiffness matrix has the following form:

$$\mathbf{C} = \begin{bmatrix} c_{11} & c_{12} & c_{13} & 0 & 0 & 0 \\ c_{12} & c_{11} & c_{13} & 0 & 0 & 0 \\ c_{13} & c_{13} & c_{33} & 0 & 0 & 0 \\ 0 & 0 & 0 & c_{44} & 0 & 0 \\ 0 & 0 & 0 & 0 & c_{44} & 0 \\ 0 & 0 & 0 & 0 & 0 & c_{66} \end{bmatrix} \tag{1.39}$$

where $c_{66} = (c_{11} - c_{12})/2$. For the VTI rock, Young's modulus and Poisson's ratio must satisfy $E_1 = E_2$, $\nu_{12} = \nu_{21}$, $\nu_{31} = \nu_{32}$, $\nu_{13} = \nu_{23}$.

The elastic stiffnesses (c_{ij}) in the TI rock in Eq. (1.39) can be obtained from the acoustic velocities (dynamic stiffnesses) and from lab compression tests (static stiffnesses). The stiffnesses can also be related to Young's moduli, Poisson's ratios, and bulk moduli (King, 1964; Mavko et al., 2009).

For the VTI rock the compliance matrix has the following form (Bower, 2010):

$$\mathbf{S} = \begin{bmatrix} 1/E_1 & -\nu_{12}/E_1 & -\nu_{31}/E_3 & 0 & 0 & 0 \\ -\nu_{12}/E_1 & 1/E_1 & -\nu_{31}/E_3 & 0 & 0 & 0 \\ -\nu_{13}/E_1 & -\nu_{13}/E_1 & 1/E_3 & 0 & 0 & 0 \\ 0 & 0 & 0 & 1/G_3 & 0 & 0 \\ 0 & 0 & 0 & 0 & 1/G_3 & 0 \\ 0 & 0 & 0 & 0 & 0 & 1/G_1 \end{bmatrix} \tag{1.40}$$

where $G_1 = E_1/[2(1+\nu_{12})]$; Poisson's ratios are not symmetric, but satisfy $\nu_{31}/E_3 = \nu_{13}/E_1$.

Hooke's law in the VTI rock can be expressed as follows:

$$\begin{bmatrix} \varepsilon_{11} \\ \varepsilon_{22} \\ \varepsilon_{33} \\ 2\varepsilon_{23} \\ 2\varepsilon_{13} \\ 2\varepsilon_{12} \end{bmatrix} = \begin{bmatrix} 1/E_1 & -\nu_{12}/E_1 & -\nu_{31}/E_3 & 0 & 0 & 0 \\ -\nu_{12}/E_1 & 1/E_1 & -\nu_{31}/E_3 & 0 & 0 & 0 \\ -\nu_{13}/E_1 & -\nu_{13}/E_1 & 1/E_3 & 0 & 0 & 0 \\ 0 & 0 & 0 & 1/G_3 & 0 & 0 \\ 0 & 0 & 0 & 0 & 1/G_3 & 0 \\ 0 & 0 & 0 & 0 & 0 & 1/G_{12} \end{bmatrix} \times \begin{bmatrix} \sigma_{11} \\ \sigma_{22} \\ \sigma_{33} \\ \sigma_{23} \\ \sigma_{13} \\ \sigma_{12} \end{bmatrix} - \Delta T \begin{bmatrix} \alpha_{T1} \\ \alpha_{T1} \\ \alpha_{T3} \\ 0 \\ 0 \\ 0 \end{bmatrix} \tag{1.41}$$

The minimum and maximum horizontal stresses in the VTI rock can be derived from Eq. (1.41). In the principal stress state, shear stresses and shear strains are zero; therefore, the first two equations in Eq. (1.41) can be rewritten as follows:

$$\varepsilon_1 = \frac{\sigma_1}{E_1} - \frac{\nu_{12}\sigma_2}{E_1} - \frac{\nu_{31}\sigma_3}{E_3} - \alpha_{T1}\Delta T \tag{1.42}$$

$$\varepsilon_2 = \frac{\sigma_2}{E_1} - \frac{\nu_{12}\sigma_1}{E_1} - \frac{\nu_{31}\sigma_3}{E_3} - \alpha_{T1}\Delta T \tag{1.43}$$

where σ and ε are principal stresses and strains, respectively.

Solving Eqs. (1.42) and (1.43), the principal stresses (σ_1 and σ_2) can be obtained:

$$\sigma_1 = \frac{E_1\nu_{31}}{E_3(1-\nu_{12})}\sigma_3 + \frac{E_1}{1-\nu_{12}^2}\varepsilon_1 + \frac{E_1\nu_{12}}{1-\nu_{12}^2}\varepsilon_2 + \frac{E_1\alpha_{T1}}{1-\nu_{12}}\Delta T \tag{1.44}$$

$$\sigma_2 = \frac{E_1\nu_{31}}{E_3(1-\nu_{12})}\sigma_3 + \frac{E_1}{1-\nu_{12}^2}\varepsilon_2 + \frac{E_1\nu_{12}}{1-\nu_{12}^2}\varepsilon_1 + \frac{E_1\alpha_{T1}}{1-\nu_{12}}\Delta T \tag{1.45}$$

where the principal stresses, Young's moduli, and Poisson's ratio are illustrated in Fig. 1.15. If the two horizontal axes (1 and 2) and the vertical

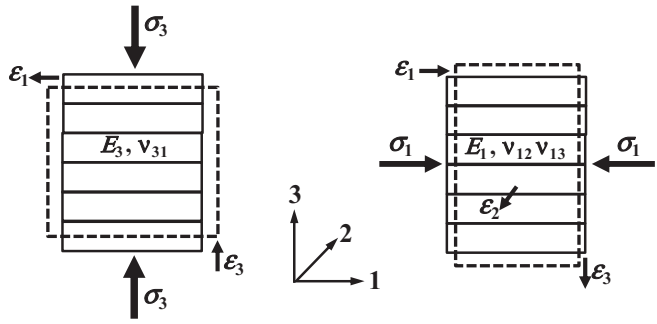

Figure 1.15 Two compression tests in vertical and horizontal directions to obtain all Young's moduli and Poisson's ratios in the rock withvertical transverse isotropy.

axis (3-axis) are represented by h, H, and V (e.g., $E_h = E_1$, $E_V = E_3$, $\nu_h = \nu_{12}$, $\nu_V = \nu_{31}$, $\alpha_{Th}=\alpha_{T1}$), and for a porous rock the effective stresses replace the total stresses, then the above equations can be rewritten as the following forms for the effective in situ stresses:

$$\sigma'_h = \frac{E_h \nu_V}{E_V(1-\nu_h)}\sigma'_V + \frac{E_h}{1-\nu_h^2}\varepsilon_h + \frac{E_h \nu_h}{1-\nu_h^2}\varepsilon_H + \frac{E_h \alpha_{Th}}{1-\nu_h}\Delta T \tag{1.46}$$

$$\sigma'_H = \frac{E_h \nu_V}{E_V(1-\nu_h)}\sigma'_V + \frac{E_h}{1-\nu_h^2}\varepsilon_H + \frac{E_h \nu_h}{1-\nu_h^2}\varepsilon_h + \frac{E_h \alpha_{Th}}{1-\nu_h}\Delta T \tag{1.47}$$

where σ'_h and σ'_H are the minimum and maximum effective horizontal stresses, respectively; σ'_V is the effective vertical stress; E_h and E_V are Young's moduli in horizontal and vertical directions, respectively; ν_h and ν_V are Poisson's ratios in horizontal and vertical directions, respectively; ε_h and ε_H are the strains in the minimum and maximum horizontal stress directions, respectively.

Substituting Eq. (1.9) of the effective stress law into above equations, the minimum and maximum horizontal stresses can be obtained, i.e.,

$$\sigma_h = \frac{E_h \nu_V}{E_V(1-\nu_h)}(\sigma_V - \alpha_V p_p) + \alpha_h p_p + \frac{E_h}{1-\nu_h^2}\varepsilon_h + \frac{E_h \nu_h}{1-\nu_h^2}\varepsilon_H + \frac{E_h \alpha_{Th}}{1-\nu_h}\Delta T \tag{1.48}$$

$$\sigma_H = \frac{E_h \nu_V}{E_V(1-\nu_h)}(\sigma_V - \alpha_V p_p) + \alpha_h p_p + \frac{E_h}{1-\nu_h^2}\varepsilon_H + \frac{E_h \nu_h}{1-\nu_h^2}\varepsilon_h + \frac{E_h \alpha_{Th}}{1-\nu_h}\Delta T \tag{1.49}$$

where α_h and α_V are Biot's coefficients in the horizontal and vertical directions, respectively.

Eqs. (1.48) and (1.49) are similar to the ones presented by Thiercelin and Plumb (1994), where they did not consider thermal effects. If $E_h = E_V = E$, $\nu_h = \nu_V = \nu$, $\alpha_h = \alpha_V = \alpha$, $\alpha_{Th} = \alpha_T$, Eqs. (1.48) and (1.49) can be simplified to the isotropic case, as follows:

$$\sigma_h = \frac{\nu}{1-\nu}(\sigma_V - \alpha p_p) + \alpha p_p + \frac{E}{1-\nu^2}(\varepsilon_h + \nu\varepsilon_H) + \frac{E\alpha_T}{1-\nu}\Delta T \tag{1.50}$$

$$\sigma_H = \frac{\nu}{1-\nu}(\sigma_V - \alpha p_p) + \alpha p_p + \frac{E}{1-\nu^2}(\varepsilon_H + \nu\varepsilon_h) + \frac{E\alpha_T}{1-\nu}\Delta T \tag{1.51}$$

If $\varepsilon_h = \varepsilon_H = 0$, then Eqs. (1.48) and (1.49) can be simplified to the case of the TI rocks in the uniaxial strain condition:

$$\sigma_h = \frac{E_h\nu_V}{E_V(1-\nu_h)}(\sigma_V - \alpha_V p_p) + \alpha_h p_p + \frac{E\alpha_{Th}}{1-\nu_h}\Delta T \tag{1.52}$$

References

Amadei, B., 1996. Importance of anisotropy when estimating and measuring in situ stresses in rock. Int. J. Rock Mech. Min. Sci. Geomech. Abstr. 33 (3), 293–325.

Amadei, B., Savage, W., Swolfs, H., 1987. Gravitational stresses in anisotropic rock masses. Int. J. Rock Mech. Min. Sci. Geomech. Abstr. 24 (1), 5–14.

Barton, A., Zoback, M., Moos, D., 1995. Fluid flow along potentially active faults in crystalline rock. Geology 23 (8), 683–686.

Biot, M.A., 1941. General theory of three-dimensional consolidation. J. Appl. Phys. 12 (1), 155–164.

Bower, A.F., 2010. Applied Mechanics of Solids. CRC Press.

Detournay, E., Cheng, A.H.-D., 1993. Fundamentals of poroelasticity. In: Fairhurst, C. (Ed.), Comprehensive Rock Engineering: Principles, Practice and Projects, Analysis and Design Method, vol. II. Pergamon Press, pp. 113–171. Chapter 5.

Dohmen, T., Zhang, J., Barker, L., Blangy, J.P., 2017. Microseismic magnitudes and b-values for delineating hydraulic fracturing and depletion. SPE J. 22 (5), 1624–1633. SPE-186096.

Havens, J.B., 2012. Mechanical Properties of the Bakken Formations. M.S. thesis, Colorado School of Mines.

Hudson, J., Harrison, J., 1997. Engineering Rock Mechanics: An Introduction to the Principles. Pergamon.

Jeager, J.C., Cook, N.G.W., 1979. Fundamentals of Rock Mechanics, third ed. Chapman and Hall.

Jeager, J.C., Cook, N.G.W., Zimmerman, R., 2007. Fundamentals of Rock Mechanics, fourth ed. Blackwell Publishing.

King, M.S., 1964. Wave Velocities and Dynamic Elastic Moduli of Sedimentary Rocks. Ph.D. thesis, University of California, Berkeley.

Mavko, G., Mukerji, T., Dvorkin, J., 2009. The Rock Physics Handbook: Tools for Seismic Analysis of Porous Media. Cambridge University Press.
Murrell, S.A.F., 1965. The effect of triaxial stress systems on the strength of rocks at atmospheric temperatures. Geophys. J. R. Astron. Soc. 10, 231–281.
Parry, R.H.G., 2004. Mohr Circles, Stress Paths and Geotechnics, second ed. Taylor & Francis.
Thiercelin, M.J., Plumb, R.A., 1994. Core-based prediction of lithologic stress contrasts in east Texas formations. SPE Form. Eval. 9 (4), 251–258.
Zhang, J., 2013. Borehole stability analysis accounting for anisotropies in drilling to weak bedding planes. Int. J. Rock Mech. Min. Sci. 60, 160–170.
Zhang, J., Zhang, Y., Yin, S., 2018. PKN solution revisit: 3-D hydraulic fracture size and stress anisotropy effects. Rock Mech. Rock Eng. 51 (2), 653–660.

CHAPTER 2

Rock physical and mechanical properties

Contents

Applied Petroleum Geomechanics
ISBN 978-0-12-814814-3
https://doi.org/10.1016/B978-0-12-814814-3.00002-2

Abstract

Rock physical and mechanical properties are introduced, and methods to obtain these properties are discussed. Rock properties, including bulk density, porosity, permeability, sonic velocity, transit time, Young's modulus, Poisson's ratio, and Biot's coefficient are the fundamental inputs for geomechanical modeling and geological engineering design. The anisotropy and stress-dependent behaviors in rock properties are addressed to better characterize the rock, and these are particularly important for hydraulic fracturing design in unconventional plays. The fluid impact on sonic velocities is also investigated, and the slowdown of the compressional velocity by gas-bearing formation is studied. Empirical equations and new correlations for obtaining rock properties are examined with considerations of anisotropy for both conventional and unconventional reservoirs. Dynamic and static properties and their relationships are also evaluated.

Keywords: Anisotropy; Biot's coefficient; Bulk density; Dynamic and static relationship; Poisson's ratio; Porosity and permeability; Rock properties; Sonic velocity; Young's modulus.

2.1 Rock density

2.1.1 Bulk and matrix densities

Rock density, or bulk density, is a measure of mass of the rock contained in a given unit volume. It is a very important parameter for obtaining the overburden stress. Rock bulk density is controlled by densities and volumetric fractions of components of which the rock is composed. For a porous rock it is dependent on not only the density of each solid matrix but also the density of each pore fluid as well as fluid saturation. Therefore, bulk density has a strong correlation with minerals, fluids, and porosity, which can be obtained from the following equation:

$$\rho_b = (1 - \phi)\rho_m + \phi\rho_f \tag{2.1}$$

where ρ_b is the bulk density of the rock; ρ_m is the matrix or mineral density; ϕ is the porosity of the rock; ρ_f is the fluid (water, oil, or gas, etc.) density in the rock. If the fluid is water, ρ_f is the density of formation water.

The density of formation water is a function of water salinity, temperature, and content of dissolved gases. Normally, it varies from 1.0 to

1.08 g/cm^3 in sedimentary basins. For example, in general cases, $\rho_f =$ 1.07 g/cm^3 in the Gulf of Mexico; $\rho_f = 1.02$ g/cm^3 in the Rocky Mountains; $\rho_f = 1.08$ g/cm^3 in the Niger Delta; and $\rho_f = 1.02$ g/cm^3 in the North Sea.

Tables 2.1 and 2.2 list the matrix densities for common minerals (Schön, 1996) and bulk density for various rock types. For most rocks and soils, the matrix density is about 2.65 g/cm^3, roughly the density of quartz and clay minerals (Table 2.1). Therefore, bulk density of a rock can be calculated from Eq. (2.1) if the formation porosity is known. Fig. 2.1 shows an example of bulk density variations with depth below the sea floor in the Gulf of Mexico. The densities in the figure were calculated from core porosity data (Ostermeier et al., 2001) using Eq. (2.1). It shows that bulk density of the formation is very low at the shallow depth (<100 m below the sea floor), and this mostly is due to that the formation is unconsolidated with very high porosity. Bulk density increases as the burial depth increases because formation compaction causes porosity reduction with depth.

Rock bulk density can be measured in the laboratory using core samples. For subsurface rocks, it is more convenient to obtain the bulk density from density log in a borehole. However, density log data, particularly the

Table 2.1 Average matrix densities in common minerals and fluids.

Mineral or fluid	Density ρ_m (g/cm^3)
Quartz	2.65
Calcite	2.71
Dolomite	2.87
Montmorillonite	2.06
Illite	2.64
Kaolinite	2.59
Chlorite	2.88
K-Feldspar	2.56
Biotite	2.90
Halite	2.165
Anhydrite	2.96
Sylvite	1.99
Plagioclase (Na)	2.62
Plagioclase (Ca)	2.76
Barite	4.48
Oil	0.85
Fresh water	1.0

Table 2.2 Bulk densities and porosities in various rock types.

Rock type	Density ρ_b (g/cm^3)	Porosity ϕ (%)
Granite	2.5–2.8	0.5–1.5
Dolerite	3.0–3.1	0.1–0.5
Limestone	2.5–2.8	5–20
Dolomite	2.5–2.87	1–5
Quartzite	2.65	0.1–0.5
Sandstone	2.0–2.6	5–25
Shale	2.0–2.7	10–30
Coal–Anthracite	1.3–1.6	
Coal–Bituminous	1.1–1.4	
Sediments	1.7–2.3	
Metamorphic rocks	2.6–3.0	

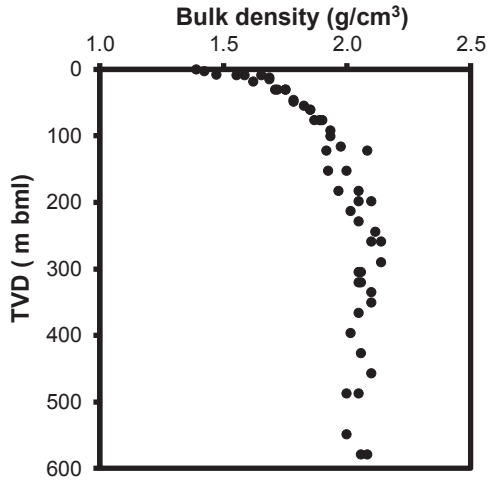

Figure 2.1 Bulk density variations with the true vertical depth (TVD) below the sea floor in the Gulf of Mexico. The bml represents below the mudline or below the sea floor in offshore drilling.

shallow density data, are not always available; then, Gardner's method can be used to convert acoustic compressional transit time or velocity to bulk density (Gardner et al., 1974).

$$\rho_b = aV_p^b \tag{2.2}$$

where V_p is the velocity of the compressional wave; a and b are empirical constants, and the default values are $a = 1.74$ and $b = 0.25$ in the metric system (ρ_b in g/cm^3 and V_p in km/s). In the English unit (ρ_b in g/cm^3

and V_p in ft/s), $a = 0.23$ and $b = 0.25$ are used as the default values by Gardner et al. (1974).

Eq. (2.2) represents a fair average for a large number of laboratory and field observations of different brine-saturated rock types. For practical applications, a calibration is needed to adjust two constants of a and b in Eq. (2.2). Additionally, the compressional velocity can be slowed down by hydrocarbon formations. In this case the compressional velocity should be corrected to take out hydrocarbon impacts in oil- and gas-bearing formations (refer to Section 2.3.5).

2.1.2 Bulk density at the shallow depth

As mentioned above, bulk density in the shallow formation may not be available in most cases, but it is a required parameter for calculating the overburden stress. Fig. 2.2 shows some available data of the shallow densities. This figure plots bulk density variations with depth, where the shallow formation density was obtained by soil boring, and the deep density was measured from formation density log in the Gulf of Mexico. It can be observed from Figs. 2.1 and 2.2 that the density at the shallow depth (<2000 ft), particularly near the sea floor, is significantly lower than that in the deeper formation.

The shallow density and porosity in the deepwater of the Gulf of Mexico have been studied in various purposes, e.g., Ostermeier et al. (2001),

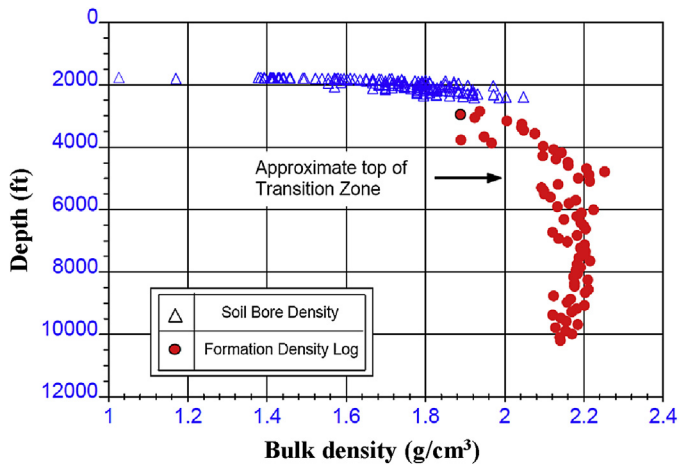

Figure 2.2 Formation bulk density versus depth (plotted from the sea level) for the Green Canyon area in the Gulf of Mexico. The water depth is 1749 ft (533 m) (Bender et al., 1996).

Bender et al. (1996), and the Ocean Drilling Program (ODP, 2008). Dr. Terry Miller obtained the shallow density correlation based on the measured porosity and density data. Miller's shallow density method (KSI/Halliburton internal research published by Zhang et al., 2008 with KSI's permission) addresses the problem that in deepwater, the shallow sediments may have very high porosities and thus low densities cannot be correctly described using seismic interval velocities. Using shallow porosity data from Ostermeier et al. (2001) and the Ocean Drilling Program, the Miller shallow porosity can be expressed in the following form:

$$\phi_s = \phi_a + \phi_b e^{-kd^{1/n}} \tag{2.3}$$

where ϕ_s is the shallow porosity; $\phi_a + \phi_b$ is the mudline porosity, d is the depth below the mudline in ft, and k and n are empirically determined parameters that provide the reasonable fit to the data.

The porosity data can then be applied to calculate near mudline bulk density, ρ_s, directly by the following relationship:

$$\rho_s = \rho_m(1 - \phi_s) + \rho_w\phi_s \tag{2.4}$$

where ρ_m is the average density of the sediment grains (typically 2.65 g/cm^3 for shales); ρ_w is the density of formation water (typically 1.03–1.05 g/cm^3).

Fig. 2.3 plots the measured porosity data in the deepwater Gulf of Mexico locations versus Miller's near mudline density correlation obtained from Eqs. (2.3) and (2.4), using $\phi_a = 0.35$, $\phi_b = 0.35$, $k = 0.0035$, $\rho_m = 2.675$ g/cm^3, $\rho_w = 1.05$ g/cm^3, and $n = 1.09$ (Zhang et al., 2008). In a similar region where has a low formation density at the shallow depth, Eqs. (2.3) and (2.4) may be applicable after certain calibrations to the local core tests or density log data.

2.2 Porosity

2.2.1 Porosity from density, velocity, and resistivity

Porosity (ϕ) is an important property to analyze volumes of the oil and gas reservoirs. It is defined to be the ratio of a volume of void spaces within a rock to the total bulk volume of the rock, i.e.,

$$\phi = \frac{V_{pores}}{V_{rock}} \tag{2.5}$$

where V_{pores} and V_{rock} are the volumes of pores and the rock, respectively.

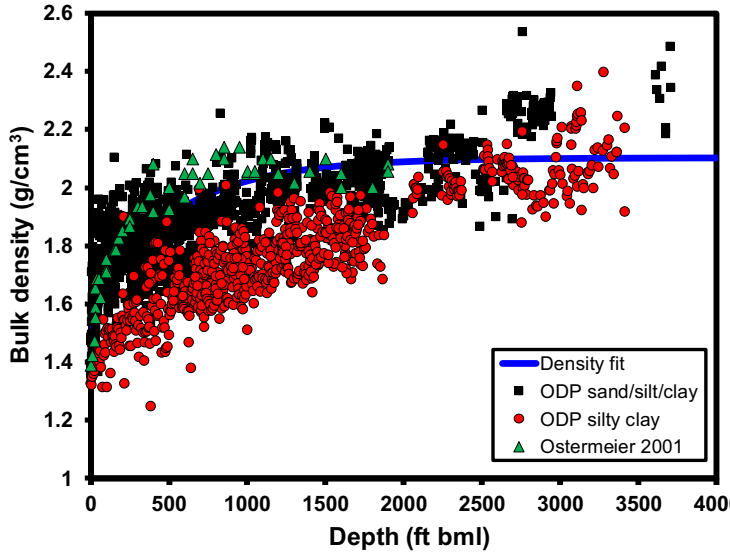

Figure 2.3 Density curve (the line) obtained from Eqs. (2.3) and (2.4) compared to the measured shallow bulk density from the Ocean Drilling Program (ODP) and Ostermeier et al. (2001) (Zhang et al., 2008).

In engineering practice, porosity has several descriptions, but the two most common terms are total porosity (defined as the above) and effective porosity. Effective porosity represents the ratio of the interconnected pore space to the total bulk volume of the rock. Therefore, effective porosity is also called interconnected porosity. The fluids in the interconnected pores contribute to fluid flow. Porosity is not only primarily controlled by the shapes, sizes, and arrangements of the rock grains but also dependent on rock mechanical processes (such as compaction, deformation, fracture evolution) and geochemical processes (e.g., dissolution, precipitation, mineralogical changes). Rock grain packing types have important effects on porosity, and Table 2.3 lists the effects of several ideal packing types on porosity, assuming that the rock consists of identical spherical rock grains.

Table 2.3 Porosity in different packing types of spherical rock grains.

Packing type	ϕ
Cubic	0.48
Orthorhombic	0.40
Tetragonal	0.30
Rhombohedral	0.26

Porosity can be determined by lab experiments in core samples and by well logs, such as density, resistivity, neutron, and NMR (Nuclear Magnetic Resonance) logs. The density–porosity equation (Eq. 2.1) can be rewritten to the following form for calculating porosity purpose:

$$\phi = \frac{\rho_m - \rho_b}{\rho_m - \rho_f} \tag{2.6}$$

Fig. 2.4 illustrates how to use the density log to calculate porosity from Eq. (2.6). The calculated porosities are also compared to the measured porosities from core samples in the Haynesville shale gas formation. In the calculation, the following parameters are used: $\rho_m = 2.67$ g/cm^3, $\rho_f = 1.05$ g/cm^3, and bulk density ρ_b was obtained from the density log shown in the left plot of Fig. 2.4.

For clean sandstones with moderate porosities, porosity is often estimated by the empirical time–average equation (Wyllie et al., 1956):

$$\phi = \frac{\Delta t - \Delta t_m}{\Delta t_f - \Delta t_m} \tag{2.7}$$

where Δt, Δt_m, and Δt_f are the sonic (or acoustic) compressional transit time of the formation, rock matrix, and pore fluid, respectively.

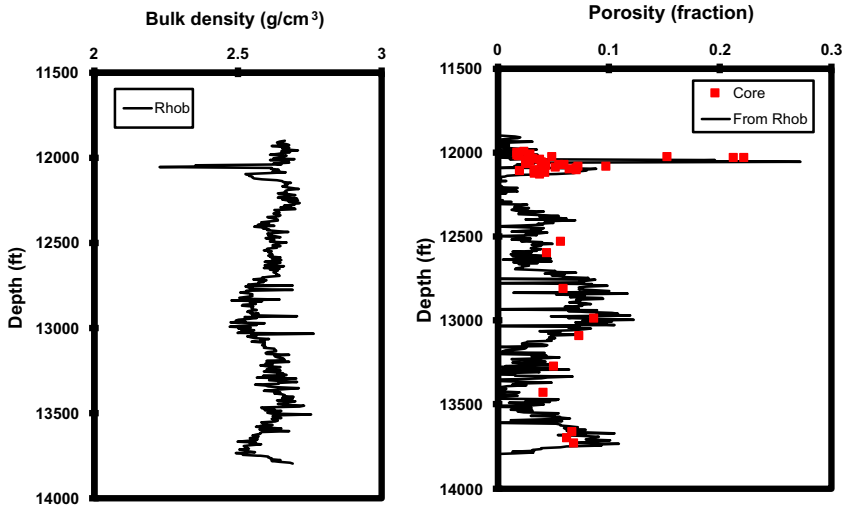

Figure 2.4 Porosity measured from core samples and calculated from density log using Eq. (2.6) in the Haynesville shale gas formation.

This equation can be rewritten, in terms of acoustic velocity, as the following form:

$$\phi = \frac{1/V_p - 1/V_m}{1/V_f - 1/V_m} \tag{2.8}$$

where V_p, V_m, and V_f are the compressional velocities of the formation, rock matrix, and pore fluid, respectively.

If pore spaces contain oil or gas, Δt will increase. Therefore, the porosity calculated from Eqs. (2.6) and (2.7) is optimistic porosity, and corrections for the gas or oil effect are needed. Fluid effect in high porosity formation with high hydrocarbon saturation can be corrected by the following empirical relations, respectively: for oil, $\phi_o = 0.9\phi$; for gas $\phi_g = 0.7\phi$.

The Wyllie equation (Eq. 2.7) represents consolidated and compacted formations, generally for a porosity of less than 0.25 in sandstones. Unconsolidated sandstones, such as those in the US Gulf Coast, Nigeria, and Venezuela, often have much higher porosity (0.28–0.50). If this equation is used in unconsolidated sandstones, the correction for the less compaction effects is necessary. Additionally, the presence of clays within the sand matrix will increase Δt by an amount proportional to the bulk-volume fraction of the clay. The following empirical equation can be used for calculating porosity in sandstones in which adjacent shale values (Δt_{sh}) exceed 100 μs/ft:

$$\phi = \frac{\Delta t - \Delta t_m}{\Delta t_f - \Delta t_m} \frac{1}{C_p} \tag{2.9}$$

where C_p is a "lack of compaction" correction factor, ranging commonly from 1 to 1.3, with values as high as 1.8 occasionally observed (Raymer et al., 1980). A variety of methods are used to estimate C_p. The simplest is to use the sonic compressional transit time observed in nearby shales (Δt_{sh}, in μs/ft) divided by 100, or $C_p = \Delta t_{sh}/100$.

Raymer et al. (1980) proposed an empirical velocity to porosity transform for $0 < \phi < 0.37$:

$$V_p = (1 - \phi)^2 V_m + \phi V_f \tag{2.10}$$

Raiga-Clemenceau et al. (1988) proposed another empirical relationship of porosity and sonic transit time in a porous medium:

$$\phi = 1 - \left(\frac{\Delta t_m}{\Delta t}\right)^{1/x} \tag{2.11}$$

Table 2.4 Bulk density and porosity for various rock types.

Matrix or rock type	Δt_m (μs/ft)	x	Reference
Silica	55.5	1.60	Raiga-Clemenceau et al. (1988)
Calcite	47.6	1.76	Raiga-Clemenceau et al. (1988)
Dolomite	43.5	2.00	Raiga-Clemenceau et al. (1988)
Mudstone	67.1	2.19	Issler (1992)
Mudstone alternative fit	63.4	2.34	Issler (1992)
Mudstone and sandstone	52–70	2.19	Nelson and Bird (2005)

where x is an exponent specific for the matrix lithology. This equation does not account for the effect of the pore fluids on the formation transit time. In this equation, Raiga-Clemenceau et al. (1988) used the following parameters related to the matrix natures (Table 2.4):

Porosity can also be obtained from the resistivity log. Archie (1942) found that the resistivity of a given core sample was always related to the water resistivity by a constant factor F (he called it the formation factor), which is a function of porosity. The general form of the Archie equation can be written as follows:

$$S_w^n = \frac{a}{\phi^m}\frac{R_w}{R_t} \tag{2.12}$$

where S_w is the water saturation; R_w is the resistivity of formation water; R_t is the formation resistivity; the constants a, m, and n need to be determined for a formation being evaluated.

The above equation can be approximately expressed in a simplified form for a 100% water-saturated formation ($S_w = 1$):

$$\phi = \sqrt{\frac{R_w}{R_t}} \tag{2.13}$$

where the formation resistivity R_t can be obtained from the deep resistivity log and again need to take off the oil and gas effects. The resistivity of formation water R_w should be verified in as many ways as possible, including calculations from the spontaneous potential log, water catalog, calculations from nearby water-bearing formation, and/or formation water sample measurement.

2.2.2 Depth-dependent porosity and normal compaction

Field tests and lab experiments have shown that rock porosity decreases as the burial depth increases. The following equation, first proposed by Athy (1930), is the most commonly used one to describe porosity and depth relationship:

$$\phi = ae^{-bZ} \tag{2.14}$$

where a and b are constants; Z is the depth; $a = \phi_0$; and ϕ_0 is the porosity when Z is zero. For example, in the Northern North Sea the constants are $a = 0.49$ and $b = 2.7 \times 10^{-4}$ for sandstones and $a = 0.803$ and $b = 5.1 \times 10^{-4}$ for shales, if Z is in meters (Schön, 1996).

Zhang and Wieseneck (2011) analyzed the porosity data measured from wireline density logs in several wells of the Bossier and Haynesville shale gas formations in North Louisiana and obtained the following relation in normally compacted shales:

$$\phi = 0.5e^{-0.00036Z} \tag{2.15}$$

where ϕ is in fractions; Z is the true vertical depth in feet.

Athy's compaction equation indicates that porosity reduces exponentially with depth because of normal compaction of the formations, causing formations to be more compacted and consolidated. Porosity is not only dependent on depth (decreasing with depth) but also controlled by different mudstone mineralogy (Mondol et al., 2007). The smectite, compared to other clay minerals, has the largest porosity and is less compacted (the curve 19 in Fig. 2.5). It can be also observed in Fig. 2.5 that the normal compaction trends are very different for different shales, and this behavior is particularly important when one uses normal compaction trends for pore pressure prediction.

2.2.3 Stress-dependent porosity

Lab experimental tests show that rock porosity decreases as the applied stress increases. For example, lab measurements in sandstone specimens cored 1000 m below the sea floor (Peng and Zhang, 2007) show that the stress and porosity have a negative exponential relation, i.e.,

$$\phi = 0.336e^{-0.0023\sigma} \tag{2.16}$$

where ϕ is the porosity (fraction); σ is the axial stress (MPa).

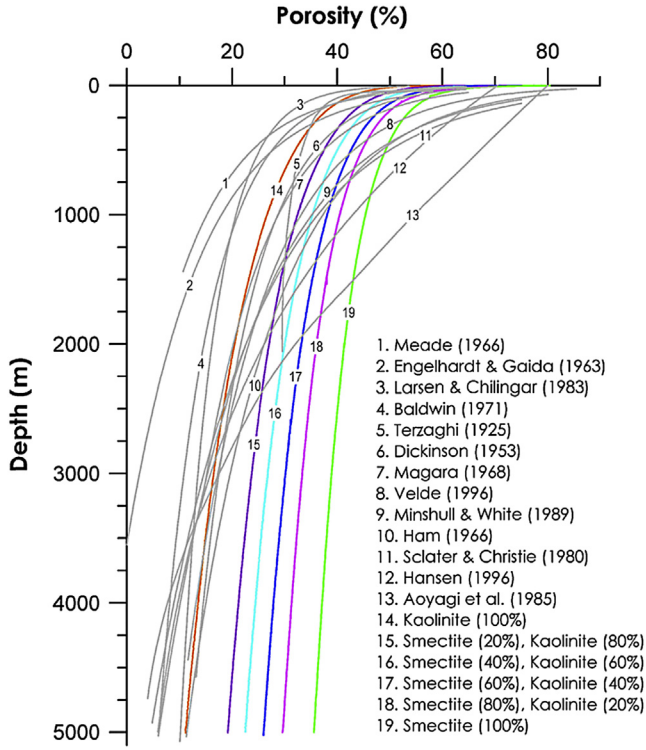

Figure 2.5 A comparison of published porosity–depth trends for shales and argillaceous sediments (curves 1–13) and experimentally compacted curves of brine-saturated smectite, kaolinite, and their mixtures (curves 14–19) (Mondol et al., 2007).

Therefore, the effective stress and porosity can be expressed as a generalized form in the following:

$$\phi = \phi_0 e^{-c\sigma'} \tag{2.17}$$

where ϕ_0 is the initial porosity; c is a compaction parameter; σ' is the effective stress. For instance, the parameters are $\phi_0 = 0.386$ and $c = 0.0313\ \text{MPa}^{-1}$ in the EI 330 shale in the Gulf of Mexico (Flemings et al., 2002).

Eberhart-Phillips et al. (1989) conducted a comprehensive suite of laboratory measurements for 64 different sandstones with varying amounts of shale. They found that porosity is also dependent on *P*-wave velocity (V_p), *S*-wave velocity (V_s), mean effective stress, and clay content. Based on

the measurements, Eberhart-Phillips et al. (1989) derived the following equations (Zoback, 2007):

$$\begin{aligned} V_p &= 5.77 - 6.94\phi - 1.73\sqrt{C} + 0.446(\sigma'_m - e^{-16.7\sigma'_m}) \\ V_s &= 3.70 - 4.94\phi - 1.57\sqrt{C} + 0.361(\sigma'_m - e^{-16.7\sigma'_m}) \end{aligned} \tag{2.18}$$

where V_p and V_s are both in units of km/s; σ'_m is the mean effective stress, in units of kbar (1 kbar = 100 MPa); C is the clay content, and $0 \leq C \leq 1$. If shales have similar relations as shown in Eq. (2.18), then they can be used for pore pressure estimate when V_p or V_s and other logging data are available.

2.3 Sonic or seismic velocities and transit time

2.3.1 Compressional and shear velocities

When a seismic or sonic wave propagates in rock formations, the compressional and shear waves are two major wave types. The wave propagation velocities are determined by the appropriate elastic moduli and densities of the materials that the waves pass through. Therefore, rock properties and pore pressure can be estimated from seismic interval velocities and the travel time in sonic log. Compressional body waves (primary or *P*-waves) propagate by alternating compression and dilation in the direction of the waves (Barton, 2007). The compressional velocity (V_p) and dynamic elastic moduli have the following relations:

$$V_p = \sqrt{\frac{K_d + (4/3)G_d}{\rho_b}} \tag{2.19}$$

$$V_p = \sqrt{\frac{E_d(1-\nu_d)}{\rho_b(1+\nu_d)(1-2\nu_d)}} \tag{2.20}$$

where K_d is the dynamic bulk modulus; G_d is the dynamic shear modulus (or expressed by symbol μ_d); E_d is the dynamic Young's modulus; ν_d is the dynamic Poisson's ratio. It can be seen that the dynamic elastic moduli can be obtained from the compressional velocity and Poisson's ratio.

Shear body waves (termed secondary, transverse or *S*-waves) propagate by a sinusoidal pure shear strain in a direction perpendicular to the direction

of the waves (Barton, 2007). Therefore, dynamic shear modulus controls the shear velocity of propagation:

$$V_s = \sqrt{\frac{G_d}{\rho_b}} = \sqrt{\frac{E_d}{\rho_b}\frac{1}{2(1+\nu_d)}} \tag{2.21}$$

For a fluid the shear modulus is zero; from the above equation, *S*-wave velocity is zero. Therefore, the *S*-wave is unable to travel through a fluid.

2.3.2 Sonic transit time

In well log measurements the sonic transit time (travel time or sonic slowness) is used to represent the acoustic wave velocity. The compressional transit time is the reciprocal of the compressional velocity and has the following form in the English unit:

$$\Delta t_p = \frac{10^6}{V_p} \tag{2.22}$$

where Δt_p is the compressional transit time of the formation, in μs/ft; V_p is the compressional velocity, in ft/s.

Time average equation of Wyllie et al. (1956) can be written in the following form in terms of the compressional transit time and porosity in the rock:

$$\Delta t_p = \phi \Delta t_f + (1-\phi)\Delta t_m \tag{2.23}$$

where Δt_m and Δt_f are the sonic transit time in the rock matrix and the pore fluid, respectively.

2.3.3 Relationship of V_p and V_s

For a gas-bearing formation, V_p is slowed down by gas, and the relations of V_p and V_s can be used to correct the measured V_p (e.g., Zhang and Wieseneck, 2011). The ratio of compressional to shear wave velocity (V_p/V_s) depends on dynamic Poisson's ratio (ν_d) according to the following theoretical equation:

$$\frac{V_p}{V_s} = \sqrt{\frac{2(1-\nu_d)}{1-2\nu_d}} \tag{2.24}$$

The ratio V_p/V_s is about $\sqrt{3}$ for hard rocks, for which ν_d is 0.25. However, in the case of unconsolidated sediments, the ratio V_p/V_s can even

reach values of 20–40 for near surface formations, for which Poisson's ratio is commonly greater than 0.45. Therefore, V_p/V_s can be used for the rock quality interpretation; for example, the mean value of $V_p/V_s = 1.89$ in the more heavily jointed rocks (perhaps a rock quality Q $\approx$ 1–10) and the mean value of $V_p/V_s = 1.80$ in sparsely jointed rocks (perhaps a rock quality Q $\approx$ 10–100) (Barton, 2007).

The ratio V_p/V_s may also be used for porosity and rock failure analysis (Zhang et al., 2009). When elastic waves travel in a rock, the wave velocities are dependent on rock lithology and rock strength. For instance, rocks with greater strengths have higher velocity values, whereas the velocities in loose, unconsolidated sediments correspond to lower velocity values. Laboratory-measured compressional and shear velocities for intermediate to high velocity rocks on limestones, dolomites, and sandstones show a distinct difference in velocity ratios (V_p/V_s) exhibited by different rocks (Pickett, 1963). The limestones have the highest V_p/V_s ratio (1.9–2.0), and the clean sandstones have the lowest V_p/V_s (1.6–1.75). Experimental data compiled by Castagna et al. (1985) show that the clay minerals and calcite without porosity have the highest velocity ratio of $V_p/V_s = 2.0$. The quartz without porosity has the lowest velocity ratio of $V_p/V_s = 1.5$.

Zhang et al. (2009) examined the in situ velocity ratios of deepwater Green Canyon wells where the sonic compressional and shear velocities were acquired from stable and unstable borehole sections; caliper logs were utilized to determine the borehole stability while gamma ray logs were used to determine lithology. Fig. 2.6 presents the V_p/V_s ratios in the stable wellbore for shales, shaly sandstones, and sandstones calculated from downhole-measured compressional and shear velocities. For shales the ratio of V_p/V_s ranges from 1.9 to 2.1; shaly sandstones from 1.85 to 2.0; and sandstones from 1.7 to 1.9, very close to the laboratory results presented by Pickett (1963).

Based on in situ sonic and field seismic measurements in mudrocks, Castagna et al. (1985) proposed the following relationship of V_p and V_s (the velocities are in km/s):

$$V_s = 0.8621\,V_p - 1.1724 \tag{2.25}$$

For sandstones, compressional and shear velocities have an easy-to-remember relationship (Han, 1986):

$$V_s = 0.79\,V_p - 0.79 \tag{2.26}$$

where the velocities are in km/s. The above equation was shown by Mavko et al. (2009) to give a very good fit to a wide variety of water-saturated

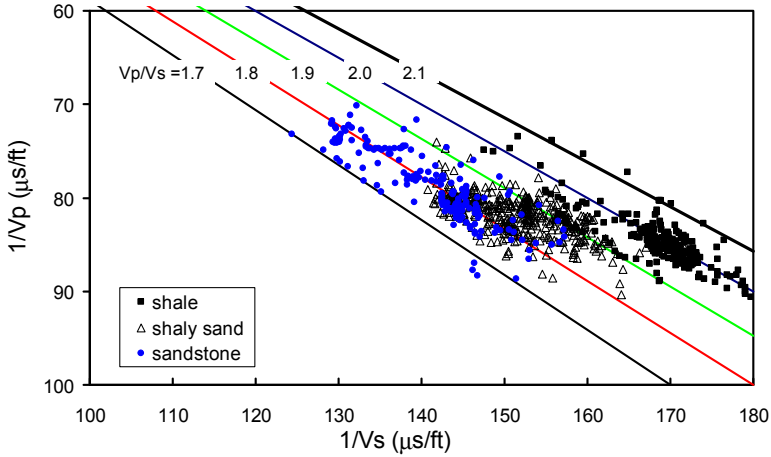

Figure 2.6 V_P/V_s plot at the true vertical depth of 27,000–30,000 ft in an ultradeep well for shale, shaly sandstone, and sandstone in the Green Canyon, the Gulf of Mexico (Zhang et al., 2009).

shaly sands, from 4% to 39% porosity, with clay volume fractions spanning 0%–55%, and over a confining pressure range of 0–40 MPa, equivalent to depths up to roughly 3 km.

2.3.4 Velocity and porosity relationship

The velocity of a wave is controlled by the elastic properties and density of material. However, porosity has a significant impact on the P-wave and S-wave velocities in the porous rock. In general, an approximate inverse proportionality is found between velocity and porosity, and time average equation proposed by Wyllie et al. (1956) can be rewritten to link the compressional velocity to porosity of the rock:

$$\frac{1}{V_p} = \frac{\phi}{V_f} + \frac{(1-\phi)}{V_m} \tag{2.27}$$

where V_p, V_m, and V_f are the compressional velocities for the formation, matrix, and pore fluid, respectively.

Analyzing laboratory-measured results in sandstones (Fig. 2.7) from literature, the following simple relation of V_p/V_s and porosity was given (Zhang et al., 2009):

$$V_p/V_s = \frac{A}{(1-\phi)^B} \tag{2.28}$$

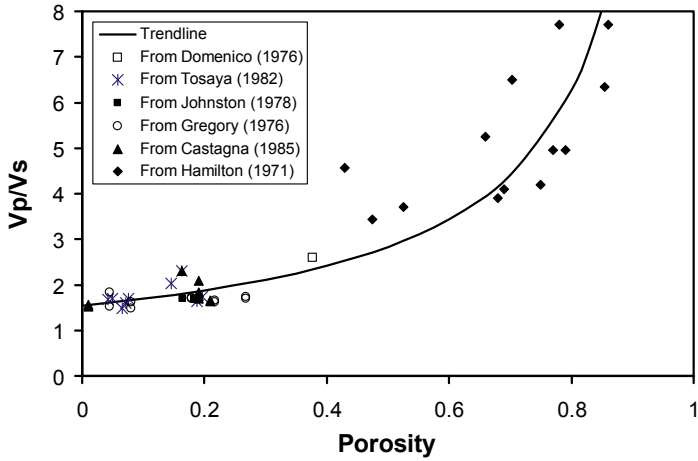

Figure 2.7 Laboratory-measured velocity ratios with respect to porosity in sandstones (the data are obtained from the references as shown in the figure legend).

where A is the V_p/V_s in the rock matrix or the rock with zero porosity, and B is a parameter to fit the observation. In the trendline of Fig. 2.7, $A = 1.55$ and $B = 0.87$.

This relationship reveals that the V_p/V_s is strongly dependent on porosity, and increasing porosity increases V_p/V_s. Porosity in fractured formations, depending on the fracture density, is normally much higher than the intact rocks. If the formation is highly fractured, porosity can be significantly higher than that in the intact rock. Therefore, according to Eq. (2.28) the heavily fractured rock has a much higher V_p/V_s.

An important distinguishing characteristic of the S-wave is its inability to propagate through a fluid. Therefore, if a rock fails or is extremely fractured, the cracks and the additional porosity degrade the propagation of the shear waves. Therefore, in a failed rock the shear velocity will be very low. Accordingly, a very high V_p/V_s ratio is produced because of the deterioration of mechanical integrity and the increase of porosity of the rock.

The triaxial compression test results indicate that the strain, stress (load), and V_p/V_s have a certain relationship, as shown in Fig. 2.8 (Zhang et al., 2009). The figure shows that at the initial loading stage, as the load (differential stress of axial load and confined pressure) increases, the velocity ratio remains unchanged. As the load increases to about 50% of the rock strength (peak load), the velocity ratio begins to increase. After the load reaches about 90% of the rock strength, the velocity ratio increases

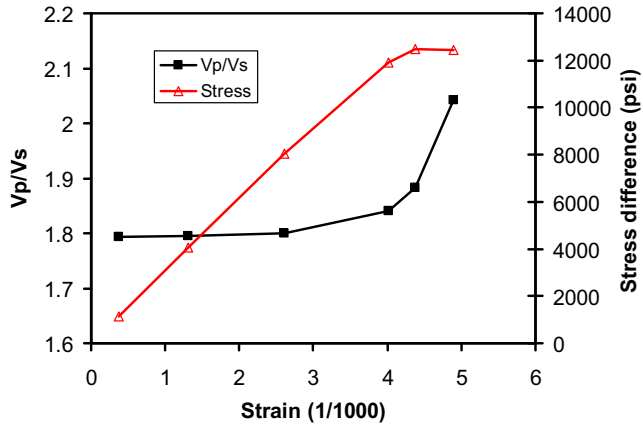

Figure 2.8 Lab test results of strain, differential stress, and V_p/V_s in a sandstone cored in a deep well of the Green Canyon in the Gulf of Mexico.

significantly. The velocity ratio continues to increase even after the rock fails or reaches the peak load. Compared to the initial loading stage, the increase of the maximum velocity ratio after failure reaches 1.14 times of the initial ratio. The increase of V_p/V_s is mainly caused by reduction of the shear velocity due to new fracture generation, when the rock approaches and reaches its strength limit. Fig. 2.9 presents the relationship of the laboratory-measured shear velocity and differential stress. It shows that at the initial loading stage the shear velocity increases slightly, which is caused by the closure of preexisting microcracks in the rock due to loading. As the

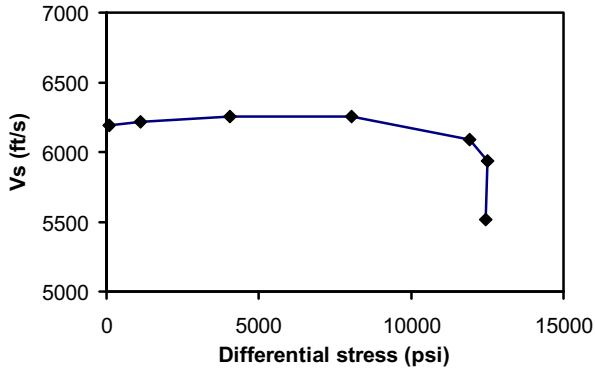

Figure 2.9 Lab test result of shear velocity versus differential stress in the same sandstone in Fig. 2.8.

load approaches and reaches the rock strength, the rock begins to fail, consequently creating new fractures. The new fractures increase porosity and cause the shear velocity to decrease dramatically (Fig. 2.9). However, the compressional velocity only changes slightly throughout the loading process. Because of this characteristic, the compressional velocity (V_p) or compressional transit time is better than the shear velocity to be used for rock property estimate.

2.3.5 Fluid (gas) effect on V_p and V_s

Fluid saturation and stress level have a significant influence on V_p. Laboratory experimental results show that nonlinear relationship of V_p and stress exists with a hydrostatic loading in sandstones (King, 1966). It is found that the water-saturated sandstone has a much higher V_p than its dry state. The kerosene-saturated sandstone has a lower velocity than that in water-saturated. However, shear wave velocity reduces when a rock sample is saturated with a liquid.

Compressional velocity or transit time plays a key role in pore pressure and fracture gradient prediction and for rock property estimates. However, gas effect in a gas-bearing formation slows V_p down. This behavior will cause errors in the V_p-based pore pressure and fracture gradient prediction. The drill gas from mud-logging data in the Haynesville shale gas formation shows the V_p reduction by gas in the shale gas formation (Fig. 2.10). Plotting compressional and shear velocities measured from downhole

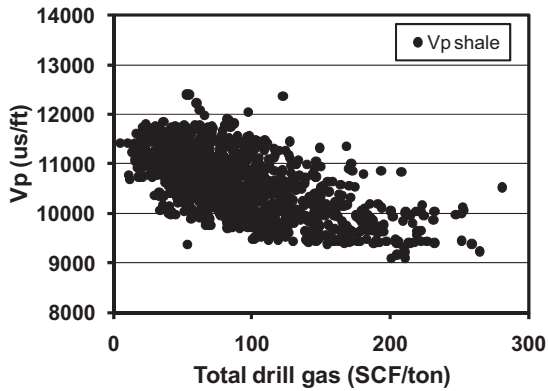

Figure 2.10 V_p versus drill gas in a well in the Bossier and Haynesville shale gas formations demonstrating that V_p decreases as the drill gas increases (Zhang and Wieseneck, 2011).

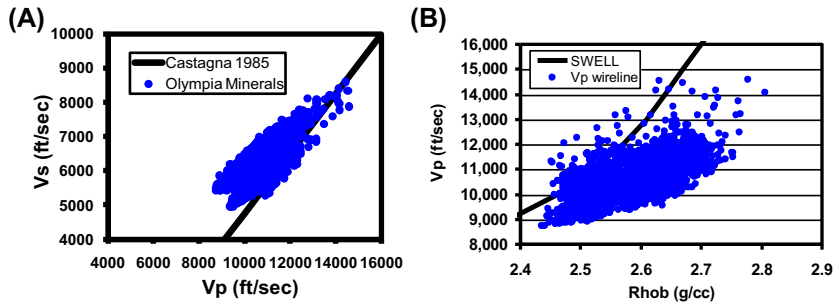

Figure 2.11 Compressional velocity affected by gas in the Bossier and Haynesville shales. (A). V_p–V_s plot showing V_p reduction compared to the normal trend; (B). V_p versus bulk density and the baseline of V_p and bulk density in the Gulf of Mexico showing gas effect on V_p (Zhang and Wieseneck, 2011).

wireline logs, it shows that the measured V_p–V_s trend in the Bossier and Haynesville shales deviates from the normal trend (Eq. 2.25), as shown in Fig. 2.11A. That is, V_p is slowed down compared to the normal V_p–V_s trend proposed by Castagna et al. (1985). This slowdown is due to the presence of gas in the shale as it occurs mainly in the compressional velocity, and because gas apparently has little impact on the shear velocity. A compressional velocity and bulk density plot in the Bossier and Haynesville shales is compared to the normal V_p–bulk density trend (without hydrocarbon effect) in Fig. 2.11B. It again shows that V_p in the Bossier and Haynesville shales is much slower than the normal trend of mudrocks in the Gulf of Mexico. Therefore, V_p and bulk density relationship is also useful to identify gas- and oil-bearing formations.

The slowdown in compressional velocity needs to be corrected for pore pressure and fracture gradient prediction and for rock property estimates. Given that the shear wave velocity has a small gas effect, compressional velocity can therefore be calculated from shear velocity to avoid gas effect, but the use of shear velocity where the rock is not affected by wellbore instability should be ensured. Using an appropriate V_p–V_s relation (e.g., Eq. 2.25), V_p can be estimated from the downhole-measured V_s. An example of the compressional transit time calculated from the shear transit time taken from a wireline log shows that the increment in the compressional transit time (i.e., slowdown in the compressional velocity) due to gas effect can reach 20 μs/ft (Zhang and Wieseneck, 2011).

2.3.6 Anisotropy of V_p and V_s

Velocity anisotropy in formations can be caused by the following reasons in the rocks (Barton, 2007): microcracks, fabric, joints, interbeddings, interfaces, faults, and stress anisotropies. Anisotropy effect is small for sandstones and carbonates, but large for shales. Lab tests illustrate that both compressional and shear velocities and their anisotropies increase as the applied stresses increase (Nur, 1971). The experiments conducted on rock samples of gneisses and shales show a clear evidence of anisotropy in Young's moduli, P-wave velocities, and thermal conductivities, as shown in Fig. 2.12 (Kim et al., 2012). Therefore, ignoring anisotropy in rock properties may lead to erroneous results.

The *P*- and *S*-wave anisotropy parameters ε and γ (Thomsen, 1986) can be calculated from the following equations:

$$\varepsilon = \frac{c_{11} - c_{33}}{2c_{33}}$$
$$\gamma = \frac{c_{66} - c_{44}}{2c_{44}} \tag{2.29}$$

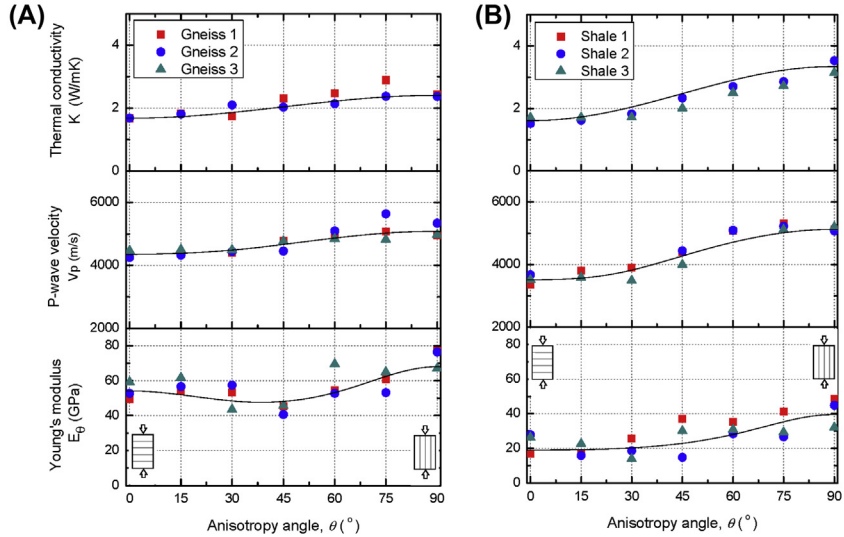

Figure 2.12 Laboratory-measured elastic modulus (E_θ), P-wave velocity (V_p), and thermal conductivity (K) variation with respect to anisotropy angle. In the right axis, values are normalized with respect to average minimum ones. (A) Asan gneiss, (B) Boryeong shale (Kim et al., 2012).

where c_{11}, c_{33}, c_{44}, and c_{66} are the elastic constants (refer to Eq. (1.39)). For VTI rocks (see Fig. 1.14), γ determines variation of horizontally polarized shear velocity with angle from vertical, and ε relates the horizontal P velocity, V_{PH}, to the vertical P velocity, V_{PV}:

$$\begin{aligned} V_{PV}^2 &= V_{PH}^2(1-2\varepsilon) \\ V_{PV} &\approx V_{PH}(1-\varepsilon) \end{aligned} \tag{2.30}$$

Wang (2002) measured velocities and anisotropies of many shales and reservoir rocks from oil and gas fields around the world. The results show that anisotropy in shales ranges from 6% to 33% for P-waves (ε) and 2%–55% for S-waves (γ). The coal sample is extremely anisotropic, showing over 40% anisotropy for both P- and S-waves. The magnitude of anisotropy decreases exponentially in shales as porosity increases.

2.4 Permeability

2.4.1 Permeability and hydraulic conductivity

Permeability is one of the most important physical properties of a porous medium. It measures quantitatively the ability of a porous medium to conduct fluid flow. Permeability of a rock depends largely on the connectedness of the void spaces, the grain size of the rock, and the cementation between rock grains. A rock could be extremely porous, but if each pore is isolated from the others, the rock would be impermeable. If rock grain size is small, then void spaces of the rock are small; therefore, the surface film of the fluid can actually choke the movement of additional fluids through the small spaces.

Permeability is a tensor in a manner similar to the stress tensor. More often the permeability is isotropic in the direction of the bedding plane but anisotropic in the direction of perpendicular to the bedding plane. Therefore, if two coordinates are in the plane of the bedding, the two permeabilities having equal values and denoted as the horizontal permeability, k_h, and the other coordinate in the direction perpendicular to the bedding denoted as the vertical permeability, k_V, then the permeability tensor can be expressed in the following form:

$$k = \begin{bmatrix} k_h & 0 & 0 \\ 0 & k_h & 0 \\ 0 & 0 & k_V \end{bmatrix} \tag{2.31}$$

In sedimentary rocks, horizontal permeability usually has a large value than vertical permeability, depending on porosity, grain size, and grain packing.

Hydraulic conductivity is a commonly used term (similar to permeability) in hydrogeology and is a measure in how easily a particular fluid (e.g., water) passes through a particular earth material. It came from Darcy's law, i.e., the rate of flow (q) in a porous medium is proportional to the cross-sectional area (A), proportional to the difference of hydraulic head ($h_1 - h_2$), and inversely proportional to the distance of the two hydraulic heads (L):

$$q = KA\frac{h_1 - h_2}{L} \tag{2.32}$$

where K is the hydraulic conductivity. The following equation gives permeability and hydraulic conductivity relationship:

$$K = \frac{\rho_f g}{\mu}k \tag{2.33}$$

where ρ_f is the fluid density; g is the gravitational acceleration; μ is the dynamic viscosity of fluid; and k is the permeability.

2.4.2 The relationship of permeability and porosity

The Kozeny–Carman equation relates the intrinsic permeability to porosity, ϕ, and grain size, d, of the rock:

$$k = \frac{d^2\phi^3}{180(1-\phi)^2} \tag{2.34}$$

Timur (1968) proposed that permeability and porosity follow the following relation for clean sandstones, i.e.,

$$k = a\frac{\phi^b}{S_{wirr}^c} \tag{2.35}$$

where S_{wirr}^c is irreducible water saturation; a, b, and c are determined from measurements on core samples. In Timur's relationship, with ϕ and S_{wirr}^c in units of v/v (fraction) and k in mD, a = 10^4, b = 4.4, and c = 2.

Timur's equation indicates that a linear relation between log(k) and ϕ exists. Laboratory core tests in tight gas sandstones in the Green River Basin and the Haynesville shale gas formation of the United States show that

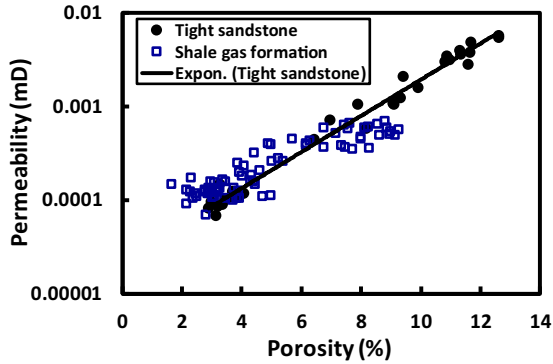

Figure 2.13 Laboratory core tests of permeability and porosity in tight sandstones in the Green River Basin and the Haynesville shale gas formation. The equation of the trend line is $\log_{10}k = 0.1934\phi - 4.65$.

log(k) and porosity follow a linear relationship (Fig. 2.13). However, this linear relation may not be true for other rocks; for example, laboratory test data in the clay-free Fontainebleau sandstone do not conform to the linear relation of log(k) and ϕ (Bourbie and Zinszner, 1985).

2.4.3 Stress-dependent permeability

Permeability is not only dependent on porosity but also has strong correlations with the burial depth and stress. The stress changes caused by subsurface engineering have important impacts on permeability. Permeability in a fractured porous medium is mainly controlled by the geometry and interconnectedness of the pores and fractures as well as stress state. It has been found that stress-deformation behavior of fractures and pores is a key factor governing permeability and fluid flow through the rocks. For example, reservoir depletion causes effective stress increase that will compact the pore spaces and reduce permeability.

Stress and permeability tests under triaxial loading conditions have been conducted to examine permeability in rock samples with respect to a complete stress–strain path (e.g., Zhang et al., 2000; Zhang et al., 2007). Experimental results show that for low permeability rocks (e.g., permeability < 1 mD), no dramatic change in permeability is exhibited as the axial stress increases within the elastic deformation range. However, significant permeability changes occur if plastic deformations are induced. From Fig. 2.14 it can be seen that, during the initial elastic deformation (region OA), permeability reduces because of compaction of existing cracks; however, permeability starts to increase as the rock begins to dilate.

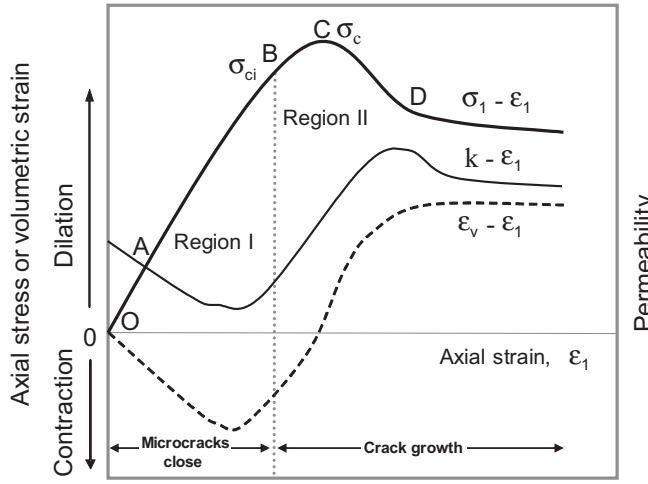

Figure 2.14 Schematic relationships among axial stress (σ_1), volumetric strain (ε_V), and permeability (k) in a triaxial compression test (Zhang et al., 2007).

In region AB of the complete stress–strain curve, the first structural damage appears randomly as elongated noninterconnected microcracks (Jaeger at al., 2007), which cause permeability to increase slightly. As the axial stress increases in this stage, the permeability slowly increases until yielding of the rock (Point B). The rock yielding leads to a jump in the permeability magnitude due to the sudden creation of microfractures. Toward the end of region BC, there is a pronounced increase in microcracking tending to coalesce along a plane in the central portion of the specimen. This corresponds to a significant increase in permeability (Fig. 2.14). After reaching the maximum stress, at point C, a macroscopic fracture plane develops, causing a significant increase in permeability. After the maximum stress, the permeability continues to increase before reaching its peak value at point D. This is likely due to the fact that in the region CD, the fracture plane extends toward the ends of the specimen and new cracks continue to appear, as reported by acoustic emissions (Jaeger at al., 2007). On reaching a maximum value (σ_c), the permeability drops again because the failed rock undergoes a second phase of compaction. The subsequent permeability changes are the result of the postfailure deformation, which continue until the axial stress reaches its minimum magnitude (residual strength) (Zhang et al., 2007).

Volumetric strain and permeability have a strong relationship, and two major regions can be distinguished in Fig. 2.14. Region I (preexisting

microcrack closing) commences from the origin until the crack-initiation stress level (σ_{ci}) is reached. This region corresponds to the closure of existing microcracks pervading the rock sample. This causes the rock volume to contract as the load increases; therefore, permeability decreases gradually. Region II (new crack growth) corresponds to the initiation of new cracks, which induces a volumetric dilation and a dramatic increase in permeability. It is obvious from Fig. 2.14 that changes of permeability and volumetric strain are coherent in trend. This phenomenon illustrates that the volumetric strain and permeability can be related by a certain function, although it is difficult to determine a correlation between stress and permeability, particularly after the peak strength (σ_c) is reached.

2.4.4 Stress and permeability relations in fractured rocks

For a single fracture, the fracture permeability can be obtained from the parallel plate model:

$$k_f = \frac{b^2}{12} \tag{2.36}$$

where k_f is the fracture permeability; b is the fracture aperture.

The single fracture model can be extended to multiple fracture systems by considering regular families of parallel fractures. The permeability through a set of parallel fractures of equal aperture, oriented parallel to flow direction, can be expressed in the following equation (the cubic law):

$$k_f = \frac{b^3}{12s} \tag{2.37}$$

where s is the mean fracture spacing.

Because natural fractures are neither smooth nor parallel, investigators have questioned the accuracy of applying the cubic law to natural fractures. Investigations show that the cubic law is valid when corrected by considering the fracture tortuosity, correction factor, or using effective fracture aperture (Witherspoon et al., 1980). The cubic law may be also applicable in hydraulic fractures for determining the stress–conductivity relation. Decrease of formation pore pressure because of depletion will increase effective stresses and cause the apertures (widths) of the hydraulic fractures to reduce; therefore, the fracture conductivity decreases.

In fractured formations, permeability variations with the stresses have been delineated through various laboratory and field tests, represented by different empirical equations.

Jones (1975) provided an empirical relation for the fracture permeability in carbonate rocks as follows:

$$k_f = k_0\left[\log\left(\frac{\sigma'_0}{\sigma'}\right)\right]^3 \tag{2.38}$$

where k_0 is the initial permeability; σ' is the effective stress; σ'_0 is the effective stress when $k_f = k_0$.

Louis (1974) suggested an alternative relationship based on well pumping tests at different depths:

$$k_f = k_0 \exp(-A\sigma') \tag{2.39}$$

where σ' is the effective stress and can be expressed as $\sigma' = \gamma H - p_p$ in which γ is the specific gravity of the rocks; H is the depth; p_p is the pore pressure; and A is a coefficient.

Walsh (1981) offered the following empirical relation derived from laboratory test data:

$$k_f = k_0\left[1 - \left(\sqrt{2}\,\xi\right)\ln(\sigma'/\sigma'_0)\right]^3 \tag{2.40}$$

where σ'_0 is the initial effective stress, and ξ is a constant related to the fracture geometry.

Bai and Elsworth (1994) presented the following equation to describe strain and permeability change (Δk):

$$\Delta k = k_0\left[1 + \Delta\varepsilon\left(\frac{k_n b}{E} + \frac{b}{s}\right)^{-1}\right]^3 \tag{2.41}$$

where $\Delta\varepsilon$ is the strain change; k_n is the normal stiffness of the fracture; and E is Young's modulus.

Based on Eq. (2.37) and large synthetic rock tests (Zhang et al., 2007), the permeability change in one direction (such as, z-direction) due to the aperture change can be directly related to the stress resultant deformations. For two mutually orthogonal sets of fractures, as shown in Fig. 2.15, the permeability change due to the aperture changes in the z-direction can be obtained as follows (Zhang et al., 2007):

$$k_z = k_{0z}\left(1 - \frac{\Delta b_x}{b_{0x}} - \frac{\Delta b_y}{b_{0y}}\right)^3 \tag{2.42}$$

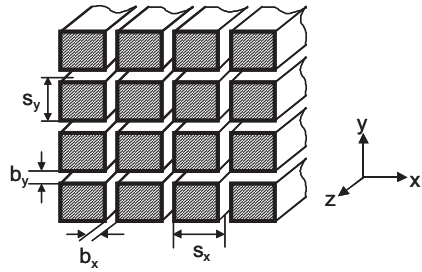

Figure 2.15 Simplified multiple fracture system for two mutually orthogonal sets of parallel fractures in the *z*-direction.

where k_z is the permeability change due to aperture increments of Δb_x and Δb_y; the compressive displacement is positive and tensile displacement is negative; k_{0z} is the original permeability in the z-direction under the initial stress condition; b_{0x} is the initial average normal aperture of the original fracture in the x-direction; b_{0y} is the initial average normal aperture of the original fracture in the y-direction.

Assuming an idealized three-dimensional regularly spaced fracture-matrix system, as illustrated in Fig. 2.16, the change of the fracture aperture along the x-direction due to the normal stress changes can be obtained (Zhang, 2002; Zhang et al., 2007). Similarly, the change of the fracture aperture along the y-direction can also be obtained. Therefore, the change of permeability in the z-direction in two mutually orthogonal sets of fractures caused by 3-D stress changes can be obtained (Zhang et al., 2007):

$$k_z = k_{z0}\left\{1 - \left(\frac{1}{K_{nx}b_x} + \frac{1}{K_{nx}s_x} + \frac{1}{E_r}\right)[\Delta\sigma_x - \nu(\Delta\sigma_y + \Delta\sigma_z)] - \left(\frac{1}{K_{ny}b_y} + \frac{1}{K_{ny}s_y} + \frac{1}{E_r}\right)[\Delta\sigma_y - \nu(\Delta\sigma_x + \Delta\sigma_z)]\right\}^3 \tag{2.43}$$

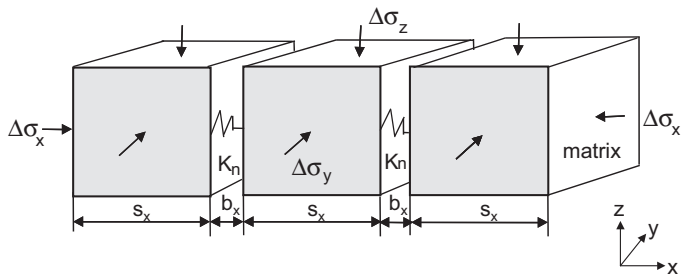

Figure 2.16 Coupled fracture–matrix system with 3-D stresses for a set of parallel fractures (Zhang, 2002).

where K_{nx} and K_{ny} are the fracture normal stiffnesses in the fractures perpendicular to the x- and y-directions, respectively; $\Delta\sigma_x$, $\Delta\sigma_y$, and $\Delta\sigma_z$ are the effective stress increments in the x-, y-, and z-directions, respectively, and the compressive stress is positive.

From Eq. (2.43), the permeability change is controlled by the stress change, fracture aperture and spacing, and normal stiffness of the fracture. It should be noted that shear stress effect is not considered in Eq. (2.43). When shear stresses are large, their effect on permeability should be considered. The permeability–stress relationship also shows that the effective stress change has a pronounced impact in permeability. This effective stress-dependent permeability is significant for the fractured reservoirs because a rapid increase in the effective stress can cause a quick closure of natural fractures, which may cause a permanent loss of permeability in the fractures. Therefore, slowing down the effective stress change during production of a fractured reservoir can decelerate the permeability reduction. For example, reducing reservoir drawdown can decrease the fast increase in the effective stress, thus reduce the permeability decrease.

2.4.5 Stress and proppant effects on permeability of hydraulic fractures

Multistage hydraulic fracturing in the horizontal well and propping the hydraulic fractures by proppants are the major completion method to enhance permeability for oil and gas production in unconventional resources. Experimental results from 88 Barnett shale samples show that the conductivity of hydraulic fractures is dependent on the proppant size and formation stresses (Zhang et al., 2014). The propped fracture conductivity increases with larger proppant size and higher proppant concentration. Longer-term laboratory fracture conductivity measurements also show that within 20 h the fracture conductivity could be reduced by as much as 20%. Laboratory results also demonstrate that higher proppant concentration leads to higher fracture conductivity with the same-sized proppant (Fig. 2.17A); larger proppant size consistently provides higher conductivity than the smaller one (Fig. 2.17B). An interesting observation is the significant conductivity increment with propped fractures (even those with a very small proppant concentration) compared with unpropped fracture. This is because the proppants support fracture surfaces to reduce the fracture closure under stress. The fracture conductivity reduces as the stress increases, but the reduction of the fracture conductivity in propped fractures is much

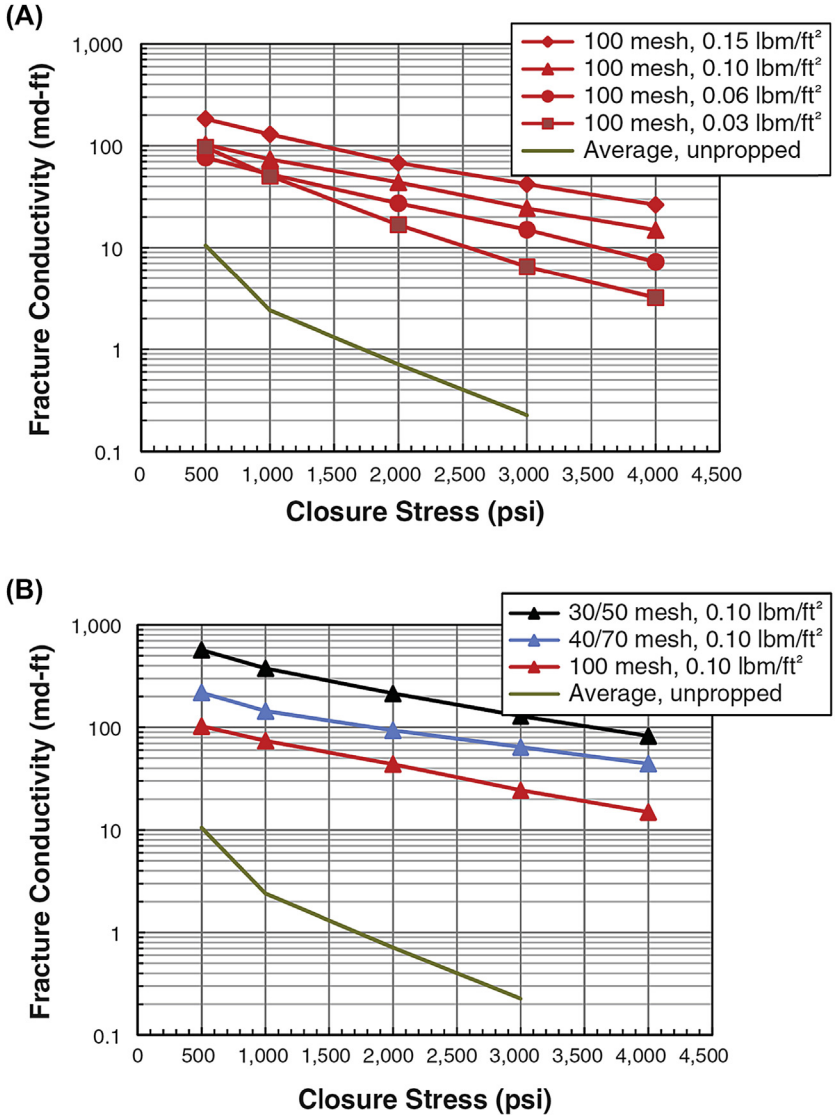

Figure 2.17 Conductivities of propped and unpropped fractures versus the minimum stress (closure stress) from laboratory tests in the outcrop samples of the Barnett shale: (A) different proppant concentrations; (B) different proppant sizes (Zhang et al., 2014).

smaller than that in unpropped fractures, as shown in Fig. 2.17. This implies that a higher proppant concentration, larger proppant size, and larger propped fracture area can enhance fracture conductivity and increase oil and gas production.

2.4.6 Stress and permeability relation in porous rocks

For porous media, fluids flow mainly through pore spaces. The variation in grain sizes or pore spaces due to the effect of an applied stress causes a change of permeability. For a simple cubical grain packing structure, the permeability k can be expressed as follows (Bai and Elsworth, 1994):

$$k = \frac{2R^2}{\pi^2} \tag{2.44}$$

where R is the grain radius of the porous rock.

When the stresses exerted on the grains change, it will cause the grain size and pore space to change and result in permeability change. From Eq. (2.44), the following equation can be used to describe the relation between the grain size and permeability:

$$k_p = k_0 \frac{R^2}{R_0^2} \tag{2.45}$$

where k_p is the permeability after the change of the grain radius (R); k_0 is the initial permeability; R_0 is the initial grain radius.

Under a three-dimensional effective stress condition, the change in grain sizes within a cubical packing (Fig. 2.18) can be determined by analyzing the elastic contact of spheres. Applying the theory of the Hertzian contact of

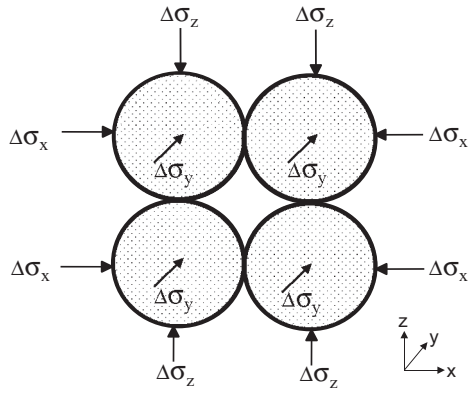

Figure 2.18 Spherical contact of grains under 3-D stresses.

spherical grains, the change of grain radius due to effective stresses changes of $\Delta\sigma_x$, $\Delta\sigma_y$, and $\Delta\sigma_z$ can be obtained from the following equations:

$$R = R_0\left\{1 - \frac{1}{2}\left\{\frac{9(1-\nu^2)}{2}\left[\pm\left(\frac{\pi\Delta\sigma_x}{E}\right)^2 \pm \left(\frac{\pi\Delta\sigma_y}{E}\right)^2 \pm \left(\frac{\pi\Delta\sigma_z}{E}\right)^2\right]\right\}^{\frac{1}{3}}\right\} \tag{2.46}$$

where the positive sign is for the compressive stress, and negative sign is for the tensile stress.

Substituting Eq. (2.46) to Eq. (2.45), the change in permeability by normal stresses can be expressed as follows:

$$k = k_0\left\{1 - \frac{1}{2}\left[\frac{9\pi^2(1-\nu^2)}{2E^2}\left(\pm\Delta\sigma_x^2 \pm \Delta\sigma_y^2 \pm \Delta\sigma_z^2\right)\right]^{\frac{1}{3}}\right\}^2 \tag{2.47}$$

where k_0 is the initial permeability. This relationship may be applicable for analyzing the stress-dependent permeability of the proppants in hydraulic fractures as described in the previous section. Hydraulic fracture conductivity changes induced by stress changes are primarily caused by the following reasons:

(1) Reduction in pore pressure due to production depletion increases the effective overburden stress, causing the formation compaction, fracture deformation, even closure of small fractures.

(2) Proppant deformation, embedment, crushing, and fines migration cause reduction in the pore spaces and permeability of the proppants in the hydraulic fractures.

2.5 Young's modulus

Young's modulus is an important parameter to define the relationship between stress and strain in a material in the linear-elastic deformation. It generally refers to the static Young's modulus, which can be obtained from laboratory core tests, e.g., uniaxial or triaxial compression test. The dynamic Young's modulus can be calculated from theoretical equations using the acoustic velocity data. However, for geomechanics analysis, static Young's modulus is needed. That is, in the stress—strain constitutive equations (refer to Chapter 1), static Young's modulus is required for the calculations. Therefore, if only dynamic modulus is available, then it needs to be converted to the static modulus. Some converting correlations will be introduced in the following sections.

2.5.1 Static Young's modulus

The static axial Young's modulus (E_s) in the laboratory core test is defined as the ratio of the axial stress change ($\Delta\sigma$) to the axial strain change ($\Delta\varepsilon$) produced by the stress change, i.e.,

$$E_s = \frac{\Delta\sigma}{\Delta\varepsilon} \tag{2.48}$$

If an axial stress and axial strain curve before reaching the ultimate strength of the rock takes approximately a linear form (Fig. 2.19), the slope of this stress–strain curve is the static Young's modulus or elastic modulus. ISRM (1979) suggested the following three methods for calculating Young's modulus from the stress–strain curve in uniaxial compression of a rock specimen of regular geometry:

(1) Tangent Young's modulus is measured at a stress level, which is some fixed percentage of the ultimate strength. It is generally taken at a stress level equal to 50% of the ultimate uniaxial compressive strength.

(2) Average Young's modulus is determined from the average slopes of the more-or-less straight line portion of the axial stress–axial strain curve (Fig. 2.19).

(3) Secant Young's modulus is usually measured from zero stress to some fixed percentage of the ultimate strength, generally at 50%.

Young's modulus describes the capacity of rock deformation, or the stiffness of a rock. A rock with a high Young's modulus is less deformable

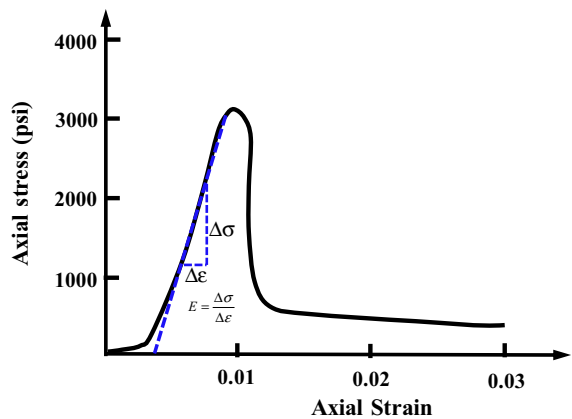

Figure 2.19 Average Young's modulus (E) from the uniaxial stress–strain curve in a shale sample cored at the depth of 25,000 ft TVD ss (from the sea level) in the Gulf of Mexico. TVD, true vertical depth

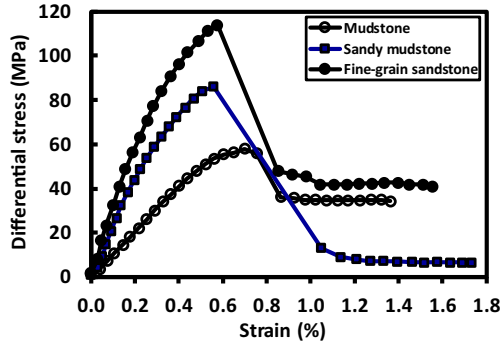

Figure 2.20 Complete stress–strain curves for sandstone, sandy mudstone, and mudstone in Eastern China's Permian formations under the triaxial compression tests (confining stress $\sigma_3 = 10$ MPa).

(i.e., stiff), and the initial part of the complete stress–strain curve of the rock will be steep. However, for a low Young's modulus (soft) rock it is more deformable, and the initial part of the complete stress–strain curve will be gentle (Hudson and Harrison, 1997). Fig. 2.20 shows three complete stress–strain curves of the triaxial compressive tests for fine-grained sandstone, sandy mudstone, and mudstone in the Permian formations in Huainan, China (Meng et al., 2006). The differential stress in the figure represents the difference of the axial and the confining stresses, i.e., $\sigma_1 - \sigma_3$. Fig. 2.20 indicates that different rocks have different Young's moduli: the sandstone has a much greater peak compressive strength and larger Young's modulus than those in mudstones.

In triaxial compression tests, Young's moduli may be different at different confining stresses. Triaxial test results show that Young's moduli could be very different even for the rocks cored in the same formation at a similar depth. Fig. 2.21 demonstrates that Young's modulus increases as the confining stress increases (Meng et al., 2006). When the confining stress is small (e.g., S3 = 0 and 5 MPa in Fig. 2.21), the difference of Young's moduli is large. Laboratory test results reported by Niandou et al. (1997) have a similar phenomenon. Triaxial compression tests indicate that Young's modulus is dependent on the confining pressure (stress) and they have a nonlinear relationship even for the same rock. This nonlinear relationship can be expressed as the following form:

$$E_s = b_2\sigma_3^2 + b_1\sigma_3 + b_0 \tag{2.49}$$

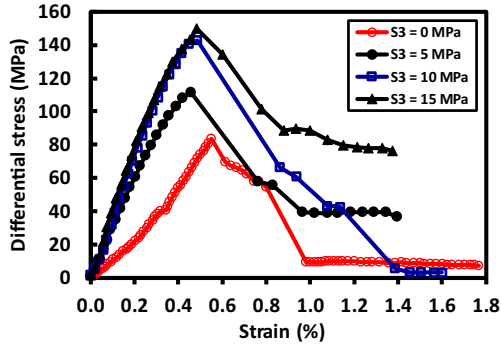

Figure 2.21 Triaxial compression tests in the medium-grained sandstone under different confining stresses (S3 in the figure).

where E_s is the static Young's modulus in GPa; σ_3 is the confining stress in MPa; b_0, b_1, and b_2 are the parameters that are dependent on lithology. For different lithologies, the parameters in Eq. (2.49) are different (Meng et al., 2006).

The confining stress dependent Young's modulus was also found from the triaxial tests in the Carboniferous sandstone by Santarelli (1987). His results indicate that the tangent Young's modulus at 50% peak strength is well represented by the following relation:

$$E_s = 17.41(1 + 0.08\sigma_3)^{0.403} \tag{2.50}$$

where E_s is Young's modulus in GPa; σ_3 is the confining stress in MPa.

2.5.2 Empirical equations to estimate static Young's modulus

When laboratory test data of Young's moduli are not available, empirical equations can be used for estimating static Young's modulus. Phani and Niyogi (1987) proposed the following empirical relation for predicting Young's modulus of the porous material from porosity:

$$E_s = E_0(1 - a\phi)^n \tag{2.51}$$

where E_s is Young's modulus of porous material with porosity ϕ; E_0 is Young's modulus of the matrix when the porosity is zero; and a and n are constants, normally $a = 1$.

A simpler empirical equation can be expressed in the following form:

$$E_s = E_0 e^{-a\phi} \tag{2.52}$$

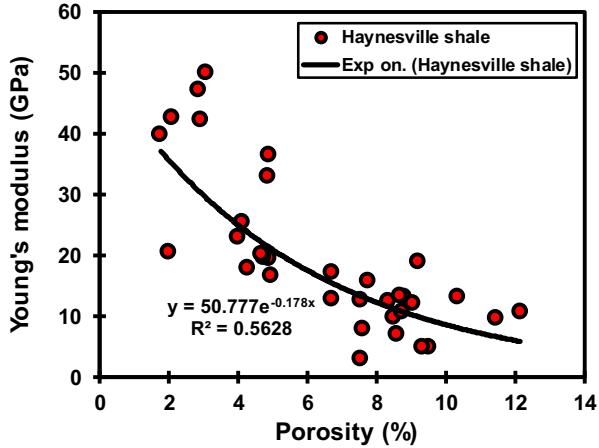

Figure 2.22 Porosity versus Young's modulus obtained from the uniaxial compression tests in the Haynesville shale gas formation.

The results of uniaxial compression tests in the Haynesville shale gas formation (porosity <14%) of several wells indicate that Young's modulus is highly dependent on porosity (Fig. 2.22). Young's modulus increases as porosity decreases and the following correlations are obtained:

$$E_s = 50.777e^{-17.8\phi} \tag{2.53}$$

$$\text{Or } E_s = 48.943(1-\phi)^{16.511} \tag{2.54}$$

where Young's modulus E_s is in GPa and the porosity ϕ is in fractions.

Using the laboratory test data and the P-wave transit time measured from the sonic log, t_p, Horsrud (2001) obtained the following correlations for the shale samples cored in the North Sea boreholes:

$$E_s = 0.076(304.8/t_p)^{3.23} \tag{2.55}$$

where E_s is in GPa; t_p is the P-wave transit time from the sonic log, in μs/ft.

$$E_s = 0.076V_p^{3.23} \tag{2.56}$$

where E_s is in GPa; V_p is the P-wave velocity, in km/s.

Using the empirical equations, continuous estimates of rock properties can be obtained directly from the sonic log for different rock intervals. To apply those empirical equations into a different field, calibrations are needed. That is, the empirical equations need to be calibrated to available lab data and to adjust parameters in the empirical equations to match the lab data.

2.5.3 Anisotropic Young's modulus

Most rocks are anisotropic materials and have a characteristic orientation, particularly in shale formations where the clay minerals are oriented in the bedding direction. The shale will be stiffer (with a higher Young's modulus) if it is loaded parallel to the bedding direction than that if it is loaded perpendicular to the same direction. Laboratory uniaxial compression tests in core samples of the Haynesville shale gas formation show that the horizontal and vertical Young's moduli are markedly different. The ratio of the horizontal to vertical Young's moduli is highly related to the vertical Young's modulus (Fig. 2.23), for which following correlation exists:

$$E_h/E_V = 10.06E_V^{-0.594} \tag{2.57}$$

where E_h and E_V are the horizontal and vertical Young's moduli (in GPa), respectively.

The other available lab test results of the horizontal and vertical Young's moduli are also plotted in Fig. 2.23. These data include the Haynesville and Bossier shales (Sone, 2012), Baxter shale (Higgins et al., 2008), sandstones and shales in the Cretaceous Travis Peak formations (Thiercelin and Plumb, 1994), and the outcrops of the Eagle Ford shale (Knorr, 2016). It can be observed from Fig. 2.23 that these core test results follow a similar trend, as presented in Eq. (2.57). Laboratory tests in several shale oil and gas formations also indicates that Young's modulus anisotropy is dependent on the clay volume, and the anisotropy increases as the clay volume increases (e.g., Sone and Zoback, 2013).

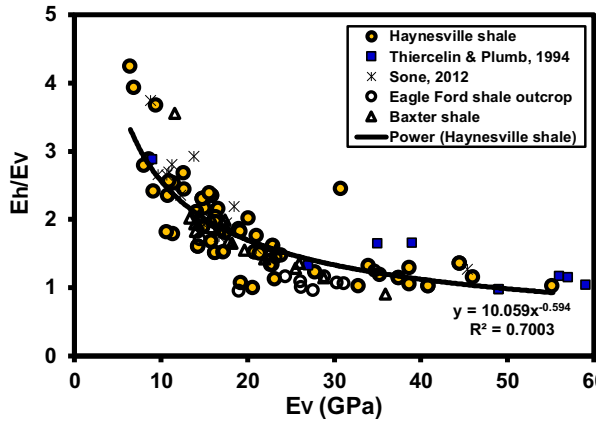

Figure 2.23 Lab test results of horizontal and vertical static Young's moduli in shales and sandstones following a similar correlation.

2.5.4 Dynamic Young's modulus

When rock samples are not available, the well logs and geophysical data can be used to analyze and interpret rock physical and mechanical parameters. The dynamic Young's modulus (E_d) can be solved from the following theoretical equation by knowing the elastic compressional and shear wave velocities of the rock:

$$E_d = \rho_b V_p^2 \frac{(1+\nu_d)(1-2\nu_d)}{(1-\nu_d)} \tag{2.58}$$

where ρ_b is the bulk density; V_p is the compressional velocity; ν_d is the dynamic Poisson's ratio.

The dynamic Young's modulus can also be expressed as the following forms if the transit time is available:

$$E_d = \frac{\rho_b}{t_p^2} \frac{(1+\nu_d)(1-2\nu_d)}{(1-\nu_d)} \tag{2.59}$$

$$E_d = \frac{2\rho_b(1+\nu_d)}{t_s^2} \tag{2.60}$$

where t_p and t_s are the compressional and shear transit time, respectively.

Therefore, if well log data (such as density log, sonic compressional transit time, and shear transit time) are available, the dynamic Young's modulus can be computed from the above equations. In the English unit, dynamic Young's modulus, Eq. (2.59), can be expressed as the following form:

$$E_d = 1.35 \times 10^4 \frac{\rho_b}{t_p^2} \frac{(1+\nu_d)(1-2\nu_d)}{(1-\nu_d)} \tag{2.61}$$

where E_d is the dynamic Young's modulus with unit of one million psi (Mpsi); t_p is in μs/ft; ρ_b is in g/cm^3.

From lab tests in over 400 core samples of sandstones, shales, limestones, dolomites, and siltstones from the Gulf of Mexico, Lacy (1997) derived the following correlation between rock dynamic Young's modulus and the compressional velocity:

$$E_d = 0.265 V_p^{2.04} \tag{2.62}$$

where the dynamic modulus (E_d) is measured in Mpsi; the compressional velocity V_p is in km/s and ranges from 1 to 6 km/s.

If the formation bulk density (ρ_b) is also known from density logs, a more accurate estimate for the dynamic modulus can be made by using the following equation (Lacy, 1997):

$$E_d = 1.13 \times 10^4 \rho_b / t_p^2 \tag{2.63}$$

where E_d is in Mpsi; t_p is in μs/ft; ρ_b is in g/cm^3. This correlation is a simplification of the theoretical equation of Eq. (2.61) with Poisson's ratio of $\nu_d \approx 0.248$.

2.5.5 Relations of dynamic and static Young's moduli

In general, the dynamic values of Young's modulus have been found to be greater than the static values. The discrepancy between the dynamic and static moduli is far greater in the soft rock (such as shale) than that in the hard rock (such as granite) (Howarth, 1984), and it has been widely attributed to microcracks and pores in the rocks. It is also believed that the differences in strain amplitude between static and dynamic measurements is the primary cause for the difference between static and dynamic moduli in dry rocks (e.g., Martin and Haupt, 1994). There are many empirical relations to correlate the dynamic and static Young's moduli. Some correlations derived from petroleum basins are listed below, Eqs. (2.64)–(2.67), where the units of the static and dynamic elastic moduli are one million psi (Mpsi, 1 Mpsi ≈ 6.895 GPa).

From ultrasonic test data of 600 core samples in the Gulf of Mexico, Lacy (1997) obtained the following correlation for sandstones:

$$E_s = 0.0293E_d^2 + 0.4533E_d \tag{2.64}$$

A similar correction exists for shales (Lacy, 1997):

$$E_s = 0.0428E_d^2 + 0.2334E_d \tag{2.65}$$

From the test data in sandstones, shales, limestones, and dolomites, the generalized correlation can be expressed as follows (Lacy, 1997):

$$E_s = 0.018E_d^2 + 0.422E_d \tag{2.66}$$

Ohen (2003) gave the following relation between dynamic and static moduli for the shales in the Gulf of Mexico:

$$E_s = 0.0158E_d^{2.74} \tag{2.67}$$

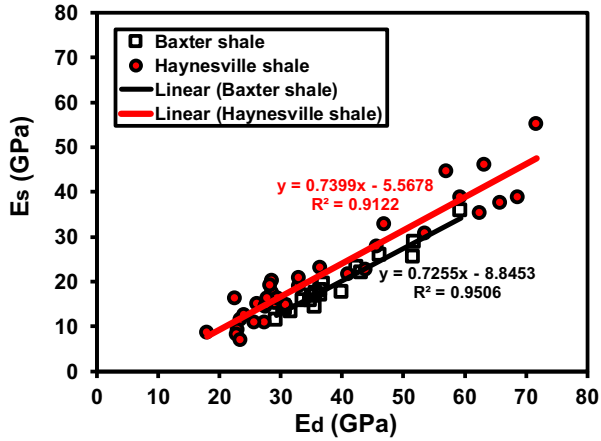

Figure 2.24 The dynamic and static moduli in the Haynesville and Baxter shales.

From uniaxial compression tests in the Haynesville shale gas cores, dynamic and static moduli have the following relation:

$$E_s = 0.6115E_d \tag{2.68}$$

For the same data in the Haynesville shale, the following correlation can be used with a higher correlation coefficient ($R^2 = 0.9122$, as shown in Fig. 2.24).

$$E_s = 0.74E_d - 5.568 \tag{2.69}$$

where E_s and E_d are in GPa.

Analyzing core test data from the Baxter shale with low total organic content in the Vermillion Basin in Wyoming presented by Higgins et al. (2008), a similar correlation is obtained in the following, as shown in Fig. 2.24:

$$E_s = 0.7255E_d - 8.8453 \tag{2.70}$$

where E_s and E_d are in GPa. This equation is not realistic when $E_s < 8.8$ GPa; in this case, a different correlation can be used, i.e.,

$$E_s = 0.5036E_d \tag{2.71}$$

Laboratory measurements of static and dynamic core mechanical properties of the Chase and Council Grove reservoirs in Kansas in limestones, dolostones, siltstones, and mudstones show that there is a good correlation between static and dynamic-undrained Young's moduli

(Yale and Jamieson, 1994). The well log derived (dynamic-undrained) values can be correlated to static, reservoir condition values of Young's modulus using a correction factors between 0.68 (for mudstones and siltstones) and 0.79 (for dolostones and limestones) depending on lithology. Combining these factors with Eqs. (2.68) and (2.71), it has the following generalized relation:

$$E_s = kE_d \tag{2.72}$$

where k is a correlation factor between 0.5 (shales, Eq. (2.71)) and 0.79 (dolostones and limestones, Yale and Jamieson, 1994).

It should be noted that the dynamic modulus, if it is calculated from lab measured V_p and V_s, is not a constant even for the same rock. For example, it increases as the axial load increases during the compression test, as shown in Fig. 2.25, because V_p and V_s increase as the load increases. Therefore, the correlations between static and dynamic moduli may be very different for different axial and confining stress conditions. For many cases in petroleum engineering there needs to be a conversion from the downhole sonic log data (transit time) into rock properties (moduli and strengths). Therefore, obtaining empirical correlations between the static moduli measured from lab compression tests and the dynamic moduli derived from the downhole-measured transit time may be more applicable. Alternatively, obtaining a correlation between static modulus and downhole transit time is more direct and easier to apply.

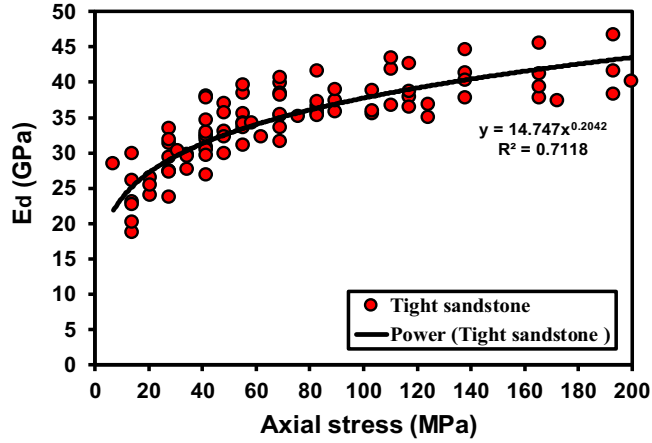

Figure 2.25 The dynamic Young's moduli, calculated from lab measured V_p and V_s, increase with the axial stresses in the cores of tight sandstones in the Green River Basin, USA.

2.6 Poisson's ratio

2.6.1 Static Poisson's ratio

Poisson's ratio is the ratio of transverse strain to corresponding axial strain on a material stressed along one axis. For a rock core subjected to an axial load, Poisson's ratio (ν) can be expressed in the following:

$$\nu = -\frac{\varepsilon_l}{\varepsilon_a} \tag{2.73}$$

where ε_l and ε_a are the lateral and axial strains, respectively. Therefore, static Poisson's ratio can be determined by measuring the lateral and axial deformations of the uniaxial compression test in the rock sample.

Static Poisson's ratio in a rock depends on lithology, confining stress, pore pressure, and porosity of the rock. Laboratory test results show that static Poisson's ratio increases as porosity increases (Fig. 2.26). This porosity-dependent Poisson's ratio is not difficult to understand because the dynamic Poisson's ratio is theoretically dependent on V_p/V_s (refer to Eq. 2.76), and V_p/V_s is directly related to porosity (Fig. 2.7 and Eq. (2.28)). The trend line in Fig. 2.26 is:

$$\nu = 0.2 + 0.61\phi \tag{2.74}$$

2.6.2 Poisson's ratio anisotropy

Similar to Young's moduli, Poisson's ratios are also anisotropic. Fig. 2.27 presents static vertical and horizontal Poisson's ratios in the Haynesville

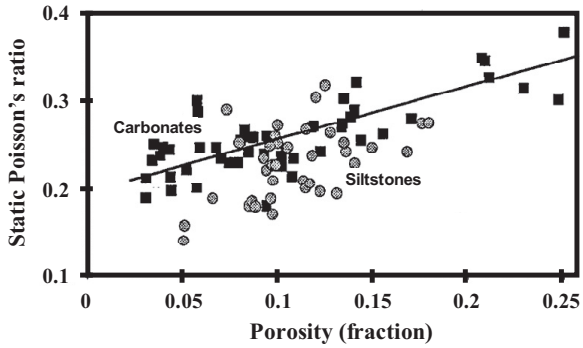

Figure 2.26 Poisson's ratio versus porosity for carbonates and siltstones (Yale and Jamieson, 1994).

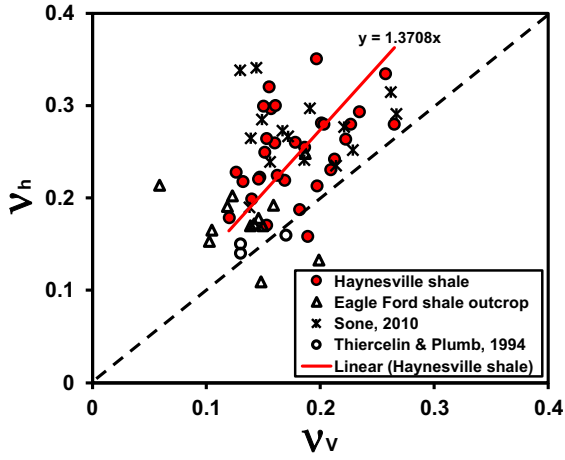

Figure 2.27 Laboratory experimental results of vertical and horizontal Poisson's ratios in the Haynesville and Bossier shale, the Eagle Ford shale outcrop, and the Cretaceous Travis Peak formations.

shale and other formations from laboratory uniaxial compression tests. The vertical Poisson's ratio ν_V (or ν_{VH}) in Fig. 2.27 is Poisson's ratio measured when the loading is in the vertical direction (perpendicular to the bedding direction). The horizontal Poisson's ratio ν_h (or ν_{hH}) is Poisson's ratio when the loading is in the horizontal direction (parallel to the bedding direction). It can be seen from Fig. 2.27 that the vertical Poisson's ratio is generally smaller than the horizontal Poisson's ratio, and the difference of horizontal and vertical Poisson's ratios is up to two times. The weak bedding plane has a larger displacement (strain) when the loading direction is perpendicular to the bedding direction; hence the displacement (strain) in the vertical direction is larger than the case where the load is parallel to the bedding direction. Therefore, from Eq. (2.73) the vertical Poisson's ratio is smaller. Fig. 2.27 also plots static vertical and horizontal Poisson's ratios in the Haynesville and Bossier shales, the Eagle Ford shale outcrop (Knorr, 2016), and the Cretaceous Travis Peak formations (Thiercelin and Plumb, 1994). There is no good correction between vertical and horizontal Poisson's ratios, but it can be approximately expressed in the following form (the trendline in Fig. 2.27):

$$\nu_h = 1.37\nu_V \tag{2.75}$$

2.6.3 The relationship of dynamic and static Poisson's ratios

Dynamic Poisson's ratio can be calculated from the compressional and shear velocities of the elastic wave (V_p, V_s), i.e.,

$$\nu_d = \frac{\frac{1}{2}(V_p/V_s)^2 - 1}{(V_p/V_s)^2 - 1} \tag{2.76}$$

Laboratory measurements of static and dynamic Poisson's ratios in mudstones, siltstones, and siltstones with dolomites in the Chase and Council Grove reservoirs in Kansas show that there is significant scatter, as shown in Fig. 2.28 (Yale and Jamieson, 1994). The core test results of static and dynamic Poisson's ratios in the Baxter shale (Higgins et al., 2008) are also plotted in Fig. 2.28, and the data are also scatter and no good correlation can be derived. A similar result was reported by Tutuncu et al. (1998). The dynamic-undrained Poisson's ratios trend with the static-drained Poisson's ratio values, and no systematic correction to acoustic (sonic) log derived Poisson's ratios is needed (Yale and Jamieson, 1994). Therefore, the sonic well log derived Poisson's ratio, which is dynamic-undrained Poisson's ratio, can be approximately used as the static Poisson's ratio.

Fig. 2.29 shows the calculated dynamic Poisson's ratio from Eq. (2.76) using sonic compressional and shear velocities in an offshore well with a water depth of 264 m. It shows that Poisson's ratio depends on both lithology and depth and is larger in shales and smaller in sandstones.

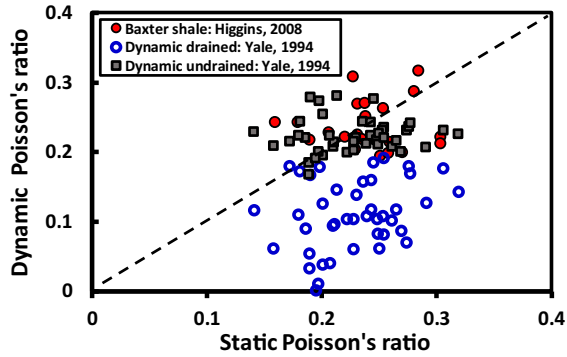

Figure 2.28 Drained static Poisson's ratio versus dynamic-undrained and drained Poisson's ratios compared to the data in the Baxter shale (plotted from the data presented by Yale and Jamieson, 1994 and Higgins et al., 2008).

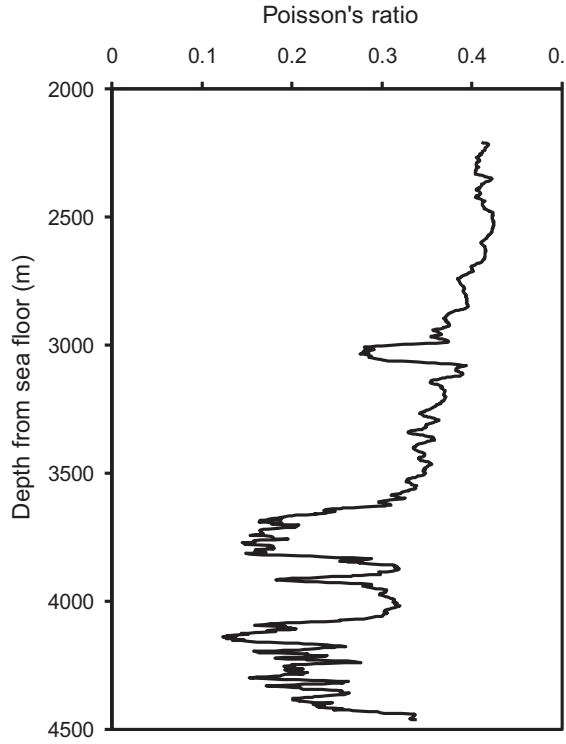

Figure 2.29 Poisson's ratio derived from sonic compressional and shear velocities obtained from wireline log in an offshore well (Peng and Zhang, 2007).

2.7 Biot's effective stress coefficient

2.7.1 Static Biot's coefficient

For a porous rock under stress, the solid and fluid parts are deformed independently. Therefore, pore pressure and effective stress needs to be considered in a fluid-saturated medium. The effective stress is dependent on the total stress, pore pressure, and Biot's coefficient (refer to Eq. (1.9)). Biot's coefficient (static) is defined as the ratio of static pore space deformation to total bulk-volume change and can be calculated from Eq. (1.10), when the frame bulk modulus or the dry bulk modulus of the porous rock (K_{dry}) and the matrix bulk modulus (K_m) are available (Nur and Byerlee, 1971); the equation is restated in the following:

$$\alpha = 1 - K_{dry}/K_m \tag{2.77}$$

Detournay and Cheng (1993) used K (the drained bulk modulus of elasticity) to replace K_{dry} in the above equation for computing Biot's coefficient.

The dry bulk modulus can be related to dry Young's modulus (E_{dry}) and dry Poisson's ratio (ν_{dry}) as shown in the following equation:

$$K_{dry} = \frac{E_{dry}}{3(1 - 2\nu_{dry})} \tag{2.78}$$

The matrix bulk modulus (K_m) is a constant, depending on the chemical composition of the minerals, e.g., for clay minerals K_m varies from 9.3 GPa in smectite up to >100 GPa in chlorite. When the matrix bulk modulus is not available, published values of the matrix bulk moduli (e.g., Mavko et al., 2009) can be used for estimating Biot's coefficient. The matrix bulk moduli in typical minerals can be found in Table 2.5.

The upper limit of Biot's coefficient is 1. For unconsolidated or high porosity rocks, Biot's coefficient is close to 1. Laboratory measurements demonstrate that for underground rocks Biot's coefficient values decrease with porosity from a value of 1 at surface conditions to values around 0.6–0.8 at porosity of 0.15–0.20 for carbonates and sandstones (Bouteca and Sarda, 1995). From triaxial compression tests in the middle Bakken rocks, Biot's coefficients are 0.6–0.79 for sandstones, 0.62–0.75 for dolomites, and 0.69–0.83 for limestones (Wang and Zeng, 2011). Biot's coefficients in shales are poorly documented. Few oedometric experiments on shales and marls indicate that Biot's coefficients are around 0.7 (Burrus, 1998). Biot's coefficients from laboratory tests in different rocks show that Biot's coefficient is a function of porosity (Cosenza et al., 2002). Experimental results also show that Biot's coefficient values decrease as the

Table 2.5 Matrix bulk and shear moduli, densities, and compressional velocities in typical minerals.

Mineral type	K (GPa)	G (GPa)	ρ (g/cm^3)	V_p (km/s)
Calcite	76.8	32	2.71	6.64
Gulf clay	25	9	2.55	3.81
Quartz	37	44	2.65	6.05
Dolomite	76.4	49.7	2.87	7.0

differential pressure (the confining pressure minus pore pressure) increases. Laboratory bulk volume test results (Fatt, 1959) on the Boise sandstone show that Biot's coefficient values range from 1 (very low differential pressure of 0.5 MPa), 0.82 (differential pressure of 20 MPa) to 0.77 (high differential pressure of 60 MPa). Therefore, Biot's coefficient values decrease as the differential confining pressure increases.

The Bakken shale samples from the Williston Basin were tested to obtain Biot's coefficient (He et al., 2016) through measuring the variations of both confining pressure and pore pressure. The experimental results show that Biot's coefficients are dependent on rock permeability and have anisotropic behavior. The vertical (perpendicular to the bedding) samples have much lower Biot's coefficients than those in the horizontal samples, i.e.,

$$\alpha_V = c\alpha_h \tag{2.79}$$

where α_V and α_h are the vertical and horizontal Biot's coefficients, respectively; c is a parameter, $c = 0.79$ to 1 from the test results.

2.7.2 Dynamic Biot's coefficient

Theoretically, Biot's coefficient cannot be calculated from the bulk modulus obtained by dynamic methods (such as P-wave and S-wave measurements) because the static modulus values are required by the theory. However, dynamic bulk modulus, compressional velocity, and other dynamic values can be used to obtain an empirical Biot's coefficient. The dynamic bulk modulus in a dry rock can be obtained from the following theoretical equation:

$$K_d = \rho_d\left(V_{pd}^2 - 4V_{sd}^2/3\right) \tag{2.80}$$

where K_d, ρ_d, V_{pd}, and V_{sd} are the dynamic bulk modulus, bulk density, compressional velocity, and shear velocity of the dry rock, respectively.

The dynamic Biot's coefficient may be obtained by replacing K_{dry} by Eq. (2.80) in Eq. (2.77), i.e.,

$$\alpha_d = 1 - \frac{\rho_d\left(V_{pd}^2 - 4V_{sd}^2/3\right)}{K_m} \tag{2.81}$$

where α_d is the dynamic Biot's coefficient.

It is rarely reported on how to convert dynamic Biot's coefficient to the static one. However, dynamic bulk modulus can be related to static bulk modulus by using empirical equations presented in Section 2.5.5. As described in Section 2.6.3, the difference of dynamic and static Poisson's ratios is small; therefore, the correlations of dynamic and static Young's moduli can be used to obtain the correlations in dynamic and static bulk moduli. For example, Eq. (2.72) can be expressed in the following form:

$$K_s = kK_d \tag{2.82}$$

where K_s and K_d are the static and dynamic bulk moduli, respectively; k is a correlation factor between 0.5 and 0.79 from Eq. (2.72).

Combining Eqs. (2.81) and (2.82), the static Biot's coefficient, α, can be obtained in the following form:

$$\alpha = 1 - \frac{k\rho_d\left(V_{pd}^2 - 4V_{sd}^2/3\right)}{K_m} \tag{2.83}$$

where k is a correlation factor between 0.5 and 0.79 from Eq. (2.72).

Combining Eqs. (2.83) and (2.81), the relation of dynamic and static Biot's coefficients can be obtained, i.e.,

$$\alpha = (1 - k) + k\alpha_d \tag{2.84}$$

For example, if $\alpha_d = 0.7$ and $k = 0.6$, then from Eq. (2.84) $\alpha = 0.82$.

Fabricius et al. (2008) studied dynamic Biot's coefficients in the North Sea chalk samples, which varied considerably in depositional texture and mineralogy. They calculated dynamic Biot's coefficients from Eq. (2.81) using the velocities of the dry chalk samples and the matrix bulk modulus of calcite. Their results indicate that dynamic Biot's coefficient tends to decrease with porosity in clay-poor samples as a reflection of calcite cementation, causing the mineral frame to stiffen as porosity is filled by cement. Samples rich in smectite or chlorite tend to have relatively high Biot's coefficient, probably because the presence of clay prevents calcite cement from bridging between particles.

2.7.3 Empirical methods for Biot's coefficient

If no measured Biot's coefficient is available, the empirical equations can be used to estimate Biot's coefficient. Experimental results show that Biot's coefficient is a function of porosity; therefore, most empirical equations for

Biot's coefficient are related to porosity. Zimmerman et al. (1986) obtained the following empirical equation for the lower bound of Biot's coefficient:

$$\alpha = 1 - (1 - \phi)\left[1 + \frac{\phi(1 + \nu_s)}{2(1 - 2\nu_s)}\right]^{-1} \tag{2.85}$$

where ν_s is drained Poisson's ratio; ϕ is the porosity.

Jizba (1991) presented laboratory-measured petrophysical data and bulk moduli of 34 tight gas sandstones and 9 shales from GRI's cooperative wells in the Travis Peak Formation in East Texas. Using the static bulk moduli presented by Jizba (1991) and assuming the matrix modulus is 39 GPa, Biot's coefficient can be computed from Eq. (2.77), and the following correlation can be obtained for tight sandstones and shales under the confining pressure of 20 MPa (Fig. 2.30):

$$\alpha = 1.278\phi^{0.22} \tag{2.86}$$

For hard formations, porosity $\phi < 0.37$, the equation in the paper of Raymer et al. (1980) was rewritten in the following form as the empirical equation of Biot's coefficient by Krief et al. (1990):

$$\alpha = 1 - (1 - \phi)^{3.8} \tag{2.87}$$

Krief et al. (1990) also gave a more general form of empirical equation of Biot's coefficient:

$$\alpha = 1 - (1 - \phi)^{\frac{3}{1-\phi}} \tag{2.88}$$

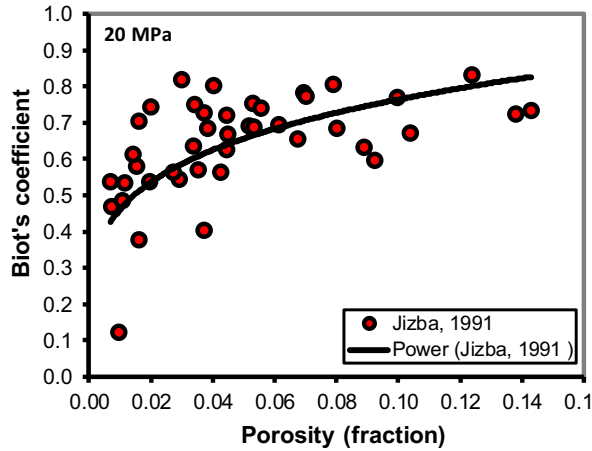

Figure 2.30 Biot's coefficient computed from laboratory results presented by Jizba (1991) in tight sandstones and shales under the confining pressure of 20 MPa.

For unconsolidated sediments Biot's coefficient is large and may approach 1, and the following empirical equation was suggested by Lee (2003):

$$\alpha = 0.99494 - \frac{184.05}{1 + e^{(\phi+0.56468)/0.10817}} \tag{2.89}$$

where porosity ϕ is in fractions.

Biot's coefficient predicted from Eq. (2.89) is adequate for a differential pressure about 20 MPa based on the calibration from the data presented by Domenico (1976). Notice that these empirical equations did not consider the effect of the differential pressure.

2.7.4 Biot's coefficient estimate from well logs

Shear deformation does not produce a pore-volume change, and consequently different fluids do not affect shear modulus. Therefore, dry rock shear modulus (μ_d) should be equal to the saturated formation shear modulus (μ_{fm}). Thus, Biot's coefficient can be approximately obtained using the formation shear modulus and matrix shear modulus (μ_{ma}) as shown in the following equation, particularly for a gas-filled formation (Krief et al., 1990):

$$\alpha = 1 - \frac{\mu_{fm}}{\mu_{ma}} \tag{2.90}$$

Therefore, dynamic Biot's coefficient can be expressed as the following form:

$$\alpha_d = 1 - \frac{\rho_b V_S^2}{\rho_m V_{Sma}^2} \tag{2.91}$$

where V_S and V_{Sma} are the shear velocities of the formation and the matrix, respectively.

From Eq. (2.90), if the dynamic formation shear and matrix shear moduli have the same constant (k) to convert to static ones, then Eq. (2.91) is also the static Biot's coefficient (α).

The formation bulk density can be expressed as a function of the matrix density (ρ_m) and porosity, i.e., $\rho_b = (1 - \phi)\rho_m + \phi\rho_f$. Substituting it to Eq. (2.91), the following equation can be obtained:

$$\alpha = 1 - [(1 - \phi) + \phi\rho_f/\rho_m]\frac{V_S^2}{V_{Sma}^2} \tag{2.92}$$

For the gas-filled low porosity formation, $(1-\phi) >> \phi\rho_f/\rho_m$. Thus, Eq. (2.92) can be simplified as:

$$\alpha = 1 - \frac{(1-\phi)V_S^2}{V_{Sma}^2} \tag{2.93}$$

where the formation shear velocity V_S can be obtained from downhole sonic log (shear transit time). The shear velocity of the matrix (V_{Sma}) can be obtained from the shear velocity in the minerals that the rock is composed of. If expressed in shear transit time, Eq. (2.93) can be rewritten in the following form:

$$\alpha = 1 - \frac{(1-\phi)\Delta t_{s\_ma}^2}{\Delta t_s^2} \tag{2.94}$$

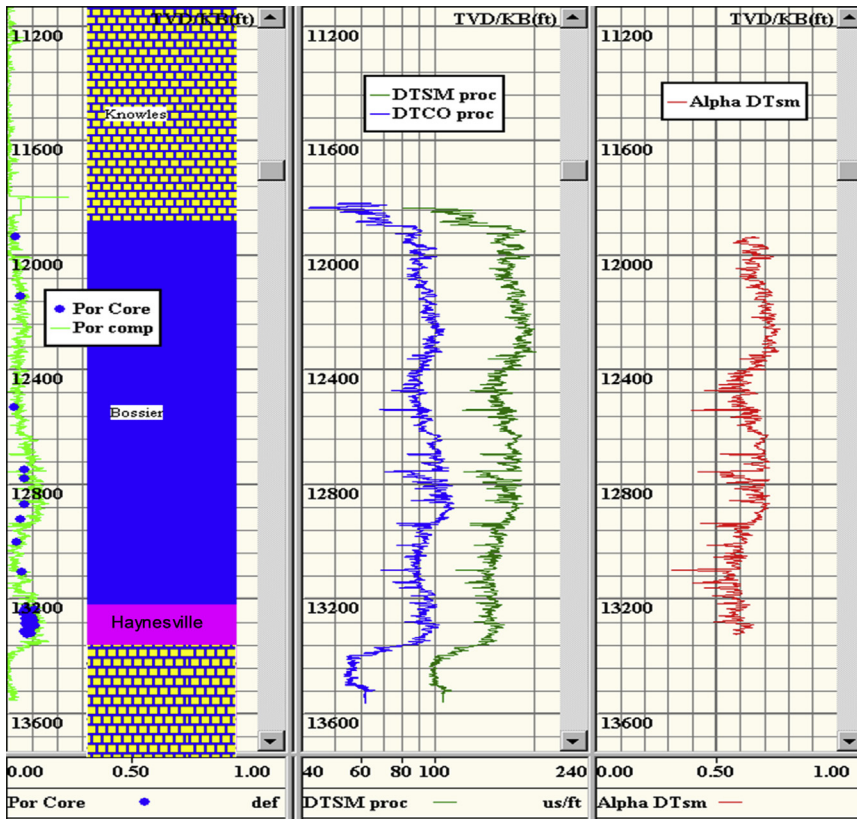

Figure 2.31 Biot's coefficient computed from downhole well log data in the Bossier and Haynesville shales. The left track shows the porosities from well log and core tests with lithology column; the middle track presents the sonic log of the compressional and shear transit time; the right track is the calculated Biot's coefficient from Eq. (2.94).

where Δt_{s_ma} is the shear transit time of the matrix; Δt_s is the shear transit time of the rock. Therefore, if well log data are available (porosity and shear velocity or shear transit time), Biot's coefficient can be obtained from Eq. (2.94).

Fig. 2.31 displays an example using well log data and Eq. (2.94) to compute Biot's coefficient by assuming $\Delta t_{s\_ma} = 100$ μs/ft.

References

Archie, G.E., 1942. The electrical resistivity log as an aid in determining some reservoir characteristics. Trans. AIME 146 (1), 54–62.

Athy, L.F., 1930. Density, porosity, and compaction of sedimentary rocks. AAPG Bull. 14 (1), 1–24.

Bai, M., Elsworth, D., 1994. Modeling of subsidence and stress-dependent hydraulic conductivity for intact and fractured porous media. Rock Mech. Rock Eng. 27, 209–234.

Barton, N., 2007. Rock Quality, Seismic Velocity, Attenuation and Anisotropy. CRC Press.

Bender, C.V., Bourgoyne, A.T., Suhayda, J.N., 1996. Estimating break-down pressure of upper marine sediments using soil boring data. J. Pet. Sci. Eng. 14, 101–114.

Bourbie, T., Zinszner, B., 1985. Hydraulic and acoustic properties as a function of porosity in Fontainebleau sandstone. J. Geophys. Res. 90, 11524–11532.

Bouteca, M., Sarda, J.-P., 1995. Experimental measurements of thermoporoelastic coefficients. In: Charlez, P. (Ed.), Mechanics of Porous Media. Balkema, Rotterdam.

Burrus, J., 1998. Overpressure models for clastic rocks, their relation to hydrocarbon expulsion: a critical reevaluation. In: Law, B.E., Ulmishek, G.F., Slavin, V.I. (Eds.), Abnormal Pressures in Hydrocarbon Environments: AAPG Memoir, vol. 70, pp. 35–63.

Castagna, J.P., Batzle, M.L., Eastwood, R.L., 1985. Relationship between compressional-wave and shear-wave velocities in clastic silicate rocks. Geophysics 50 (4), 571–581.

Cosenza, P., Ghoreychi, M., de Marsily, G., Vasseur, G., Violette, S., 2002. Theoretical prediction of poroelastic properties of argillaceous rocks from in situ specific storage coefficient. Water Resour. Res. 38, 25-1–25-12.

Detournay, E., Cheng, A.H.-D., 1993. Fundamentals of poroelasticity. In: Fairhurst, C. (Ed.), Comprehensive Rock Engineering: Principles, Practice and Projects, Analysis and Design Method, vol. II. Pergamon Press, pp. 113–171 (Chapter 5).

Domenico, S.N., 1976. Effect of brine-gas-mixture on velocity in an unconsolidated sand reservoir. Geophysics 41, 882–894.

Eberhart-Phillips, D., Han, D.-H., et al., 1989. Empirical relationships among seismic velocity, effective pressure, porosity and clay content in sandstone. Geophysics 54, 82–89.

Fabricius, I., Gommesen, L., Krogsbøll, A., Olsen, D., 2008. Chalk porosity and sonic velocity versus burial depth: influence of fluid pressure, hydrocarbons, and mineralogy. AAPG Bull. 92, 201–223.

Fatt, I., 1959. The Biot-Willis elastic coefficients for a sandstone. J. Appl. Mech. 26, 296–297.

Flemings, P.B., Stump, B.B., et al., 2002. Flow focusing in overpressured sandstones: theory, observations and applications. Am. J. Sci. 302, 827–855.

Gardner, G.H.F., Gardner, L.W., Gregory, A.R., 1974. Formation velocity and density – the diagnostic basics for stratigraphic traps. Geophysics 39 (6), 770–780.

Han, D., 1986. Effects of Porosity and Clay Content on Acoustic Properties of Sandstones and Unconsolidated Sediments. Ph.D. dissertation, Stanford University.
He, J., Rui, Z., Ling, K., 2016. A new method to determine Biot's coefficients of Bakken samples. J. Nat. Gas Sci. Eng. 35, 259–264.
Higgins, S., Goodwin, S., Donald, A., Bratton, T., Tracy, G., 2008. Anisotropic stress models improve completion design in the Baxter shale. SPE-115736.
Horsrud, P., 2001. Estimating mechanical properties of shale from empirical correlations. SPE Drill. Complet., 68–73. SPE-56017.
Howarth, D.F., 1984. Apparatus to determine static and dynamic elastic moduli. Rock Mech. Rock Eng. 17, 255–264.
Hudson, J., Harrison, J., 1997. Engineering Rock Mechanics: An Introduction to the Principles. Pergamon.
ISRM, 1979. Suggested methods for determining the uniaxial compressive strength and deformability of rock materials. Int. J. Rock Mech. Min. Sci. Geomech. Abst. 16, 135–140.
Issler, D.R., 1992. A new approach to shale compaction and stratigraphic restoration, Beaufort-Mackenzie Basin and Mackenzie Corridor, Northern Canada. AAPG Bull. 76 (8), 1170–1189.
Jaeger, J.C., Cook, N.G.W., Zimmerman, R., 2007. Fundamentals of Rock Mechanics, fourth ed. Blackwell Publishing.
Jizba, D., 1991. Mechanical and Acoustical Properties of Sandstones and Shales. Ph.D. thesis, Stanford University.
Jones, F.O., 1975. A laboratory study of the effects of confining pressure on fracture flow and storage capacity in carbonate rocks. J. Pet. Technol. 27 (1), 21–27.
King, M.S., 1966. Wave velocities in rocks as a function of changes in overburden pressure and pore fluid saturants. Geophysics 31, 50–73.
Kim, H., Cho, J.-W., Song, I., Min, K.-B., 2012. Anisotropy of elastic moduli, P-wave velocities, and thermal conductivities of Asan Gneiss, Boryeong shale, and Yeoncheon Schist in Korea. Eng. Geol. 147–148, 68–77.
Knorr, A.F., 2016. The Effect of Rock Properties on Fracture Conductivity in the Eagle Ford. M.S. thesis, Texas A & M University.
Krief, M., Garta, J., Stellingwerff, J., Ventre, J., 1990. A petrophysical interpretation using the velocities of P and S waves (full-waveform sonic). Log. Anal. 31, 355–369.
Lacy, L.L., 1997. Dynamic rock mechanics testing for optimized fracture designs. SPE-38716.
Lee, M.W., 2003. Velocity ratio and its application to predicting velocities. US Geol. Surv. Bull. 2197. US Department of the Interior and US Geological Survey.
Louis, C., 1974. Rock hydraulics. In: Muller, L. (Ed.), Rock Mechanics. Springer Verlag, Vienna, pp. 299–382.
Mavko, G., Mukerji, T., Dvorkin, J., 2009. The Rock Physics Handbook: Tools for Seismic Analysis of Porous Media. Cambridge University Press.
Martin, R., Haupt, R., 1994. Static and dynamic elastic moduli in granite: the effect of strain amplitude. In: 1st North American Rock Mechanics Symposium, 1–3 June, Austin, Texas.
Meng, Z., Zhang, J., Peng, S., 2006. Influence of sedimentary environments on mechanical properties of clastic rocks. Environ. Geol. 51 (1), 113–120.
Mondol, N.H., Bjørlykke, K., Jahren, J., Høeg, K., 2007. Experimental mechanical compaction of clay mineral aggregates—changes in physical properties of mudstones during burial. Mar. Petrol. Geol. 24 (5), 289–311.
Nelson, P.H., Bird, K.J., 2005. Porosity-Depth Trends and Regional Uplift Calculated from Sonic Logs, National Petroleum Reserve in Alaska. Scientific Investigations Report 2005–5051. U.S. Geological Survey.

Niandou, H., Shao, J.F., Henry, J.P., Fourmaintraux, D., 1997. Laboratory investigation of the behaviour of Tournemire shale. Int. J. Rock Mech. Min. Sci. 34 (1), 3–16.
Nur, A., 1971. Effects of stress on velocity anisotropy in rocks with cracks. J. Geophys. Res. 76 (8), 2022–2034.
Nur, A., Byerlee, J.D., 1971. An exact effective stress law for elastic deformation of rocks with fluids. J. Geophys. Res. 76, 6414–6419.
ODP, Ocean Drilling Program Janus Web Database (http://www-odp.tamu.edu/database/), 2008.
Ohen, H.A., 2003. Calibrated wireline mechanical rock properties method for predicting and preventing wellbore collapse and sanding. SPE-82236.
Ostermeier, R.M., Pelletier, J.H., Winker, C.D., Nicholson, J.W., 2001. Trends in shallow sediment pore pressures – deepwater Gulf of Mexico. Paper SPE/IADC 67772 presented at the SPE/IADC Drilling Conf. Held in Amsterdam, The Netherlands, 2001.
Peng, S., Zhang, J., 2007. Engineering Geology for Underground Rocks. Springer.
Phani, K.K., Niyogi, S.K., 1987. Young's modulus of porous brittle solids. J. Mater. Sci. 22, 257–263.
Pickett, G.R., 1963. Acoustic character logs and their applications in formation evaluation. J. Pet. Technol. 15, 650–667. SPE-452-PA.
Raiga-Clemenceau, J., Martin, J.P., Nicoletis, S., 1988. The concept of acoustic formation factor for more accurate porosity determination from sonic transit data. Log. Anal. 29, 54–60.
Raymer, L.L., Hunt, E.R., Gardner, J.S., 1980. An improved sonic transit time-to-porosity transform. In: Transactions of the SPWLA 21st Annual Logging Symposium, vol. 21. Society of Professional Well Log Analysts, Houston, TX, United States, pp. P1–P13.
Santarelli, F.J., 1987. Theoretical and Experimental Investigation of the Stability of the Axisymmetric Wellbore. Ph.D. thesis, University of London.
Schön, J.H., 1996. Physical properties of rocks: fundamentals and principles of petrophysics. In: Handbook of Geophysical Exploration: Seismic Exploration. Pergamon. Book 18.
Sone, H., 2012. Mechanical Properties of Shale Gas Reservoir Rocks and Its Relation to the In-Situ Stress Variation Observed in Shale Gas Reservoirs. Ph.D. dissertation, Stanford University.
Sone, H., Zoback, M., 2013. Mechanical properties of shale-gas reservoir rocks – Part 1: Static and dynamic elastic properties and anisotropy. Geophysics 78 (5), D381–D392.
Thomsen, L., 1986. Weak elastic anisotropy. Geophysics 51, 1954–1966.
Thiercelin, M.J., Plumb, R.A., 1994. Core-based prediction of lithologic stress contrasts in East Texas formations. SPE Form. Eval. 9 (4), 251–258.
Timur, A., 1968. An investigation of permeability, porosity, and residual water saturation relationship for sandstone reservoirs. Log. Anal. 9 (4).
Tutuncu, A., Podiot, A., Gregory, A., Sharma, M., 1998. Nonlinear viscoelastic behavior of sedimentary rocks, Part I: Effect of frequency and strain amplitude. Geophysics 63, 184–194.
Walsh, J.B., 1981. Effect of pore pressure and confining pressure on fracture permeability. Int. J. Rock Mech. Min. Sci. Geomech. Abstr. 18 (3), 429–435.
Wang, C., Zeng, Z., 2011. Overview of Geomechanical Properties of Bakken Formation in Williston Basin. ARMA, North Dakota, pp. 11–199.
Wang, Z., 2002. Seismic anisotropy in sedimentary rocks, Part 2: Laboratory data. Geophysics 67, 1423–1440.
Witherspoon, P.A., Wang, J.S.Y., Iwai, K., Gale, J.E., 1980. Validity of cubic law for fluid flow in a deformable rock fracture. Water Resour. Res. 16 (6), 1016–1024.
Wyllie, M.R.J., Gregory, A.R., Gardner, L.W., 1956. Elastic wave velocities in heterogeneous and porous media. Geophysics 21 (1), 41–70.

Yale, D., Jamieson, W., 1994. Static and dynamic rock mechanical properties in the Hugoton and Panoma Fields, Kansas. SPE-27939.
Zhang, J., 2002. Dual-Porosity Approach to Wellbore Stability in Naturally Fractured Reservoirs. Ph.D. dissertation, The University of Oklahoma.
Zhang, J., Standifird, W.B., Lenamond, C., 2008. Casing ultradeep, ultralong salt sections in deep water: a case study for failure diagnosis and risk mitigation in record-depth well. SPE 114273.
Zhang, J., Lang, J., Standifird, W., 2009. Stress, porosity, and failure dependent compressional and shear velocity ratio and its application to wellbore stability. J. Pet. Sci. Eng. 69, 193–202.
Zhang, J., Standifird, W., Roegiers, J.C., Zhang, Y., 2007. Stress-dependent permeability in fractured media: from lab experiments to engineering applications. Rock Mech. Rock Eng. 40 (1), 3–21.
Zhang, J., Bai, M., Roegiers, J.C., Wang, J., Liu, T., 2000. Experimental determination of stress-permeability relationship. In: Proc 4th North American Rock Mech. Symp., Seattle. Balkema, Rotterdam, pp. 817–822.
Zhang, J., Wieseneck, J., 2011. Challenges and surprises of abnormal pore pressure in shale gas formations. SPE 145964.
Zhang, J., Kamenov, A., Zhu, D., Hill, A.D., 2014. Laboratory measurement of hydraulic-fracture conductivities in the Barnett shale. SPE J. 29 (3), 216–227. SPE-163839.
Zimmerman, R.W., Somerton, W.H., King, M.S., 1986. Compressibility of porous rocks. J. Geophys. Res. 91 (B12), 12765–12777.
Zoback, M., 2007. Reservoir Geomechanics. Cambridge University Press.

CHAPTER 3

Rock strengths and rock failure criteria

Contents

Abstract

Laboratory test methods are introduced to determine stress—strain relationships and rock strengths. Rock failure mechanisms are studied based on uniaxial and triaxial

Applied Petroleum Geomechanics
ISBN 978-0-12-814814-3
https://doi.org/10.1016/B978-0-12-814814-3.00003-4

compression tests. Empirical equations and correlations between rock strengths and petrophysical and geophysical properties are presented for different lithologies. New correlations for deepwater reservoirs and shale oil and shale gas formations are proposed. These correlations enable one to obtain continuous rock strengths along the depth interval of interest from well logging and seismic data (e.g., sonic velocity, transit time, and porosity). Rock failure criteria are examined to reveal rock failure mechanisms, including linear and nonlinear Mohr—Coulomb, Drucker—Prager, true triaxial, Cam—Clay, and modified Griffith failure criteria. Their suitability and applicability for geomechanical modeling are also discussed. The anisotropy of rock strengths and its impact on rock failures are also investigated.

Keywords: Anisotropy; Failure criterion; Laboratory test; Rock strength; Strength correlation; Well log.

3.1 Laboratory tests for rock strengths

Laboratory tests usually consist of simple experiments appropriate to the nature of the rock in which important quantities, often stress and strain, are determined (Jaeger and Cook, 1979). Different types of laboratory tests can be used to obtain rock strength, Young's modulus, and other mechanical properties. Fig. 3.1 shows some typical laboratory tests, as introduced in the following:

(1) Uniaxial compression test (Fig. 3.1A): the cylindrical rock specimen is only compressed in the axial direction by the axial load or stress of σ_1;

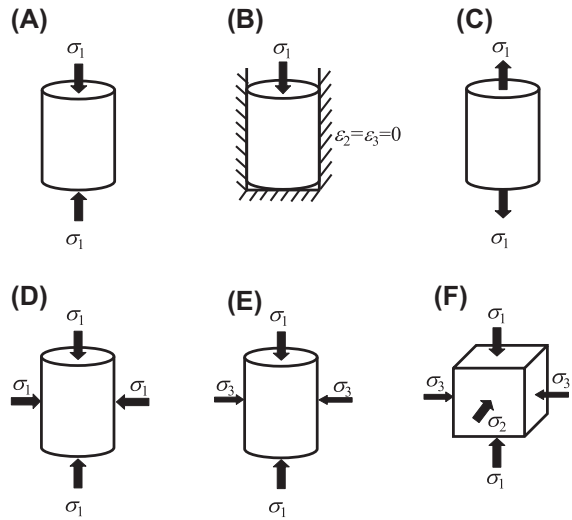

Figure 3.1 Schematic diagram showing typical laboratory tests to obtain rock mechanical properties. (A) uniaxial compression; (B) uniaxial strain; (C) tensile; (D) hydrostatic; (E) triaxial compression; (F) polyaxial compression.

(2) Uniaxial strain test (Fig. 3.1B): the cylindrical rock specimen is only loaded in the axial direction, and the lateral direction is constrained (no lateral displacement);
(3) Tensile test (Fig. 3.1C): the cylindrical rock specimen is applied tensional force (stress) in the axial direction;
(4) Hydrostatic test (Fig. 3.1D): the cylindrical rock specimen is compressed with the same stress in all directions;
(5) Triaxial compression tests (Fig. 3.1E): the cylindrical rock specimen is compressed in both axial and lateral directions. The axial stress (σ_1) is greater than the lateral stress (σ_3, confining pressure);
(6) Polyaxial (true triaxial) compression test (Fig. 3.1F): three independent and mutually perpendicular stresses (σ_1, σ_2, and σ_3) load to the faces of a rectangular prismatic specimen.

3.1.1 Uniaxial tensile test

Uniaxial tensile strength describes the capacity of the rock to resist tensile stress. It is one of the most important parameters for hydraulic fracturing design. The direct (Fig. 3.1C) and indirect (point load and Brazilian tests) methods can be used to back calculate tensile strength. The direct measurement of tensile strength can be performed by gluing both ends of a cylindrical rock specimen to metal front plates that are fixed to the platens of a load frame. The glue or cement has to be more resistant to tensile stress than the specimen (Shang et al., 2016).

The indirect methods (e.g., the Brazilian test) have been dominant in determining tensile strengths of rocks due to their ease in sample preparation and testing procedure. The Brazilian test is performed by applying a load by two platens diametrically compressed to a rock cylinder (Fig. 3.2). The technique involves loading a disc-shaped specimen in compression across its diameter. Such loading generates a tensile stress at the center of the disc in a direction perpendicular to the direction of the applied load. Failure occurs by an extensional fracture in or close to the loaded diametral plane. The tensile strength is given by the ratio of the peak load P to the diameter and thickness product (ISRM, 1978):

$$T_0 = \frac{2P}{\pi D t} \tag{3.1}$$

where D and t are the sample diameter and thickness in mm; P is the load at failure in Newtons; T_0 is the uniaxial tensile strength in MPa.

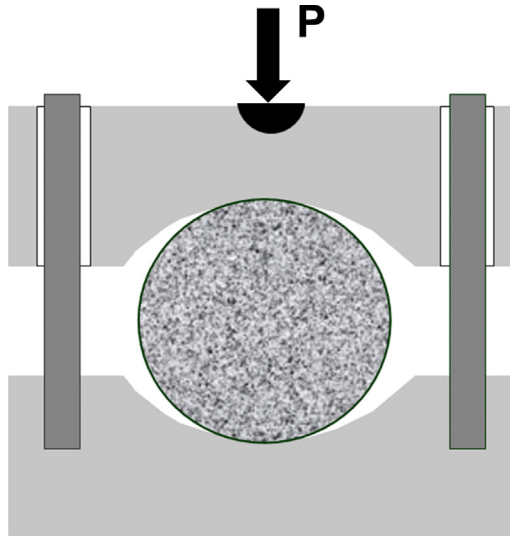

Figure 3.2 Schematic Brazilian test and the specimen.

Brazilian method often overestimates the tensile strength of the poorly consolidated rock because the line load applied during the test typically widens for a soft material (Peng and Zhang, 2007). In such a case, a line load is no longer applied and the force is distributed over a larger area. Consequently, a higher tensile strength is calculated.

3.1.2 Uniaxial compression test

Uniaxial compression test (Fig. 3.1A) is used to determine uniaxial compressive strength (UCS), Poisson's ratio, and Young's modulus. Uniaxial compression test is also called unconfined compression test. In this test, a circular cylinder of rock sample is compressed parallel to its longitudinal axis. It is the oldest and simplest test and continues to be one of the most convenient and useful ways for determining the properties of rocks. During the test, the loads in the axial direction, displacements (normally measured by linear variable displacement transformers), and strains (can be measured by extensometers) in both axial and radial directions are recorded for rock strength analyses.

In the uniaxial test, the following equation is used for calculating the UCS for the ISRM suggested samples.

$$UCS = \frac{P_{\max}}{A} \tag{3.2}$$

where P_{max} is the maximum load exerted on the rock sample; A is the area of the cross section of the sample.

ISRM (1979) recommends that the test specimen should be a right circular cylinder, having a diameter approximately 54 mm, and a height-to-diameter ratio of 2.5–3. If the sample size does not meet this requirement, the strength test results obtained from Eq. (3.2) will need to be corrected. Based on an analysis of a series of laboratory test data, Hoek and Brown (1980) found that rock UCS decreases as the sample size increases. They proposed that the UCS should be normalized by dividing individual strength of each sample to the strength of a sample with a diameter of 50 mm. The proposed correction is determined by the following equation:

$$\sigma_c = \sigma_{c50}\left(\frac{50}{d}\right)^{0.18} \tag{3.3}$$

where σ_c is the corrected UCS for rock specimen with a diameter of d (mm); σ_{c50} is the UCS for rock specimen with a diameter of $d = 50$ mm.

Based on laboratory studies the rock failure process can be broken down into a number of stages characterized by changes in the measured axial and lateral strain response recorded during uniaxial and triaxial compression tests (Fig. 3.3). In the figure the axial and lateral strains are measured and the volumetric and crack volumetric strains are calculated. These stages include (Eberhardt et al., 1999):

(1) Crack closure (at stress of σ_{cc}).

Crack closure, at stress of σ_{cc}, occurs during the initial stages of loading when existing cracks orientated at an angle to the applied load close. During crack closure, the stress–strain response is nonlinear, exhibiting an increase in axial stiffness.

(2) Linear elastic deformation (from σ_{cc} to σ_{ci}).

Once the majority of existing cracks have closed, linear elastic deformation takes place.

(3) Crack initiation and stable crack growth (from σ_{ci} to σ_{cd}).

Crack initiation, σ_{ci}, represents the stress level where the loading-induced microfracturing begins. The growth of these cracks has been shown to occur in the direction of the major principal stress, σ_1, and cracks grow along a curved path to align themselves with σ_1. The opening of cracks with faces parallel to the applied load is therefore detected as a departure from linear lateral and volumetric strain behaviors.

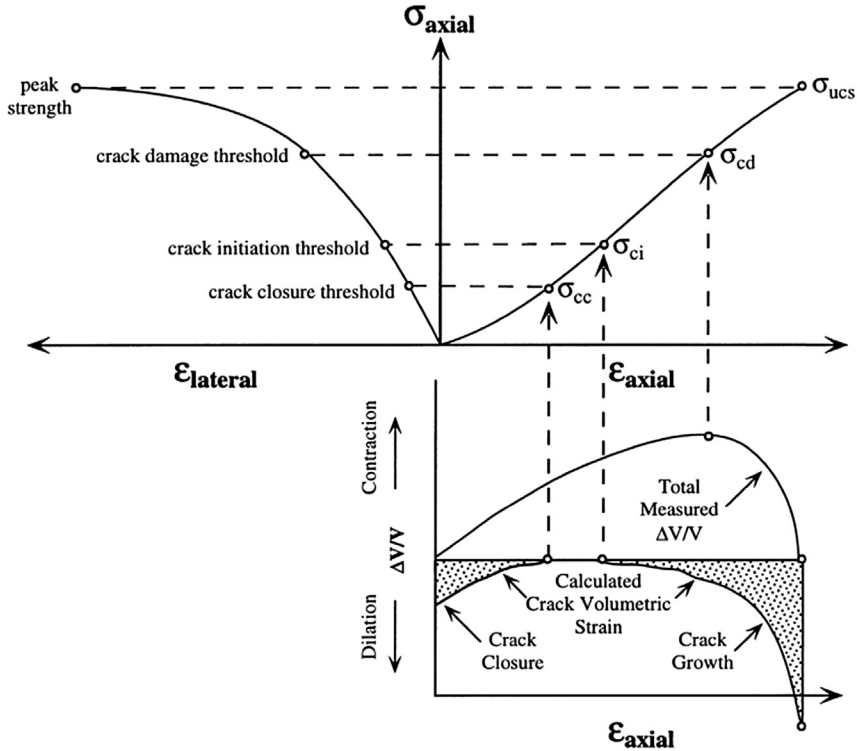

Figure 3.3 Stress–strain diagram obtained from a single uniaxial compression test for Lac du Bonnet granite showing the definition of crack initiation (σ_{ci}), crack damage (σ_{cd}), and peak strength (σ_{ucs}) (Martin and Chandler, 1994).

(4) Crack damage and unstable crack growth (from σ_{cd} to peak strength σ_{ucs}).

Crack propagation is either stable or unstable. Under stable conditions, crack growth can be stopped by controlling the applied load. Unstable crack growth, also referred to as the crack damage stress threshold, σ_{cd}, has been associated with the point of reversal in the total volumetric strain curve (Fig. 3.3). Under such conditions, crack propagation will continue until failure even if the applied loading is held constant.

(5) Failure and postpeak behavior.

Once the applied load exceeds the peak strength (UCS), rock starts failure, and the rock loses to its partial or all capacity to bear loading dependent on the plasticity of the rock. For a brittle rock, it may lose the capacity; however, for ductile (plastic) rock, it may still have capacity to partially bear the applied load.

3.1.3 Triaxial compression test and rock peak strengths

The triaxial compression test has proved to be the most useful test in the study of the mechanical properties of rocks under a wide range of stress values (Jeager, Cook et al., 2007). In a triaxial compression test, the major principal stress (σ_1) is applied along the axis of a cylindrical rock specimen, and a minor principal stress (σ_3, and $\sigma_2 = \sigma_3$) is applied to the curved surfaces of the specimen by fluid-confining pressure (confining stress). Notice that the confining pressure and confining stress are interchangeably used in the triaxial test. Fig. 3.4 shows the axial stresses, confining stresses, and strains (both axial and lateral) in a typical triaxial compression test in the Middle Bakken formation. The rock strength is the peak value of the load (applied axial stress) of each curve of Fig. 3.4. It shows that the rock strength increases as the confining pressure increases. Therefore, the rock has a higher strength when it is subjected to three-dimensional compressions. It should be noted that the UCS (i.e., when the confining stress is zero) is the lowest strength, but it is an important parameter used in rock failure criteria for geomechanical analyses. The triaxial tests also show that Young's modulus (the slope in each stress-axial strain curve in Fig. 3.5) is not a constant but increases as the confining pressure increases.

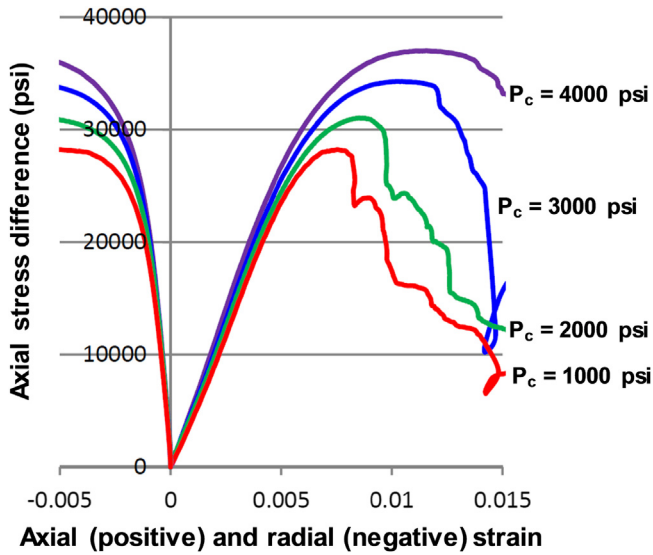

Figure 3.4 Middle Bakken stress–strain curve from triaxial compression test with various confining stresses (P_c) (Amendt et al., 2013, SPWLA).

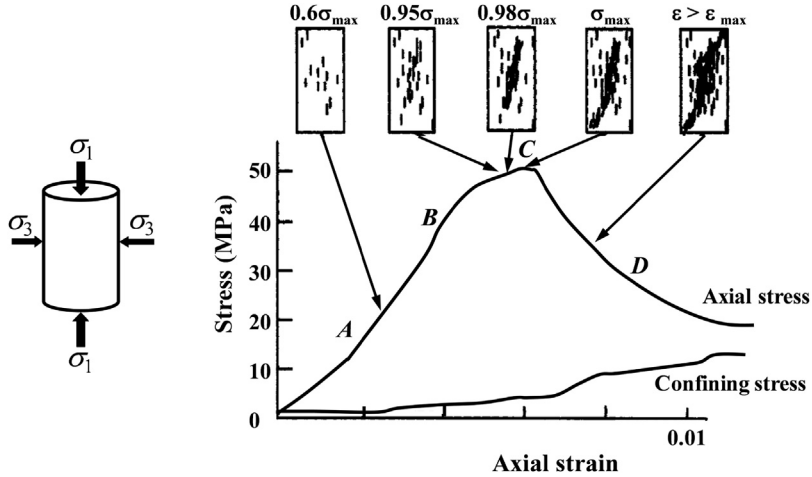

Figure 3.5 Schematic representation of the axial stress and lateral confining stress measured by Hallbauer et al. (1973) on a set of argillaceous quartzite specimens, along with cartoons of the state of microcracking observed on specimens that were loaded to the indicated points along the stress–strain curve.

Fig. 3.5 presents the triaxial compression tests conducted by Hallbauer et al. (1973) on argillaceous quartzite specimens. In the tests, they also performed macroscopic and microscopic photographic studies of longitudinal sections of each specimen and showed how the development of fractures and microcracks was related to the stress–strain curves. Careful observation of longitudinal sections cut through the axes of the specimens allowed the growth of microcracks and fractures to be observed in relation to the stress–strain curve. In region AB of the stress–strain curve, as illustrated in Fig. 3.5, the first visible structural damage appears as mainly intragranular and elongated microcracks having their axes oriented parallel (within ± 10 degrees) to the direction of maximum compressive stress (i.e., axially). The cracks are distributed throughout the sample but are concentrated in the center. Toward the end of region BC, the number of microcracks increases drastically, and the cracks begin to coalesce along a plane located in the central region of the specimen. At the point C of the maximum axial stress, the microcracks begin to link up to form a macroscopic fracture plane, which is approximately parallel to the diagonal direction of the specimen. Finally, in region CD, the fracture plane has extended through the entire specimen, and shear displacement begins to occur across the two faces of the rock (Jeager, Cook et al., 2007).

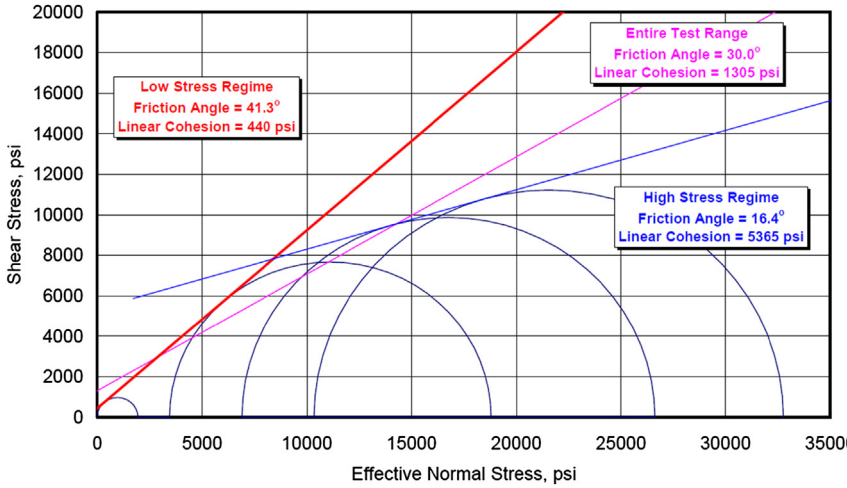

Figure 3.6 Mohr–Coulomb strength envelopes obtained from triaxial compression tests for weak sandstone at depth of 28,014 ft TVD KB in the Gulf of Mexico (Zhang et al., 2008).

When a series of triaxial compression tests are conducted, the cohesion and angle of internal friction of the rock can be obtained from the Mohr circles and strength envelopes. Fig. 3.6 plots the Mohr circles and the Mohr–Coulomb strength envelopes from three triaxial compression tests and one uniaxial test in a weak sandstone in the Gulf of Mexico. It indicates that the rock may have different strength envelopes for different confining stresses. From these tests, the cohesion and angle of internal friction of the rock can be obtained from the Mohr circles and strength envelopes (refer to Section 3.4.2). Fig. 3.6 shows that the cohesion (c) is 440 psi, when the confining stress is less than 6890 psi; whereas, when confining stress is greater than 6890 psi, the cohesion is significantly higher ($c = 5365$ psi). This observation suggests that when confining stress gets higher, the apparent rock cohesion starts to increase while the angle of internal friction tends to reduce. For example, if the mud weight is 10 ppg at a depth of 12,000 ft, the mud pressure (confining stress for the wellbore) is about 6234 psi. However, at the depth of 8000 ft, the same mud weight of 10 ppg is equivalent to a mud pressure of 4156 psi (i.e., a smaller confining stress for the wellbore). That is, for the same mud weight at a shallower depth, the wellbore has a lower cohesive strength and may be more likely to experience shear failures. Certainly, the confining stress is only one of the factors to impact wellbore stability.

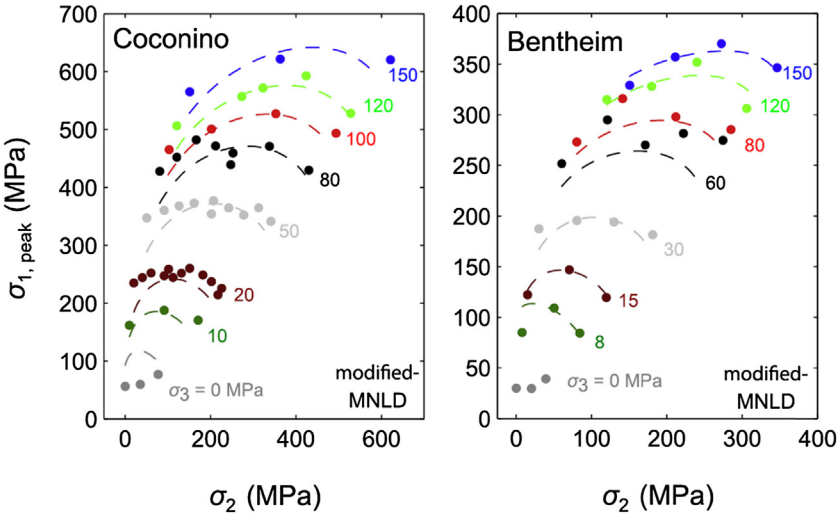

Figure 3.7 Variations of peak strength ($\sigma_{1,\ peak}$) with σ_2 in Coconino and Bentheim sandstones tested under the common loading path for all constant σ_3 levels: solid dots are the experimental data (Ma et al., 2017).

3.1.4 Polyaxial compression test

In the polyaxial compression test (also called true triaxial compression test), three independent and mutually perpendicular uniform loads apply to the faces of a rectangular prismatic specimen. That is, the maximum, intermediate, and least compressive principal stresses are applied separately. Earlier polyaxial cells built by Mogi (1971) and Spetzler et al. (1981) were mainly suited for testing deformational and strength characteristics of weak to medium strength rocks. The University of Wisconsin designed and fabricated a true triaxial testing system suitable for testing both weak and competent rocks (Haimson and Chang, 2000). The polyaxial compression tests can simulate the in situ loading scenarios in actual field condition. The results from the polyaxial compression tests experimentally demonstrate that rock strength is a function of the major principal stress (σ_1) and the minor principal stress (σ_3) as well as the intermediate stress (σ_2). Fig. 3.7 presents the true triaxial test results in two porous sandstones, Coconino and Bentheim (Ma et al., 2017). It reveals the effect of σ_2 and σ_3 on rock failures, and the rock peak strength increases as σ_2 and σ_3 increase.

3.2 Rock strengths from petrophysical and well log data

Compressive and tensile strengths are key inputs for geomechanical analyses, particularly the UCS. Rock strength parameters can be obtained from

core sample tests in laboratory experiments as described in the previous section. However, in most cases core samples are unavailable for laboratory testing, and empirical correlations between rock strength, geophysical, and petrophysical data can be used for estimation. These correlations usually are developed for some specific rock formations based on the relationships of laboratory core tests, geophysical data, and petrophysical data. Because there are multiple choices of strength correlations for various rock types in different geological settings, it is necessary to understand the characteristics of the correlations and their range of applicability before applying them.

3.2.1 Empirical equations of rock strengths in shales

3.2.1.1 From sonic velocity

In conventional reservoirs, shales make up over 75% of the drilled formations in the oil and gas industry, and over 70% of the borehole problems are related to shale instability (Lal, 1999). The oil and gas industry still fights borehole instability problems, particularly for drilling in geologically young formations of shales (weak shales), for example, in Tertiary and Cretaceous shales of the Gulf of Mexico, the North Sea, and the Gulf of Guinea. For evaluating wellbore stability and sand production, rock strength is one of the most important parameters. Some correlations were obtained using rock physical data (P-wave velocity (V_p), or equivalently, interval transit time ($\Delta t = 1/V_p$)), which were directly measured from sonic logs to relate to laboratory-measured rock strengths. Using an extensive shale database, Lal (1999) developed the following shale strength correlations tied only to compressional sonic velocity mainly for high porosity Tertiary shales in the Gulf of Mexico:

$$c = 5(V_p - 1)/\sqrt{V_p} \tag{3.4}$$

$$\sin\varphi = (V_p - 1)/(V_p + 1) \tag{3.5}$$

Based on Eqs. (3.4) and (3.5), the UCS can be obtained:

$$UCS = 10(V_p - 1) = 10(304.8/\Delta t - 1) \tag{3.6}$$

where the cohesion (c) and the uniaxial compressive strength (UCS) are in MPa; the angle of internal friction (φ) is in degrees; the compressional sonic velocity (V_p) is in km/s; and the transit time (Δt) is in μs/ft.

Through wireline log data and laboratory triaxial compression tests of shale samples obtained from deep boreholes from the North Sea,

Horsrud (2001) proposed the following correlation for estimating rock strength, mainly for high-porosity Tertiary shales:

$$UCS = 0.77 V_p^{2.93} \tag{3.7}$$

where UCS is in MPa; V_p is in km/s. Using the P-wave interval transit time from sonic log, Δt, (in μs/ft), the following correlations were obtained (Horsrud, 2001):

$$UCS = 0.77(304.8/\Delta t)^{2.93} \tag{3.8}$$

$$E = 0.076(304.8/\Delta t)^{3.23} \tag{3.9}$$

where Young's modulus (E) is in GPa.

Lal's and Horsrud's correlations predict rock strengths fairly well for shales in the Gulf of Mexico and the North Sea where high-porosity, unconsolidated Tertiary-aged, or younger shales are dominant. Therefore, these correlations after certain calibrations can be used to estimate UCSs in weak shales. In the above strength correlations, Horsrud's correlation predicts a higher shale strength than Lal's equation for the shale with higher sonic velocity (or lower transit time). Fig. 3.8 presents the shale UCS calculated from sonic well log data by using Lal's and Horsrud's correlations in an oil exploration well in the Gulf of Mexico.

3.2.1.2 From porosity

Rock strength and porosity have good correlations for various rocks, and porosity can be obtained from lab tests or from density and sonic logs. In the following equations, the rock strength UCS is in MPa and porosity is in percent (%). For shales in the North Sea (geologically young and weak shales, mostly high-porosity Tertiary shales), Horsrud (2001) proposed the following correlations for estimating rock UCS:

$$UCS = 243.6\phi^{-0.96} \tag{3.10}$$

Lashkaripour and Dusseault (1993) obtained a correlation based on 13 data points from publicly available sources and their own testing of shales. The mean of the UCS is approximately 79 MPa, and 9 of these 13 points have 10% porosity or less. The following is their correlation:

$$UCS = 193.4\phi^{-1.143} \tag{3.11}$$

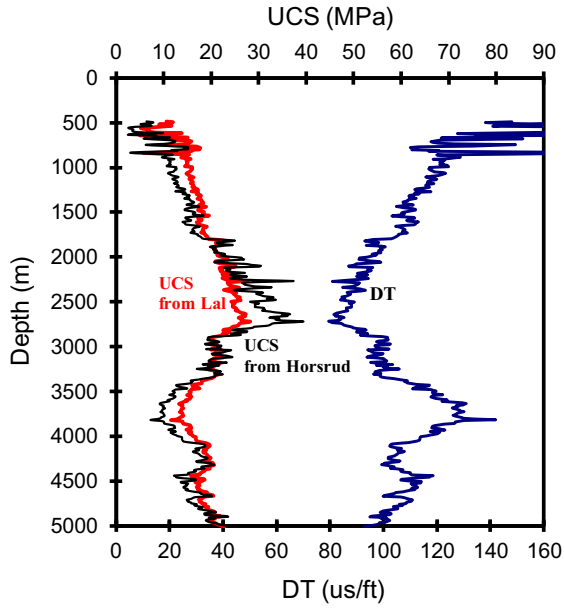

Figure 3.8 The UCSs in the Gulf of Mexico shales calculated from measured sonic transit time (Δt or DT) using Lal's and Horsrud's correlations.

For high porosity ($\phi > 27\%$) shale, Chang et al. (2006) gave the following correlation:

$$UCS = 955.8\phi^{-1.762} \tag{3.12}$$

The Haynesville shale gas formations of the Jurassic period in Northern Louisiana are tight ($\phi < 14\%$) and have very high UCSs. The laboratory measured UCS and porosity have the following relation:

$$UCS = 233.22\phi^{-0.553} \tag{3.13}$$

Gas presence in the gas-bearing shale can slow down compressional velocity of the formation (Zhang and Wieseneck, 2011); therefore, the rock strength predicted using the compressional velocity (transit time) may not be accurate. Alternatively, porosity can be used to estimate rock strength.

The above porosity-strength correlations for low porosity cases are plotted in Fig. 3.9 and compared to laboratory test results in the Haynesville shale gas formations. It shows that the Haynesville shale has a very high UCS, and this high strength is one of the major characteristics in many shale

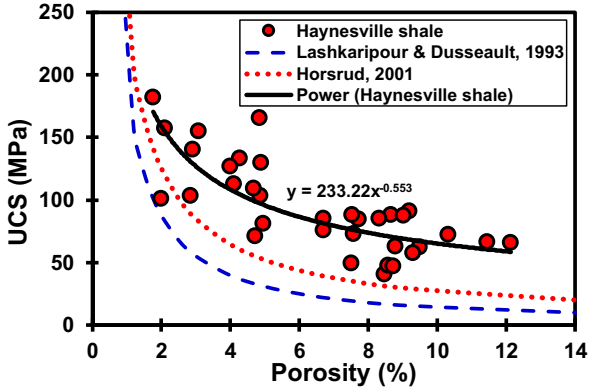

Figure 3.9 Laboratory-measured uniaxial compressive strengths versus porosities for the Haynesville shales compared to UCS-porosity correlations.

gas and shale oil formations because they normally are geologically older formations than the rocks in conventional reservoirs.

3.2.1.3 From Young's modulus

Rock UCS can also be related to Young's modulus. Chang et al. (2006) proposed the following correlation between rock strength (in MPa) and Young's modulus (in GPa) for shales:

$$UCS = 7.22E^{0.712} \tag{3.14}$$

For the data in the Tertiary shales in the deepwater ultradeep wells (7600–9000 m below the sea level) of the Gulf of Mexico (e.g., Zhang et al., 2008), the laboratory measured UCS (in MPa) and Young's modulus E (in GPa) have the following relation (see Fig. 3.10 and 3.11):

$$UCS = 14.035E^{0.5734} \tag{3.15}$$

Laboratory test data in the North Sea shale samples cored from deep boreholes (from the Tertiary to the Triassic) and three outcrop shales (Horsrud, 2001) are also plotted in Fig. 3.10 for comparison. It can be observed that the North Sea shales have a similar trend as the one in the Gulf of Mexico.

For the same data in the Haynesville shale gas formations ($\phi < 14\%$) shown previously, the laboratory-measured UCS (in MPa) and Young's modulus E (in GPa) have the following relation (refer to Fig. 3.11):

$$UCS = 23.524E^{0.4775} \tag{3.16}$$

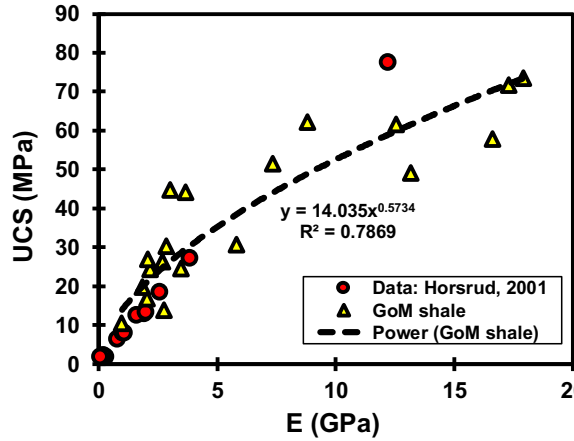

Figure 3.10 Laboratory-measured uniaxial compressive strengths (symbols) versus Young's moduli from the deep wells in the Gulf of Mexico (GoM) shales compared to the data in the North Sea.

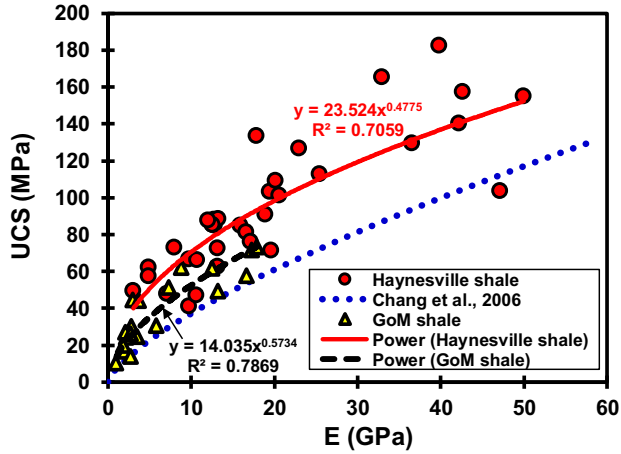

Figure 3.11 Correlations of uniaxial compressive strength and Young's modulus compared to laboratory measured results in the Haynesville shale gas formation and the Gulf of Mexico shales.

The above Young's modulus-strength correlations and laboratory test data are plotted in Fig. 3.11. It shows that rock strengths are very different in different regions, and the Haynesville shale has very high UCS magnitudes. Therefore, calibrations by local lab test data are needed for applying these correlations to a new region.

3.2.2 Empirical equations of rock strengths in sandstones

3.2.2.1 From sonic velocity and transit time

For fine grained, both consolidated and unconsolidated sandstones in the Bowen Basin of Australia, McNally (1987) presented the following strength estimation using sonic logs:

$$UCS = 1200\exp(-0.036\Delta t) \tag{3.17}$$

where UCS is in MPa and the transit time Δt is in μs/ft.

For the Tertiary reservoir sandstones in the Gulf of Mexico and the Jurassic reservoir sandstones in the North Sea, the following correlation exists between the lab-measured UCS and the compressional transit time from sonic log measurements (Fig. 3.12) :

$$UCS = 156318(1/\Delta t)^{2.064} \tag{3.18}$$

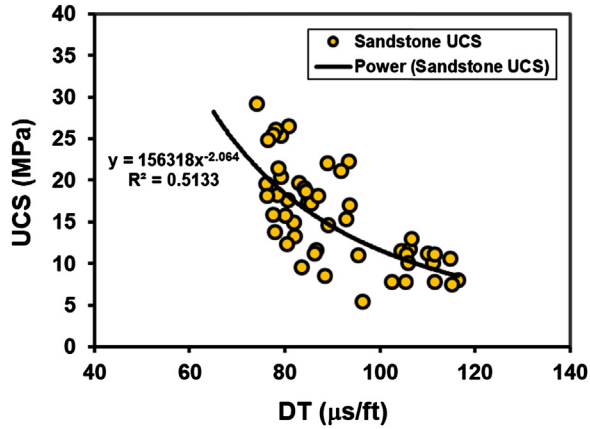

Figure 3.12 Lab-measured uniaxial compressive strengths versus sonic compressional transit time in some deep wells in the Gulf of Mexico and the North Sea.

The same units are used as those in Eq. (3.17).

Some high-porosity (~20%) sandstones are even weaker than shales, such as the Tertiary formations in the Gulf of Mexico. In this case, the wellbore breakout and sand production are expected while drilling and after reservoir production. Based on the laboratory test data in the Tertiary formations of the Gulf of Mexico and the North Sea, Zhang (2013) obtained the following empirical equation to estimate the UCS for weak (poorly consolidated) sandstones:

$$UCS = 0.68(304.8/\Delta t)^{2.5} \tag{3.19}$$

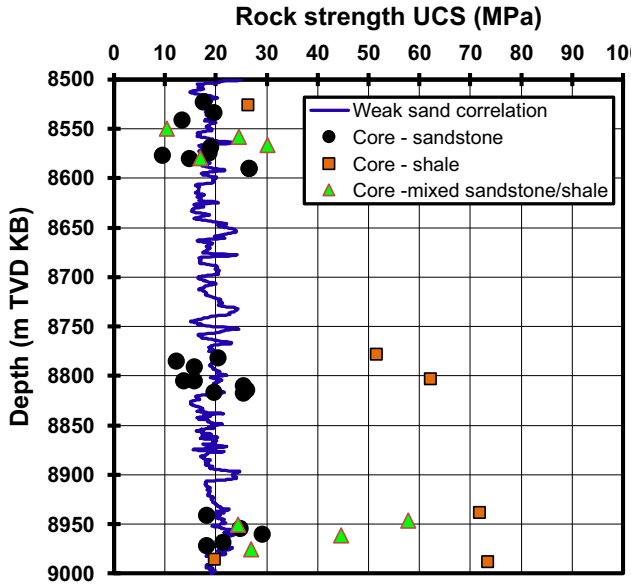

Figure 3.13 Rock uniaxial compression strengths obtained from lab compression tests in the Gulf of Mexico and calculated from sonic transit time (Δt) using the weak rock correlation (Eq. 3.19).

The same units are used as those in Eq. (3.17).

Fig. 3.13 demonstrates the UCSs from core tests in sandstones, shales, and mixed lithology of shales and sandstones in the Gulf of Mexico (Zhang et al., 2008). The data have the following characteristics: (1) there are two groups in the rock strength data—a lower UCS group and a higher UCS group. Most rocks in the higher UCS group are shale formations; (2) Lal's and Horsrud's correlations underestimate the strengths of shales. (3) the UCSs in sandstones (circles in Fig. 3.13) are lower than those in shales; therefore, most sandstones are weak rocks because of high porosity. Using Eq. (3.19), the UCSs in weak sandstones are calculated and compared to the core test data, as shown in Fig. 3.13. The figure shows that the calculated UCSs from Eq. (3.19) give a reasonable prediction of rock strengths in sandstones and mixed lithology. This weak rock strength correlation (Eq. 3.19) may also be suitable for weak shales, as shown in Fig. 3.13.

For stronger sandstones (porosity <10%), Moos et al. (1999) presented the following relation for coarse-grained sandstones and conglomerates in the Cook Inlet, Alaska:

$$UCS = 1.745\rho V_p^2 - 21 \tag{3.20}$$

where UCS is in MPa, bulk density ρ is in g/cm^3, and V_p is in km/s. Note that Eq. (3.20) is different from their original equation because a different unit is used here.

For very strong and consolidated sandstones in Australia ($0.05 < \phi < 0.12$ and UCS > 80 MPa), the following empirical equation was developed (Chang et al., 2006):

$$UCS = 42.1 \exp\left(1.9 \times 10^{-2} \rho V_p^2\right) \tag{3.21}$$

where UCS is in MPa, bulk density ρ is in g/cm^3, and V_p is in km/s.

The above correlations (equations) were obtained either from limited data or from the datasets in local conditions. For applications to a new area, calibration is extremely important before using any of these strength correlations.

3.2.2.2 From Young's modulus and porosity

Based on the data presented by Plumb (1994), Bradford et al. (1998) used the following correlation between the UCS and Young's modulus for weak reservoir sandstones with risks of sand production:

$$UCS = 2.28 + 4.1089E \tag{3.22}$$

where UCS is in MPa and E is in GPa.

For the Tertiary sandstones in the deepwater ultradeep wells (7600–9000 m below the sea level) of the Gulf of Mexico (GoM), the laboratory-measured UCS (in MPa) and Young's modulus E (in GPa) have the following relation (see Fig. 3.14):

$$UCS = 14.86E^{0.464} \tag{3.23}$$

Fig. 3.14 plots the lab-measured data of the UCSs and Young's moduli compared to the correlations of Eqs. (3.22) and (3.23). It shows that reservoir sandstones in the Everest Complex of the North Sea (Bradford et al., 1998) have much lower UCSs than those in the Gulf of Mexico, and Eq. (3.22) can be applied to the weak reservoir rocks.

Vernik et al. (1993) obtained the following correlation between porosity and the UCS for very clean, grain-supported, and well-consolidated sandstones (clean arenites and arenites, $\phi \leq 15\%$):

$$UCS = 254(1 - 0.027\phi)^2 \tag{3.24}$$

Plumb (1994) found an empirical correlation for average upper bound on the UCS for well-cemented clay-free sandstones obtained from 784

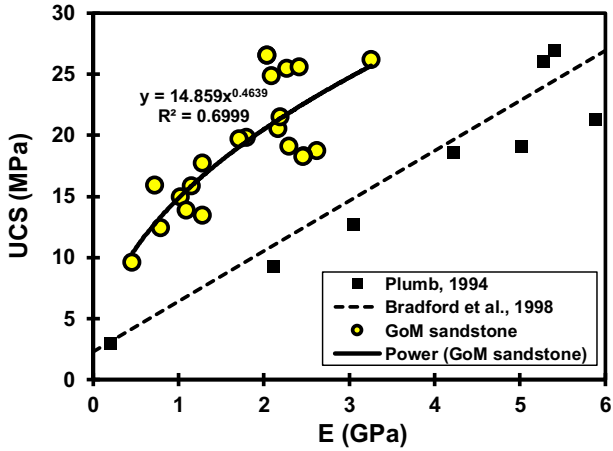

Figure 3.14 Correlations and laboratory-measured uniaxial compressive strengths versus Young's moduli in sandstones from ultradeep Gulf of Mexico wells.

rocks in oil field cores and quarries. The upper bound UCS is a strong negative function of porosity in the low to intermediate porosity range, but it becomes relatively independent of porosity at high porosity where sand production is a problem. The average upper bound is approximated by:

$$UCS = 357(1 - 0.028\phi)^2 \tag{3.25}$$

In Eqs. (3.24) and (3.25), UCS is in MPa and porosity ϕ is in %. Eq. (3.25) represents an upper bound UCS of sandstones and predicts a higher UCS than that from Eq. (3.24). For sandstones which contain clays, the strength falls well below the trend suggested by Eq. (3.25).

Weingarten and Perkins (1992) presented the following relation to predict sandstone internal friction angle φ (degrees) using porosity ϕ (fraction):

$$\varphi = 57.8 - 105\phi \tag{3.26}$$

3.2.3 Empirical equations of rock strengths in carbonate rocks

3.2.3.1 From sonic velocity

Milizer and Stoll (1973) obtained the following relation between the UCS and compressional transit time for the limestone and dolomite (Chang et al., 2006):

$$UCS = (7682/\Delta t)^{1.82}/145 \tag{3.27}$$

Golubev and Rabinovich (1976) proposed the following empirical equation for the limestone and dolomite (Chang et al., 2006):

$$UCS = 10^{(2.44+109.14/\Delta t)}/145 \tag{3.28}$$

In Eqs. (3.27) and (3.28), UCS is in MPa and Δt is in μs/ft.

Eq. (3.27) predicts a much lower strength than Eq. (3.28); therefore, Eq. (3.27) may be more suitable for low-strength carbonates.

Najibi et al. (2015) presented the following rock strength correlation for the limestones from core test data in two Iran oil fields:

$$UCS = 3.67 V_p^{2.14} \tag{3.29}$$

where UCS is in MPa and V_p is in km/s.

3.2.3.2 From Young's modulus and porosity

Chang et al. (2006) obtained the following relation between the UCS (in MPa) and Young's modulus (in GPa) for the limestone with $10 < \text{UCS} < 300$ MPa:

$$UCS = 13.8E^{0.51} \tag{3.30}$$

For the limestone and dolomite with low to moderate porosity ($0.05 < \phi < 0.2$) and high UCS ($30 < \text{UCS} < 150$ MPa) in the Middle East, the following empirical equation was obtained (Chang et al., 2006):

$$UCS = 143.8 \exp(-6.95\phi) \tag{3.31}$$

Another empirical equation for $0.05 < \phi < 0.2$ and $30 < \text{UCS} < 300$ MPa is (Chang et al., 2006):

$$UCS = 135.9 \exp(-4.8\phi) \tag{3.32}$$

where ϕ is porosity (fraction).

The North Sea chalk has been widely studied because of the prominent chalk reservoirs (Ekofisk, Eldfisk, Valhall, Tommeliten, and others). Havmøller and Foged (1996) compiled a large amount of the North Sea reservoir and outcrop chalk data to establish correlations between mechanical properties and porosity (Fjær et al., 2008). The overall trends they found (for the North Sea chalk) can be summarized in the following equations:

$$UCS = 174e^{7.57\phi} \tag{3.33}$$

$$UCS \approx 8T_0 \tag{3.34}$$

where UCS and tensile strength (T_0) are in MPa; ϕ is in a fraction.

Table 3.1 Field estimates of rock uniaxial compressive strength (UCS).

	UCS (MPa)	Field characteristics	Examples
Extremely strong	>250	Specimen can only be chipped with a geologic hammer	Fresh basalt, chert, diabase, gneiss, granite, quartzite
Very strong	100–250	Specimen requires many blows of a geological hammer to fracture it	Amphibolite, sandstone, basalt, gabbro, gneiss, granodiorite, limestone, marble, rhyolite, tuff
Strong	50–100	Specimen requires more than one blow to fracture it	Limestone, marble, phyllite, sandstone, schist, shale
Medium strong	25–50	Cannot be scraped or peeled with a pocket knife. Specimen can be fractured with a single blow from a geological hammer.	Claystone, coal, concrete, schist, shale, siltstone
Weak	2–25	Can be peeled with a pocket knife with difficulty. Shallow indentation made by firm below with point of a geological hammer.	Chalk, rocksalt, potash
Very weak	1–5	Crumbles under firm blows with point of a geological hammer, can be peeled by a pocket knife	Highly weathered or altered rock
Extremely weak	0.25–1	Indented by thumbnail	Stiff fault gouge

3.2.4 Field methods for estimating rock uniaxial compressive strength

When laboratory tests are not possible, field estimates of rock strength can be conducted by examining rock samples and drilling cuttings. Table 3.1 presents the field methods to estimate rock UCS proposed by Hoek and Brown (1997).

3.3 Rock strength anisotropy

In general, rocks or rock masses always present certain degree of anisotropy, particularly in fractured (jointed) rock masses or slates, shales, and schists.

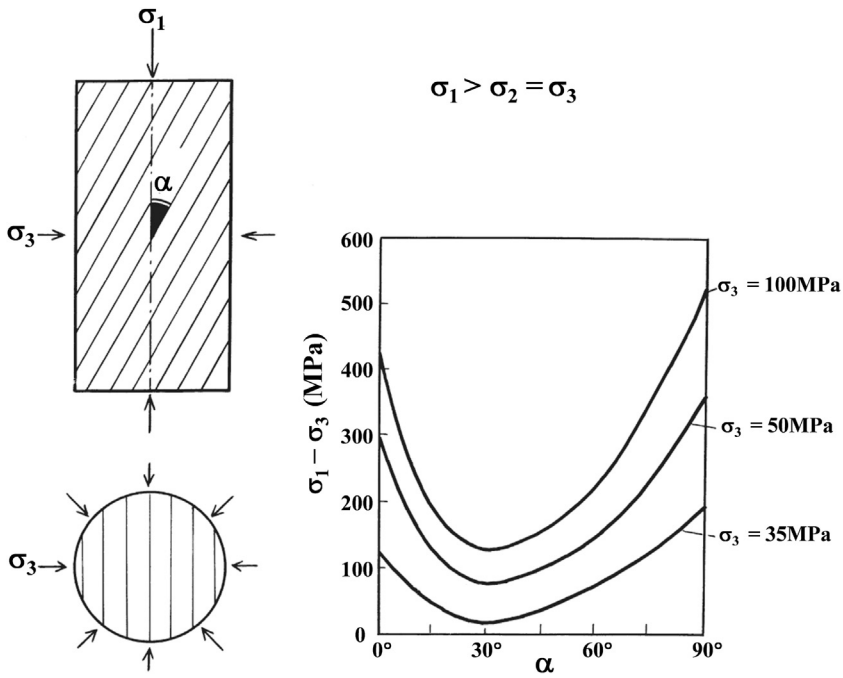

Figure 3.15 Compressive strength (or $\sigma_1 - \sigma_3$) of the anisotropic rocks as function of the angle α between the maximum principal stress (σ_1) and weak planes under the conventional triaxial compression (Donath, 1964).

The effect of the stress states on failure behavior in anisotropic rocks has been studied by many researchers (e.g., Donath, 1964; McLamore and Gray, 1967; Niandou et al., 1997; Brady and Brown, 2004; Mogi, 2007) using triaxial compressive tests ($\sigma_1 > \sigma_2 \geq \sigma_3$). Donath extensively studied the strong influence of planar anisotropy on rock strength. Fig. 3.16 shows schematically his experimental method and the observed results (Donath, 1964). The right graph in Fig. 3.15 shows the differential stress ($\sigma_1 - \sigma_3$) at failure as a function of angle α for different confining pressure ($P_c = \sigma_2 = \sigma_3$). Here α is the angle between the maximum stress (σ_1) and the orientation of the weak planes (or bedding planes). As can be seen in this figure, the compressive strength of the anisotropic rock is the lowest at around $\alpha = 30°$. Fig. 3.16 presents laboratory test results of the compressive strength of Tournemire shale versus the plane of weakness. Again, it shows that the compressive strength of the anisotropic rocks is the lowest at $\alpha \approx 30°$. These results show that failure of anisotropic rocks is likely to occur when the angle α is nearly equal to the shear failure angle of isotropic

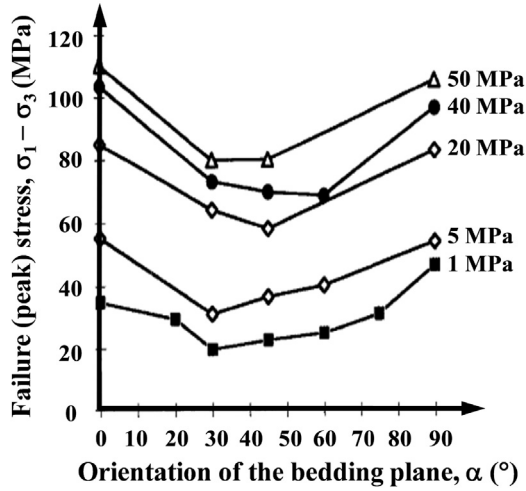

Figure 3.16 Triaxial compressive test results for Tournemire shale showing the variation of peak principal stress difference ($\sigma_1 - \sigma_3$) with the angle of inclination of the major principal stress to the plane of weakness (α), for the confining pressures (σ_3) indicated (Niandou et al., 1997).

rocks with roughly similar solidity, because the failure angles of isotropic rocks are nearly $\alpha = 30°$ in many cases.

The bedding planes in rock formations cause rock strength anisotropy. Willson et al. (2007) presented the following equation to calculate rock UCS variation relative to the bedding planes:

$$UCS_\vartheta = UCS_{\max}(\cos\vartheta + k_1 \sin\vartheta)(1 - \sin\vartheta\cos\vartheta) \times \left[1 - 2\sin\vartheta\cos\vartheta\left(1 - \frac{4k_2}{\sqrt{2}(1+k_1)}\right)\right] \tag{3.35}$$

where UCS_ϑ is the uniaxial compressive strength at ϑ with consideration of bedding effects; ϑ is the angle between the stress concentration orientation and the bedding plane, $\vartheta = 0$ represents loading perpendicular to bedding; and $\vartheta = 90°$ represents loading parallel to bedding; $UCS_{\max}$ is the maximum strength at any orientation; k_1 and k_2 are defined in the following:

$$k_1 = q_{//}/q_\perp$$

$$k_2 = UCS_{\min}/UCS_{\max}$$

where, $q_{//}$ is the strength with the bedding parallel to the sample axis; $q_{\perp}$ is the strength with the bedding perpendicular to the sample axis; $\mathrm{UCS}_{\min}$ is the minimum strength at any orientation.

3.4 Rock failure criteria

3.4.1 Rock failure types

A rock fails when the surrounding stress exceeds its tensile, compressive, or shear strength, whichever is reached first. There are several failure types depending on rock lithology, rock microstructures, and applied stresses. Jaeger and Cook (1979) described rock failures at various confining pressures, as shown in Fig. 3.17. In unconfined compression (Fig. 3.17A), irregular longitudinal splitting is observed. With a moderate amount of confining pressures, the rock failure is characterized by a single plane of fracture, inclined at an angle of less than 45 degrees to the direction of σ_1, as shown in Fig. 3.17B. This is a typical shear failure under compressive stresses, and a shear displacement along the surface of the shear fracture is generated. If the confining pressure is increased so that the rock becomes fully ductile (Jaeger et al., 2007), a network of shear fractures accompanied by plastic deformation appears, as shown in Fig. 3.17C. The second basic type of failure is tensile failure, which appears typically in uniaxial tension. Its characteristic feature is a clean separation with no offset between the surfaces (Fig. 3.17D). If a slab is compressed between line loads as shown in Fig. 3.17E, a tensile fracture appears between the loads.

There are various failure (strength) criteria applied to compare the stresses to rock strength to determine whether the rock fails or not. For the porous media the effective stress concentrations near an underground

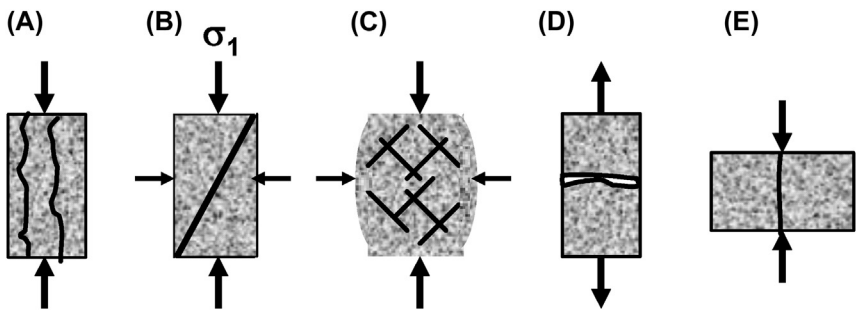

Figure 3.17 Rock failure types. (A). splitting; (B). shear failure; (C). multiple shear fractures; (D). tensile failure; (E). tensile failure induced by point loads.

excavation because of the far-field stresses and pore pressure need to be considered for failure initiation. It is commonly accepted that rock failure is controlled by Terzaghi's effective stress because Biot's effective stress coefficient approaches 1.0 when rock failure is approached (e.g., Zhang, 2002; Zhang et al., 2003). Terzaghi's effective stress can be expressed as follows:

$$\sigma'_{ij} = \sigma_{ij} - \delta_{ij} p_p \tag{3.36}$$

where σ'_{ij} is the effective stress tensor, p_p is the pore pressure and δ is the Kronecker delta, and $\delta = 1$ when $i = j$; $\delta = 0$ when $i \neq j$.

3.4.2 Mohr–Coulomb failure criterion

3.4.2.1 Linear Mohr–Coulomb failure criterion

Shear failure occurs when the shear strength of a formation is exceeded. Even for compressive loading, shear failure can also happen in the rock as shown in Fig. 3.17B and C. Fig. 3.18 is field-observed Z-shape sigmoidal veins (shear fractures) developed by the shear stresses.

When a rock is loaded by the far-field principal stresses, shear stresses can be generated on an inclined plane where shear and normal stresses can be obtained from Eq. (1.12), as shown in Fig. 3.19. Shear failures will occur in the rock when shear stress overcomes the friction stress ($\mu\sigma_n$ or $\sigma_n \tan\varphi$) plus rock inherent shear strength or cohesion (c). The Mohr–Coulomb failure criterion uses this principle to describe shear failure mechanism. For dry

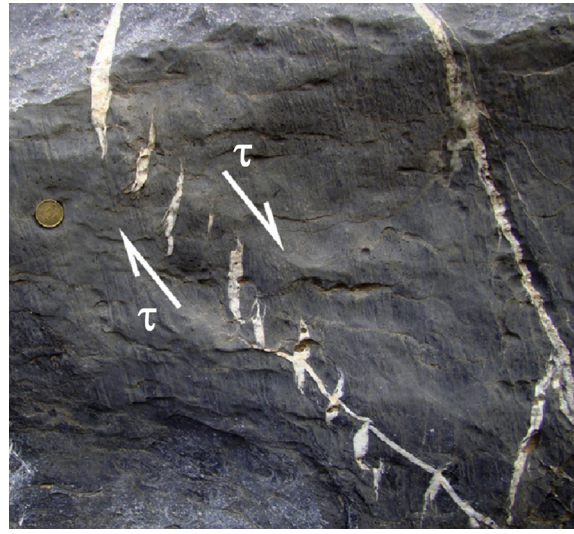

Figure 3.18 Field example of shear failures in sigmoidal veins (Bons et al., 2012).

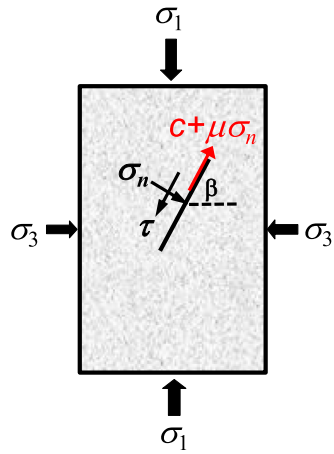

Figure 3.19 Shear stresses developed in an inclined plane in the rock under far-field compressive stresses.

rocks, the Mohr—Coulomb failure criterion says that when the shear stress, τ, is greater than $c + \sigma_n \tan\varphi$, the shear failure occurs. The Mohr—Coulomb failure criterion can be written as the following linear form between shear and normal stresses (originally proposed by Coulomb in 1785):

$$\tau = c + \sigma_n \tan\varphi \tag{3.37}$$

where σ_n is the normal stress; τ is the shear stress; c is the cohesion (also called the inherent shear strength); φ is the angle of internal friction, $\mu = \tan\varphi$; μ is the coefficient of friction. For a fractured rock, it can be assumed $c = 0$.

In the principal stress space, (σ_1, σ_2, σ_3), the Mohr—Coulomb failure criterion can be expressed as follows:

$$\sigma_1 = UCS + q\sigma_3 \tag{3.38}$$

where σ_1 and σ_3 are the maximum and minimum principal stresses, respectively; and

$$q = \frac{1 + \sin\varphi}{1 - \sin\varphi} \tag{3.39}$$

Based on the Mohr—Coulomb failure criterion, the UCS, angle of internal friction and cohesion have the following relation:

$$UCS = \frac{2c\cos\varphi}{1 - \sin\varphi} \tag{3.40}$$

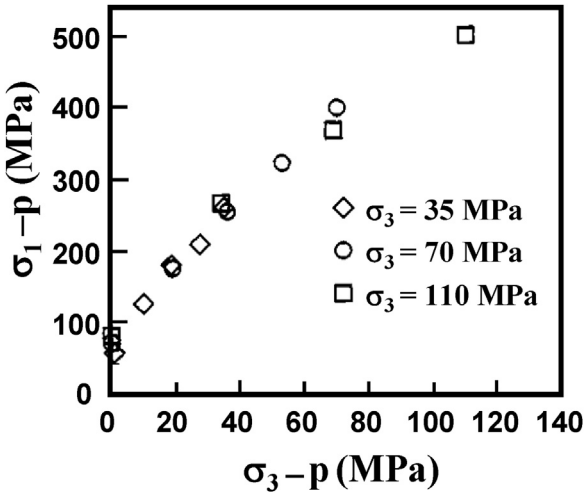

Figure 3.20 Effective stresses at failure in a Darley Dale sandstone. *(Based on the data of Murrell, S.A.F., 1965.)*

When the experimental results of the maximum and minimum effective stresses (difference of total stress and pore pressure) are plotted at failure in a Darley Dale sandstone (Murrell, 1965), the failure data nearly form a single failure curve, which in this particular case is nearly a straight line, but slightly concave downward (Fig. 3.20). Therefore, for the porous rock in the principal effective stress space, the Mohr–Coulomb failure criterion can be expressed as the following:

$$\sigma'_1 = UCS + q\sigma'_3 \tag{3.41}$$

where σ'_1 and σ'_3 are the maximum and minimum effective principal stresses, respectively.

Therefore, the Mohr–Coulomb failure envelope of Eq. (3.37) can be expressed in the effective stress forms as follows:

$$\tau = c + (\sigma_n - p_p)\tan\varphi \tag{3.42}$$

$$\tau = c + \sigma'_n \tan\varphi \tag{3.43}$$

It can be observed from Eq. (3.42) that pore pressure reduces rock shear strength. A simple physical interpretation of this condition is that, while the normal stress tends to strengthen a fracture inside the rock, by pushing the two opposing rock faces together, the pore pressure acts to weaken it, by pushing the two opposing rock faces apart.

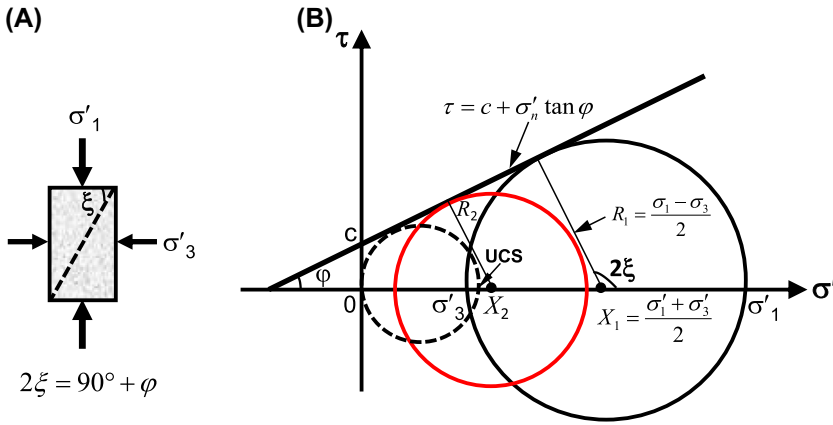

Figure 3.21 The Mohr–Coulomb failure criterion in the effective stress domain. (A). shear failure plane under triaxial compression condition; (B). the Mohr circles and the linear shear failure envelope (tangent line of the Mohr circles).

The Mohr–Coulomb failure criterion can be depicted by the Mohr circle diagram. Fig. 3.21 shows the Mohr circle and Mohr–Coulomb failure envelope. Shear failure will not occur if the values of (σ'_n, τ) of a point in Fig. 3.21 lie below the failure envelope. In the Mohr–Coulomb criterion, two conclusions should be noted: (1) the intermediate principal stress σ'_2 does not affect shear failure and this may overestimate rock failure; (2) the plane of the shear fracture passes through the direction of the intermediate stress. These conclusions can be applied to determine the direction of the in situ intermediate stress, when the stress regime is known (refer to Chapter 5). The most likely shear failure plane can be obtained from the Mohr circles and the Mohr–Coulomb envelope, when the Mohr circle touches the failure envelope as shown in Fig. 3.21. The angle of the shear failure plane can be obtained from the geometric relationship in Fig. 3.21:

$$\xi = 45^\circ + \varphi/2 \tag{3.44}$$

From triaxial compression test results, the Mohr circles and Mohr–Coulomb failure envelope can be obtained. If several experimental datasets are available, the Mohr circles can be drawn, as shown in Fig. 3.21. Then, the cohesion and angle of internal friction can be calculated according to the geometric relationship shown in Fig. 3.21. Using two Mohr circles as an example, the following relations can be obtained:

$$\sin\varphi = \frac{R_2 - R_1}{X_2 - X_1} \tag{3.45}$$

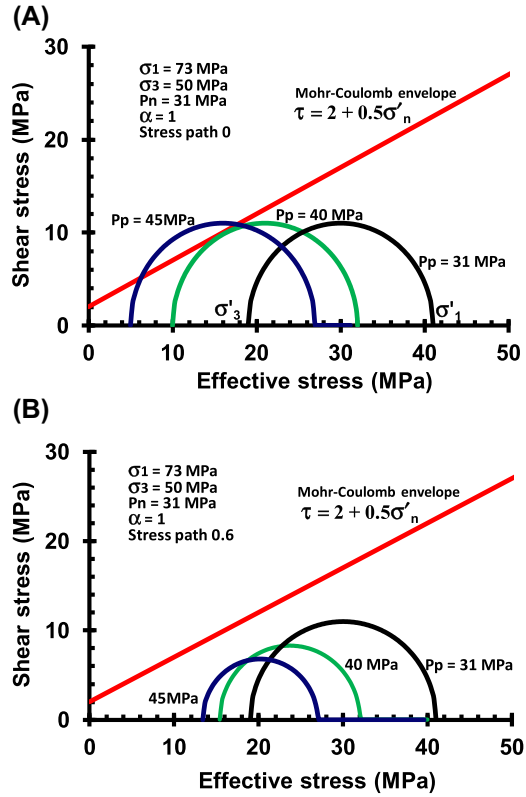

Figure 3.22 Overpressured pore pressure (p_p from the normal pressure of $p_n = 31$ MPa increasing to 40 and 45 MPa) moving the Mohr circles to the left. (A) both total stresses (σ_1 and σ_3) have no change with pore pressure variations; (B) the minimum stress (σ_3) increases as the pore pressure increases (assuming the stress path $\Delta\sigma_h/\Delta p_p = 0.6$) but no change in vertical stress σ_1.

$$c = \left[\frac{R_1}{\sin\varphi} - X_1\right]\tan\varphi \tag{3.46}$$

where $R_2 = \frac{\sigma_1 - \sigma_3}{2}$ in circle 2; $R_1 = \frac{\sigma_1 - \sigma_3}{2}$ in circle 1; $X_2 = \frac{\sigma'_1 + \sigma'_3}{2}$ in circle 2; $X_1 = \frac{\sigma'_1 + \sigma'_3}{2}$ in circle 1; R_1 and R_2 are the radii of circles 1 and 2, respectively; X_1 and X_2 are the distances from the origin to the circle center in circles 1 and 2, respectively. Notice that the values of σ_1 and σ_3 in circle 1 are different from those in circle 2.

Fig. 3.22 illustrates how pore pressures affect the Mohr circles and rock failures. It shows a case for a shale oil formation at depth of 3100 m, where the vertical stress $\sigma_V = \sigma_1 = 73$ MPa, the minimum horizontal stress

$\sigma_3 = 50$ MPa, and the hydrostatic pressure $p_n = 31$ MPa. Two scenarios on how pore pressure variations impact the minimum stress are examined here. If the total stresses (σ_1, σ_2, and σ_3) keep unchanged with pore pressure variations, the increase in pore pressure (or overpressure) will reduce the minimum and maximum effective stresses (σ'_1, σ'_3). This will move the Mohr circle to the left side, making the Mohr circle touch or cross the shear failure envelope and causing shear failures (Fig. 3.22A). However, in most cases the increase of pore pressure may also cause the minimum horizontal stress σ_3 to increase as field observed (e.g., Hillis, 2000; Engelder and Fischer, 1994). Therefore, the other scenario is that the increase in the minimum horizontal stress induced by the increase of pore pressure causes the Mohr circle size reduction (Fig. 3.22B) with assumption of no change in vertical stress σ_V. The rock in this case is much less likely to have shear failures than the one shown in Fig. 3.22A. By contrast, the decrease in pore pressure (e.g., the reservoir depletion) increases the Mohr circle size and moves the circle to the right side (Dohmen et al., 2013, 2017), and the increased Mohr circle sizes may, then, cross the shear failure envelope and cause shear failures (see Fig. 3.22B).

3.4.2.2 Modified Mohr–Coulomb failure criterion

Triaxial tests have found that the Mohr–Coulomb failure envelope has a nonlinear behavior (e.g., Fig. 3.23). It was recognized in 1970s that the shear strength envelopes for intact rocks, when tested over a wide range of confining stress, would have an obvious curvature, and eventually reach a horizontal stage with no further increase in strength (Barton, 2013). This was termed the "critical state," and the simple relation $\sigma_1 = 3\sigma_3$ suggested

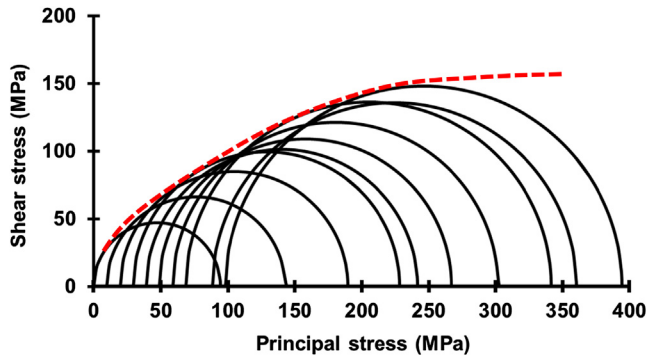

Figure 3.23 Nonlinear failure envelope from triaxial compression tests for Daye marble. *(Plotted from the data presented by Ouyang, Z., Elsworth, D., 1991.)*

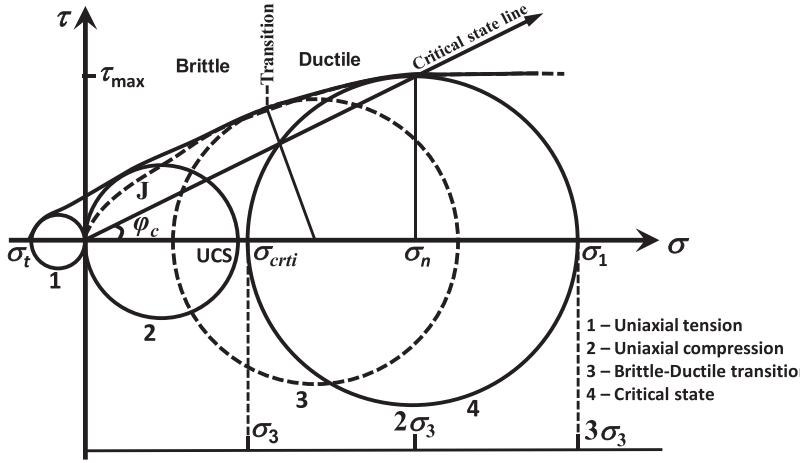

Figure 3.24 Critical state line (defined by $\sigma_1 = 3\sigma_3$) suggested by numerous high-pressure triaxial strength tests in dry rocks. Note the closeness of the unconfined strength (UCS) circle to the confining pressure σ_{crti} (Barton, 1976). 'J' represents jointed rock. The magnitude of φ_c is 26.6 degrees when $\sigma_1 = 3\sigma_3$. For porous rocks, effective stresses should be used to replace the total stresses.

itself, as illustrated in Fig. 3.24. This critical state can be considered as the separation between the brittle and ductile deformation of the rock as illustrated in Fig. 3.24. In ductile and brittle deformation stages, the rock behaviors are very different (Mogi, 1974). The rock loaded at a low confining pressure (small $\sigma_1 - \sigma_3$) is brittle as shown in Fig. 3.25, meaning

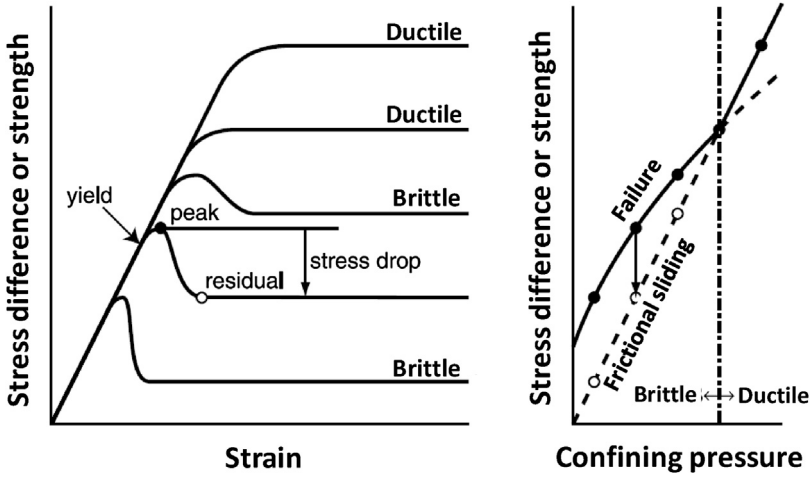

Figure 3.25 Schematic triaxial stress–strain curves for rock loaded at different confining pressures and the brittle–ductile transition. *(Plotted based on Mogi, K., 1974.)*

that after reaching the peak stress the strength decreases to a residual value determined by frictional sliding (Schöpfer et al., 2013). The difference between the peak and residual strengths is the stress drop (Fig. 3.25). At a high confining pressure, however, no stress drop occurs, and the rock is in elastic perfectly plastic deformation. The transition of the confining pressure at which no loss in strength occurs is a possible definition of the brittle–ductile transition (Schöpfer et al., 2013).

A study by Singh et al. (2011), involving reanalysis of thousands of reported triaxial tests, has revealed the astonishing simplicity of the following equality: UCS $\approx \sigma_{\text{crti}}$ (i.e., critical σ_3) for the majority of rock types. In other words, the two Mohr circles referred to in Fig. 3.24 are touching at their circumference. The curvature of peak shear strength envelopes is more correctly described, so that few triaxial tests are required, only needed to be performed at low confining stress, to delineate the whole strength envelope. This simplicity does not of course apply to the case, where triaxial tests are required over a wide range of confining stress, to correct the envelope, usually to adjust to greater local curvature.

Singh et al. (2011) basically modified the Mohr–Coulomb criterion by absorbing the critical state defined in Barton (1976) and then quantifying the necessary deviation from the linear form, using a large body of experimental test data. This modified Mohr–Coulomb nonlinear failure criterion may be written in the effective stress form as follows:

$$\sigma'_1 - \sigma'_3 = UCS + \frac{2\sin\varphi}{1-\sin\varphi}\sigma'_3 - A\sigma'^{2}_3 \tag{3.47}$$

where A is an empirical constant for the rock type under consideration. Eq. (3.47) is the linear Mohr–Coulomb failure criterion (Eq. 3.41) except the last team $-A\sigma'^{2}_3$. For $0 \le \sigma'_3 \le \sigma'_{crti}$, Singh et al. (2011) found that parameter A has the following form:

$$A = \frac{1}{\sigma'_{crti}}\frac{\sin\varphi}{1-\sin\varphi} \tag{3.48}$$

where σ'_{crti} is the critical effective confining stress and $\sigma'_{\text{crti}} \approx$ UCS.

In the tensile stress area (i.e., $\sigma_3 < 0$) in Fig. 3.24, the Griffith failure criterion described by a parabolic Mohr envelope can be used (refer to Section 3.4.9, Eq. (3.83) and Fig. 3.31 for details).

3.4.3 Weak plane sliding failure criterion

Because most sedimentary and metamorphic rocks are anisotropic, the effect of anisotropy on strength is of great importance. The simplest situation is the planar anisotropy in which a rock mass has a set of parallel planes of weakness, as shown in the experimental results (Fig. 3.15). Using the Mohr–Coulomb failure criterion, Jaeger and Cook (1979) gave the following equation to calculate the maximum and minimum principal stresses associated with the weak plane sliding along preexisting planes of weakness for a rock mass having a set of parallel planes of weakness:

$$\sigma_1 - \sigma_3 = \frac{2(c_w + \mu_w \sigma_3)}{(1 - \mu_w \cot \beta)\sin 2\beta} \tag{3.49}$$

where, β is the angle between σ_1 and the normal to the planes of weakness, and $\varphi_w < \beta < 90°$ (refer to Fig. 3.26); it should be noted that the angle of β is different from α in Fig. 3.15, and $\alpha = 90° - \beta$; σ_1 and σ_3 are the maximum and minimum principal stresses, respectively; c_w is the cohesion of the plane of weakness; φ_w, μ_w are the angle and coefficient of internal

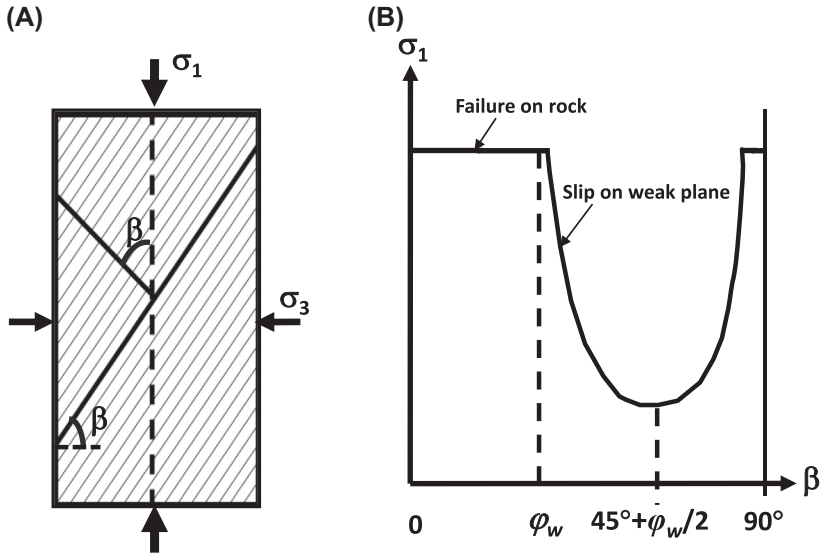

Figure 3.26 (A). Transversely isotropic specimen with a set of parallel weak planes in a triaxial compression test; (B). Schematic rock peak strength variation with the angle, β, in the triaxial test at a constant confining stress (σ_3) inspired by experimental tests and Eq. (3.49).

friction in the plane of weakness, respectively; $\mu_w = \tan\varphi_w$; and φ_w is the angle of internal friction in the plane of weakness.

In terms of effective stresses, Eq. (3.49) can be expressed in the following form:

$$\sigma_1' - \sigma_3' = \frac{2\left(c_w + \mu_w \sigma_3'\right)}{(1 - \mu_w \cot\beta)\sin 2\beta} \tag{3.50}$$

The value of σ_1 required to cause failure, as given by Eqs. (3.49) and (3.50), trends to infinity as $\beta \to 90°$ or $\beta \to \varphi_w$ (i.e., failure in the rock). In other words, when $0 < \beta < \varphi_w$ and $\beta = 90°$, the planes of weakness have no impact on the rock strength. If $\varphi_w < \beta < 90°$, shear failure will occur in the weak planes at a finite value of σ_1 that varies with β, as shown in Fig. 3.26B. The minimum strength occurs in the following condition (refer to Fig. 3.26B):

$$\beta_{\min} = 45° + \varphi_w/2 \tag{3.51}$$

Compared to the experimental results in the outcrop of the Mancos shale, the model of the planes of weakness Eq. (3.49) gives a good prediction (Fig. 3.27). For multiple sets of parallel planes of weakness, superposition principle can be used in Eq. (3.50) to solve the complex problem.

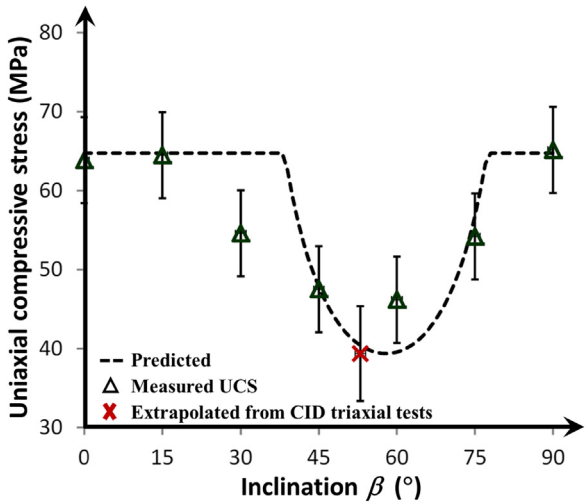

Figure 3.27 Measured uniaxial compressive strengths versus β and the strength predicted by the planes of weakness model in the Mancos shale (Eq. 3.49). *(After Fjær, E., Nes, O.M., 2013. with permission of ARMA).*

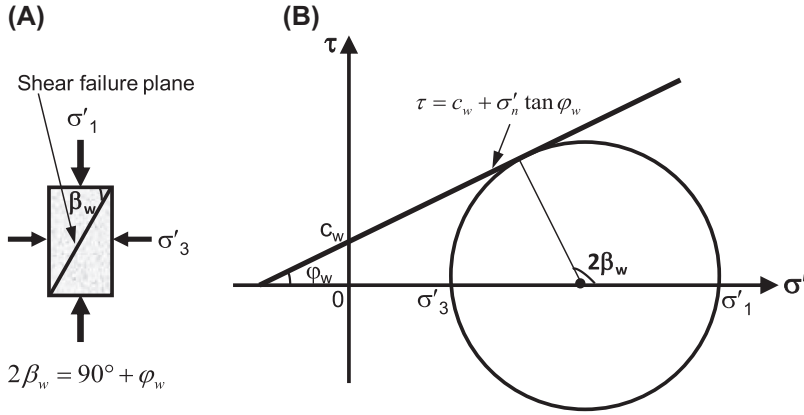

Figure 3.28 Shear failure plane (A) and the Mohr circle (B) in the rock with a set of parallel planes of weakness.

Fig. 3.28 plots the Mohr–Coulomb failure envelope and the Mohr circle representation of the rock containing a set of parallel planes of weakness. The shear failure angle (β_w) in the shear failure plane of the rock can be obtained from the Mohr circle, i.e., $\beta_w = 45° + \varphi_w/2$. Compared to Eq. (3.51), the minimum strength or the shear failure that the anisotropic rock is most likely to occur is when the bedding angle, β, is equal to the shear failure angle (β_w), i.e., $\beta = \beta_w = \beta_{\min}$.

3.4.4 Drucker–Prager failure criterion

The Mohr–Coulomb failure criterion does not consider the effect of the intermediate principal stress. Laboratory data have shown that the intermediate principal stress plays an important role in the failure of rocks. The Drucker–Prager failure criterion can describe rock failures in the domain of three principle stresses (Drucker and Prager, 1952). The Drucker–Prager failure criterion can be expressed in the effective stress form, i.e.,

$$\sqrt{J_2} = \alpha_0 I_1' + \kappa \tag{3.52}$$

where α_0 and κ are material constants; I'_1 and J_2 are the stress invariants, which can be expressed as:

$$I_1' = \sigma_1' + \sigma_2' + \sigma_3' \tag{3.53}$$

$$J_2 = \frac{1}{6}\left[(\sigma_1 - \sigma_2)^2 + (\sigma_2 - \sigma_3)^2 + (\sigma_3 - \sigma_1)^2\right] \tag{3.54}$$

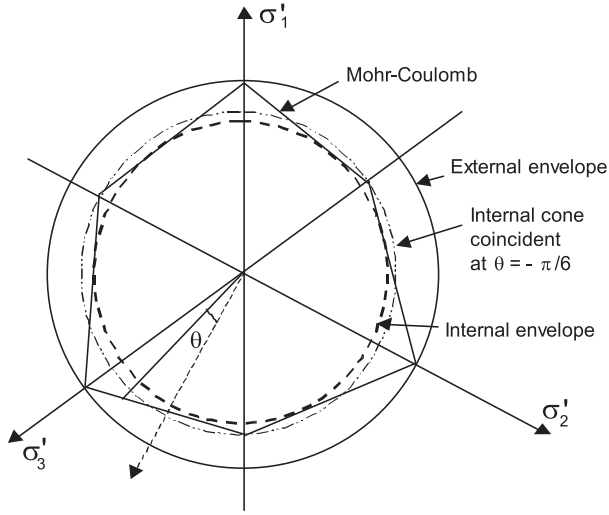

Figure 3.29 The Mohr–Coulomb failure surface and different possibilities to correspond to the Drucker–Prager failure conditions.

The Drucker–Prager failure criterion is an extended form of the Mohr–Coulomb failure criterion. In the principal stress space, a section in the deviatoric plane shows that it is possible in various ways to relate the two failure criteria (Fig. 3.29). For the plane-strain condition it is recommended that the inside cone tangent to the pyramid is used (Kovari, 1977). In this case, the conversions of the material parameters from the Mohr–Coulomb criterion to the Drucker–Prager criterion are:

$$\alpha_0 = \frac{\tan \varphi}{\sqrt{9 + 12 \tan^2 \varphi}} \tag{3.55}$$

$$\kappa = \frac{3c}{\sqrt{9 + 12 \tan^2 \phi}} \tag{3.56}$$

When the external envelope is used, the conversion equations in the material parameters from the Mohr–Coulomb criterion to the Drucker–Prager criterion are as follows:

$$\alpha_0 = \frac{2 \sin \varphi}{\sqrt{3}(3 - \sin \varphi)} \tag{3.57}$$

$$\kappa = \frac{6c \cos \phi}{\sqrt{3}(3 - \sin \phi)} \tag{3.58}$$

If the internal cone envelope coincident at $\theta = \pi/6$ is used, the conversion equations of the material parameters from the Mohr–Coulomb criterion to the Drucker–Prager criterion become:

$$\alpha_0 = \frac{2\sin\varphi}{\sqrt{3}(3+\sin\varphi)} \tag{3.59}$$

$$\kappa = \frac{6c\cos\phi}{\sqrt{3}(3+\sin\phi)} \tag{3.60}$$

3.4.5 Modified Lade failure criterion

The modified Lade criterion was presented by Ewy (1998) based on the Lade strength criterion (Lade, 1984) for studying wellbore stability. In this criterion, all three effective principal stresses (σ'_1, σ'_2, σ'_3) were considered. The modified Lade can be expressed as the following form:

$$\frac{\left(I_1''\right)^3}{I_3''} = 27 + \eta \tag{3.61}$$

where

$$I_1'' = \left(\sigma_1' + S\right) + \left(\sigma_2' + S\right) + \left(\sigma_3' + S\right)$$

$$I_3'' = \left(\sigma_1' + S\right) + \left(\sigma_2' + S\right) + \left(\sigma_3' + S\right)$$

$$S = \frac{c}{\tan\varphi}$$

$$\eta = \frac{4\tan^2\varphi(9 - 7\sin\varphi)}{1-\sin\varphi}$$

Compared to the Mohr–Coulomb criterion, the modified Lade criterion considers the effect of intermediate principal stress (σ_2) on rock failures. The wellbore stability predicted by the modified Lade criterion has less failure (therefore, needs to design a smaller mud weight) than that by the Mohr–Coulomb criterion because the latter ignores the effect of intermediate principal stress. Therefore, critical mud weight values predicted by the modified Lade criterion are less conservative than those predicted by the Mohr–Coulomb criterion. However, the modified Lade predicts a larger wellbore failure than that predicted by the Drucker–Prager criterion because the Drucker–Prager criterion predicts a greater strengthening effect from intermediate principal stress.

3.4.6 Hoek–Brown failure criterion

By studying experimental results of a wide variety of rocks, Hoek and Brown (1980) presented the following empirical failure criterion for jointed rock masses:

$$\sigma'_1 = \sigma'_3 + UCS\left(m\sigma'_3/UCS + s\right)^a \tag{3.62}$$

where σ'_1 and σ'_3 are the maximum and minimum effective principal stresses, respectively; m and s are the constants depending on the properties of the rock and on the extent to which it has been broken before being subject to the stresses; a is a constant depended on the rock mass characteristics; m ranges from 0.001 (extremely weak rock) to 25 (extremely strong rock) and $s = 1$ for intact rock; $s < 1$ for previously broken rock.

For intact rocks that make up the rock mass, Eq. (3.62) simplifies to:

$$\sigma'_1 = \sigma'_3 + \sqrt{mUCS\sigma'_3 + sUCS^2} \tag{3.63}$$

For clastic sediments, Hoek and Brown (1997) suggested using the following values for m:

$m = 22$ for conglomerate; $m = 19$ for sandstone; $m = 9$ for siltstone; and $m = 4$ for claystone.

3.4.7 True triaxial failure criterion

Polyaxial compression (true triaxial) tests demonstrate that rock strength is a function of the major principal stress (σ_1) and the minor principal stress (σ_3) as well as the intermediate stress (σ_2). Therefore, rock failure characteristic depends on the effects of all three principal stresses. For ductile materials, the von Mises criterion is defined as the following form to consider all three principal stresses:

$$\tau_{oct} = \frac{1}{3}\sqrt{(\sigma_1 - \sigma_2)^2 + (\sigma_1 - \sigma_3)^2 + (\sigma_3 - \sigma_1)^2} = d \tag{3.64}$$

where τ_{oct} is the octahedral shear stress; d is a material-dependent constant, $d = \frac{\sqrt{2}}{3}\sigma_y$; σ_y is the yield strength of the material (UCS for the rock). Eq. (3.64) states that the yield point is reached when the distortional energy, represented by the octahedral shear stress increases to a constant d. Nadai (1950) recommended that the von Mises yield criterion for ductile metals can be adapted to rocks by replacing the constant d with a monotonically rising function f_N of the octahedral normal stress σ_{oct} or the mean stress σ_m:

$$\tau_{oct} = f_N(\sigma_{oct}) \tag{3.65}$$

where $\sigma_{oct} = \sigma_m = \frac{\sigma_1+\sigma_2+\sigma_3}{3}$. It can be seen that the Drucker–Prager criterion, Eq. (3.52), is a specific form of Eq. (3.65)

Mogi (1971) plotted his experimental data for the Dunham dolomite and the Mizuho trachyte and found that σ_{oct} and $\sigma_{m,2}$ have a single monotonically rising curve for each rock, i.e.,

$$\tau_{oct} = g_1(\sigma_{m,2}) \tag{3.66}$$

where $\sigma_{m,2} = \frac{\sigma_1+\sigma_3}{2}$

Eq. (3.66) was used to fit the KTB amphibolite and the Westerly granite as a monotonically increasing power function (Haimson and Chang, 2000; Haimson, 2006) as the following form:

$$\tau_{oct} = A\sigma_{m,2}^B \tag{3.67}$$

where A and B are the fitting parameters. If the stress unit is in MPa, then for the KTB amphibolite the parameters are $A = 1.77$ and $B = 0.86$; for the Westerly granite $A = 1.51$ and $B = 0.89$ (Haimson, 2006).

Alternately, the linear Mogi model can be used for true triaxial data of rocks, which also provides a good fit and is easier to use:

$$\tau_{oct} = a + b\sigma_{m,2} \tag{3.68}$$

where a and b are the fitting parameters. Table 3.2 shows the values of a and b obtained from several true triaxial tests in different rocks.

Some new failure criteria for true triaxial strength criteria have been proposed (e.g., You, 2009; Ma et al., 2017). However, for the conventional triaxial tests ($\sigma_2 = \sigma_3$), the octahedral shear stress can be simplified into the following form:

$$\begin{aligned}\tau_{oct} &= \frac{1}{3}\sqrt{(\sigma_1-\sigma_2)^2+(\sigma_1-\sigma_3)^2+(\sigma_3-\sigma_1)^2} \\ &= \frac{\sqrt{2}}{3}(\sigma_1-\sigma_3)\end{aligned} \tag{3.69}$$

Table 3.2 The values of a and b obtained from true triaxial tests.

Rock type	a (MPa)	b	Reference
KTB amphibolite	40.1	0.636	Haimson (2006)
Westerly granite	30.19	0.712	Haimson (2006)
Mancos shale	10.779	0.5857	Vachaparampil and Ghassemi (2013)
Barnett shale	36.542	0.4807	Vachaparampil and Ghassemi (2013)
Eagle ford shale	30.412	0.5634	Vachaparampil and Ghassemi (2013)

The linear Mogi criterion, Eq. (3.68), then reduces to (Al-Ajmi and Zimmerman, 2005):

$$\frac{\sqrt{2}}{3}(\sigma_1 - \sigma_3) = a + \frac{b}{2}(\sigma_1 + \sigma_3) \tag{3.70}$$

Comparison with the linear Mohr–Coulomb failure criterion shows that for triaxial compression case, the linear Mogi criterion, Eq. (3.70), coincides with the Mohr–Coulomb criterion, if the following relations are satisfied:

$$\begin{aligned} a &= \frac{2\sqrt{2}}{3} c \cos\varphi \\ b &= \frac{2\sqrt{2}}{3} \sin\varphi \end{aligned} \tag{3.71}$$

Under this condition the linear Mogi criterion given by Eq. (3.68) is exactly equivalent to the Mohr–Coulomb criterion.

The equations presented in this section are expressed in total stresses. They need to be expressed in effective forms for porous rocks by considering pore pressure effect, i.e., replacing σ by σ'.

3.4.8 Cam-Clay failure criterion

The Cam-Clay model was developed to describe soil yield by researchers at the University of Cambridge (hence its name) (Roscoe et al., 1958, 1963). Roscoe and Burland (1968) proposed the modified Cam-Clay model. It is a very influential soil yield model and recently has been used to model the compaction of sediments and rock failures. The primary assumptions of the Cam-Clay and modified Cam-Clay models are characterized by the following three parameters:

(1) Effective mean stress, p', can be calculated in terms of principal stresses σ'_1, σ'_2, and σ'_3 as:

$$p' = \frac{1}{3}\left(\sigma'_1 + \sigma'_2 + \sigma'_3\right) \tag{3.72}$$

(2) Deviatoric (shear stress) q:

$$q = \frac{1}{\sqrt{2}}\sqrt{(\sigma'_1 - \sigma'_2)^2 + (\sigma'_2 - \sigma'_3)^2 + (\sigma'_1 - \sigma'_3)^2} \tag{3.73}$$

(3) Specific volume, v, is defined as:

$$v = 1 + e \tag{3.74}$$

where e is the void ratio and can be related to porosity by $e = \phi/(1 - \phi)$.

The yield functions of the Cam-Clay and modified Cam-Clay models are determined from the following equations:

Cam-Clay:

$$q + Mp' \ln\left(\frac{p'}{p'_0}\right) = 0 \tag{3.75}$$

Modified Cam-Clay:

$$\frac{q^2}{p'^2} + M^2\left(1 - \frac{p'_0}{p'}\right) = 0 \tag{3.76}$$

In p'–q space, the Cam-Clay yield surface is a logarithmic curve while the modified Cam-Clay yield surface plots as an elliptical curve (Fig. 3.30). The parameter p'_0 (known as the yield stress or preconsolidation pressure) controls the size of the yield surface. The parameter M is the slope of the Critical State Line (CSL) in p'–q space, i.e., $M = q/p'$. A key characteristic of the CSL is that it intersects the yield curve at the point at which the maximum value of q is attained.

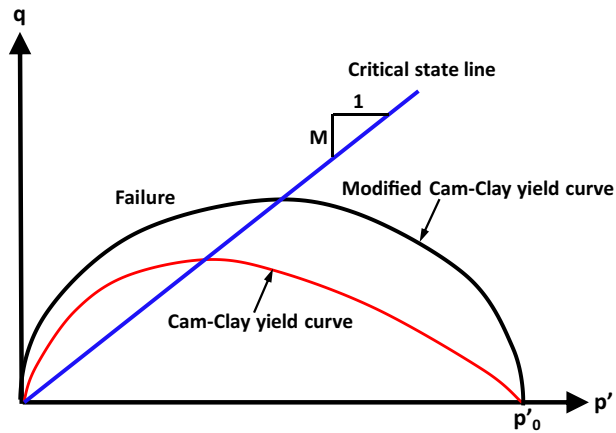

Figure 3.30 The Cam-Clay and modified Cam-Clay yield surfaces (in p'–q space). Failure occurs in the left side of the critical state line.

In $p'-q$ plane the CSL, similar to the shear failure envelope in the Mohr–Coulomb failure criterion, is a straight line passing through the origin with the slope equal to M, one of the characteristic of the material (see Fig. 3.30). The size of the yield surface is determined by p'_0 and M. The Cam-Clay model has been widely used to simulate pore-collapse related reservoir compaction and surface subsidence analysis.

3.4.9 Tensile and Griffith failure criteria

It is commonly assumed that the tensile failure in rock will occur when the effective stress becomes tensile and equals or exceeds rock tensile strength, i.e.,

$$\sigma'_3 = -T_0 \tag{3.77}$$

where T_0 is the uniaxial tensile strength; σ'_3 is the minimum effective principal tensile stresses (σ'_3 is negative when it is tensile).

Griffith (1921) proposed that fractures are caused by stress concentration at the tips of minute Griffith elliptical cracks supposed to pervade the material. A fracture is initiated when the maximum stress near the tip of most favorably oriented crack reaches a critical value of the material. The Griffith failure takes place if the following equations are satisfied for a dry material:

If $\sigma_1 + 3\sigma_3 \geq 0$,

$$(\sigma_1 - \sigma_3)^2 = 8T_0(\sigma_1 + \sigma_3) \tag{3.78}$$

If $\sigma_1 + 3\sigma_3 < 0$,

$$\sigma_3 = -T_0 \tag{3.79}$$

When $\sigma_3 = 0$, it is uniaxial compression, so that the UCS predicted by Eq. (3.78) ($\sigma_1 = \text{UCS}$) is:

$$UCS = 8T_0 \tag{3.80}$$

From Eq. (3.80), the Griffith theory predicts that a ratio of uniaxial compressive to tensile strengths is 8. It should be noted that for some rocks, Eq. (3.80) underestimates the UCS. An extension of the Griffith criterion examines the stresses induced around open penny-shaped cracks in a semi-infinite body subjected to triaxial compressive stresses σ_1, σ_2, and σ_3. It is shown that the intermediate principal stress σ_2 has no significant influence on the tensile failure initiation. Hence, this extended Griffith criterion is

essentially equivalent to loading a penny-shaped crack in a biaxial stress field (Hoek and Martin, 2014; Murrell, 1963). The equation governing tensile failure initiation is:

$$\sigma_1 = \frac{12T_0(1 + 2\sigma_3/\sigma_1)}{(1 - \sigma_3/\sigma_1)^2} \tag{3.81}$$

This penny-shaped crack version of the Griffith criterion predicts that the UCS is 12 times of the tensile strength:

$$UCS = 12T_0 \tag{3.82}$$

The Griffith criterion can be presented by a parabolic Mohr envelope (Whittaker et al., 1992) as given by the following equation:

$$\tau^2 = 4T_0(T_0 + \sigma) \tag{3.83}$$

where τ is the shear stress acting along the crack plane surface; σ is the normal stress acting perpendicular to the crack surface.

The Griffith criterion in Eq. (3.83) can be plotted in $\tau - \sigma$ space, similar to the nonlinear Mohr–Coulomb envelope, as shown in Fig. 3.31. This figure shows that the Griffith envelope intersects the τ axis at $2T_0$; however, the intercept in the Mohr–Coulomb envelope (Fig. 3.21) is the cohesion c. If the Griffith and Mohr–Coulomb envelopes have the same intercept, then the cohesion and tensile strength have the following relation:

$$c = 2T_0 \tag{3.84}$$

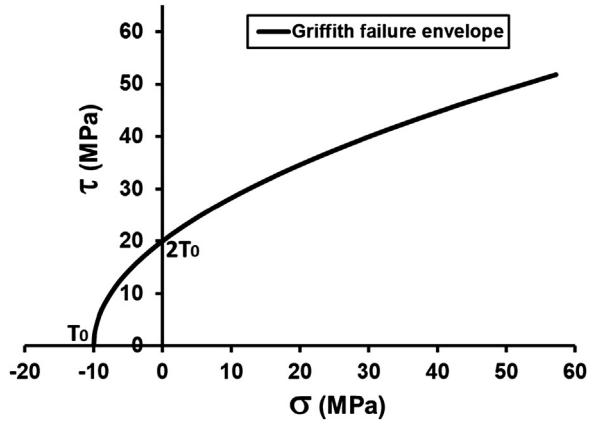

Figure 3.31 Griffith failure criterion Eq. (3.84) plotted in terms of the Mohr–Coulomb envelope with tensile strength $T_0 = 10$ MPa.

References

Al-Ajmi, A., Zimmerman, R.W., 2005. Relation between the Mogi and the Coulomb failure criteria. Int. J. Rock Mech. Min. Sci. 42, 431–439.

Amendt, D., Wenning, Q., Busetti, S., 2013. Mechanical characterization in unconventional reservoirs: a facies based methodology. SPWLA 54th Annual Logging Symp. Held in New Orleans, LA.

Barton, N., 1976. The shear strength of rock and rock joints. Int. J. Rock Mech. Min. Sci. Geomech. Abstr. 13, 255–279.

Barton, N., 2013. Shear strength criteria for rock, rock joints, rockfill and rock masses: problems and some solutions. J. Rock Mech. Geotech. Eng. 5 (4), 249–261.

Bons, P., Elburg, M., Gomez-Rivas, E., 2012. A review of the formation of tectonic veins and their microstructures. J. Struct. Geol. 43, 33–62.

Bradford, L.D.R., Fuller, J., Thompson, P.J., Walsgrove, T.R., 1998. Benefits of assessing the solids production risk in a North Sea reservoir using elasto-plastic modeling. SPE/ISRM-47360, Eurock'98 held in Trondheim Norway, pp. 261–269.

Brady, B.H.G., Brown, E.T., 2004. Rock Mechanics for Underground Mining. Springer.

Chang, C., Zoback, M., Khaksar, A., 2006. Empirical relations between rock strength and physical properties in sedimentary rocks. J. Pet. Sci. Eng. 51, 223–237.

Dohmen, T., Zhang, J., Li, C., Blangy, J.P., Simon, K.M., Valleau, D.N., Ewles, J.D., Morton, S., Checkles, S., 2013. A new surveillance method for delineation of depletion using microseismic and its application to development of unconventional reservoirs. Paper SPE 166274 presented at the SPE Annual Technology Conference in New Orleans, Louisiana.

Dohmen, T., Zhang, J., Barker, L., Blangy, J.P., 2017. Microseismic magnitudes and b-values for delineating hydraulic fracturing and depletion. SPE J. 22 (5), 1624–1633. SPE-186096.

Donath, F.A., 1964. Strength variation and deformational behavior in anisotropic rock. In: Judd, W.R. (Ed.), State of Stress in the Earth's Crust. American Elsevier, New York, pp. 281–297.

Drucker, D.C., Prager, W., 1952. Soil mechanics and plastic analysis or limit design. Q. Appl. Math. 10, 157–165.

Eberhardt, E., Steadb, D., Stimpson, B., 1999. Quantifying progressive pre-peak brittle fracture damage in rock during uniaxial compression. Int. J. Rock Mech. Min. Sci. 36, 361–380.

Engelder, T., Fischer, M.P., 1994. Influence of poroelastic behavior on the magnitude of minimum horizontal stress, S_h, in overpressured parts of sedimentary basins. Geology 22, 949–952.

Ewy, R.T., 1998. Wellbore stability prediction using a modified Lade criterion. Paper SPE-47251 presented at SPE/ISRM Eurock'98 held in Trondheim, Norway.

Fjær, E., Nes, O.-M., 2013. Strength anisotropy of Mancos shale. ARMA 13–519, the 47th US Rock Mechanics/Geomechanics Symposium held in San Francisco, CA, USA.

Fjær, E., Holt, R.M., Horsrud, P., Raaen, A.M., Risnes, R., 2008. Petroleum Related Rock Mechanics. Elsevier, Amsterdam.

Golubev, A.A., Rabinovich, G.Y., 1976. Resultaty primeneia appartury akusticeskogo karotasa dlja predeleina proconstych svoistv gornych porod na mestorosdeniaach tverdych isjopaemych. Prikl. Geofiz. Moskva 73, 109–116.

Griffith, A.A., 1921. The phenomena of rupture and flow in solids. Phil. Trans. Roy. Soc. Lond. A221, 163–198.

Haimson, B., 2006. True triaxial stresses and the brittle fracture of rock. Pure Appl. Geophys. 163, 1101–1130.

Haimson, B., Chang, C., 2000. A new true triaxial cell for testing mechanical properties of rock and its use to determine rock strength and deformability of Westerly granite. Int. J. Rock Mech. Min. Sci. 37, 285–296.
Hallbauer, D.K., Wagner, H., Cook, N.G.W., 1973. Some observations concerning the microscopic and mechanical behaviour of quartzite specimens in stiff, triaxial compression tests. Int. J. Rock Mech. Min. Sci. Geomech. Abstr. 10 (6), 713–726.
Havmøller, O., Foged, N., 1996. Review of rock mechanical data for chalk. Proc. 5th North Sea Chalk Sym. France, 7–9 October.
Hillis, R., 2000. Pore pressure/stress coupling and its implications for seismicity. Explor. Geophys. 31, 448–454.
Hoek, E., Brown, E.T., 1980. Underground excavations in rock. Inst. Min. Metall. London.
Hoek, E., Brown, E.T., 1997. Practical estimates of rock mass. Int. J. Rock Mech. Min. Sci. 34 (8), 1165–1186.
Hoek, E., Martin, C.D., 2014. Fracture initiation and propagation in intact rock – a review. J. Rock Mech. Geotech. Eng. 6 (4), 287–300.
Horsrud, P., 2001. Estimating mechanical properties of shale from empirical correlations. SPE-56017, SPE Drilling & Completion, pp. 68–73.
ISRM, 1978. Suggested methods for determining tensile strength of rock materials. Int. J. Rock Mech. Min. 15 (3), 99–103.
ISRM, 1979. Suggested methods for determining uniaxial compressive strength and deformability of rock materials, ISRM Committee on Standardization of Laboratory Tests. Int. J. Rock Mech. Min. Sci. 16, 137–140.
Jaeger, J.C., Cook, N.G.W., 1979. Fundamentals of Rock Mechanics, third ed. Chapman & Hall.
Jaeger, J.,C., Cook, N.G.W., Zimmerman, R., 2007. Fundamentals of Rock Mechanics, fourth ed. Blackwell Publishing.
Kovari, K., 1977. The elasto-plastic analysis in the design practice of underground openings. In: Gudehus, G. (Ed.), Finite Elements in Geomechanics. John Wiley & Sons, pp. 377–412.
Lade, P.V., 1984. In: Gallager, R.H. (Ed.), Failure Criterion for Frictional Materials. Mechanics of Engineering Materials Desai CS. John Wiley & Sons.
Lal, M., 1999. Shale Stability: Drilling Fluid Interaction and Shale Strength. Paper SPE 54356.
Lashkaripour, G.R., Dusseault, M.B., 1993. A statistical study on shale properties; relationship among principal shale properties. In: Proc. Conf. on Probabilistic Methods in Geotechnical Engineering, Canberra, Australia, pp. 195–200.
Ma, X., Rudnickib, J., Haimson, B., 2017. The application of a Matsuoka-Nakai-Lade-Duncan failure criterion to two porous sandstones. Int. J. Rock Mech. Min. Sci. 92, 9–18.
Martin, C.D., Chandler, N.A., 1994. The progressive fracture of Lac du Bonnet granite. Int. J. Rock Mech. Min. Sci. Geomech. Abstr. 31, 643–659.
McLamore, R., Gray, K.E., 1967. The mechanical behavior of anisotropic sedimentary rocks. J. Eng. Ind. 89, 62–73.
McNally, G.H., 1987. Estimation of coal measures rock strength using sonic and neutron logs. Geoexploration 24 (4–5), 381–395.
Militzer, H., Stoll, R., 1973. Einige Beitrageder geophysics zur primadatenerfassung im Bergbau, Neue Bergbautechnik. Lipzig 3, 21–25.
Mogi, K., 1971. Fracture and flow of rocks under high triaxial compression. J. Geophys. Res. 76, 1255–1269.
Mogi, K., 1974. On the pressure dependence of strength of rocks and the Coulomb-fracture criterion. Tectonophysics 21, 273–285.

Mogi, K., 2007. Experimental Rock Mechanics. Taylor & Francis/Balkema.
Moos, D., Zoback, M.D., Bailey, L., 1999. Feasibility study of the stability of openhole multilaterals, Cook Inlet, Alaska. Paper SPE-52186, SPE Mid-continent Operations Symposium held in Oklahoma City, Oklahoma.
Murrell, S.A.F., 1963. A criterion for brittle fracture of rocks and concrete under triaxial stress and the effect of pore pressure on the criterion. In: Fairhurst, C. (Ed.), Proc 5th Rock Mech Symp. In Rock Mechanics. Pergamon, pp. 563–577.
Murrell, S.A.F., 1965. The effect of triaxial stress systems on the strength of rocks at atmospheric temperatures. Geophys. J. R. Astron. Soc. 10, 231–281.
Nadai, A., 1950. Theory of Flow and Fracture of Solids, vol. 1. McGraw-Hill, New York, 1950.
Najibi, A.R., Ghafoori, M., Lashkaripour, G.R., 2015. Empirical relations between strength and static and dynamic elastic properties of Asmari and Sarvak limestones, two main oil reservoirs in Iran. J. Pet. Sci. Eng. 126, 78–82.
Niandou, H., Shao, J.F., Henry, J.P., Fourmaintraux, D., 1997. Laboratory investigation of the behaviour of Tournemire shale. Int. J. Rock Mech. Min. Sci. 34 (1), 3–16.
Ouyang, Z., Elsworth, D., 1991. A phenomenological failure criterion for brittle rock. Rock Mech. Rock Eng. 24, 133–153.
Peng, S., Zhang, J., 2007. Engineering Geology for Underground Rocks. Springer.
Plumb, R., 1994. Influence of composition and texture on the failure properties of clastic rocks. SPE-28022, presented at the 1994 Eurock Rock Mechanics in Petroleum Engineering, 29–31 August, Delft, Netherlands.
Roscoe, K.H., Burland, J.B., 1968. On the generalised stress-strain behaviour of 'wet' clay. Engineering Plasticity. Cambridge University Press, pp. 535–609.
Roscoe, K.H., Schofield, A.N., Wroth, C.P., 1958. On the yielding of soils. Geotechnique 8 (1), 22–52.
Roscoe, K.H., Schofield, A.N., Thurairajah, A., 1963. Yielding of clays in states wetter than critical. Geotechnique 13 (3), 211–240.
Schöpfer, M.P.J., Childs, C., Manzocchi, T., 2013. Three-dimensional failure envelopes and the brittle-ductile transition. J. Geophys. Res. Solid Earth. 118, 1378–1392.
Shang, J., Hencher, S.R., West, L.J., 2016. Tensile strength of geological discontinuities including incipient bedding, rock joints and mineral veins. Rock Mech. Rock Eng. 49, 4213–4225.
Singh, B., Raj, A., Singh, B., 2011. Modified Mohr–Coulomb criterion for non-linear triaxial and polyaxial strength of intact rocks. Int. J. Rock Mech. Min. Sci. 48 (4), 546–555.
Spetzler, H.A., Sobolev, G.A., Sondergeld, C.H., Salov, B.G., Getting, I.C., Koltsov, A., 1981. Surface deformation, crack formation, and acoustic velocity changes in pyrophyllite under polyaxial loading. J. Geophys. Res. 86, 1070–1080.
Vachaparampil, A., Ghassemi, A., 2013. Failure characteristics of three shales under true-triaxial compression. Int. J. Rock Mech. Min. Sci. 100, 151–159.
Vernik, L., Bruno, M., Bovberg, C., 1993. Empirical relations between compressive strength and porosity of siliciclastic rocks. Int. J. Rock Mech. Min. Sci. Geomech. Abstr. 30, 677–680.
Weingarten, J.S., Perkins, T.K., 1992. Prediction of sand production in gas wells: methods and Gulf of Mexico case studies. Paper SPE-24797 Washington DC, 4–7, October.
Whittaker, B.N., Singh, R.N., Sun, G., 1992. Rock Fracture Mechanics: Principles, Design and Applications. Developments in Geotechnical Engineering. Elsevier. Book 71.
Willson, S.M., Edwards, S.T., Crook, A., Bere, A., Moos, D., Peska, P., 2007. Assuring stability in extended-reach wells – analyses, practice, and mitigations. SPE/IADC 105405.

You, M., 2009. True-triaxial strength criteria for rock. Int. J. Rock Mech. Min. Sci. 46, 115–127.
Zhang, J., 2002. Dual-porosity Approach to Wellbore Stability in Naturally Fractured Reservoirs. Ph.D. dissertation. Univ. of Oklahoma.
Zhang, J., 2013. Borehole stability analysis accounting for anisotropies in drilling to weak bedding planes. Int. J. Rock Mech. Min. Sci. 60, 160–170.
Zhang, J., Wieseneck, J., 2011. Challenges and surprises of abnormal pore pressure in shale gas formations. Paper SPE 145964.
Zhang, J., Bai, M., Roegiers, J.C., 2003. Dual-porosity poroelastic analyses of wellbore stability. Int. J. Rock Mech. Min. Sci. 40, 473–483.
Zhang, J., Standifird, W., Lenamond, C., 2008. Casing ultradeep, ultralong salt sections in deep water: A case study for failure diagnosis and risk mitigation in record-depth well. Paper SPE 114273.

CHAPTER 4

Basic rock fracture mechanics

Contents

Abstract

Stress concentration occurs owing to the presence of cracks and sharp corners, causing rock failures; even the intact rock has a very high strength. Inglis and Griffith theories are introduced to study the stress and displacement relationships when fractures exist in the rock. Stress distributions around the fracture tips in three fracture modes are introduced. The stresses and fracture intensity factors in an inclined fracture under anisotropic far-field stresses are also discussed, which may be applicable for inclined wellbore and hydraulic fracturing problems. Sneddon's solutions of fracture widths in both 2-D and 3-D conditions are discussed, which can be applied to hydraulic fracturing modeling and wellbore strengthening design. Fracture propagation

Applied Petroleum Geomechanics
ISBN 978-0-12-814814-3
https://doi.org/10.1016/B978-0-12-814814-3.00004-6

in rock is characterized by the generation of microcracks around the crack tip, i.e., an inelastic zone or the fracture process zone is formed. This zone is examined using fracture mechanics theory. The mechanical properties and stress-deformation behaviors in fractured rock mass are also discussed.

Keywords: Fracture mechanics; Fracture process zone (FPZ); Fracture toughness; Fracture width; Stress at fracture tip; Stress intensity factor.

4.1 Stress concentration at the crack tip

Inglis (1913) calculated stresses and strains in an elastic plate due to the presence of cracks and sharp corners. Fig. 4.1 shows an elliptic hole or crack in a thin plate subjected to a tensile stress (σ_L), and the major and minor axes of the crack are $2a$ and $2b$, respectively. He found that the maximum stress at the crack tip, $\sigma_{\max}$, could be given by:

$$\sigma_{\max} = \left(1 + \frac{2a}{b}\right)\sigma_L \tag{4.1}$$

The ratio of the maximum stress to the applied stress is referred to as the elastic stress concentration factor (F_σ):

$$F_\sigma = \left(1 + \frac{2a}{b}\right) \tag{4.2}$$

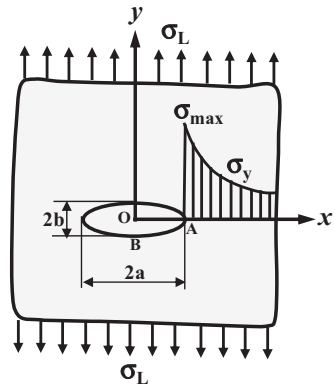

Figure 4.1 An elliptic hole in a thin plate subjected to uniform tension, causing stress concentration.

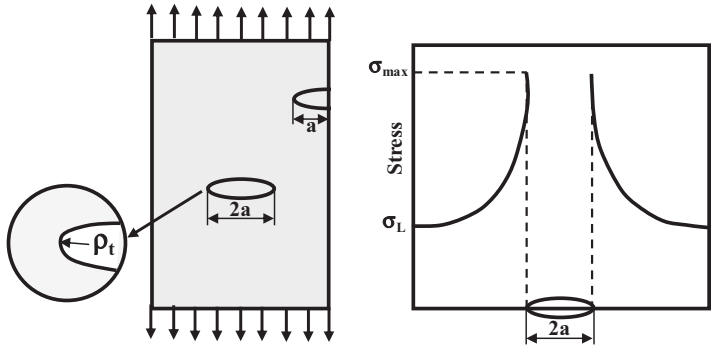

Figure 4.2 A surface crack and an internal crack in a thin plate subjected to uniform tension (left) and the stress concentration induced by the internal crack (right).

From Eq. (4.2), it is evident that the stress concentration factor can be considerably larger than unity for narrow holes. For a circular borehole ($a = b$), the stress concentration factor is 3. However, for a very narrow hole (e.g., a flat crack), the stress concentration factor is 21 if $a = 10b$. This means that the induced maximum stress will reach 21 times of the applied stress. These effects become more obvious as the ratio a/b increases, e.g., when $a/b = 1000$, the maximum tension at the point A is 2001 times the applied tensile stress. The ellipse in this case would appear as a fine straight crack, and a very small pull applied to the plate across the crack would set up a tension at the tips sufficient to start a tear in the material. The rapidity with which the induced stress decreases with the distance from this edge of the hole is also very noticeable (Inglis, 1913).

The maximum stress at the crack tip can also be expressed in the following form:

$$\sigma_{\max} = \left(1 + 2\sqrt{\frac{a}{\rho_t}}\right)\sigma_L \tag{4.3}$$

where ρ_t is the radius of curvature at the crack tip, and a is the half length of an internal crack, or the length of a surface crack (Suni, 2012), as shown in Fig. 4.2.

4.2 Linear-elastic fracture mechanics

4.2.1 Griffith crack theory

Inglis's theory shows that the stress increase at the tip of a crack is dependent only on the geometrical shape of the crack and not its absolute

size. Griffith (1921) found that this seemed contrary to the well-known fact that larger cracks are propagated more easily than smaller ones. This anomaly led Griffith to a theoretical analysis of fractures based on the point of view of minimum potential energy (Fischer-Cripps, 2007). Griffith proposed that the reduction in strain energy due to the formation of a crack must be equal to or greater than the increase in surface energy required by the new crack faces. According to Griffith, there are two conditions necessary for crack growth:

(1) The bonds at the crack tip must be stressed to the point of failure. The stress at the crack tip is a function of the stress concentration factor, which is dependent on the ratio of its radius of curvature to its length.

(2) For an increment of crack extension, the amount of strain energy released must be greater than or equal to that required for the surface energy of the two new crack faces.

Based on the fact that tensile strength of an actual material is much lower than that theoretically predicted, Griffith (1921) postulated that typical brittle materials inevitably contain numerous submicroscopic flaws, microcracks, or other discontinuities of heterogeneity, which are distributed with random orientation throughout the volume of the material (Whittaker et al., 1992). These cracks serve as stress concentrators, and fracture initiation is caused by the stress concentrations at the tips of these minute internal cracks. These cracks have since been referred to as the Griffith flaws or the Griffith cracks.

The fundamental concept of the Griffith theory is that the bounding surfaces of a solid possess a surface tension, just as those of a liquid do, and when a crack spreads the decrease in the strain energy is balanced by an increase in the potential energy due to this surface tension (Sneddon, 1946). The calculation of the effect of the presence of a crack on the energy of an elastic body is based on Inglis's solution (Inglis, 1913) of the two-dimensional equations of elastic equilibrium in the space bounded by two concentric ellipses, the crack being then taken to be an ellipse of zero eccentricity. Denoting the surface tension of the material of the solid body by T, the length of the crack by 2a, and Young's modulus of the material of the body by E, Griffith showed that, in the case of plane stress, the crack will spread when the tensile stress P, applied normally to the direction of the crack, exceeds the critical value P_c:

$$P_c = \sqrt{\frac{2ET}{\pi a}} \tag{4.4}$$

A formula differing from (Eq. 4.4) by a factor 0.8 has been derived by Orowan (1934) from rather similar assumptions. In the case of plane strain, it has the following form:

$$P_c = \sqrt{\frac{2ET}{\pi a(1-\nu^2)}} \tag{4.5}$$

where ν is Poisson's ratio.

Sack (1946) extended Griffith's theory to three dimensions and calculated the conditions of failure for a solid containing a plane crack bounded by a circle: a "penny-shaped" crack, when one of the principal stresses is acting normally to the plane of the crack. By treating the crack as an oblate spheroid whose elliptic section has zero eccentricity, Sack proposed that failure will occur when the tensile stress P normal to the crack exceeds the critical value P_c:

$$P_c = \sqrt{\frac{\pi ET}{2a(1-\nu^2)}} \tag{4.6}$$

The three-dimensional model introduced by Sack thus gives a critical tensile stress differing from the Griffith value (Eq. 4.4) by a factor $\pi/[2(1-\nu^2)^{1/2}]$.

4.2.2 Stress intensity factor and fracture toughness

The stress intensity factor, K, is used in fracture mechanics to describe the stress state at a crack tip. It is related to the rate of crack growth and used to establish failure criteria due to fracture. The stress intensity factor was developed by George R. Irwin (Irwin, 1957), the father of fracture mechanics. It is one of the most fundamental and useful parameters in fracture mechanics. For an elliptical crack, the stress intensity factor in Mode I fracture (K_I) is defined as:

$$K_I = \sigma\sqrt{\pi a} \tag{4.7}$$

where σ is the far-field stress; a is the half length of the crack.

A critical value of K can be obtained by experiments. Crack initiation will take place if the stress intensity factor K reaches its critical value or fracture toughness, K_C. Fracture toughness is a property that describes the ability of a material to resist fracture. The linear-elastic fracture toughness of a material is determined from the stress intensity factor at which a thin crack

in the material begins to grow. If the stress intensity factor of a fracture is equal or greater than its critical stress intensity factor or toughness, then the fracture starts to grow or be unstable, as shown in the following equation for Mode I fractures.

$$K_I = \sigma\sqrt{\pi a} \geq K_{IC} \tag{4.8}$$

where K_{IC} is the fracture toughness of Mode I fracture.

4.2.3 Three basic fracture modes

Different loading configurations at the crack tips lead to different modes of crack tip surface displacements. Three single loading configurations form three basic fracture modes, i.e., mode I, mode II, and mode III, as illustrated in the following (Fig. 4.3):

(1) Mode I: opening mode. The crack tip is subjected to a normal stress σ, and the crack faces separate symmetrically with respect to the crack front so that the displacements of the crack surfaces are perpendicular to the crack plane (Whittaker et al., 1992).

(2) Mode II: in-plane shearing mode. The crack tip is subjected to an in-plane shear stress τ_i, and the crack faces slide relative to each other so that the displacements of the crack surfaces are in the crack plane but perpendicular to the crack front.

(3) Mode III: tearing mode or out-of-plane shearing mode. The crack tip is subjected to an out-of-plane shear stress τ_0, and the crack faces move relative to each other so that the displacements of the crack surfaces are in the crack plane but parallel to the crack front.

A combination of any two of the three fracture modes constitutes a mixed mode, such as I-II, I-III, II-III, and I-II-III.

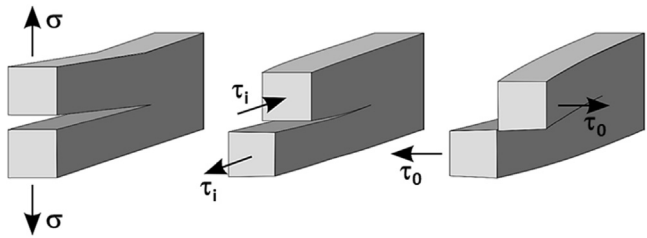

Figure 4.3 Mode I, opening mode (left); Mode II, in-plane shearing mode (middle); Mode III, out-of-plane shearing mode (right).

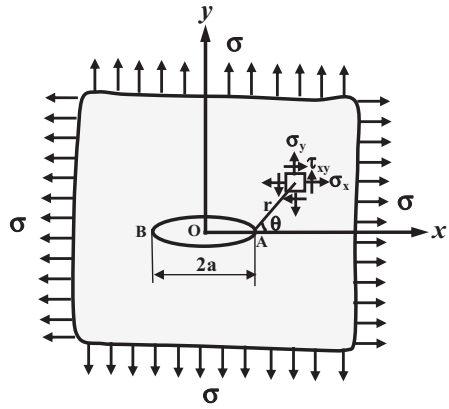

Figure 4.4 An infinite plate containing a fracture under biaxial tension.

4.2.4 Fracture tip stresses and displacements

4.2.4.1 Model I fracture

The stress and displacement equations at the fracture tip can be derived from the well-known Westergaard function. For the mode I fracture under biaxial tension, the stresses in the vicinity of the crack tip (point A in Fig. 4.4) can be expressed in the following (Whittaker et al., 1992):

$$\begin{bmatrix} \sigma_x \\ \sigma_y \\ \tau_{xy} \end{bmatrix} = \frac{K_I}{\sqrt{2\pi r}} \cos\frac{\theta}{2} \begin{bmatrix} 1 - \sin\frac{\theta}{2}\sin\frac{3\theta}{2} \\ 1 + \sin\frac{\theta}{2}\sin\frac{3\theta}{2} \\ \sin\frac{\theta}{2}\cos\frac{3\theta}{2} \end{bmatrix} \tag{4.9}$$

$$\text{For plane strain: } \sigma_z = \nu(\sigma_x + \sigma_y) \tag{4.10}$$

$$\text{For plane stress: } \sigma_z = \tau_{xz} = \tau_{yz} = 0 \tag{4.11}$$

where σ is the far-field stress; σ_x, σ_y, σ_z, and τ_{xy} are the normal and shear stresses in the vicinity of the fracture tip; r is the distance from the fracture tip; θ is an angle as shown in Fig. 4.4; and $K_I = \sigma\sqrt{\pi a}$.

In this chapter, tensile stress is positive and compressive stress is negative to be consistent with the fracture mechanics sign convention.

Using Hooke's law, the displacement components at the fracture tip can be obtained from Eq. (4.9):

$$\begin{bmatrix} u \\ v \end{bmatrix} = \frac{K_I}{4G}\sqrt{\frac{r}{2\pi}} \begin{bmatrix} (2k-1)\cos\dfrac{\theta}{2} - \cos\dfrac{3\theta}{2} \\ (2k+1)\sin\dfrac{\theta}{2} - \sin\dfrac{3\theta}{2} \end{bmatrix} \tag{4.12}$$

where u and v are the displacements along x- and y-axes, respectively; G is the shear modulus.

For plane strain: $k = 3 - 4\nu$ and $w = 0$.

For plane stress: $k = (3-\nu)/(1+\nu)$ and $w = -\frac{\nu}{E}\int(\sigma_x + \sigma_y)dz$

where w is the displacement along z-axis.

The principal stresses (σ_1, σ_2, σ_3) at the fracture tip can be obtained from Eqs. (4.9)–(4.11):

$$\begin{bmatrix} \sigma_1 \\ \sigma_2 \end{bmatrix} = \frac{K_I}{\sqrt{2\pi r}}\cos\frac{\theta}{2} \begin{bmatrix} 1 + \left|\sin\dfrac{\theta}{2}\right| \\ 1 - \left|\sin\dfrac{\theta}{2}\right| \end{bmatrix} \tag{4.13}$$

$$\text{For plane strain: } \sigma_3 = \nu(\sigma_1 + \sigma_2) = 2\nu\frac{K_I}{\sqrt{2\pi r}}\cos\frac{\theta}{2} \tag{4.14}$$

$$\text{For plane stress: } \sigma_3 = 0 \tag{4.15}$$

4.2.4.2 Model II fracture

For the mode II fracture under in-plane shear stresses in the far field, the stresses in the vicinity of the crack tip (point A in Fig. 4.5) can be expressed as follows (Whittaker et al., 1992):

$$\begin{bmatrix} \sigma_x \\ \sigma_y \\ \tau_{xy} \end{bmatrix} = \frac{K_{II}}{\sqrt{2\pi r}} \begin{bmatrix} -\sin\dfrac{\theta}{2}\left(2 + \cos\dfrac{\theta}{2}\cos\dfrac{3\theta}{2}\right) \\ \sin\dfrac{\theta}{2}\cos\dfrac{\theta}{2}\cos\dfrac{3\theta}{2} \\ \cos\dfrac{\theta}{2}\left(1 - \sin\dfrac{\theta}{2}\sin\dfrac{3\theta}{2}\right) \end{bmatrix} \tag{4.16}$$

For plane strain: $\sigma_z = \nu(\sigma_x + \sigma_y)$

For plane stress: $\sigma_z = \tau_{xz} = \tau_{yz} = 0$.

where K_{II} is the mode II fracture tip stress intensity factor, and $K_{II} = \tau_i\sqrt{\pi a}$; τ_i is the in-plane shear stresses in the far field.

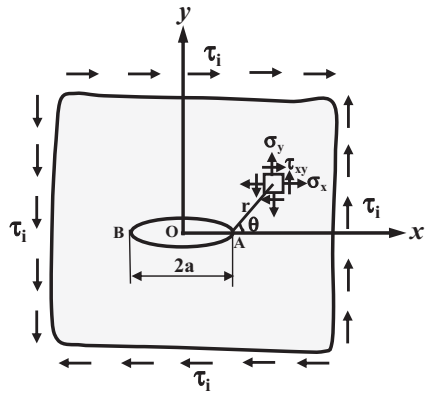

Figure 4.5 An infinite plate containing a fracture under in-plane shear stresses.

The displacement components at the fracture tip of the Mode II fracture can be obtained as follows:

$$\begin{bmatrix} u \\ v \end{bmatrix} = \frac{K_{II}}{4G}\sqrt{\frac{r}{2\pi}}\begin{bmatrix} (2k+3)\sin\dfrac{\theta}{2} + \sin\dfrac{3\theta}{2} \\ -(2k-3)\cos\dfrac{\theta}{2} - \cos\dfrac{3\theta}{2} \end{bmatrix} \tag{4.17}$$

For plane strain: $w = 0$.

For plane stress: $w = -\frac{\nu}{E}\int(\sigma_x + \sigma_y)dz$.

4.2.4.3 Model III fracture

For the mode III fracture under an antiplane shear stress τ_0 in the far field, the stresses in the vicinity of the crack tip can be expressed as follows (Whittaker et al., 1992):

$$\begin{bmatrix} \tau_{xz} \\ \tau_{yz} \end{bmatrix} = \frac{K_{III}}{\sqrt{2\pi r}}\begin{bmatrix} -\sin\dfrac{\theta}{2} \\ \cos\dfrac{\theta}{2} \end{bmatrix} \tag{4.18}$$

where K_{III} is the mode III fracture tip stress intensity factor, and $K_{III} = \tau_0\sqrt{\pi a}$.

And only the displacement w exists, i.e.,

$$w = \frac{2K_{III}}{G}\sqrt{\frac{r}{2\pi}}\sin\frac{\theta}{2} \tag{4.19}$$

4.2.5 Stresses and displacements in an inclined fracture

For a mixed mode (a fracture is exposed to two or more different loading systems), the resulting total stresses and displacements at the fracture tip can be superimposed to obtain because the principle of superposition is applicable in linear-elastic fracture mechanics. Using this feature the complex fracture problems with complicated loadings can be solved. For a plane cracked body having a line crack, arbitrary in size and shape (e.g., an inclined crack), and loaded arbitrarily along its outer boundaries (see Fig. 4.6), the elastic stress components in the immediate vicinity of the crack front can be obtained by superposing those resulting from Model I and Model II loadings (Eqs. 4.9 and 4.16), i.e.,

$$\begin{bmatrix}\sigma_x\\ \sigma_y\\ \tau_{xy}\end{bmatrix} = \frac{K_I}{\sqrt{2\pi r}}\cos\frac{\theta}{2}\begin{bmatrix}1-\sin\frac{\theta}{2}\sin\frac{3\theta}{2}\\ 1+\sin\frac{\theta}{2}\sin\frac{3\theta}{2}\\ \sin\frac{\theta}{2}\cos\frac{3\theta}{2}\end{bmatrix} + \frac{K_{II}}{\sqrt{2\pi r}}\begin{bmatrix}-\sin\frac{\theta}{2}\left(2+\cos\frac{\theta}{2}\cos\frac{3\theta}{2}\right)\\ \sin\frac{\theta}{2}\cos\frac{\theta}{2}\cos\frac{3\theta}{2}\\ \cos\frac{\theta}{2}\left(1-\sin\frac{\theta}{2}\sin\frac{3\theta}{2}\right)\end{bmatrix} \tag{4.20}$$

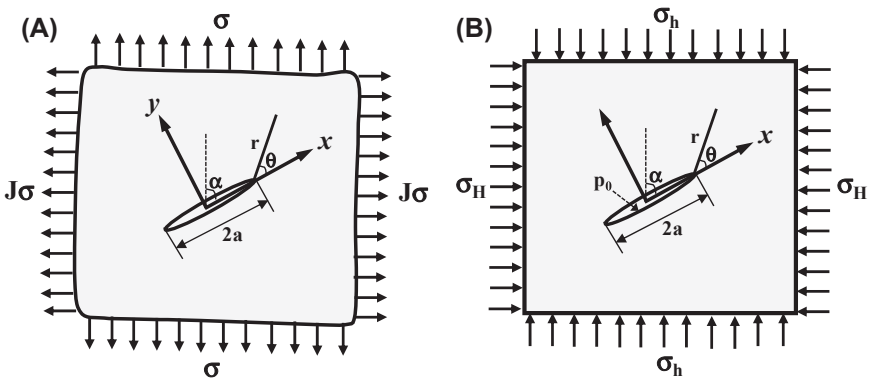

Figure 4.6 An inclined center-crack subjected to biaxial stresses. (A) far-field tensile stresses; (B) far-field compressive stresses and internal pressure.

Similarly, the crack tip displacement components can be obtained as follows (Eftis and Subramonian, 1978):

$$\begin{bmatrix} u \\ v \end{bmatrix} = \frac{K_I}{G}\sqrt{\frac{r}{2\pi}}\begin{bmatrix} \frac{1}{2}(k-1)\cos\frac{\theta}{2} - \cos\frac{\theta}{2}\sin^2\frac{\theta}{2} \\ \frac{1}{2}(k+1)\sin\frac{\theta}{2} - \sin\frac{\theta}{2}\cos^2\frac{\theta}{2} \end{bmatrix} + \frac{K_{II}}{G}\sqrt{\frac{r}{2\pi}}\begin{bmatrix} \frac{1}{2}(k+1)\sin\frac{\theta}{2} + \sin\frac{\theta}{2}\cos^2\frac{\theta}{2} \\ \frac{1}{2}(1-k)\cos\frac{\theta}{2} + \cos\frac{\theta}{2}\sin^2\frac{\theta}{2} \end{bmatrix} \tag{4.21}$$

where r is the radius started from the crack tip; k is expressed in terms of Poisson's ratio ν by $k = (3 - 4\nu)$ for plane strain and $k = (3 - \nu)/(1 + \nu)$ for idealized plane stress. The expression for stress hold provided $0 < (r/a) << 1$, while for displacement $0 \leq (r/a) << 1$.

By detailed study of the infinite sheet with a flat crack subject to biaxial loads, it was shown that use of Eqs. (4.20) and (4.21) leads to predictions that are, in general, qualitatively as well as quantitatively incorrect (Eftis and Subramonian, 1978). They extended their previous work to treat the biaxially loaded infinite sheet with an inclined crack. The stress and displacement components in the immediate vicinity of the crack front are as follows (Eftis and Subramonian, 1978):

$$\begin{aligned} \sigma_x &= \frac{K_I}{\sqrt{2\pi r}}\cos\frac{\theta}{2}\left[1 - \sin\frac{\theta}{2}\sin\frac{3\theta}{2}\right] - \frac{K_{II}}{\sqrt{2\pi r}}\sin\frac{\theta}{2}\left[2 + \cos\frac{\theta}{2}\cos\frac{3\theta}{2}\right] \\ &\quad + \sigma(1 - J)\cos 2\,\alpha \\ \sigma_y &= \frac{K_I}{\sqrt{2\pi r}}\cos\frac{\theta}{2}\left[1 + \sin\frac{\theta}{2}\sin\frac{3\theta}{2}\right] + \frac{K_{II}}{\sqrt{2\pi r}}\sin\frac{\theta}{2}\cos\frac{\theta}{2}\cos\frac{3\theta}{2} \\ \tau_{xy} &= \frac{K_I}{\sqrt{2\pi r}}\sin\frac{\theta}{2}\cos\frac{\theta}{2}\cos\frac{3\theta}{2} + \frac{K_{II}}{\sqrt{2\pi r}}\cos\frac{\theta}{2}\left[1 - \sin\frac{\theta}{2}\sin\frac{3\theta}{2}\right] \end{aligned} \tag{4.22}$$

$$u_x = \frac{K_I}{G}\sqrt{\frac{r}{2\pi}}\cos\frac{\theta}{2}\left[\frac{1}{2}(k-1)+\sin^2\frac{\theta}{2}\right]+\frac{K_{II}}{G}\sqrt{\frac{r}{2\pi}}\sin\frac{\theta}{2}\left[\frac{1}{2}(k+1)+\cos^2\frac{\theta}{2}\right]$$
$$+\frac{(1-J)\sigma}{8G}\{r[\cos(\theta+2\alpha)+k\cos(\theta-2\alpha)$$
$$-2\sin\theta\sin 2\alpha]+(k+1)a\cos 2\alpha\}$$
$$u_y = \frac{K_I}{G}\sqrt{\frac{r}{2\pi}}\sin\frac{\theta}{2}\left[\frac{1}{2}(k+1)-\cos^2\frac{\theta}{2}\right]+\frac{K_{II}}{G}\sqrt{\frac{r}{2\pi}}\cos\frac{\theta}{2}\left[\frac{1}{2}(1-k)+\sin^2\frac{\theta}{2}\right]$$
$$+\frac{(1-J)\sigma}{8G}\{r[\sin(2\alpha-\theta)+k\sin(2\alpha+\theta)-2\sin\theta\cos 2\alpha]$$
$$+(k+1)a\sin 2\alpha\} \tag{4.23}$$

where σ is the far-field stress in y-direction (see Fig. 4.6A); J is the ratio of the far-field stress in x-direction to the far-field stress in y-direction.

The crack intensity factors K_I and K_{II} can be obtained from the following equations:

$$K_I = \sigma_n\sqrt{\pi a} \tag{4.24}$$

$$K_{II} = \tau_n\sqrt{\pi a} \tag{4.25}$$

where σ_n is the normal stress perpendicular to the fracture surface; and τ_n is the shear stress parallel to the fracture surface. For the loading conditions shown in Fig. 4.6A, the intensity factors are specified by the following equations (Eftis and Subramonian, 1978):

$$K_I = \frac{\sigma\sqrt{\pi a}}{2}[(1+J)-(1-J)\cos 2\alpha] \tag{4.26}$$

$$K_{II} = \frac{\sigma\sqrt{\pi a}}{2}(1-J)\sin 2\alpha \tag{4.27}$$

The equations proposed by Eftis and Subramonian (1978) indicate that presence of the horizontal load for the inclined crack shows up both in the terms involving K_I and K_{II}, as well as in Eqs. (4.22) and (4.23). Both are necessary to give full account of load biaxiality.

Consider a pressurized crack subjected to an internal pressure, p_0, and the far-field compressive stresses σ_h and σ_H (see Fig. 4.6B), the stress

intensity factors can be obtained as follows (Rice, 1968; Abou-Sayed et al., 1978):

$$K_I = \sqrt{\pi a}(p_0 - \sigma_H \cos^2 \alpha - \sigma_h \sin^2 \alpha) \tag{4.28}$$

$$K_{II} = \sqrt{\pi a}\left[\frac{1}{2}(\sigma_H - \sigma_h)\sin 2\alpha\right] \tag{4.29}$$

4.2.6 Plastic zone and fracture process zone at the fracture tip

4.2.6.1 Plastic process zone at the fracture tip

Fracture tip plastic zone or yield zone can be obtained by applying the failure criteria to the stresses at the fracture tip. For metallic materials, the Von Mises failure criterion can be used and is given by the following expression:

$$(\sigma_1 - \sigma_2)^2 + (\sigma_2 - \sigma_3)^2 + (\sigma_1 - \sigma_3)^2 = 2\sigma_0^2 \tag{4.30}$$

where σ_1, σ_2, and σ_3 are the principal stresses at the fracture tip region; σ_0 is the yield strength.

Substituting the principal stresses at the fracture tip (Eqs. 4.13–4.15) into Eq. (4.30), the plastic zone at the fracture tip for Mode I fracture can be solved as follows:

$$\text{For plane stress: } r(\theta) = \frac{1}{4\pi}\left(\frac{K_I}{\sigma_0}\right)^2\left(1 + \frac{3}{2}\sin^2\theta + \cos\theta\right) \tag{4.31}$$

$$\text{For plane strain: } r(\theta) = \frac{1}{4\pi}\left(\frac{K_I}{\sigma_0}\right)^2\left[\frac{3}{2}\sin^2\theta + (1 + \cos\theta)(1 - 2\nu)^2\right] \tag{4.32}$$

It can be seen that as the fracture intensity factor increases, the size of the plastic zone that develop around the tip will be greater. The plastic zone length (r_p), the distance to the boundary ahead of the crack tip, can be solved from Eqs. (4.31) and (4.32) when $\theta = 0$ as follows:

$$\text{For plane stress: } r_p = \frac{1}{2\pi}\left(\frac{K_I}{\sigma_0}\right)^2 \tag{4.33}$$

$$\text{For plane strain: } r_p = \frac{1}{2\pi}\left(\frac{K_I}{\sigma_0}\right)^2(1 - 2\nu)^2 \tag{4.34}$$

4.2.6.2 Fracture process zone at the fracture tip in rock

A fracture in rock propagates generally in a brittle manner than in plastic yielding; therefore, the plastic zone at the crack front of the rock is very different from metallic materials. Fracture propagation in rock is characterized by the generation of microcracks around the crack tip and interlocking in a portion of the crack where displacement has not reached a critical value. This zone of inelastic behavior is called the fracture process zone (FPZ), analogous to the plastic zone in metals (Labuz et al., 1985). However, there are no sound theoretical models available to fully describe the shape and size of the crack tip FPZ, and it is often described by the approximate models developed to describe the plastic zone in metals (Whittaker et al., 1992).

Schmidt (1980) suggested a maximum normal stress criterion to describe the shape of the crack tip FPZ in rock. The criterion is that when the local maximum principal stress in the vicinity of the crack tip reaches the uniaxial tensile strength of the rock (T_0), the FPZ is generated, i.e.,

$$\sigma_1 = T_0 \tag{4.35}$$

Here the tensile stress is positive and compressive stress is negative to be consistent with the fracture mechanics notation.

Substituting Eq. (4.13) into the above equation yields the shape of the FPZ in Mode I fracture as follows:

$$r(\theta) = \frac{1}{2\pi}\left(\frac{K_I}{T_0}\right)^2 \cos^2\frac{\theta}{2}\left(1 + \left|\sin\frac{\theta}{2}\right|\right)^2 \tag{4.36}$$

The length of the FPZ can be obtained from the above equation by substituting $\theta = 0$:

$$r_p = \frac{1}{2\pi}\left(\frac{K_I}{T_0}\right)^2 \tag{4.37}$$

This is the same form as that of metallic materials for plane stress from the Von Mises criterion (Eq. 4.33) if the yield strength (σ_0) is equal to the uniaxial tensile strength (T_0). The shape and size of the FPZ is independent of whether the crack is under plane stress or plane strain condition because the out-of-plane stress does not enter onto the expression for $r(\theta)$ as given by Eq. (4.36). Because the maximum normal stress criterion does not consider the stress redistribution outside the FPZ, the actual size of the FPZ should be much larger than the one predicted from Eq. (4.36).

The cohesive crack model can be used to describe the nonlinear deformation ahead of a crack tip in rock. It is actually a modification to Dugdale's crack model originally developed for metals (Dugdale, 1960). In this model a notional crack with an effective crack length is assumed. This effective crack length consists of a traction-free portion (true crack length) and a length of the FPZ over which a cohesive stress, tending to close the crack, is distributed (refer to Fig. 4.7). Such a hypothesized crack is also referred to as a fictitious crack (Whittaker et al., 1992). The cohesive crack model has the following assumptions (Labuz et al., 1985; Whittaker et al., 1992):

(a) The rock in the FPZ is partially damaged but still able to carry closing stress σ (x), which is transferred from one surface to the other of the crack. The rock outside the FPZ is assumed to be linear elastic.

(b) The FPZ starts to develop when the maximum principal stress reaches the tensile strength T_0 and the corresponding true crack tip opening displacement δ_t is zero. With increasing δ_t, the stress is decreased until zero and the corresponding δ_t reaches a critical value δ_c.

(c) The closing cohesive stress is a function of true crack tip opening displacement δ_t.

(d) Overall stress intensity factor at the notional crack tip no longer exists, i.e., stress singularity at the notional crack tip disappears.

In Dugdale's crack model a constant closing stress distribution was used. For rocks, the closing stress, σ (x), should probably be a function of the

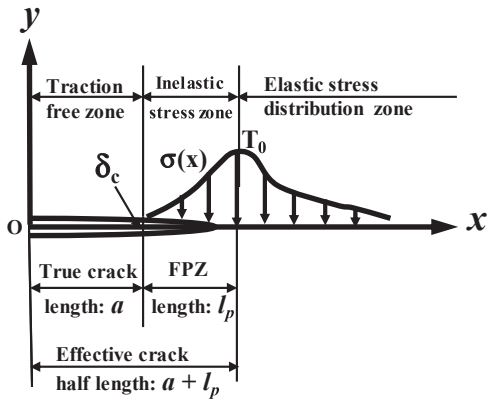

Figure 4.7 Representation of the fracture process zone of rock in the cohesive crack model.

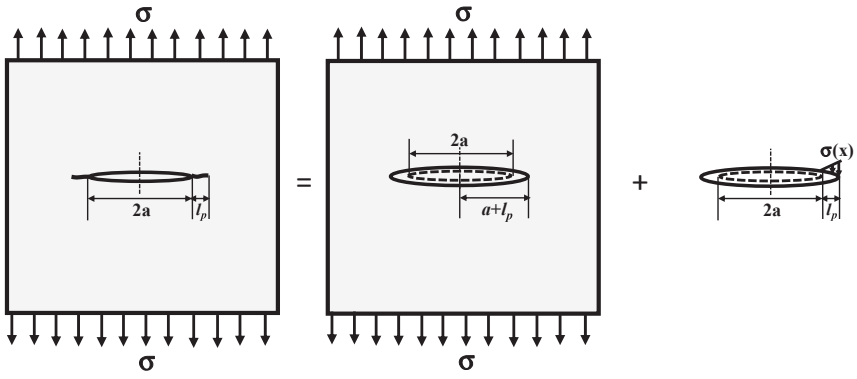

Figure 4.8 Schematic presentation of the Dugdale–Barenblatt model with a linear closing stress (σ (x)).

crack opening. As a first estimate of varying σ (x), Labuz et al. (1985) proposed a linear distributed σ (x) over the length of the FPZ (l_p),

$$\sigma(x) = \frac{x-a}{l_p} T_0 \tag{4.38}$$

where x is the distance from the center of the true crack tip along the x-axis.

Consider a crack of length 2a in an infinite plate (plane stress) acted on by a uniform tensile stress, σ, as shown in Fig. 4.8. A nonlinear zone of length l_p is formed (assuming $a > l_p$). Using a similar formulation of Barenblatt (1962), Labuz et al. (1985) derived a solution of the length l_p of the FPZ zone as follows:

$$l_p = \frac{9\pi}{32}\left[\frac{K_{IC}}{T_0}\right]^2 \tag{4.39}$$

Therefore, with the assumption of a linear distribution of closing stress and smooth crack closure (the singularity is zero), the nonlinear region is over twice as long as with the constant distribution as derived by Dugdale (1960), suggesting that the FPZ zone in rock is bigger than that in metal.

4.2.7 Fracture toughness of rock and its correlation to tensile strength

The fracture toughness of rock is an important parameter for modeling fracture failure and can be measured from laboratory tests. Gunsallus and

Kulhawy (1984) and Bhagat (1985) experimentally found that Mode I fracture toughnesses of several types of rocks and soils are directly proportional to their tensile strengths. Experimental data show that a very soft sedimentary rock (including coal), having a low tensile strength, has either a very low fracture toughness or a very low resistance to fracture initiation. In contrast, a hard rock, having a high tensile strength, has accordingly a high fracture toughness or has a very high resistance to fracture initiation. Whittaker et al. (1992) obtained some approximate relations between fracture toughness and tensile strength, compressive strength, point load strength, hardness, and velocity of acoustic wave of rock on the basis of experimental data from many references. According to Whittaker et al. (1992), the relations between Mode I and Mode II fracture toughnesses and tensile strengths of various types of rocks including coal can be expressed as follows:

$$K_{IC} = 0.27 + 0.107T_0 \tag{4.40}$$

$$K_{IIC} = 0.05 + 0.086T_0 \tag{4.41}$$

where T_0 is the tensile strength (MPa); and K_{IC} and K_{IIC} are Mode I and Mode II fracture toughnesses (MPa·m$^{1/2}$), respectively.

Using public data and their own experimental results, Zhang (2002) obtained a relation between Mode I fracture toughness and tensile strength for several rock types:

$$T_0 = 6.88K_{IC} \tag{4.42}$$

where T_0 is in MPa and K_{IC} is in MPa·m$^{1/2}$. This equation should be valid for general rocks from soft to hard under the condition of quasi-static or low-speed impact loading.

Chandler et al. (2016) conducted fracture toughness measurements on the Mancos shale samples; combined with public data, they obtained a similar correlation as Eq. (4.42), i.e., $T_0 = 6.76K_{IC}$

Through analyzing laboratory test data, Whittaker et al. (1992) obtained the following relations between fracture toughness and uniaxial compressive strength (UCS):

$$K_{IC} = 0.708 + 0.006UCS \tag{4.43}$$

$$K_{IIC} = 0.114 + 0.005UCS \tag{4.44}$$

4.3 Sneddon solutions of fracture widths

4.3.1 2-D plane strain solution of the Griffith fracture

Numerous analytical or semi-analytical solutions for estimating fracture width have been proposed. The line crack solution proposed by Sneddon (1946) and Sneddon and Elliott (1946) can be used to determine the width of a 2-D plane strain crack (fracture) in an isotropic stress environment without the presence of a borehole. Sneddon and Elliott (1946) considered the distribution of stresses in the interior of an infinite two-dimensional elastic medium when a very thin internal crack is opened under the action of a pressure, which may be considered to vary in magnitude along the length of the crack. Sneddon (1946) derived stress distributions in the interior of an infinite two-dimensional elastic medium produced by the opening of an internal crack (the length was $2c$ in his paper, and here $2L$ is used as shown in Fig. 4.9) under the action of a pressure in the crack in the plane strain condition. For the case of a uniform pressure (p_0), Sneddon and Elliott (1946) proposed the following solution for the fracture width (two-side displacements in y-direction):

$$w(x) = \frac{4(1-\nu^2)}{E} p_o \sqrt{L^2 - x^2} \tag{4.45}$$

where $w(x)$ is the fracture width; E is Young's modulus of the rock; ν is Poisson's ratio; p_0 is the internal pressure in the fracture; L is the fracture half length; x is the distance from the fracture center, as shown in Fig. 4.9.

The maximum fracture width appears at the center of the fracture, which can be obtained from Eq. (4.45) when $x = 0$.

Sneddon (1946) recognized that an adjustment might be required to the analytical solution for the effects of shorter height fractures when he stated that "the most striking feature of the analysis in the three-dimensional case is that the expressions for the components of stress in the neighborhood of

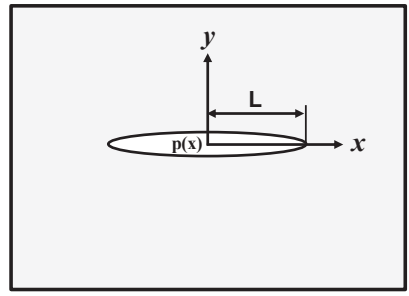

Figure 4.9 2-D plane strain fracture model.

the crack differ from those of the two-dimensional case by a numerical factor only."

4.3.2 General solution for fracture width of the Griffith fracture

The possibility of solving crack (fracture) problems by reducing them to a mixed boundary values for a half-plane or a half-space was first pointed out by Sneddon (1946) and Sneddon and Elliott (1946). Sneddon (1966) considered a case of stress field in the xy-plane owing to the application of a symmetrical pressure $p(x)$ to the faces of the Griffith fracture $|x| \leq L$, $y = 0$, as shown in Fig. 4.9. The symmetrical pressure means that $p(x)$ is an even function of x and that the pressure on the face $y = 0-$ of the crack is identical to that applied on the face $y = 0+$. It is sufficient to calculate the components of the stress tensor at the point (x, y) in the half-plane $y \geq 0$ when the line $y = 0$ is subjected to the boundary conditions:

$$\begin{aligned} \sigma_{yy}(x,0) &= -p(x), \quad 0 \leq x \leq L \\ u_y(x,0) &= 0, \qquad x > L \\ u_{xy}(x,0) &= 0, \qquad x \geq L \end{aligned}$$

These are readily established by considering the symmetry of the problem. Sneddon's integral equations can be applied to obtain the analytical solution of the fracture width (displacements of two sides of the fracture) caused by the internal pressure $p(x)$, i.e.,

$$w(x) = \frac{8(1-\nu^2)}{\pi E} \int_x^L \frac{tg(t)dt}{\sqrt{t^2 - x^2}}, \quad |x| < L \tag{4.46}$$

where $g(t)$ is a function of the internal pressure ($p(x)$ or σ_y) in the fracture, and $g(t) = \int_0^t \frac{p(x)dx}{\sqrt{t^2 - x^2}} = \int_0^t \frac{\sigma_y dx}{\sqrt{t^2 - x^2}}$ (Sneddon, 1966). The internal pressure may not be a constant or uniformly distributed. If $p(x)$ is a constant (e.g., $p(x) = p_0$), then $g(t) = \pi p_0/2$. Substituting it into Eq. (4.46), the solution of Eq. (4.45) can be obtained.

4.3.3 3-D solution for a penny-shaped fracture

A penny-shaped crack is a typical 3-D fracture in the interior of an infinite elastic medium, occupying the circle $r^2 = x^2 + y^2 = L^2$ in the plane $z = 0$, under the action of an internal pressure as a function of the radius r (Fig. 4.10). For this 3-D circular fracture with a constant internal pressure

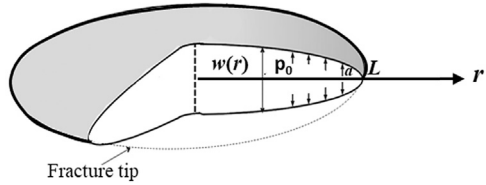

Figure 4.10 Model of a penny-shaped fracture.

(p_0) acting over the whole circular area, Sneddon (1946) derived the following equation to calculate the fracture width:

$$w(r) = \frac{8(1-\nu^2)}{\pi E} p_o \sqrt{L^2 - r^2} \tag{4.47}$$

If the applied pressure $p(r)$ is constant over a circular area of radius $a \leq L$ (i.e., the internal pressure only acts on a certain area of $0 < r < a$), then it has:

$$p(r) = p_0, \quad 0 < r < a$$
$$p(r) = 0, \quad a < r < L$$

The fracture width can be obtained in the following form (Sneddon, 1946):

$$w(r) = \frac{8(1-\nu^2)}{\pi E} p_o \sqrt{L^2 - r^2}\left(1 - \sqrt{1 - a^2/L^2}\right) \tag{4.48}$$

The maximum fracture width appears at the center of the circular fracture (when $r = 0$):

$$w_{\max} = \frac{8(1-\nu^2)p_o L}{\pi E}\left(1 - \sqrt{1 - a^2/L^2}\right) \tag{4.49}$$

Sneddon's solution has been applied into oil and gas industry for hydraulic fracturing modeling and wellbore strengthening design (e.g., Perkins and Kern, 1961; Khristianovic and Zheltov, 1955; Geertsma and de Klerk, 1969; Alberty and McLean, 2004; Zhang et al., 2016).

4.4 Natural fractures and mechanical behaviors of discontinuities

4.4.1 Discontinuities and discrete fracture network

One of the most prominent features of the earth's upper crust is the presence of joints and fractures (discontinuities) at all scales. A rock mass

consists of both intact rock blocks and discontinuities. An intact rock and a rock mass have significant different geomechanical behaviors (Peng and Zhang, 2007). Nearly every rock property is determined to some extent on the discontinuities and the fluids they contain. The success of many applications such as efficient recovery from fractured reservoirs, hazardous waste disposal, and geothermal energy extraction depends on a thorough understanding of fracture behaviors. Many petroleum reservoirs are situated in fractured porous formations, in which discontinuities have significantly different mechanical properties that control the behaviors of the reservoirs. The discontinuities can be the single most important factor governing the deformability, strength, and permeability of the rock mass. Moreover, a particularly large and persistent discontinuity could critically affect the stability of any underground excavation (Hudson and Harrison, 1997). For these reasons, it is necessary to understand the geomechanical properties of discontinuities and to know how the discontinuities affect rock behaviors.

There are many types of discontinuities in rock formations. Bedding, a discontinuity, is one of the most common geologic phenomena in sedimentary rocks. The bedding plane or interface between two layers in the sedimentary rock mass represents geologically the transitive interface from one sedimentary environment to another, and it also represents an interruption of sedimentary planes. A bedding plane generally consists of plant detritus, mica, and other weak minerals. Therefore, it is usually treated mechanically as a weak plane, as shown in Fig. 4.11.

The other discontinuities include unconformity planes and tectonic structural planes, such as faults, fractures, and joints induced by tectonic activities. Fig. 4.12 shows steep bedding planes and a fault in the Arbuckle

Figure 4.11 Thin bedding planes in the Marcellus shale outcrop.

Figure 4.12 The outcrop showing steep bedding planes (right side) and a fault (in the middle) in Arbuckle mountain, Oklahoma.

Figure 4.13 Two orthogonal sets of joints within siltstones and black shales of the Utica shale outcrop near Fort Plain, New York.

mountain, Oklahoma. Fig. 4.13 demonstrates rectangular joint networks within siltstones and black shales of the Utica shale outcrop, a similar behavior found in the Marcellus shale, where two orthogonal joints (J_1 and J_2) exist. Natural fractures can also be found in cores, and Fig. 4.14 displays that natural fractures are perpendicular to the bedding planes in the Wolfcamp cores. Those vertical fractures may be beneficial for hydraulic fracturing and enhancing oil production.

For complicated fracture networks, a computational model is needed and named "discrete fracture network" (DFN). The DFN is a three-dimensional geometric representation of joints present in a rock mass. It explicitly represents the geometrical properties of each individual fracture

Figure 4.14 Core pictures of the Wolfcamp C showing partially filled natural fractures perpendicular to the bedding planes.

(e.g., orientation, size, position, shape, and aperture) and the topological relationship between individual fractures and fracture sets. The DFN modeling grew out of attempts by early researchers in the 1970s and 1980s to develop a technology to characterize and model the flow and transport in natural fractures for the emerging high-level nuclear waste repository studies in the United States and Sweden. Although much early work was done to support nuclear waste repository performance assessment, the usefulness of DFN modeling became readily apparent to engineers and geologists working in the mining, oil and gas, civil engineering, and groundwater protection/remediation areas, where the use has greatly increased over the past 20 years. There are now several commercial vendors of DFN codes, and the use of DFN models has become part of the standard workflow in many areas of rock engineering (La Pointe, 2017). The DFN can be generated from geological mapping, stochastic realization, or geomechanical simulation to represent different types of rock fractures including joints, faults, veins, and bedding planes (Lei et al., 2017).

4.4.2 Mechanical behaviors of discontinuities

A discontinuity (e.g., a bedding plane) generally is a weak plane compared to the rock matrix and has prominently lower strength and higher compressibility. Therefore, the bedding plane has much lower compression resistance, shear resistance, and tension resistance. Failures are more likely to occur in bedding planes or preexisting fractures.

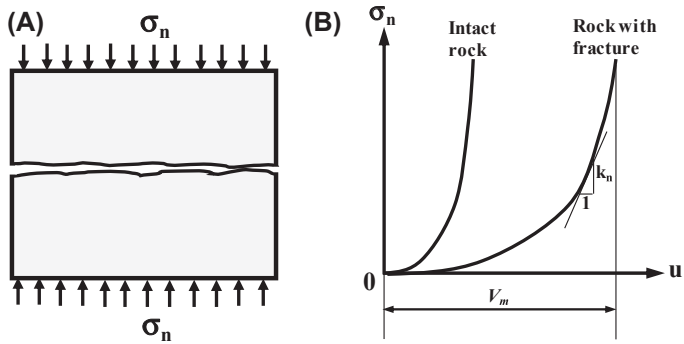

Figure 4.15 (A) A discontinuity loaded in compression; (B) normal stress and normal displacement relationship.

The normal and shear stiffnesses are two basic parameters used to describe mechanical behaviors of a discontinuity. The normal stiffness is defined as the slope in the normal stress and displacement curve when a discontinuity is loaded under a normal stress perpendicular to the direction of the discontinuity (Fig. 4.15), i.e.,

$$k_n = \frac{\partial \sigma_n}{\partial u} \tag{4.50}$$

where k_n is the normal stiffness of the discontinuity; σ_n is the normal stress applied perpendicularly to the discontinuity; u is the normal displacement of the discontinuity.

The shear stiffness (k_s) is the slope in the curve of the applied shear stress (τ) and resulted shear displacement (v) and can be expressed in the following (refer to Fig. 4.16):

$$k_s = \frac{\partial \tau}{\partial v} \tag{4.51}$$

Laboratory test results show that the shear stiffness in the discontinuity is much smaller than the normal stiffness. In other words, the discontinuity is much weaker to resist shear stress.

For an interlocked joint (discontinuity) when a normal compressive stress is exerted on the discontinuity as shown in Fig. 4.15, the normal stress and discontinuity displacement have a hyperbolic (nonlinear) relation (Goodman, 1976):

$$\sigma_n = \left(\frac{\Delta V_j}{V_m - \Delta V_j}\right)\sigma_i + \sigma_i \tag{4.52}$$

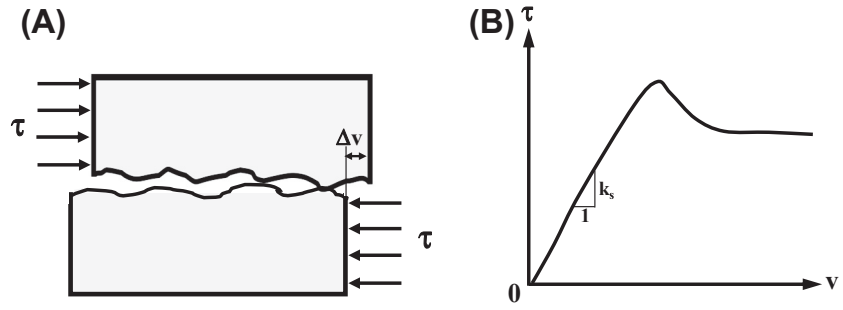

Figure 4.16 (A) A discontinuity sheared under a constant normal stress; (B) shear stress versus shear displacement.

where ΔV_j is the joint closure under a given normal stress σ_n; V_m is the maximum closure (displacement); and σ_i is the initial stress level. An alternative version of Eq. (4.52) was given by Goodman (1976) in the following dimensionless form:

$$\frac{\sigma_n - \sigma_i}{\sigma_i} = C\left(\frac{\Delta V_j}{V_m - \Delta V_j}\right)^t \tag{4.53}$$

where C and t are constants.

Bandis et al. (1983) proposed another empirical normal stress–displacement model for an interlocked joint:

$$\sigma_n = \frac{\Delta V_j}{a - b\Delta V_j} \tag{4.54}$$

where a and b are constants; a represents the reciprocal of the initial normal stiffness k_{ni} ($a = 1/k_{ni}$); $a/b = V_m$; V_m is the maximum closure of the joint and

$$V_m = A + B(JRC) + C\left(\frac{JCS}{a_j}\right)^D \tag{4.55}$$

where A, B, C, and D are constants determined from cyclic loading tests; JRC is the joint roughness coefficient from 0 to 20; JCS is the joint wall compression strength.

The initial normal stiffness can be obtained from the following relation (Bandis, 1980):

$$k_{ni} = -7.15 + 1.75JRC + 0.02\left(\frac{JCS}{a_j}\right) \tag{4.56}$$

where k_{ni} is the initial normal stiffness in MPa/mm; a_j is the initial mechanical aperture in mm; *JCS* is in MPa.

The above equations are for interlocked joints. However, for a dislocated joint the normal stress and displacement have the following relation:

$$\log \sigma_n = k_{ni} + M\Delta V_j \tag{4.57}$$

where M is a constant.

Based on laboratory tests on fractured concrete blocks, Zhang et al. (1999) found that the applied stress and fracture displacement follow an exponential relation. For example, for the uniaxial loading perpendicular to the fracture plane, the fracture displacement (aperture) decreases as the applied stress increases, which can be expressed in the following form:

$$u = b_0 e^{-a\sigma_n} \tag{4.58}$$

where b_0 is the initial fracture width (aperture); a is a testing constant ($a > 0$).

Eq. (4.58) indicates that the normal stress, which is perpendicular to the fracture plane, causes the fracture to close. However, for the uniaxial loading parallel to the fracture plane, the fracture aperture increases as the applied stress increases. This is because the tensile stress is induced in the direction of perpendicular to the fracture plane. The fracture displacement can be defined by the following relation (Zhang et al., 1999):

$$u = b_0 e^{b\sigma_x} \tag{4.59}$$

where σ_x is the applied stress parallel to fracture plane; b is a constant ($b > 0$).

The shear stress and shear displacement of a rough discontinuity depend on the normal stress and the discontinuity surface characteristics because the shear deformation involves dilation and fracture asperities. A hyperbolic function is frequently used to describe the shear stress and shear displacement relationship for a discontinuity in the prepeak stress regime:

$$\tau = \frac{v}{a + bv} \tag{4.60}$$

where v is the shear displacement of the discontinuity; τ is the shear stress; and c and d are constants.

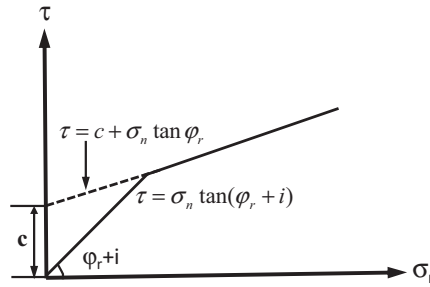

Figure 4.17 Shear failure criterion in the fractured rock compared to that in the intact rock.

Newland and Allely (1957) developed an equation to explain and predict the shear resistance of nonplanar rock joints based on the observed dilatant behavior of granular material such as sand:

$$\tau = \sigma_n \tan(\phi_r + i) \tag{4.61}$$

where τ is the maximum shear strength under the normal stress σ_n; i is the average angle of deviation of the fracture from the direction of the applied shear stress (see Fig. 4.17), and φ_r is the angle of internal friction of the intact rock or residual angle of internal friction used by Barton (1976).

Compared to the Mohr–Coulomb criterion, the cohesion in the fractured rock is zero in Eq. (4.61). Barton (1973, 1976) proposed a similar equation to describe the fracture shear failure based on shear tests for the rough tension fractures:

$$\tau = \sigma_n \tan\left[\phi_r + JRC \log\left(\frac{JCS}{\sigma_n}\right)\right] \tag{4.62}$$

Eqs. (4.61) and (4.62) can be used as the shear failure criterion for fractured rocks.

4.4.3 Mechanical behaviors of rock masses

Research shows that the deformation behaviors of a rock matrix and a rock mass are different. For a simple case, if a set of structure planes (such as bedding planes) are parallel and equally spaced in the rock mass, Young's moduli of rock mass and rock matrix can be expressed as:

$$\frac{1}{E_m} = \frac{1}{E_r} + \frac{1}{k_n s} \tag{4.63}$$

where E_m is Young's modulus of the rock mass; E_r is Young's modulus of the rock matrix; k_n is the normal stiffness of the structure plane; and s is the spacing of structure planes.

The weak planes or fractures in a rock mass make the compressive strength of the rock mass far less than that of the rock matrix. The presence of bedding or other discontinuities also causes anisotropies in both mechanical properties and mechanical behaviors; for example, rock strength, Young's modulus, and deformation are considerably different in the parallel and perpendicular directions of the bedding, as described in Chapters 2 and 3. These behaviors should be considered in the subsurface engineering design and operations.

References

Abou-Sayed, A., Brechtel, C., Clifton, R., 1978. In situ stress determination by hydrofracturing: a fracture mechanics approach. J. Geophys. Res. 83 (B6), 2851–2862.

Alberty, M., McLean, M., 2004. A physical model for stress cages. SPE-90493. SPE Annual Technical Conference and Exhibition, Houston, 26–29 September.

Bandis, S.C., 1980. Experimental Studies of Scale Effects on Shear Strength and Deformation of Rock Joints. Ph.D. thesis. Univ. of Leeds, 385pp.

Bandis, S.C., Lumsden, A.C., Barton, N.R., 1983. Fundamentals of rock joint deformation. Int. J. Rock Mech. Min. Sci. Geomech. Abstr. 20, 249–268.

Barenblatt, G.I., 1962. Mathematical theory of equilibrium cracks in brittle fracture. Adv. Appl. Mech. 7, 55–129.

Barton, N., 1973. Review of a new shear strength criterion for rock joints. Eng. Geol. 7 (4), 287–332.

Barton, N., 1976. The shear strength of rock and rock joints. Int. J. Rock Mech. Min. Sci. Geomech. Abstr. 13, 255–279.

Bhagat, R.B., 1985. Mode I fracture toughness of coal. Int. J. Min. Eng. 3, 229–236.

Chandler, M.R., Meredith, P.G., Brantut, N., Crawford, B.R., 2016. Fracture toughness anisotropy in shale. J. Geophys. Res. Solid Earth 121 (3), 1706–1729.

Dugdale, D.C., 1960. Yielding of steel sheets containing slits. J. Mech. Phys. Solids 8, 100–104.

Eftis, J., Subramonian, N., 1978. The inclined crack under biaxial load. Eng. Fract. Mech. 10 (1), 43–67.

Fischer-Cripps, A.C., 2007. Introduction to Contact Mechanics, second ed. Springer.

Geertsma, J., de Klerk, F., December 1969. A rapid method of predicting width and extent of hydraulically induced fractures. J. Pet. Technol. Paper SPE-2458.

Goodman, R.E., 1976. Methods of Geological Engineering in Discontinuous Rocks. West Publishing.

Griffith, A.A., 1921. The phenomena of rupture and flow in solids. Phil. Trans. Roy. Soc. Lond. A221, 163–198.

Gunsallus, K.L., Kulhawy, F.H., 1984. A comparative evaluation of rock strength measures. Int. J. Rock Mech. Min. Sci. Geomech. Abstr. 21 (5), 233–248.

Hudson, J., Harrison, J., 1997. Engineering Rock Mechanics: An Introduction to the Principles. Pergamon.

Inglis, C.E., 1913. Stresses in plates due to the presence of cracks and sharp corners. Transactions of the Institute of Naval Architects 55, 219–241.
Irwin, G.R., 1957. Analysis of stresses and strains near the end of a crack traversing a plate. J. Appl. Mech. 24, 361–364.
Khristianovich, S.A., Zheltov, Y.P., 1955. Formation of vertical fractures by means of highly viscous liquid. In: Proc., Fourth World Petro. Congress, Rome, vol. 2, pp. 579–586.
La Pointe, P., 2017. Special issue on Discrete Fracture Network (DFN) modeling – preface. ARMA e-Newsletter, 20.
Labuz, J.F., Shah, S.P., Dowding, C.H., 1985. Experimental analysis of crack propagation in granite. Int. J. Rock Mech. Min. Sci. Geomech. Abstr. 22, 85–98.
Lei, Q., Latham, J.-P., Tsang, C.-F., 2017. The use of discrete fracture networks for modelling coupled geomechanical and hydrological behaviour of fractured rocks. Comput. Geotech. 85, 151–176.
Newland, P.L., Allely, B.H., 1957. Volume changes in drained triaxial tests on granular materials. Geotechnique 7, 17–34.
Orowan, E., 1934. Die mechanischen festigkeitseigenschaften und die realstruktur der kristalle. Z. Kristallogr. 89, 327–343.
Peng, S., Zhang, J., 2007. Engineering Geology for Underground Rocks. Springer.
Perkins, T.K., Kern, L.R., 1961. Widths of hydraulic fractures. SPE Annual Fall Meeting, Dallas, 8–11 October. SPE-89-PA.
Rice, J.R., 1968. Mathematical analysis in the mechanics of fracture. In: Liebowitz, H. (Ed.), Treatise on Fracture, vol. II. Academic, New York, pp. 191–311 chap. 3.
Sack, R.A., 1946. Extension of Griffith's theory of rupture to three dimensions. Proc. Phys. Soc. 58 (6), 729–736.
Schmidt, R.A., 1980. A microcrack model and its significance to hydraulic fracturing and fracture toughness testing. In: Proc. 21st US Symp. on Rock Mech., pp. 581–590.
Sneddon, I.N., 1946. The distribution of stress in the neighbourhood of a crack in in an elastic solid. Proc. Roy. Soc. Lond. Math. Phys. Sci. 187, 229–260.
Sneddon, I.N., 1966. Crack problems in the theory of elasticity. In: Shaw, W.A. (Ed.), Developments in Theoretical and Applied Mechanics.
Sneddon, I.N., Elliott, H.A., 1946. The opening of a Griffith crack under internal pressure. Q. Appl. Math. 4, 262–266.
Suni, I., 2012. Materials Science and Engineering I: ES 260 Notes. Chap. 9. Clarkson University.
Whittaker, B.N., Singh, R.N., Sun, G., 1992. Rock Fracture Mechanics: Principles, Design and Applications. Developments in Geotechnical Engineering. Book 71. Elsevier.
Zhang, Z.X., 2002. An empirical relation between mode I fracture toughness and the tensile strength of rock. Int. J. Rock Mech. Min. Sci. 39, 401–406.
Zhang, J., Bai, M., Roegiers, J.-C., Liu, T., 1999. Determining stress-dependent permeability in the laboratory. In: Amadei, B., Kranz, R.L., Scott, G.A., Smeallie, P.H. (Eds.), Proc. 37th US Rock Mech. Symp. Colorado. Rotterdam, Balkema, pp. 341–347.
Zhang, J., Alberty, M., Blangy, J.P., 2016. A semi-analytical solution for estimating the fracture width in wellbore strengthening applications. Paper SPE-180296 presented at SPE Deepwater Drilling & Completions Conf. held in Galveston, TX, USA.

CHAPTER 5

In situ stress regimes with lithology-dependent and depletion effects

Contents

Abstract

Three in situ stress regimes are introduced, which can be used to describe the relationship of the vertical stress and two horizontal stresses. From Anderson's faulting theory, the lower and upper bound horizontal stresses are obtained either from the coefficient of friction of the fault or from Poisson's ratio of the formation. Both the coefficient of friction of the fault and the horizontal stresses are lithology-dependent. If formations in a fault are composed of shales, the coefficient of friction of the fault is small. This implies that the fault zone that is composed of shales is weaker and more likely to have shear failures than the fault zone composed of sandstones. An improved lithology-dependent (Poisson's ratio-dependent) stress polygon is presented, which can reduce the uncertainty of in situ stress estimate by narrowing the area of the conventional stress polygon. Pore pressure depletion by oil and gas extraction decreases the minimum and maximum horizontal stresses. Field-measured depletion-induced stress paths are also examined. Continuous depletion makes the formation approach the critical stress state (shear failures), and in this state fluid injection or repressurization may cause the formation shear failures.

Keywords: Depletion and injection; Horizontal stresses; In situ stresses; Lithology-dependent; Poisson's ratio dependent stress polygon; Stress polygon; Stress regimes.

Applied Petroleum Geomechanics
ISBN 978-0-12-814814-3
https://doi.org/10.1016/B978-0-12-814814-3.00005-8

5.1 In situ stresses in various faulting regimes

In situ stresses are the most important parameters for geomechanics modeling and geoengineering design, particularly in the oil and gas industry. For example, the minimum horizontal stress is very critical for fracture gradient prediction, casing design and wellbore stability assessment in drilling operations, and planning hydraulic fracturing in tight reservoirs. Generally, in situ stresses include three mutually orthogonal principal stresses in the subsurface, which can be defined as the vertical (overburden) stress and the maximum and minimum horizontal stresses (σ_V, σ_H, and σ_h). In different geographic, geologic, and tectonic regions, in situ stress magnitudes and orientations are very different. Three in situ stresses correspond to three principal stresses, namely the greatest stress (σ_1), the intermediate stress (σ_2), and the least stress (σ_3). According to the relationship of these three principal stresses, three in situ stress regimes (refer to Fig. 5.1) can be used to describe in situ stress states (e.g., Zoback et al., 2003; Peng and Zhang, 2007) based on the faulting theory (Anderson, 1951). Assuming that the faults were formed by shear failures caused by in situ stresses, the following three stress regimes can be classified based on the relationship of shear failures and principal stresses:

1. Normal faulting stress regime (Fig. 5.1A). The vertical stress drives normal faulting (shear failure), and the shear slip occurs to form the normal fault when the minimum stress reaches a sufficiently low value. In this stress state, the vertical stress is the greatest principal stress, and

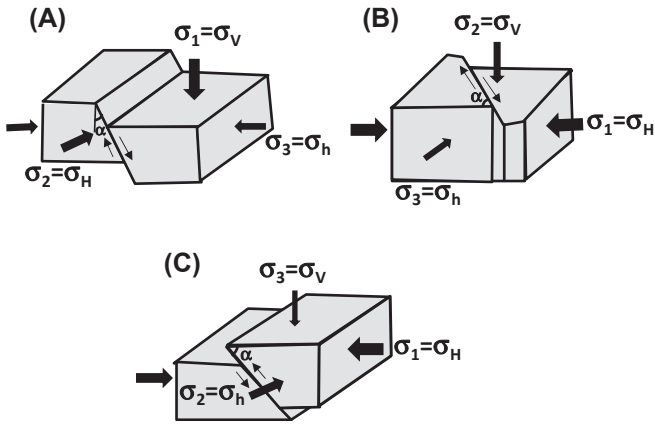

Figure 5.1 Illustration of different faulting stress regimes: (A) Normal faulting; (B) Strike-slip faulting; and (C) Reverse faulting.

two horizontal stresses are the intermediate and minimum principal stresses, i.e.,

$$\sigma_V \geq \sigma_H \geq \sigma_h \tag{5.1}$$

From the Mohr circle (see Fig. 3.21) the angle between the shear failure plane (the fault plane) and the maximum stress (σ_V) is:

$$\alpha = 45^\circ - \varphi/2 \tag{5.2}$$

where φ is the angle of internal frication of the rock. It can be seen from Eq. (5.2) that $\alpha < 45$ degrees. Therefore, the angle of dip of the fault plane in the normal fault is 90 degrees $-\alpha$ (> 45 degrees, see Fig. 5.1A).

2. Strike-slip faulting stress regime (Fig. 5.1B). In this case, the vertical stress is the intermediate principal stress, i.e.,

$$\sigma_H \geq \sigma_V \geq \sigma_h \tag{5.3}$$

The maximum horizontal stress causes faulting (shear failure). The angle between the shear plane of the fault and the maximum horizontal stress is $\alpha = 45^\circ - \varphi/2$.

3. Reverse (or thrust) faulting stress regime (Fig. 5.1C). In this case, the vertical stress is the least principal stress, i.e.,

$$\sigma_H \geq \sigma_h \geq \sigma_V \tag{5.4}$$

The maximum horizontal stress causes thrust faulting (shear failure). The angle between the fault plane and the maximum horizontal stress is $\alpha = 45^\circ - \varphi/2$, i.e., the angle of dip of the fault $\alpha < 45$ degrees, a low angle fault.

It should be noted that current stress state may be different from observed fault types in the formations, particularly for the reverse faulting stress regime. For example, the presence of reverse faults is not necessary to represent a reverse faulting stress regime in the contemporary stress field. The reason is that the paleostresses in this case might be in the reverse faulting stress regime; however, it was an unstable stress state and more likely to be changed to the strike-slip or normal faulting stress regime because of stress relaxation or other reasons.

5.2 In situ stress bounds and stress polygons

Assuming that there are critically oriented faults constraining stress magnitudes, the Mohr–Coulomb criterion (Jaeger and Cook, 1979) expressed

in the principal effective stress domain for a fault is shown in the following equation, if there is no shear failure/sliding:

$$\sigma'_1 \le \frac{2c_f \cos\varphi_f}{1-\sin\varphi_f} + \frac{1}{k_f}\sigma'_3 \tag{5.5}$$

where σ'_1 is the maximum effective stress; σ'_3 is the minimum effective stress; φ_f is the angle of internal friction of the fault; c_f is the cohesion of the fault; and

$$k_f = \frac{1-\sin\varphi_f}{1+\sin\varphi_f} = \left(\sqrt{\mu_f^2+1}+\mu_f\right)^{-2} \tag{5.6}$$

where μ_f is the coefficient of friction of the fault, and $\mu_f = \tan\varphi_f$.

For deep formations, the cohesion of the fault is often neglected and Eq. (5.5) can be simplified. Therefore, to avoid a fault from frictional sliding, the in situ stresses should satisfy the following equation—a similar equation used by Sibson (1974) and Zoback et al. (2003):

$$\sigma'_1 \le \frac{1}{k_f}\sigma'_3 \tag{5.7}$$

Substituting the total principal stresses into Eq. (5.7), the in situ stresses can be expressed in the following equations for different faulting stress regimes (as shown in Fig. 5.1):

Normal faulting regime:

$$\frac{\sigma'_1}{\sigma'_3} = \frac{\sigma_V - \alpha p_p}{\sigma_h - \alpha p_p} \le \frac{1}{k_f} \tag{5.8}$$

where α is Biot's coefficient; p_p is the pore pressure.

Strike-slip faulting regime:

$$\frac{\sigma'_1}{\sigma'_3} = \frac{\sigma_H - \alpha p_p}{\sigma_h - \alpha p_p} \le \frac{1}{k_f} \tag{5.9}$$

Reverse faulting regime:

$$\frac{\sigma'_1}{\sigma'_3} = \frac{\sigma_H - \alpha p_p}{\sigma_V - \alpha p_p} \le \frac{1}{k_f} \tag{5.10}$$

Hence, from Eq. (5.8) the lower bound minimum horizontal stress (σ_h^{LB}) can be obtained:

$$\sigma_h^{LB} = \left(\sqrt{\mu_f^2+1}+\mu_f\right)^{-2}(\sigma_V - \alpha p_p) + \alpha p_p \tag{5.11}$$

From Eq. (5.10), the upper bound maximum horizontal stress (σ_H^{UB}) can be expressed as:

$$\sigma_H^{UB} = \left(\sqrt{\mu_f^2 + 1} + \mu_f\right)^2 (\sigma_V - \alpha p_p) + \alpha p_p \tag{5.12}$$

It should be noted that Biot's effective stress coefficient, α, approaches 1 when the rocks are near the state of failures. Therefore, it can be assumed that $\alpha = 1$ in Eqs. (5.8)–(5.12).

Fig. 5.2 plots the in situ stress and pore pressure profiles in a deepwater well with water depth of 858 m (Zhang and Zhang, 2017). The figure displays the measured sand pore pressure, vertical stress from density logs, and the calculated lower and upper bound horizontal stresses from Eqs. (5.11) and (5.12). In the normal faulting stress regime, the minimum horizontal stress should range from the lower bound minimum horizontal

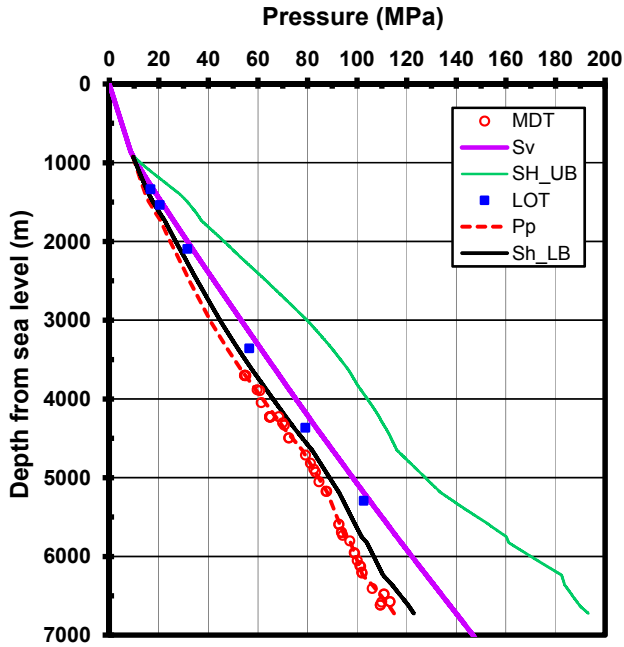

Figure 5.2 In situ stresses and pore pressure (p_p and MDT) versus depths in a deepwater well with the lower bound minimum horizontal stress (Sh_LB) and upper bound maximum horizontal stress (SH_UB) calculated from Eqs. (5.11) and (5.12) assuming a constant μ_f of 0.6. The MDT points are the measured formation pore pressures from the borehole after drilling; S_V is the vertical stress; LOT data are the measured formation leak-off pressures.

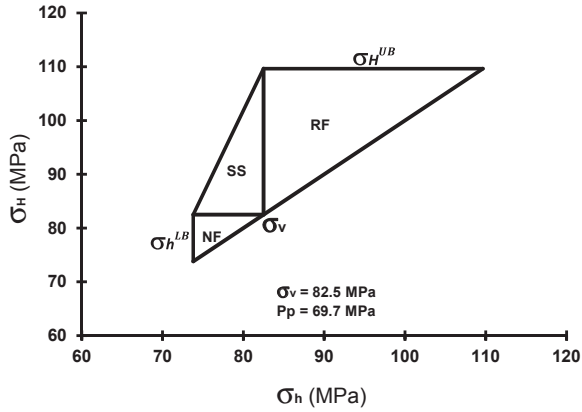

Figure 5.3 Stress polygon obtained from Eqs. (5.11) and (5.12) with measured pore pressure of 69.7 MPa and vertical stress of 82.5 MPa in a borehole, assuming that the coefficient of friction of the fault (μ_f) is 0.6. In the plot, NF, SS, and RF represent the normal, strike-slip, and reverse faulting stress regimes, respectively.

stress to the overburden stress. However, in the strike-slip and thrust faulting stress regimes, the maximum horizontal stress should be located between the overburden stress and the upper bound maximum horizontal stress. It can be observed that the range between the lower bound and the upper bound horizontal stresses is significant, which therefore requires dedicated efforts to better constrain horizontal stresses.

A stress polygon at a given depth can be drawn using the relationships of in situ stresses and pore pressure in different stress regimes from Eqs. (5.11) and (5.12). This is shown in Fig. 5.3 assuming $\mu_f = 0.6$. Fig. 5.3 uses the example shown in Fig. 5.2, where the vertical stress and measured pore pressure at depth of 4316 m from the sea level are $\sigma_V = 82.5$ MPa and $p_p = 69.7$ MPa. Biot's coefficient of 1 is applied to Eqs. (5.11) and (5.12) to calculate the lower and upper bound horizontal stresses. From these data, an in situ stress polygon is plotted, as shown in Fig. 5.3. The maximum and minimum horizontal stresses are constrained inside the stress polygon in three different stress regimes.

5.3 Lithology-dependent in situ stresses and improved stress polygon

5.3.1 Lithology-dependent coefficient of friction of the fault

The stress polygon has been used for decades to constrain in situ stresses (e.g., Zoback et al., 2003). To plot the stress polygon, the coefficient of

friction of the fault is needed, which is not possible to be measured directly in subsurface. Conventionally, it is assumed that the coefficient of friction of the fault is a constant across the entire fault plane ($\mu_f = 0.6-0.7$) based on Byerlee's law (Byerlee, 1978). This assumption may lead to uncertainty in in situ stress estimation because of the difficulty in μ_f estimate. In fact, some faults are weaker with much lower μ_f. For example, Bird and Kong (1994) and Carena and Moder (2009) concluded that all faults in the vicinity of the transform plate boundary of the western United States are frictionally weak to very weak ($\mu_f \leq 0.2$). Iaffaldano (2012) inferred that the coefficient of friction of large-scale plate boundaries is in the range of 0.01–0.07. Byerlee (1978) pointed out that if the sliding surfaces are separated by gouge composed of some clay minerals, the friction is very low. Engelder and Fischer (1994) concluded that the minimum horizontal stress calculated from $\mu_f = 0.6$ underestimates the minimum stress in the central North Sea Graben and does not match the measured data in the Scotian Shelf, Canada. Not surprisingly, research work shows that the coefficient of friction of the fault is highly related to the lithology or mineralogy of the fault gouge. For example, extreme fault weakness ($\mu_f \sim 0.1$) occurs within a 3-m wide creeping fault core (Zoback et al., 2010) in the San Andreas of central California because of the presence of weak clay minerals (Carpenter et al., 2011; Collettini et al., 2011). Saffer and Marone (2003) observed a coefficient of friction in the fault gouge of 0.42–0.68 for illitic shale; however, under identical conditions, a low friction ($\mu_f = 0.15 - 0.32$) is inferred in a smectitic shale. There are also questions concerning whether μ_f is the same for all faults in a region, whether it is even constant along strike on the same fault (Carena and Model, 2009), or whether it is depth-dependent.

Studies and experiments (e.g., Takahashi et al., 2007) in clay–quartz gouges show that the clay content has a significant effect on the frictional strength of the fault, i.e., as clay content increases, the coefficient of friction decreases (e.g., when clay content is 100%, $\mu_f < 0.1$ for smectite). Analyzing the data given by Takahashi et al. (2007), the following linear relationship can be obtained for a smectite and quartz mixture:

$$\mu_f = 0.68 - 0.6C_S \tag{5.13}$$

where C_S is the weight fraction of smectite clay content and C_S is between 0 and 1.

Analyzing experimental data presented by Tembe et al. (2010), the following linear relationship can be obtained for illite–quartz mixture:

$$\mu_f = 0.68 - 0.42C_I \tag{5.14}$$

where C_I is the weight fraction of illite clay content and C_I is between 0 and 1.

Therefore, the coefficient of friction of the fault is lithology-dependent, which needs to be considered when one applies Eqs. (5.11) and (5.12) to estimate in situ stresses.

Field measurements of in situ stresses show that the horizontal stresses are highly dependent on lithologies (e.g., Warpinski and Teufel, 1989; Wileveau et al., 2007; Gunzburger and Cornet, 2007; Gunzburger and Magnenet, 2014). For instances, coal seams and shales have much higher minimum horizontal stresses than the adjacent sandstones, as shown in Fig. 5.4. Measured data from West Texas (Miller et al., 1994) also show that shale formations have much larger minimum horizontal stresses than those in adjacent sandstones, as shown in Fig. 5.5. The minimum horizontal stress results analyzed from leak-off test data in the North Sea (Breckels and van Eekelen, 1982) have the same conclusion.

Fig. 5.6 shows the comparison of two stress polygons: one in a sandstone with $\mu_f = 0.6$ (the case shown in Fig. 5.3) and the other in a shale with a

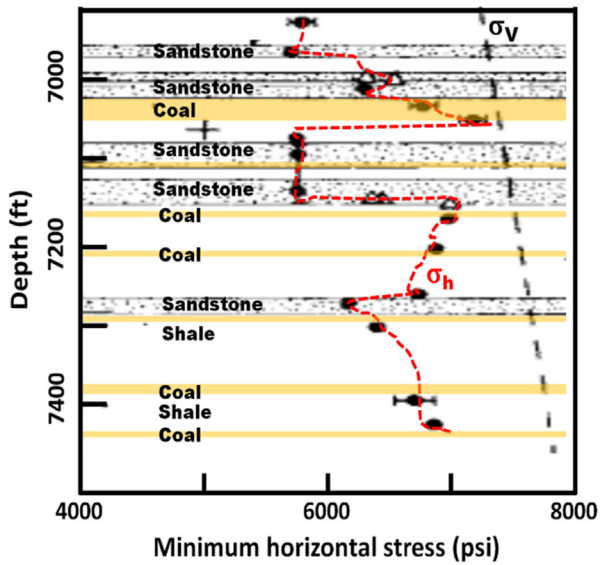

Figure 5.4 The minimum horizontal stress profile (σ_h) measured from mini-frac tests in Colorado. *(Modified from Warpinski and Teufel, 1989.)*

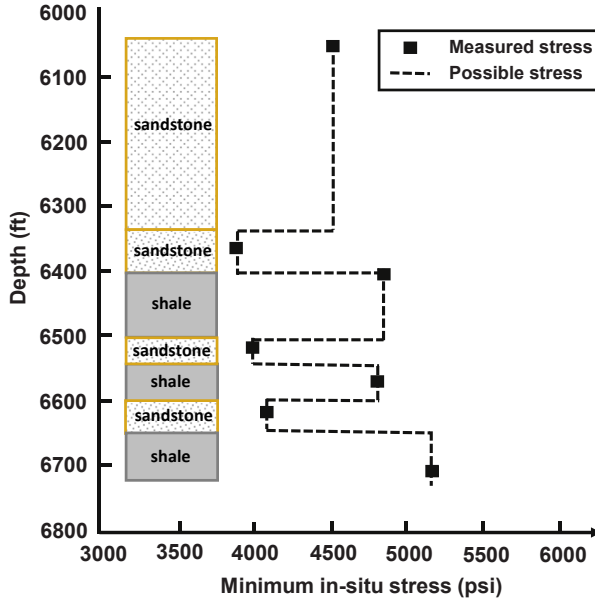

Figure 5.5 The minimum horizontal stress measured from overcoring of open-hole hydraulic fracture tests in the Canyon Sands in West Texas (plotted based on the data in Miller et al., 1994).

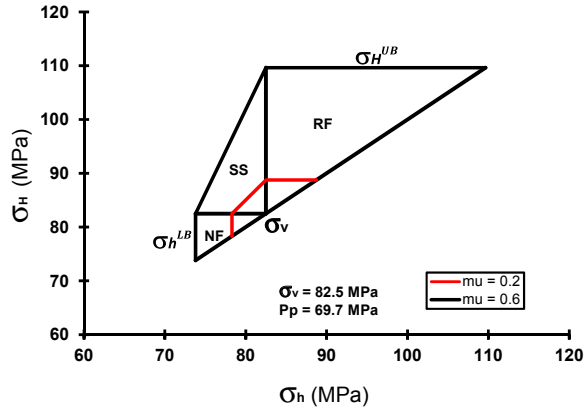

Figure 5.6 Stress polygons plotted with the same vertical stress and pore pressure as shown in Fig. 5.3, but with two different coefficients of friction of the fault $\mu_f = 0.6$ and $\mu_f = 0.2$. A smaller μ_f (mu in the figure) corresponds to a smaller stress polygon.

smaller coefficient of friction of the fault ($\mu_f = 0.2$). The stress polygon in the shale is much smaller (Fig. 5.6).

5.3.2 Poisson's ratio–dependent stress polygon

Zhang and Zhang (2017) verified that the horizontal stress calculated from the uniaxial strain method is the minimum value of the minimum horizontal stress, which can be used as the lower bound horizontal stress to draw the stress polygon. This lower bound minimum horizontal stress (σ_h^{LB}) can be expressed in the following equation:

$$\sigma_h^{LB} = \frac{\nu}{1-\nu}(\sigma_V - \alpha p_p) + \alpha p_p \tag{5.15}$$

where ν is Poisson's ratio of the formation and can be obtained from the compressional and shear velocities (V_p and V_s) from Eq. (2.77).

The upper bound of the maximum horizontal stress (σ_h^{UB}) in strike-slip and reverse faulting regimes can be obtained from the following equation:

$$\sigma_H^{UB} = \frac{1-\nu}{\nu}(\sigma_V - \alpha p_p) + \alpha p_p \tag{5.16}$$

Based on Eqs. (5.15) and (5.16), the new stress polygon (Fig. 5.7) can be drawn when Poisson's ratio of the formation is available. Fig. 5.7 plots two

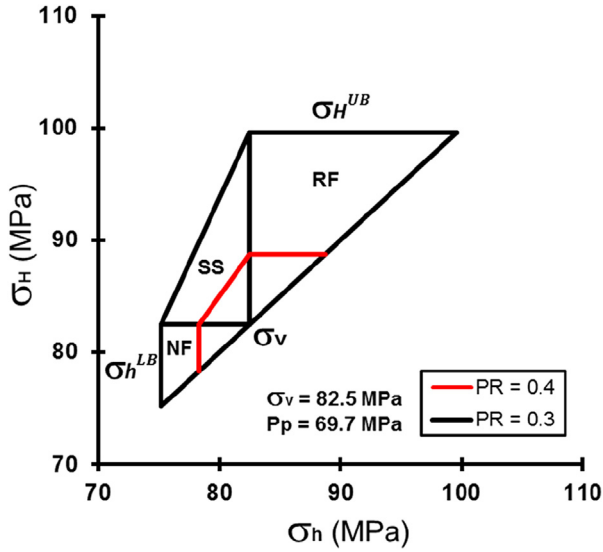

Figure 5.7 Poisson's ratio dependent stress polygons and stress bounds calculated from Eqs. (5.15) and (5.16) in a sandstone and a shale with $\alpha = 1$ and Poisson's ratios (PR) of 0.3 and 0.4, respectively.

stress polygons: one in a sandstone with Poisson's ratio of 0.3 and the other in a shale with Poisson's ratio of 0.4. It indicates that the stress polygon is markedly related to Poisson's ratio of the rock. Fig. 5.7 shows that Poisson's ratio–based stress polygon can narrow the area of the conventional stress polygon, particularly in shales. Using this Poisson's ratio–dependent stress polygon and combining with other methods (borehole breakouts and drilling-induced tensile fractures; refer to Chapters 6 and 10), in situ stresses can be estimated.

5.3.3 Relationship of the coefficient of friction of the fault and Poisson's ratio

As indicated before, two methods can be used to calculate the lower bound minimum horizontal stress: one from the uniaxial strain model (Eq. 5.15), the other from the faulting stress regime constraint (Eq. 5.11). Assuming that the two lower bounds are equal, the coefficient of friction can be estimated, as shown in the following:

$$\left(\sqrt{\mu_f^2+1}+\mu_f\right)^{-2}=\frac{\nu}{1-\nu} \tag{5.17}$$

Therefore, one obtains:

$$\mu_f=\frac{1-2\nu}{2\sqrt{\nu(1-\nu)}} \tag{5.18}$$

This equation is applicable in the following range of Poisson's ratio: $0.16<\nu<0.5$.

Fig. 5.7 shows that the stress polygon depends highly on Poisson's ratio. Because Poisson's ratio is dependent on lithology and depth, the coefficient of friction of the fault also depends on lithology and depth. For example, a sandstone normally has a lower Poisson's ratio than a shale; hence, the sandstone in the fault has a larger coefficient of friction (e.g., when $\nu=0.23$, $\mu_f=0.64$ from Eq. 5.18) than that in the shale. This explains why the sandstone normally has a smaller horizontal stress. A shale normally has a higher Poisson's ratio, thus a smaller coefficient of friction (e.g., if $\nu=0.4$, then $\mu_f=0.2$ from Eq. 5.18). This is verified by the following experimental results: the measurements by Ikari et al. (2011) show that fault gouges containing clay minerals are frictionally weak ($\mu_f<0.5$), whereas gouges rich in silicate minerals (e.g., quartz, feldspar) are stronger ($\mu_f>0.6$). From the well data in claystone sequences containing polygonal fault systems in

the Central North Sea, Goulty and Swarbrick (2005) estimated that the slip on fault surfaces is consistent with $\mu_f = 0.11 \pm 0.02$.

Therefore, the common assumption of a fault strength of $\mu_f = 0.6 - 0.7$ would only correspond to a low Poisson's ratio rock (e.g., sandstone, limestone). For shales and other ductile rocks, μ_f values should be lower from Eq. (5.18). Therefore, the strength or the coefficient of friction of the fault may not be as large as that previously assumed (i.e., $\mu_f = 0.6 - 0.7$). It should be smaller (e.g., as small as $\mu_f = 0.1 - 0.2$) in shales or mudstones.

Using the same example as shown in Fig. 5.2, in situ stresses can be better constrained by using the new lower bound and upper bound horizontal stresses from Eqs. (5.15) and (5.16). Fig. 5.8 presents the calculated horizontal stresses, Poisson's ratio, and the calculated μ_f from Eq. (5.18). The formations are mainly shales from 3200 to 5800 m with Poisson's ratio of 0.35—0.42, which corresponds to a higher minimum horizontal stress. At the depth greater than 6000 m the formations are mostly sandstones, which have smaller Poisson's ratio (0.25—0.35). Compared to Fig. 5.2, the range of the new stress bounds calculated from Eqs. (5.15) and (5.16) is much smaller (see Fig. 5.8); therefore, in situ stress is better constrained and the uncertainty in the stress estimation is reduced. The other advantage of the

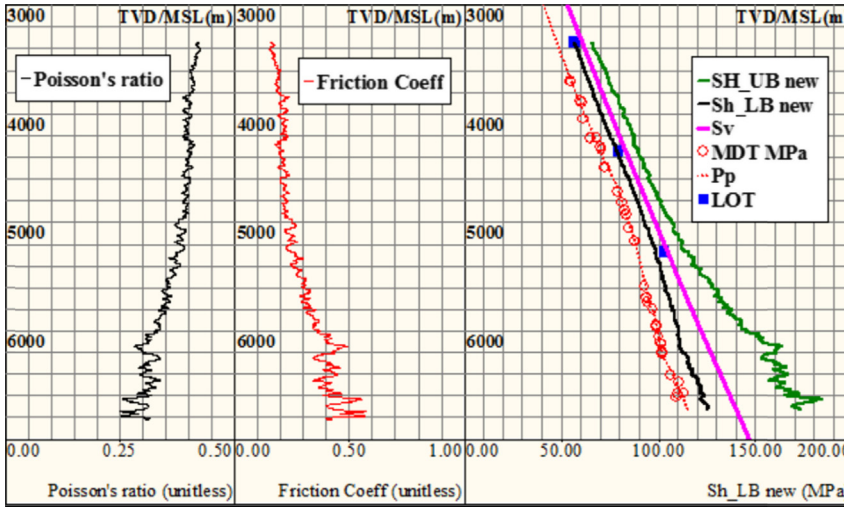

Figure 5.8 In situ stress profile versus depth below the sea level for the same case as shown in Fig. 5.2. The left track plots Poisson's ratios derived from sonic logs; the middle track shows the coefficients of friction calculated from Poisson's ratios from Eq. (5.18); the right track displays vertical stress, pore pressure, the minimum and maximum horizontal stress bounds calculated from Eqs. (5.15) and (5.16).

new equations is that Poisson's ratio of the rock is much easier to be obtained than the coefficient of friction of the fault.

5.3.4 Lithology-dependent minimum and maximum horizontal stresses

To illustrate the relationship between lithology and horizontal stresses, the minimum and maximum horizontal stresses can be schematically plotted in Fig. 5.9 based on the explanation in the previous sections. It can be observed in Fig. 5.9A that in normal faulting regime, a sandstone normally has a smaller minimum horizontal stress because of its smaller Poisson's ratio. By contrast, a shale has a higher minimum horizontal stress. Therefore, the shale can be used as a barrier of hydraulic fracture propagation when hydraulic fracturing is performed in the adjacent sandstone (Zhang et al., 2018). It should be noted that in the strike-slip and reverse faulting stress regimes, this lithology-dependent effect in the horizontal stresses may be smaller (Fig. 5.9B and C) or even reverse because of the larger tectonic stresses. In highly tectonically stressed environment both the minimum and maximum horizontal stresses can approach or exceed the overburden stress, and tectonic strain effect on the sandstone/shale sequence becomes significant (Blanton and Olson, 1999). Therefore, in strong tectonic compressional settings, a mechanically stiffer formation (with higher Young's modulus), commonly a sandstone, may be more stressed by the tectonic stresses than a softer formation, such as a shale. The following equation can be used to illustrate the impact of the tectonic strains on the horizontal stresses:

$$\sigma_{x\_tect} = \frac{E}{1-\nu^2}(\varepsilon_x + \nu\varepsilon_y) \tag{5.19}$$

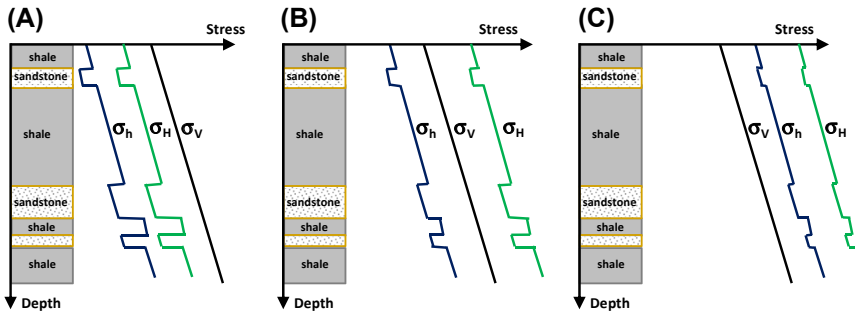

Figure 5.9 Schematic representation of the lithology-dependent horizontal stresses in three different faulting stress regimes: (A) Normal faulting; (B) Strike-slip faulting; and (C) Reverse faulting.

where σ_{x_tect} is the tectonic stress, an additional stress, applied in one of the horizontal directions, i.e., x-direction; ε_x and ε_y are the horizontal strains in x and y directions caused by tectonic stresses, respectively.

Eq. (5.19) shows that the formation with a higher Young's modulus (e.g., a sandstone) has a higher tectonic stress, if the tectonic strains are the same. Therefore, the sandstone may become a high stress interval in a strong tectonic stress (strain) region. This may create a dilemma on where and how to perforate the formations for hydraulic fracturing if based on conventional practice (Yuan et al., 2013).

5.4 Fault strength and in situ stresses

The relationship of fault strength (coefficient of friction of the fault) and in situ stresses can be explicitly illustrated by the Mohr circles, as shown in Fig. 5.10. The linear Mohr–Coulomb failure envelope and the maximum shear stress ($\tau_{f\max}$) along a fault can be expressed as:

$$\tau_f = \mu_f \sigma'_n \tag{5.20}$$

$$\tau_{f\max} = \frac{\sigma'_V - \sigma'_h}{2} \tag{5.21}$$

where σ'_n is the effective normal stress; σ'_V and σ'_h are the maximum and minimum effective stresses, respectively; τ_f and $\tau_{f\max}$ are the shear and maximum shear stresses in the fault, respectively.

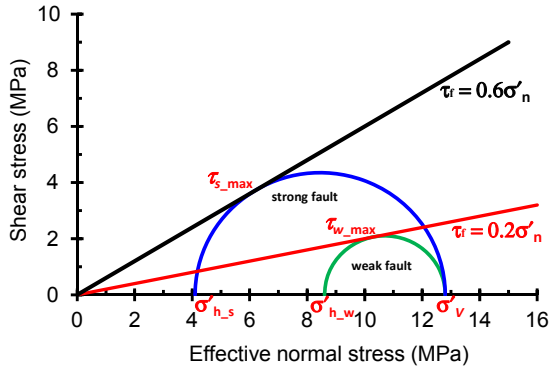

Figure 5.10 Mohr circle diagrams showing the interaction of the coefficients of friction of the fault, shear stresses, and effective stresses in critically stressed state. The vertical stress and pore pressure are the same to the one shown in Fig. 5.6 but with two coefficients of friction: $\mu_f = 0.6$ for a stronger fault and $\mu_f = 0.2$ for a weak fault. The frictionally weak fault requires a much larger minimum stress (or lower maximum shear stress) to maintain its stability.

Fig. 5.10 indicates that in the critically stressed condition (before shear failure) a stronger fault ($\mu_f = 0.6$) has a smaller effective minimum stress (σ'_{h_s}), or higher maximum shear stress (τ_{s_max}). However, a frictionally weak fault (e.g., $\mu_f = 0.2$ in Fig. 5.10) needs a higher effective minimum stress (σ'_{h_w}) (thus smaller Mohr circle and much lower maximum shear stress, τ_{w_max}) to keep the fault stability. This may potentially explain the low inferred shear stresses along strike-slip faults, such as the San Andreas (e.g., Hickman, 1991; Townend and Zoback, 2004). The link between the frictional strength and the minimum stress has important implications for slip behavior on natural faults. For instance, an unstable natural fault, to keep the frictionally weak fault from slip, would require modification of the minimum stress (increase of the minimum stress, as suggested by Zhang and Zhang (2017)) or the fault gauge composition (as suggested by Ikari et al., 2011).

5.5 Depletion and injection impacts

5.5.1 Depletion-reducing horizontal stresses

Data from hydrocarbon basins document the systematic relationship where pore pressure depletion from oil and gas extraction in both conventional and unconventional reservoirs is associated with a reduction in both the minimum and maximum horizontal stresses (e.g., Salz, 1977; Teufel et al., 1991; Segall and Fitzgerald, 1998; Lang et al., 2011; Dohmen et al., 2013). Fig. 5.11 presents pore pressure and in situ stress profiles before depletion and after 4285 psi of depletion in the Middle Bakken unconventional oil reservoir at an equivalent depth of 10,000 ft (Dohmen et al., 2014). It shows that depletion in pore pressure greatly reduces the minimum and maximum horizontal stresses. Measurements from the diagnostic fracture injection tests (DFIT) in the Middle Bakken and Three Forks plays show that the minimum horizontal stress decreases linearly with reservoir pressure (Fig. 5.12A). It has the following correlation (Dohmen et al., 2017):

$$\sigma_h = 0.79 p_p + 2240 \tag{5.22}$$

where σ_h is the minimum horizontal stress, in psi; and p_p is the reservoir pressure, in psi. The depletion-induced stress path (the slope of the line in Fig. 5.12A) is $c = \Delta\sigma_h / \Delta p_p = 0.79$.

By analyzing the instantaneous shut-in pressure data in a tight, low-porosity, low-permeability sandstone of the Vicksburg formation,

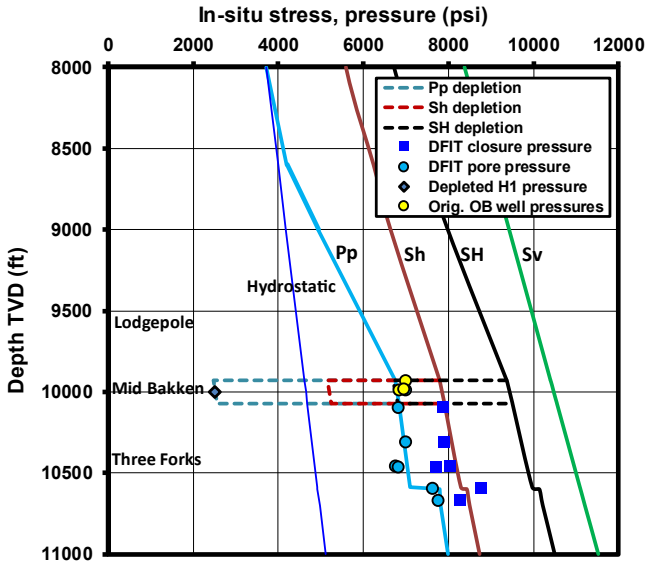

Figure 5.11 Measured and estimated pore pressure and in situ stresses with 4285 psi production depletion in the Middle Bakken reservoir from the DFIT and pressure gauge measurements (symbols in the figure). DFITs were performed in the Bakken and Three Forks formations (without depletion) in the observation and nearby wells. Gauge pressure measurements are also plotted for the depleted pressure in the production well and undepleted pressures in three observation (OB) vertical wells (Dohmen et al., 2014).

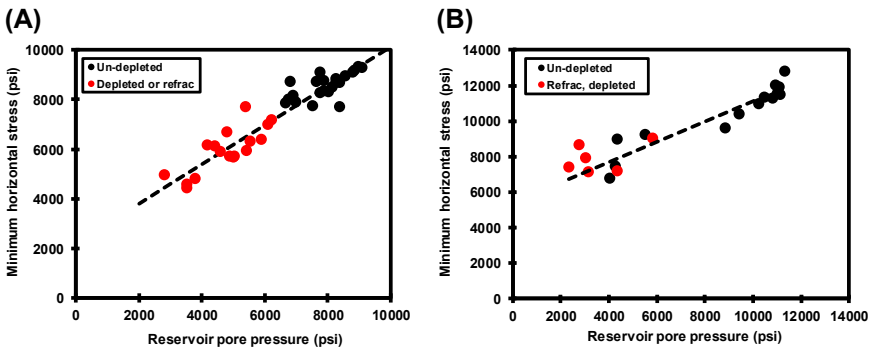

Figure 5.12 Measured minimum horizontal stresses as a function of the reservoir pressure and depletion. (A) The Middle Bakken and Three Forks reservoirs; (B) tight sandstone of the Vicksburg formation.

Salz (1977) obtained the following linear relationship between the minimum horizontal stress and the reservoir pressure (Fig. 5.12B):

$$\sigma_h = 0.57p_p + 5385 \tag{5.23}$$

where the minimum horizontal stress and the reservoir pressure are in psi, and the stress path $c = 0.57$.

Addis (1997) analyzed the stress-depletion response in several petroleum reservoirs. The depletion-induced stress path ($\Delta\sigma_h/\Delta p_p$) is very different in different fields. Furthermore, it can be different even in the same field, e.g., in the Ekofisk field, the North Sea, $\Delta\sigma_h/\Delta p_p = 0.84$ in the basin crest, $\Delta\sigma_h/\Delta p_p = 0.82$ in the flank, but $\Delta\sigma_h/\Delta p_p = 0.77$ in the outer flank (Teufel et al., 1991). Table 5.1 lists the measured stress paths in some petroleum

Table 5.1 The ratios of measured depletion-induced minimum stresses to the reservoir pressures in some petroleum basins.

Field or formation	Rock type	Stress measurement method	Stress path c ($\Delta\sigma_h/\Delta p_p$)	References
Middle Bakken, ND	Calcitic dolomitic siltstone	DFIT	0.79	Dohmen et al. (2017)
Vicksburg formation, TX	Sandstone	Shut-in	0.57	Salz (1977)
Waskom, TX	Sandstone	Shut-in	0.46	Whitehead et al. (1987)
Magnus, North Sea	Sandstone	Fracture opening	0.68	Shepherd (1991)
West Sole, North Sea	Sandstone	Shut-in	1.18	Addis (1997)
Wytch Farm, UK	Sandstone	Wellhead injection	0.63	Colter and Havard (1981)
Ekofisk, North Sea	Chalk	Shut-in	~0.8	Teufel et al. (1991)
Tor reservoir, Valhall, North Sea.	Chalk	LOT	0.7 in the crest, 0.84 in the flank.	Zoback and Zinke (2002)
CPSE field, Brunei	Sandstone	Repeated LOT	0.84	Nelson et al. (2005)
Gulf of Mexico, USA	Sandstone	LOT	~0.65	

basins. When the measured data are not available, the depletion-induced minimum stress reduction may be estimated based on the assumption of the minimum horizontal stress in the uniaxial strain boundary condition in the following equation (Aadnoy, 1991; Engelder and Fischer, 1994):

$$\Delta\sigma_h = \alpha\left(\frac{1-2\nu}{1-\nu}\right)\Delta p_p \tag{5.24}$$

where $\Delta\sigma_h$ and Δp_p are the incremental minimum stress and reservoir pressure, respectively. It should be noted that Poisson's ratio may also change after depletion. From Eq. (5.24) the depletion-induced stress path can be expressed as:

$$c = \alpha\left(\frac{1-2\nu}{1-\nu}\right) \tag{5.25}$$

where $c = \Delta\sigma_h/\Delta p_p$. It can be seen that the stress path is dependent on Poisson's ratio or the lithology.

After depletion the minimum horizontal stress may also be estimated from the following equation, if the pore pressure after depletion is known:

$$\sigma_{hd} = k(\sigma_V - \alpha p_{pd}) + \alpha p_{pd} \tag{5.26}$$

where σ_{hd} and p_{pd} are the minimum horizontal stress and the reservoir pressure after depletion, respectively; k is a parameter that can be obtained from the measured data, such as DFIT.

Several attempts have been made to experimentally predict the in situ stress changes with depletion and injection (Teufel et al., 1991; Rafieepour et al., 2017). However, laboratory-measured stress paths under uniaxial strain condition have large discrepancies with field stress measurements from hydraulic fracturing tests. For example, the stress path measurements via hydraulic fracturing stimulation in the Ekofisk Field (Teufel et al., 1991) are very different from laboratory-derived stress paths under uniaxial strain conditions ($c \approx 0.8$ from the field and $c = 0.5 - 0.6$ from the lab). These discrepancies might be due to several factors such as scale effects, stress arching, and faulting contributions (Addis, 1997; Holt, 1999). Holt (1999) argued that the damaged core and scale effects are two sources of discrepancies between the lab and field measurements. Another important parameter contributing the difference between the field and lab measurements might be the fact that the dominant boundary condition in the reservoir is not the generalized uniaxial strain. Experimental results (Rafieepour et al., 2017) show that the changes of stress paths are larger for

constrained conditions than unconstrained conditions. The stress path order is as uniaxial strain > generalized plane strain > plane strain > unconstrained. In their experiments a permanent stress change was also observed during the production and injection cycle for all boundary conditions. This indicates that most of stress changes during production are irrecoverable on repressurization. Therefore, decreasing depletion or slowing down production may reduce the irrecoverable reservoir damage.

5.5.2 Depletion and Mohr's circle representation

The Mohr circle plots are useful for representing the depletion effect on the reservoir rock and for demonstrating how stress changes in the reservoir during its production history. As described in the previous section, the minimum horizontal stress decreases as the reservoir depletion increases. However, the vertical stress (overburden stress) does not change much (e.g., Segall and Fitzgerald, 1998); therefore, vertical effective stress increases as the depletion increases. Thus, a large stress difference in the effective vertical and minimum effective horizontal stresses is created as depletion increases, and the Mohr circle becomes larger. Fig. 5.13 presents the Mohr circles and the relationship of the minimum effective horizontal stress, effective vertical stress, shear stress, and the failure envelope for different degrees of depletion (Dohmen et al., 2017). Two cases are considered in the Mohr circle plots in Fig. 5.13 to allow for the uncertainty in Biot's coefficient (i.e., $\alpha = 0.5$ and 0.75). Lower values of α, such as 0.3, shift the Mohr circles farther to the right (Fig. 5.13A), whereas higher values (e.g., $\alpha > 0.75$) shift the Mohr circles farther to the left (Fig. 5.13B), making the

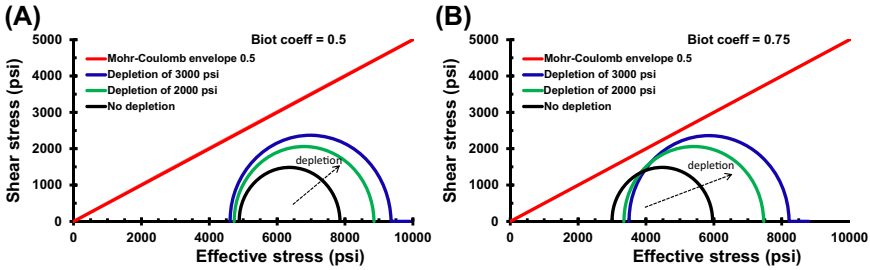

Figure 5.13 Mohr circle representation showing the effects before (smallest circle) and after depletion of 2000 psi (intermediate circle) and 3000 psi (largest circle) in the Middle Bakken reservoir at the depth of 11,087 ft with the Mohr–Coulomb shear failure envelope ($\mu = 0.5$) in a fractured formation (the line). (A) Biot's coefficient $\alpha = 0.5$; (B) $\alpha = 0.75$.

stress conditions approach the shear failure envelope and appear critically stressed. If the Mohr circle touches the Mohr–Coulomb failure envelope, then slip on optimally oriented fractures will occur. The smallest Mohr circle in Fig. 5.13 represents the initial effective stress state before production with a pore pressure of 7539 psi, and with total stresses of $\sigma_h = 8648$ psi and $\sigma_V = 11{,}619$ psi. The intermediate circle represents the pore pressure of 5539 psi after 2000 psi of depletion. The largest circle has a pore pressure of 4539 psi after 3000 psi of depletion. In either case shown in Fig. 5.13, the Mohr circle grows and approaches critical stress with continued depletion.

5.5.3 Injection and shear failures

After sufficient depletion pushes the reservoir rock to a critically stressed state, a small volume of water injected into the fracture system should trigger shear slip by increasing the pore pressure internal to the fractures and lowering the effective stress that otherwise clamps them shut. Fig. 5.14 is a Mohr circle illustrating the mechanism of shear failure induced by repressurization (Dohmen et al., 2017). Although depletion takes years and slowly changes the reservoir pressure, the pore pressure increase from either direct well injection or from intersecting propagating hydraulic fractures occurs over a short time period of hours. The rapid pore pressure increase does not diffuse significantly into the matrix, and the injection does not change the total stresses (horizontal stresses) immediately, but simply reduces the effective stresses, moving the Mohr circle to the left. This effect sets up the condition for shear failure on critically stressed, optimally

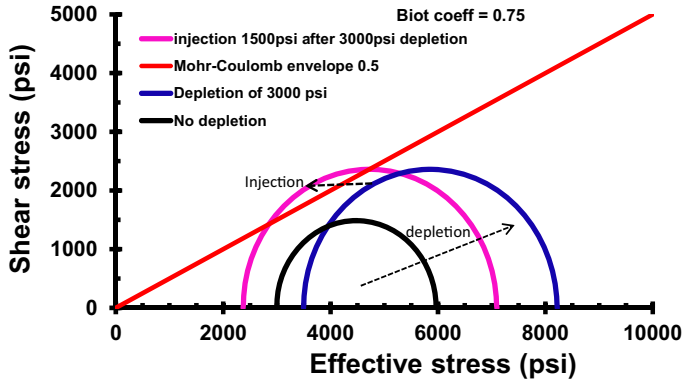

Figure 5.14 Mohr circle representation showing how repressurization impacts the depleted reservoir (after drawdown of 3000 psi) with an injection of 1500 psi.

oriented fractures. Therefore, repressurization may cause formation shear failures, which can enhance production for a depleted reservoir.

References

Aadnoy, B.S., 1991. Effect of reservoir depletion on borehole stability. J. Pet. Sci. Eng. 6, 57–61.

Addis, M.A., 1997. The stress-depletion response of reservoirs. SPE-38720 Presented at SPE Ann. Conf. Exhib., San Antonio.

Anderson, E.M., 1951. The Dynamics of Faulting and Dyke Formation with Application to Britain, second ed. Oliver and Boyd, Edinburgh.

Bird, P., Kong, X., 1994. Computer simulations of California tectonics confirm very low strength of major faults. Bull. Geol. Soc. Am. 106, 159–174.

Blanton, T.L., Olson, J.E., 1999. Stress magnitude from logs: effects of tectonic strains and temperature. SPE Reservoir Eval. Eng. 2 (1).

Breckels, I.M., van Eekelen, H.A.M., 1982. Relationship between horizontal stress and depth in sedimentary basins. SPE-10336, JPT, pp. 2191–2199.

Byerlee, J., 1978. Friction of rocks. Pure Appl. Geophys. 116, 615–626.

Carena, S., Moder, C., 2009. The strength of faults in the crust in the Western United States. Earth Planet. Sci. Lett. 287, 373–384.

Carpenter, B.M., Marone, C., Saffer, D.M., 2011. Weakness of the San Andreas fault revealed by samples from the active fault zone. Nat. Geosci. 4, 251–254.

Collettini, C., Niemeijer, A., Viti, C., Smith, S., Marone, C., 2011. Fault structure, frictional properties and mixed-mode fault slip behavior. Earth Planet. Sci. Lett. 311, 316–327.

Colter, V.S., Havard, D.J., 1981. The Wytch farm oil field. In: Dorset, L.V.I., Hobson, G.D. (Eds.), Petroleum Geology of the Continental Shelf of North-West Europe. Heyden, London, pp. 494–503.

Dohmen, T., Zhang, J., Li, C., Blangy, J.P., Simon, K.M., Valleau, D.N., Ewles, J.D., Morton, S., Checkles, S., 2013. A new surveillance method for delineation of depletion using microseismic and its application to development of unconventional reservoirs. SPE-166274 presented at SPE Ann. Tech. Conf. Exhib.

Dohmen, T., Blangy, J.P., Zhang, J., 2014. Microseismic depletion delineation. Interpretation 2 (3). SG1–SG13.

Dohmen, T., Zhang, J., Barker, L., Blangy, J.P., 2017. Microseismic magnitudes and b-values for delineating hydraulic fracturing and depletion. SPE-186096. SPE J. 22 (5), 1624–1634.

Engelder, T., Fischer, M.P., 1994. Influence of poroelastic behavior on the magnitude of minimum horizontal stress, S_h in overpressured parts of sedimentary basins. Geology 22, 949–952.

Goulty, N.R., Swarbrick, R.E., 2005. Development of polygonal fault systems: a test of hypotheses. J. Geol. Soc. 162, 587–590.

Gunzburger, Y., Cornet, F.H., 2007. Rheological characterization of a sedimentary formation from a stress profile inversion. Geophys. J. Int. 168, 402–418.

Gunzburger, Y., Magnenet, V., 2014. Stress inversion and basement-cover stress transmission across weak layers in the Paris basin, France. Tectonophysics 617, 44–57.

Hickman, S.H., 1991. Stress in the lithosphere and the strength of active faults. Rev. Geophys. 759–775. U.S. Natl. Rep. to Int. Union of Geodesy and Geophys.

Holt, R.M., 1999. Reservoir stress path: evaluation of core and field data. In: Amadei, Kranz, Scott, Smeallie (Eds.), Rock Mechanics for Industry. Balkerma, Rotterdam.

Iaffaldano, G., 2012. The strength of large-scale plate boundaries: constraints from the dynamics of the Philippine sea plate since ~5Ma. Earth Planet. Sci. Lett. 357–358, 21–30.

Ikari, M.J., Marone, C., Saffer, D.M., 2011. On the relation between fault strength and frictional stability. Geology 1, 83–86.

Jaeger, J.C., Cook, N.G.W., 1979. Fundamentals of Rock Mechanics, third ed. John Wiley & Sons.

Lang, J., Li, S., Zhang, J., 2011. Wellbore stability modeling and real-time surveillance for deepwater drilling to weak bedding planes and depleted reservoirs. Paper SPE/IADC-139708.

Miller II, W.K., Peterson, R.E., Stevens, J.E., Lackey, C.B., Harrison, C.W., 1994. In-situ stress profiling and prediction of hydraulic fracture azimuth for the West Texas Canyon Sands formation. SPE Prod. Facil. 9 (3), 204.

Nelson, E.J., Hillis, R.R., Meyer, J.J., Mildren, S.D., Van Nispen, D., Briner, A., 2005. The reservoir stress path and its implications for water-flooding, Champion Southeast field, Brunei. ARMA/USRMS paper 05-775. 40th US Symp. on Rock Mechanics.

Peng, S., Zhang, J., 2007. Engineering Geology for Underground Rocks. Springer, 2007.

Rafieepour, S., Miska, S., Ozbayoglu, E., Yu, M., Takach, N., Zhang, J., Majidi, R., 2017. Experimental study of reservoir stress path and hysteresis during depletion and injection under different deformational conditions. ARMA17-416 presented at 51st US Rock Mechanics/Geomech. Symp.

Saffer, D.M., Marone, C., 2003. Comparison of smectite- and illite-rich gouge frictional properties: application to the updip limit of the seismogenic zone along subduction megathrusts. Earth Planet. Sci. Lett. 215, 219–235.

Salz, L.B., 1977. Relationship between fracture propagation pressure and pore pressure. Paper SPE-6870.

Segall, P., Fitzgerald, S.D., 1998. A note on induced stress changes in hydrocarbon and geothermal reservoirs. Tectonophysics 289, 117–128.

Shepherd, M., 1991. The Magnus field, blocks 211/7a, 12a, UK North Sea. In: Abbotts, I.L. (Ed.), United Kingdom Oil and Gas Fields 25 Years Commemorative Volume, Geological Society Memoir No. 14, pp. 153–157.

Sibson, R.H., 1974. Frictional constraints on thrust, wrench and normal faults. Nature 247, 542–544.

Takahashi, M., Mizoguchi, K., Kitamura, K., Masuda, K., 2007. Effects of clay content on the frictional strength and fluid transport property of faults. J. Geophys. Res. 112. B08206.

Tembe, S., Lockner, D.A., Wong, T.F., 2010. Effect of clay content and mineralogy on frictional sliding behavior of simulated gouges: binary and ternary mixtures of quartz, illite, and montmorillonite. J. Geophys. Res. 115. B03416.

Teufel, L.W., Rhett, D.W., Farrell, H.E., 1991. Effect of reservoir depletion and pore pressure drawdown on in situ stress and deformation in the Ekofisk field, North Sea. In: Roegiers, J.-C. (Ed.), Rock Mechanics as a Multidisciplinary Science, Proc. 32nd US Rock Mech. Symp.

Townend, J., Zoback, M.D., 2004. Regional tectonic stress near the San Andreas fault in Central and Southern California. Geophys. Res. Lett. 31. L15S11.

Warpinski, N.R., Teufel, L.W., 1989. In-situ stresses in low permeability, nonmarine rocks. J. Pet. Technol. 41 (4), 405–414. SPE-16402-PA.

Whitehead, W.S., Hunt, E.R., Holditch, S.A., 1987. The effects of lithology and reservoir pressure on the in-situ stress in the Waskom (Travis peak) field. Paper SPE/DOE-16403.

Wileveau, Y., Cornet, F.H., Desroches, J., Plumling, P., 2007. Complete in situ stress determination in an argillite sedimentary formation. Phys. Chem. Earth 32, 866–878.

Yuan, R., Jin, L., Zhu, C., Zhou, M., Vitthal, S., 2013. Vertical or horizontal? -hydraulic fracture geometry as a make or break to a tight gas field in the Western Sichuan basin. Int. Petroleum Technology Conf. Beijing, China, 26–28 March 2013, IPTC-16757.
Zhang, Y., Zhang, J., 2017. Lithology-dependent minimum horizontal stress and in-situ stress estimate. Tectonophysics 703–704, 1–8.
Zhang, Y., Zhang, J., Yuan, B., Yin, S., 2018. In-situ stresses controlling hydraulic fracture propagation and fracture breakdown pressure. J. Pet. Sci. Eng. 164, 164–173.
Zoback, M., Zinke, J., 2002. Production-induced normal faulting in the Valhall and Ekofisk oil fields. Pure Appl. Geophys. 159, 403–420.
Zoback, M., Hickman, S., Ellworth, W., 2010. Scientific drilling into the San Andreas fault zone. Eos 92, 197–204.
Zoback, M.D., et al., 2003. Determination of stress orientation and magnitude in deep wells. Int. J. Rock Mech. Min. Sci. 40, 1049–1076.

CHAPTER 6

In situ stress estimate

Contents

Applied Petroleum Geomechanics
ISBN 978-0-12-814814-3
https://doi.org/10.1016/B978-0-12-814814-3.00006-X

Abstract

Theoretical and practical methods for determining in situ stresses are discussed. Measurements and interpretations of the horizontal stresses (e.g., diagnostic fracture injection test, leak-off test, and mini-frac test) are investigated in both impermeable and permeable rocks. Empirical equations in various petroleum basins are given to estimate in situ stresses. Overburden stress and overburden gradient for both onshore and offshore drilling are analyzed. Integrated methods for calculating the minimum and maximum horizontal stresses are studied in different faulting stress regimes. Poisson's ratio–based stress polygons are applied to constrain in situ stresses using both drilling-induced tensile fractures and wellbore breakouts. Methods for interpreting directions of horizontal stresses are also introduced.

Keywords: Hydraulic fracture test; In situ stresses; Maximum horizontal stress; Minimum horizontal stress; Overburden gradient; Overburden stress; Poisson's ratio and stress polygon.

6.1 Overburden stress

6.1.1 Overburden stress from bulk density

Overburden stress, or vertical stress, is caused by the weight of the overlying formations. If the overlying formations have an average density of ρ_a, then overburden stress (σ_V) can be calculated by:

$$\sigma_V = \rho_a g Z \tag{6.1}$$

where g is the acceleration due to gravity; Z is the depth.

If bulk densities of the rocks vary with depth, the vertical stress can be calculated by integration of the densities to the depth of interest, Z, i.e.,

$$\sigma_V = \rho_w g Z_w + g \int_{Z_w}^{Z} \rho_b(z) dz \tag{6.2}$$

where ρ_b (z) is the formation bulk density as a function of depth and can be obtained from density log; ρ_w is the density of sea water; Z_w is the water depth, for onshore drilling $Z_w = 0$.

However, density log is usually not recorded at the shallow depth. Some empirical methods can be used to estimate shallow formation bulk density. One method is Miller's near surface or mudline density correlation, which can be found in Eq. (2.4) or from Zhang et al. (2008). The other was proposed by Athy (1930) to interpolate shallow formation bulk density

based on analyzing the observed depth–density curve in density measurements of shales in northern Oklahoma. It has the following relation:

$$\rho_z = \rho_0 + A_m(1 - e^{-bZ}) \tag{6.3}$$

where ρ_z is the density at the depth of Z, in g/cm^3; ρ_0 is the formation density at the surface; A_m is the possible maximum density increase ($A_m = \rho_m - \rho_0$ and $A_m = 1.3$ in Athy (1930)); ρ_m is the matrix density or the grain density of the rock; b is a fitting constant. When bulk density data (ρ_z) are available at certain depths, by fitting the density curve to Eq. (6.3), the shallow density (ρ_0) can be obtained.

Fig. 6.1 presents an example to calculate overburden stress and overburden gradient using density log in an offshore subsalt well. To calculate overburden stress, the first step is to build a density profile with depth. In this example the water depth is 1085 m and the shallow density below the sea floor (mudline) is calculated from Miller's equation, Eq. (2.4). Then, composite bulk density data are built by considering salt density (about 2.165 g/cm^3) and bulk densities in formations. Notice that the sea

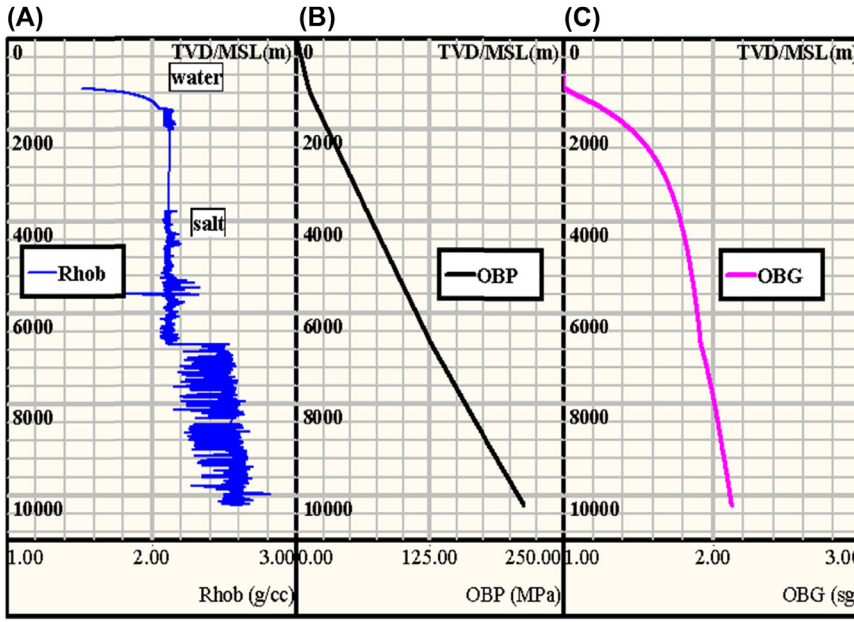

Figure 6.1 Density log versus the true vertical depth from the sea level (in m) and calculated overburden stress and overburden gradient in deepwater subsalt formations of the Gulf of Mexico: (A) composite density data below the sea floor in g/cm^3; (B) overburden stress (OBP) in MPa; and (C) overburden gradient (OBG) in sg or g/cm^3.

water density (1.03 g/cm^3) is also needed for overburden calculation. Integrating this composite density (Eq. 6.2), overburden stress and overburden gradient can be obtained, as shown in Fig. 6.1.

It should be noted that the density log may be affected by the borehole quality. When the borehole has washouts or breakouts, the density tool cannot give a reliable density measurement. In this case the density log data need to be corrected before using it for overburden stress calculation.

6.1.2 Overburden stress from empirical equations

6.1.2.1 Overburden stress for offshore drilling

Formation overburden stress gradient in onshore drilling can be estimated using 1.0–1.1 psi/ft (0.0227–0.025 MPa/m). However, it is not recommended for deepwater overburden gradient interpretations. Traugott (1997) presented the following empirical equation for overburden stress gradient based on drilling and well logging data in the Gulf of Mexico:

$$OBG = \frac{\rho_w Z_w + \rho_a (Z - Z_w - Z_{ag})}{Z} \tag{6.4}$$

where OBG is the overburden stress gradient in offshore wells, in ppg; Z is the true vertical depth (TVD) in the Kelly Bushing (KB) level; Z_w and Z_{ag} are the water depth and air gap, respectively; the density of sea water $\rho_w = 8.5–8.7$ ppg; ρ_a is the average density of the sediments in ppg, and

$$\rho_a = \rho_{ml} + \left(\frac{Z - Z_w - Z_{ag}}{3125}\right)^{0.6} \tag{6.5}$$

where ρ_{ml} is the density at the mudline (sea floor) and $\rho_{ml} = 16.3$ ppg (1.956 g/cm^3); the depth unit is ft.

It should be noted that the depth datum used for overburden gradient calculation in Eq. (6.4) is the KB level for drilling purpose. From Eqs. (6.4) to (6.5), overburden stress can be obtained from the following equation:

$$\sigma_V = \left\{\rho_w Z_w + \left[16.3 + \left(\frac{Z - Z_w - Z_{ag}}{3125}\right)^{0.6}\right](Z - Z_w - Z_{ag})\right\}/19.25 \tag{6.6}$$

where σ_V is in psi; water density is in ppg and the depth is in ft.

Barker and Wood (1997), assuming plastic deepwater formations, derived an expression for the cumulative average density from the mudline to a depth of interest using leak-off test (LOT) data from 70 deepwater wells. The essence of the plastic formation assumption is that the pressure

required to open a fracture is equal to the overburden gradient. When combined with the contribution of the overlying sea water (Barker and Woods suggested $\rho_w = 8.55$ ppg as the average density of sea water for deepwater Gulf of Mexico wells), the following expression was presented:

$$OBG = \frac{\rho_w Z_w + 5.3(Z - Z_w - Z_{ag})^{1.1356}}{Z} \tag{6.7}$$

where OBG is in ppg, water density is in ppg and the depth is in ft.

Fig. 6.2 displays the overburden gradient profiles calculated from empirical equations of Eqs. (6.4) and (6.7) compared to the one obtained from the density log in a deepwater well in the Green Canyon of the Gulf of Mexico. In the calculations, sea water density of 8.58 ppg is used. Fig. 6.2 shows that Traugott's empirical method has a better match to the one calculated from the density log.

Van Ruth et al. (2004) analyzed 37 offshore wells in the Carnarvon Basin, offshore Western Australia. By integrating density values from density logs and from check-shot velocities empirically transformed to densities, they obtained the following equation for vertical stress estimation:

$$\sigma_V = 20.4 Z_{bml}^{1.06} + p_{hyd} Z_w \tag{6.8}$$

where σ_V is the vertical stress in kPa; Z_{bml} is the depth below sea floor (mudline) in meters; p_{hyd} is the hydrostatic pore pressure gradient, for sea water p_{hyd} is about 10.3 kPa/m; and Z_w is the water depth in meters.

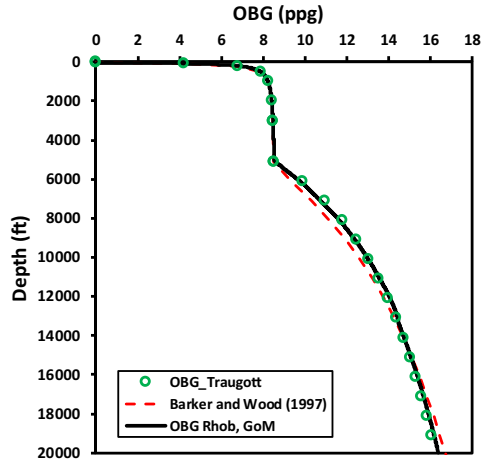

Figure 6.2 Calculated overburden profiles from the empirical equations (Eqs. (6.4) and (6.7)) and density log data (OBG Rhob) in a deepwater well in the Green Canyon of the Gulf of Mexico, where the water depth is 5060 ft and air gap is 42 ft.

Tingay et al. (2013) developed an average overburden stress equation for the northern Malay basin:

$$\sigma_V = 0.0064 Z_{ss}^{1.1599} \tag{6.9}$$

where σ_V is in MPa; Z_{ss} is the true vertical depth below sea level (TVDSS) in meters. This equation is accurate to ±1.35 MPa over all calculated vertical stress magnitudes in the studied depth range of 100–3500 m (Tingay et al., 2013).

Using density log data, another overburden stress equation was obtained in offshore Northern Malay basin:

$$\sigma_V = 0.023 Z_{bml} \tag{6.10}$$

where σ_V is the overburden stress below the sea floor (MPa); Z_{bml} is the true vertical depth (TVD) starting from the sea floor (m).

Vertical stress trend for the North Sea was established using data from 10 North Sea wells (Yang and Aplin, 2004). The equation is as follows:

$$\sigma_V = 0.01799 Z_{bml} + 9.95 \times 10^{-7} Z_{bml}^2 \tag{6.11}$$

where σ_V is in MPa; Z_{bml} is in meters. They suggested that the equation can be used to calculate the vertical stress to the depth at which the density log starts its run.

6.1.2.2 Overburden stress for onshore drilling

For onshore drilling, overburden calculation is simpler than that in offshore. Dohmen et al. (2013) presented the following equation to calculate overburden stress in the Bakken play in North Dakota:

$$\sigma_V = 0.0231 Z \tag{6.12}$$

where σ_V is in MPa; Z is the TVD below the surface in meters. This expression is similar to Eq. (6.10) for offshore Northern Malay basin.

Zhang and Wieseneck (2011) analyzed reliable density log data and obtained the following equation to estimate overburden stress in the Haynesville and Bossier plays:

$$\sigma_V = 0.6186 Z^{1.061} \tag{6.13}$$

where σ_V is in psi; and Z is in feet.

From density log, Warpinski (1989) obtained the following equation for overburden stress estimate at DOE's Multiwell Experiment (MWX) site in the Piceance basin of western Colorado:

$$\sigma_V = 0.0238 Z \tag{6.14}$$

where σ_V is in MPa; Z is in meters.

By analyzing in situ stress data measured in mining industry, Hoek and Brown (1980) proposed that overburden stress can be estimated from the overburden gradient of 0.0272 MPa/m. This implies that the rock average bulk density is about 2.77 g/cm^3, which is too high for most sedimentary rocks in petroleum basins, where the overburden gradient is about 0.0231−0.0238 MPa/m, as shown in Eqs. (6.12) and (6.14). Therefore, if it is possible, it is best to compute vertical stress from reliable density log data.

6.2 Minimum horizontal stress from measurements

Ljunggren et al. (2003) reviewed methods for determining in situ stresses, which can be classified into two main categories. The first category consists of methods that disturb the in situ rock conditions, i.e., by inducing strains, deformations, or crack opening. The following methods may be included in this category:

- hydraulic methods, including hydraulic fracturing and hydraulic tests on preexisting fractures,
- borehole relief methods, and
- surface relief methods.

The second category consists of methods based on the observation of rock behaviors without any major influence on the rocks. The following methods belong to this category:

- statistics of measured data (database),
- core-discing,
- borehole breakouts,
- relief of large rock volumes (back analysis),
- acoustic methods (Kaiser effect),
- strain recovery methods,
- geological observational methods, and
- earthquake focal mechanisms.

In the oil and gas industry, the minimum horizontal stress is commonly measured from downhole hydraulic fracturing tests, such as LOT, extended leak-off test (XLOT), diagnostic fracture injection test (DFIT), mini-frac text, and micro-frac test.

6.2.1 Leak-off tests in normal and strike-slip faulting stress regimes

The minimum horizontal stress can be determined by direct measurements, and the commonly used method is hydraulic fracturing (e.g., Haimson and Cornet, 2003), or its oil field equivalent, LOT, XLOT (e.g., Raaen et al., 2006),

DFIT, mini-frac and wireline tests, or LWD micro-frac tests (Ramakrishnan et al., 2009). In a hydraulic fracture test, an interval of borehole is isolated and sealed with inflatable packers as shown in Fig. 6.3. In a typical LOT, it is simpler than the one presented in Fig. 6.3 because the casing in the borehole seals the shallower formations; therefore, only the hole below the casing and any new formation drilled before the test are exposed (Edwards et al., 2002). The fluid is then pumped into the hole with a constant flowrate. The pressure increase in the hole is typically linear as long as there are no leaks in the system, and the exposed formation is not highly permeable. As the pressure increases at some point, the rate of pressure increase varies such that the pressure—time curve departs from linearity (Fig. 6.4). This departure from linearity is the fracture initiation pressure (p_i).

After departure from linearity, pressure is typically seen to increase at a lower rate until a maximum pressure is reached, and this pressure is the formation breakdown pressure (p_b). After the rock is broken down (i.e., major hydraulic fracture is created), at some point the pressure in the hole levels off and remains fairly constant (p_{prop}) at the same flowrate. During this stage, the fracture is propagating (Zhang and Roegiers, 2010).

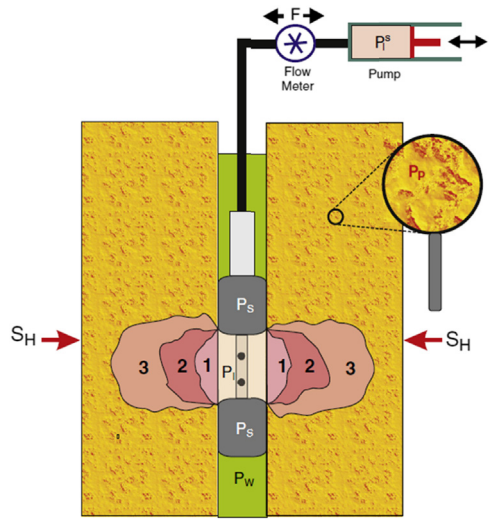

Figure 6.3 Outline of the principal components of a hydraulic fracturing stress measurement. A test interval along the borehole is isolated by two inflatable packers. The pressure in the interval is then increased by pumping fluid in. The induced fracture extends successively with each of three pressurization cycles in the direction of the maximum horizontal stress S_H and opens against the minimum horizontal stress S_h (Schmitt et al., 2012).

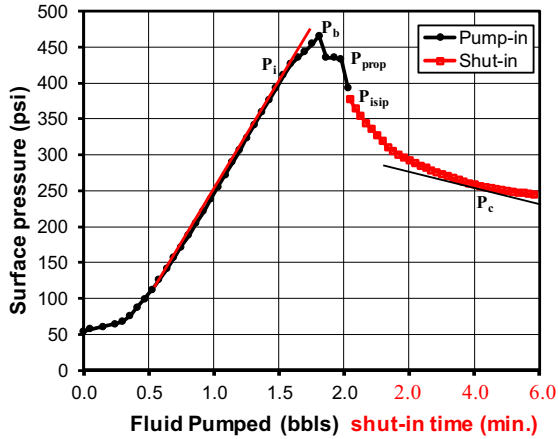

Figure 6.4 A typical one-cycle XLOT performed in a borehole showing the relationship of the fracture initiation and breakdown pressures versus the injection volume.

When the pump is turned off, the pressure begins to decline and the pressure drops to the instantaneous shut-in pressure (p_{isip}). As the pressure declines, the fracture starts to close. If the generated fracture is vertical and largely in the far field, then the stress acting to close the fracture is equal to the minimum horizontal stress (σ_h). Therefore, the minimum horizontal stress is equal to the closure pressure (p_c), i.e., the inflection point in the pressure decline curve (Zhang and Yin, 2017), as shown in Fig. 6.4.

$$\sigma_h = p_c \tag{6.15}$$

Eq. (6.15) is for the case in the normal and strike-slip faulting stress regimes, and the created fracture is not affected by preexisting fractures. If natural fractures exist, the hydraulic injection may not create new fractures but open preexisting arbitrary-oriented fractures. In this condition, the interpretation of closure pressure from Eq. (6.15) provides an unreliable estimate of the minimum horizontal stress. However, an inversion type stress analysis introduced by Cornet and Valette (1984) or Baumgartner and Rummel (1989) can be used to analyze in situ stresses in preexisting fractures. The method is based on the shut-in pressure P_{si} as a measure of the normal stress S_n acting across the fracture plane considered:

$$S_n = P_{si} \tag{6.16}$$

Assuming that the vertical stress S_V is overburden stress (a principal stress) and the stress field linearly varies with depth, the normal stress $S_{n,i}$

acting on the fracture plane can be expressed in the following equation (Klee et al., 2011):

$$S_{n,i} = S_V \cos^2 \alpha + \frac{1}{2}\sin^2 \alpha\{[S_{Ho} + S_{ho} + (dS_H/dz + dS_h/dz)z_i] - [S_{Ho} + S_{ho} + (dS_H/dz + dS_h/dz)z_i]\cos 2(\theta - \theta_1)\} \quad (6.17)$$

where θ and α are the strike and dip angles of the particular fracture plane at depth z_i; S_{Ho} and S_{ho} are the principal horizontal stresses at the upper limit of the investigated borehole section; the stress derivatives are the horizontal principal stress gradients and θ_1 is the orientation of S_{Ho} with respect to north. The equation includes six unknowns; the solution therefore requires a minimum of six measurements of S_n at various depths on fractures with different orientations. This method is attractive because shut-in pressures are easy to identify and are usually reliable (Klee et al., 2011). In addition, no assumptions on pore pressure are required.

6.2.2 Leak-off tests in the reverse faulting stress regime

In a strong tectonic stress regime, particularly the reverse faulting stress regime, vertical stress is the minimum stress and the injection-induced fracture is horizontal, and the closure pressure is equal to vertical stress σ_V, i.e.,

$$\sigma_V = p_c \quad (6.18)$$

Therefore, the closure pressure measured from a hydraulic injection test in the reverse faulting stress regime is not a true reflection of the minimum horizontal stress. Alternative methods are needed; for instance, the minimum horizontal stress can be interpreted from drilling-induced fractures using Kirsch's wellbore solution (refer to Section 6.4.2.2).

6.2.3 Minimum stress interpretations from leak-off tests

As stated in Eq. (6.15), σ_h is equal to the closure pressure (at the inflection point) during the pressure decline in Fig. 6.4; however, this method can be difficult to apply when the inflection point is less well-defined, as pointed out by Jones and Sargeant (1993) and Desroches and Kurkjian (1999). One approach to determine the minimum horizontal stress is to use the instantaneous shut-in pressure (p_{isip}). However, this is not an exact relationship. Although p_{isip} is an adequate approximation of closure stress, it is usually difficult to determine accurately. If large amounts of fluid have been pumped

into the formation interval, the value of stress will increase because of the additional stresses created by the presence of this extra fluid, and this could distort the results.

By examining the pressure falloff data after several injection periods, the point at which the fracture closes can be observed, and closure pressure can be better estimated (Whitehead et al., 1986). When the pump is shut in, the pressure decline behavior should represent linear flow of fluid from the fracture into the reservoir (Jones and Sargeant, 1993). During infinite-conductivity fracture flow, pressure in the wellbore varies as described by the following equation:

$$\Delta p = At^{1/2} \tag{6.19}$$

A similar relation exists for finite-conductivity fracture flow:

$$\Delta p = A't^{1/4} \tag{6.20}$$

where Δp is the difference between the final injection pressure and shut-in bottomhole pressure; t is the elapsed time; A and A' are constants.

Therefore, the pressure decline in the fracture should be a linear relationship with $t^{1/2}$ or $t^{1/4}$. When the fracture closes, the slope of the pressure decline curve versus $t^{1/2}$ or $t^{1/4}$ should change. Fig. 6.5 presents an example plot of the pressure decline curve versus $t^{1/2}$. The change point of the slope in the pressure decline curve versus $t^{1/2}$ or $t^{1/4}$ is the closure pressure (Thiercelin and Roegiers, 2000), which is easier to be picked up and interpreted.

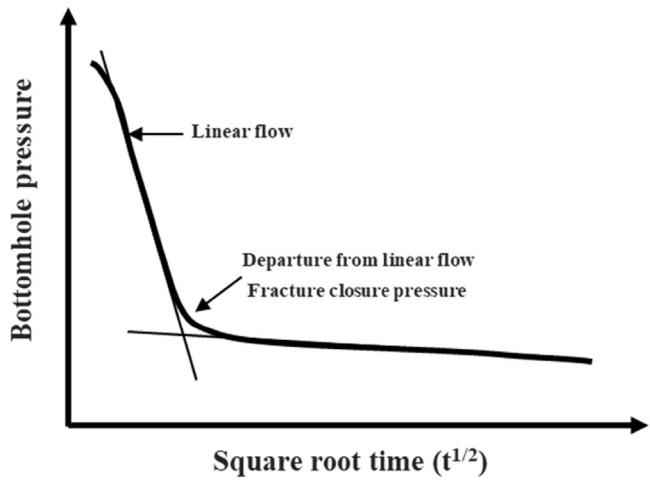

Figure 6.5 Pressure falloff data plotted with square root of time from a leak-off test.

There are several other methods used to determine the closure pressure from the pressure decline following shut-in. The G-time function technique uses a plot of pressure as a function of pressure versus G-time (Nelson et al., 2007). The G-time function was constructed to account for the temporal and spatial variations of leak-off observed in the rock as the created hydraulic fracture propagates and recedes. It is a dimensionless time function relating shut-in time (t) to total pumping time (t_p) (at an assumed constant rate). The dimensionless pumping time used in the G-function is defined as follows (Barree et al., 2009):

$$\Delta t_D = (t - t_p)/t_p \tag{6.21}$$

where t is the elapsed total time from the start of fracture initiation; t_p is the total pumping time (elapsed time from fracture initiation to shut-in) in consistent time units.

The G-function can be expressed in the following:

$$G(\Delta t_D) = \frac{4}{\pi}[g(\Delta t_D) - g_0] \tag{6.22}$$

where g_0 is the dimensionless loss-volume function at shut-in ($t = t_p$ or $\Delta t_D = 0$). It is the computed value of g at shut-in (Eq. (6.23) or (6.24)).

For the assumption of low leak-off, or high efficiency where the open fracture area after shut-in varies approximately linearly with time in low-permeability formations, the intermediate function $g(\Delta t_D)$ is computed in the following equation (Barree et al., 2009):

$$g(\Delta t_D) = \frac{4}{3}\left[(1 + \Delta t_D)^{1.5} - \Delta t_D^{1.5}\right] \tag{6.23}$$

For high leak-off, or low-efficiency fluids where the fracture surface area varies with the square root of time after shut-in, the intermediate function $g(\Delta t_D)$ is as follows:

$$g(\Delta t_D) = (1 + \Delta t_D)\sin^{-1}\left[(1 + \Delta t_D)^{-0.5}\right] + \Delta t_D^{0.5} \tag{6.24}$$

On a plot of pressure and its derivatives versus G-function calculated from Eqs. (6.22) to (6.23) (Barree et al., 2009), as shown in Fig. 6.6, the fracture closure pressure can be easily determined.

There are two ways to record the pressures when performing the LOT or FPIT (formation pressure integrity test). One is to record the pump pressure from the surface; the other is to measure it through downhole pressure gauges or tools, such as the pressure while drilling (PWD or APWD).

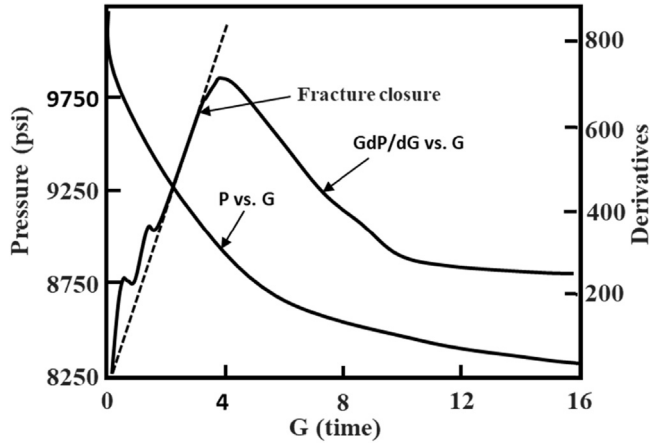

Figure 6.6 Pressure-dependent leak-off G-function plot to determine the closure pressure.

However, these two measurements may give different results, and the downhole measurement gives a lower value than the one from the surface measurement. The downhole measurement gives a more realistic result because it represents the downhole pressure of the tested formation. If the injection pressure (pump pressure) is recorded at the surface, the bottomhole pressure gradient can be calculated from the following equation:

$$P_l = P_{mw} + \frac{p_s}{0.051948D} \tag{6.25}$$

where P_l is the bottomhole pressure gradient (ppg); p_s is the measured pump pressure at the surface (psi); P_{mw} is the downhole mud weight (or ESD) when the LOT test is performed (ppg); D is the depth of the tested formation (ft).

It should be noted that if the LOT does not reach the formation breakdown pressure, it is not a good test for in situ stress determination.

6.2.4 Minimum stress from diagnostic fracture injection test

The DFIT is another method to determine the closure pressure (e.g., Martin et al., 2012). It can be used to discern both hydraulic fracturing character and the reservoir pressure. It is often performed before the stimulation treatment of a formation. It usually consists of pumping a certain amount (500–2000 gal) of water (often containing a clay control additive) into a reservoir rock at rates of 2–10 bbls/min. The pressure and injection rates are measured throughout the fracture-injection test and recorded for subsequent analysis. The principle in determination of closure pressure in the DFIT is

very similar to the LOT, and interpretation of the closure pressure is the same as the methods introduced in the previous sections. The major difference between LOT and DFIT is that the DFIT uses a larger injection rate (volume) and creates a much longer hydraulic fracture. The formation breakdown pressure may be measured larger for a higher pumping rate. It should be noted that the recorded pressure in the DFIT normally is the gauge pressure. The mud pressure in the borehole should be added for the purpose of calculating in situ stresses (refer to Eq. 6.25).

6.2.5 Case example of in situ minimum stress measurement

The MWX was sponsored by the US Department of Energy to increase natural gas production from low-permeability sandstone reservoirs. Three vertical wells, MWX-1, MWX-2, and MWX-3, spaced several hundred feet apart were drilled in the Piceance Basin of northwestern Colorado. The MWX involved strata of the Mesaverde Group, which comprises the Cretaceous Iles and the Williams Fork Formations (Nelson, 2003). The major stress measurement techniques used were small-volume hydraulic fractures and anelastic strain recovery (ASR) (Warpinski and Teufel, 1989).

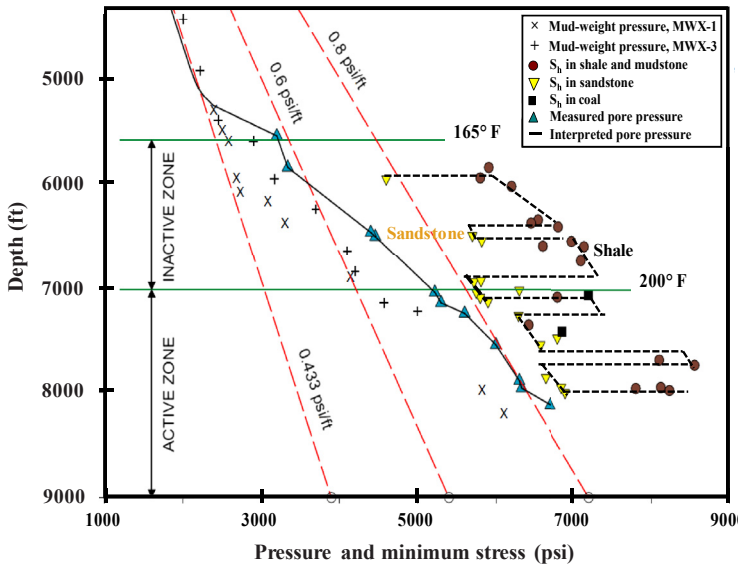

Figure 6.7 Pore pressure and minimum horizontal stress (S_h) measurements as a function of depth at the MWX site in the Piceance Basin of Colorado. *(Modified from Nelson (2003) courtesy of the U.S. Geological Survey, data from Spencer (1989) and Warpinski et al. (1985))*

Fig. 6.7 presents pore pressure and measured minimum horizontal stress profiles with depth. The pore pressure is highly overpressured starting from 5200 ft probably because of gas generation. The minimum horizontal stress in the shale or mudstone at any given depth is consistently greater than that in the sandstone. This might be caused by the sandstone, which has a lower Poisson's ratio than that in the shale or by the lithology-dependent phenomenon as described by Zhang and Zhang (2017) (refer to Section 5.3 of Chapter 5).

6.3 Minimum horizontal stress calculation

The LOT, FPIT, and DFIT are useful methods to determine the minimum horizontal stress in some sections of a borehole. However, measured data normally are not available at the location and depth of interest. Furthermore, most LOT tests only provide fracture initiation pressures or formation breakdown pressures and do not indicate fracture closure pressures (i.e., the minimum stress). Micro-frac tests can be performed while drilling, which provide real-time measurements of horizontal stresses. However, for a very tight rock the micro-frac test may not be able to break the formation. Therefore, challenges still exist for efficiently, routinely, and accurately determining and predicting the minimum horizontal stress (e.g., Schmitt et al., 2012; Zhang, 2013). In the following sections, the conventional uniaxial strain model and its improved forms are examined for estimating the minimum horizontal stress.

6.3.1 Minimum horizontal stress without tectonic impact

In the normal faulting stress regime, the minimum horizontal stress is the minimum principal stress and can be calculated by assuming the uniaxial strain condition. For the isotropic rocks and without tectonic stress effect, the minimum horizontal stress can be expressed in the following:

$$\sigma_h = \frac{\nu}{1-\nu}(\sigma_V - \alpha p_p) + \alpha p_p \tag{6.26}$$

where σ_h is the minimum horizontal stress; σ_V is the overburden stress; ν is Poisson's ratio; p_p is the pore pressure; α is Biot's coefficient. This equation indicates that the minimum horizontal stress is strongly dependent on vertical stress and pore pressure. Notice that Eq. (6.26) is the lower bound minimum horizontal stress (Zhang and Zhang, 2017).

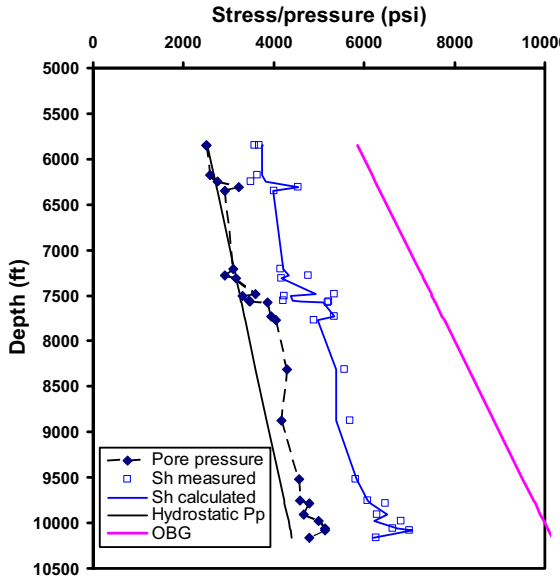

Figure 6.8 The minimum horizontal stress calculated by Eq. (6.26) with $\alpha = 0.95$ using the data of Whitehead et al. (1987) measured in Texas. The measured pore pressure, hydrostatic pore pressure, and overburden stress are also plotted.

A case example in the following is presented to examine the applicability of this equation. Whitehead et al. (1987) presented field measurements for in situ stresses and pore pressure in the Travis Peak Field of tight gas sandstone play, Harrison County, Texas. The minimum horizontal stresses were measured from 34 stress tests in 5 wells in the Travis Peak formation using mini-frac and other tests (Whitehead et al., 1986). The formation pore pressures were obtained in many zones by either wireline formation tests or pressure buildup tests. Poisson's ratio values are available in their paper and can be used to calculate the stresses from Eq. (6.26). Fig. 6.8 plots the measured reliable pore pressure, overburden stress, measured and calculated minimum horizontal stresses. It shows that the minimum horizontal stress calculated from the uniaxial strain model (Eq. 6.26) gives a very reasonable estimation.

Warpinski et al. (1985) presented another field test results of in situ stresses in well MWX-2 located near Rifle, Colorado. Poisson's ratios are calculated from sonic logging data. Based on the data, the minimum horizontal stress is calculated using Eq. (6.26) (assuming $\alpha = 1$) and compared to the measured minimum horizontal stresses. Fig. 6.9 demonstrates that the calculated minimum horizontal stresses based on Eq. (6.26)

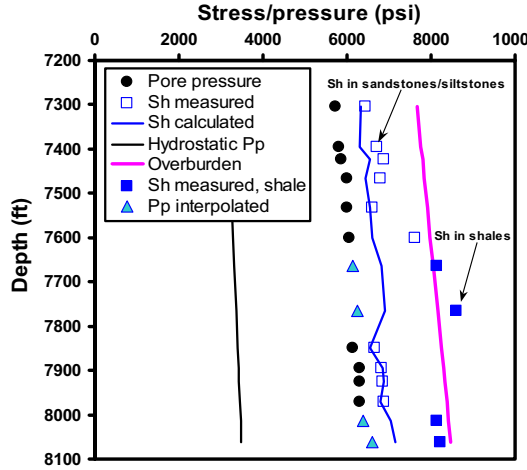

Figure 6.9 Pore pressure, measured and calculated minimum horizontal stresses (S_h), and overburden stress versus depth in Well MWX-2 based on the data of Warpinski et al. (1985).

match the measured results in sandstones and siltstones, where measured pore pressure data are available. The calculated results do not match the measured results in shales, and this may be caused by the unreliable pore pressure estimate in the shales. There were no measured pore pressures in shales, and the pore pressures provided in shales were interpolated from the pressures measured in adjacent sandstones (Warpinski et al., 1985). The mismatch in the minimum horizontal stress calculation may also be caused by the tectonic stress.

6.3.2 Minimum horizontal stress with tectonic impact

The uniaxial strain model is oversimplified for estimating the minimum horizontal stress in a tectonic region. Therefore, modification is needed. If the tectonic stress is considered (as proposed by Daines, 1982), the minimum horizontal stress can be written as:

$$\sigma_h = \frac{\nu}{1-\nu}(\sigma_V - \alpha p_p) + \alpha p_p + \sigma_{tect}^{\min} \tag{6.27}$$

where $\sigma_{tect}^{\min}$ is the tectonic stress in the minimum horizontal stress direction. It is also named as the excess minimum horizontal stress, and

$$\sigma_{tect}^{\min} = \frac{E}{1-\nu^2}(\varepsilon_h + \nu\varepsilon_H) \tag{6.28}$$

Therefore, Eq. (6.27) can be rewritten as follows:

$$\sigma_h = \frac{\nu}{1-\nu}(\sigma_V - \alpha p_p) + \alpha p_p + \frac{E}{1-\nu^2}(\varepsilon_h + \nu\varepsilon_H) \tag{6.29}$$

where E is Young's modulus of the rock; ε_h and ε_H are the tectonic strains or excess applied strains in the minimum and maximum horizontal stress directions, respectively. Eq. (6.29) can be derived from Hooke's law (refer to Eq. (1.50) in Chapter 1 with thermal effect or Warpinski (1989)).

To apply the above method the tectonic strains have to be obtained, which can be back-calculated either from in situ stress measurements or from calibrations of observed wellbore shear and tensile failures. Dolinar (2003) presented how to use the measured horizontal stress results to obtain the excess applied strain in mining areas for the eastern United States. He considered that the excess strains could be obtained from Eq. (6.29) after the effects of gravity (effect of Eq. 6.26) were removed from the measured horizontal stresses. The stress measurements were mainly obtained by overcoring method from 37 sites in the northern (7 sites) and central (19 sites) Appalachian regions as well as from the eastern Mid-Continent region (11 sites) with the depths ranging from 275 to 2500 feet. Examining the excess strains obtained from the stress measurements indicates that for most of the eastern United States the maximum applied excess or tectonic strain (ε_H) ranges from 300 to 550 micro strains (Table 6.1). However, in a high strain zone in the central Appalachian region, the maximum applied tectonic strains range from 700 to 1000 micro strains.

Table 6.1 Average excess applied horizontal strain by region for the eastern United States (Dolinar, 2003).

Region	Number of sites	Max. Strain ε_H (10^{-6})	Max. Strain range (10^{-6})	Min. Strain ε_h (10^{-6})	Strain ratio $\varepsilon_H/\varepsilon_h$
Northern Appalachian	7	440	300–540	260	1.69
Central Appalachian: Low strain zone	7	370	300–480	170	2.17
Central Appalachian: High strain zone	12	760	550–970	410	1.85
Eastern Mid-Continent	10	370	240–530	80	4.6

Very high tectonic stresses are found in the Longmen Shan fault belt near China's Sichuan basin, where the margin zone between the Tibetan Plateau and Sichuan basin is located. In this fault belt the rate of the maximum tectonic compressive strain (ε_H) measured from the surface by GPS reaches to 40–50 nano-strains per year (Pan and Shen, 2017). This has imposed large tectonic strains to the Sichuan basin, which can reach $\varepsilon_H = 2\text{–}20 \times 10^{-9}$/yr. If the subsurface formations have the same strain rates and the rock properties are $E = 30$ GPa, $\nu = 0.25$, and $\varepsilon_h = 0$, then the minimum tectonic stress can be obtained from Eq. (6.28), i.e., $\sigma_{tect}^{\min} = 1.6 \times 10^{-5}\text{–}1.6 \times 10^{-4}$ MPa/yr and the maximum tectonic stress $\sigma_{tect}^{\max} = 6.4 \times 10^{-5}\text{–}6.4 \times 10^{-4}$ MPa/yr (refer to Eq. 6.73). The high tectonic strain rates and high tectonic stresses have caused very high horizontal stresses in the geologic time scale in this region. Cui et al. (2014) reported abnormally high horizontal stresses from in situ stress measurements by ASR in the Wenchuan Earthquake Fault Scientific Drilling Project, borehole-1 (WFSD-1). The borehole, located in the Longmen Shan thrust fault zone, was drilled to a vertical depth of 1179 m with an average deviation angle of 11 degrees. The obtained minimum and maximum horizontal stresses (Cui et al., 2014) are plotted in Fig. 6.10 along

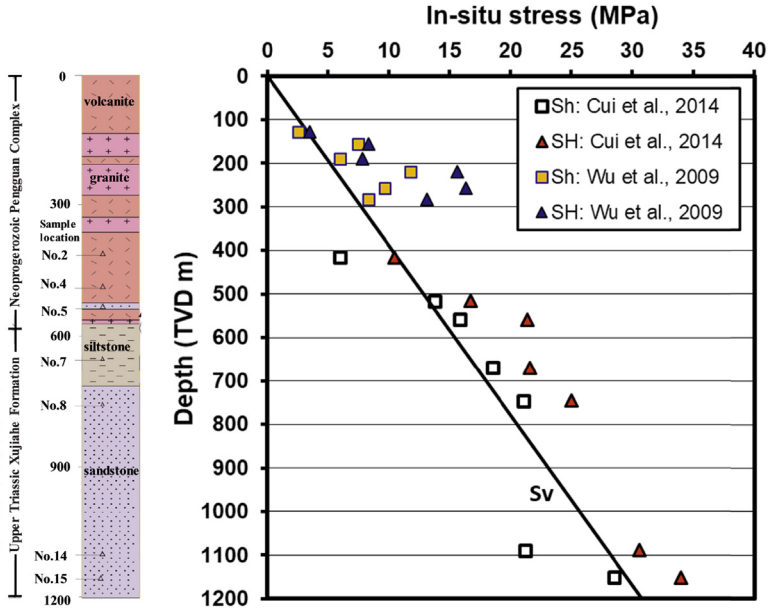

Figure 6.10 Geological column of the WFSD-1 and measured minimum and maximum horizontal stresses in the Longmen Shan Fault area, Sichuan, China.

with the main lithologic units and rock types. The overburden stress and depth (Z) have the following relation: $\sigma_V = 0.0257Z$. The data at shallower depths (< 400 m) are also plotted in Fig. 6.10 for comparison, which were measured using hydraulic fracturing method in the Yingxiu area (Wu et al., 2009), near the WFSD-1 site. It can be observed from Fig. 6.10 that two horizontal stresses are mostly higher than the overburden stress, so that this area is in the thrust faulting stress regime.

When the excess strains are not available, empirical correlations can be used to estimate tectonic stresses or strains. Calibrating the minimum stress data obtained from downhole tests, the tectonic stress can be approximately estimated from the following relation:

$$\sigma_{tect}^{\min} = b\sigma_V \tag{6.30}$$

where b is the ratio of the tectonic to overburden stresses or tectonic stress constant, and $b \geq 0$.

Therefore, the minimum horizontal stress Eq. (6.27) can be rewritten as follows:

$$\sigma_h = k(\sigma_V - \alpha p_p) + \alpha p_p + b\sigma_V \tag{6.31}$$

where $k = \nu/1{-}\nu$.

Several examples are given in the following to illustrate tectonic stress constants in different basins. Tingay et al. (2009) presented in situ stress measurements in the Champion field, offshore Brunei. This field is in normal faulting stress regime, and average in situ stress gradients are $\sigma_V = 21.8$ MPa/km, $\sigma_h = 16.5$ MPa/km, and $\sigma_H = 18{-}21$ MPa/km. Based on the measured stress and pore pressure data, they obtained the following pore pressure and in situ stress relation:

$$\sigma_h/\sigma_V = 0.58(p_p/\sigma_V) + 0.54 \tag{6.32}$$

where σ_h, σ_V, and p_p are in MPa, the same unit used in the following equations.

Compared this equation to Eq. (6.31) and assuming $\alpha = 1$, it can be found that $b = 0.12$, hence Eq. (6.32) can be rewritten as follows:

$$\sigma_h = 0.42(\sigma_V - p_p) + p_p + 0.12\sigma_V \tag{6.33}$$

The LOT data in deepwater Gulf of Mexico wells show that the tectonic stress constant is much lower, but with a much higher $\nu/(1\text{-}\nu)$, e.g., in the Mississippi Canyon $b = 0.04$, and

$$\sigma_h = 0.68(\sigma_V - p_p) + p_p + 0.04\sigma_V \tag{6.34}$$

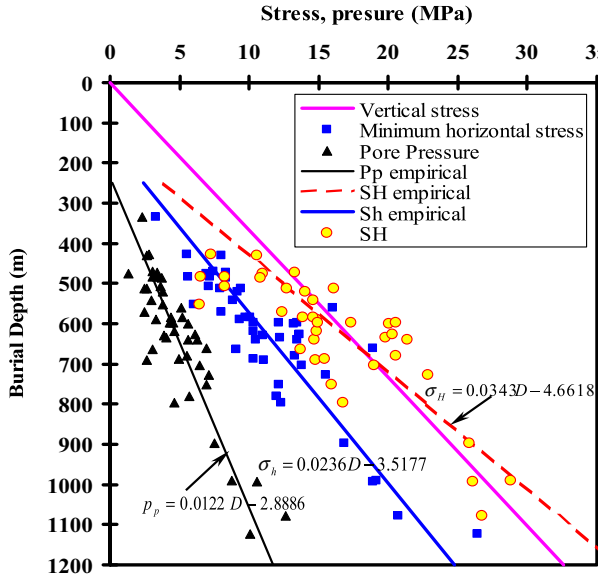

Figure 6.11 Measured σ_h and p_p data and empirical correlations of the maximum and minimum horizontal stresses, overburden stress, and pore pressure in coalbed methane reservoir of the Qinshui basin, China.

Analyzing measured minimum horizontal stress data from mini-frac tests, Meng et al. (2011) obtained the following relation (with constant $b = 0.035$) for the minimum horizontal stress in the Qinshui coalbed methane basin (Fig. 6.11):

$$\sigma_h = 0.45(\sigma_V - p_p) + p_p + 0.035\sigma_V \tag{6.35}$$

It can be seen from Eqs. (6.33–6.35) that k and b values are different in different areas. If the measured minimum horizontal stress data (e.g., LOT, DFIT) are available, k and b values can be back-calculated from Eq. (6.31), which can be used to estimate the minimum horizontal stress in a similar area.

6.3.3 Minimum horizontal stress in anisotropic rocks

Some sedimentary rocks, particularly shales, are transversely isotropic, and rock properties (e.g., Young's modulus and Poisson's ratio) are very different in horizontal and vertical directions. For transversely isotropic rocks the minimum horizontal stress can be expressed as follows, if the uniaxial strain model is applicable (refer to Chapter 1, Section 1.5.2 for derivations):

$$\sigma_h = \frac{E_h \nu_V}{E_V(1-\nu_h)}(\sigma_V - \alpha_V p_p) + \alpha_h p_p \tag{6.36}$$

where subscripts h and V represent rock properties in horizontal and vertical directions, respectively. For example, if rock properties have the following relations: $E_h/E_V = 2.0$, $\nu_h/\nu_V = 1.4$, $\nu_V = 0.2$, $\nu_h = 0.28$, and $\alpha_V = \alpha_h = \alpha$, the minimum horizontal stress in anisotropic and isotropic cases can be calculated as follows:

Anisotropic case, from Eq. (6.36): $\sigma_{h\_VTI} = 0.56(\sigma_V - \alpha p_p) + \alpha p_p$,

Isotropic case, from Eq. (6.26): $\sigma_h = 0.25(\sigma_V - \alpha p_p) + \alpha p_p$

The results in the above calculations indicate that the effective minimum horizontal stress in the transversely isotropic case is more than two times of that in the isotropic case. The difference in this example is significant; therefore, the anisotropy of the rock needs to be considered.

Because the uniaxial strain model cannot describe the real state of in situ stresses in most cases, the minimum stress model in Eq. (6.36) can be modified by considering the tectonic strains. The equation considering the horizontal strains derived in Chapter 1, Section 1.5.2 (Eq. 1.48) can be used for the transversely isotropic formations:

$$\sigma_{h\_VTI} = \frac{E_h \nu_V}{E_V(1-\nu_h)}(\sigma_V - \alpha_V p_p) + \alpha_h p_p + \frac{E_h}{1-\nu_h^2}(\varepsilon_h + \nu_h \varepsilon_H) \quad (6.37)$$

The difficulty in applying this equation is to determine the minimum and maximum horizontal strains ε_H and ε_h. To solve this issue, two methods can be used: one is to use local or regional empirical equations to estimate the minimum horizontal stress; the other is to back-calculate the horizontal strains or tectonic stresses from stress measurements using the following equation and Eq. (6.73):

$$\sigma_{tect}^{\min} = \frac{E_h}{1-\nu_h^2}(\varepsilon_h + \nu_h \varepsilon_H) \quad (6.38)$$

6.3.4 Minimum horizontal stress from empirical equations

When measured data in the study area are not available, regional empirical equations can be used as a first estimate. Empirical equations in several petroleum basins are presented in the following. For application of any of these empirical equations, calibrations from local data in the studied area are needed because these equations might be obtained with some limitations, e.g., for a certain formation or rock type without considering lithology effects.

Using more than 300 reliable data from leak-off tests and hydraulic fracture tests from the US Gulf Coast region, Breckels and van Eekelen (1982) proposed several relationships between the minimum horizontal

stress and depth (mainly for shales). The following correlations are the lower bound of the measured data for normally pressured formations in this region:

$$\begin{aligned}\sigma_h &= 0.197D^{1.145} \quad (D \le 11,500ft)\\ \sigma_h &= 1.167D - 4596 \quad (D > 11,500ft)\end{aligned} \tag{6.39}$$

where D is the depth in ft; σ_h is the minimum horizontal stress in psi. The same units are used from Eqs (6.39–6.42).

The minimum horizontal stress in abnormally pressured formations in the US Gulf Coast region can be estimated from the following correlations (Breckels and van Eekelen, 1982):

$$\begin{aligned}\sigma_h &= 0.197D^{1.145} + 0.46(P_c - P_{cn}) \quad (D \le 11,500ft)\\ \sigma_h &= 1.167D - 4596 + 0.46(P_c - P_{cn}) \quad (D > 11,500ft)\end{aligned} \tag{6.40}$$

where P_c is the pore pressure gradient in psi/ft; P_{cn} is the normal pore pressure gradient; and $P_{cn} = 0.465$ psi/ft.

A similar correlation was obtained from hydraulic fracturing tests in Venezuela for 5900 ft < D < 9200 ft (Breckels and van Eekelen, 1982):

$$\sigma_h = 0.21D^{1.145} + 0.56(P_c - P_{cn}) \tag{6.41}$$

where $P_{cn} = 0.433$ psi/ft.

The mini-frac test data in the offshore Brunei appear to be subject to higher compressive stresses than those in the US Gulf Coast; based on 15 data points, Breckels and van Eekelen (1982) obtained the following relation (depth D < 10,000 ft):

$$\sigma_h = 0.227D^{1.145} + 0.49(P_c - P_{cn}) \tag{6.42}$$

From LOTs, Gibson-Poole et al. (2002) obtained the following correlation between the minimum horizontal stress and depth in the Mesozoic formations of the Petrel Sub-basin, NW Australia:

$$\sigma_h = 0.0184Z \tag{6.43}$$

where σ_h is in MPa; Z is the depth in meters. The same units are used from Eqs. (6.43–6.47).

A similar correlation was obtained in the North Sea basins (Lønø, 1995) based on XLOT data in the Ekofisk field:

$$\sigma_h = 0.0185Z_{bml} - 2 \quad (500 \le Z_{bml} \le 2,900m) \tag{6.44}$$

In the central Graben of the North Sea, the minimum horizontal stress calculated from shut-in data from both LOT and XLOT data follows the following expression (Amundsen, 1995; Addis et al., 1998):

$$\sigma_h = 0.017Z - 1.09 \quad (Z \leq 3,500m) \tag{6.45}$$

The minimum horizontal stresses measured from acid-gas injection wells in the Alberta Basin, Canada, have a basin-wide average gradient of 16.6 kPa/m, although stress gradients vary locally between 13.6 and 19.5 kPa/m (Hawkes et al., 2005), i.e.:

$$\sigma_h = 0.0166Z \tag{6.46}$$

In situ stress results measured by hydraulic fracturing tests (e.g., DFIT) in tight gas reservoirs (Xujiahe sandstones) in the Sichuan basin of China show that the maximum horizontal stress is greater than the overburden stress ($\sigma_V = 0.024-0.0245Z$ and $\sigma_H \approx 0.03Z$). This area is located in high tectonic stress regime, and the pore pressures in deep formations are overpressured. The minimum horizontal stress in this area is close to or even higher than the overburden stress, which generally has the following relation (refer to Fig. 7.26):

$$\sigma_h = 0.0224Z \tag{6.47}$$

6.4 Maximum horizontal stress

Predicting the maximum horizontal stress is much more challenging than predicting the minimum horizontal stress. This section attempts to provide various approaches and methods. In very complicated conditions, such as in a strong tectonic stress region, multiple methods and integrated approaches need to be applied to verify each other and calibrate the model.

6.4.1 Maximum horizontal stress from extended leak-off test

6.4.1.1 No fluid penetration in the formation

In normal and strike-slip faulting stress regimes, the maximum horizontal stress can be estimated from the multicycle XLOT or DFIT, as shown in Fig. 6.12. Assuming that the rock behaves like elastic and isotropic material and no fluid penetrates into the fracture, Haimson and Fairhurst (1967) derived the following equation to calculate the fracture initiation pressure that can be used for the leak-off test analysis in a vertical well, and they

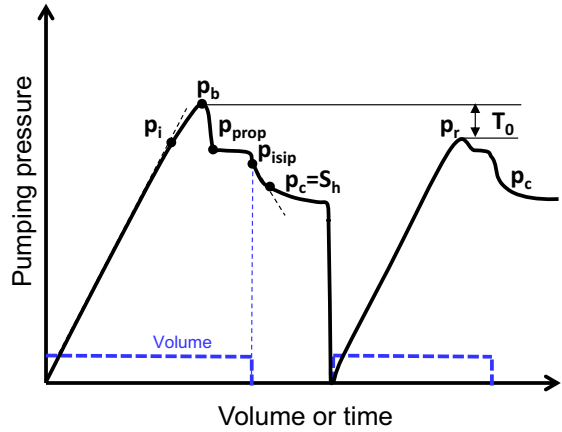

Figure 6.12 Schematic relationship between pumping pressure and time or volume of injected fluid in a typical two-cycle XLOT in a vertical well.

stated that this equation might be able to predict formation breakdown pressure:

$$p_b = 3\sigma_h - \sigma_H - p_p + \sigma_T + T_0 \tag{6.48}$$

where p_b is the formation breakdown pressure; p_p is the pore pressure; T_0 is the tensile strength of the rock. The thermal stress (σ_T) in Eq. (6.48) is considered, which can be expressed in the following form:

$$\sigma_T = \frac{\alpha_T E(T_m - T_f)}{1 - \nu} \tag{6.49}$$

where σ_T is the thermal stress arising from the difference (ΔT) between the mud temperature (T_m) and the formation temperature (T_f); α_T is the thermal expansion coefficient of the rock; E is Young's modulus of the rock.

Some laboratory hydraulic fracturing experiments indicate that the prediction from Eq. (6.48) underestimates the breakdown pressure obtained from the laboratory test results (e.g., Zoback et al., 1977). Zhang et al. (2018) proposed a new model to estimate formation breakdown pressure in Eq. (6.50), which predicts a higher formation breakdown pressure than that obtained from Eq. (6.48), implying a better prediction:

$$p_b = 3\sigma_h - \sigma_H - p_p + \sigma_T + kT_0 \tag{6.50}$$

where k is a parameter and the default value is $k = \sqrt{2}$. If $k = 1$, Eq. (6.50) simplifies to Eq. (6.48).

It can be observed that the tensile strength effect is stronger in Eq. (6.50) than that in Eq. (6.48) proposed by Haimson and Fairhurst (1967). The equation, Eq. (6.50), predicts a higher tensile strength effect; therefore, it may be used as the upper bound formation breakdown pressure.

For a vertical borehole and no fluid penetration in the formation before the fracture is initiated, the upper bound maximum horizontal stress can be obtained by rearranging Eq. (6.50):

$$\sigma_H = 3\sigma_h - p_b - p_p + \sigma_T + kT_0 \tag{6.51}$$

To obtain reliable and repeatable closure pressure and rock tensile strength data, a second pressurization cycle needs to be performed from the initial hydraulic fracture test (Fig. 6.12) to obtain fracture reopening data. Because a fracture has been created by the first cycle of the XLOT, there should be no tensile strength in the fracture reopening process. The pressure at the time of reopening of the fracture created from the previous cycle can be used to estimate rock tensile strength (T_0):

$$T_0 = p_b - p_r \tag{6.52}$$

where p_r is the fracture reopening pressure (refer to Fig. 6.12).

Fig. 6.13 presents an example of a two-cycle XLOT in an offshore well of the North Sea. Normally, the recorded pump pressure is the gauge

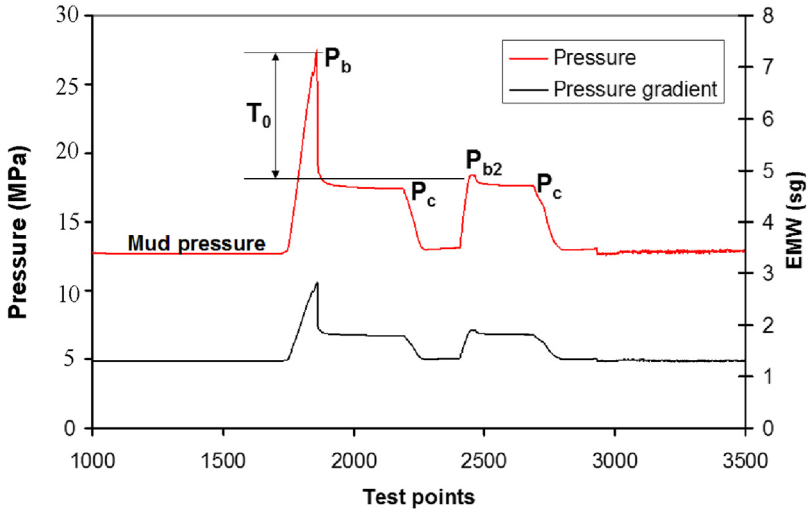

Figure 6.13 Measured pump pressure and pressure gradient with consideration of downhole mud pressure versus time (test points) in a two-cycle XLOT at a vertical depth of 1000 m. In the figure the equivalent mud weight (EMW) is in sg (or g/cm^3).

pressure without considering mud weight (mud pressure). Therefore, the mud pressure should be added to obtain the bottomhole pressure (see Eq. 6.25). Based on the pressure data in Fig. 6.13, the calculation of the maximum horizontal stress is shown in the following:

- The minimum horizontal stress is equal to the closure pressure $\sigma_h = p_c = 18$ MPa.
- Using Eq. (6.52), the tensile strength equals the difference of the formation breakdown pressure and reopening fracture ($p_{b2} = p_r$): $T_0 = p_b - p_{b2} = 9.4$ MPa.
- The maximum horizontal stress can be calculated from Eq. (6.51) with $p_b = 28.2$ MPa, $p_p = 11$ MPa, $\sigma_V = 18.7$ MPa, $k = \sqrt{2}$. Therefore, $S_H = 28.1$ MPa.
- The results show $\sigma_H > \sigma_V > \sigma_h$; this well is in strike-slip faulting stress regime.

6.4.1.2 For permeable fractures

Eqs. (6.48) and (6.51) specially assume that fluid pressure does not penetrate into the fracture from the borehole before the fracture begins to open. However, there are good grounds to believe that the fracture remains permeable to a significant degree even when closed (Ito et al., 1999). If the fracture is slightly conductive, the fluid pressure at the wellbore wall may only partially penetrate, and the pressure inside the fracture at the wellbore wall is equal to the well pressure (Ito et al., 1999), i.e., $p_p = p_r$. Substituting $p_p = p_r$ and Eq. (6.52) into Eq. (6.51) with assumption of no thermal effect and $\alpha = 1$, the maximum horizontal stress can be obtained by:

$$\sigma_H = 3\sigma_h + (k-1)p_b - (k+1)p_r \tag{6.53}$$

In the extreme case with a more conductive fracture, the fluid pressure may completely penetrate to the crack tip. This implies that the reopening is dominated by total force formed by the fluid pressure on the fracture surfaces, and reopening pressure would be equal to the minimum horizontal stress (Rutqvist et al., 2000):

$$\sigma_h = p_r \tag{6.54}$$

Detournay and Cheng (1988) considered the effect of flow from the hydraulic fracture into the formation. A poroelastic solution of the breakdown pressure (Eq. 6.55) was proposed to take into account this effect for permeable rocks (Haimson and Fairhurst, 1967; Detournay and

Cheng, 1988). This breakdown pressure can be used as the lower bound breakdown pressure:

$$p_{bl} = \frac{3\sigma_h - \sigma_H - 2\eta p_p + T_0}{2(1-\eta)} \tag{6.55}$$

The maximum horizontal stress for permeable rocks can be obtained from the above equation:

$$\sigma_H = 3\sigma_h - 2(1-\eta)p_b - 2\eta p_p + T_0 \tag{6.56}$$

where $\eta = \alpha\frac{1-2\nu}{2(1-\nu)}$.

Eqs. (6.56) and (6.53) can be used as the lower bound maximum horizontal stress, while the upper bound maximum horizontal stress can be obtained from Eq. (6.51).

6.4.2 Maximum horizontal stress from drilling-induced tensile fractures

6.4.2.1 In normal and strike-slip faulting stress regimes

If the mud pressure used for drilling is too high, then drilling-induced tensile fractures are generated (Fig. 6.14). Fig. 6.14A presents an example of drilling-induced tensile fractures in a six-pad electrical image log (EMI)

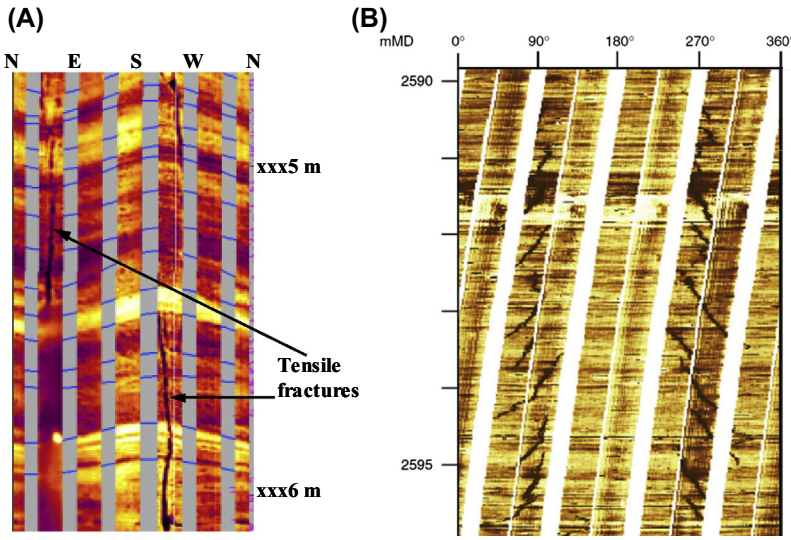

Figure 6.14 Electrical resistivity image logs. (A) the direction of the drilling-induced tensile fracture orientation aligned with borehole axis in a vertical well. (B) normalized formation micro imager (FMI) log showing en echelon drilling-induced tensile fractures in an inclined borehole (Thorsen, 2011).

in a vertical well. The azimuth in the image log along the wellbore starts from North, to East, South, West, and goes back to North. The drilling-induced fractures are thin and long fractures parallel to the borehole axis and can be identified from resistivity image (darker color) in the image log, as shown in Fig. 6.14A.

Assuming that the downhole mud pressure is equal to the formation initiation pressure when drilling-induced tensile fractures occur, Eq. (6.48) can be used to calculate the maximum horizontal stress for the vertical hydraulic fracture in a vertical well, i.e.,

$$\sigma_H = 3\sigma_h - p_m - p_p + T_0 \tag{6.57}$$

where p_m is the downhole mud pressure when drilling-induced tensile fractures occur.

The other method is to assume that the tensile fractures are generated at the wellbore wall when the minimum effective tangential stress (absolute value, because tensile stress is a negative value) becomes less than the tensile strength of the rock. Kirsch's equation can be used to calculate the effective tangential stress. The minimum effective tangential stresses at the wellbore wall in a vertical well (σ'_θ) can be obtained from Kirsch's equation as follows:

$$\sigma'_\theta = 3\sigma_h - \sigma_H - p_m - \alpha p_p \tag{6.58}$$

When vertical tensile fractures are generated in elastic, impermeable rocks in a vertical wellbore, the following relation is satisfied: $\sigma'_\theta + T_0 \leq 0$. When the rock starts to fail, Biot's coefficient can be assumed as $\alpha = 1$. Therefore, Eq. (6.58) can be rewritten as:

$$\sigma_H \geq 3\sigma_h - p_m - p_p + T_0 \tag{6.59}$$

where T_0 is the tensile strength of the rock to the horizontal tensile stress (absolute value is used in the equation). Therefore, Eq. (6.59) is similar to Eq. (6.57).

Plotting Eq. (6.59) in the stress polygon diagram and combining with other methods (e.g., wellbore breakout), the maximum horizontal stress can be constrained (refer to Section 6.4.4).

For an inclined borehole, the drilling-induced fractures are no longer created along the borehole axial direction, but en echelon fractures (Fig. 6.14B) are generated (e.g., Sun et al., 2017; Thorsen, 2011) because of shear stress presence in the far field of the wellbore. Inversion methods of

drilling-induced tensile fracture and wellbore breakout data (Aadnoy, 1990; Peska and Zoback, 1995; Okabe et al., 1998; Huang et al., 2010; Thorsen, 2011) can be applied to obtain in situ stresses in inclined wellbores.

In the normal stress regime for a horizontal well drilled in one of the horizontal stress directions, the tensile stress (absolute value) is the largest at the top and bottom in the cross section of the borehole; hence, the tensile fractures (vertical ones) initiate at the top and bottom of the horizontal well.

6.4.2.2 In the reverse faulting stress regime

6.4.2.2.1 For a vertical well

In the reverse faulting stress regime, the vertical stress is the minimum in situ stress; therefore, horizontal hydraulic fracture stress will be generated (Hubbert and Willis, 1957). The drilling-induced tensile fractures can also be horizontal in a vertical well, as shown in Fig. 6.15. In the reverse faulting stress regime, hydraulic fractures are opening or closing against the vertical stress because the axial stress in the borehole axial direction induces these tensile fractures. This suggests that the closure pressure in the vertical well in

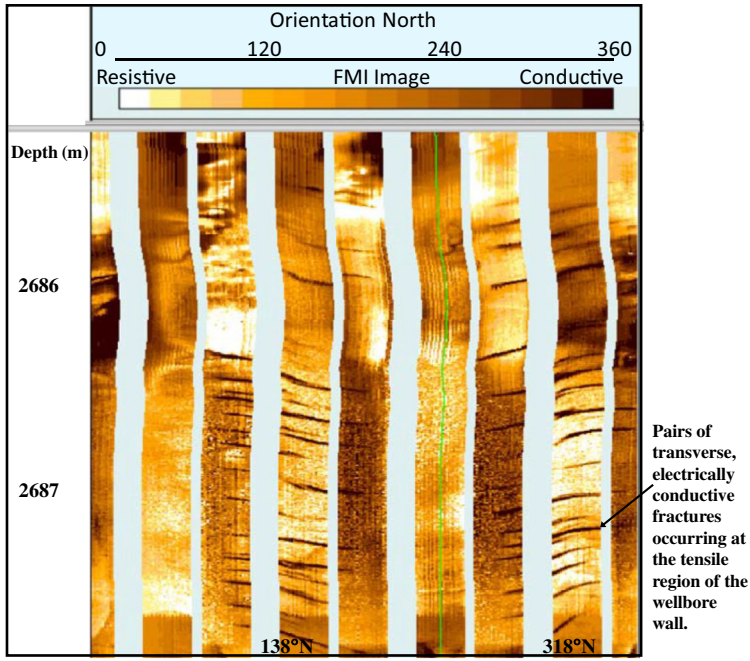

Figure 6.15 Drilling-induced horizontal tensile fractures interpreted on an image log from the West Tuna 39 well of Australia. The fractures are electrically conductive, transverse (the azimuth of σ_H: 138°N and 318°N), restricted to the tensile stress region of the vertical wellbore (Nelson et al., 2005).

hydraulic fracture tests (e.g., DFIT, LOT) may not be representative of the minimum horizontal stress. This closure pressure is the vertical stress instead. Hence, an alternative method is needed for estimating the minimum horizontal stress.

Horizontal fractures observed to open and dilate in the near-wellbore environment can be used to constrain in situ stresses. Using Kirsch's equation, the minimum effective axial stress (σ'_z) at the wellbore wall in a vertical well can be written as (refer to Eq. (10.30) in Chapter 10):

$$\sigma'_z = \sigma_V - 2\nu(\sigma_H - \sigma_h) - \alpha p_p \tag{6.60}$$

Assuming that horizontal fractures are generated when $\sigma'_z + T_V \leq 0$ (generating horizontal fracture) and $\sigma'_\theta + T_0 > 0$ (opposite to Eq. 6.59, i.e., not generating vertical fracture), as shown in Fig. 6.16. Therefore, Eqs. (6.60) and (6.58) can be rewritten as follows, assuming $\alpha = 1$:

$$\sigma'_z + T_V = \sigma_V - 2\nu(\sigma_H - \sigma_h) - p_p + T_V \leq 0 \tag{6.61}$$

$$\sigma'_\theta + T_0 = 3\sigma_h - \sigma_H - p_m - p_p + T_0 > 0 \tag{6.62}$$

where T_V is the rock tensile strength for the vertical tensile stress (absolute values for T_V and T_0 are used in the equations), and it is the strength for resistance to generate a horizontal tensile fracture and open it vertically. If preexisting horizontal and low-angle fabrics or weaknesses (e.g., beddings and interfaces) are presence, then T_V is negligible. T_0 is the rock tensile strength for the horizontal tensile stress.

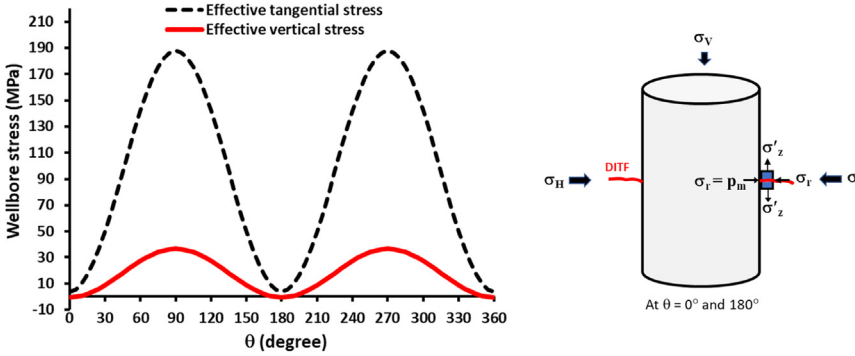

Figure 6.16 Plot of effective tangential and axial (vertical) stresses along the wellbore circumference in a vertical well in the reserve faulting stress regime (for $\sigma_V < \sigma_h$). It shows the condition for generating horizontal drilling-induced tensile fractures at $\sigma'_z + T_V \leq 0$, which occurs at 0°, 180°, and 360°. The plot is drawn from Eqs. (6.58) and (6.60) for $\nu = 0.2$, $\alpha = 1$, $\sigma_V = 78$ MPa, $p_m = 62$ MPa, and $p_p = 60$ MPa.

From Eqs. (6.61) to (6.62), the maximum horizontal stress can be constrained in the following equations, and this condition represents the case where only drilling- or injection-induced horizontal tensile fractures are generated, i.e.,

$$\text{Generating horizontal fractures}: \ \sigma_H \geq \frac{\sigma_V + 2\nu\sigma_h - p_p + T_V}{2\nu} \tag{6.63}$$

$$\text{Not generating vertical fractures}: \ \sigma_H < 3\sigma_h - p_m - p_p + T_0 \tag{6.64}$$

When Eqs. (6.63) and (6.64) are satisfied, only drilling- or injection-induced horizontal fractures are generated. Fig. 6.17 presents how to use stress polygon to constrain the ranges of the minimum and maximum horizontal stresses from Eqs. (6.63) to (6.64). The stress polygon needs to be drawn based on the lower bound minimum horizontal stress from Eq. (5.15) and upper bound maximum horizontal stress from Eq. (5.16) in Chapter 5. A case example is examined in Fig. 6.17 for Poisson's ratio $\nu = 0.2$ (or $\mu = 0.75$ from Eq. 5.18), Biot coefficient $\alpha = 1$, vertical stress $\sigma_V = 78$ MPa, mud pressure $p_m = 62$ MPa, and pore pressure $p_p = 60$ MPa. The simplified equations of Eqs. (6.61) and (6.62) (i.e., $\sigma'_z + T_V = 0$ and $\sigma'_\theta + T_0 = 0$) are applied to analyze the range of the minimum and maximum horizontal stresses. From these equations two lines are plotted in the stress polygon (dashed lines in Fig. 6.17). The area between these two lines (shaded area) in the reverse faulting stress regime (RF) is the allowable horizontal stress region when the drilling- or injection-induced horizontal tensile fractures are generated. Additionally, the maximum horizontal stress should not be greater than the upper bound of the stress

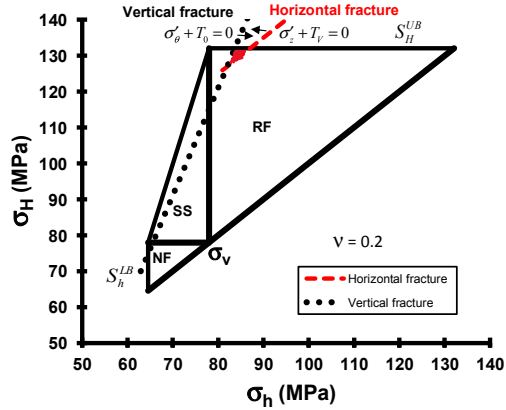

Figure 6.17 Allowable area of the minimum and maximum horizontal stresses constrained from stress polygon and drilling- or injection-induced horizontal fractures.

polygon, i.e., $\sigma_H \leq S_H^{UB}$. Therefore, the ranges of horizontal stresses can be obtained from Fig. 6.17, i.e., $\sigma_h = 82-87$ MPa and $\sigma_H = 129-132$ MPa.

6.4.2.2.2 For a horizontal well

For a horizontal well, drilling- or injection-induced horizontal fractures in the reverse faulting stress regime are much easier to be generated because the minimum effective tangential stress is very small. The minimum effective tangential stress in a horizontal well drilled in the minimum horizontal direction can be expressed in the following:

$$\sigma'_\theta = 3\sigma_V - \sigma_H - p_m - \alpha p_p \tag{6.65}$$

When the horizontal fractures (the fractures parallel to the axial direction of the horizontal well) are generated, the following relation is satisfied, i.e., $\sigma'_\theta + T_V \leq 0$. Notice that in this case σ'_θ is the stress to generate horizontal fractures at the side of the horizontal wellbore, as shown in Fig. 6.18. Therefore, Eq. (6.65) can be rewritten in the following form when the horizontal fractures are generated assuming $\alpha = 1$:

$$\sigma'_\theta + T_V = 3\sigma_V - \sigma_H - p_m - p_p + T_V \leq 0 \tag{6.66}$$

Fig. 6.19 plots the effective tangential stress along the wellbore circumference in a horizontal well located in the strike-slip and reverse faulting stress regimes. In this figure the in situ stresses, mud pressure, pore pressure, and other parameters are the same to those in Fig. 6.16. Comparing Fig. 6.19 to Fig. 6.16, the horizontal well is much easier to

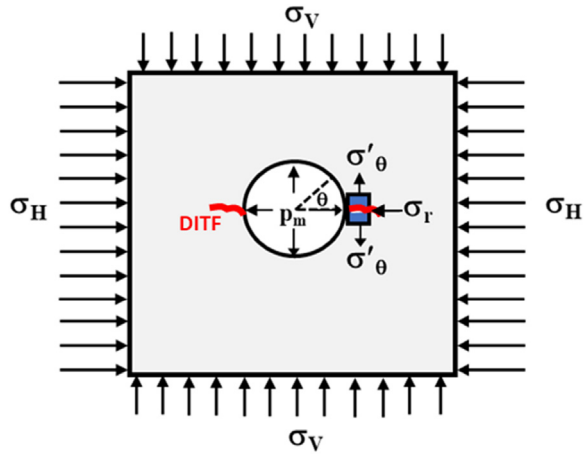

Figure 6.18 Effective tangential stresses and DITFs at the sides of the cross section of a horizontal well drilled in the minimum horizontal stress direction (for $\sigma_V < \sigma_H$).

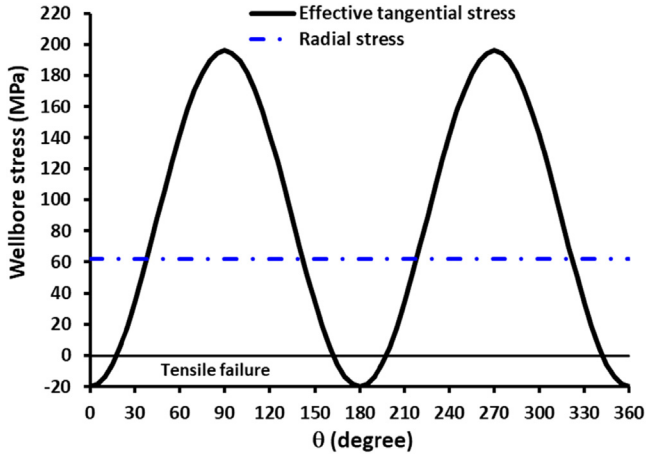

Figure 6.19 Effective tangential stress and total radial stress (mud pressure) along the wellbore circumference in a horizontal well drilled in the minimum horizontal stress direction and located in the reserve faulting stress regime.

generate horizontal fractures because a much larger tensile stress (absolute value) is created at the wellbore wall (this can be found by comparing Eq. (6.61) to Eq. (6.66)). It may imply that for hydraulic fracturing operations in a vertical well, the vertical fractures may be initiated first; these vertical fractures will rotate and eventually develop into horizontal fractures after penetrating through the near-wellbore zone into the undisturbed formation because σ_V is the minimum in situ stress.

Because the maximum horizontal stress is the largest in situ stress in the reverse faulting stress regime, the tensile fractures (horizontal ones) will initiate at the side of the horizontal well (as shown in Figs. 6.18 and 6.19). However, when the horizontal wellbore is not aligned with a principal horizontal stress direction, the shear stress at the wellbore wall is not zero. The borehole wall subjected to the maximum tension is at an angle (γ) to the borehole axis, and en echelon fractures are generated, as shown in Fig. 6.14B. At the wellbore wall the effective principal tensile stress is equal to the minimum effective principal stress and can be obtained by the following equations:

$$\sigma'_{t\max} = \frac{\sigma'_z + \sigma'_\theta}{2} - \sqrt{\left(\frac{\sigma'_z - \sigma'_\theta}{2}\right)^2 + \tau_{\theta z}} \tag{6.67}$$

$$\gamma = \frac{1}{2}\tan^{-1}\left(\frac{2\tau_{\theta z}}{\sigma'_z - \sigma'_\theta}\right) \tag{6.68}$$

where $\sigma'_{t\,\max}$ is the effective principal tensile stress at the wellbore wall; σ'_z and σ'_θ are the effective axial and tangential stresses at the wellbore wall, respectively; $\tau_{\theta z}$ is the shear stress at the wellbore wall (refer to Kirsch's equation in Chapter 10); γ is the angle between borehole axis and the tensile fractures.

6.4.3 Maximum horizontal stress from wellbore breakouts

When stress concentration around a wellbore exceeds rock compressive strength, breakouts are induced around the wellbore. Barton et al. (1988) presented the following equation to determine the maximum horizontal stress utilizing observations of breakout width in a vertical well:

$$\sigma_H = \frac{UCS + p_p + p_m - \sigma_h(1 + 2\cos 2\,\theta)}{1 - 2\cos 2\,\theta} \tag{6.69}$$

where UCS is the uniaxial compressive strength of the rock; (180°-2θ) is the wellbore breakout angle.

In the above equation, Barton et al. (1988) assumed the wellbore breakout occurs when the maximum tangential compressive stress is equal to the uniaxial compressive strength. This assumption may be oversimplified. Failure criteria should be applied to analyze wellbore shear failure (breakout) and calculate the maximum horizontal stress.

Using the Mohr—Coulomb failure criterion, the following equation can be obtained for calculating the maximum horizontal stress in a vertical well (refer to Chapter 10, Section 10.5 for derivations):

$$\sigma_H = \frac{UCS - \alpha(q-1)p_p + (q+1)p_m - (1 - 2\cos 2\,\beta_b)\sigma_h}{1 + 2\cos 2\,\beta_b} \tag{6.70}$$

where $2\beta_b$ is the wellbore breakout angle (degrees); $2\beta_b = 180° - 2\theta$; $q = (1+\sin\varphi)/(1-\sin\varphi)$; φ is the angle of internal friction of the rock.

If the wellbore is in uniaxial loading condition, then $q = 0$, and Eq. (6.70) is simplified to Eq. (6.69). For borehole breakouts in inclined boreholes, in situ stresses can be obtained from inversion of borehole breakout data (e.g., Zajac and Stock, 1997).

6.4.4 Maximum horizontal stress from breakouts and drilling-induced fractures

When both borehole breakouts and drilling-induced tensile fractures (DITFs) occur in a vertical well, a stress polygon combined with wellbore failure data can be used to determine the minimum and maximum

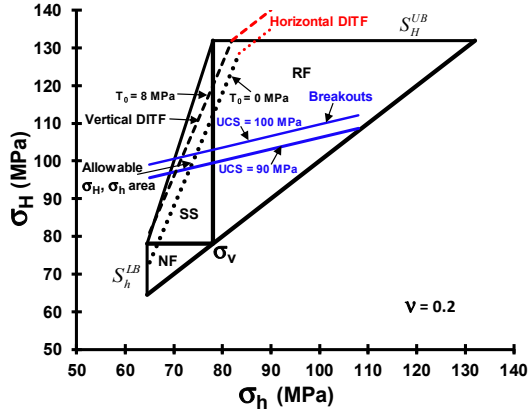

Figure 6.20 Allowable region of the minimum and maximum horizontal stresses constrained from stress polygon by borehole breakouts and drilling-induced tensile fractures (DITF in the figure) in a vertical well.

horizontal stresses. For determining horizontal stresses, a stress polygon is built first as illustrated in Fig. 6.20, which is similar to Fig. 6.17. Lines of breakouts and DITFs are then plotted in the stress polygon diagram in Fig. 6.20. The "breakout line" is drawn based on Eq. (6.70) if breakouts occur at a given mud weight (here $p_m = 62$ MPa), and the UCS of the rock is known. The "DITF line" consists of two segments: vertical and horizontal DITF lines. Vertical DITFs are the vertical tensile fractures generated in elastic, impermeable rocks in normal and strike-slip faulting stress regimes, i.e., Eq. (6.59) should be satisfied, or $\sigma'_\theta + T_0 \leq 0$. However, in the reverse faulting stress regime, horizontal DITFs may be initiated, hence Eq. (6.61) needs to be satisfied, or $\sigma'_z + T_V \leq 0$. Combing these two cases, a composite DITF line can be drawn, as shown in Fig. 6.20. From the stress polygon plot the allowable horizontal stress area can then be determined, which is the area within the intersection of "breakout lines" and "DITF lines".

6.4.5 Maximum horizontal stress from excess horizontal strains

Similar to the method for estimating the minimum horizontal stress in Eq. (6.29), the maximum horizontal stress in isotropic rocks can be obtained from the following equation, if the horizontal strains are available:

$$\sigma_H = \frac{\nu}{1-\nu}(\sigma_V - \alpha p_p) + \alpha p_p + \frac{E}{1-\nu^2}(\varepsilon_H + \nu\varepsilon_h) \tag{6.71}$$

In transversely isotropic formations, the maximum horizontal stress can be expressed in the following form (refer to Chapter 1, Section 1.5.2 for derivations):

$$\sigma_H = \frac{E_h \nu_V}{E_V(1-\nu_h)}(\sigma_V - \alpha_V p_p) + \alpha_h p_p + \frac{E_h}{1-\nu_h^2}(\varepsilon_H + \nu_h \varepsilon_h) \tag{6.72}$$

where subscripts h and V represent the rock properties in the horizontal and vertical directions, respectively.

The major barrier for applying these equations is the difficulty in accurately determining the horizontal strains. Similar to Section 6.3, the horizontal strains can be back-calculated from stress measurements using the following relation:

$$\sigma_{tect}^{\max} = \frac{E_h}{1-\nu_h^2}(\varepsilon_H + \nu_h \varepsilon_h) \tag{6.73}$$

The maximum horizontal stress may also be estimated from the following empirical equation:

$$\sigma_H = \frac{\nu}{1-\nu}(\sigma_V - \alpha p_p) + \alpha p_p + c\sigma_V \tag{6.74}$$

where c is a calibration constant.

6.4.6 Maximum horizontal stress from equilibrium of in situ stresses and pore pressure

To keep the stress–strain equilibrium, the three in situ stresses in elastic formations should satisfy Hooke's law. According to Hooke's law, the maximum effective horizontal stress (σ'_H) can be written as the following form:

$$\sigma'_H = \frac{\sigma'_h - E\varepsilon_h}{\nu} - \sigma'_V \tag{6.75}$$

where ε_h is the strain in the minimum horizontal stress direction.

Replacing the effective stresses by total stresses, the in situ stresses have the following relation:

$$\sigma_H = \frac{(\sigma_h - \alpha p_p) - E\varepsilon_h}{\nu} - \sigma_V + 2\alpha p_p \tag{6.76}$$

Eq. (6.76) shows that if the minimum horizontal stress and horizontal strain are available, the maximum horizontal stress can be calculated.

Normally rock formations extend very long in horizontal directions; therefore, the strain in the minimum horizontal direction is much smaller than the strains in the vertical stress direction. Particularly, when the interested formations are constrained by stiffer formations, the stress state is similar to the condition of uniaxial strain loading. In this extreme case, ε_h is equal to zero if there is no tectonic strain in the minimum horizontal stress direction; therefore, the maximum horizontal stress can be expressed as (Li and Purdy, 2010):

$$\sigma_H = \frac{(\sigma_h - \alpha p_p)}{\nu} - \sigma_V + 2\alpha p_p \tag{6.77}$$

Eq. (6.77) is applied to estimate the maximum horizontal stress in an oil field—Field 1 of the Visund field in the northern part of the North Sea. The vertical stress, minimum horizontal stress, pore pressure, and mud weight are available from Wiprut (2001). Applying Eq. (6.77) and assuming $\alpha = 1$ and $\nu = 0.25$, the maximum horizontal stresses at different depths are calculated, as shown in Fig. 6.21, which are consistent with Wiprut's results.

Eq. (6.76) can be plotted to the stress polygon diagram to constrain in situ stresses. A stress polygon in Fig. 6.22 is drawn for Poisson's ratio of 0.25 (or $\mu = 0.58$ from Eq. 5.18) based on the lower and upper bound horizontal stresses Eqs. (5.15) and (5.16). The following parameters are used

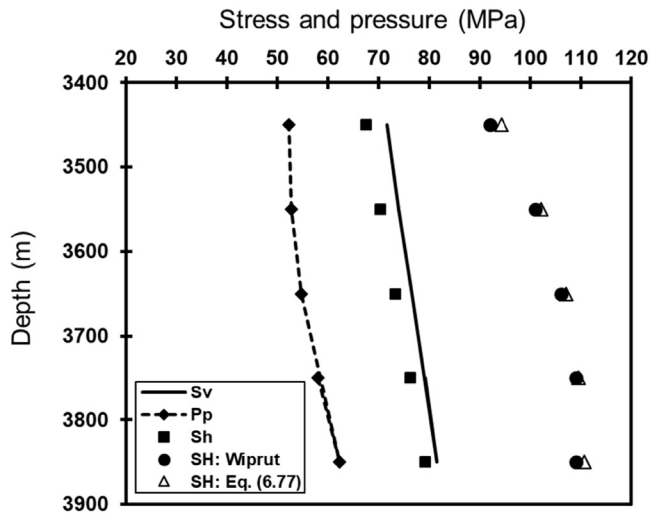

Figure 6.21 Calculated maximum horizontal stress (S_H) from Eq. (6.77) compared to the results of Wiprut (2001) in Well 1S of Field 1, the Visund Field, northern North Sea.

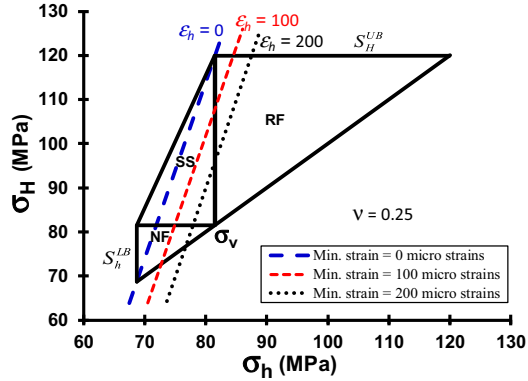

Figure 6.22 Stress polygon for the cases of different minimum horizontal strains (dashed lines) calculated from Eq. (6.76).

in the stress polygon: $\sigma_V = 81.5$ MPa, $p_p = 62.3$ MPa, $\nu = 0.25$, E = 30 GPa, and $\alpha = 1$. Eq. (6.76) is plotted in the stress polygon for three cases of $\varepsilon_h = 0$, $\varepsilon_h = 100$, $\varepsilon_h = 200$ microstrains, the dashed lines in Fig. 6.22. It can be seen that in situ stress state changes to the reverse faulting stress regime as the tectonic strain, ε_h, increases. Combining this plot to wellbore breakouts and other data, the maximum stress can be obtained.

6.4.7 Maximum horizontal stress estimate

If no direct measurements are available for determining the magnitude of the maximum horizontal stress, the following relation can provide a rule-of-thumb estimation:

$$\sigma_H = \sigma_h + m(\sigma_V - \sigma_h) \tag{6.78}$$

where m is a constant. In the normal faulting stress regime, m can generally be taken as 0.5 for a rule-of-thumb estimate.

The maximum horizontal stress estimated from Eq. (6.78) needs calibrations to obtain a reasonable value. This can be done by, for example, using the estimated maximum horizontal stress to calculate wellbore shear and tensile failures in offset wells and then comparing the calculated results to the observed breakouts and drilling-induced tensile fractures.

6.5 Maximum horizontal stress orientation

The orientation of the maximum horizontal stress is a crucially important parameter for designing hydraulic fracturing and optimizing drilling direction.

For a vertical or near vertical borehole, the maximum horizontal stress orientation is aligned with the direction of drilling-induced tensile fractures and is perpendicular to the direction of borehole breakouts. Oriented caliper and image logs can be used to identify the directions of wellbore breakouts and drilling-induced tensile failures. In hydraulic fracturing operations, the direction of the hydraulic fracture propagation (except natural fractures) is parallel to the maximum horizontal stress direction, and microseismic measurements can identify it (Dohmen et al., 2017).

6.5.1 From borehole breakouts

Borehole breakouts are stress-induced enlargements of a wellbore. When a borehole is drilled, the formations removed from the borehole are no longer supporting the surrounding rocks. As a result, the stresses become concentrated around the wellbore. Borehole breakout occurs when the critical stress (obtained from a failure criterion; e.g., the Mohr-Coulomb criterion) around the borehole exceed rock strength. Breakouts are mostly caused by shear failures, including maybe compressive or tensile spalling failures of the wellbore (Zhang, 2002; Zhang et al., 2003). Shear failures in a wellbore are primarily caused by the development of intersecting conjugate shear planes, causing pieces of the borehole wall to spall off, as shown in Fig. 6.23. Around a vertical borehole, stress concentration (e.g., the tangential stress) is the greatest in the direction of the minimum horizontal stress (S_h in Fig. 6.23). Hence, the long axes of borehole breakouts are oriented approximately parallel to the minimum horizontal stress orientation (S_h), as shown in Fig. 6.23.

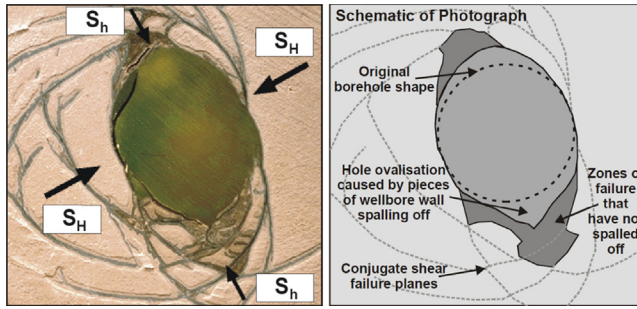

Figure 6.23 Results of a hollow cylinder lab test simulating borehole breakouts (performed by the CSIRO Division of Geomechanics). Intersection of conjugate shear failure planes results in enlargement of the cross-sectional shape of the wellbore (Reinecker et al., 2003).

Borehole image log can also be used to identify wellbore breakouts. Fig. 6.24 displays a section of ultrasonic borehole imager (UBI) log data processing for the GPK1 vertical well. It shows the wellbore breakouts (two symmetric bands at N95 ± 7°E in the image log), azimuth of wellbore breakouts, and schematic wellbore cross sections. The azimuth of wellbore breakouts in the vertical well is the direction of the minimum horizontal stress. For inclined boreholes, Eq. (6.68) can be applied to calculate the principal stress direction or γ (the angle between the borehole axis and the principal stress direction).

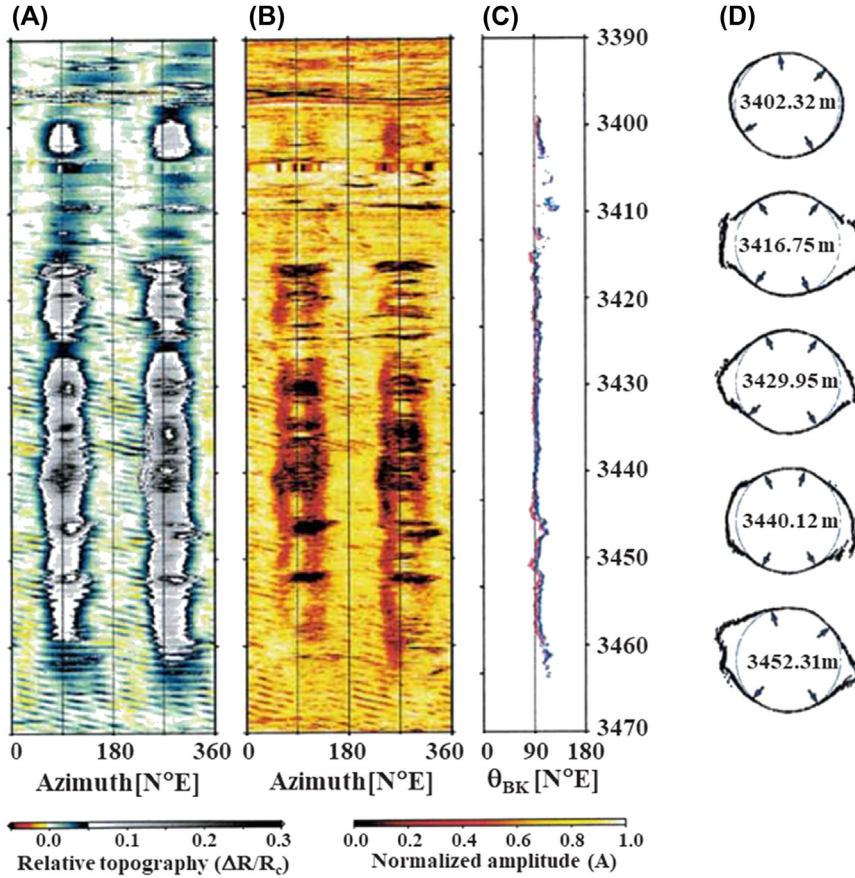

Figure 6.24 Results of UBI data processing for GPK1 well. (A) Unwrapped maps of the relative topography ΔR/Rc: (B) Unwrapped maps of the normalized amplitude. (C) Breakout azimuth θ_{BK}. (D) wellbore cross-section views (Bérard and Cornet, 2003).

6.5.2 From drilling-induced tensile fractures

Drilling-induced tensile fractures (DITFs) can be identified by borehole image log. Fig. 6.25 shows a section of electrical image log in the left and a schematic wellbore cross section in the right with tensile fractures and breakouts annotated. The DITFs and breakouts in the image log have low resistivity for water-based mud (darker color). In the image log the breakouts are wider and darker than the DITFs, and the directions of the breakouts and DITFs are different in 90 degrees. For a vertical or nearly vertical borehole, the orientation of the maximum horizontal stress is parallel to the direction of DITFs. For inclined boreholes the angle (γ) between borehole axis and DITFs can be obtained using Eq. (6.68), when en echelon DITFs in image logs are available (e.g., Fig. 6.14B). From the image logs the maximum stress magnitudes can also be obtained for the inclined boreholes (Thorsen, 2011).

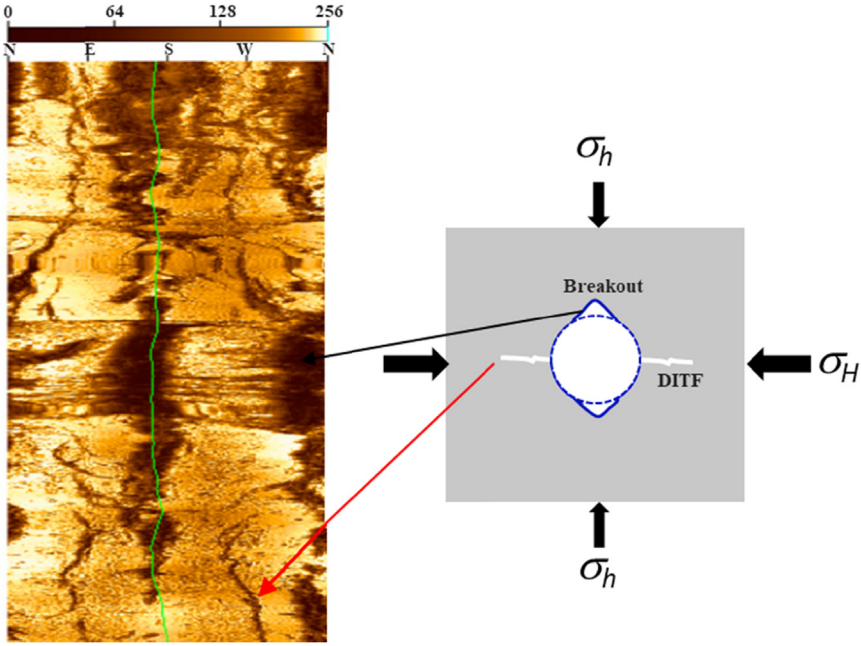

Figure 6.25 Electrical image log (left) showing drilling-induced fractures and breakouts in a vertical well with a schematic wellbore cross section (right) displaying the directions of the DITFs and breakouts.

References

Aadnoy, B.S., 1990. In situ stress direction from borehole fracture traces. J. Pet. Sci. Eng. 4, 143–153.

Addis, M.A., Hanssen, T.H., Yassir, N., Willoughby, D.R., Enever, J., 1998. A comparison of leak-off test and extended leak-off test data for stress estimation. Paper SPE/ISRM 47235.

Amundsen, O., 1995. Determination of In-Situ Stresses from Leak Off and Extended Leak Off Tests in the Oseberg Field, North Sea. M.Sc. thesis, New Mexico Inst. of Mining and Tech.

Athy, L.F., 1930. Density, porosity, and compaction of sedimentary rocks. Am. Assoc. Pet. Geol. Bull. 14 (1), 1–24.

Barker, J.W., Wood, T.D., 1997. Estimating shallow below mud-line deepwater Gulf of Mexico fracture gradients. Presented at the Houston AADE Chapter Annual Technical Forum.

Barree, R.D., Barree, V.L., Craig, D.P., 2009. Holistic fracture diagnostics: consistent interpretation of prefrac injection tests using multiple analysis methods. SPE Prod. Oper. 24 (3), 396–496. SPE 107877.

Barton, C.A., Zoback, M.D., Burns, K.L., 1988. In-situ stress orientation and magnitude at the Fenton Geothermal Site, New Mexico, determined from wellbore breakouts. Geophys. Res. Lett. 15, 467–470.

Baumgartner, J., Rummel, F., 1989. Experience with "fracture pressurization tests" as a stress measuring technique in a jointed rock mass. Int. J. Rock Mech. Min. Sci. Geomech. Abstr. 26 (6), 661–672.

Bérard, T., Cornet, F.H., 2003. Evidence of thermally induced borehole elongation: a case study at Soultz, France. Int. J. Rock Mech. Min. Sci. 40, 1121–1140.

Breckels, I.M., van Eekelen, H.A.M., 1982. Relationship between horizontal stress and depth in sedimentary basins. J. Pharm. Technol., 2191–2199. SPE 10336.

Cornet, F.H., Valette, B., 1984. In situ stress determination from hydraulic injection test data. J. Geophys. Res. 89, 11527–11537.

Cui, J., Lin, W., Wang, L., Gao, L., Wang, W., Sun, D., Li, Z., Zhou, C., Qian, H., Peng, H., Xia, K., Li, K., 2014. Determination of three-dimensional in situ stresses by anelastic strain recovery in Wenchuan Earthquake Fault Scientific Drilling Project Hole-1 (WFSD-1). Tectonophysics 619–620, 123–132.

Daines, S.R., 1982. The prediction of fracture pressures for wildcat wells. J. Pharm. Technol. 34 (4), 863–872. SPE-9254-PA.

Desroches, J., Kurkjian, A.L., 1999. Applications of wireline stress measurements. SPE Reservoir Eng. 2, 451–461.

Detournay, E., Cheng, A.H.-D., 1988. Poroelastic response of a borehole in a non-hydrostatic stress field. Int. J. Rock Mech. Min. Sci. Geomech. Abstr. 25, 171–182.

Dohmen, T., Zhang, J., Li, C., Blangy, J.P., Simon, K.M., Valleau, D.N., Ewles, J.D., Morton, S., Checkles, S., 2013. A new surveillance method for delineation of depletion using microseismic and its application to development of unconventional reservoirs. SPE166274 presented at SPE Ann. Tech. Conf. Exhib.

Dohmen, T., Zhang, J., Barker, L., Blangy, J.P., 2017. Microseismic magnitudes and b-values for delineating hydraulic fracturing and depletion. SPE J. 22 (5), 1624–1634. SPE-186096.

Dolinar, D.R., 2003. Variation of horizontal stresses and strains in mines in bedded deposits in the eastern and midwestern United States. In: Proc. 22nd Int. Conf. on Ground Control in Mining, Morgantown, WV.

Edwards, S.T., Bratton, T.R., Standifird, W.B., 2002. Accidental geomechanics – capturing in-situ stress from mud losses encountered while drilling. SPE/ISRM 78205 presented at the SPE/ISRM Rock Mechanics Conference Held in Irving, Texas.

Gibson-Poole, C.M., Lang, S.C., Streit, J.E., Kraishan, G.M., Hillis, R.R., 2002. Assessing a basin's potential for geological sequestration of carbon dioxide: an example from the Mesozoic of the Petrel Sub-basin, NW Australia. In: Keep, M., Moss, S. (Eds.), Sedimentary Basins of Western Australia, vol. 3. Oilfield Publications, pp. 439–463.

Haimson, B.C., Cornet, F.H., 2003. ISRM suggested methods for rock stress estimation – part 3: hydraulic fracturing (HF) and/or hydraulic testing of pre-existing fractures (HTPF). Int. J. Rock Mech. Min. Sci. 40, 1011–1020.

Haimson, B.C., Fairhurst, C., 1967. Initiation and extension of hydraulic fractures in rocks. SPE J. 7, 310–318.

Hawkes, C., Bachu, S., Haug, K., Thompson, A., 2005. Analysis of in-situ stress regime in the Alberta basin, Canada, for performance assessment of CO_2 geological sequestration sites. In: 4th Annual Conf. on Carbon Capture and Sequestration, DOE/NETL, May 2–5, 2005.

Hoek, E., Brown, E.T., 1980. Underground Excavations in Rock. Institution of Mining and Metallurgy, London.

Huang, J., Griffiths, D.V., Wong, S.W., 2010. In situ stress determination from inversion of hydraulic fracturing data. Int. J. Rock Mech. Min. Sci. 48, 476–481.

Hubbert, M.K., Willis, D.G., 1957. Mechanics of hydraulic fracturing. Pet. Trans. AIME 210, 153–168.

Ito, T., Evans, K., Kawai, K., Hayashi, K., 1999. Hydraulic fracture reopening pressure and the estimation of maximum horizontal stress. Int. J. Rock Mech. Min. Sci. 36 (6), 811–826.

Jones, C., Sargeant, J.P., 1993. Obtaining the minimum horizontal stress from microfracture test data: a new approach using a derivative algorithm. SPE Prod. Facil. Feb., 39–44.

Klee, G., Bunger, A., Meyer, G., Rummel, F., Shen, B., 2011. In situ stresses in borehole Blanche-1/South Australia derived from breakouts, core discing and hydraulic fracturing to 2 km depth. Rock Mech. Rock Eng. 44, 531–540.

Li, S., Purdy, C., 2010. Maximum horizontal stress and wellbore stability while drilling: modeling and case study. Paper SPE 139280.

Ljunggren, C., Chang, Y., Janson, T., Christiansson, R., 2003. An overview of rock stress measurement methods. Int. J. Rock Mech. Min. Sci. 40 (7/8), 975–989.

Lønø, G., 1995. In Situ Measurements and Rock Mechanics Testing of Overburden Rock from the Ekofisk Field, North Sea. M.Sc. thesis, New Mexico Inst. of Mining and Tech.

Martin, R., Cramer, D., Nunez, O., Roberts, N., 2012. A method to perform multiple diagnostic fracture injection tests simultaneously in a single wellbore. SPE-152019.

Meng, Z., Zhang, J., Wang, R., 2011. In-situ stress, pore pressure and stress-dependent permeability in the Southern Qinshui Basin. Int. J. Rock Mech. Min. Sci. 48, 122–131.

Nelson, P.H., 2003. A review of the multiwell experiment, Williams Fork and Iles Formations, Garfield County, Colorado. In: Petroleum Systems and Geologic Assessment of Oil and Gas in the Uinta-Piceance Province, Utah and Colorado. U.S. Geol. Survey Digital Data Series DDS-69-B, pp. 1–14 (Chapter 15).

Nelson, E.J., Meyer, J.J., Hillis, R.R., Mildren, S.D., 2005. Transverse drilling induced tensile fractures in the West Tuna area, Gippsland Basin, Australia: implications for the in situ stress regime. Int. J. Rock Mech. Min. Sci. 42, 361–371.

Nelson, E.J., Chipperfield, S.T., Hillis, R.R., Gilbert, J., McGrowen, J., Mildren, S.D., 2007. The relationship between closure pressure from fluid injection tests and the minimum principal stress in strong rocks. Int. J. Rock Mech. Min. Sci. 44, 787–801.

Okabe, T., Hayashi, K., Shinohara, N., Takasugi, S., 1998. Inversion of drilling-induced tensile fracture data obtained from a single inclined borehole. Int. J. Rock Mech. Min. Sci. 35 (6), 747–758.

Pan, Y., Shen, W.-B., 2017. Contemporary crustal movement of southeastern Tibet: constraints from dense GPS measurements. Sci. Rep. 7. Article number: 45348.

Peska, P., Zoback, M.D., 1995. Compressive and tensile failure of inclined well bores and determination of in situ stress and rock strength. J. Geophys. Res. 100 (B7), 12791–12811.

Raaen, A.M., Horsrud, P., Kjørholt, H., Økland, D., 2006. Improved routine estimation of the minimum horizontal stress component from extended leak-off tests. Int. J. Rock Mech. Min. Sci. 43, 37–48.

Ramakrishnan, H., Waters, G., Boratko, E.C., Latifzai, A.S., Bentley, D., 2009. Application of downhole injection stress testing in the Barnett shale formation. SPE-124147 presented at the Annual Technical Conference Exhibition.

Reinecker, J., Tingay, M., Müller, B., 2003. Borehole Breakout Analysis from Four-Arm Caliper Logs. World Stress Map Project.

Rutqvist, J., Tsang, C.F., Stephansson, O., 2000. Uncertainty in the maximum principal stress estimated from hydraulic fracturing measurements due to the presence of the induced fracture. Int. J. Rock Mech. Min. Sci. 37, 107–120.

Schmitt, D.R., Currie, C.A., Zhang, L., 2012. Crustal stress determination from boreholes and rock cores: fundamental principles. Tectonophysics 580, 1–26.

Spencer, C.W., 1989. Comparison of overpressuring at the Pinedale anticline area, Wyoming, and the Multiwell Experiment site, Colorado. In: Law, B.E., Spencer, C.W. (Eds.), Geology of Tight Gas Reservoirs in the Pinedale Anticline Area, Wyoming, and at the Multiwell Experiment Site, Colorado, vol. 1886. U.S. Geological Survey Bulletin, 16 pp. (Chapter C).

Sun, D., Sone, H., Lin, W., Cui, J., He, B., Lv, H., Cao, Z., 2017. Stress state measured at ~7 km depth in the Tarim Basin, NW China. Sci. Rep. 7, 4503.

Thiercelin, M.C., Roegiers, J.-C., 2000. Formation characterization: rock mechanics. In: Economides, M.J., Nolte, K.G. (Eds.), Reservoir Stimulation, third ed. Wiley (Chapter 3).

Thorsen, K., 2011. In situ stress estimation using borehole failures — even for inclined stress tensor. J. Pet. Sci. Eng. 79 (3–4), 86–100.

Tingay, M.R.P., Hillis, R.R., Morley, C.K., King, R.C., Swarbrick, R.E., Damit, A.R., 2009. Present-day stress and neotectonics of Brunei: implications for petroleum exploration and production. Am. Assoc. Pet. Geol. Bull. 93 (1), 75–100.

Tingay, M.R., Morley, C.K., Laird, A., Limpornpipat, O., Krisadasima, K., Pabchanda, S., Macintyre, H.R., 2013. Evidence for overpressure generation by kerogen-to-gas maturation in the northern Malay Basin. Am. Assoc. Pet. Geol. Bull. 97 (4), 639–672.

Traugott, M., 1997. Pore pressure and fracture gradient determinations in deepwater. Deepwater Technology Supplement, World Oil, 68–70.

Van Ruth, P., Hillis, R., Tingate, P., 2004. The origin of overpressure in the Carnarvon Basin, Western Australia: implications for pore pressure prediction. Petrol. Geosci. 10, 247–257.

Warpinski, N.R., 1989. Elastic and viscoelastic calculations of stresses in sedimentary basins. SPE Form. Eval. 4 (4), 522–530.

Warpinski, N.R., Teufel, L.W., 1989. In-situ stresses in low permeability, nonmarine rocks. J. Pet. Technol. 41 (4), 405–414. SPE-16402-PA.

Warpinski, N.R., Branagan, P., Wilmer, R., 1985. In-situ stress measurements at U.S. DOE's multiwell experiment site, Mesaverde Group, Rifle, Colorado. J. Petrol. Technol., 527–536. SPE 12142.

Whitehead, W.S., Hunt, E.R., Finley, R.J., Holditch, S.A., 1986. In-situ stresses: a comparison between log-derived values and actual field-measured values in the Travis Peak formation of East Texas. Paper SPE-15209.

Whitehead, W.S., Hunt, E.R., Holditch, S.A., 1987. The effects of lithology and reservoir pressure on the in-situ stress in the Waskom (Travis peak) field. Paper SPE/DOE 16403.

Wiprut, D., 2001. Stress, Borehole Stability, and Hydrocarbon Leakage in the Northern North Sea. Ph.D. dissertation, Stanford University, pp. 51–62.

Wu, M., Zhang, Y., Liao, C., Chen, Q., Ma, Y., Wu, J., Yan, J., Ou, M., 2009. Preliminary results of in-situ stress measurements along the Longmenshan fault zone after the Wenchuan M_s 8.0 earthquake. Acta Geol. Sin. 83 (4), 746–753.

Yang, Y., Aplin, A.C., 2004. Definition and practical application of mudstone porosity-effective stress relationships. Petrol. Geosci. 10, 153–162.

Zajac, B.J., Stock, J.M., 1997. Using borehole breakouts to constrain the complete stress tensor: results from the Sijan Deep Drilling Project and offshore Santa Maria Basin, California. J. Geophys. Res. B 102 (B5), 10083–10100.

Zhang, J., 2002. Dual-Porosity Approach to Wellbore Stability in Naturally Fractured Reservoirs. Ph.D. dissertation, The University of Oklahoma.

Zhang, J., 2013. Borehole stability analysis accounting for anisotropies in drilling to weak bedding planes. Int. J. Rock Mech. Min. Sci. 60, 160–170.

Zhang, J., Roegiers, J.-C., 2010. Discussion on "Integrating borehole-breakout dimensions, strength criteria, and leak-off test results, to constrain the state of stress across the Chelungpu Fault, Taiwan". Tectonophysics 492, 295–298.

Zhang, J., Wieseneck, J., 2011. Challenges and surprises of abnormal pore pressure in shale gas formations. In: SPE Annual Technical Conference and Exhibition, 30 October-2 November, Denver, Colorado, USA. SPE-145964.

Zhang, Y., Zhang, J., 2017. Lithology-dependent minimum horizontal stress and in-situ stress estimate. Tectonophysics 703–704, 1–8.

Zhang, J., Bai, M., Roegiers, J.-C., 2003. Dual-porosity poroelastic analyses of wellbore stability. Int. J. Rock Mech. Min. Sci. 40, 473–483.

Zhang, J., Standifird, W., Lenamond, C., 2008. Casing ultradeep, ultralong salt sections in deep water: a case study for failure diagnosis and risk mitigation in record-depth well. Paper SPE 114273.

Zhang, J., Yin, S., 2017. Fracture gradient prediction: an overview and an improved method. Pet. Sci. 14, 720–730.

Zhang, Y., Zhang, J., Yuan, B., Yin, S., 2018. In-situ stresses controlling hydraulic fracture propagation and fracture breakdown pressure. J. Pet. Sci. Eng. 164, 164–173.

Zoback, M.D., Rummel, F., Jung, R., Raleigh, C.B., 1977. Laboratory hydraulic fracturing experiments in intact and pre-fractured rock. Int. J. Rock Mech. Min. Sci. 14, 49–58.

CHAPTER 7

Abnormal pore pressure mechanisms

Contents

Abstract

Abnormal pore pressures, mostly overpressures, exist in many sedimentary formations. The overpressures deteriorate drilling safety and may cause borehole influxes, kicks, and even blowouts. To reduce these risks, origins and mechanisms of abnormal pore pressures are analyzed, including compaction disequilibrium, hydrocarbon generation, smectite diagenesis, formation uplift, and unloading. If formation overpressures were

Applied Petroleum Geomechanics
ISBN 978-0-12-814814-3
https://doi.org/10.1016/B978-0-12-814814-3.00007-1

generated by compaction disequilibrium, it is often recognized by higher-than-expected porosities at a given depth and the porosities deviated from the normal porosity trend. Hydrocarbon generation is a process of the creation of mobile fluids from an original solid immobile kerogen, which greatly increases fluid volume or porosity and causes a great increase in pore pressure. Case studies show that hard overpressures created from hydrocarbon generation are consistent with the increase in vitrinite reflectance. In addition, a composite normal compaction trendline for pore pressure prediction is proposed to honor smectite and illite transformation and pore pressure generation. Abnormal pore pressures in several petroleum basins and shale oil and gas plays are examined to illustrate the mechanisms of abnormal pressure generations.

Keywords: Abnormal pore pressure; Compaction disequilibrium; Hydrocarbon generation; Overpressure; Pore pressure gradient; Smectite–illite transformation; Uplift and unloading.

7.1 Normal and abnormal pore pressures

Pore pressure is the fluid pressure in pore spaces of the porous formation. It varies from hydrostatic pressure (normal pore pressure) to severe overpressure, which can be more than two times of the hydrostatic pressure in a subsurface formation. Overpressures exist in many geologic basins in the world. If the abnormal pore pressure is not accurately predicted before drilling or while drilling, drilling risks and incidents will increase greatly. For example, in deepwater of the Gulf of Mexico, incidents associated with pore pressure and wellbore instability accounted for 5.6% of drilling time in non-subsalt wells and 12.6% of drilling time in the subsalt wells (York et al., 2009). The abnormally high pore pressures have caused serious drilling incidents, such as the kicks and well blowouts (Skalle and Podio, 1998; Holand and Skalle, 2001). Therefore, pore pressure prediction is critically important for drilling planning and operations in the oil and gas industry. Abnormally high pressures also induced geologic hazards and disasters, such as weakness in faults (e.g., Bird, 1995; Tobin and Saffer, 2009) and mud volcanoes (Davies et al., 2007; Tingay et al., 2009).

7.1.1 Hydrostatic pressure and normal pore pressure

Normal pore pressure is the hydrostatic pressure caused by the column of pore fluid from the surface to the interested depth. For the formations with normal fluid pressure, the pore pressure gradient follows the hydrostatic pressure gradient. The magnitude of hydrostatic pressure is proportional to

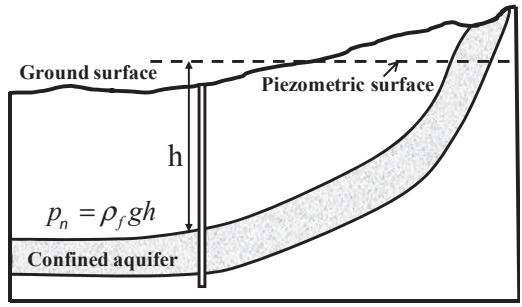

Figure 7.1 Schematic cross-section showing the hydrostatic pressure caused by water column in a subsurface formation (aquifer).

the depth below the surface and to the density of the fluid in the pores. Thus, hydrostatic pressure can be calculated using the following equation:

$$p_n = \rho_f gh \tag{7.1}$$

where p_n is the hydrostatic pressure; g is the acceleration due to gravity; ρ_f is the fluid density; and h is the vertical height of the fluid column (or depth), as shown in Fig. 7.1 (Zhang, 2013).

Practically the following equation can be used to calculate the hydrostatic pressure in the metric unit:

$$p_n = 0.00981\rho_f h \tag{7.2}$$

where p_n is in MPa; ρ_f is in g/cm^3; and h is in meters.

In the English unit, the hydrostatic pressure can be expressed as follows:

$$p_n = 0.4335\rho_f h \tag{7.3}$$

where p_n is in psi; ρ_f is in g/cm^3; and h is in ft.

7.1.2 Salinity effect on hydrostatic pressure

Hydrostatic pore pressure depends on water density (Fig. 7.2), while the density of water is a function of water salinity, temperature, and content of dissolved gases (Chillingar et al., 2002). There is a general variation in hydrostatic pressure gradient ($\rho_f g$) at different locations owing to different water densities. For instance, the average hydrostatic pressure gradient is usually taken as 0.465 psi/ft (1.074 kg/cm^3) in the Gulf of Mexico, and this corresponds to water with a salinity of 80,000 parts per million (ppm) of sodium chloride at 77°F (25°C) (Dickinson, 1953). Formation water varies

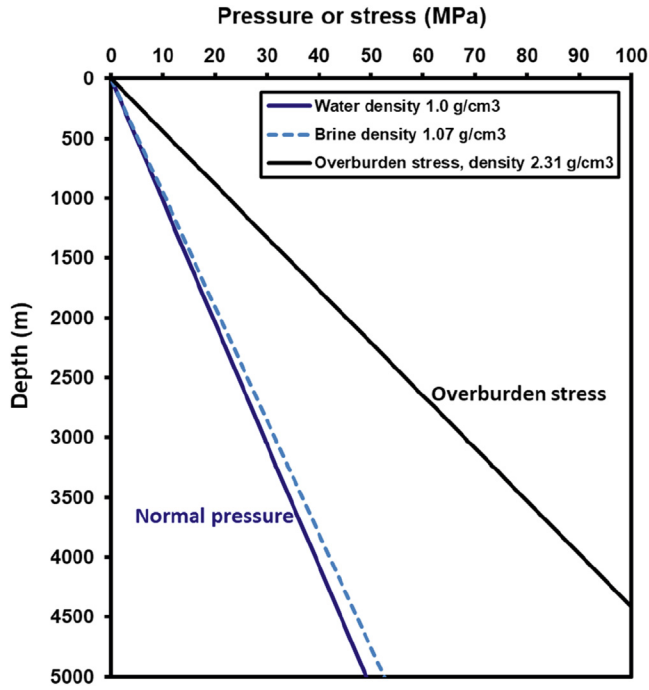

Figure 7.2 Normal pore pressure profiles for pore fluids of fresh water and brine compared to overburden stress in the subsurface.

greatly in salinity; therefore, formation pore pressure also changes with salinity, as shown in Table 7.1.

Generally, the density of water in sedimentary basins varies from 1.0 to 1.08 g/cm^3 (for the saturated saltwater, $\rho_w = 1.2$ g/cm^3), for example:

Gulf Coast (Mississippi delta): $\rho_w = 1.07$ g/cm^3;

Rocky Mountains and the North Sea: $\rho_w = 1.02$ g/cm^3;

Nigeria delta: $\rho_w = 1.08$ g/cm^3.

7.1.3 Overpressure and underpressure

When pore pressure is lower or higher than the hydrostatic pressure, it is abnormal pore pressure. Pore pressure that is greater than the hydrostatic pressure is termed overpressure or excess pressure (Fig. 7.3). Likewise, pore pressure that is less than the hydrostatic pressure is termed underpressure, or subnormal pressure. Underpressure and overpressure together are composed of the classification of abnormal pressures. The terms of abnormal pressure and overpressure are sometimes used interchangeably

Table 7.1 Water salinity, density, and pressure gradient variations (at 20°C, standard conditions).

Water type	Salinity: Cl^- (mg/L)	Salinity: NaCl (mg/L)	Water density (g/cm^3)	Pressure gradient (kPa/m)	Pressure gradient (psi/ft)	Equivalent mud weight (ppg)
Fresh water	0–1500	0–2500	1.00	9.81	0.433	8.335
Sea water	18,000	30,000	1.02	10.0	0.442	8.50
Sea water	33,000	–	1.035	10.18	0.448	8.63
Formation water	10,000	16,500	1.01	9.91	0.437	8.41
Formation water	36,000	60,000	1.04	10.2	0.450	8.67
Formation water	48,000	80,000	1.05	10.3	0.455	8.75
Formation water	60,000	100,000	1.07	10.5	0.463	8.92
Saturated saltwater	192,667	317,900	1.20	11.77	0.520	10.0

Modified from Mouchet, J.C., Mitchell, A., 1989. Abnormal Pressures while Drilling. Editions TECHNIP, Paris.

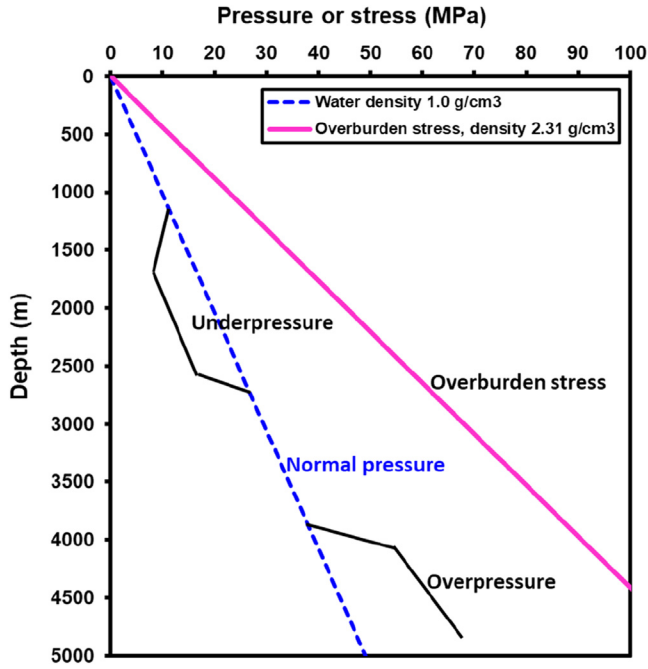

Figure 7.3 Underpressure, overpressure, hydrostatic pressure (normal pressure), and overburden stress in the subsurface.

because underpressures uncommonly occur in the sedimentary formations (excluding those caused by depletion from oil and gas production).

7.1.4 Pore pressure and pore pressure gradient

The hydrostatic pressure and formation pore pressure in a typical oil and gas well are plotted in Fig. 7.4. The pore pressure profile with depth in this well is similar to many geologically young sedimentary basins where overpressure is encountered at depth. At relatively shallow depths (less than 2000 m), pore pressure is hydrostatic, indicating that a continuous, interconnected column of pore fluid extends from the surface to that depth. At a depth of more than 2000 m the overpressure starts, and pore pressure increases with depth rapidly, implying that the deeper formations are hydraulically isolated from the shallower ones. By 3800 m, pore pressure reaches a value close to the overburden stress, a condition referred to as hard overpressure. The effective stress in pore pressure prediction community is conventionally defined to be the subtraction of pore pressure from overburden stress, as shown in Fig. 7.4. The increase of overpressure causes reduction in the effective stress.

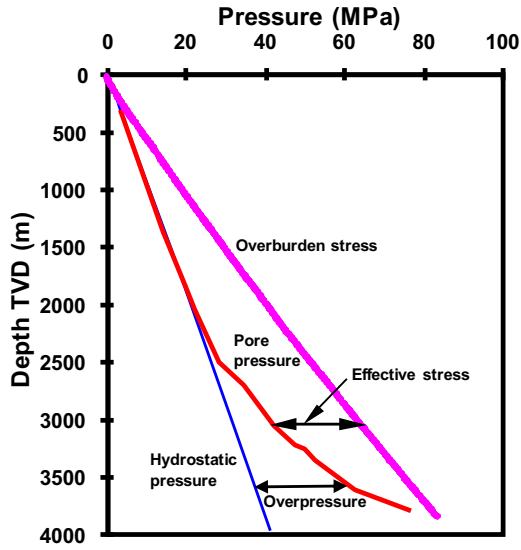

Figure 7.4 Hydrostatic pressure, pore pressure, overburden stress, and effective stress in a borehole. TVD is the true vertical depth.

Pore pressure gradient is more practically used in drilling engineering because it is more convenient to be used for determining mud weight (mud density), as shown in Fig. 7.5. Pore pressure gradient at a given depth is the pore pressure divided by the true vertical depth. The mud weight should be appropriately selected based on pore pressure gradient, wellbore stability, and fracture gradient before setting and cementing a casing. The drilling fluid (mud) is applied in the form of mud pressure to support the wellbore walls for preventing influx and wellbore collapse during drilling. To avoid fluid influx and wellbore instability in an open hole section, a heavier mud pressure than the pore pressure is needed. However, when mud weight is higher than the fracture gradient of the drilling section, it may break the formation, causing mud losses or even lost circulation. To prevent a wellbore from unintentional hydraulic fracturing by the high mud weight, as needed where there is overpressure, a casing needs to be set to protect the overlying formations from fracturing, as illustrated in Fig. 7.5.

Pressure gradients and mud weight are expressed in the metric unit, SG or g/cm^3 (i.e., specific gravity) in Fig. 7.5. However, pressure gradients and mud weight are often reported in the English or the US unit system in the oil and gas industry. The pressure gradient conversions between the US and metric units can be found in Table 7.2. In the drilling industry, the

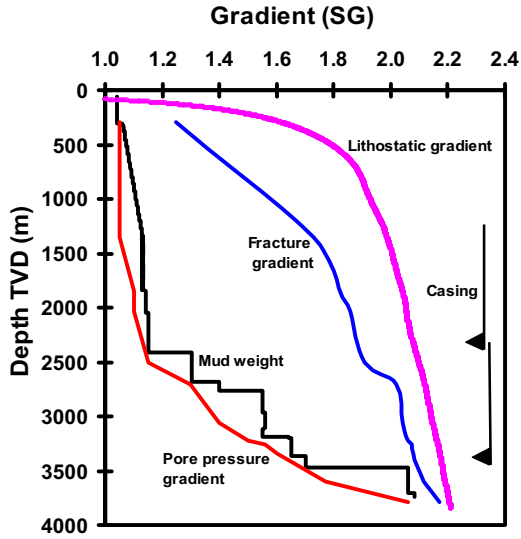

Figure 7.5 Pore pressure gradient, fracture gradient, overburden stress gradient (lithostatic gradient), mud weight, and casing shoes with depth. In this figure pore pressure and overburden gradients are converted from the pore pressure and overburden stress plotted in Fig. 7.4 (Zhang, 2011).

Table 7.2 Conversions of pore pressure gradients in the metric and the US unit systems.

Conversions	Conversions
1 g/cm^3 = 9.81 MPa/km	1 ppg = 0.051948 psi/ft
1 g/cm^3 = 0.00981 MPa/m	1 ppg = 0.12 g/cm^3
1 g/cm^3 = 1 SG	1 ppg = 0.12 SG
1 MPa/km = 0.102 SG = 0.102 g/cm^3	1 ppg = 1.177 MPa/km
1 MPa/km = 0.0442 psi/ft	1 ppg = 1.177 kPa/m
1 g/cm^3 = 8.345 ppg	1 psi/ft = 19.25 ppg
1 g/cm^3 = 0.4335 psi/ft	1 psi/ft = 2.31 g/cm^3
1 SG = 8.345 ppg	1 psi/ft = 22.62 MPa/km
1 SG = 0.4335 psi/ft	1 psi/ft = 2.31 SG
1 SG = 62.428 pcf (lb/ft^3)	1 ppg = 7.4805 pcf

pressure gradient in the subsurface formation is normally converted to an equivalent mud weight (EMW) at surface for display and interpretation. In the US unit system, the unit of the pressure gradient is lbs/gallon, or ppg, which is a commonly used unit for pressure gradients and mud weight in the drilling industry in some countries, such as the United States.

Converting a pressure into the EMW at a given depth can use the following equation:

$$EMW(ppg) = \frac{pressure \quad (psi)}{0.051948 \times \ TVD \quad (ft)} \tag{7.4}$$

where TVD is the true vertical depth in ft.

7.2 Origins of abnormal pore pressures

Overpressures can be generated by many mechanisms, such as compaction disequilibrium (undercompaction); hydrocarbon generation and gas cracking; aquathermal expansion; tectonic compression (lateral stress); mineral transformations (e.g., illitization); and osmosis, hydraulic head, and hydrocarbon buoyancy (Swarbrick and Osborne, 1998). The following mechanisms will be examined in the following sections:

- Compaction disequilibrium;
- Hydrocarbon generation;
- Formation uplift and unloading;
- Smectite diagenesis.

7.2.1 Overpressures by compaction disequilibrium

In many cases, compaction disequilibrium or undercompaction has been determined to be the primary cause of overpressure, particularly in geologically young rocks (such as formations in the Tertiary, i.e. Neogene and Paleogene periods) and fast subsided basins (sedimentation rate $>$ 500 ft/m.y. or 152 m/m.y.). Examples of areas where compaction disequilibrium is cited as the primary reason of abnormal pressure include the US Gulf Coast, Alaska Cook Inlet; Beaufort Sea; Mackenzie Delta; North Sea; Adriatic Sea; Niger Delta; Mahakam Delta; Nile Delta; Malay Basin; Eastern Venezuelan Basin (Trinidad); and Potwar Plateau of Pakistan (Law and Spencer, 1998; Burrus, 1998; Heppard et al., 1998; Powley, 1990; Nelson and Bird, 2005). In these areas, the abnormally pressured rocks are mainly located in the Tertiary and late Mesozoic sedimentary formations, the depositional setting is dominantly deltaic, and the lithology is dominantly shale.

When sediments compact normally, formation porosity is reduced at the same time as pore fluid is expelled. During burial, formation overburden stress increase is the prime cause of fluid expulsion. If the sedimentation rate is low, normal compaction occurs, i.e., equilibrium between increasing

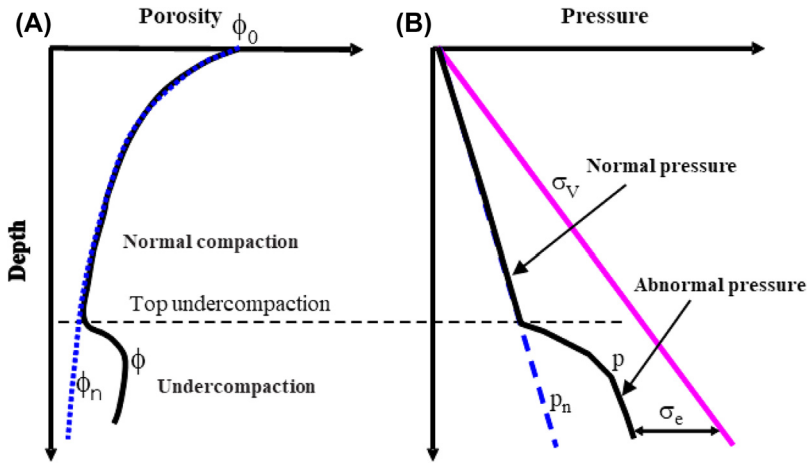

Figure 7.6 Schematic porosity (A) and corresponding pore pressure (B) in a sedimentary basin. The dashed porosity profile represents normally compacted formation. In the undercompaction section, porosity (ϕ) is larger than that in the normal compaction trend (ϕ_n), and the porosity reversal occurs, corresponding to overpressure.

overburden and ability to expel fluids is maintained (Mouchet and Mitchell, 1989). The normal compaction generates hydrostatic pore pressure in the formation, as shown in the shallow section of Fig. 7.6. When the sediments subside rapidly and the formation has extremely low permeability, fluids can only be partially expelled, and the remained fluid in the pores must support all or part of the weight of overburden sediments. Consequently, the pores are less compacted, which results in a higher porosity than the normally compacted formation. This generates abnormally high pore pressure, causing porosity to decrease less rapidly than it should be with depth, and formations are undercompacted, i.e., in the state of undercompaction or compaction disequilibrium. It mainly occurs in mudstones (shales) because of their low permeability. The compaction disequilibrium is often recognized by higher-than-expected porosities at a given depth and the porosities deviated from the normal porosity trend (e.g., the deep section of Fig. 7.6.).

Fig. 7.6 illustrates how to identify undercompaction and overpressure from porosity profile. In a normally compacted formation, porosity should decrease gradually as depth increases. When this porosity—depth relation is reversed, the undercompaction occurs and overpressure generates. The starting point of the porosity reversal is the top of undercompaction or top

of overpressure. In the formation with undercompaction, porosity and pore pressure are higher than those in the normally compacted formation.

To predict abnormal pore pressure generated by compaction disequilibrium, one needs to obtain the porosity under normal compaction condition. It is commonly accepted that porosity decreases exponentially as depth increases in normally compacted formations (e.g., Athy, 1930):

$$\phi_n = \phi_0 e^{-cZ} \tag{7.5}$$

where ϕ_n is the porosity in normally compacted formation; ϕ_0 is the porosity of the mudline; Z is the true vertical depth below the mudline; c is the compaction constant in 1/m or 1/ft.

This relation has been widely applied because in many shales and some sandstones, normal porosity profiles generally show a concave downward curvature (Fig. 2.5), as described in Eq. (7.5). A similar relationship (Eq. 2.17) exists between porosity and effective stress (e.g., Dutta, 2002; Flemings et al., 2002; Zhang, 2011). Using porosity, effective stress, and pore pressure relationship, the pore pressure can be obtained from porosity data based on compaction equilibrium theory (Zhang, 2011; Zhang and Wieseneck, 2011). Fig. 7.7 presents an example on how to use compaction disequilibrium to calculate pore pressure. Firstly, bulk density or sonic log in offset wells are analyzed to obtain the porosity in normally compacted shales, including to pick shale formations from the gamma ray log and calculate porosity from bulk density log in the picked shales (e.g., Eq. 2.6). By doing so, the porosity points of shales at different depths can be obtained (the black points as shown in Fig. 7.7). The normal compaction trendline (NCT) can be obtained ($\phi_n = 0.46e^{-0.001118Z}$, Z is in meters) from Eq. (7.5) based on the shallow porosity data. Fig. 7.7 plots the porosity variations with depth compared to the NCT in both linear and logarithmic scales. It shows that the shale is in normal compaction condition when depth is less than 3200 m. From 3200 to 3600 m, the formations are slightly undercompacted with a higher porosity than the normal compaction trend. This implies that the pore pressure gradient starts to increase. The porosity at depth of >3600 m is significantly higher than the normal compaction trend, and the pore pressure is highly overpressured (Fig. 7.7) (refer to Chapter 8 for more details in pore pressure calculations).

7.2.2 Overpressures from hydrocarbon generation

Generation of liquid and gaseous hydrocarbons from kerogen maturation is kinetically controlled and dependent on a combination of time and

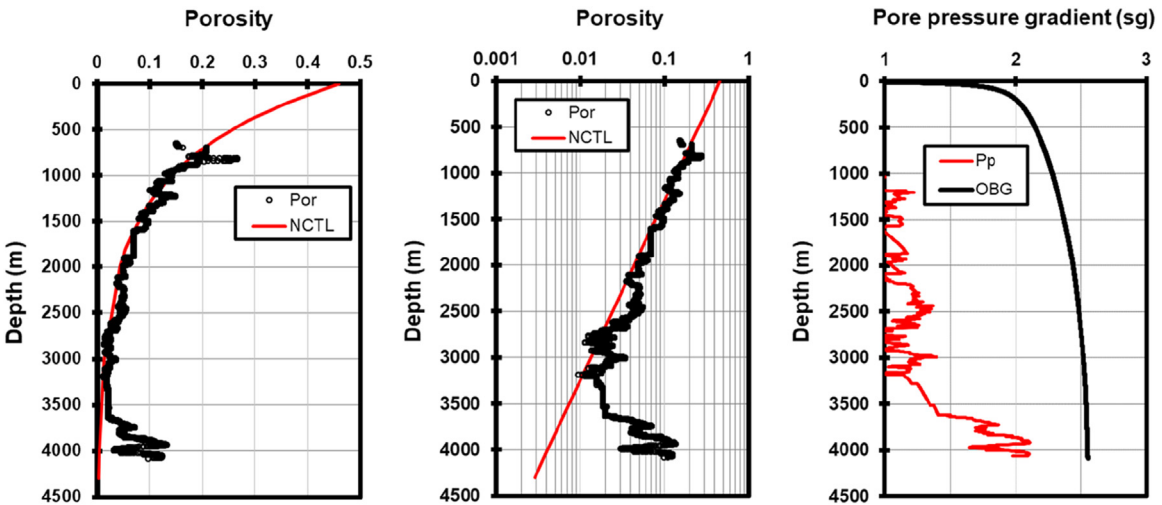

Figure 7.7 Density-derived shale porosity versus depth in both linear (left) and logarithmic (middle) scales compared to the normal compaction trendline, and pore pressure profile (right) calculated from the porosity.

temperature. Hydrocarbon generation is the creation of mobile fluids (mainly oil and hydrocarbon gases) from an original solid immobile kerogen, causing fluid volume or porosity increase if the fluids cannot be expelled. The coincidence of overpressure and hydrocarbon generation was given early prominence by the study of the Bakken shale in the Williston Basin, Montana and North Dakota, USA (Meissner, 1978a,b). The abnormal pressure was attributed by Meissner (1978a) to two processes: (1) increased volume of hydrocarbons and residue relative to unaltered organic material, and (2) inhibited structural collapse of the rock framework as overburden-supporting solid organic matter was converted to hydrocarbon pore fluid. He estimated the fluid volume increased at about 25%, with even greater increases in volume when maturation proceeded from oil to wet gas, and later to dry gas (Fig. 7.8). Spencer (1987) extended the link between overpressure and volume increase during oil generation to most of the deeper parts of the Rocky Mountain basins. Sweeney et al. (1995) modeled volume increases from organic maturation during oil generation, leading to 25% of the total overpressure found in the La Luna Formation source rocks in the Maracaibo Basin, Venezuela. The distribution of hydrocarbon generation with depth indicates that considerable hydrocarbon expulsion and migration occurred in the US Gulf Coast wells at below 10,000 ft, where vitrinite reflectance values ranged from Ro = 0.65 to 0.9% through the hydrocarbon generation interval. Results in four wells indicate a close relationship between the intervals of high overpressures (pressure gradient ranging from 0.76 to 0.86 psi/ft) and the petroleum generation and expulsion windows; however, the porosity versus depth plot in each well does not show an obvious change (Hunt et al., 1998).

The conversion of kerogen to methane from source rocks is the most aggressive overpressure mechanism. The rising temperature that accompanies increasing burial depth converts oil in a reservoir into thermal gas. A consideration of hydrogen balance shows that approximately one volume of

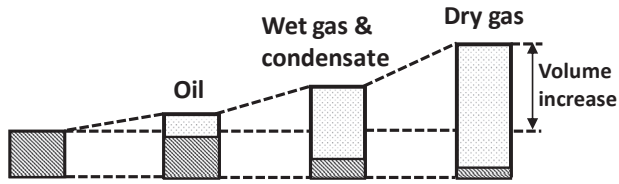

Figure 7.8 Estimation of volume change when Type II kerogen in the Bakken shale of the Williston Basin matures to produce oil, then wet gas and condensate, and finally dry gas. *(Redrawn from Meissner, 1978b.)*

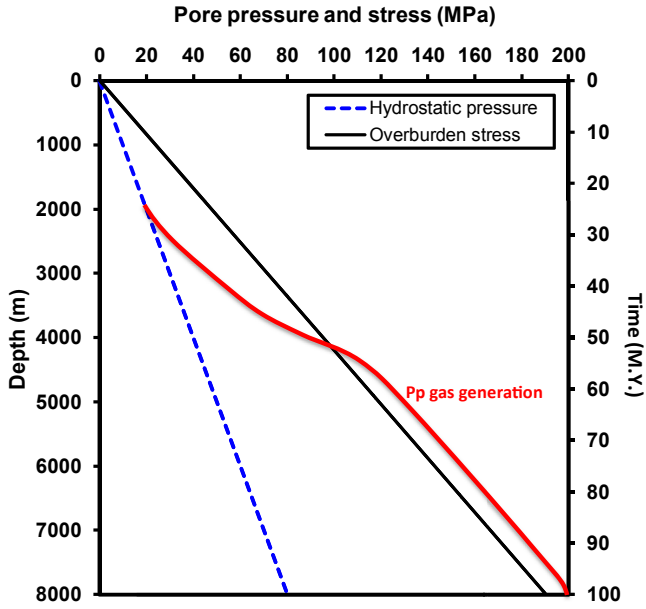

Figure 7.9 Pore pressure build-up with depth and deposition time showing the pore pressure generation trend developed in an isolated system when oil cracks to gas (Carcione and Helle, 2002).

oil thermally cracks to 534.3 volumes of gas at standard temperature and pressure during deep burial (Barker, 1990). This extremely high volume will develop very high overpressures, if the reservoir is an effectively isolated system. Fig. 7.9 displays the calculated pore pressure generated from oil cracking into gas. It demonstrates clearly the potential for generating very high overpressures, most of which are in the geologically unreasonable range of greater than the overburden stress.

Calculations by Barker (1990) show that if the reservoir system remains open (i.e., at hydrostatic pressure) and is initially filled with oil that is subsequently cracked to gas, then roughly 75% of the gas will be lost or the reservoir volume must effectively increase in size, for example, by moving the gas—water contact downward. If the reservoir is sealed and totally filled with oil, cracking of as little as 1% of the oil is enough to raise pressures to 1 psi/ft (22.6 MPa/km). When these pressures exceed the fracture gradient, the induced fracturing will break the seals, causing gas loss and pressure decrease. The induced overpressures from hydrocarbon generation also create microfractures in the source rock. Laboratory measurements of ultrasonic velocity and anisotropy in kerogen-rich black shales of varying

maturity in the Bakken formation, North Dakota, suggest that extensive, bedding-parallel microcracks exist in situ in most mature source rocks (Vernik, 1994). Core samples of the Bossier and Haynesville shales show that bedding-parallel fractures exist in most cores, and some cores are highly fractured with poke-chipping fractures and other microfractures. This could be caused by the fracturing from induced overpressures by hydrocarbon generation.

Gas generation in low permeable rocks causes high overpressure in many onshore gas plays in the United States. For example, in the Greater Green River Basin in Wyoming, Colorado, and Utah, the overpressures are mainly caused by gas generation and occurrence in low-permeability upper Cretaceous and lower Tertiary rocks (Law, 1984; Law and Dickinson, 1985). Fig. 7.10 shows the pressure gradient in the Wagon Wheel well in the Green River Basin, Wyoming. The pore pressures constructed by C. W. Spencer (Law, 1984, 2002) were based on mud weight data from mud logs, well logs, and drill stem tests (DST). The total gas-bearing interval has been divided into three pressure-related intervals that are defined on the basis of specific geologic conditions.

The uppermost interval, referred to as the inactive zone, extends from a depth of 8035 ft to about 10,500 ft where there is an abrupt increase in the pressure gradient. The inactive zone corresponds to an interval in which significantly large volumes of gas have previously been thermally generated.

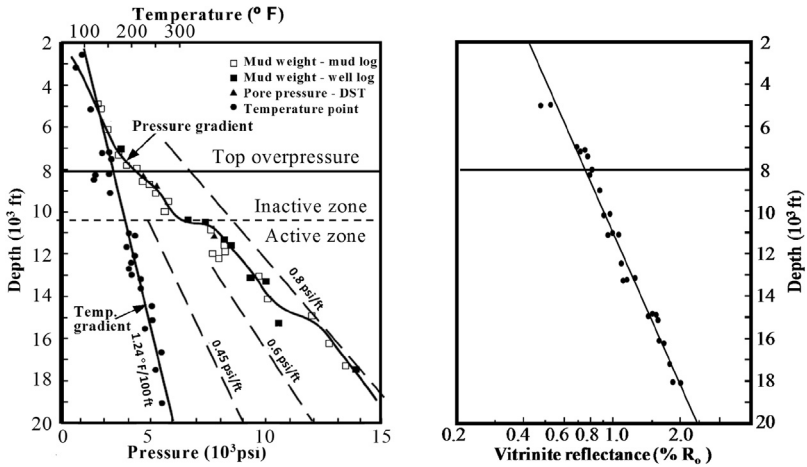

Figure 7.10 Pore pressure and temperature (left) and vitrinite reflectance (right) in the Wagon Wheel well, the Green River Basin, Wyoming. *(From Charpentier et al., 1987; Law, 2002)*

However, because a cooling event occurred 2–4 million years ago, the thermal generation of gas has either ceased or diminished to low rates such that it is lost from the reservoirs faster than it accumulates (Charpentier et al., 1987).

Below the inactive zone is the active zone that is further subdivided into two intervals. Within the active zone thermogenic gas is thought to be actively generated. The upper part of the active zone extends from a depth of about 10,500 ft to about 14,700 ft where another abrupt increase in the pressure gradient occurs. The pressure gradient in the upper part of the active zone appears to be due to a thermal effect elaborated on by the lower part of the active zone that extends from a depth of about 14,700 ft to 17,700 ft where the base of the Rock Springs Formation occurs. The pressure gradient in the lower part of the active zone is coincident with the top of a coal-bearing zone. The elevated pressure gradient through this interval has been interpreted to the increased gas generation of the coal zone (Charpentier et al., 1987).

With subsequent burial and exposure to higher temperatures, the accumulated oil undergoes thermal cracking to gas, accompanied by a significant increase of fluid volume and pressures (Barker, 1990). The level of thermal maturity at which oil is transformed to gas is commonly thought to be about 1.35% vitrinite reflectance (R_o) for a liquid-prone (Type I/II organic matter) source rock (Tissot and Welte, 1984; Hunt, 1996). For a gas-prone source rock (Type III organic matter), when $R_o > 0.6\%$, gas generation and overpressuring start, such as in the Greater Green River Basin (Law, 2002), as shown in Fig. 7.10, where the increase of R_o is closely related to the overpressures.

Oudin and Picard (1982) found that there is a good correlation between the top of hard overpressure and the increase in vitrinite reflectance in the Handil Field in Indonesia while Bates (1996) obtained a similar correlation in the Nilam Field. According to Lambert et al. (2003), gas generation starts at a vitrinite reflectance of 0.6%. In the fields of the Sisi-Nubi, Tunu, Peciko, Handil, and Nilam in the Lower Kutai Basin, Indonesia, the top of the transition zone from normal pressure into hard overpressure coincides with the vitrinite reflectance threshold value of 0.6% for gas generation (Ramdhan, 2010). Vitrinite reflectance data and measured pore pressures show coincidence in gas generation and overpressures, as shown in Fig. 7.11.

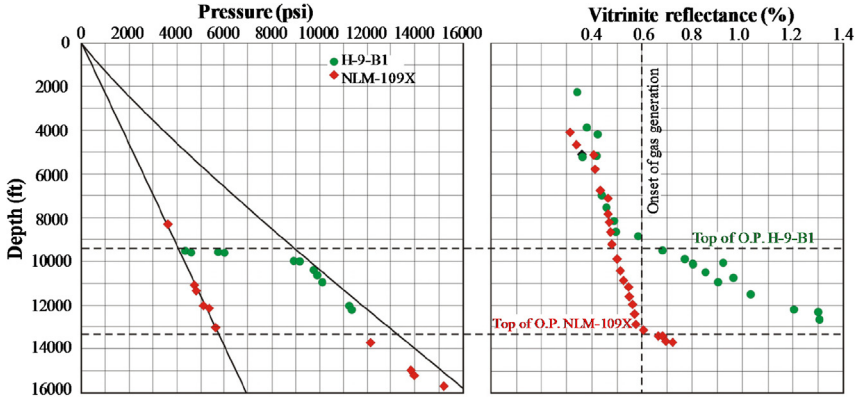

Figure 7.11 Pressure–depth plot and vitrinite reflectance data for wells H-9-B1, Handil Field, and NLM-109X, Nilam Field (Ramdhan, 2010). The top of the overpressure occurs at $R_o = 0.6\%$.

7.2.3 Overpressures by uplift and unloading

Formation uplift and erosion cause overpressures, for example the Sabine uplift in the Haynesville shale gas formation is one of reasons for overpressure generation (Zhang and Wieseneck, 2011). Evidence is also found in other petroleum basins, for example, in the Cassia field, Trinidad (Heppard et al., 2008), where the uplift made the top of the abnormal pressure become shallower.

Assume that a formation is perfectly sealed at burial depth D_0, retaining a normal pressure of P_{f0}. If it is uplift to the depth D_1, then the pore pressure will keep the original value after uplift (the fluid expansion and other factors are not considered here), i.e., $P_{f\,1} = P_{f\,0}$ (for a perfect seal), as shown in Fig. 7.12. If the formation keeps the original pressure after uplift, it will have a pressure elevation or overpressure compared to the current hydrostatic pore pressure at the new burial depth. The pore pressure elevation due to uplift is

$$\Delta p_{f1} = \rho_f g D_e \tag{7.6}$$

where, D_e is the height of the uplift or erosion.

Taking into account the factors of hydrocarbon compositions, thermal history, initial pressure, and sealing conditions, Xia et al. (2013) analyzed the fluid pressure variation of unconventional reservoirs during uplift. Their

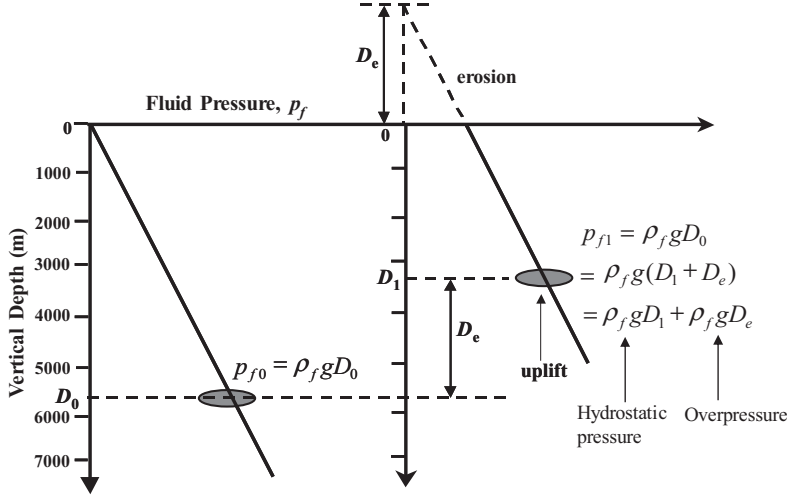

Figure 7.12 Formation uplift causing pore pressure increase in a perfectly sealed condition.

calculation considered both fluid dynamics (Darcy flow and diffusion) and thermodynamics (pressure–volume–temperature relationships), and their results showed that uplift with an ideal sealing condition may enhance overpressures of gas reservoirs and most volatile oil reservoirs with gas to oil ratio (GOR) > 1000 scf/bbl and decrease overpressures of black oil reservoirs with GOR < 500 scf/bbl.

Owing to formation uplift or unloading, the relationship of the effective stress and sonic or seismic velocity does not follow the loading curve, and unloading happens, as demonstrated by laboratory-measured compaction data in Fig. 7.13. The unloading defines the rebound curves in the original compaction/loading curve (Bowers, 2001). The unloading occurs along a flatter effective stress path than the initial compaction curve in the velocity and density curves, as shown in Fig. 7.13. In the unloading case, a higher pore pressure exists for the same velocity value than the one without unloading because it has a smaller effective stress in the unloading case. Fig. 7.13 also indicates that the sediment density typically changes very little in the unloading condition.

Zhang and Wieseneck (2011) studied the relationship of pore pressure (calculated from the fluid kicks), vertical effective stress, and corresponding sonic velocities and densities in the Bossier and Haynesville shale gas formations (Fig. 7.14). Unloading may exist in Fig. 7.14 compared to Bowers' loading curve. Even in the unloading case a power relation can be used to

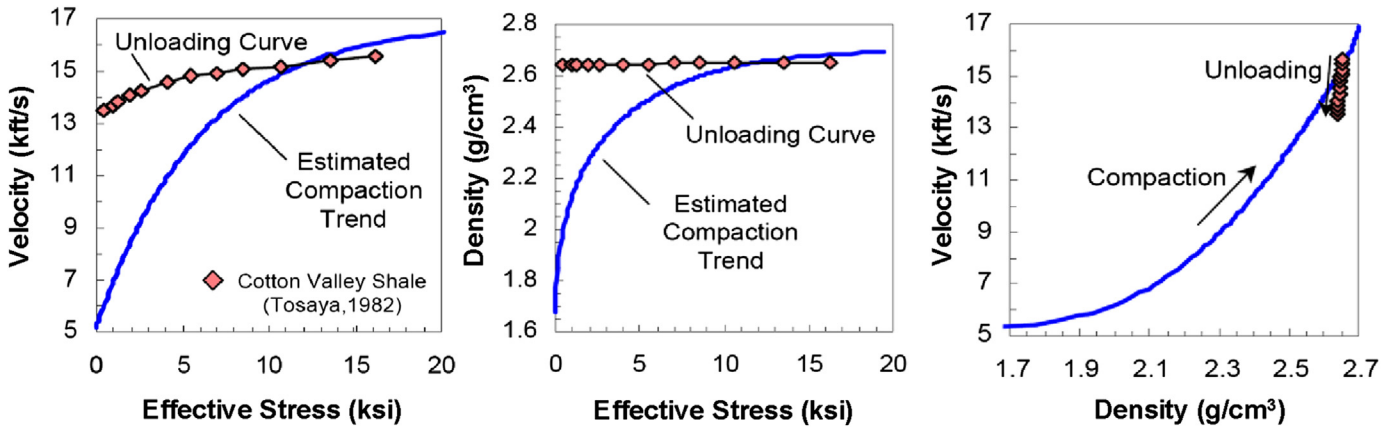

Figure 7.13 Typical unloading responses from velocity—effective stress, density—effective stress, and velocity—density plots (Tosaya, 1982; Bowers, 2001).

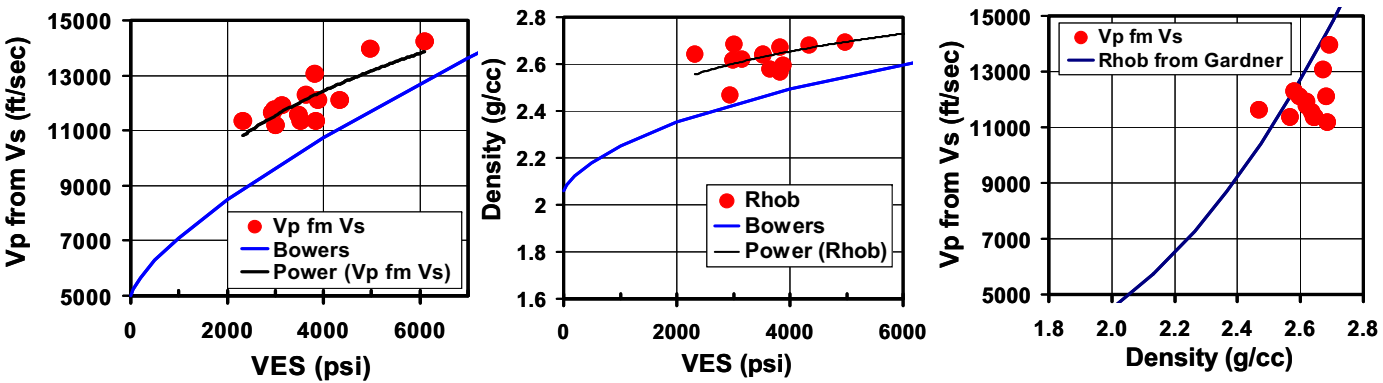

Figure 7.14 Velocity—vertical effective stress (VES), density—vertical effective stress, and velocity—density plots in several wells showing unloading behavior may exist in the Bossier and Haynesville shale gas formations (Zhang and Wieseneck, 2011).

describe sonic velocity and effective stress relation, as shown in the following equation (Zhang and Wieseneck, 2011):

$$V_p = 1467\sigma_e^{0.2577} \tag{7.7}$$

where V_p is the compressional velocity, in ft/s; and σ_e is the effective stress, in psi.

7.3 Overpressures and smectite–illite transformation

Several common mineral transformations in sediments involve the release of bound water. The most common of these involves the dehydration of smectite, a multilayered, mixed-layered clay commonly found in mudrocks. Smectite represents a family of montmorillonite, beidellite, saponite, and nontronite, and it is one of the frequently observed clay mineral in nature. Smectite transforms to a new mineral, illite, involving the release of water at certain temperatures; during this process, the bound water in smectite is expelled into pore space, causing the increase of pore volume and pore pressure because the bound water expands about 1.04–1.1 times as it turns into pore water. Experimental results (Hunnur, 2006) show that during smectite to illite transformation, an increase in pore pressure of up to 3% was observed between day 3 and day 7 from the start of the experiment. Other dehydration reactions include gypsum to anhydrite in evaporitic sediments and coalification.

7.3.1 Overpressure mechanism of smectite to illite transformation

Evaluation of interlayer water loss (dehydration) by smectites under diagenetic conditions indicates that smectites in compacting shales, where the vertical effective stress is greater than zero, will expel one of the two remaining water layers at temperatures of 67–81°C, a temperature range coincident with the onset of smectite to illite transformation (Colten-Bradley, 1987). The last water layer will be lost at 172–192°C. The loss of water generated by dehydration from the minerals into pore space causes fluid volume increase in low permeable shale due to smectite to illite transformation, which will increase pore pressure, if the water cannot be expelled to other formations.

The overall volume change accompanying the complex smectite–illite reaction is not fully understood. Calculations indicate a total increase in volume of 4% occurring in three pulses of water release (Swarbrick and

Osborne, 1998). The first two are likely to take place within the top 1 km of burial, with only the last pulse at depths where significant amounts of overpressure are measured. However, the volume of water released is only about 1.4% and will not create significant overpressure unless the rock is completely sealed. Colton-Bradley (1987) suggested that overpressure would inhibit the dehydration reaction because the dehydration temperatures are elevated with increasing pore fluid pressure. The smectite dehydration reaction is therefore thought to be a secondary rather than a major cause of overpressure but may be additive to overpressure created by compaction disequilibrium.

In several shale-dominated basins a gradual and systematic change from smectite to illite downwards in the stratigraphic section is observed, broadly coincident with the transition to high amounts of overpressure (Bruce, 1984). The transition occurs over a temperature range of 70–150°C and appears to be independent of sediment age and burial depth. By contrast, in the highly overpressured Caspian Sea basin, there is no change in smectite to illite ratio to a depth of 6 km and temperature of 96°C (Bredehoeft et al., 1988). Hence the origin of overpressure by smectite diagenesis is not conclusive. However, the coincidence of overpressure at the same stratigraphic levels as smectite to illite transformation may be related to the ensuing changes in the rock fabric, trapping excess fluids generated by another mechanism, e.g., compaction disequilibrium. Another consequence of the mineral transformation from smectite to illite may develop a hydraulic seal by the growth of coalescing illite packets and reduce permeability. This would help to retain fluids and hence contribute to the preservation of overpressure (Freed and Peacor, 1989).

7.3.2 Smectite and illite transition identified by rock properties

In some area, an obvious transition from smectite to illite (S–I) occurred in shallow depths (e.g., around 1000–2000 m). This transition not only changes rock properties (e.g., sonic velocity, bulk density, elastic modulus) but also affects pore pressure prediction. From the cross-plot of bulk density and sonic transit time, the smectite–illite transition with depths can be observed in the offset wells. Alberty (2005) found that bulk density and sonic transit time have different empirical relations for smectite and illite in the Gulf of Mexico:

$$\text{Smectite}: \ \rho_s = 2.918 - 0.00517\Delta t \tag{7.8}$$

$$\text{Illite}: \ \rho_i = 3.044 - 0.00505\Delta t \tag{7.9}$$

where ρ_s and ρ_i are the bulk densities in smectite and illite (g/cm^3), respectively; Δt is the sonic transit time (μs/ft).

Therefore, the following relation can be used to identify smectite and illite transition:

$$\Delta\rho_s = \rho_b - (a - b\Delta t) \tag{7.10}$$

where $\Delta\rho_s$ is the difference between the bulk density measured from density log and the bulk density in the smectite (g/cm^3); $a = 2.981$, $b = 0.00511$ from Eq. (7.8).

When $\Delta\rho_s \leq 0$, the shale should be smectite-dominated. Otherwise, when $\Delta\rho_s > 0$, the shale should be illite-dominated. Therefore, the S—I transition can also be identified from the bulk density curve where an obvious increase in density appears. The cross-plot of bulk density and sonic transit time in different depths in a well (Fig. 7.15) demonstrates that at a certain depth there is a rapid increase in density at the same velocity (or transit time, DT in the plot), e.g., at the transit time of 110 μs/ft, the density increases from around 2.3 to 2.6 g/cm^3. This density increase is a typical behavior caused by smectite—illite transformation. The smectite and illite trend lines (Eqs. 7.8 and 7.9) are also plotted into the cross-plots in Fig. 7.15 for comparisons.

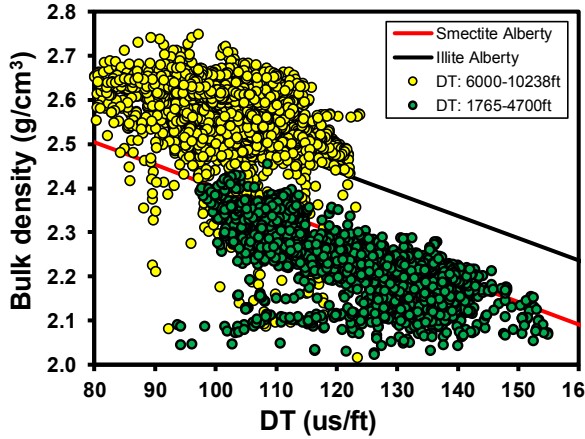

Figure 7.15 Cross-plot of bulk density and sonic transit time from wireline log in a well with smectite and illite trendlines. At a shallow depth of < 4700 ft, the points follow the smectite trend and when depth > 6000 ft, data points follow the illite trend (Reilly and Zhang, 2015).

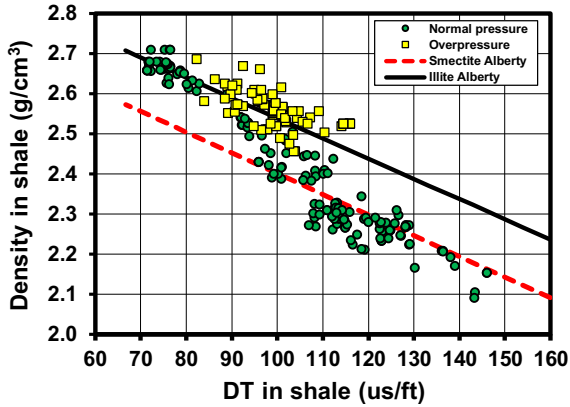

Figure 7.16 Sonic DT and bulk density relationship for 14 wells where the pore pressures were measured in wet sand and the shale properties were obtained from well logs in the bounding shales. The smectite and illite trends are also plotted for comparisons (Reilly and Zhang, 2015).

Fig. 7.16 shows a cross-plot of bulk density and sonic transit time for the measured sand pore pressure points in 14 wells. The transit time DT and density data were picked in the adjacent bounding shales of each measured pore pressure data point in the north Malay basin. Compared to the velocity–density data in the Gulf of Mexico reported by Alberty (2005) and Lahann and Swarbrick (2011), the Malaysian data are consistent to the smectite–illite diagenesis in the Gulf of Mexico. The plot in Fig. 7.16 shows that overpressures are mainly located in the illite trend. This indicates that pore pressure generation might be associated with smectite to illite transformation (Reilly and Zhang, 2015). Some normal pressure points are also in the illite trend, but these points are in deep formations and from the wells located in the basin flank with majority of sands interbedded with thin shales. The reason to generate normal pressure might be due to that these thin shales could not retain high pore pressures, even pressures were generated.

7.3.3 Unloading caused by smectite and illite transformation

There are two different unloadings (Katahara, 2006): elastic unloading and unloading caused by the S–I transformation. The latter can be used to explain the generation of pore pressure induced by the S–I transformation in shales. The cross-plot of shale bulk density and vertical effective stress (vertical stress subtract measured pore pressure, or VES) shows two different

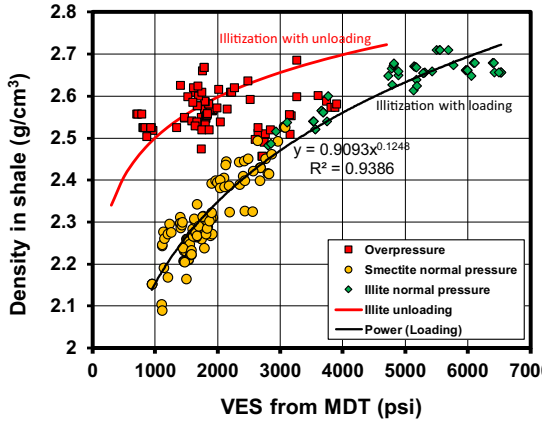

Figure 7.17 Cross-plot of bulk density and vertical effective stress (VES in the figure) in several wells showing illitization with loading and unloading.

behaviors of the shale diagenesis: illitization loading and unloading (Fig. 7.17). From smectite shales to illite shales with normal pressure and slight overpressure, the shales experience illitization as the loading (VES) increases, i.e., bulk density increases as the loading increases. This mainly appears at a shallow depth. Fig. 7.17 also indicates that a great shift occurs in the overpressure data (most red squares) in the latter stages of illitization, in which the overpressure data do not follow the stress–density loading path. This stage can be considered as the illitization with unloading, a similar behavior reported in Lahann et al. (2001). From Fig. 7.17 the illitization unloading curve corresponds to overpressures; however, the illitization loading curve coincides to normal pressures. This implies that only the illitization with unloading generates overpressures. The following correlations can be used to describe the loading and unloading curves:

Illitization with loading: $\rho_l = 0.909\sigma_e^{0.1248}$

Illitization with unloading: $\rho_u = 1.71\sigma_e^{0.055}$

where ρ_l and ρ_u are the bulk densities in loading and unloading cases, respectively; σ_e is the vertical effective stress.

7.3.4 Smectite and illite normal compaction trend and overpressure

For the basins with smectite-dominated shales, the transformation from smectite to illite may increase pore pressure. For pore pressure prediction, the normal compaction trends in smectite and illite should be different, and a composite NCT is needed. Transition from smectite to illite is primarily

driven by temperature; and therefore, the composite normal compaction trend will be dependent on the temperature gradient. Alberty and McLean (2003) pointed out that in reality, it should have a compaction trend honoring the smectite and illite characterizations, to follow the smectite trend down to the onset of the diagenetic conversion and then cross over to the illite trend within the diagenetic window and then follow the illite trend thereafter.

Zhang and Yin (2017a) proposed a multisegmental NCT, which has different compaction parameters (c_s and c_i), as shown in Fig. 7.18, i.e.,

$$\text{For smectites}: \ \Delta t_s = \Delta t_m + (\Delta t_{ml} - \Delta t_m)e^{-c_s Z} \tag{7.11}$$

$$\text{For illites}: \Delta t_i = \Delta t_m + (\Delta t_{ml} - \Delta t_m)e^{-c_i Z} \tag{7.12}$$

$$\text{For a linear S} - \text{I transition}: \ \Delta t_t = \frac{(Z - Z_1)\Delta t_i + (Z_2 - Z)\Delta t_s}{(Z_2 - Z_1)} \tag{7.13}$$

where Δt_s, Δt_i, Δt_m, Δt_{ml} are the transit time in smectite, illite, matrix and mudline, respectively; c_s and c_i are the compaction parameters for smectite and illite, respectively; Z_1 is the depth of the smectite; Z_2 is the depth of the illite; Z_1 and Z_2 can be determined from mineral test results in offset wells or estimated from the regional temperature profile, which is associated with the S–I transformations.

This composite NCT can be used to predict the overpressure that is solely caused by smectite to illite transformation. It can also be used for the

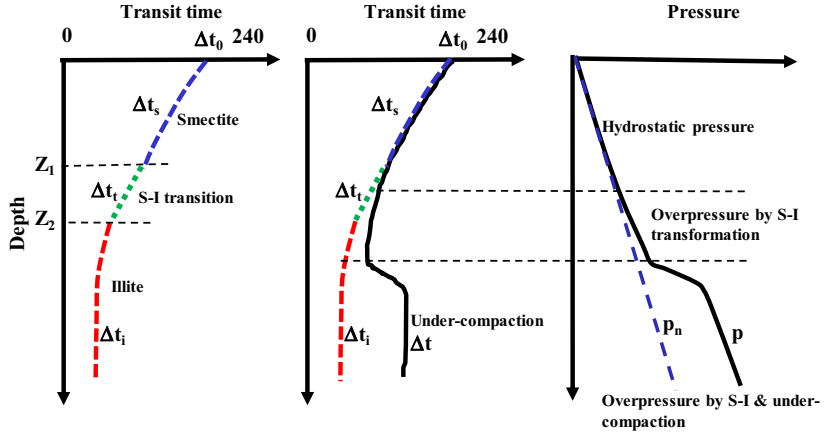

Figure 7.18 The NCTs in the transit time versus depth for a shale composed of smectite and illite. Left: composite NCT; middle: composite NCT and transit time; right: overpressure caused by smectite to illite transformation and undercompaction.

case that smectite to illite transformation is only as an addition to the overpressure, and primary abnormal pressure is caused by under-compaction, as shown in Fig. 7.18. Because rock properties change greatly from smectite to illite, it should use two different NCTs (or a composite one); otherwise, if only illite NCT is used, the shallow pore pressure will be overestimated, particularly if this NCT is calibrated by the measured pore pressures in the deep formations.

7.4 Pore pressure seals and compartments

Pressure seal and compartment are two important concepts in pore pressure prediction. A seal is formed by impermeable or extremely low permeability lithology such as evaporite, salt, or shale. Pressure compartment has impermeable outer seals and an internal volume (e.g., sandstone). Each compartment exhibits effective internal hydraulic communication and has a similar pressure gradient. Effective pressure seals are of critical importance to maintain pore pressures in a pressure compartment. The pressure seals may be formed by faults, salt and mud diapirs, and vertical or lateral facies changes. The overall rate of pressure change across seals in shale has been observed to be as great as 15 psi/ft (0.34 MPa/m) (Powley, 1990). Fig. 7.19 shows the pressure difference of more than 15 MPa across a seal. Fig. 7.20 displays that the difference of pore pressure gradients is 0.8 ppg (~0.1 SG)

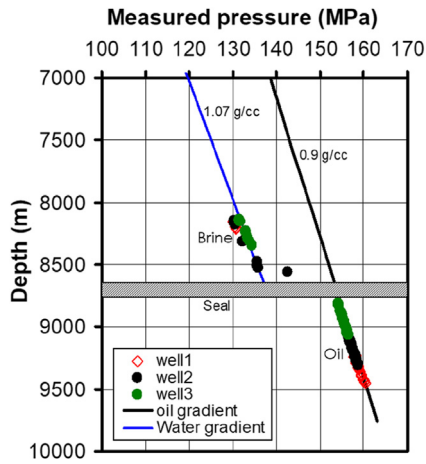

Figure 7.19 Measured fluid pressures in two sandstone formations showing that there are obvious pressure compartments, implying a seal between the two sandstones exists.

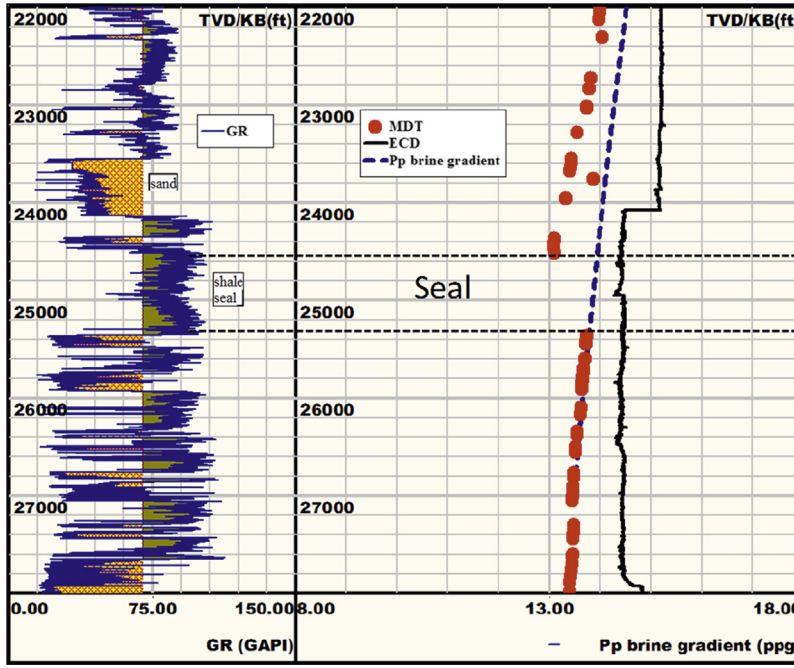

Figure 7.20 Gamma ray and pore pressure gradients measured from the modular formation dynamic tester (MDT, in ppg) showing two pressure compartments and a thick seal in a well.

in two sandstones across a thick seal. Seal integrity is critical to maintain pore pressures in a compartment or a hydrocarbon reservoir, particularly the integrity of the top seal in the crest. If pore pressure gradient in a reservoir at the crest is higher than the fracture gradient of the seal, then the seal would be broken, causing the oil or gas to bleed off.

7.5 Abnormal formation pressures in some petroleum basins

7.5.1 Global distribution

Abnormal pressures occur in a wide range of geographic and geologic conditions. Based on the compilation of the occurrence of abnormal pressures (Law and Spencer, 1998), there are approximately 150 geographic locations around the world known to be abnormally pressured. Hunt (1990) indicated that abnormal pressures were identified in about 180 basins. Nearly all the abnormally pressured regions are overpressured. All

the causes of abnormal pressures in the literature are referred to the following reasons (Law and Spencer, 1998): compaction disequilibrium, aquathermal expansion, hydrocarbon generation, mineral transformations, tectonics, and osmosis. The most common cause of abnormally high pressure is compaction disequilibrium; the age of the abnormally pressured rocks is primarily Tertiary. In pre-Tertiary rocks, the main causes of abnormal pressure include hydrocarbon generation, aquathermal expansion, mineral transformations, and tectonic deformation; however, hydrocarbon generation was cited as the most common cause. As these deltaic sediments are buried deeper and experience higher temperatures, hydrocarbon generation may supplant compaction disequilibrium as the main cause of abnormally high pressure. In deltaic rock sequences where the hydrocarbon source rock occurs stratigraphically below the compaction disequilibrium-affected sediments, the generation of hydrocarbons from these source rocks may result in the development of overpressure, which could be physically transferred upward into the region of compaction disequilibrium. This causes further increase of the overpressure generated by compaction disequilibrium (Law and Spencer, 1998). In the following sections, typical pore pressure profiles are analyzed in several petroleum basins.

7.5.2 Abnormal pressure in the Macondo well of the Gulf of Mexico

The Macondo well, MC 252-1 (BP) is an oil exploration well, located 133 miles SE of New Orleans in the Mississippi Canyon block 252, deepwater Gulf of Mexico, USA. The mudline of the well was 5067 ft including the air gap of 75 ft. On April 20, 2010, the Deepwater Horizon blowout of the Macondo well occurred.

The Macondo pore pressure profile (Fig. 7.21) shows that the first abnormal pore pressure indicator at 7500 ft TVD SS (below the sea level) confirms the shallow onset of overpressure, and this is very common in deepwater Gulf of Mexico (e.g., Flemings et al., 2002). From 7500 to 17,640 ft, pore pressure gradually increases and approximately parallels to the overburden stress, with the maximum pore pressure gradient of 13.9 ppg. Thereafter, pore pressure decreases abruptly by 1200 psi over 370 ft as the main sandstone reservoir (M56) is approached (Pinkston, 2018). The M56, a Miocene-aged sandstone, is part of a larger hydraulically connected aquifer and has a large pore pressure regression presented at the Macondo (Pinkston, 2018). Case study in some Green Canyon wells show

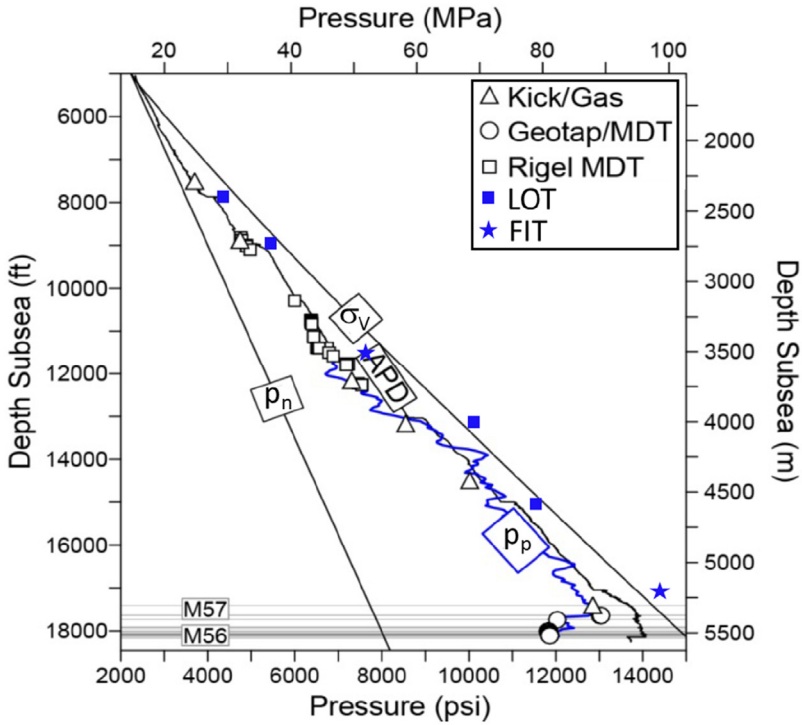

Figure 7.21 Pore pressure profile in the Macondo well (redrawn from Pinkston, 2018) with downhole mud weight (APD) and LOT, FIT. p_n and p_p are the normal pressure and pore pressure.

a similar behavior, i.e., the reservoir pressure regression occurred compared to adjacent shales and isolated sands owing to lateral drainage in the reservoir (Zhang et al., 2008).

The leak-off test (LOT) and formation integrity test (FIT) data points (related to fracture gradient) from BP's report (BP, 2010) are also plotted in Fig. 7.21. It shows that the drilling window between pore pressure and fracture gradient is very narrow in some sections although the maximum fracture gradient is greater than 16 ppg (the value of FIT tested at 17,082 ft TVD ss).

7.5.3 Abnormal pressures in the Scotian Shelf, Canada

The Scotian Basin is located beneath the outer part of the Scotian Shelf, offshore Nova Scotia, eastern Canada. The gas-bearing sandstones in the Cretaceous and upper Jurassic formations are the major target in the basin. Overpressures are encountered throughout the Scotian Shelf south of the

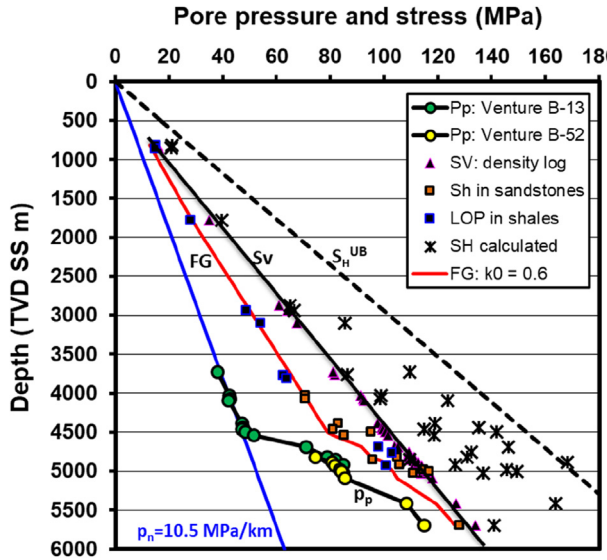

Figure 7.22 Measured pore pressures (p_p) from drill stem test (DST) and repeat formation tester (RFT) in four wells in the Venture field, Canada (plotted based on the data presented by Ervine and Bell, 1987). The hydrostatic pressure (p_n), measured leak-off pressure (LOP), the minimum horizontal stress (S_h), and calculated maximum horizontal stress (S_H) are also plotted.

hinge zone (Yassir and Bell, 1994). Most of the research on overpressures in the Scotian Shelf has concentrated on the Venture field, where the overpressures begin at approximately 4500 m, as shown in Fig. 7.22. Pore pressure increases in steps, reaching a value close to the lithostatic stress (S_V in the figure) in deep formations. Overpressures occur in high-porosity sands interbedded with shales. The shales act as seals to overpressured fluids (Wade, 1991; Drummond, 1992). Disequilibrium compaction for abnormal pressure generation is ruled out because of the low sedimentation rates in the region. Gas generation is a key cause of overpressuring because the overpressured zone is related to a sharp increase in vitrinite reflectance tested in some wells. Additionally, Wade (1991) noted that the top of overpressure corresponds with the 130°C isotherm (related to hydrocarbon maturation).

Fig. 7.22 also shows that there is a consistent relationship between overpressures and in situ stresses in the basin. The minimum horizontal stress increases dramatically starting from the top of overpressure at ~4500 m. This implies that contemporary stresses in these sediments are causally related to overpressuring. The maximum horizontal stress is greater than the

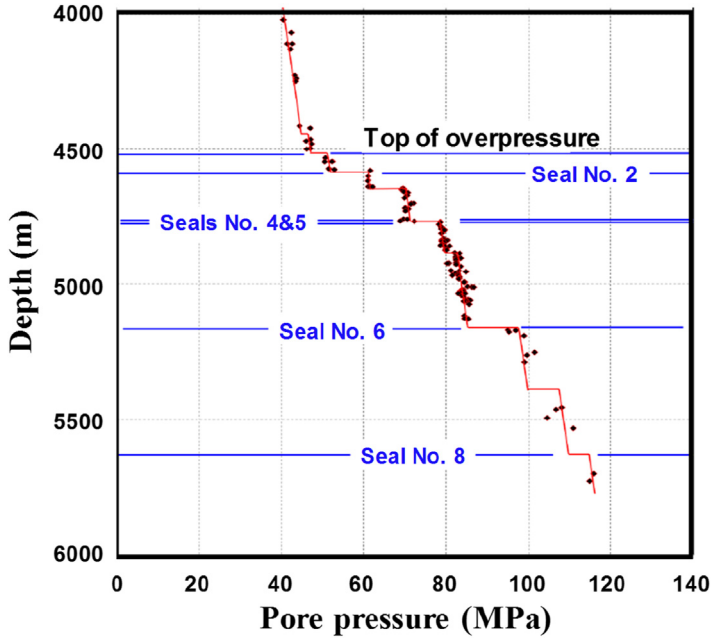

Figure 7.23 Seals and pressure compartments retaining overpressures in the Venture field, Canada. *(Based on Wheeler, 2011.)*

vertical stress; therefore, in situ stress state in this region belongs to the strike-slip faulting stress regime.

Fig. 7.23 shows that deeper than the top of overpressure at 4500 m, several shale seals and sandstone pressure compartments are recognized in the Venture field. These seals make the rapid transitions to high overpressures possible and are key factors to retain overpressures.

7.5.4 Abnormal pressures in the Central Graben, the North Sea

The Central Graben of the North Sea is one of the world's most prolific oil-producing provinces. It contains major reserves of oil, gas, and condensate presented in reservoirs ranging in age from the Devonian to Early Eocene. These include super giant fields such as the Ekofisk. The Upper Jurassic sandstones in the Central Graben vary from being normally pressured, 0.01 MPa/m (0.44 psi/ft) near the graben margins, to pressure gradients exceeding 0.02 MPa/m (0.88 psi/ft) in the center of the graben. The Paleocene sandstones consist of sheet sandstones forming a normally pressured regional aquifer, and the Chalk Group, where overlain by these

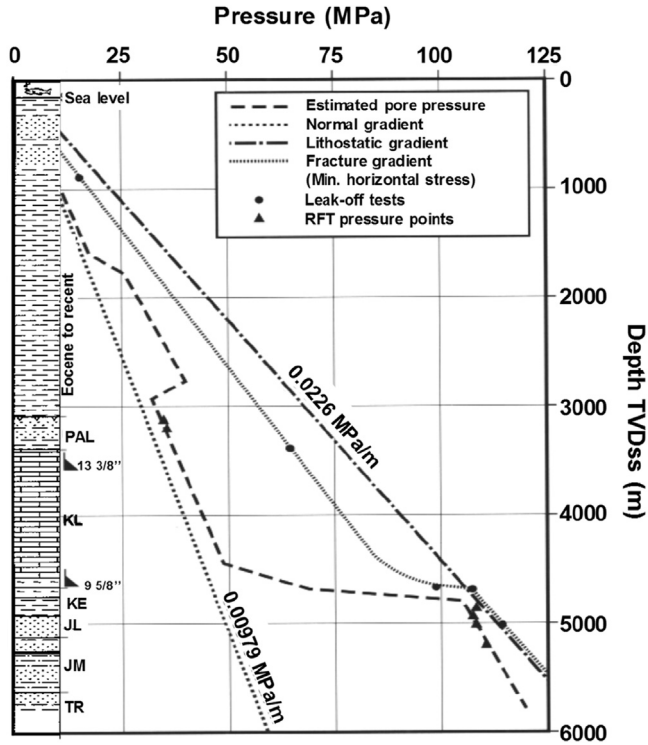

Figure 7.24 Pressure–depth profile for a well drilled in the center of the Central Graben (Holm, 1998). Notice that the chalk in the Late Cretaceous has a lower pore pressure, slightly higher than the hydrostatic pressure. The hard overpressure occurs below the chalk.

sandstones, is similarly normally pressured. Fig. 7.24 displays a pressure–depth profile for a well drilled in the center of the Central Graben (Holm, 1998). It has normal pore pressure in the chalk of the Late Cretaceous, but the hard overpressure occurs in the Jurassic rocks below the chalk.

Compaction disequilibrium and hydrocarbon generation are important processes in the development of overpressures within rocks of the Chalk Group and pre-Cretaceous of the Central Graben, with hydrocarbon generation considered as the dominant cause of overpressure in rocks below depths of 4500 m (Holm, 1998). In a study of the Norwegian Central Graben, Leonard (1993) subdivided the observed pressure regime into three vertically stacked compartments, the Tertiary, the Chalk Group, and the pre-Cretaceous. The lowermost compartment is highly overpressured in

the range 38–52 MPa, which might be caused by thermal cracking from oil to gas.

Gaarensstroom et al. (1993) studied the generation of overpressure and sealing mechanisms in the Central Graben of the United Kingdom and proposed that overpressure was initiated by rapid sedimentation and burial of low permeability claystones. This early pressure generation was then followed by an increase in the magnitude of the overpressure due to hydrocarbon generation. Finally, as the pore pressure continued to increase, the fracture gradient was exceeded with subsequent loss of fluid and pressure.

7.5.5 Abnormal pressures in the Cooper Basin, Australia

The Nappamerri Trough contains a thick Permian section of sandstones, coals, siltstones, and shales, and extensive drilling has proved up many commercial gas fields. The Roseneath Shale, Epsilon Formation, and Murteree Shale (REM) were initially the main focus of shale gas assessment in the Nappamerri Trough of the Cooper Basin in Australia. The thick shale units of the Roseneath and Murteree are considered to be regional seals. The Nappamerri Trough contains a thick Permian section of sandstones, coals, siltstones, and shales deposited in a cold climate fluviolacustrine setting (Trembath et al., 2012).

The prospective REM section has a high vitrinite reflectance of 2%–4% with the level of thermal maturity depending on location within the Trough. With the high level of maturity, the Permian sequence is expected to be within the dry gas window. DSTs and mud weights in offset wells indicate that the Epsilon and Patchawarra Formations are highly overpressured and that the overpressure is confined to the Nappamerri Trough. The regional pressure gradient is 0.43 psi/ft (hydrostatic pressure gradient), while the pressure gradient in the Nappamerri Trough, based on DST data over the Epsilon and Patchawarra Formations, is about 0.72 psi/ft (Fig. 7.25). The top of overpressure starts at 2800 m and the maximum overpressure compared to the hydrostatic pressure can reach 3000 psi. This overpressure might be caused by gas generation.

7.5.6 Abnormal pressures in China

Abnormal pore pressures exist in many geologic basins in China. For example, overpressures have developed over large parts of the Yinggehai, Qiongdongnan, Sichuan, and Bohai Bay basins. Overpressures in the

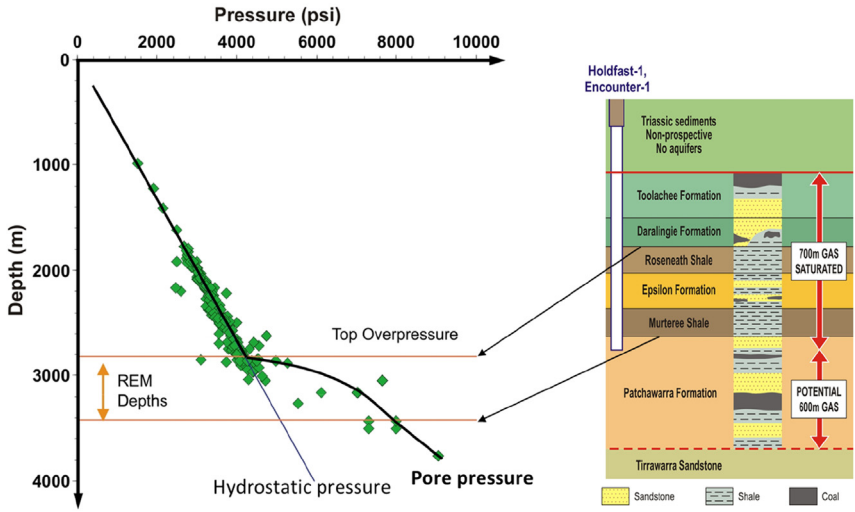

Figure 7.25 Cooper Basin pressure–depth trends with the Central Nappamerri Trough deviating from the regional trend indicating overpressure (left) and schematic representation of the potential thickness of gas saturated interval in Encounter-1 and Holdfast-1 (right) (Trembath et al., 2012, with permission from the APPEA Journal).

Junggar basin are widely spread in the central and southern parts. Overpressures in the Tarim basin occur mainly in the Kuche depression (Hao et al., 2007). Most shale gas and tight gas formations in the Sichuan basin are overpressured, such as the Longmaxi shale gas formation in the Fushun-Yongchuan block. Abnormally low pressures are widely spread in the Ordos basin where basin-centered gas systems had been found.

Triassic-aged Xujiahe sandstones are tight gas formations located in the western Sichuan basin, pore pressures in these tight sandstones and source rocks are highly overpressured (Fig. 7.26). For example, pore pressure in gas formation Xu 2 (T_3X^2) is 1.5–1.7 times greater than the hydrostatic pressure; pore pressures in the Xu 3 (T_3X^3) and the Xu 4 (T_3X^4) have even higher magnitudes, around 1.85–2.1 times greater than the hydrostatic pressure. This region belongs to active tectonic stress regime because of the strong compression in the Longmenshan fault belt, which might be one of the reasons for abnormal pressure generation. In situ stresses measured from borehole hydraulic fracturing tests (e.g., mini-frac) indicate that the maximum horizontal stress is greater than the vertical stress ($\sigma_V = 0.024–0.025Z$). At the shallow depth, both horizontal stresses are

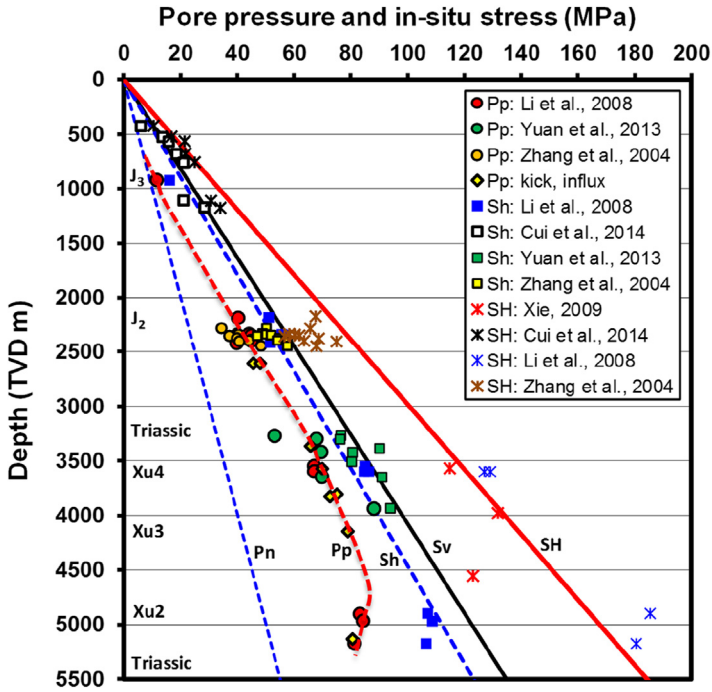

Figure 7.26 The measured pore pressure (p_p), minimum horizontal stress (S_h), maximum horizontal stress (S_H), and vertical stress (S_V) in the western Sichuan basin, China. The deep data (Z > 3000 m) were obtained from the Xujiahe sandstone reservoirs, and the shallow data (Z < 2000 m) were obtained from the WFSD-1 (Fig. 6.10) in the Longmenshan fault belt.

greater than the vertical stress (Fig. 7.26). In the deeper formation (>900 m), the measured horizontal stresses and depth have the following approximate relations:

$$\sigma_h = 0.0224Z \tag{7.14}$$

$$\sigma_H = 0.0335Z \tag{7.15}$$

where σ_h and σ_H are the minimum and maximum horizontal stresses in MPa; Z is the depth in meters.

7.5.7 Abnormal pressures in the Malay Basin

The Malay Basin is a Tertiary transtensional rift basin located offshore east of Peninsular Malaysia, between the Gulf of Thailand and Borneo in SE Asia. Northern part of the Malay Basin is elongated NW to SE and has been a prolific area for hydrocarbon exploration in Malaysia. In the deep

formations, particularly in the center of the basin, the pore pressure and temperature are markedly high, and these pose a direct threat to safe drilling. It was reported that in the past 80% of the exploration and appraisal wells in the Malay Basin were terminated because of overpressure (Shariff and Leslie, 1995).

Singh and Ford (1982) suggested that the abnormal pressure in the Malay Basin is a complex origin attributed to a combination of rapid burial of certain stratigraphic units, uplift of initially normally pressured strata, faulting, and hydrocarbon column effects. Shariff and Leslie (1995) found that the margins of the Malay Basin are normally pressured, and the central portion of the Malay Basin is overpressured. Madon (2004, 2007) considered that compaction disequilibrium was the primary causal mechanism for overpressures in the basin center, when the sedimentation burial rates were very high (>1000 m/m.y.). Hoesni (2004) proposed that the overpressure in the Malay Basin was mainly caused by compaction disequilibrium with potential contribution from clay diagenesis or chemical compaction processes. He also pointed out that the occurrence of chemical compaction was evident from a distinctive profile (rapidly increasing density with almost constant velocity) observed on the velocity−density cross-plots, and the onset of chemical compaction was observed between 105 and 120°C. Duffy et al. (2011) found that chemical compaction existed in the South Malay Basin, and their XRD analysis on mudstone cuttings showed evidence of different mineralogy with depth, with reduction of expandable clays occurring below 2200 m. Tingay et al. (2013) concluded that overpressure was generated by kerogen to gas maturation in the northern Malay Basin. Satti et al. (2015) considered that the overpressure in the southwestern Malay Basin was mainly caused by unloading. Reilly and Zhang (2015) pointed out that pore pressure generations in the northern Malay Basin were related to multiple factors, and the clay diagenesis could be one of the causes of overpressures.

Measured pore pressure data in dozens of wells in the northern Malay Basin show that wells drilled in different areas in the basin have very different pore pressure regimes (Fig. 7.27). Wells drilled in the basin flank have normal pressures or slight overpressures even in very deep formations (>10,000 ft). However, wells drilled in the basin center are highly overpressured, probably due to more shaly and much thicker shales for building more pressures. Many overpressured wells also have a pressure regression following a significant pressure increase. That is, the normal pressure and hard overpressure coexist in deep formations. In this case, the normally

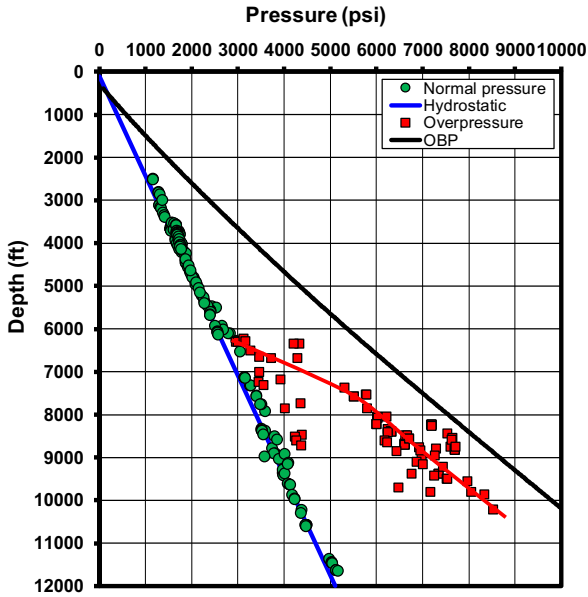

Figure 7.27 Measured pore pressures, hydrostatic and overburden stress in the Northern Malay Basin (Reilly and Zhang, 2015).

pressured formation has a very low fracture gradient. If this normally pressured formation and its adjacent overpressured formation are drilled in the same casing interval, it will have a very narrow drilling window. Additionally, gas-phase pressures in thin sands are very different from wet sands, which results in a narrow drilling window due to water and gas phase pressure dichotomy. This brings challenges for drilling because of potential gas kicks (Reilly and Zhang, 2015).

Cross-plots of sonic transit time and bulk density versus vertical effective stress show that normally pressured data points are located on the loading curve (Fig. 7.28). However, most of overpressured data points are on unloading curve. This unloading could be caused by elastic unloading and/or illitization unloading. Therefore, this unloading behavior needs to be considered for pore pressure prediction.

7.5.8 Abnormal formation pressures in major US shale plays

7.5.8.1 Pore Pressure Gradient in Major US Shale Plays

Most shale oil and gas plays in the US have abnormal pore pressures, and high overpressures are very common (see Table 7.3). For example, in the

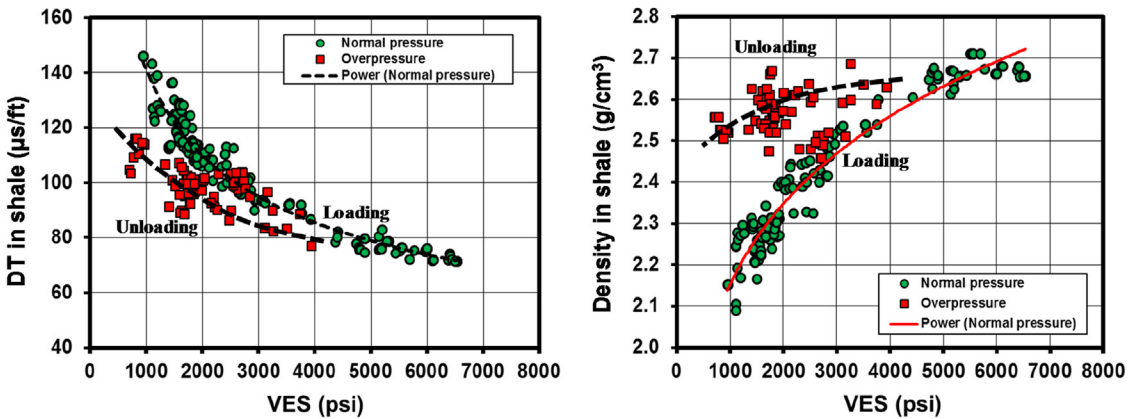

Figure 7.28 Cross-plots of vertical effective stress (VES in the figure) versus sonic transit time (left) and bulk density (right) in dozens of wells showing loading and unloading behaviors (Reilly and Zhang, 2015).

Table 7.3 Pore pressure gradients and mechanical properties in major US shale plays.

Plays	Barnett	Haynesville	Fayetteville	Marcellus	Wolfcamp	Bakken	Eagle ford
Depth (ft)	5000–8500	9600–13,500	1000–7000	2000–8500	5500–11,000	3100–11,000	2500–15,000
Pore pressure gradient (psi/ft)	0.49–0.54	0.75–0.94	0.44	0.40–0.67	0.46–0.62	0.5–0.82	0.4–0.8
Young's modulus (Mpsi)	5–7	1.45–8	1–1.45 outcrop samples	4.4–29	4–11.9	2.67–9.8	2–8.4
Poisson's ratio	0.15–0.21	0.1–0.26	0.1–0.26	0.15–0.35	0.15–0.4	0.25–0.33	0.15–0.35

Plays	Utica	Woodford	Monterey	Niobrara	Mancos	Antrim	New Albany
Depth (ft)	4000–14,000	6000–16,000	4000–15,000	5500–8500	5000–8000	500–2000	500–4500
Pore pressure gradient (psi/ft)	0.56–0.8	0.6–0.65	0.44–0.8	0.41–0.67	0.45–0.9	0.35–0.38	0.43
Young's modulus (Mpsi)	1–7	0.28–2.2	1.3–2.7	6.1–9	3.4–4.2	0.6–2.2	1.6–3.8
Poisson's ratio	0.22–0.35	0.15–0.25	0.1	0.18–0.27	0.08–0.25	0.2	0.16–0.2

From various sources: Major references are Sandrea and Sandrea (2014), Burnaman et al. (2009), Wang and Zeng, 2011

Haynesville and Bossier shale gas plays in Louisiana and Texas, the pore pressure gradient is very high and ranges from 0.75 to 0.94 psi/ft (1.73–2.17 g/cm^3); the upside of the high pressure gradient has been abnormally high well IPs (9.5 MMscf/d), almost five times those of the benchmark Barnett (Sandrea and Sandrea, 2014). However, some shale gas plays have normal pore pressures or even underpressures, such as the Fayetteville, New Albany, and Antrim.

7.5.8.2 Bakken and Three Forks plays

The Bakken shale oil play is mainly located in the Williston Basin in North Dakota and Montana of USA and Saskatchewan of Canada. The Mississippian- and Devonian-aged Bakken formations consist of the Upper, Middle, and Lower Bakken members. The Middle Bakken reservoir is a calcitic and dolomitic siltstone lying between the Upper and Lower Bakken shales, which are the source rocks for the play (Dohmen et al., 2013). The Three Forks, beneath the Bakken formation, is also an oil-bearing formation. Pore pressures in the Bakken and Three Forks indicate an inverted continuous system with pressure leaking off at top, apart from the Parshall pressure cell (Fig. 7.29). The most likely regional normal pressure gradient is 0.47 psi/ft because of high salinity in the formations. The top of overpressure occurs at about 9000 ft; thereafter, the pore pressure is highly overpressured in the Bakken and Three Forks formations, as shown in Fig. 7.29. Comparisons indicate a higher overpressure in the Three Forks at the same depth level than that in the Middle Bakken.

Meissner (1978a) pointed out that abnormal pressures associated with mature Bakken source rocks are basically caused by:

1. the inhibited structural collapse of the rock framework as overburden-supporting solid organic material (estimated to be at least 25 volume percent of the rock) converted to nonoverburden-supporting hydrocarbon pore fluid (e.g., oil and/or gas); and
2. the increased volume occupied by metamorphosed organic residue plus generated hydrocarbon fluids above those occupied by the unaltered organic material.

Therefore, anomalous pressures in the Bakken formations are believed to be maintained by the combination of large hydrocarbon volumes generated at high rates and the relative isolation of the Bakken by extremely tight rocks in the underlying Three Forks and overlying Lodgepole Formations (Meissner, 1978b). Theloy (2014) also found that the intense oil

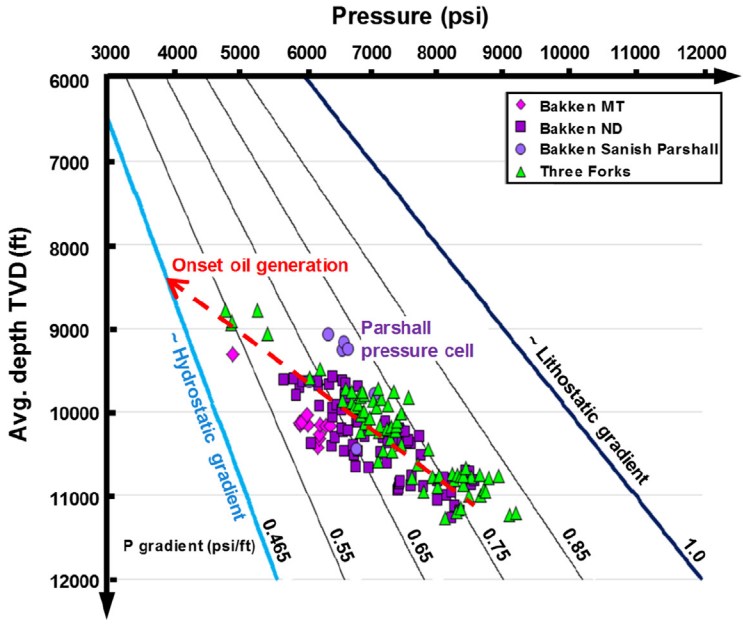

Figure 7.29 Pore pressure profile in ND and MT, USA based on analyzing 92 bottomhole pressure and DFIT data points, a number of hydrostatic points at eastern margin, six Sanish-Parshall points in the Middle Bakken and additional data of the Three Forks (Theloy, 2014).

generation in both Upper and Lower Bakken shales correlates to formation overpressures.

7.5.8.3 Haynesville and Bossier shale plays

The Bossier and Haynesville shales are tight shale gas reservoirs with very low matrix permeability (0.00007–0.0007 mD). The lithology comprises the Tertiary-, Cretaceous-, and Jurassic-aged stratigraphic units characterized primarily by claystones (shales) and sandstones. There are also limestone formations, such as the Knowles limestone in the Cotton Valley Group and the Smackover limestone at bottom of the Haynesville shale (Fig. 7.30). Regional correlation sections across northern Louisiana reveal a prominent mid-Cretaceous unconformity, suggesting a later uplift event affecting the area. It appears that the present-day Sabine High represents a Tertiary uplift event. The maximum missing section due to the Tertiary uplift is estimated in orders of several thousand feet. Timing of the uplift and erosion appears to be the Oligocene Epoch (Zhang and Wieseneck, 2011).

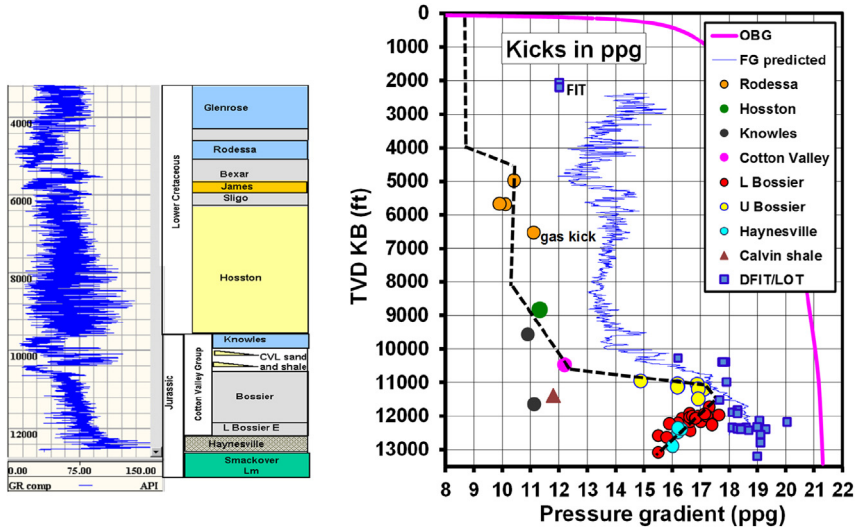

Figure 7.30 Gamma ray log and typical stratigraphic column (left) in the Bossier and Haynesville plays; pore pressure gradient from kicks in different wells plotted on the same formation tops with measured DFIT and LOT data compared to the calculated minimum stress (right) (Zhang and Wieseneck, 2011).

Several pressure gradients were identified from the kick data, as shown in Fig. 7.30. That is, a normal pressure gradient from the surface to the top of the Rodessa limestone; thereafter, pore pressure becomes slightly overpressured to the top of the Hosston (Travis peak) shale. The pore pressure gradient then increases gradually from the Hosston shale to the Knowles limestone. At the upper Bossier shale, the pore pressure gradient increases significantly and has a transition zone to hard overpressure in the lower Bossier. From the lower Bossier to the Haynesville shales, the hard overpressure exists. Based on this lithology-dependent pore pressure gradient profile, pore pressure can be predicted when one knows the prognosed formation tops in the predrill well. The measured fracture gradient data from the DFIT and LOT are consistent to the fracture gradient computed from the minimum stress method (Zhang and Yin, 2017b).

References

Alberty, M., 2005. Pore pressure detection: moving from an art to a science. Paper SPE-108787.

Alberty, M., Mclean, M., 2003. Emerging trends in pressure prediction. OTC-15290.

Barker, C., 1990. Calculated volume and pressure changes during the thermal-cracking of oil to gas in reservoirs. AAPG Bull. 74, 1254–1261.

Bates, J.A., 1996. Overpressuring in the Kutai Basin: distribution, origins, and implications for the petroleum system. In: Indonesian Petroleum Association, Proc. 25th Ann. Convention, pp. 93–115.
Bird, P., 1995. Lithosphere dynamics and continental deformation. Rev. Geophys. (Suppl. l), 379–383.
BP, 2010. Deepwater Horizon Accident Investigation Report. Public report online. Sept. 8, 2010, p. 19.
Bowers, G.L., 2001. Determining an appropriate pore-pressure estimation strategy. Paper OTC-13042.
Bruce, C.H., 1984. Smectite dehydration - its relation to structural development and hydrocarbon accumulation in Northern Gulf of Mexico Basin. AAPG (Am. Assoc. Pet. Geol.) Bull. 68, 673–683.
Burnaman, M., Xia, W., Shelton, J., 2009. Shale gas play screening and evaluation criteria. China Petrol. Exploration 14, 51–64.
Bredehoeft, J.D., Djevanshir, R.D., Belitz, K.R., 1988. Lateral fluid flow in a compacting sand-shale sequence: South Caspian Basin. AAPG Bull. 72, 416–424.
Burrus, J., 1998. Overpressure models for clastic rocks, their relation to hydrocarbon expulsion: a critical reevaluation. In: Law, B.E., Ulmishek, G.F., Slavin, V.I. (Eds.), Abnormal Pressures in Hydrocarbon Environments: AAPG Memoir, vol. 70, pp. 35–63.
Carcione, J.M., Helle, H., 2002. Rock physics of geopressure and prediction of abnormal pore fluid pressures using seismic data. CSEG Recorder 27 (7), 8–32.
Charpentier, R.R., Law, B.E., Prensky, S.E., 1987. Quantitative model of overpressured gas resources of the Pinedale anticline, Wyoming. SPE/DOE 16404 in Low Permeability Reservoirs Symposium, 18–19 May, 1987, Denver, Colorado.
Chillingar, G.V., Serebryakov, V.A., Robertson, J.O., 2002. Origin and Prediction of Abnormal Formation Pressures. Elsevier.
Colten-Bradley, V.A., 1987. Role of pressure in smectite dehydration; effects on geopressure and smectite-to-illite transformation. AAPG (Am. Assoc. Pet. Geol.) Bull. 71, 1414–1427.
Cui, J., Lin, W., Wang, L., Gao, L., Wang, W., Sun, D., Li, Z., Zhou, C., Qian, H., Peng, H., Xia, K., Li, K., 2014. Determination of three-dimensional in situ stresses by anelastic strain recovery in Wenchuan Earthquake Fault Scientific Drilling Project Hole-1 (WFSD-1). Tectonophysics 619–620, 123–132.
Davies, R.J., Swarbrick, R.E., Evans, R.J., Huuse, M., 2007. Birth of a mud volcano: East Java, 29 May 2006. GSA Today (Geol. Soc. Am.) 17 (2).
Dohmen, T., Zhang, J., Li, C., Blangy, J.P., Simon, K.M., Valleau, D.N., Ewles, J.D., Morton, S., Checkles, S., 2013. A new surveillance method for delineation of depletion using microseismic and its application to development of unconventional reservoirs. Paper SPE 166274 presented at the SPE Annual Technology Conference in New Orleans, Louisiana.
Duffy, L.M., Aplin, A.C., Hoesni, M.J., 2011. Rock property analysis of Malay Basin mudrocks. SP16 presented at 72nd EAGE Conference & Exhibition Incorporating SPE EUROPEC 2010.
Dutta, N.C., 2002. Geopressure prediction using seismic data: current status and the road ahead. Geophysics 67 (6), 2012–2041.
Drummond, K.J., 1992. Geology of venture, a geopressured gas field, offshore Nova Scotia. In: Halbouty, M.T. (Ed.), Giant Oil and Gas Fields of the Decade 1978 to 1988: AAPG Memoir, vol. 54, pp. 55–72.
Ervine, W.B., Bell, J.S., 1987. Subsurface in situ stress magnitudes from oil-well drilling records: an example from the Venture area, offshore Eastern Canada. Can. J. Earth Sci. 24, 1748–1759.

Flemings, P.B., Stump, B.B., Finkbeiner, T., Zoback, M., 2002. Flow focusing in overpressured sandstones: theory, observations, and applications. Am. J. Sci. 302, 827–855.
Freed, R.L., Peacor, D.R., 1989. Geopressured shale and sealing effect of smectite to illite transition. AAPG (Am. Assoc. Pet. Geol.) Bull. 73, 1223–1232.
Gaarenstroom, L., Tromp, R.A.J., De Jong, M.C., Brandenburg, A.M., 1993. Overpressures in the North Sea: implications for trap integrity. In: Parker, J.R. (Ed.), Petroleum Geology of Northwest Europe: Proceedings of the 4th Conference. Geological Society of London, pp. 1305–1314.
Hao, F., Zou, H., Gong, Z., Yang, S., Zeng, Z., 2007. Hierarchies of overpressure retardation of organic matter maturation: case studies from petroleum basins in China. AAPG Bull. 91 (10), 1467–1498.
Heppard, P.D., Cander, H.S., Eggertson, E.B., 1998. Abnormal pressure and the occurrence of hydrocarbons in offshore Eastern Trinidad, West Indies. In: Law, B.E., Ulmishek, G.F., Slavin, V.I. (Eds.), Abnormal Pressures in Hydrocarbon Environments: AAPG Memoir, vol. 70, pp. 215–246.
Hoesni, M.J., 2004. Origins of Overpressure in the Malay Basin and Its Influence on Petroleum Systems. Ph.D. thesis, Durham University.
Holand, P., Skalle, P., 2001. Deepwater Kicks and BOP Performance. SINTEF Report for U.S. Minerals Management Service.
Holm, G.M., 1998. Distribution and origin of overpressure in the Central Graben of the North Sea. In: Law, B.E., Ulmishek, G.F., Slavin, V.I. (Eds.), Abnormal Pressures in Hydrocarbon Environments: AAPG Memoir, vol. 70, pp. 123–144.
Hunnur, A.T., 2006. Smectite to Illite Transformation: Relevance to Pore Pressure in the Subsurface. M.S. thesis, University of Oklahoma.
Hunt, J.M., 1996. Petroleum Geochemistry and Geology, second ed. W. H. Freeman and Co, New York, p. 743.
Hunt, J.M., 1990. Generation and migration of petroleum from abnormally pressured fluid compartments. AAPG (Am. Assoc. Pet. Geol.) Bull. 74 (1), 1–12.
Hunt, J.M., Whelan, J.K., Eglinton, L.B., Cathles III, L.M., 1998. Relation of shale porosities, gas generation, and compaction to deep overpressures in the U. S. Gulf Coast. In: Law, B.E., Ulmishek, G.F., Slavin, V.I. (Eds.), Abnormal Pressures in Hydrocarbon Environments: AAPG Memoir, vol. 70, pp. 87–104.
Katahara, K., 2006. Overpressure and shale properties: stress unloading or smectite–illite transformation? In: Expanded Abstracts, 76th SEG Annual Meeting, New Orleans, 1–6 October, pp. 1520–1524.
Lahann, R.W., McCarty, D.K., Hsieh, J.C.C., 2001. Influence of clay diagenesis on shale velocities and fluid-pressure. OTC 13046.
Lahann, R.W., Swarbrick, R.E., 2011. Overpressure generation by load transfer following shale framework weakening due to smectite diagenesis. Geofluids 11, 362–375.
Lambert, B., Duval, B.C., Grosjean, Y., Umar, I.M., Zaugg, P., 2003. The Peciko case history: impact of an evolving geological model on the dramatic increase of gas reserves in the Mahakam Delta. In: Halbouty, M.T. (Ed.), Giant Oil and Gas Fields of the Decade 1990–1999, vol. 78. American Association of Petroleum Geologists Memoir, pp. 297–320.
Leonard, R.C., 1993. Distribution of sub-surface pressure in the Norwegian Central Graben and applications for exploration. In: Parker, J.R. (Ed.), Petroleum Geology of the Northwest Europe: Proceedings of the 4th Conference. Geological Society of London, pp. 1295–1303.
Law, B.E., 1984. Relationships of source rocks, thermal maturity, and overpressuring to gas generation and occurrence in low permeability Upper Cretaceous and lower Tertiary rocks, Greater Green River basin, Wyoming, Colorado, and Utah. In: Woodward, et al.

(Eds.), Hydrocarbon Source Rocks of the Greater Rocky Mountain Region: Rocky Mountain Association of Geologists Guidebook, pp. 469–490.
Law, B.E., Dickinson, W.W., 1985. Conceptual model for origin of abnormal pressured gas accumulation in low permeability reservoirs. AAPG (Am. Assoc. Pet. Geol.) Bull. 69, 1295–1304.
Law, B.E., 2002. Basin-centered gas systems. AAPG (Am. Assoc. Pet. Geol.) Bull. 86 (11), 1891–1919.
Law, B.E., Spencer, C.W., 1998. Abnormal pressures in hydrocarbon environments. In: Law, B.E., Ulmishek, G.F., Slavin, V.I. (Eds.), Abnormal Pressures in Hydrocarbon Environments: AAPG Memoir, vol. 70, pp. 1–11.
Li, L., Wu, J., Long, X., Lian, Z., 2008. Study and it application of tectonic stress distribution in Xinchang field, western Sichuan. Nat. Gas. Ind. 28 (9), 1–3 (in Chinese).
Madon, M., 2004. Overpressure history of the Malay Basin, offshore Peninsular Malaysia. In: Petroleum Geology Conf. & Exhib, December 15–16, 2006, Malaysia.
Madon, M., 2007. Overpressure development in rift basins: an example from the Malay Basin, offshore Peninsular Malaysia. Petrol. Geosci. 13, 169–180.
Meissner, F.F., 1978a. Petroleum geology of the Bakken Formation, Williston Basin, North Dakota and Montana. In: 24th Annual Conference, Williston Basin Symposium. Montana Geological Society, pp. 207–227.
Meissner, F.F., 1978b. Patterns of source rock maturity in non-marine source rocks of some typical Western interior basins. In: Nonmarine Tertiary and Upper Cretaceous Source Rocks and the Occurrence of Oil and Gas in West-Central U.S.: Rocky Mountain Association of Geologists Continuing Education Lecture Series, pp. 1–37.
Mouchet, J.-C., Mitchell, A., 1989. Abnormal Pressures While Drilling. TECHNIP, Paris.
Nelson, H.N., Bird, K.J., 2005. Porosity-Depth Trends and Regional Uplift Calculated from Sonic Logs, National Reserve in Alaska. Scientific Investigation Report 2005-5051. U.S. Dept. of the Interior and USGS.
Oudin, J.L., Picard, P.F., 1982. Genesis of hydrocarbons in Mahakam Delta and the relationship between their distribution and the overpressured zone. In: Indonesian Petroleum Association, Proceedings 11th Annual Convention, pp. 181–202.
Pinkston, F.W.M., 2018. Pore Pressure and Stress at the Macondo Well, Mississippi Canyon, Gulf of Mexico. M.S. thesis, The University of Texas at Austin.
Powley, D.E., 1990. Pressures and hydrogeology in petroleum basins. Earth Sci. Rev. 29, 215–226.
Reilly, M.J., Zhang, J., 2015. Overpressure generation mechanism accounting for clay diagenesis and gas-charging in North Malay Basin. Extended Abstract and Presentation, Geopressure 2015, Durham University.
Ramdhan, A.M., 2010. Overpressure and Compaction in the Lower Kutai Basin, Indonesia. Doctoral thesis, Durham University.
Sandrea, R., Sandrea, I., 2014. New well-productivity data provides us shale potential insights. Oil Gas J. 112 (11). Nov. 3, 2014.
Satti, I.A., Ghosh, D., Yusoff, W., Hoesni, M.J., 2015. Origin of overpressure in a field in the Southwestern Malay Basin. Paper SPE 176034. SPE Drilling & Completion.
Shariff, K.M., Leslie, W.C., 1995. Occurrence, origin and implications of overpressure in the Malay and Penyu basins, offshore Malaysia. Bull. Geol. Soc. Malays. 37, 191–204.
Skalle, P., Podio, A.L., 1998. Trends extracted from 1,200 Gulf Coast blowouts during 1960–1996. World Oil. June, 67–72.
Singh, I., Ford, C.H., 1982. The occurrence, causes and detection of abnormal pressure in the Malay Basin. Paper SPE 10463 presented at the Offshore South East Asia 82 Conference, Singapore.

Spencer, C.W., 1987. Hydrocarbon generation as a mechanism for overpressuring in Rocky-Mountain region. AAPG (Am. Assoc. Pet. Geol.) Bull. 71, 368–388.
Swarbrick, R.E., Osborne, M.J., 1998. Mechanisms that generate abnormal pressures: an overview. In: Law, B.E., Ulmishek, G.F., Slavin, V.I. (Eds.), Abnormal Pressures in Hydrocarbon Environments: AAPG Memoir, vol. 70, pp. 13–34.
Sweeney, J.J., Braun, R.L., Burnham, A.K., Talukdar, S., Vallejos, C., 1995. Chemical kinetic model of hydrocarbon generation, expulsion, and destruction applied to the Maracaibo Basin, Venezuela. AAPG (Am. Assoc. Pet. Geol.) Bull. 79, 1515–1532.
Theloy, C., 2014. Integration of Geological and Technological Factors Influencing Production in the Bakken Play, Williston Basin. Ph.D. thesis, Colorado School of Mines, Golden, CO.
Tingay, M.R.P., Hillis, R.R., Swarbrick, R.E., Morley, C.K., Damit, A.R., 2009. Origin of overpressure and pore-pressure prediction in the Baram province, Brunei. AAPG (Am. Assoc. Pet. Geol.) Bull. 93 (1), 51–74.
Tingay, M.R., Morley, C.K., Laird, A., Limpornpipat, O., Krisadasima, K., Pabchanda, S., Macintyre, H.R., 2013. Evidence for overpressure generation by kerogen-to-gas maturation in the northern Malay Basin. AAPG (Am. Assoc. Pet. Geol.) Bull. 97 (4), 639–672.
Tissot, B.P., Welte, D.H., 1984. Petroleum Formation and Occurrence, second rev. ed. Springer-Verlag, Berlin. 699 pp.
Tobin, H.J., Saffer, D.M., 2009. Elevated fluid pressure and extreme mechanical weakness of a plate boundary thrust, Nankai Trough subduction zone. Geology 37 (8), 679–682.
Tosaya, C.A., 1982. Acoustical Properties of Clay Bearing Rocks. Ph.D. dissertation, Stanford University.
Trembath, C., Elliott, L., Pitkin, M., 2012. The Nappamerri Trough, Cooper Basin unconventional plays: proving a hypothesis. The APPEA Journal 52 (2), 662-662.
Vernik, L., 1994. Hydrocarbon-generation-induced microcracking of source rocks. Geophysics 59 (4), 555–563.
Wade, J.A., 1991. Lithostratigraphy 11, Overpressure 1. Atlantic Geoscience Centre, Geological Survey of Canada. East Coast Basin Atlas Series: Scotian Shelf, p. 71.
Wang, C., Zeng, Z., 2011. Overview of geomechanical properties of Bakken formation in Williston Basin, North Dakota. ARMA 11-199 presented at 45th US Rock Mechanics/Geomechanics Symp.
Wheeler, J.W., 2011. Non-stratigraphic implications of barostratigraphic analysis. Presented at Geopressure 2011, Galveston, Texas.
Xia, X., Wallace, J., Du, L., 2013. Modeling of abnormal fluid pressure in unconventional plays due to uplift. URTeC-1619787 presented at Unconventional Resources Tech. Conf., Denver, CO, August 12–14.
Xie, R., 2009. Stress Interpretation and Wellbore Stability Evaluation of Xujiahe Formation of Exploration Wells in Western Sichuan Depression. Ph.D. dissertation, Chengdu University of Technology (in Chinese).
York, P., Prithard, D., Dodson, J.K., Dodson, T., Rosenberg, S., Gala, D., Utama, B., 2009. Eliminating non-productive time associated drilling trouble zone. OTC20220 presented at the 2009 Offshore Tech. Conf. Held in Houston.
Yassir, N.A., Bell, J.S., 1994. Relationships between pore pressure, stresses and present day geodynamics in the Scotian Shelf, offshore Eastern Canada. Bull. Am. Assoc. Pet. Geol. 78, 1863–1880.
Yuan, R., Jin, L., Zhu, C., Zhou, M., Vitthal, S., 2013. Vertical or horizontal? Hydraulic fracture geometry as a make or break to a tight gas field in the Western Sichuan basin. In: Int. Petroleum Technology Conf, Beijing, China, IPTC 16757.

Zhang, S., Wan, T., Chen, J., 2004. Tectonic stress field modeling and fracture prediction in T_3x^{2-4} strata in Xiaoquan-Xinchang area, western Sichuan depression. Oil Gas Geol. 25 (1), 70–74, 80.

Zhang, J., Standifird, W.B., Lenamond, C., 2008. Casing ultradeep, ultralong salt sections in deep water: a case study for failure diagnosis and risk mitigation in record-depth well. In: Paper SPE 114273.

Zhang, J., 2011. Pore pressure prediction from well logs: methods, modifications, and new approaches. Earth Sci. Rev. 108, 50–63.

Zhang, J., Wieseneck, J., 2011. Challenges and surprises of abnormal pore pressures in the shale gas formations. In: Paper SPE 145964 Presented at SPE Annual Technical Conference and Exhibition, 30 October–2 November, 2011, Denver, Colorado, USA.

Zhang, J., 2013. Effective stress, porosity, velocity and abnormal pore pressure prediction accounting for compaction disequilibrium and unloading. Mar. Petrol. Geol. 45, 2–11.

Zhang, J., Yin, S., 2017a. Real-time pore pressure detection: indicators and improved methods. Geofluids 2017, 12. Article ID 3179617.

Zhang, J., Yin, S., 2017b. Fracture gradient prediction: an overview and an improved method. Petrol. Sci. 14, 720–730.

CHAPTER 8

Pore pressure prediction and monitoring

Contents

Applied Petroleum Geomechanics
ISBN 978-0-12-814814-3
https://doi.org/10.1016/B978-0-12-814814-3.00008-3

Abstract

This chapter systematically introduces pore pressure prediction methods. Pore pressure prediction in hydraulically connected formations is studied with consideration of the centroid effect. Pore pressure elevation by hydrocarbon columns or faults is investigated to examine shallow gas flow. The commonly used methods for pore pressure prediction from well logs are reviewed. Resistivity, sonic, porosity, and d-exponent methods are modified using depth-dependent normal compaction trends for easy applications. Methods and procedures of real-time pore pressure detection and monitoring are presented. Abnormal pore pressure indicators in the real-time drilling are summarized, which can be used for identifying underbalanced drilling conditions to reduce drilling risks. Case studies in deepwater wells and shale oil and gas reservoirs illustrate how to conduct pore pressure prediction in sedimentary formations.

Keywords: Normal compaction trend; Pore pressure indicators; Pore pressure prediction; Real-time detection; Resistivity; Porosity; Velocity and transit time; Well logs.

8.1 Introduction

Numerous hydrocarbon reservoirs are situated in abnormally high pore pressure or overpressure formations. Drilling through these formations poses serious challenges and potential risks to operations, if the overpressures are not accurately predicted before drilling or while drilling. Abnormal pore pressures can greatly increase drilling nonproductive time and cause serious drilling incidents (e.g., fluid influx, pressure kick, well blowout). The ability to safely drill through abnormal pressure zones requires a multidisciplinary approach in understanding overpressure mechanisms, accurately predicting

pore pressure before drilling, and correctly detecting and interpreting abnormal pressures in the real time. Predrill pore pressure prediction can be conducted by using seismic interval velocity in the planned well location as well as using well logging and drilling data in the analog wells. In the cases of new prospects and deepwater subsalt wells, high uncertainties and serious challenges exist in the predrill prediction; therefore, real-time pore pressure detection and analysis are highly needed to reduce drilling risks.

Pore pressure analyses mainly include three aspects: predrill pore pressure prediction, pore pressure prediction while drilling (real time), and postwell pore pressure analysis (e.g., Li et al., 2012). Predrill pore pressure can be predicted using seismic interval velocity data in the planned well location, as well as using geological, well logging, and drilling data in the offset wells, as shown in Fig. 8.1. If a large uncertainty exists in the predrill prediction, real-time pore pressure detection and updates while drilling are recommended to reduce uncertainty. Real-time pore pressure detection generally relies on the following measurements and data: logging-while-drilling (LWD), measurement-while-drilling (MWD), measured pore pressure and drilling parameters, and mud logging (Fig. 8.1).

It should be noted that the seismic interval velocity and well log-based pore pressure predictions are based on the shale (mudrock) properties, and the pore pressures obtained from these methods are the pressures in shales.

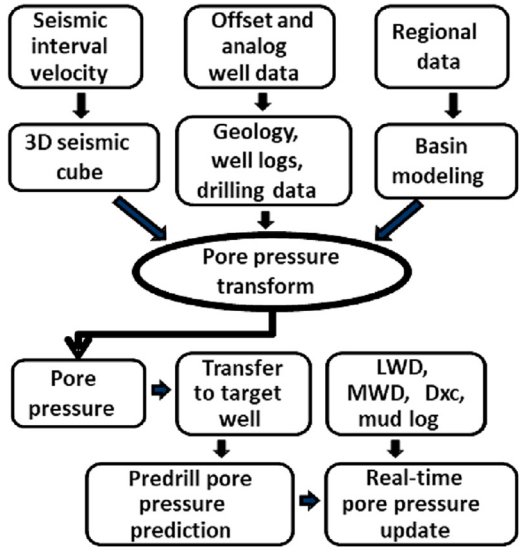

Figure 8.1 Schematic workflow for pore pressure analyses.

For a sandstone or other permeable formation, pore pressure can be obtained based on hydraulic theory by assuming that the permeable formation is hydraulically connected.

8.2 Pore pressure prediction from hydraulics

8.2.1 Pore pressure in a hydraulically connected formation

In a sandstone, limestone, or other permeable formation, the pore pressure can be obtained by assuming the formation being hydraulically connected and fully saturated, and theory of hydraulics can be applied. For an inclined aquifer or a hydrocarbon-bearing formation, if a deeper overpressured section is connected to the shallower sections by a permeable pathway, the pressures in such a hydraulically connected formation can be calculated based on the difference of the heights of fluid columns, i.e.,

$$p_2 = p_1 + \rho_f g(Z_2 - Z_1) \tag{8.1}$$

where p_1 is the formation fluid pressure at depth of Z_1; p_2 is the formation fluid pressure at depth of Z_2; ρ_f is the in situ fluid density; g is the acceleration of gravity.

Therefore, for a permeable formation if formation pressure at a certain depth is available, then the pressures at other depths can be obtained from Eq. (8.1). The calculation and principle are relatively simple. However, to perform this calculation, the connectivity and extension area of the formation need to be understood firstly. In other words, each individual fluid compartment and seal need to be distinguished, which can be determined from regional geology, well logging data and drilling data (Powley, 1990). Fig. 8.2 shows an example of calculating formation pressure in an oil-bearing sandstone using the hydraulic communication model (Eq. 8.1). When the formation pressure and fluid density in Well 1 are known, the pressures in other wells can be calculated using Eq. (8.1). If the formation is hydraulically connected and saturated with the same fluid, the formation pressures in the four wells should follow a single fluid gradient. Fig. 8.2 demonstrates that Eq. (8.1) gives an excellent prediction. Therefore, when geological structure, fluid pressure, and density in a well are known, the fluid pressures in other wells located in this hydraulically connected formation can be fairly predicted. It should be noted that the permeability magnitude and its variation may affect hydraulic connectivity of a formation. For extremely low permeable formations (e.g., shales), the applicability of Eq. (8.1) may be limited.

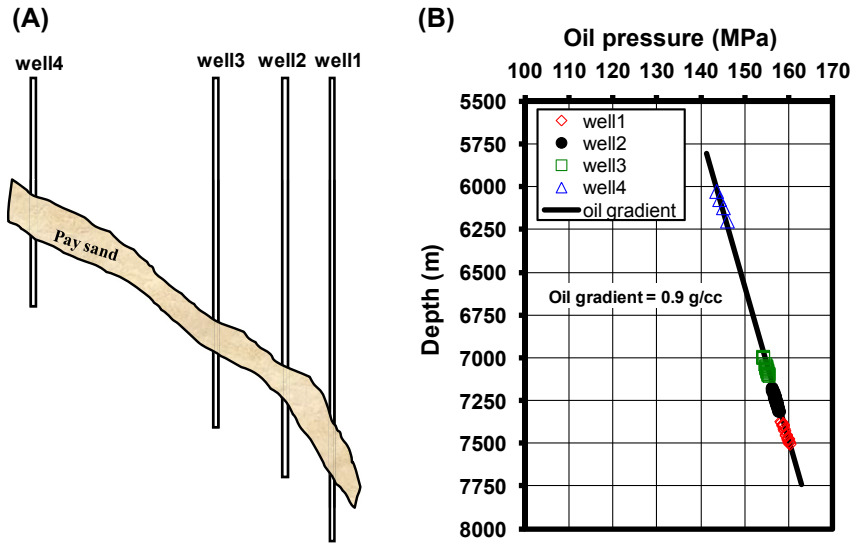

Figure 8.2 Schematic cross section (A) showing four wells in a hydraulically connected oil-bearing sandstone compartment and fluid pressures in different wells (B). Measured fluid pressures (dots) in these wells match the calculated pore pressures (line) with an oil gradient of 0.9 g/cm^3 (Zhang, 2011).

Pore pressure gradient is different in a formation when it is saturated with different fluids. In each fluid column, the pore pressure can be calculated using Eq. (8.1) with the density of the fluid saturated in this column. Fig. 8.3 displays a hydraulically connected formation filled with gas, oil, and water (brine). If fluid pressure at a depth is known; fluid densities and depths of water–oil contact (WOC) and oil–gas contact (OGC) are also known, then the pressures at other depths can be obtained by using Eq. (8.1). For instance, the gas pressure at depth A (the crest) can be obtained from the following equation:

$$p_A = p_B - \rho_g g(Z_B - Z_A) \tag{8.2}$$

where ρ_g is the in situ gas density; p_B is the pore pressure at depth B; p_A is the pore pressure at depth A.

At depth B (oil–gas contact), the oil pressure can be obtained from the following equation:

$$p_B = p_C - \rho_o g(Z_C - Z_B) \tag{8.3}$$

where ρ_o is the in situ oil density; p_C is the pore pressure at depth C.

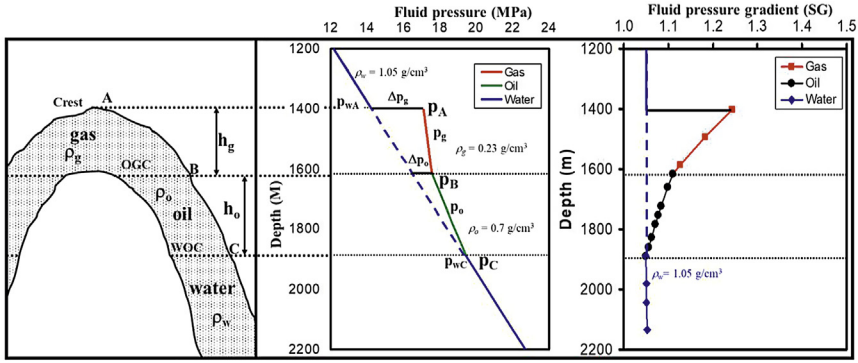

Figure 8.3 A schematic reservoir saturated with gas, oil and water (left), pore pressure (middle), and pore pressure gradient (right) elevated by oil and gas columns and density contrast between water, oil, and gas in a reservoir. This density contrast causes pore pressure increase at depth A compared to the one caused only by water gradient (Zhang, 2011).

If the formation is only saturated with water, then the pressure at depth A is:

$$p_{wA} = p_C - \rho_w g(Z_C - Z_A) \tag{8.4}$$

Comparing the pressure (p_A) in the crest to the water pressure (p_{wA}) at the same depth, the pore pressure increment induced by oil and gas columns in the crest (depth A in Fig. 8.3) can be expressed in the following form (i.e., $\Delta p_{og} = p_A - p_{wA}$):

$$\Delta p_{og} = (\rho_w - \rho_o)gh_o + (\rho_w - \rho_g)gh_g \tag{8.5}$$

where Δp_{og} is the pore pressure increment induced by oil and gas columns; ρ_w is the in situ water (brine) density; h_g is the height of gas column; h_o is the height of oil column.

It should be noted that gas density is highly dependent on pressure. Therefore, the in situ gas density should be used for the calculations. Normally, the gas column height is not very large; hence, in the aforementioned equations gas density is assumed to be a constant value.

The pore pressure elevation (Δp_{og} in Eq. 8.5) is caused by hydrocarbon buoyancy effect due to density contrasts between the hydrocarbon and water. The pressure elevation due to the difference in densities gradually decreases from the maximum value at the top of the reservoir to zero at the water and hydrocarbon contact.

8.2.2 Shallow gas flow and pore pressure elevation by gas columns

When a sandstone, or other permeable formation (called "sand" in the context) at a shallower depth A is connected to a deeper gas formation at depth B by a permeable (leaking) fault (as shown in Fig. 8.4), the fault increases the gas column in the shallower sand. Therefore, the pore pressure at depth A induced by gas column can be calculated from Eq. (8.2). Expressed in the English system, it has:

$$p_A = p_B - \rho_g(Z_B - Z_A) \tag{8.6}$$

where p_A and p_B are the pore pressures at depths A and B, in psi; ρ_g is the in situ gas density, in psi/ft; and depths are in ft.

Fig. 8.5 illustrates that gas pressure at a shallower depth (2700 ft) is elevated by a deeper gas sand formation (at 3300 ft) through a permeable fault. The pore pressure at the shallow depth increases from 8.8 ppg (normal pore pressure) to 11.9 ppg (overpressure).

Fig. 8.6 displays an example of pore pressure elevations by gas columns in two shallow gas formations. The shallower gas formation at 2750 ft has a higher gas pressure induced by a larger gas column, whereas the deeper one (at 3200 ft) with a smaller gas column has a lower gas pressure. Before drilling, identifying potential shallow gas (or shallow water) formations and accurately predicting their pore pressures can avoid shallow gas (or shallow water) flow.

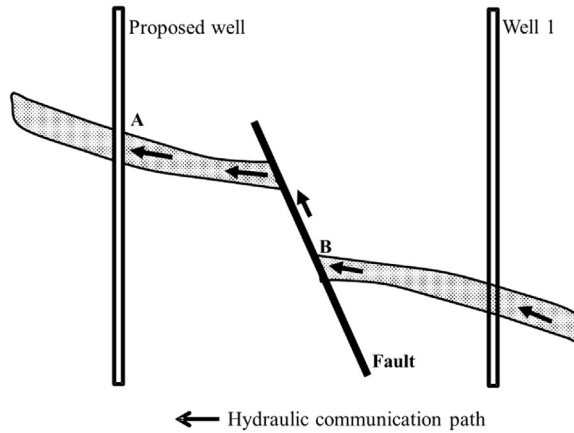

Figure 8.4 Schematic cross section showing two wells in a hydraulically connected gas-bearing sand. The pore pressure in the proposed well is elevated by the deep gas formation through a permeable fault.

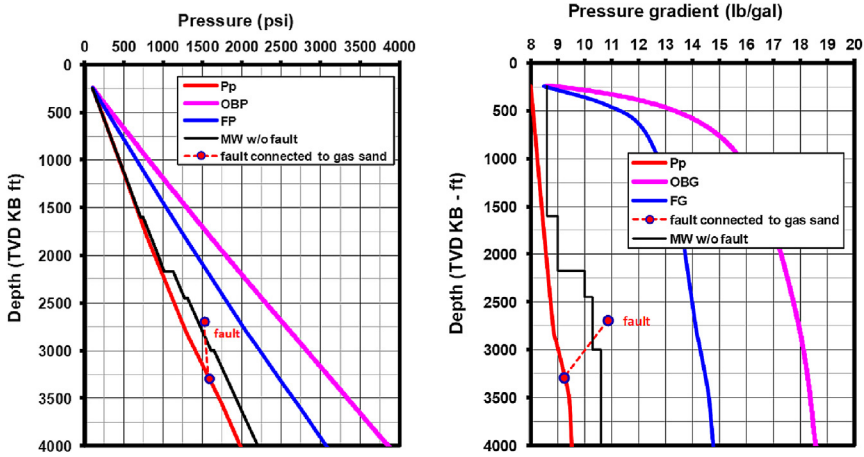

Figure 8.5 Gas pressure (left) and pressure gradient (right) elevated by a deeper gas formation through a permeable fault (see Fig. 8.4).

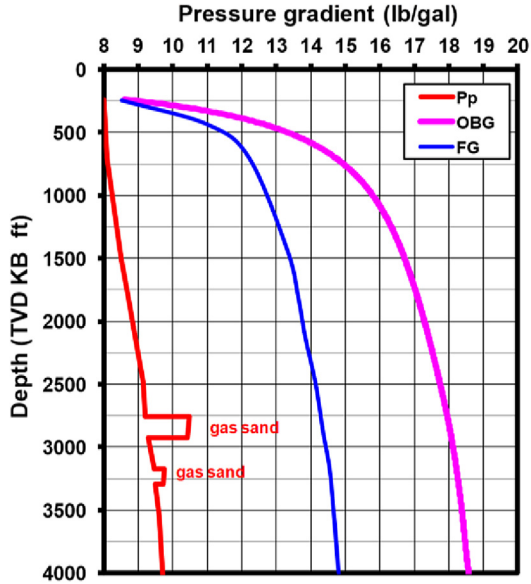

Figure 8.6 Shallow gas pore pressure gradients induced by two different gas columns.

8.2.3 Centroid effect

Pore pressure in a tilted sand encased in an overpressured shale, is different from its adjacent shale because the shale has a much lower permeability. The centroid concept arose from the observation that the shale pressure and sand pressure must follow different local gradients (Bruce and Bowers, 2002).

For a sand, its pore pressure follows a hydrostatic, oil or gas gradient depending on the fluid type it contains. The sand acts as a conduit to transfer pressures updip, as described in the previous sections. However, the shale does not. It is assumed that the shale pore pressure is caused by disequilibrium compaction and normally follows the overburden (lithostatic) stress gradient. At depth, shale pore pressure exceeds sand pore pressure. At shallow depth, however, sand pore pressure exceeds shale pore pressure. The centroid is the depth at which sand and shale pore pressures are equal (e.g., Dickinson, 1953; Traugott, 1997; Bowers, 2001; Flemings et al., 2002; Shaker, 2002). The centroid concept is an empirical method for predicting pore pressure at the crest of a tilted sand (Fig. 8.7A). This concept states that the pore pressure in the sand and its adjacent shale are only equal at one depth (Fig. 8.7B), i.e., the centroid depth, approximately at the mid height of the reservoir. Away from this point, the pore pressure in the shale is assumed to vary with depth along a lithostatic-pressure parallel gradient, which has a gentle slope (Fig. 8.7B). In shale-dominated sequences pore pressure is most likely subparallel to lithostatic-pressure gradient as the overburden is mainly supported by pore fluids rather than the grain structure in the undercompaction condition. However, in an aquifer (sand) the pore pressure variation with depth follows a hydrostatic parallel gradient, which has a steeper slope as shown in Fig. 8.7C. If the sand is a hydrocarbon-bearing reservoir, the sand pressure should be parallel to the hydrocarbon fluid gradient.

Fig. 8.8 illustrates how to apply the centroid concept to predict sand pressures in an aquifer when the wells are drilled above and below

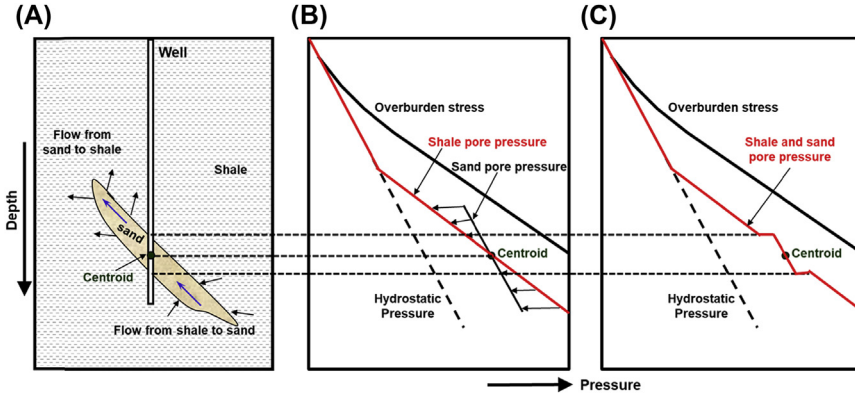

Figure 8.7 Centroid concept: (A) a tilted sand body surrounding by shales; (B) different pore pressures in the sand and shale; (C) the composite pore pressure in both sand and shale where a well penetrates the centroid.

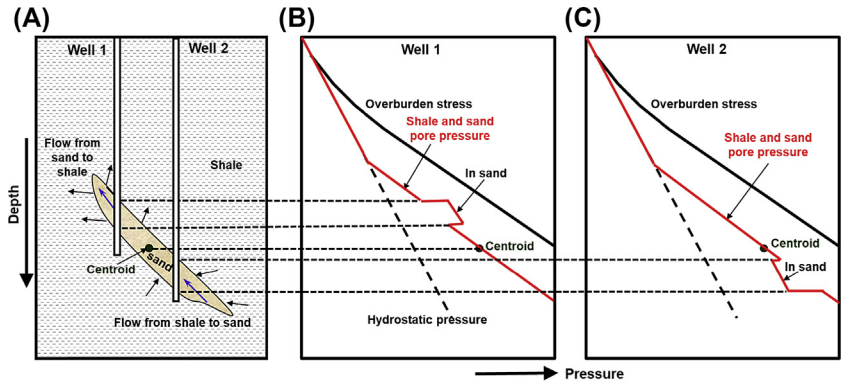

Figure 8.8 (A) Two wells drilled in a tilted sand; (B) pore pressure for the well penetrating the tilted sand above the centroid; and (C) pore pressure below the centroid.

the centroid depth. If a well is drilled in the updip of the centroid (Well 1 in Fig. 8.8A), the penetrated sand has a higher pore pressure than the shale (Fig. 8.8B). However, if a well is drilled in the downdip of the centroid (Well 2 in Fig. 8.8A), the penetrated sand has a lower pore pressure than the shale (Fig. 8.8C). The sand pressures can be calculated from Eq. (8.1) using the centroid as the reference depth. The shale pore pressure can be obtained from well log data or estimated from Eq. (8.1), but in the equation ρ_f should be replaced by overburden formation density.

Sharp pressure transitions exist at the sand–shale interface, predicted by the centroid concept in Figs. 8.7 and 8.8. However, dynamic fluid models show that there is a smooth pressure transition at the sand–shale interface. Therefore, using the centroid concept to predict sand fluid pressure may result in an overestimation of the crest pressure compared to the fluid flow model (Yardley and Swarbrick, 2000).

For applying centroid theory, the centroid depth (the equal-pressure-depth) needs to be determined. The rule of thumb of estimate assumes the centroid to be the mean elevation of the sand. Czerniak (2011) proposed a permeability weighting method of 3-D centroid modeling workflow, which allows for complex structuring and lateral changes in formation pressures. It was based on that the flow into and flow out of the sand body at the centroid were equal. Using a similar concept, a one-dimensional flow model was proposed (Gao and Flemings, 2017) to capture complicated two- and three-dimensional flow presented in a dipping permeable reservoir encased in overpressured mudrocks. In their model, the variation of mudrock permeability with effective stress and the effect of reservoir geometry were also incorporated.

8.2.4 Vertical and lateral transfer and drainage

Vertical transfer of overpressured fluid from lower sequences is mainly through faults or fractures, as shown in Figs. 8.4 and 8.5. This essentially inflates the pressures in shallow sand sequences but with no influence on the porosity. However, most pressure change in a permeable formation is caused by lateral transfer and drainage (Fig. 8.9), and the pressures in the permeable formation can be calculated by Eqs. (8.2)–(8.4). Fig. 8.10 presents a comparison of two cases with vertical transfer and lateral drainage.

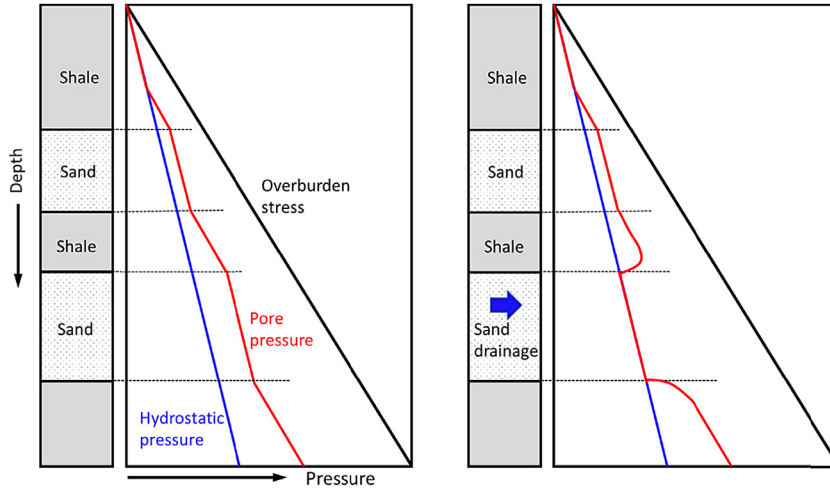

Figure 8.9 Schematic plot of pore pressures in two wells without sand pressure drainage (left) and with pressure drainage (right).

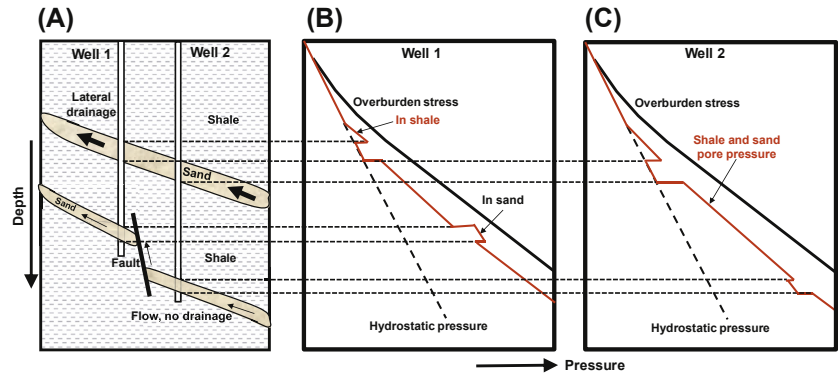

Figure 8.10 (A) Two wells drilled through tilted sands (the shallower sand with lateral drainage and the deeper one with vertical transfer); (B) sand and shale pore pressures for the wells penetrating in the updip and (C) in the downdip.

If the fluid bleeds off in the sandstone because of lateral drainage, its pore pressure could be close to hydrostatic pressure (Figs. 8.9 and 8.10). Case studies in the Green Canyon wells of the Gulf of Mexico show this behavior, i.e., owing to lateral drainage, the reservoir pressure can be very low and pressure regression occurred compared to adjacent shales and isolated sand pressures (Zhang et al., 2008; Hauser et al., 2013).

8.3 Principle of pore pressure prediction for shales

Hottmann and Johnson (1965) were probably the first ones to make pore pressure prediction from shale properties derived from well log data (acoustic travel time or velocity and resistivity). They found that porosity decreases as a function of depth from analyzing acoustic travel time (transit time) in the Miocene and Oligocene shales in the Upper Texas and Southern Louisiana Gulf Coast. This trend represents the "normal compaction trend" as a function of burial depth, and fluid pressure exhibited within this normal trend is the hydrostatic pressure. If intervals of abnormal compaction are penetrated, the resulting data points diverge from the normal compaction trend, which represents an abnormal pore pressure.

Analyzing the data presented by Hottmann and Johnson (1965), Gardner et al. (1974) proposed an equation that can be written in the following form to predict pore pressure:

$$p_f = \sigma_V - \frac{(\alpha_V - \beta)(A_1 - B_1 \ln \Delta t)^3}{Z^2} \tag{8.7}$$

where p_f is the formation fluid pressure (psi); σ_V is the overburden stress expressed in psi; α_V is the normal overburden stress gradient (psi/ft); β is the normal fluid pressure gradient (psi/ft); Z is the depth (ft); Δt is the sonic transit time (μs/ft); A_1 and B_1 are the constants, $A_1 = 82776$ and $B_1 = 15695$.

Later on, many empirical equations for pore pressure prediction were proposed based on resistivity, sonic transit time (interval velocity), and other well logging data. The fundamental theory for pore pressure prediction is Terzaghi's or Biot's effective stress law (Terzaghi et al., 1996; Biot, 1941). Based on it, pore pressure in the vertical direction in one-dimensional condition can be expressed as the following:

$$p_p = (\sigma_V - \sigma_e)/\alpha \tag{8.8}$$

where p_p is the pore pressure; σ_e is the vertical effective stress; α is the Biot effective stress coefficient. It is conventionally assumed $\alpha = 1$ in geopressure community.

Pore pressure can be calculated from Eq. (8.8) when one knows overburden and effective stresses. Overburden stress can be easily obtained from bulk density logs and empirical equations (refer to Section 6.1), while effective stress can be correlated to seismic velocity and well log data, such as resistivity, sonic transit time, seismic or sonic interval velocity, bulk density, and drilling parameters (e.g., d-exponent).

Although in situ stresses include three mutually orthogonal principal stresses, i.e., vertical, maximum horizontal, and minimum horizontal stresses (σ_V, σ_H, σ_h), it is commonly assumed that the formation compaction is mainly caused by the vertical (overburden) stress and formation undercompaction is primarily related to the vertical stress (e.g., Chapman, 1983; Osborne and Swarbrick, 1997). Therefore, the pore pressure caused by compaction and undercompaction can be calculated from Eq. (8.8). However, in a strong tectonic stress regime, horizontal stresses may play an important role in abnormal pore pressure generation. In this case, the mean stress should be used for pore pressure calculation, i.e.,

$$p_p = (\sigma_m - \sigma_e)/\alpha \tag{8.9}$$

where σ_m is the mean stress and $\sigma_m = \frac{1}{3}(\sigma_V + \sigma_H + \sigma_h)$.

In the following sections (Sections 8.4–8.6), commonly used methods of pore pressure prediction for shales are introduced, in which Eq. (8.8) is applied. For a strong tectonic stress regime, the mean stress can be used, i.e., replacing σ_V by σ_m.

8.4 Pore pressure prediction from porosity

8.4.1 Depth-dependent porosity method

As introduced in Chapter 7, undercompaction or compaction disequilibrium is the primary cause of formation overpressures, which occur mainly in rapidly subsided basins and in rocks with low permeability. The indicators of undercompaction are higher pore pressure and larger formation porosity than those in the normal compaction condition. Efforts have been made to use porosity data for predicting pore pressure in shales or mudstones. For instance, Heppard et al. (1998) used an empirical porosity equation similar to Eaton's sonic method to predict pore pressure using shale porosity data. Holbrook et al. (2005) presented a porosity-dependent

effective stress method for pore pressure prediction. Flemings et al. (2002) and Schneider et al. (2009) also applied porosity–stress relationships to predict overpressures in mudstones.

Porosity change is an indicator of effective stress and pore pressure, particularly for the overpressures generated from undercompaction (as shown in Fig. 7.6) and hydrocarbon cracking. Therefore, pore pressure can be estimated from formation porosity. Zhang (2011) derived a theoretical equation for pore pressure prediction from porosity based on normal compaction trend of porosity. The pore pressure gradient can be calculated from the following equation (refer to Appendix 8.1 for details):

$$P_{pg} = \left[OBG - (OBG - P_{ng}) \frac{\ln \phi_0 - \ln \phi}{cZ} \right] \tag{8.10}$$

where P_{pg} and P_{ng} are the pore pressure and normal pore pressure gradients, respectively (normally $P_{ng} = 0.45$ psi/ft or 1.03 g/cm^3, dependent on water salinity); OBG is the overburden gradient; ϕ is the porosity in shale at depth of Z, which can be obtained from sonic or density log; ϕ_0 is the porosity of the mudline (the surface or sea floor); Z is the depth below the mudline; c is the compaction constant and can be obtained from the normal compaction porosity (ϕ_n) trendline (i.e., from the following equation), as shown in Fig. 7.6.

$$\phi_n = \phi_0 e^{-cZ} \tag{8.11}$$

From Eq. (8.10) the pore pressure, overburden stress, and porosity have the following relation:

$$p_p = \left[\sigma_V - (\sigma_V - p_n) \frac{\ln \phi_0 - \ln \phi}{cZ} \right] \tag{8.12}$$

where p_p is the pore pressure; σ_V is the overburden stress; p_n is the normal pore pressure.

The primary difference between Eq. (8.12) and other existing pore pressure–porosity equations is that the pressures obtained from Eq. (8.12) are dependent on depth. In other words, the normal compaction trendline of porosity is a function of depth.

8.4.2 Case application of the porosity method

A case study is examined to illustrate the porosity method presented in Eq. (8.10). It is a deepwater field located in the Green Canyon of the Gulf

of Mexico, USA. The water depth is about 5000 ft, and the formations are mainly shales with some sandstones. The target reservoir is located in the Miocene sandstones. Several offset wells are analyzed to examine pore pressures in this field. An important step in performing pore pressure analysis is to select the clean shales in well log data because pore prediction theory is based on the undercompaction mechanism of shale. Before applying the porosity model, one needs to obtain the shale porosity from density log or sonic log. Clay minerals have a crystalline structure that can contain more radioactive elements than sandstones. Therefore, gamma ray data in well logs can be used to differentiate shale intervals from those of other lithologies. Drawing shale base lines in gamma ray data is the first step to identify and separate shale from other rocks, as shown in Fig. 8.11. The high gamma ray values (>75−110 API) are assumed to be shales, whereas points where gamma ray values are less than the shale base lines are not used for analysis. Shale points defined on the gamma ray log are then transferred to the corresponding well log data used for pore pressure analysis (KSI, 2001).

In Fig. 8.11, porosity is calculated from the shale transit time from Wyllie's equation (Eq. 2.7) using $\Delta t_f = 200$ μs/ft and $\Delta t_m = 70$ μs/ft. Using

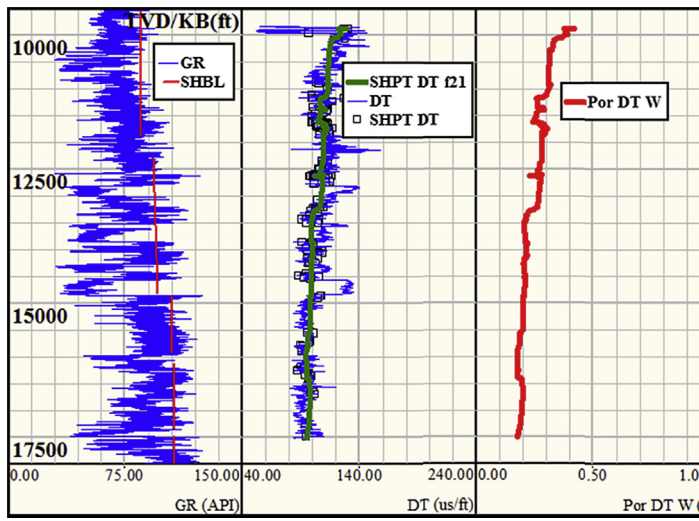

Figure 8.11 Log data and the calculated porosity from sonic transit time by Wyllie's equation in a deepwater well of the Gulf of Mexico. The gamma ray (GR) and shale base lines (SHBL) are shown in the left track; the sonic transit time (DT), shale points of the transit time (SHPT DT), and filtered shale transit time in shale (SHPT DT f21) are plotted in the middle track; and the calculated porosity from the filtered shale transit time is shown in the right track.

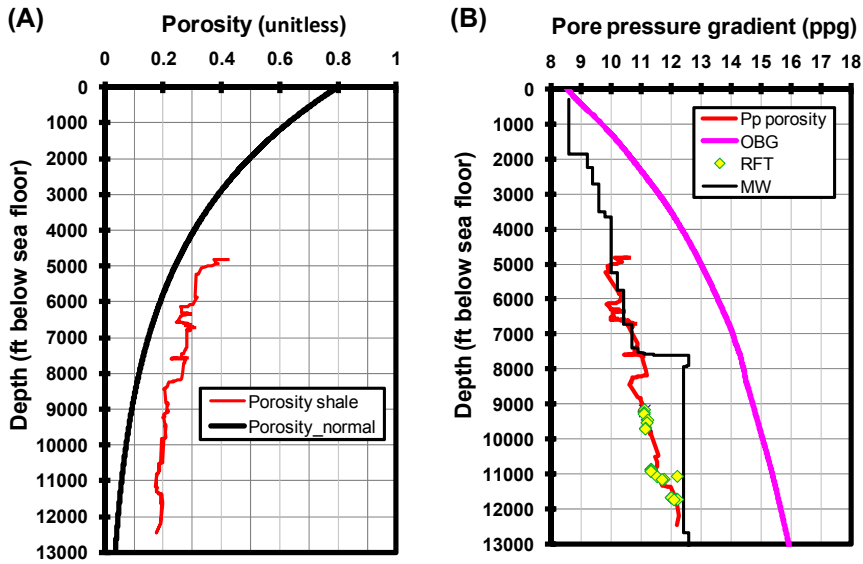

Figure 8.12 Pore pressure analysis from the porosity method. (A) presents porosity of shales obtained from Fig. 8.11 and normal compaction trendline of porosity calculated from Eq. (8.11). (B) plots overburden stress gradient (OBG), mud weight used while drilling (MW), measured pore pressure (RFT), and pore pressure profile calculated from the porosity by Eq. (8.10).

this porosity data, the normal compaction trend in porosity is analyzed based on Eq. (8.11) with the parameters of $\phi_0 = 0.8$ and $c = 0.00024$, as shown in Fig. 8.12A. Then, pore pressure gradient is calculated from the porosity model (Eq. 8.10) with parameters (ϕ_0 and c) obtained from Fig. 8.12A (assuming $P_{ng} = 8.7$ ppg). The calculated pore pressure gradient is compared to the measured pore pressure from the repeat formation tests (RFT) and mud weight, as shown in Fig. 8.12B. The porosity method gives a good result in terms of matching measured pore pressures.

Fig. 8.13 presents another example for pore pressure analysis using porosity data in the Bossier and Haynesville shale gas plays. In the figure, the porosity is obtained from density log and calibrated to the core data, and Eq. (8.11) is used for the normal compaction porosity trend line with the parameters of $\phi_0 = 0.5$ and $c = 0.00036$. The calculated pore pressure increases from the Sligo to Hosston formations because of a higher porosity than the normal trend. In the Bossier or Haynesville shale, the porosity is significantly higher than the normal porosity trend and hard overpressure exists. Pore pressures obtained from the porosity method and sonic method have a similar result and match the kick data.

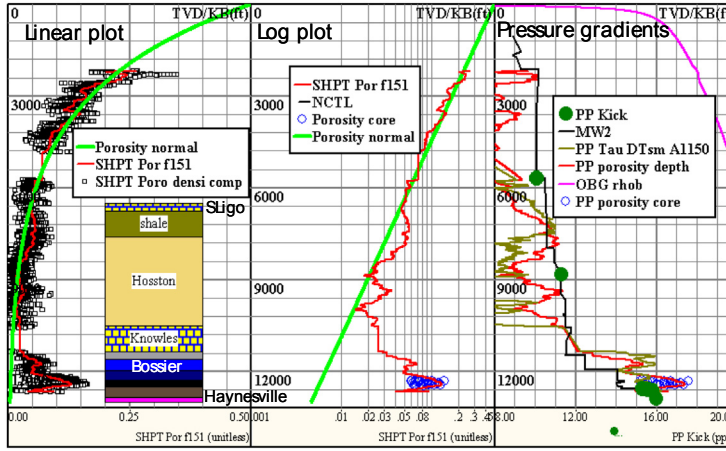

Figure 8.13 Pore pressure estimations from porosity and sonic log with comparison to kick data. The porosity data are shown in the left and middle tracks. The right track presents the pore pressure profiles calculated from the porosity method by Eq. (8.10) (red curve) and from the sonic log compared to mud weight and kicks (dots) (Zhang and Wieseneck, 2011).

8.5 Pore pressure prediction from resistivity

8.5.1 Eaton's resistivity method

Shale resistivity can be used to calculate pore pressure. The general rule is that a low resistivity corresponds with a high pore pressure. In young sedimentary basins where undercompaction is the major cause of overpressure (e.g., the Gulf of Mexico and the North Sea), the well log-based resistivity method can fairly predict pore pressure. Eaton (1972, 1975) presented the following equation to predict pore pressure gradient in shales using resistivity log:

$$P_{pg} = OBG - (OBG - P_{ng})\left(\frac{R}{R_n}\right)^n \tag{8.13}$$

where R is the shale resistivity obtained from well log; R_n is the shale resistivity at the normal (hydrostatic) pressure; n is an exponent varied from 0.6 to 1.5, and normally $n = 1.2$.

Eaton's resistivity method is particularly applicable in pore pressure prediction for geologically young sedimentary basins (e.g., Lang et al., 2011), if the normal shale resistivity is properly determined. For applying Eaton's method, R_n is an important parameter needed to be obtained; therefore, the normal compaction trendline needs to be accurately determined.

8.5.2 Modified Eaton's resistivity method

In Eaton's original equation, it is difficult to determine the normal shale resistivity or the shale resistivity in the condition of hydrostatic pore pressure (i.e. resistivity normal compaction trend). One approach is to assume that the normal shale resistivity is a constant. However, the normal resistivity (R_n) is not a constant in most cases, but a function of the burial depth, as shown in Fig. 8.14. Thus the normal compaction trendline needs to be determined for pore pressure prediction.

Based on the relationship of measured resistivity and burial depth in the formations with normal pressures, the following equation of the normal compaction trend of resistivity was proposed (Zhang, 2011):

$$\ln R_n = \ln R_0 + bZ$$

or

$$R_n = R_0 e^{bZ} \tag{8.14}$$

where R_n is the shale resistivity in the normal compaction condition; R_0 is the shale resistivity of the mudline; Z is the depth below the mudline; b is the slope of logarithmic resistivity in the normal compaction trendline (Fig. 8.14).

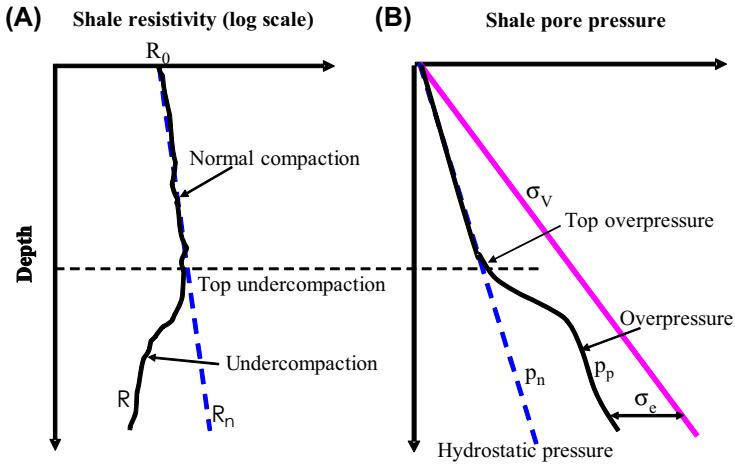

Figure 8.14 Schematic plot showing resistivity and pore pressure relationship in an undercompacted basin. The dash line in (A) represents the resistivity in normally compacted formation (normal resistivity, R_n). In the undercompacted section the resistivity (R) reversal occurs, corresponding to an overpressured formation in (B). In the undercompacted (overpressured) section, resistivity (R) is lower than the normal compaction trend (R_n).

Substituting Eq. (8.14) into Eq. (8.13), the depth-dependent Eaton's resistivity equation can be expressed in the following form:

$$P_{pg} = OBG - (OBG - P_{ng})\left(\frac{R}{R_0 e^{bZ}}\right)^n \tag{8.15}$$

The same case study as shown in Figs. 8.11 and 8.12 is used to verify the modified Eaton's resistivity method. Fig. 8.15 shows the pore pressure postwell analysis from the modified Eaton's resistivity method (Eq. 8.15). Before the pore pressure analysis, the normal resistivity compaction trend is firstly analyzed based on Eq. (8.14), as shown in Fig. 8.15A. With calibration of the measured pore pressure data, the normal compaction trendline is obtained with the following parameters in this basin: $R_0 = 1.28$ ohms, $b = 0.000034$. Pore pressure calculated from the modified Eaton's method (Eq. 8.15 with $n = 1.2$, $P_{ng} = 8.7$ ppg) is compared to the measured pore pressures and downhole mud weight. Fig. 8.15 indicates that the formation is in normal compaction when depth is less than 4900 ft below the sea floor. Deeper than this depth (from 4900 to 7600 ft), the

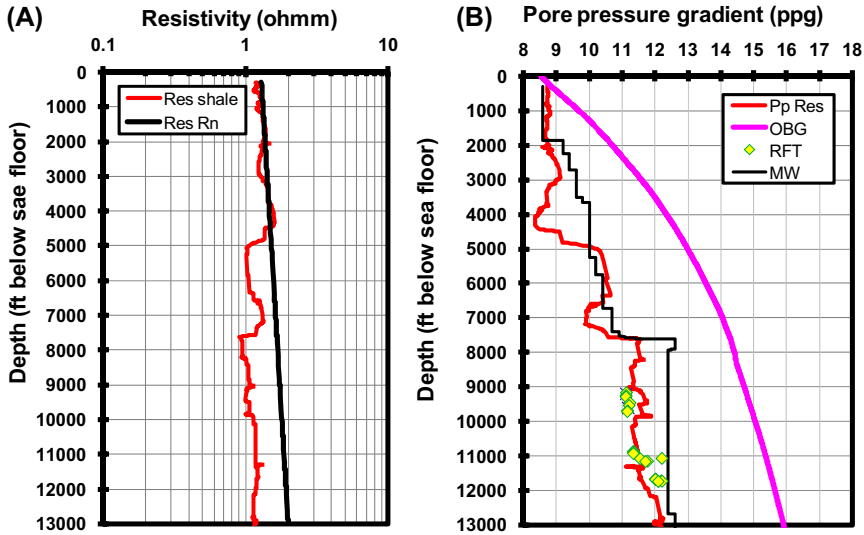

Figure 8.15 Pore pressure calculated from the modified Eaton's resistivity method with depth-dependent compaction trend in a deepwater well in the Gulf of Mexico. The left figure (A) plots the resistivity in shale and the normal resistivity trend calculated from Eq. (8.14), and the resistivity is plotted in logarithmic scale. The right figure (B) shows the overburden stress gradient (OBG), mud weight used while drilling (MW), measured pore pressure gradient (RFT), and pore pressure gradient (Pp Res) calculated from resistivity using Eq. (8.15).

formation is slightly undercompacted with a lower resistivity than the normal compaction trend (Fig. 8.15A), implying that the pore pressure increases, as shown in Fig. 8.15B. From 7600 to 13000 ft, the formation is further undercompacted and more elevated pore pressures exist. Compared to the measured pore pressure, the modified Eaton's resistivity method gives a fairly good result in pore pressure calculation (Fig. 8.15B).

It should be noted that the pore pressure and rock properties in the formation near the wellbore are affected by drilling-induced stresses. Therefore, the deep resistivity is needed for pore pressure calculation.

8.5.3 From Archie's resistivity equation

Because formation resistivity is an indicator of porosity, it can be used for pore pressure calculation. Archie's resistivity equation for a fully water-saturated rock can be written as the following:

$$S_w^n = \frac{a}{\phi^m}\frac{R_w}{R_t} = 1 \tag{8.16}$$

where R_w and R_t are the formation water resistivity and measured formation resistivity, respectively; a, m, and n are constants needed to be determined for a particular field; for shales, normally $a = 1$.

The porosity can be derived from Eq. (8.16) as the following form:

$$\phi = \left(\frac{aR_w}{R_t}\right)^{\frac{1}{m}} \tag{8.17}$$

Similarly, the porosity at depth of the mudline can be obtained:

$$\phi_0 = \left(\frac{aR_{w0}}{R_0}\right)^{\frac{1}{m}} \tag{8.18}$$

where R_{w0} and R_0 are the formation water resistivity and measured formation resistivity at the mudline, respectively.

Substituting the above two equations into porosity equation Eq. (8.12) by assuming $a = 1$, the following equation can be derived:

$$p_p = \left[\sigma_V - (\sigma_V - p_n)\frac{(\ln R_t - \ln R_0) + (\ln R_{w0} - \ln R_w)}{kZ}\right] \tag{8.19}$$

where $k = cm$, a new constant need to be determined for a particular field; R_0 can be obtained from Eq. (8.14) or from the normal compaction trendline.

8.5.4 Resistivity corrections from temperature and salinity

Resistivity changes with temperatures. Because formation temperatures vary with depths, formation resistivity should be corrected to a common temperature before applying for pore pressure prediction. Formation resistivity may be corrected by use of a chart found in most logging manuals or by the following empirical equation (Arp, 1953):

For temperature unit of Fahrenheit:

$$R_2 = R_1 \frac{T_1 + 6.77}{T_2 + 6.77} \tag{8.20}$$

where R_1 is the measured formation resistivity at temperature T_1 (°F); R_2 is the corrected formation resistivity; T_1 is the measured formation temperature (°F); T_2 is the desired common temperature (normally $T_2 = 70$ or 100°F).

For the temperature unit in Centigrade or Celsius:

$$R_2 = R_1 \frac{T_1 + 21.5}{T_2 + 21.5} \tag{8.21}$$

Formation salinity has impacts on the resistivity response, which also affects accuracy of resistivity-based pore pressure prediction. For example, resistivity may not be useful near salt bodies because of the potential for highly varying salinity (R_w). Salinity profile with depth can be computed from well log data (Revil et al., 1998). If large salinity variations exist with depth, resistivity should be corrected for pore pressure prediction purpose.

8.6 Pore pressure prediction from velocity and transit time

Shale velocity either from sonic log or seismic survey can be used to predict pore pressure generated by compaction disequilibrium because the velocity is a good indicator of porosity. The general rule is that a lower velocity (higher transit time) corresponds to a higher pore pressure.

In the sonic log, interval transit time is a more popular form to represent the velocity. The compressional transit time is the inverse of the compressional velocity and can be expressed in the following form:

$$V_p = \frac{10^6}{\Delta t} \tag{8.22}$$

where V_p is the compressional interval velocity in ft/s; Δt is the compressional transit time in μs/ft.

8.6.1 Eaton's method and its improvement

8.6.1.1 Eaton's method

Eaton (1975) proposed the following empirical equation for pore pressure gradient prediction from sonic compressional transit time:

$$P_{pg} = OBG - (OBG - P_{ng})\left(\frac{\Delta t_n}{\Delta t}\right)^n \tag{8.23}$$

where n is an exponent, and normally $n = 3$; Δt_n is the sonic compressional transit time or slowness in shales at the normal pressure conditions; Δt is the sonic transit time in shales obtained from sonic log, and it can also be derived from seismic interval velocity.

This method is applicable in some petroleum basins, but it does not consider unloading effects. This limits its application in geologically complicated area, such as formations with uplifts. To apply this method, the normal transit time (Δt_n) needs to be determined.

8.6.1.2 Modified Eaton's method

Eaton's equation can be rewritten in terms of the effective stress and velocity by converting the transit time to the velocity via Eq. (8.22):

$$\frac{\sigma}{\sigma_N} = \left(\frac{V}{V_N}\right)^n \tag{8.24}$$

where V is the measured compressional velocity; V_N is the compressional velocity under normal pore pressure; σ is the effective stress; σ_N is the effective stress under normal pressure condition.

Katahara (2003) pointed out that Eaton's method, Eq. (8.24), is unphysical at low effective stress condition. From Eaton's equation (Eq. 8.24), clearly $\sigma = 0$ only if $V = 0$. In water-saturated sediments, at a low effective stress the velocity V will approach a value close to the water compressional velocity, rather than 0; therefore, Eaton's method is incorrect in this limit. One modification that gives the correct low-stress limit is to subtract the zero-stress velocity, V_{mud} (mudline velocity) from both numerator and denominator on the right-hand side of Eq. (8.24) (Katahara, 2003):

$$\frac{\sigma}{\sigma_N} = \left(\frac{V - V_{mud}}{V_N - V_{mud}}\right)^m \tag{8.25}$$

where m is an exponent.

Zhang (2011) proposed a modified Eaton's method for calculating pore pressure gradient using depth-dependent normal compaction trendline, i.e.,

$$P_{pg} = OBG - (OBG - P_{ng})\left(\frac{\Delta t_m + (\Delta t_{ml} - \Delta t_m)e^{-cZ}}{\Delta t}\right)^n \tag{8.26}$$

where Δt_m is the compressional transit time in the shale matrix (normally 65 μs/ft); Δt_{ml} is the transit time of the mudline (normally 200 μs/ft); Z is the depth below the mudline; c is the compaction constant.

The normal compaction trend (Δt_n) in this modified Eaton's method decreases exponentially with depth in the following form, as illustrated in Fig. 8.16, (refer to Appendix 8.2 for derivation):

$$\Delta t_n = \Delta t_m + (\Delta t_{ml} - \Delta t_m)e^{-cZ} \tag{8.27}$$

where Δt_n is the transit time of shales in the normal pressure (normal compaction) condition.

This normal compaction trend allows the normal transit time to approach the matrix transit time at a very large depth, which is physically correct as Chapman (1983) pointed out. A similar normal compaction trend for shale acoustic transit time with depth in the Carnarvon Basin was established by fitting an exponential relationship to averaged acoustic transit times from 17 normally pressured wells (van Ruth et al., 2004):

$$\Delta t_n = 225 + 391e^{-0.00103Z}$$

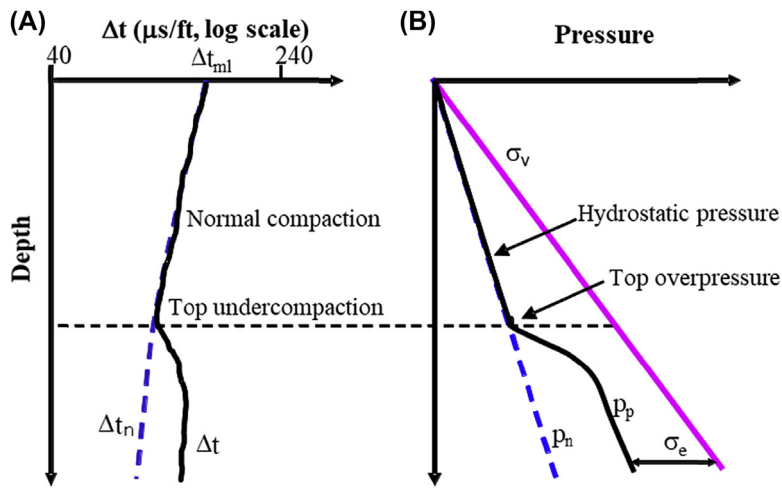

Figure 8.16 Schematic diagram showing (A) sonic transit time (Δt) measured in shale, the normal compaction trend of the transit time in the normal pressure condition (Δt_n) and (B) the pore pressure response to the transit time (Δt).

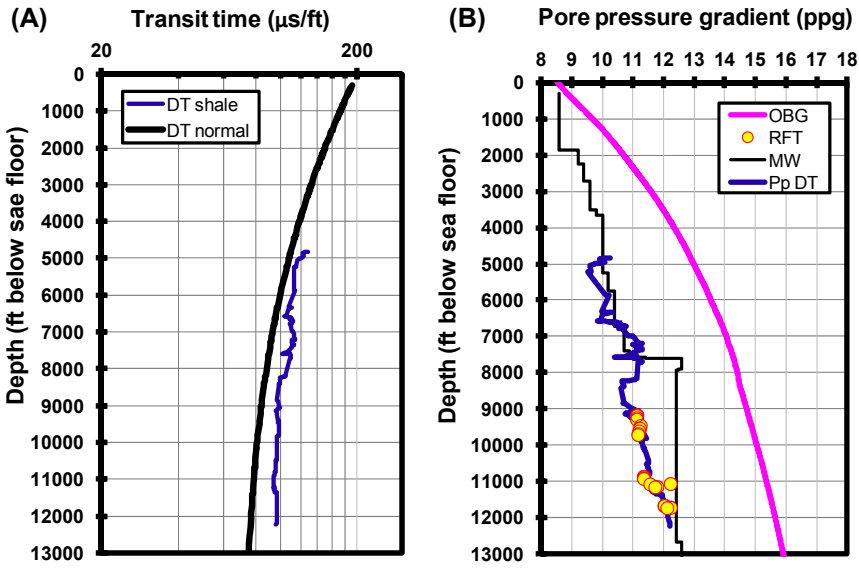

Figure 8.17 Pore pressure calculated by modified Eaton's sonic method in a deepwater well in the Gulf of Mexico. The left figure (A) plots sonic transit time in shale and normal transit time calculated from Eq. (8.27). The right figure (B) shows the overburden gradient (OBG), mud weight used while drilling (MW), measured pore pressure (RFT), and pore pressure gradient (Pp DT) calculated from sonic transit time using Eq. (8.26).

For a petroleum basin in Brunei the following relationship was obtained (Tingay et al., 2009):

$$\Delta t_n = 176.5 + 461.5e^{-0.0007Z}$$

In the above two equations, Δt_n is in μs/m and Z is in meters.

The same case study, as presented in Section 8.5.2 (Fig. 8.15), is used to examine the modified Eaton's sonic transit time method. Fig. 8.17 shows pore pressure computed from the modified Eaton's sonic method (Eq. 8.26). By calibrating the measured pore pressure data, the normal compaction trend is determined from Eq. (8.27) with the following parameters: $\Delta t_m = 70$ μs/ft, $\Delta t_{ml} = 200$ μs/ft, and $c = 0.000245$. Compared to the measured pore pressure data, the pore pressure calculated from Eq. (8.26) gives a very good result (Fig. 8.17).

8.6.2 Bowers' method

Bowers (1995) calculated the effective stresses from measured pore pressure data of the shales and overburden stresses and analyzed the corresponded

sonic interval velocities from well logging data in the Gulf of Mexico slope. He proposed the sonic velocity and effective stress having a power relationship:

$$V_p = V_{ml} + A\sigma_e^B \tag{8.28}$$

where V_p is the compressional velocity at a given depth; V_{ml} is the compressional velocity of the mudline (i.e., the sea floor or the ground surface, normally $V_{ml} = 5000$ ft/s, or 1520 m/s); A and B are the parameters calibrated with offset velocity and effective stress data.

Rearranging Eq. (8.28) and considering $\sigma_e = \sigma_V - p_p$, the pore pressure can be obtained from the velocity data in the following equation:

$$p_p = \sigma_V - \left(\frac{V_p - V_{ml}}{A}\right)^{\frac{1}{B}} \tag{8.29}$$

For the Gulf of Mexico wells, $A = 10-20$ and $B = 0.7-0.75$ in the English units (with p_p, σ_V in psi and V_p, V_{ml} in ft/s). Eq. (8.29) can be rewritten in terms of transit time simply by substituting $10^6/\Delta t$ for V_p and $10^6/\Delta t_{ml}$ for V_{ml}:

$$p_p = \sigma_V - \left(\frac{10^6\left(\frac{1}{\Delta t} - \frac{1}{\Delta t_{ml}}\right)}{A}\right)^{\frac{1}{B}} \tag{8.30}$$

where Δt_{ml} is the compressional transit time of the mudline in psi, normally $\Delta t_{ml} = 200$ μs/ft or 660 μs/m.

The effective stress and compressional velocity do not follow the loading curve if formation uplift or unloading occurs, and a higher velocity in the unloading curve than that in the loading curve appears at the same effective stress (refer to Fig. 7.13). Bowers (1995) proposed the following empirical relation to account for the effect of unloading:

$$V_p = V_{ml} + A\left[\sigma_{\max}(\sigma_e/\sigma_{\max})^{1/U}\right]^B \tag{8.31}$$

where σ_e, V_p, V_{ml}, A, and B are as before; U is the uplift parameter; and

$$\sigma_{\max} = \left(\frac{V_{\max} - V_{ml}}{A}\right)^{\frac{1}{B}}$$

where $\sigma_{\max}$ and $V_{\max}$ are the estimates of the effective stress and velocity at the onset unloading. In absence of major lithology changes, $V_{\max}$ is usually set equal to the velocity at the start of the velocity reversal.

Rearranging Eq. (8.31) the pore pressure can be obtained for the unloading case:

$$p_{ulo} = \sigma_V - \left(\frac{V_p - V_{ml}}{A}\right)^{\frac{U}{B}} (\sigma_{\max})^{1-U} \tag{8.32}$$

where p_{ulo} is the pore pressure in the unloading case.

8.6.3 Miller's method

The Miller sonic method describes a relationship between velocity and effective stress that can be used to relate sonic/seismic transit time to formation pore pressure. In Miller's sonic method an input parameter "maximum velocity depth", $d_{\max}$, controls whether unloading has occurred or not. If $d_{\max}$ is less than the depth (Z), then unloading has not occurred, the pore pressure can be obtained from the following equation (Zhang et al., 2008):

$$p_p = \sigma_V - \frac{1}{\lambda}\ln\left(\frac{V_m - V_{ml}}{V_m - V_p}\right) \tag{8.33}$$

where V_m is the sonic interval velocity in the matrix of the shale (asymptotic travel time at infinite effective stress, $V_m = 14{,}000{-}16{,}000$ ft/s); V_p is the measured compressional velocity at a given depth; λ is the empirical parameter defining the rate of increase in velocity with effective stress (normally 0.00025).

If $d_{\max} \geq Z$, then unloading behavior is assumed, the pore pressure in the unloading case can be calculated from the following equation:

$$p_{ulo} = \sigma_V - \frac{1}{\lambda}\ln\left[a_m\left(1 - \frac{V_p - V_{ulo}}{V_m - V_{ml}}\right)\right] \tag{8.34}$$

where a_m is the ratio of slopes of the virgin (loading) and unloading velocities in the effective stress curves σ_{ul} (normally $a_m = 1.8$) and $a_m = V_p/V_{ulo}$; σ_{ul} is the effective stress from unloading of the sediments; V_{ulo} is the velocity where unloading begins.

8.6.4 Tau model

A velocity-dependent pore pressure prediction method was proposed by Shell through introducing a "Tau" variable into the effective stress equation (Lopez et al., 2004; Gutierrez et al., 2006):

$$\sigma_e = A_s \tau^{B_s} \tag{8.35}$$

where A_s and B_s are the fitting constants; τ is the Tau variable and $\tau = (C - \Delta t)/(\Delta t - D)$; Δt is the compressional transit time either from sonic log or seismic velocity; C is a constant related to the mudline transit time (normally $C = 200$ μs/ft); and D is a constant related to the matrix transit time (normally $D = 50$ μs/ft).

Then, the pore pressure can be calculated from Eq. (8.35) using $\sigma_e = \sigma_V - p_p$, i.e.,

$$p_p = \sigma_V - A_s\left(\frac{C - \Delta t}{\Delta t - D}\right)^{B_s} \tag{8.36}$$

The best fitting parameters in the Gulf of Mexico are $A_s = 1989.6$ and $B_s = 0.904$ (Gutierrez et al., 2006).

Tau model and Miller's method are similar to Bowers' method. The advantage of Miller's method and Tau model is that both the effects of the matrix and mudline velocities are considered in pore pressure prediction.

8.6.5 Depth-dependent sonic method

Porosity can be approximately obtained by the empirical time average equation presented by Wyllie et al. (1956). Substituting the porosity-transit time equation Eq. (2.7) into Eqs. (8.10) and (8.12), the following equations can be derived for estimating pore pressure gradient (P_{pg}) and pore pressure (p_p) (Zhang, 2011):

$$P_{pg} = \left[OBG - (OBG - P_{ng})\frac{\ln(\Delta t_{ml} - \Delta t_m) - \ln(\Delta t - \Delta t_m)}{cZ}\right] \tag{8.37}$$

$$p_p = \left[\sigma_V - (\sigma_V - p_n)\frac{\ln(\Delta t_{ml} - \Delta t_m) - \ln(\Delta t - \Delta t_m)}{cZ}\right] \tag{8.38}$$

In Eqs. (8.37) and (8.38), the normal compaction trendline of the transit time is Eq. (8.27), and from it, the parameter c can be calculated. The normal compaction trendline of Eqs. (8.37) and (8.38) is asymptotic to matrix transit time and therefore better represents the compaction mechanism of the sediments. The other advantage of this method is that the calculated pore pressures are dependent on depth and both effects of the matrix and mudline transit time are considered.

The pore pressure in unloading case can be obtained from the following equation (Zhang, 2013a):

$$p_{ulo} = \left[\sigma_V - \frac{(\sigma_V - p_n)}{bZ}\left(\frac{b - c}{c}\ln\frac{\Delta t_{ml} - \Delta t_m}{\Delta t_{u0} - \Delta t_m} + \ln\frac{\Delta t_{ml} - \Delta t_m}{\Delta t - \Delta t_m}\right)\right] \tag{8.39}$$

where b is the compaction constant in the unloading case; $b = c$ if no unloading occurs, and $b > c$ in unloading case; Δt_{u0} is the transit time at the starting point of the unloading.

It can be derived from Eq. (8.38) that the sonic or seismic travel time and effective stress have an exponential relation in both normal compaction and undercompaction conditions (Zhang, 2013a):

$$\Delta t = \Delta t_m + (\Delta t_{ml} - \Delta t_m) e^{-cZ(\sigma_e/\sigma_n)} \tag{8.40}$$

In normal compaction case ($\sigma_e = \sigma_n$), Eq. (8.40) becomes Eq. (8.27) —the normal compaction trend for normal pressure case.

The depth-dependent sonic method, Eq. (8.37) or Eq. (8.38), has been applied in several petroleum basins, e.g., the Gulf of Mexico, the North Sea, India (Dasgupta et al., 2016), China (Xu et al., 2018), and shale gas formations. A case study in Fig. 8.18 displays the pore pressure analysis in a postdrill deepwater well with water depth of 3560 ft (Zhang et al., 2008). The subsalt formations are primarily Neogene shales and sandstones.

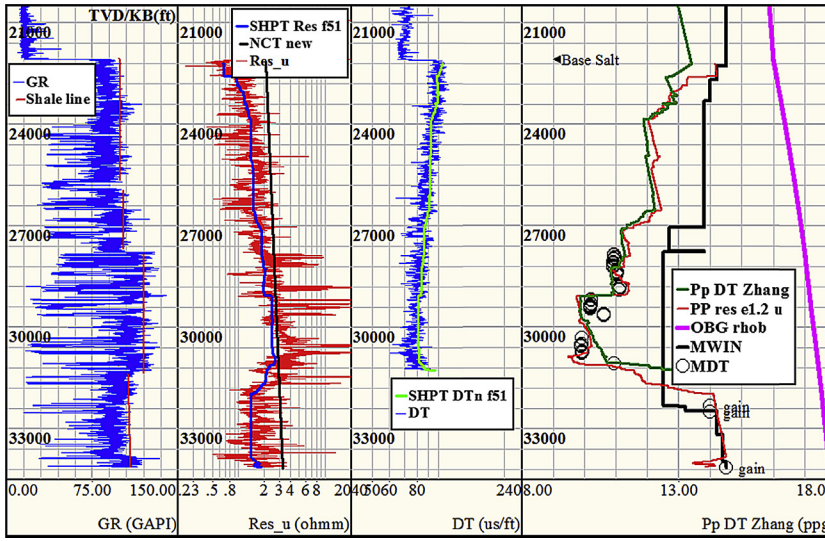

Figure 8.18 Pore pressure calculation from sonic transit time using Eq. (8.37) in subsalt formations of deepwater Gulf of Mexico. In this figure, the gamma ray and shale base lines are shown in the left track; the resistivity (Res) and filtered shale points of resistivity (SHPT Res) are plotted in the second track; the sonic transit time (DT) and filtered shale points of the transit time (SHPT DT) are shown in the third track; and the calculated pore pressure gradients from the filtered shale transit time (Pp DT) and resistivity (PP res e1.2) are shown in the right track with comparison to the measured formation pressures (MDT) and mud weights (MWIN).

Pore pressure gradient is calculated from Eq. (8.37) using $\Delta t_{ml} = 131$ μs/ft, $\Delta t_m = 73$ μs/ft, $P_{ng} = 8.75$ ppg, and $c = 0.00009$ ft^{-1}. The pore pressure gradient is also estimated using Eaton's resistivity method (Eq. 8.15). Compared to the measured pore pressure results (MDT), well influxes (fluid gains), and pore pressure calculated from resistivity log, Eq. (8.37) gives an excellent result in pore pressure calculation. It should be noted that the mudline transit time needs to be adjusted to $\Delta t_{ml} = 131$ μs/ft (instead of ~200 μs/ft in conventional cases) to make a better pore pressure estimation in subsalt formations. Fig. 8.18 also demonstrates that the pore pressure calculation from the depth-dependent sonic method can catch the pore pressure regression, which is a common phenomenon in some areas of the Gulf of Mexico.

8.6.6 Distinguishing gas effect on compressional transit time

The shear and compressional waves respond differently to reservoir fluids and pressures. These facts offer an opportunity to predict pore pressure and fluid content using seismic or sonic velocities. The challenge for pore pressure prediction is to distinguish between the presence of overpressure and gas-saturated formation from the velocity response. A lower compressional velocity or higher transit time may not only correspond to an overpressured formation but may also be related to a gas-bearing formation because the gas slows the compressional velocity down or increases the compressional transit time. The shear transit time can be used to identify whether a higher compressional transit time is caused by overpressures or by gas effect (Chilingar et al., 2002). The gas in the formation has little effect on shear transit time; however, an overpressured formation causes both compressional and shear transit time to increase (Fig. 8.19). Therefore, shear transit time or shear velocity can be used as an indicator of overpressure. Using this behavior, overpressure can be identified, as shown in Fig. 8.20, where a very high shear transit time (at depth of 27,900–28,000 ft) corresponds to a high pore pressure.

8.6.7 Smectite and illite impacts on pore pressure prediction

For the basin with smectite to illite transformation, the normal compaction trends for pore pressure calculation in smectite, illite, and transition zone should be different, as discussed in Chapter 7. The composite normal compaction trendline (NCT) can be constructed from Eqs. (7.11)–(7.13).

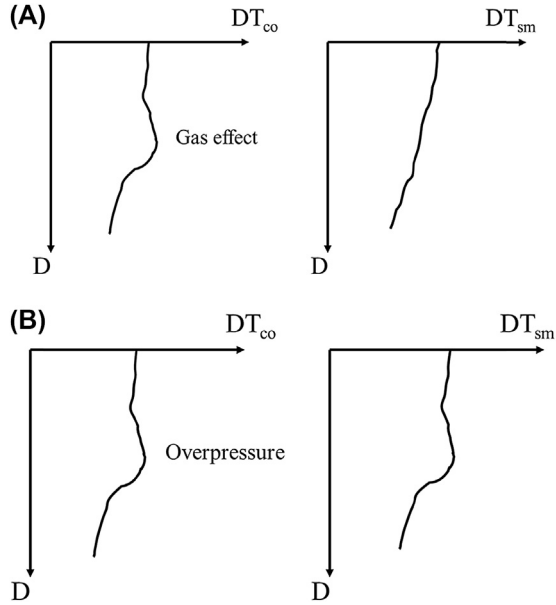

Figure 8.19 Schematic plots showing differences of compressive transit time (DT_{co}) and shear transit time (DT_{sm}) profiles for a gas-saturated zone (A) and an overpressure zone (B).

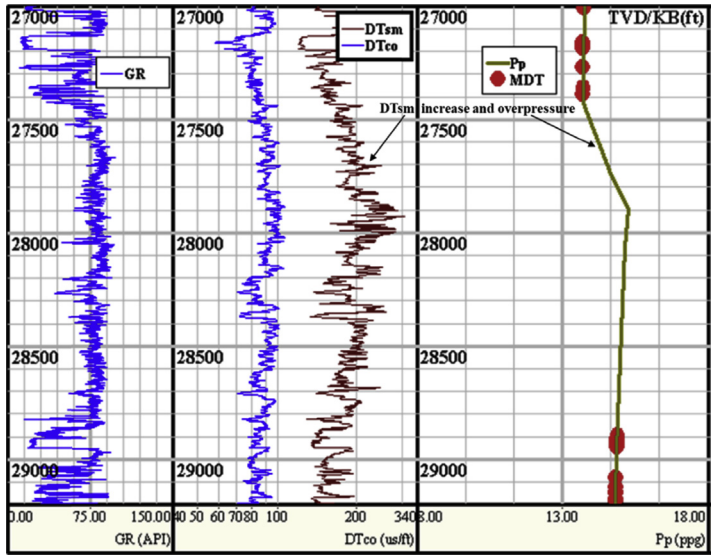

Figure 8.20 Very high shear transit time corresponding to a high pore pressure. The left track shows the gamma ray, the middle track plots compressional and shear transit time, and right track displays the measured (MDT) and estimated pore pressure.

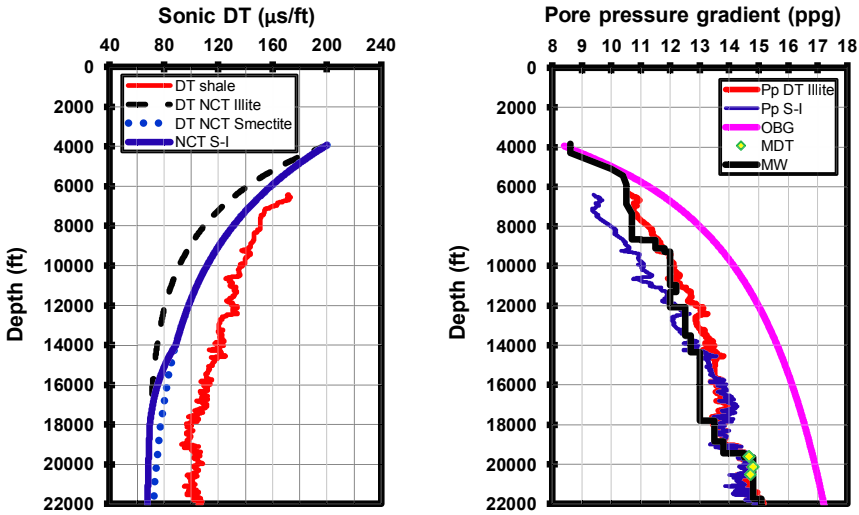

Figure 8.21 Pore pressure computations from the sonic transit time using composite NCT in a postwell analysis. The left figure presents the transit time of shales obtained from sonic log and normal compaction trendlines in smectite, illite, and the composite NCT (NCT S–I). The right track plots overburden stress gradient, mud weight used while drilling, measured pore pressure from MDT, and pore pressure profiles calculated from the transit time using single NCT (Pp DT illite) and composite NCT (Pp S–I).

Fig. 8.21 illustrates that multiple normal compaction trendlines can better predict pore pressure for the shales with different rock properties with depth. In the figure, the smectite NCT is obtained from Eq. (7.11) with the following parameters: $\Delta t_{ml} = 200$ μs/ft and $\Delta t_m = 67$ μs/ft, $c_s = 0.00018$. The illite NCT is computed from Eq. (7.12) with the following parameters: $\Delta t_{ml} = 200$ μs/ft and $\Delta t_m = 67$ μs/ft, $c_i = 0.00028$. The NCT in the transition zone is obtained from Eq. (7.13). Using the composite NCT (Δt_n) of the three segments, the pore pressure is computed from Eaton's method (Eq. 8.23 with $P_{ng} = 8.75$ ppg and $n = 3$), as shown in Fig. 8.21. The pore pressure gradient is also computed using a single NCT (e.g., illite trend). Fig. 8.21 indicates that the composite NCT gives a better result in pore pressure calculation than the one obtained from the single NCT method, particularly in the shallow section, where other methods may overestimate pore pressures.

8.7 Predrill pore pressure prediction and calibration

Before conducting pore pressure prediction in a prospect well, it needs to do pore pressure analysis in the offset or analog wells and build a pore

pressure prediction model, which should be calibrated by measured data in offset wells.

8.7.1 Calibration from formation pressure tests

There are many formation test methods for permeable formations, including real-time LWD tests or formation pressure tests while drilling (e.g., StethoScope, Geotap) and formation fluid pressure tests after drilling (e.g., MDT, RFT, DST; Schlumberger, 2006). For low-permeability rocks, the DFIT can not only be used for evaluating hydraulic fracturing ability but also for estimating formation pore pressure (e.g., Martin et al., 2012). To apply the pressure test data in permeable formations to the shale model of pore pressure prediction, it may need to consider the centroid effect (refer to Section 8.2.3).

Fig. 8.22 displays a postwell pore pressure analysis calibrated by measured formation pressures. This is a deepwater subsalt well, and the field description can be found in Zhang et al. (2008). Pore pressure gradient is calculated from the depth-dependent sonic method (Eq. 8.37) using $\Delta t_{ml} = 120$ μs/ft, $\Delta t_m = 73$ μs/ft, $P_{ng} = 8.75$ ppg, and $c = 0.00009$. The measured formation pressures from the MDT and Geotap are used to calibrate the parameters (Δt_{ml}, Δt_n, c) in Eq. (8.37).

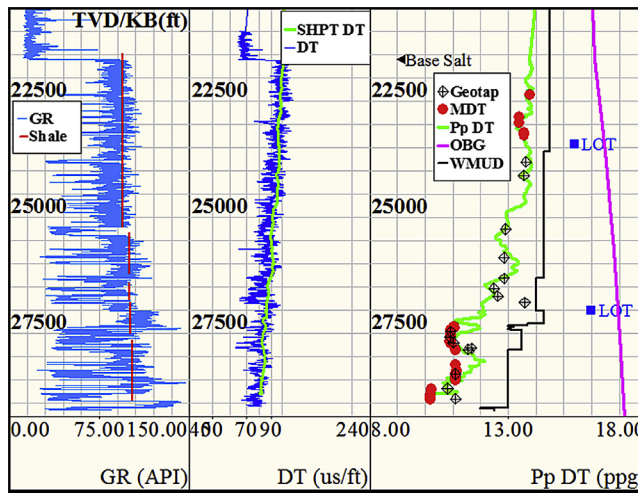

Figure 8.22 Pore pressure calculation from the sonic transit time (Eq. 8.37) in deepwater subsalt formations of the Gulf of Mexico. The gamma ray and shale base lines are shown in the left track; the sonic transit time (DT) and filtered shale points of the transit time (SHPT DT) are plotted in the second track; and the calculated pore pressure from the filtered shale transit time (Pp DT) is shown in the right track with comparison to the measured formation pressures from the MDT and Geotap.

8.7.2 Calibration from well influx, kick, and connection gas

In drilling operations, if the downhole mud weight is lower than the formation pressure, particularly for the permeable formations, the fluid influx or pressure kick will occur, causing mud pit gains. The pore pressure gradient can be calculated from the kick pressure using the following equation:

$$P_k = P_{mw} + \frac{p_{sidp}}{0.051948D} \tag{8.41}$$

where P_k is the formation pressure gradient when the influx or kick occurs (ppg); p_{sidp} is the drill pipe shut-in pressure in psi, P_{mw} is the downhole mud weight or equivalent circulating density (ECD) when the influx or kick occurs (ppg); D is the depth of the influx or kick, in ft.

Fluid influxes or pressure kicks are important data points for calibrating pore pressure prediction model. Fig. 8.18 shows an example to use the MDTs and pit gains (fluid influxes) for calibrating pore pressure prediction and Fig. 8.13 displays to use gas kicks to calibrate pore pressure model.

When a connection gas occurs, it normally indicates that the formation pore pressure is higher than the downhole mud weight. This is particularly useful for the shale formation to estimate pore pressure in real time drilling because formation pressure tests normally cannot measure pore pressures in the low permeable shale. Fig. 8.23 displays the calculated pore pressure from the connection gas values using Eq. (8.49). It indicates that the connection gas occurrence is strongly related to pore pressure increase.

8.7.3 Calibration from wellbore instability events

If pore pressure is higher, a heavier mud weight is required to keep wellbore stability because the wellbore collapse pressure increases as the pore pressure increases. Therefore, wellbore breakout can be used to detect pore pressure increase. Fig. 8.24 displays the caliper log and formation pressure measurements in a postwell analysis. The mud weight was reduced at depth of 24,000 ft, and then wellbore breakout (hole size enlargement in the caliper log) occurred in the deeper formation (a shale from 24,400 to 25,200 ft), indicating a higher mud weight needed to maintain wellbore stability. It might imply that the shale had a higher pore pressure than the measured formation pressure in the overlying sandstone. Therefore, wellbore instability can be used as an indicator of a higher pore pressure than expected.

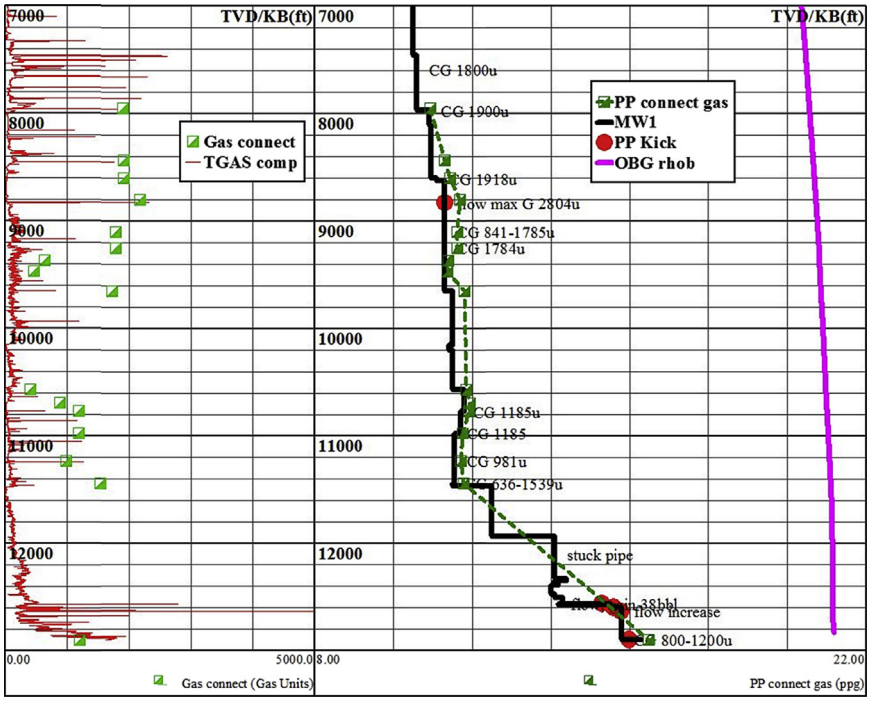

Figure 8.23 Connection gas (CG) and pore pressure relationship. The left track plots the connection gas and total gas with depth; the right track displays the calculated pore pressure from the connection gas. It also shows mud weight, CG values, inflow, and other drilling events.

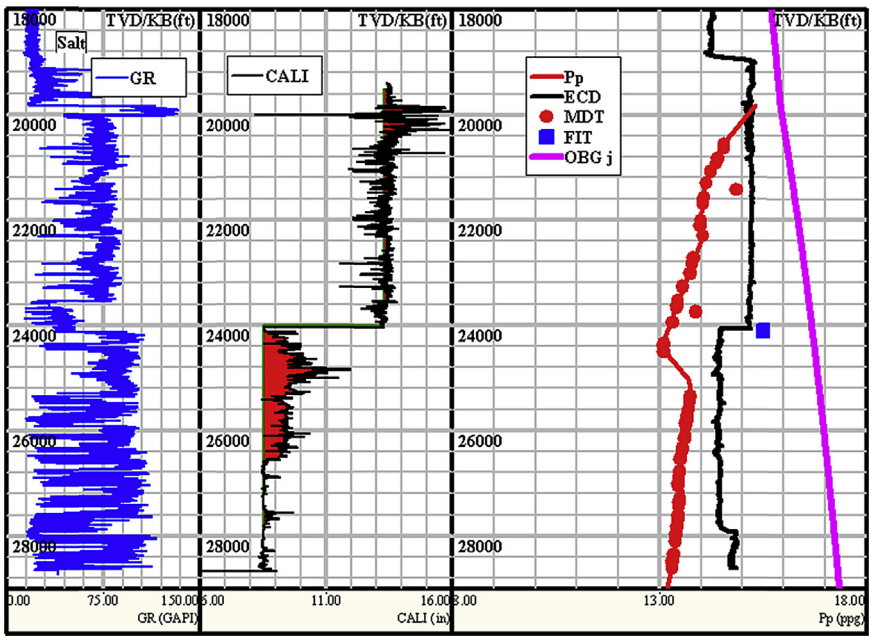

Figure 8.24 Pore pressure and wellbore breakout relationship. The left track shows the gamma ray; the middle track plots the caliper log where the shaded area is the wellbore breakout; the right track displays the measured and interpreted pore pressure gradient, mud weight, and overburden stress gradient.

8.7.4 Predrill pore pressure prediction in the prospect well

8.7.4.1 From seismic interval velocity

Seismic interval velocity at the proposed well location can be used to predict pore pressure. Fig. 8.25 shows an example of pore pressure prediction from the seismic interval velocity. Before pore pressure prediction, the seismic interval velocity should be calibrated and corrected with the sonic velocity data in the offset wells. The seismic interval velocities are the combination of different formations. However, for pore pressure prediction only shale interval velocities are needed, and the current seismic processing may not be able to extract the shale velocities. As a result, pore pressure prediction from seismic velocities has large uncertainties. Therefore, the pore pressures predicted from seismic velocities need to combine with other prediction methods (e.g., the prediction from analog wells) to obtain a composite pore pressure prediction.

8.7.4.2 From analog wells

For pore pressure prediction in a new prospect, pore pressures in the offset or analog wells need to be analyzed first, then the following steps may need:

For the hydraulically connected sandstones, hydraulic communication model can be used for pore pressure prediction (Eq. 8.1) based on the measured pore pressures in analog wells.

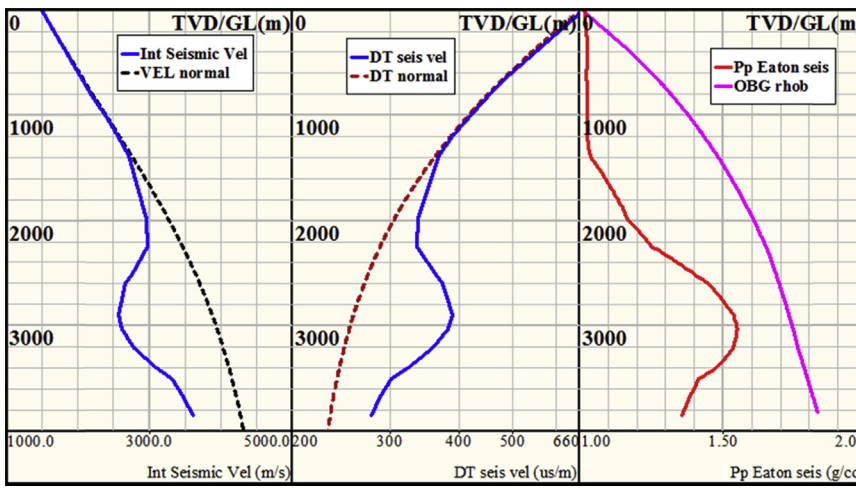

Figure 8.25 Smoothed seismic interval velocity (transit time), normal compaction trendline from Eq. (8.27) and pore pressure prediction from Eq. (8.26). The depth is in meters and plotted from the sea floor.

For shales, one of the following methods may be used for pore pressure prediction in the prospect well:

(1) Depth-shift effective stresses from analog wells based on formation tops to the prospect well and use this depth-shifted effective stresses and the overburden stress in the new well to calculate pore pressures and pressure gradients. This method assumes that at the same formation top, the effective stress in the proposed well is equal to that in the analog well.

(2) Depth-shift a composite sonic transit time from the analog wells based on formation tops to the prospect well and apply this transit time for pore pressure prediction using the parameters obtained from the analog wells.

Fig. 8.26 displays a plot of pore pressure prediction obtained from an integration of pore pressure predictions from the seismic interval velocities and from the offset well data (as described in this section). In the prediction, the pore pressures in the most likely case, in the low and high cases are given to handle the uncertainties.

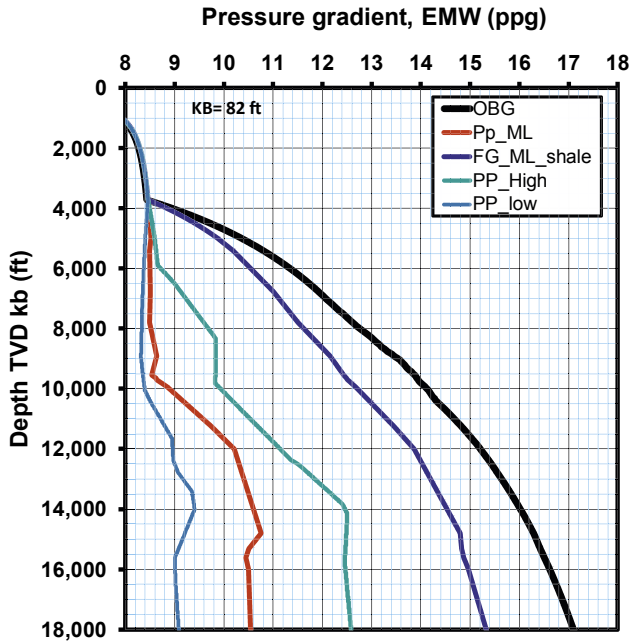

Figure 8.26 An example of predrill pore pressure prediction for a new prospect. In the figure the curves from left to right are the low case, most likely and high case pore pressures, fracture gradient in shales, and overburden gradient.

8.8 Real-time pore pressure detection

If predrill pore pressure prediction has a big uncertainty, real-time pore pressure detection is needed to update predrill pore pressure prediction and advise drilling operations in real-time to adjust the mud weight to reduce drilling risks. Real-time pore pressure detection generally relies on the following data for analyses and interpretations when the data are available, i.e., LWD including PWD (pressure while drilling), MWD, measured pore pressures, drilling parameters, and mud logging data (e.g., connection and total gases).

It should be noted that some real-time measurements (e.g., drill gas from the mud log and cuttings on the surface) have lag time. The LWD sensors (such as resistivity and sonic tools) also have certain distances behind the drill bit. These disadvantages make the real-time monitoring difficult to detect the pore pressure at the bit (excluding the d-exponent, Dxc). However, if a formation follows a certain compaction or undercompaction trend, then, the pore pressure at the bit can be interpreted.

For real-time pore pressure detection, it needs to firstly build a predrill or real-time pore pressure model based on all available data in offset wells, and then incorporate real-time abnormal pressure indicators to calibrate the model. The real-time pore pressure model mainly includes the LWD-based (e.g., resistivity and sonic transit time) and MWD-based (e.g., Dxc) methods. To apply these methods, normal compaction trends are the key parameters. The normal compaction trendlines (NCTs) need to be calibrated by offset data, real-time measured pore pressures and other indicators to finalize the trendlines. To reduce uncertainties, the pore pressure model needs to be integrated with real-time measurements and indicators, such as real-time pore pressure measurements, well influx and kick, mud logging (total gas, trip gas, connection gas), PWD, MWD, ROP, ECD, equivalent static mud density (ESD) measurements, and borehole instability events (e.g., abnormal torque and drag, tight holes, abnormal cuttings and cavings, hole enlargement and breakout, hole fill and pack-off).

8.8.1 Procedures of real-time pore pressure detections

For real-time pore pressure detection and monitoring, the following steps can be performed (Zhang and Yin, 2017a):

1. To construct predrill petrophysical and pore pressure model as introduced in the previous section and calibrate the predrill model to offset wells if they are available. The model includes methods of resistivity,

sonic, Dxc, etc. The model should include uncertainties and address drilling challenges and potential issues.

2. To apply the model to a real-time well. It particularly needs to have a calibrated NCT for each method.
3. To connect the model to stream real-time data (e.g., use ConnectML WITS and ConnectML WITSML to connect LWD and MWD tools), so that the real-time data can be automatically loaded to the model. The model can then automatically compute pore pressures based on the NCTs using real-time LWD and MWD data.
4. To compare the real-time—calculated pore pressure to downhole mud weight (ESD or ECD) for determining if the mud weight is sufficient, particularly it needs to identify whether the ESD or ECD is less than pore pressure gradient or greater than fracture gradient. Only comparing the real-time—calculated pore pressure gradient to the mud weight is not enough to conclude an underbalanced drilling status. It also needs to combine with other real-time indicators of abnormal pore pressures.
5. To adjust the model based on the following data if they are available: real-time pore pressure measurements, well influxes, mud pit gains, kicks, mud gas data, mud losses, drilling parameters, and borehole instability events (e.g., cavings, torque, hole fills, pack-offs).
6. To alert and inform the rig for action when the pore pressure is close to or higher (underbalanced) than the downhole mud weight.
7. To liaise with technical expert group on all issues related to unplanned drilling operations, ECD, and pore pressure.
8. To make postwell knowledge capture and transfer within the appropriate organizations and systems.

The real-time monitoring should ensure that:

1. Pore pressure is continuously monitored, and indicators of the abnormal pressures are identified.
2. Real-time pore pressure methods, estimates, and updates are discussed routinely with all involved monitoring parties to provide a consistent interpretation to the rig operations.
3. Abnormal pore pressure events are identified as soon as possible.
4. These abnormal events, including any significant observations, changes, or updates in pore pressure estimates, if they are occurring or imminent, need to be communicated to the operations (e.g., operation geologist and drilling engineer) quickly.
5. Appropriate actions of operations (e.g., raising mud weight when pore pressure gradient is higher than downhole mud weight) are taken quickly.

8.8.2 Real-time pore pressure detection—resistivity and sonic methods

For real-time pore pressure detection, the pore pressure calculation needs to be adapted to fit the real-time needs. Resistivity logging data can be used to calculate pore pressure in shales using Eaton's method (Eq. 8.13). Determining the NCT is critically important for the real-time pore pressure detection. Eq. (8.14) can be used as the depth-dependent resistivity NCT, in which parameters of R_0 and b can be obtained from offset data. When the calculated pore pressure matches the measured pore pressure, it indicates that the NCT (i.e., the parameters R_0 and b) is applicable for the real-time pore pressure detection in this area. Certainly, this NCT also needs to be adjusted based on the pore pressure indicators in the real-time drilling. Therefore, before real-time pore pressure detection, a critical step is to determine the NCT from the offset wells. It should be noted that the NCT may have different sets of calibration parameters for different offset wells. In this case, the calibration parameters in the closer well or wells should be used and adjusted based on the pore pressure indicators shown in the real-time drilling.

Sonic methods can also be used for real-time pore pressure detection. Similar to the resistivity method, before applying the sonic method to the real-time detection, the sonic NCT needs to be obtained (e.g., Eq. 8.27) and calibrated by the offset well data. After calibrations, the NCT is ready for real-time applications.

8.8.3 Real-time pore pressure detection—corrected d-exponent method

It has been found that the rate of penetration (ROP) increases when drilling into an undercompacted or an overpressured shale. That is, an increased ROP may be indicative to an abnormal increase in pore pressures. However, there are also many other factors affecting ROP, such as lithology, differential pressure, weight of the bit, rotating speed, torque, bit type, and change of bits. Therefore, the ROP is too random to be used as a detection method for abnormal pore pressure (Mouchet and Mitchell, 1989). Instead, d-exponent can be used as one of real-time pore pressure detection methods. Jorden and Shirley (1966) proposed the following d-exponent equation:

$$D_x = \frac{\log(ROP/60N)}{\log(12W/10^6 D)} \tag{8.42}$$

where D_x is the d-exponent; ROP is the rate of penetration (ft/hr); N is the rotary speed (rpm); W is the weight on bit (lbs); D is the hole diameter (inches).

The d-exponent is highly dependent on the differential pressure, i.e., the difference of mud pressure and pore pressure. If mud weight changes, then d-exponent will change. Therefore, d-exponent needs to be corrected to reflect the change of mud weight. Rehm and McClendon (1971) suggested the following correction:

$$D_{xc} = D_x \frac{P_{ng}}{P_{MW}} \tag{8.43}$$

where D_{xc} is the corrected d-exponent; P_{MW} is the downhole mud weight, and the ECD is recommended for P_{MW} in pore pressure calculation; P_{ng} is the hydrostatic pore pressure gradient.

Using the corrected d-exponent, the empirical equation (Eaton, 1975) for pore pressure estimate can be written in the following form, which is similar to the resistivity method:

$$P_{pg} = OBG - (OBG - P_{ng})\left(\frac{D_{xc}}{D_n}\right)^n \tag{8.44}$$

where D_n is the shale d-exponent in the normal pressure condition; n is an exponent, and normally $n = 1.2$.

It should be noted that d-exponent method initially was used for the rolling cutter bits. However, the PDC bits are widely used in the drilling industry. Because the PDC-type bits cut rocks with a shear cutting action instead of the chipping action that Jorden and Shirley (1966) assumed in their chip-hold down model, the corrected d-exponent in the PDC bit will differ from the tri-cone or bi-cone bit in the same formation. Therefore, a careful calibration is needed before real-time applications of the corrected d-exponent method.

Determining d-exponent NCT (i.e. D_n) is a key step for using this method to compute pore pressure in the real time. The following depth-dependent equation can be used as the NCT of the corrected d-exponent (Zhang and Yin, 2017a):

$$D_n = D_0 + dZ \tag{8.45}$$

where D_0 is the shale d-exponent of the mudline; d is a calibration parameter; Z is the depth below the mudline. However, if the hole size, weight of bit, and other parameters change, the normal compaction trend may change.

Another depth-dependent equation of the NCT can also be used for the corrected d-exponent:

$$D_n = D_0 e^{d_e Z} \tag{8.46}$$

where d_e is a calibration constant.

The corrected d-exponent gives a good indication of the state of compaction and pore pressure (Mouchet and Mitchell, 1989). To reduce lithology effect in different lithologies, the corrected d-exponents only in the shale formations should be used for the pore pressure detection. Fig. 8.27 presents a postwell analysis in a shale gas well for applying the corrected d-exponent method to compute pore pressures using the depth-dependent NCT. After calibrations, the NCT can be used for real-time pore pressure detection.

The primary advantage of this method is that the parameters needed for pore pressure calculation are obtained or measured from the drill bit (the BHA). Therefore, the pore pressure obtained from the corrected d-exponent method reflects the pore pressure at the bottom of the hole (near the bit). The other advantage is that it can be used in the case even if

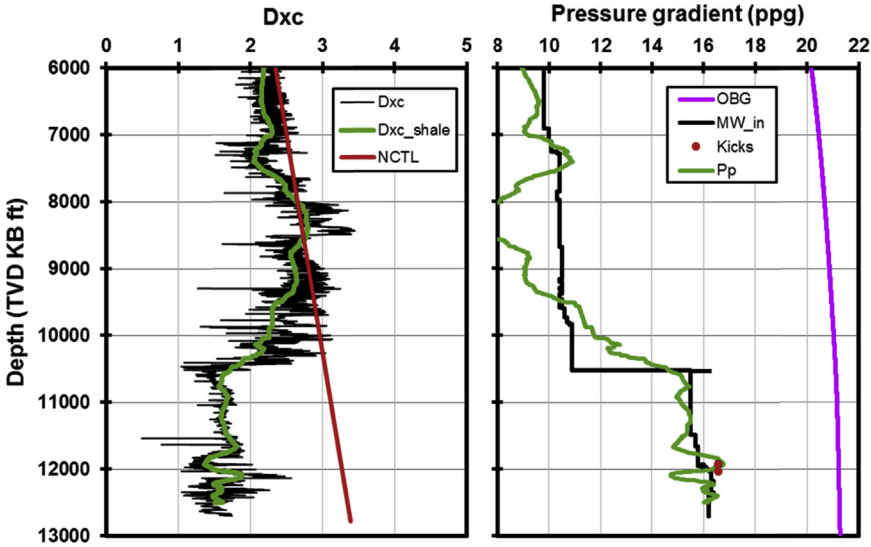

Figure 8.27 Pore pressure obtained from the corrected d-exponent method with depth-dependent compaction trendline for the postwell analysis in a shale gas well. The left track plots the corrected d-exponent in the shale and the d-exponent NCT calculated from Eq. (8.45) with $D_0 = 1.5$ and $d = 0.00015$. The right track shows the overburden gradient, mud weight, kicks, and pore pressure gradient calculated from the corrected d-exponent (Eq. 8.44).

there are no LWD data. However, this method is not applicable for the controlled drilling (e.g., controlled ROP). Based on the limitation of the d-exponent (highly dependent on ROP, lithology, bits, hole size), this method should be associated with other methods for real-time pore pressure detection.

8.8.4 Real-time pore pressure detection—from connection gas or total gas

If a gas flow from the formation into the wellbore occurs, the reservoir pore pressure should be greater than the downhole mud pressure (p_{MW}). Assuming the gas flow rate and pressures following Darcy's law, the following relation exists:

$$q = C\frac{kA}{\mu}\frac{p_p - p_{MW}}{\Delta L} \tag{8.47}$$

where q is the gas flow rate; C is a constant; k is the permeability; A is the cross-sectional area of the flow; μ is the fluid viscosity; ΔL is the flow distance.

Gas flow is not only dependent on differential pressure as described by Darcy's law but also on gas absorption and other factors. A simplified approach (i.e., using Eq. (8.47) to describe gas flow from the formation into the wellbore) can be used. Therefore, from the above equation, the pore pressure can be calculated from the following equation:

$$p_p = \frac{\mu \Delta L}{CkA} q + p_{MW} \tag{8.48}$$

Assuming that the connection gas is the gas flow, Eq. (8.48) can be simplified as the following form:

$$p_p = aQ_c + p_{MW} \tag{8.49}$$

where Q_c is the connection gas; a is a calibration parameter.

If the total gas is very high, the connection gas may not be observed, then total gas and background gas can be used to estimate pore pressure:

$$p_p = c(Q_t - Q_b) + p_{MW} \tag{8.50}$$

where Q_t and Q_b are the total gas and background gas, respectively; c is a calibration parameter.

When the calibration data are available, constant a or c can be obtained; therefore, pore pressure can be estimated using the connection gas or total gas.

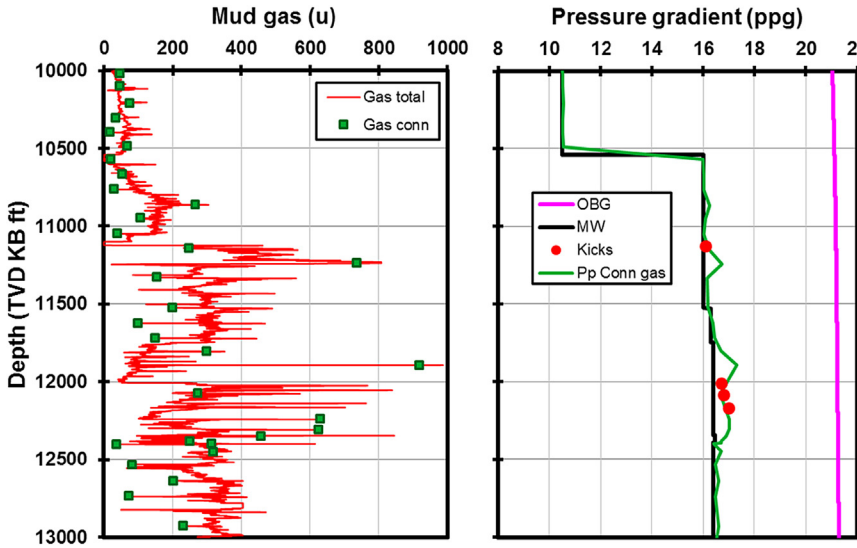

Figure 8.28 Pore pressure estimated from the connection gas using Eq. (8.49) in a postdrill shale gas well. The left track shows total gas and connection gas; the right track presents the calculated pore pressures compared to the kicks, mud weight (MW), and overburden stress (OBG).

Eqs. (8.49) and (8.50) describe the case where the downhole mud weight is lower than the pore pressure, i.e., the borehole has gas influx from the formation (e.g., connection gas). Therefore, these equations can be applicable only if the downhole mud weight is lower than the pore pressure. Fig. 8.28 presents a postwell analysis of pore pressure calculation from connection gas in a gas-bearing formation using Eq. (8.49). It should also be noted that the total gas and connection gas have lag time (e.g., 2–3 h, depending on the depth). The lag time is the time that it takes for gas to come out from the formation at the bottom hole and travel to the gas trap (gas collector) on the drilling deck. This lag time needs to be corrected for the pore pressure estimate.

8.8.5 Abnormal pore pressure indicators and detections in real-time drilling

Well influxes, kicks, blowouts, and mud losses are potential risks for drilling operations, particularly for the well with a narrow mud weight window. Real-time pore pressure monitoring can update the predrill model to reduce uncertainties in pore pressure prediction and reduce drilling risks. Real-time pore pressure detection can be performed either on the rig site or

remotely with an access of the real-time data. The real-time data for pore pressure detection mainly include the LWD resistivity and sonic transit time, mud gas log, and drilling parameters (for calculating Dxc). The pore pressure measurement while drilling is important for calibrating real-time pore pressure model. Other calibration data include mud logging data and drilling monitoring data, hole fill monitoring, torque and drag, cuttings and cavings, well flow, and mud losses. Abnormal changes in these data may be related to an abnormal pore pressure, but they could also be caused by other factors (e.g., changes of lithology, salinity, temperature, hole size, and mud weight). Therefore, it is necessary to use all available data to analyze and interpret the indicators of abnormal pore pressure.

8.8.5.1 Indicators from logging-while-drilling logs

The primary methods for real-time pore pressure calculation are the well log-based methods (e.g., from the LWD resistivity and sonic transit time), and the resistivity log is normally available in the real time. General rule for the LWD-based prediction is that the decrease in resistivity or increase in transit time (which is not caused by hydrocarbon presence) compared to the NCT is indicative of pore pressure increase. The NCTs are very critical for applying these methods and should be properly calibrated from offset wells before drilling. A fine adjustment of the NCT may be needed based on real-time pore pressure indicators. It should be noted that the LWD sensors have certain distances behind the bit (e.g., 20−100 ft, depending on the tools and the BHA). Normally, the resistivity tool is closer to the drill bit than the sonic tool. Even using the resistivity data, the detected pore pressure from the LWD logs is not the one at the bottom hole. Therefore, the log-based methods should be combined to other methods (e.g., Dxc method, in which the parameters are obtained from the bit measurements) to determine the pore pressure at the bit.

Fig. 8.29 presents an example of real-time pore pressure monitoring from the LWD resistivity in a deepwater well in the Gulf of Mexico, in which the NCT is obtained from the offset wells by using Eq. (8.14) and the pore pressure is calculated from Eq. (8.13) based on the NCT and real-time shale resistivity. The predicted pore pressure result was used to guide drilling engineers for real-time mud weight adjustments. Wellbore fluid flow and trip gas below 32,000 ft in Fig. 8.28 were due to a lower downhole MW (or ECD) than the formation pore pressure. The real-time calculated pore pressure was close to or higher than the ECD (Fig. 8.29), meaning the formation fluid flow into the wellbore would occur in

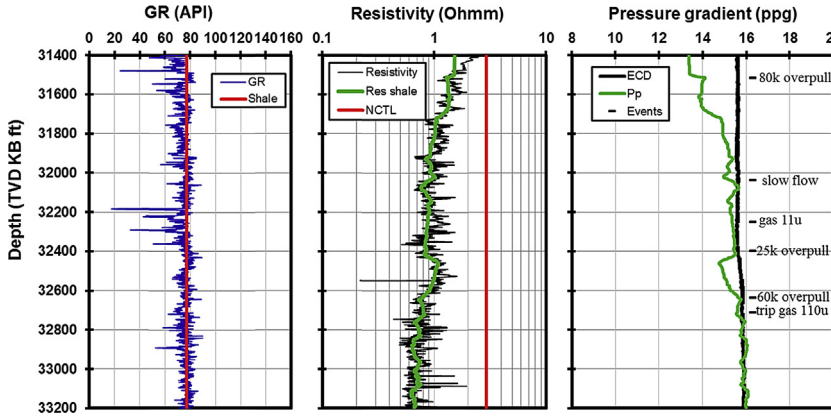

Figure 8.29 Real-time pore pressure detection from the LWD resistivity. The left track shows the real-time gamma ray and shale lines; the middle track presents the resistivity (black curve), picked shale resistivity (green curve) and NCT (red line); the right track displays the real-time calculated pore pressure (green curve) and measured data (ECD, well flow, and mud gas indicators).

the permeable formation. This is consistent to the abnormal pressure indication (well flow and trip gas show) observed in the real time.

8.8.5.2 Direct indicators of pore pressure—well influxes and mud losses

Well flow, mud pit gain, and kicks are, normally, direct indicators of a higher pore pressure than the applied mud weight. In these cases, increasing mud weight is needed. It should be noted that a well will not have fluid flow if formations are impermeable (e.g., shales). However, for impermeable formations, other indicators of underbalanced drilling status may be noticeable, such as wellbore instability (e.g., tight hole, caving, pack-off). These indicators need to be analyzed to determine whether it is in underbalanced drilling status or not. If mud losses or lost circulation are observed, it normally indicates that the applied mud weight is higher than the fracture gradient (excluding mud losses into open fractures or vuggy zones; more details can be found in Zhang and Yin, 2017b); therefore, it may need to reduce the mud weight. When the hole ballooning occurs, it normally implies that the mud weight is very close to the fracture gradient.

8.8.5.3 Indicators from mud gas

Mud gas is an important indicator of the abnormal pore pressure in drilling operations, particularly in shale formations because there are no good methods to measure pore pressures in shales. If a large volume of the

formation gas flows into the wellbore, the downhole mud weight is reduced because of the nature of low density of gas. This is "gas cut mud," indicating that the actual density of the mud coming out of the hole is less than the density of the mud being pumped into the hole. If the volume of gas influxes is large, the gas cut mud can cause a marked reduction of the downhole mud weight, and this could result in a gas kick or blowout. Therefore, the gas cut mud might be an important indicator of the abnormal pore pressure. Connection and total gas measurements in the mud log have been used qualitatively for decades in drilling oil and gas wells to identify overbalanced, underbalanced, or near underbalanced pressure conditions. Fig. 8.30 plots the relationship of the ECD and the peak total gas in a shale gas formation for an underbalanced drilling condition in the Utica shale. The well was drilled horizontally when the borehole reached to the shale gas formation at the vertical depth of 8500 ft. Fig. 8.30 shows that when the ECD was at 12–12.7 ppg, the observed maximum total gas reached 37%. When the ECD was increased and exceeded the pore pressure gradient (14.6 ppg), the total gas reduced markedly to 17%. Therefore, mud gas data from mud logs can be used as an indicator of the abnormal pore pressure. General rule for the mud gas is that an increase in the mud gas relative to the background gas is an indication of pore pressure increasing. The drawback of this method is that mud gas data have a lag time behind the bit. That is, they are only available after the gas is circulated with the mud from the bottom hole (or the gas-bearing formation) to the surface, and this can have several hours of delay depending on the hole depth. Six principles were proposed to quantitatively interpret mud gases

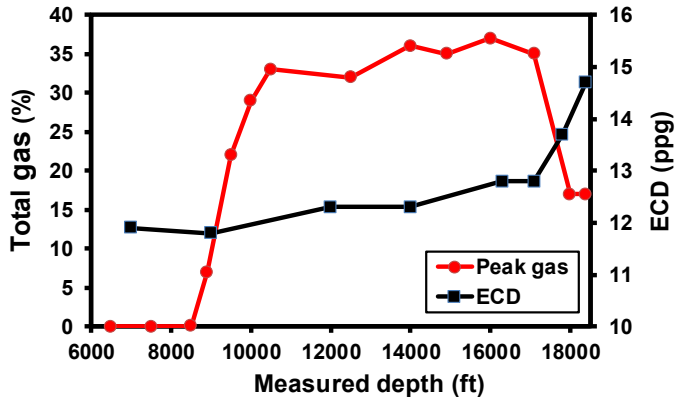

Figure 8.30 The total gas versus the downhole mud weight for drilling in a shale gas formation in a horizontal well (the estimated pore pressure from the DFIT is 14.6 ppg).

relative to formation pore pressure (Alberty and Fink, 2013). These principles for total gas displays are restated in the following:

- normal background and no reported connection gases, then $P_p <$ Swab $<$ ESD $<$ ECD.
- normal background and sporadic connection gases, then Swab $<$ $P_p <$ ESD $<$ ECD.
- normal background and consistent connection gases, then Swab $<$ ESD $< P_p <$ ECD.
- elevated background and either sporadic or consistent connection gases, then Swab $<$ ESD $<$ ECD $< P_p$.
- greatly elevated background and difficult to recognize connection gases, then Swab $<$ ESD $<$ ECD $<< P_p$.
- and if total gas drops in response to an ECD increase, then $P_p >$ ECD.

where Swab is the downhole swab pressure gradient resulted from the drill string movement; P_p is the pore pressure gradient; ESD is the equivalent static mud density; ECD is the equivalent circulating mud density.

8.8.6 Abnormal pore pressure interpretation from wellbore instability

8.8.6.1 Indicators from wellbore failures

When applied mud weight is inappropriate, wellbore instability events occur while drilling, which can help to diagnose abnormal pressures and to adjust mud weight in real-time drilling operations. Wellbore instability can be classified into two categories: shear and tensile failures. When the downhole mud weight is less than the shear failure gradient, the wellbore experiences shear failures. The indicators of shear failures while drilling include hole enlargement (borehole breakout), hole closure, tight hole (over-pull), high torque, hole fill after trip, hole bridging, hole pack-off, and hole collapse. Some of these indicators may not be caused by shear failures but by other factors; e.g., a swelling shale when the water-based mud is used because of the chemical reaction between the mud and the shale formation. Therefore, it needs to identify the causes of the failures.

Here a vertical well is used as an example to illustrate the relationship of wellbore instability and pore pressure. Based on the Mohr–Coulomb failure criterion, the minimum mud weight to avoid borehole shear failure can be obtained from the following equation (Zhang, 2013b):

$$p_m = \frac{1-\sin\phi}{2}(3\sigma_H - \sigma_h - UCS) + p_p \sin\phi \tag{8.51}$$

where p_m is the minimum mud pressure or collapse (shear failure) pressure, φ is the angle of internal friction of the rock; UCS is the rock uniaxial compressive strength; σ_H and σ_h are the maximum and minimum horizontal stresses, respectively.

Eq. (8.51) shows that shear failure is directly related to pore pressure, i.e., a higher pore pressure needs a heavier mud weight to keep the wellbore from shear failures. Therefore, wellbore instability can be used as an indicator of an overpressured formation.

Tensile failure, however, occurs when the mud pressure exceeds the capacity of the near-wellbore rock to bear tensile stress. If the downhole mud weight is higher than the fracture gradient, the formation will be fractured to create hydraulic fractures (drilling-induced tensile fractures). Real-time indicators of drilling-induced tensile failures include borehole ballooning, mud losses, and lost circulation. Reducing mud weight, adding lost circulation materials, or applying wellbore strengthening technique (refer to Chapter 9) are the possible cures for the drilling-induced tensile failures.

8.8.6.2 Indicators from abnormal cuttings

General rule is that the insufficient mud weight produces more and larger cuttings. There are generally four types of cuttings (cavings): normal cuttings, cavings from preexisting fractures, cavings owing to underbalanced drilling, and cavings owing to shear failures.

1. Normal cuttings. If the mud weight is appropriate, i.e., higher than pore pressure and collapse pressure but lower than fracture gradient, the wellbore is in a good condition. In this case, normal cuttings are generated with the PDC cutting marks when a PDC bit is used, as shown in Fig. 8.31A.

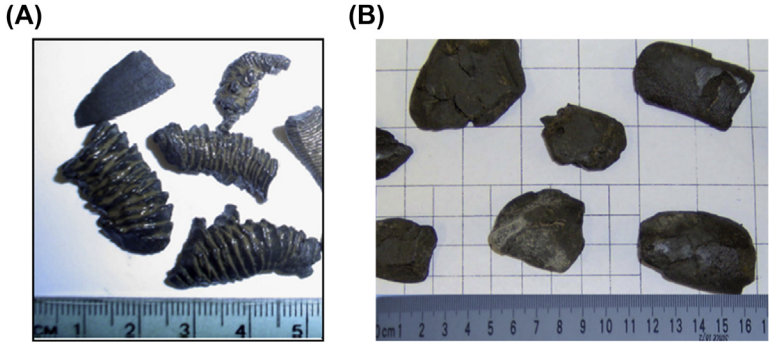

Figure 8.31 Drilling cuttings. (A) normal PDC cuttings of shales; (B) blocky cuttings from a formation with preexisting fractures.

2. Cavings from preexisting fractures. In a formation with preexisting fractures or in a faulted section, the rock may have a lower compressive strength and lower fracture gradient. In this case, it may generate blocky cavings in which the naturally fractured planes may be observed; therefore, mud losses probably occur in the preexisting fractures. Fig. 8.31B presents a picture of blocky cavings in a subsalt formation where mud losses occurred.
3. Cavings owing to underbalanced drilling. If downhole mud weight is less than formation pore pressure gradient, the wellbore experiences splintering failure or spalling. In this case, large amounts of spiky and concaved cavings are generated, as shown in Fig. 8.32, and wellbore collapse and fluid kick (if a permeable formation is encountered) may occur.
4. Cavings owing to shear failures. Shear failures cause angular or splintered cavings in the wellbore. In this case, the rock failure of the wellbore wall is similar to a triaxial compressive core test, where angular or splintered rock pieces are formed, as shown in Fig. 8.33.

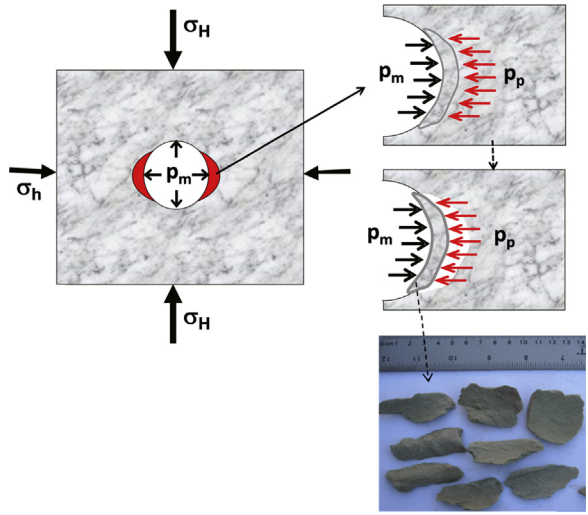

Figure 8.32 Schematic representation of wellbore spalling/chips for a higher pore pressure than the mud pressure (underbalanced drilling condition) in a vertical borehole. The upper figure illustrates the high pore pressure blowing rock chips into the wellbore; the bottom picture shows spiky and concaved cuttings resulted from the insufficient mud weight.

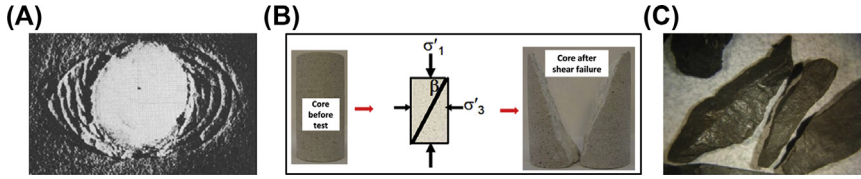

Figure 8.33 Angular or splintered cavings caused by shear failures: a case of lower mud weight than the shear failure gradient. (A) Borehole breakout from shear failures in a laboratory experiment (Addis et al., 1990); (B) triaxial compressive core test creating angular rock pieces caused by shear failures; (C) angular/splintered cavings induced by shear failures from a subsalt borehole.

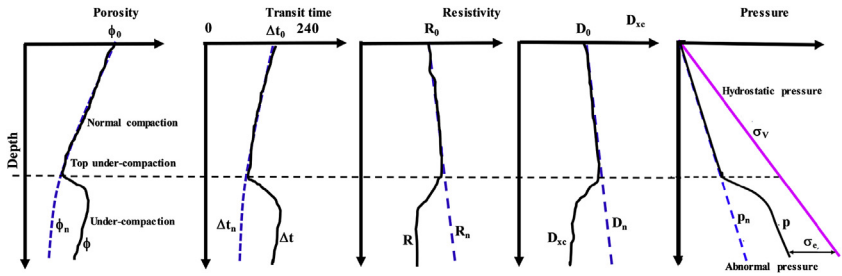

Figure 8.34 Generalized normal compaction trends and the abnormal pressure caused by undercompaction. From left to right: porosity, transit time, resistivity, d-exponent, and pore pressure plots.

8.8.7 Summary of real-time indicators for abnormal pore pressures

Table 8.1 summarizes the indicators of abnormal pore pressures in the real-time monitoring as described in the previous sections. These indicators can be used to identify abnormal pore pressures and to calibrate and update the real-time pore pressure models.

Appendix 8.1. Derivation of pore pressure prediction from porosity

It is well known that the formation porosity and effective stress have the following relationship:

$$\phi = \phi_0 e^{-a\sigma_e} \tag{A1}$$

Therefore, the effective stress can be obtained from Eq. (A1):

$$\sigma_e = \frac{1}{a}\ln\frac{\phi_0}{\phi} \tag{A2}$$

Table 8.1 Real-time indicators of abnormal pore pressures.

Indicators	General behaviors
Total gas	Total gas should increase when an underbalanced drilling occurs in a gas-bearing formation.
Background gas	Background gas should increase with ROP. For a constant ROP, background gas is expected to increase as the pore pressure increases.
Connection gas and pump-off gas	Connection gas, swab gas, or pumps-off gas occurring may indicate that the pore pressure is higher than the ESD.
Gas cut mud	Gas cut mud is a sign of abnormal pore pressure that may indicate an underbalanced drilling.
ROP	ROP increase may indicate the pore pressure gradient increase.
Dxc	Gradual decrease in Dxc compared to its NCT may indicate the pore pressure gradient increase (Fig. 8.34).
Resistivity	Gradual decrease in resistivity compared to its NCT may indicate the pore pressure gradient increase (Fig. 8.34).
DT	Gradual increase in sonic transit time (DT) compared to its NCT may indicate pore pressure gradient increasing (Fig. 8.34).
PWD and temperature	Sudden increase in PWD with increase in MWD temperature may indicate an influx or kick.
Mud volume	Mud pit volume increasing may indicate a kick.
Cuttings	Increase in percentage of cuttings may indicate wellbore instability or abnormal pore pressure. Splintery cavings may indicate underbalanced drilling, and large amounts of splintery and angular cavings indicate a wellbore collapse.
Hole fill	Hole fills (i.e., cavings falling in) after connections indicate wellbore instability and it may need to increase mud weight.
High torque, over-pull, tight hole, pack-off	Hole pack-off, over-pull, tight hole, and increasing torque and drag are likely to be caused by a higher collapse pressure or higher pore pressure than the applied mud weight. It needs to increase mud weight.

The effective stress at the normal pressure condition can also be obtained from Eq. (A1), when the porosity is the normal porosity, a condition that formations are normally compacted, i.e.,

$$\phi_n = \phi_0 e^{-a\sigma_n} \tag{A3}$$

$$\sigma_n = \frac{1}{a}\ln\frac{\phi_0}{\phi_n} \tag{A4}$$

Combining Eqs. (A2) and (A4), the following equation can be obtained:

$$\frac{\sigma_e}{\sigma_n} = \frac{\ln\phi_0 - \ln\phi}{\ln\phi_0 - \ln\phi_n} \tag{A5}$$

Or,

$$\sigma_e = \sigma_n \frac{\ln\phi_0 - \ln\phi}{\ln\phi_0 - \ln\phi_n} \tag{A6}$$

The effective stress and pore pressure have the following relation:

$$p_p = (\sigma_V - \sigma_e)/\alpha \tag{A7}$$

Substituting Eq. (A6) into Eq. (A7) and noticing $\sigma_n = \sigma_V - \alpha p_n$, the relation of pore pressure, overburden stress, and porosity can be obtained:

$$p_p = \left[\sigma_V - (\sigma_V - \alpha p_n)\frac{\ln\phi_0 - \ln\phi}{\ln\phi_0 - \ln\phi_n}\right] \Big/ \alpha \tag{A8}$$

where ϕ_n is the porosity in the normal compaction condition.

The normal compaction porosity can be obtained from the following equation (Athy, 1930):

$$\phi_n = \phi_0 e^{-cZ} \tag{A9}$$

Substituting Eq. (A9) into Eq. (A8), the relation of pore pressure and porosity can be obtained:

$$p_p = \left[\sigma_V - (\sigma_V - \alpha p_n)\frac{\ln\phi_0 - \ln\phi}{cZ}\right] \Big/ \alpha \tag{A10}$$

where p_p is the pore pressure; σ_V is the overburden stress; p_n is the normal pore pressure; ϕ is porosity in shale, ϕ_0 is the porosity of the mudline (the ground surface or sea floor for the offshore drilling); Z is the depth below the mudline; α is Biot's coefficient; and c is the compaction constant.

The pore pressure gradient can be easily obtained from Eq. (A10).

$$P_{pg} = \left[OBG - (OBG - \alpha P_{ng})\frac{\ln\phi_0 - \ln\phi}{cZ}\right] \Big/ \alpha \tag{A11}$$

where P_{pg} is the pore pressure gradient; OBG is the overburden stress gradient; P_{ng} is the normal pressure gradient.

Appendix 8.2. Derivation of sonic normal compaction equation

From the Wyllie equation, the porosity at the normal compaction condition (ϕ_n) can be expressed in the following (refer to Eq. 2.7):

$$\phi_n = \frac{\Delta t_n - \Delta t_m}{\Delta t_f - \Delta t_m} \tag{B1}$$

And the porosity of the mudline (ϕ_{ml}) can be written as follows:

$$\phi_{ml} = \frac{\Delta t_{ml} - \Delta t_m}{\Delta t_f - \Delta t_m} \tag{B2}$$

From Eq. (A9), it has the following relation between the normal porosity and mudline porosity:

$$\phi_n = \phi_{ml} e^{-cZ} \tag{B3}$$

Substituting Eqs. (B1) and (B2) into Eq. (B3), the transit time in the normal compaction condition (Δt_n) can be obtained, i.e.,

$$\Delta t_n = \Delta t_m + (\Delta t_{ml} - \Delta t_m) e^{-cZ} \tag{B4}$$

References

Addis, M.A., Barton, N.R., Bandis, S.C., Henry, J.P., 1990. Laboratory studies on the stability of vertical and deviated boreholes. Paper SPE-20406.

Arp, J.J., 1953. The effect of temperature on the density and electrical resistivity of sodium chloride Solutions. In: Petroleum Transaction, vol. 198. American Institute of Mining, Metallurgical, and Petroleum Engineers, pp. 327–330. SPE-953327-G.

Athy, L.F., 1930. Density, porosity, and compaction of sedimentary rocks. AAPG Bull. 14 (1), 1–24.

Alberty, M., Fink, K., 2013. Using connection and total gases quantitatively in the assessment of shale pore pressure. Paper SPE166188.

Biot, M.A., 1941. General theory of three-dimensional consolidation. J. Appl. Phys. 12 (1), 155–164.

Bowers, G.L., June 1995. Pore pressure estimation from velocity data; accounting for overpressure mechanisms besides under compaction. SPE Drill. Complet. 89–95.

Bowers, G.L., 2001. Determining an appropriate pore-pressure estimation strategy. Paper OTC-13042.

Bruce, B., Bowers, G., 2002. Pore pressure terminology. The Leading Edge. February 2002. Lead. Edge. Dec. 2006 170–173.

Chapman, R.E., 1983. Petroleum Geology. Elsevier.

Chilingar, G.V., Serebryakov, V.A., Robertson, J.O., 2002. Origin and Prediction of Abnormal Formation Pressures. Elsevier.
Czerniak, M., 2011. The role of permeability weighting in centroid positioning. Geopressure Conf. Galveston, Texas.
Dasgupta, S., Chatterjee, R., Mohanty, S.P., 2016. Prediction of pore pressure and fracture pressure in Cauvery and Krishna-Godavari basins, India. Mar. Petrol. Geol. 78, 493–506.
Dickinson, G., 1953. Geological aspects of abnormal reservoir pressures in Gulf Coast Louisiana. AAPG Bull. 37 (2), 410–432.
Eaton, B.A., 1972. Graphical method predicts geopressures worldwide. World Oil, pp. 51–56. May 1976.
Eaton, B.A., 1975. The equation for geopressure prediction from well logs. Society of Petroleum Engineers of AIME, Paper SPE-5544.
Flemings, P.B., Stump, B.B., Finkbeiner, T., Zoback, M., 2002. Flow focusing in over-pressured sandstones: theory, observations, and applications. Am. J. Sci. 302, 827–855.
Gao, B., Flemings, P.B., 2017. Pore pressure within dipping reservoirs in overpressured basins. Mar. Petrol. Geol. 80, 94–111.
Gardner, G.H.F., Gardner, L.W., Gregory, A.R., 1974. Formation velocity and density – the diagnostic basis for stratigraphic traps. Geophysics 39 (6), 2085–2095.
Gutierrez, M.A., Braunsdorf, N.R., Couzens, B.A., 2006. Calibration and ranking of pore-pressure prediction models. Lead. Edge. Dec. 2006 1516–1523.
Hauser, M.R., Petitclerc, T., Branusdorf, N.R., Winker, C.D., 2013. Pressure prediction implications of a Miocene pressure regression. Lead. Edge. Jan. 100–109.
Heppard, P.D., Cander, H.S., Eggertson, E.B., 1998. Abnormal pressure and the occurrence of hydrocarbons in offshore eastern Trinidad, West Indies. In: Law, B.E., Ulmishek, G.F., Slavin, V.I. (Eds.), Abnormal Pressures in Hydrocarbon Environments: AAPG Memoir, vol. 70, pp. 215–246.
Holbrook, P.W., Maggiori, D.A., Hensley, R., 2005. Real-time pore pressure and fracture gradient evaluation in all sedimentary lithologies. SPE Form. Eval. 10 (4), 215–222.
Hottmann, C.E., Johnson, R.K., 1965. Estimation of formation pressures from log-derived shale properties. Paper SPE1110 JPT 17, 717–722.
Jorden, J.R., Shirley, O.J., 1966. Application of drilling performance data to overpressure detection. J. Pet. Technol. 18 (11), 1387–1394.
Katahara, K., 2003. Analysis of overpressure on the Gulf of Mexico shelf. OTC-15293.
KSI, 2001. Best Practice Procedures for Predicting Pre-drill Geopressures in Deep Water Gulf of Mexico. DEA Project 119 Report Knowledge Systems Inc.
Lang, J., Li, S., Zhang, J., 2011. Wellbore stability modeling and real-time surveillance for deepwater drilling to weak bedding planes and depleted reservoirs. Paper SPE/IADC-139708.
Li, S., George, J., Purdy, C., 2012. Pore-pressure and wellbore-stability prediction to increase drilling efficiency. SPE144717, J. Pet. Technol. 98–101.
Lopez, J.L., Rappold, P.M., Ugueto, G.A., Wieseneck, J.B., Vu, K., 2004. Integrated shared earth model: 3D pore-pressure prediction and uncertainty analysis. Lead. Edge. Jan. 52–59.
Martin, R., Cramer, D., Nunez, O., Roberts, N., 2012. A method to perform multiple diagnostic fracture injection tests simultaneously in a single wellbore. SPE-152019.
Mouchet, J.-C., Mitchell, A., 1989. Abnormal Pressures while Drilling. Editions TECHNIP, Paris.
Osborne, M.J., Swarbrick, R.E., 1997. Mechanisms for generating overpressure in sedimentary basins: a reevaluation. AAPG Bull. 81, 1023–1041.
Powley, D.E., 1990. Pressures and hydrogeology in petroleum basins. Earth Sci. Rev. 29, 215–226.

Rehm, B., McClendon, R., 1971. Measurement of formation pressures from drilling data. Paper SPE-3601.
Revil, A., Cathles III, L.M., Losh, S., 1998. Electrical conductivity in shaly sands with geophysical applications. J. Geophys. Res. B 103 (B10), 23925–23936.
Schlumberger, 2006. Fundamentals of Formation Testing. Schlumberger.
Schneider, J., Flemings, P.B., Dugan, B., Long, H., Germaine, J.T., 2009. Overpressure and consolidation near the seafloor of Brazos-Trinity Basin IV, northwest deepwater Gulf of Mexico. J. Geophys. Res. 114, B05102.
Shaker, S., 2002. Predicted vs. measured pore pressure: pitfalls and perceptions. OTC-14073.
Terzaghi, K., Peck, R.B., Mesri, G., 1996. Soil Mechanics in Engineering Practice, third ed. John Wiley & Sons.
Tingay, M.R.P., Hillis, R.R., Swarbrick, R.E., Morley, C.K., Damit, A.R., 2009. Origin of overpressure and pore-pressure prediction in the Baram province, Brunei. AAPG Bull. 93 (1), 51–74.
Traugott, M., 1997. Pore pressure and fracture gradient determinations in deepwater. World Oil, p. 1997. August.
van Ruth, P., Hillis, R., Tingate, P., 2004. The origin of overpressure in the Carnarvon Basin, Western Australia: implications for pore pressure prediction. Petrol. Geosci. 10, 247–257.
Xu, Y., Pang, X., Hu, T., Xu, T., Zheng, X., 2018. Selection of formation pressure prediction methods based on mudstone interval transit time. Special Oil Gas Reservoirs 25 (4), 46–50.
Yardley, G.S., Swarbrick, R.E., 2000. Lateral transfer: a source of additional overpressure? Mar. Petrol. Geol. 17, 523–537.
Zhang, J., Standifird, W.B., Lenamond, C., 2008. Casing ultradeep, ultralong salt sections in deep water: a case study for failure diagnosis and risk mitigation in record-depth well. Paper SPE-114273.
Zhang, J., 2011. Pore pressure prediction from well logs: methods, modifications, and new approaches. Earth Sci. Rev. 108, 50–63.
Zhang, J., Wieseneck, J., 2011. Challenges and surprises of abnormal pore pressures in the shale gas formations. In: Paper SPE-145964 Presented at SPE Annual Technical Conference and Exhibition, Denver, Colorado, USA.
Zhang, J., 2013. Effective stress, porosity, velocity and abnormal pore pressure prediction accounting for compaction disequilibrium and unloading. Mar. Petrol. Geol. 45, 2–11.
Zhang, J., 2013. Borehole stability analysis accounting for anisotropies in drilling to weak bedding planes. Int. J. Rock Mech. Min. Sci. 60, 160–170.
Zhang, J., Yin, S., 2017. Real-time pore pressure detection indicators and improved methods. Geofluids 2017. Article ID 3179617.
Zhang, J., Yin, S., 2017. Fracture gradient prediction: an overview and an improved method. Petrol. Sci. 14 (4), 720–730.

CHAPTER 9

Fracture gradient prediction and wellbore strengthening

Contents

Abstract

Fracture gradient is a critical parameter for mud weight design in the drilling industry. In this chapter, fracture gradient prediction methods are reviewed. Analyses of field-measured leak-off test data in several petroleum basins show that fracture gradient is dependent not only on the overburden stress and pore pressure but also on depth. This phenomenon is considered in fracture gradient prediction. Leak-off test

Applied Petroleum Geomechanics
ISBN 978-0-12-814814-3
https://doi.org/10.1016/B978-0-12-814814-3.00009-5

data in the salt formations are investigated, and fracture gradient prediction method in the salt is studied. Case applications are examined to compare different fracture gradient methods, and the reasons why the leak-off test value can be higher than the overburden gradient are also explained. A depleted reservoir usually has a very low fracture gradient, and wellbore strengthening techniques can be used to increase formation fracture gradient and reduce mud losses during drilling operations. For applying a wellbore strengthening technique, it requires to estimate the width of an induced fracture at a target fracture length for a given wellbore pressure. 2-D and 3-D semianalytical solutions are presented for calculating the fracture width, which consider the effects of in situ stress anisotropy, the borehole inclinations, and trajectories.

Keywords: Breakdown pressure; Fracture gradient in salt; Fracture gradient prediction; Fracture width; Leak-off test; Mud losses; Wellbore strengthening.

9.1 Fracture gradient in drilling operations

9.1.1 Concept of fracture gradient

Fracture gradient is defined by the Schlumberger Oilfield Glossary as the pressure gradient required to induce fractures in the rock at a given depth. Based on this definition, it is the maximum mud weight that a well can hold without mud losses and without uncontrolled tensile failures (fracture growth) in drilling operations. If the downhole mud weight is higher than the formation fracture gradient, then the wellbore will have tensile failures (i.e., the formation will be fractured), causing losses of drilling mud or even lost circulation (total losses of the mud). Therefore, fracture gradient prediction is directly related to drilling safety. However, there is no consensus on how to calculate fracture gradient in the oil and gas industry. Some pore pressure specialists may use the minimum stress gradient as fracture gradient, but others may use the maximum leak-off pressure (LOP) gradient (it could be the formation breakdown pressure gradient) or the fracture initiation pressure gradient as fracture gradient. In this chapter, the maximum LOP gradient (the peak value in the LOT test) is used for fracture gradient analysis. For fracture gradient prediction the effects of the minimum stress, tensile strength, and the wellbore stress concentrations need to be considered.

Pore pressure gradient and fracture gradient are two most important parameters practically used for determining the mud weight window in drilling engineering, as shown in Fig. 9.1. The mud weight should be

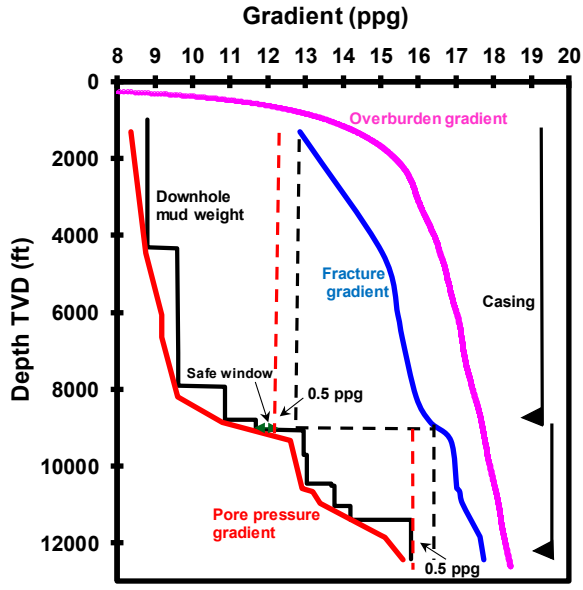

Figure 9.1 Pore pressure gradient, fracture gradient, overburden stress gradient, static downhole mud weight, and casing shoes versus depth. The "0.5 ppg" is required by the BSEE for offshore drilling.

appropriately selected based on pore pressure gradient, wellbore stability, and fracture gradient before setting a casing. The drilling mud is applied in the form of mud pressure to support borehole walls for preventing formation fluid influx and wellbore collapse during drilling operations. To avoid fluid influxes, pressure kicks, and wellbore instabilities in an openhole section, a heavier downhole mud weight than the pore pressure gradient is required. For offshore drilling, the US Bureau of Safety and Environmental Enforcement (BSEE) requires that the safe drilling margins must meet the following conditions: (1) static downhole mud weight must be greater than estimated pore pressure; (2) static downhole mud weight must be a minimum of one-half (0.5) pound per gallon (ppg) below the lesser of the casing shoe pressure integrity test or the lowest estimated fracture gradient. Otherwise, the hole is undrillable except when applying wellbore strengthening technology, or a casing needs to be set to protect the overlying formations from being fractured, as demonstrated in Fig. 9.1. Fracture gradient can be measured from leak-off tests (LOTs) or estimated from empirical equations, as stated in the following sections.

9.1.2 Fracture gradient from leak-off tests

Typically, a formation pressure integrity test or the formation LOT is performed in drilling operations to evaluate cement jobs, determine the casing setting depth, test the resistance of tensile failures of a casing shoe, and estimate the formation fracture gradient (Postler, 1997). Based on the injection pressure, volume, and time, three pressure integrity tests can be defined, i.e., formation integrity test (FIT), LOT, and extended leak-off test (XLOT). The purpose of conducting a FIT is to test the formation fracture pressure required for kick tolerance and safe drilling mud weight margin. The maximum pressure in the FIT test is less than the fracture initiation pressure. The LOT or FIT, a routine in the drilling industry, is typically conducted after drilling a few feet below a new casing shoe to determine the upper mud weight limit (i.e., fracture gradient) for the next hole section.

In an XLOT test at a casing shoe, only the open hole below the casing and any new formation (~10 ft) drilled before the test are exposed (Edwards et al., 2002) to the injection fluid that is pumped at a constant rate. The pressure increase in the hole is typically linear as long as there are no leaks in the system, and the exposed formation is not highly permeable. At some point, the rate of pressurization changes such that the pressure–time curve departs from linearity, as shown in Fig. 9.2A. This departure from linearity is referred to as the fracture initiation pressure (P_i). The pressure is then typically seen to increase at a lower rate until a maximum pressure is reached, i.e., the breakdown pressure (P_b). After this point, the pressure falls rapidly. After the rock is broken down (hydraulic fracture

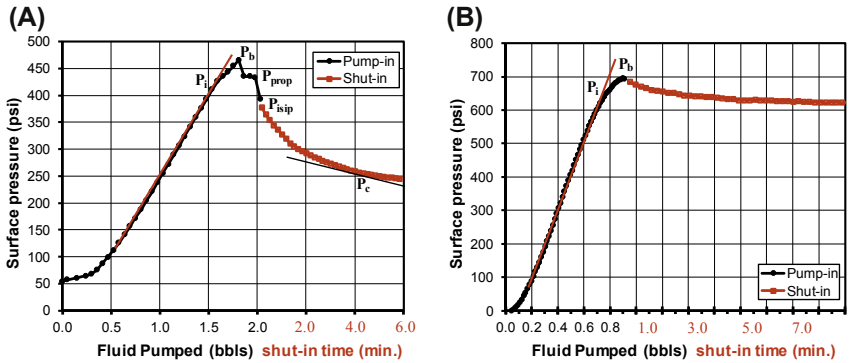

Figure 9.2 Typical leak-off tests showing the relationships between fluid pumping pressures and injection time or volumes during drilling operations. (A) XLOT; (B) LOT.

created), at some point the pressure in the hole levels off and remains fairly constant (P_{prop}) at the same flowrate, and the fracture is propagating. When the pump is turned off, the pressure immediately drops to the instantaneous shut-in pressure (P_{isip}). After the well is shut-in, the pressure begins to decline as the fracture starts to close; the stress acting to close the fracture is the closure pressure (P_c) or the minimum stress (σ_{min}). To obtain formation tensile strength and more accurate closure pressure data, a second pressurization cycle may then be performed. Because a fracture has been created by the first cycle of XLOT, there is no tensile strength in the fracture reopening (Zhang and Roegiers, 2010).

For a typical LOT test, once the peak pressure, or the breakdown pressure, is reached, the pump is shut down to record the 10-second pressure reading and then continue recording the shut-in pressure for more than 10 min, as shown in Fig. 9.2B. Fracture pressures can also be obtained from other tests, e.g., mini-frac test and diagnostic fracture injection test (DFIT).

9.1.3 Fracture gradient and mud losses in drilling operations

Understanding the mechanism of mud losses can help to better determine fracture gradient. The possible reasons of mud losses in drilling operations are presented in the following cases. For different cases, the methods for mud loss control and fracture gradient design are different.

Case 1. Seepage mud loss: For permeable rocks (excluding those with highly fractured preexisting fractures), once the mud pressure applied in the borehole is greater than the formation pore pressure ($p_{mud} > p_p$), the mud will invade and flow into the formation through pores due to the high permeability. This is the seepage mud loss, which can easily happen in permeable sandstones and limestones, particularly for the low pore pressure or depleted reservoirs. Seepage mud loss is a slow mud volume escape or loss into the formation through porous rocks or small holes. Therefore, seepage loss in most cases is minimal (normally, the loss < 10 bbl/h for oil-based mud and < 25 bbl/h for water-based mud). This will have little effect for drilling operations. Because the seepage mud loss is mainly caused by the connected pores or by formation permeability, lost circulation material pills can be used to block the flow path.

Case 2. Small loss: If the mud pressure is greater than the fracture initiation pressure, but less than the breakdown pressure ($P_i \leq p_{mud} < P_b$) in the intact shale, there will be only small volume of drilling fluid lost into the well. It can be seen from the XLOT in Fig. 9.2 that it only needs

0.3 bbls of fluid pumped into the well from the initiation pressure (P_i) to the breakdown pressure (P_b). Therefore, mud loss may be minor in this case.

Case 3. Partial loss: If the mud pressure is slightly greater than the fracture breakdown pressure ($p_{\text{mud}} \geq P_b$) in the intact shale, this will be a situation when some volume of drilling fluid is lost into the formation, but some drilling mud volume still circulates back to the surface. In this case, not only the mud volume has losses but the borehole may also have the ballooning issue to deal with.

Case 4. Partial loss and total loss in natural fractures: Once the mud pressure is greater than the minimum stress ($p_{\text{mud}} > \sigma_{\text{min}}$) in the preexisting uncemented fractures, the fractures will open and the mud will flow into the natural fractures. The degree of mud loss depends on both fracture properties (e.g., fracture aperture and spacing) and the difference of the mud pressure and the minimum stress.

Case 5. Total loss or lost circulation: It occurs either in intact rocks with $p_{\text{mud}} >> P_b$ or in the rocks having preexisting natural fractures and faults with $p_{\text{mud}} > \sigma_{\text{min}}$. This is the worst situation because there is no mud returning to the surface, and the mud level will drop to any level down in the hole. Losing a lot of drilling fluid into the well will directly affect hydrostatic pressure at the bottom. If the mud cannot be kept full in the hole, it might be the time when the hydrostatic pressure of the mud is less than the reservoir pore pressure, and a kick may happen.

It should be noted that mud loss mechanisms described above are mainly for clastic formations but may not be relevant to carbonate formations. Some carbonate reservoirs contain different sizes of vugs or caves that are interconnected by natural fractures. As a result, a large amount of mud could be lost once the drilling mud weight is greater than the reservoir pore pressure ($p_{\text{mud}} > p_p$). The same applies for those reservoirs with highly fractured preexisting open fractures. Therefore, fracture gradient in this case is not much higher than the reservoir pressure. This case is not considered in this chapter.

For most cases, fracture gradient should be equal to or less than the breakdown pressure gradient (i.e., FG $\leq P_b$) to avoid uncontrollable mud losses.

9.2 Fracture gradient prediction methods

The measured data (e.g., LOT, DFIT) show that fracture gradients in shales and sandstones are different. Normally, a shale has a higher fracture gradient

than that in a sandstone, the reason may be due to that the shale has a higher minimum stress than that in the sandstone. Therefore, fracture gradient prediction methods for shale and sandstone are different.

The concept and calculation of fracture gradient probably first came from the minimum injection pressure proposed by Hubbert and Willis (1957). They assumed that the minimum injection pressure to hold open and extend a fracture is equal to the minimum stress:

$$P_{inj}^{\min} = \sigma'_h + p_p = \sigma_h \tag{9.1}$$

where $P_{inj}^{\min}$ is the minimum injection pressure; σ'_h is the effective minimum stress; σ_h is the minimum stress; p_p is the pore pressure.

Hubbert and Willis (1957) assumed that under conditions of incipient normal faulting, the effective minimum stress is horizontal and has a value of approximately one-third the effective overburden stress, i.e., $\sigma'_h = (\sigma_V - p_p)/3$. Therefore, they obtained the minimum injection pressure or fracture pressure in the following form:

$$P_{inj}^{\min} = \frac{1}{3}(\sigma_V - p_p) + p_p \tag{9.2}$$

where σ_V is the vertical stress.

Later on, many empirical and theoretical equations for fracture gradient prediction were proposed (e.g., Haimson and Fairhurst, 1967; Matthews and Kelly, 1967; Eaton, 1969; Anderson et al., 1973; Althaus, 1977; Pilkington, 1978; Daines, 1980; Breckels and van Eekelen, 1982; Constant and Bourgoyne, 1988; Aadnoy and Larson, 1989; Wojtanowicz et al., 2000; Barker and Meeks, 2003; Fredrich et al., 2007; Wessling et al., 2009; Keaney et al., 2010; Zhang, 2011; Oriji and Ogbonna, 2012; Zhang and Yin, 2017). In the following sections, some commonly-used methods are reviewed.

9.2.1 Matthews and Kelly method

Matthews and Kelly (1967) introduced a variable of the "matrix stress coefficient (k_1)," equivalent to effective stress coefficient, for calculating fracture gradient of sedimentary formations:

$$FG = k_0(OBG - P_p) + P_p \tag{9.3}$$

where FG is the fracture gradient; OBG is the overburden stress gradient; P_p is the pore pressure gradient; k_0 is the matrix stress or effective stress coefficient (it was k_1 in their original equation), and $k_0 = (\sigma_h - p_p)/(\sigma_V - p_p)$.

In their paper, Matthews and Kelly (1967) obtained k_0 from the fracture initiation pressures. Consequently, this fracture gradient is higher than the fracture extension gradient (the minimum stress gradient).

Zhang and Yin (2017) analyzed more than 200 publicly available LOT datasets from exploration and production drilling wells in several offshore petroleum basins (the Gulf of Mexico, the North Sea, South America, the Gulf of Guinea and Asia). The LOT data are chosen only for those tests in which each test passed the initiation pressure, then reached a peak pressure value (i.e., excluding FIT tests) and performed in shale or shaly formations, excluding those tests conducted in sandstones or other permeable formations. Most of the data are from LOT tests, and only some are from XLOT tests; therefore, the peak pressure values of the tests (here called LOT values) may not be the breakdown pressures, but greater than the initiation pressures. These wells are located in young sediments, mostly in the Neogene and Paleogene formations and in the normal faulting stress regime. By assuming that the LOT is the measured fracture gradient, they analyzed the LOT, OBG (overburden stress gradient), and P_p (pore pressure gradient) relationship. Fig. 9.3 plots the net LOT pressure or effective LOT pressure gradient ($LOT-P_p$) versus the effective overburden stress gradient

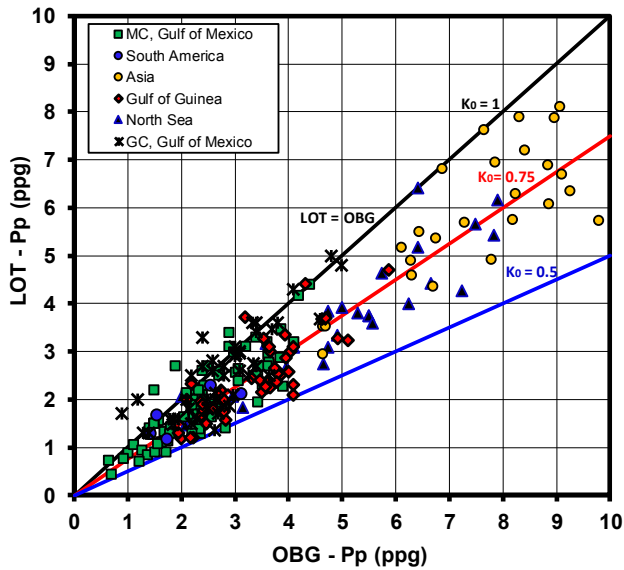

Figure 9.3 The effective LOT pressure gradient versus the effective overburden gradient (OBG) in 229 LOT datasets from offshore wells in several petroleum basins. The lines are the upper and lower bound k_0 and the average value of the bounds (Zhang and Yin, 2017).

$(OBG-P_p)$ for all 229 LOT datasets in which the pore pressures and overburden stresses are reliable. The effective stress coefficients $(k_0 = (LOT - P_p)/(OBG - P_p))$ are also plotted in Fig. 9.3. It shows that most measured data are located within $k_0 = 0.5-1$. The average value of the effective stress coefficient from $k_0 = 0.5$ to 1 is $k_0 = 0.75$. Therefore, $k_0 = 0.75$ can be used as the most likely value to calculate fracture gradient by plugging $k_0 = 0.75$ into Matthews and Kelly's equation (Eq. 9.3).

For sandstones, Eq. (9.3) can still be used for fracture gradient prediction, but a smaller k_0 should be used, e.g., $k_0 = 0.5$ and this value needs to be calibrated using measured data or mud loss events in sandstones.

9.2.2 Depth-dependent k_0 method

Fig. 9.3 shows that k_0 is scattered and is not a constant. The scattered k_0 may be caused by the fact that the LOT data were measured from different basins. For a specific basin or oil field, the LOT data should not be so scattered. To analyze what factor mostly affects variable k_0, Zhang and Yin (2017) calculated the k_0 value in each measured LOT data point as presented in Fig. 9.3 based on $k_0 = (LOT - P_p)/(OBG - P_p)$ and then plotted the k_0 values versus depths, as shown in Fig. 9.4. It demonstrates that k_0 is highly dependent on the depth, and the wells in the Green Canyon of the Gulf Mexico have higher LOT values, but the wells in the North Sea and the Gulf of Guinea have lower LOT values. Fig. 9.4 indicates that k_0 has a higher value at a shallower depth and decreases as the depth increases, i.e., k_0 is depth-dependent. Therefore, fracture gradient is also depth-dependent. The k_0 value from the LOT data in Fig. 9.4 can be expressed in the following equation:

$$k_0 = k + a/e^{Z/b} \tag{9.4}$$

where Z is the depth below the mudline or below the sea floor (in ft); k_0 is the effective stress coefficient and is dependent on the depth:

- for the low case of fracture gradient: $k = 0.5$, $a = 0.1$, $b = 5100$ (left line in Fig. 9.4);
- for the high case of fracture gradient: $k = 0.9$, $a = 0.4$, $b = 12500$ (right line in Fig. 9.4);
- for the most likely case of fracture gradient: $k = 0.75$, $a = 0.15$, $b = 7200$ (middle line in Fig. 9.4).

Based on author's field applications, the low case of k_0 shown above may be used for estimating the most likely fracture gradient in sandstones or sandy formations.

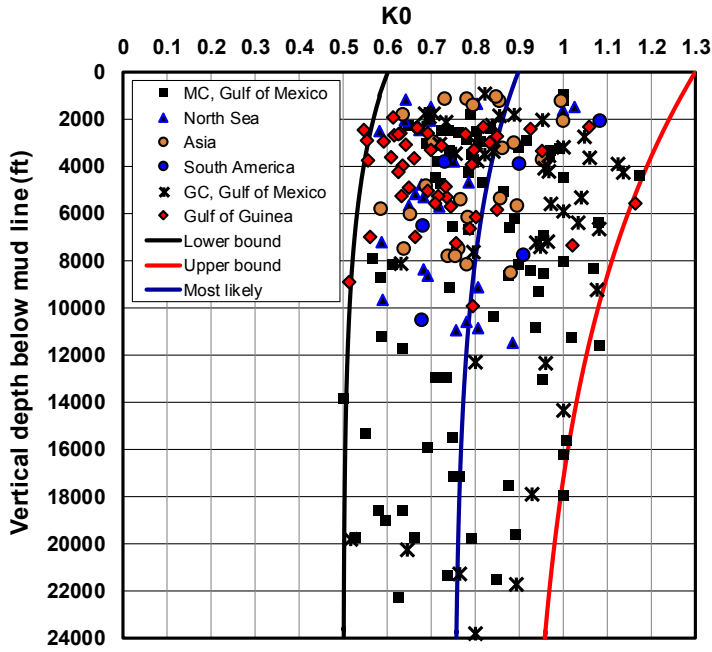

Figure 9.4 The effective stress coefficients from LOT data in offshore wells in worldwide petroleum basins.

It should be noted that k_0 varies markedly in different basins or fields; therefore, the parameters of k, a, and b in Eq. (9.4) should be obtained from each field for a better application, if the measured LOT data are available.

Based on this depth-dependent k_0, an improved fracture gradient of the Mathews and Kelly method (depth-dependent k_0 method) can be written in the following form:

$$FG = \left(k + a/e^{Z/b}\right)(OBG - P_p) + P_p \tag{9.5}$$

where Z is in ft, as defined in Eq. (9.4); k, a, and b are variables, which can be determined from the LOT data in offset wells. From the data shown in Fig. 9.4, the following parameters can be used:

- for the most likely fracture gradient in shales: $k = 0.75$, $a = 0.15$, $b = 7200$;
- for sandstones, the low case of shale fracture gradient in Fig. 9.4 may be used for the most likely sandstone fracture gradient (i.e., $k = 0.5$, $a = 0.1$, $b = 5100$), but it needs calibrations before applications.

9.2.3 Eaton's method or the minimum stress method

Eaton (1969) used Poisson's ratio of the formations to calculate fracture gradient based on the concept of the minimum injection pressure proposed by Hubbert and Willis (1957):

$$FG = \frac{\nu}{1-\nu}(OBG - P_p) + P_p \tag{9.6}$$

where ν is Poisson's ratio, which can be obtained from the compressional and shear velocities (V_p and V_s):

$$\nu = \frac{\frac{1}{2}(V_p/V_s)^2 - 1}{(V_p/V_s)^2 - 1} \tag{9.7}$$

Eaton's method enables to account for the effect of different rocks (e.g., shale, sandstone) on fracture gradient prediction because the lithology effect is considered in Poisson's ratios calculated from Eq. (9.7). Therefore, if one uses Eq. (9.6) with Eq. (9.7) for fracture gradient prediction, it will give a lithology-dependent fracture gradient; hence, there is no need to distinguish shales, sandstones, and other lithologies. In fact, Eq. (9.6) is the equation of the minimum value of the minimum stress derived from a uniaxial strain condition (Zhang and Zhang, 2017). However, in the industry applications the apparent Poisson's ratios in different rocks are used to calculate fracture gradients for simplifications, e.g., using $\nu = 0.43$ for shales (or $\nu/(1-\nu) = 0.75$) and $\nu = 0.3$ for sandstones (or $\nu/(1-\nu) = 0.5$). In this case, Eaton's equation is equivalent to Matthews and Kelly's equation, if $k_0 = \nu/(1-\nu)$.

For some old formations, such as the Cretaceous-aged and older formations, Eaton's method (Eq. 9.6) with Poisson's ratios calculated from sonic logs (Eq. 9.7) is applicable, as shown in Fig. 9.5 (Zhang and Wieseneck, 2011). The calculated fracture gradient from Eaton's method in Fig. 9.5 is compared to the measured fracture gradient results from the DFIT and LOT data in several shale gas wells. In Fig. 9.5, the DFIT and LOT measurements and pore pressures in offset wells are depth-shifted to a target well based on the same formation tops in these offset wells and plotted in the pressure form. The fracture pressure in Fig. 9.5 is calculated from Eaton's method (Eq. 9.6) using the measured pore pressures from the influxes and kicks (including the Bossier and Haynesville shale gas formations) in the offset wells, and Poisson's ratios are calculated from the sonic log using Eq. (9.7). The calculated fracture pressures match the measured DFIT and LOT data very well (Fig. 9.5).

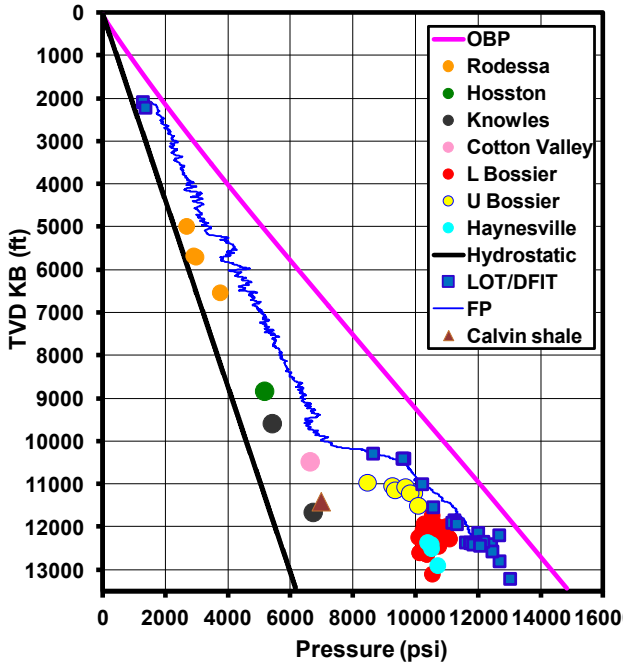

Figure 9.5 Fracture pressure (FP) profile calculated from Eaton's method (Eq. 9.6) compared to the measured DFIT and LOT pressure data plotted on the same formation tops in the Haynesville shale gas wells. Circles and triangle are the pressures of fluid kicks and influxes in the offset wells. OBP is the overburden pressure.

9.2.4 Daines' method

Daines (1980) superposed a horizontal tectonic stress σ_t to Eaton's equation. Expressing in the stress form, he called it as "minimum pressure within the borehole to hold open and extend an existing fracture", which can be written in the following equation:

$$\sigma_f = \frac{\nu}{1-\nu}(\sigma_V - p_p) + p_p + \sigma_t \tag{9.8}$$

where σ_f is the fracture pressure; σ_t is the superposed horizontal tectonic stress and a function of effective vertical (overburden) stress, i.e., $\sigma_t = \beta(\sigma_V - p_p)$ and β is a constant. Therefore, Daines' equation can be rewritten to the following form:

$$\sigma_f = \left(\beta + \frac{\nu}{1-\nu}\right)(\sigma_V - p_p) + p_p \tag{9.9}$$

9.2.5 Fracture gradient from wellbore tensile failure

Wellbore tensile failure pressure is related to and may be used for fracture gradient. When the mud pressure is higher enough, tensile stresses and tensile failures on the wellbore are initiated. The fracture initiation pressure can be calculated from Kirsch's wellbore solution. In the case of non-penetrating fluid (impermeable case) in a vertical borehole, Haimson and Fairhurst (1967) derived the following equation (Eq. 9.10) when the tensile failure occurs, and they named the pressure (p_b) to be the formation breakdown pressure:

$$p_b^V = 3\sigma_h - \sigma_H - p_p + T_0 \tag{9.10}$$

where p_b^V is the breakdown pressure in a vertical borehole; σ_h and σ_H are the minimum and maximum horizontal stresses, respectively; T_0 is the tensile strength of the rock.

In the case of penetrating fluid (permeable case), Detournay and Cheng (1988) proposed the following equation to calculate the breakdown pressure, which represents a lower bound breakdown pressure:

$$p_{bp} = \frac{3\sigma_h - \sigma_H - 2\eta p_p + T_0}{2(1-\eta)} \tag{9.11}$$

where η is a poroelastic coefficient ranging from 0 to 0.5 and $\eta = (1-2\nu)/[2(1-\nu)]$; ν is the drained Poisson's ratio.

For example, in a case of $\nu = 0.3$, then $\eta = 0.23$, the breakdown pressure is $p_{bp} = 0.7(3\sigma_h - \sigma_H - 0.58p_p + T_0)$. Comparing it to Eq. (9.10), the breakdown pressure in the permeable case is smaller than that in the impermeable case.

For inclined boreholes (including horizontal wells) and considering temperature effect (σ_T), formation breakdown pressure can be approximately written in the following form:

$$p_b = 3\sigma_{\min} - \sigma_{\max} - p_p + \sigma_T + T_0 \tag{9.12}$$

and

$$\sigma_T = \frac{\alpha_T E(T_{mud} - T_f)}{1-\nu}$$

where σ_T is the steady state thermal stress caused by the difference of the mud temperature (T_{mud}) and formation temperature (T_f); α_T is the coefficient of thermal expansion of the formation; $\sigma_{\max}$ and $\sigma_{\min}$ are the maximum and minimum far-field stresses in the borehole cross section

perpendicular to the hole axis, which can be approximately obtained from the following equations (Zhang, 2013), if the shear stresses are neglected in the inclined well:

$$\begin{aligned}\sigma_x^0 &= (\sigma_H \cos^2\alpha + \sigma_h \sin^2\alpha)\cos^2 i + \sigma_V \sin^2 i \\ \sigma_y^0 &= \sigma_H \sin^2\alpha + \sigma_h \cos^2\alpha \\ \sigma_{\max} &= \max\left(\sigma_x^0, \quad \sigma_y^0\right) \\ \sigma_{\min} &= \min\left(\sigma_x^0, \quad \sigma_y^0\right)\end{aligned} \tag{9.13}$$

where i is the borehole inclination, for a vertical well $i = 0°$ and for a horizontal well $i = 90°$; α is the angle of drilling direction with respect to the maximum horizontal stress (σ_H) direction of the borehole; σ_x^0 and σ_y^0 are the local in situ stresses in the cross section perpendicular to the axis of the inclined borehole; σ_V is the vertical stress.

Eq. (9.12) indicates that wellbore inclination affects formation breakdown pressure, and field measurements confirm this conclusion. For example, Rai et al. (2014) examined fracture gradients in nine wells drilled in three different pad locations in an onshore oil field in Asia. The measured LOPs (or formation breakdown pressures) at the 9 5/8″ casing shoe show a scatter of 1200 psi or 3 ppg mud weight equivalent. They believed that the LOP differences were caused by the well inclinations and trajectories.

9.3 Drilling direction impacts on fracture gradient in horizontal wells

If fracture initiation or breakdown pressure is used as fracture gradient, then the fracture gradient is dependent on the well inclination and drilling directions because the wellbore tensile failures in these cases are different. For a horizontal well, the fracture initiation or breakdown pressure is highly dependent on in situ stresses and drilling directions.

(1) In the normal or strike-slip faulting stress regime, for a horizontal well drilled in the minimum horizontal stress direction the formation breakdown pressure has the following forms:

$$p_b^H = 3\sigma_H - \sigma_V - p_p + T_0, \text{ if } \sigma_V > \sigma_H (\text{normal faulting stress}) \tag{9.14}$$

$$p_b^H = 3\sigma_V - \sigma_H - p_p + T_0, \text{ if } \sigma_V < \sigma_H (\text{strike-slip faulting stress}) \tag{9.15}$$

where p_b^H is the formation breakdown pressure in the horizontal well.

Comparing it to the breakdown pressure in the vertical well (i.e., Eq. 9.10), Eq. (9.15) has a higher breakdown pressure. That is, in the strike-slip faulting stress regime, a horizontal well drilled in the minimum horizontal stress direction has a higher breakdown pressure or higher fracture gradient.

From Eq. (9.14) it cannot be explicitly found whether the horizontal well has a higher or lower breakdown pressure than that in a vertical well, which depends on the magnitudes of three in situ stresses. The difference of the breakdown pressures in the horizontal and vertical wells is $p_b^H - p_b^V = 4\sigma_H - 3\sigma_h - \sigma_V$. If two horizontal stresses are very close, then, the difference $p_b^H - p_b^V \approx -(\sigma_V - \sigma_H) < 0$. This means that in the normal faulting stress regime, a horizontal well drilled in the minimum horizontal stress direction has a lower breakdown pressure or lower fracture gradient if two horizontal stresses are very close.

(2) In the normal faulting stress regime, for a horizontal well drilled in the maximum horizontal stress direction the breakdown pressure (or fracture gradient) can be expressed in the following form:

$$p_b^H = 3\sigma_h - \sigma_V - p_p + T_0 \tag{9.16}$$

Comparing it to the case in the vertical well (Eq. 9.10), the difference $p_b^H - p_b^V = -(\sigma_V - \sigma_H) < 0$; therefore, for the horizontal well in this case Eq. (9.16) has a lower breakdown pressure (or fracture gradient) than that in the vertical well, because of $\sigma_V > \sigma_H$.

(3) In the strike-slip faulting stress regime for a horizontal well drilled in the maximum horizontal stress direction:

From Eqs. (9.10) and (9.16), $p_b^H - p_b^V = -(\sigma_V - \sigma_H) > 0$ because $\sigma_V < \sigma_H$; therefore, the horizontal well has a higher breakdown pressure (or fracture gradient) than that in the vertical well.

(4) In the reverse faulting stress regime, for a horizontal well drilled in the minimum horizontal stress direction:

$$p_b^H = 3\sigma_V - \sigma_H - p_p + T_0 \tag{9.17}$$

Comparing Eq. (9.17) to Eq. (9.10), the horizontal well has lower breakdown pressure than that in the vertical well.

(5) In reverse faulting stress regime, for a horizontal well drilled in the maximum horizontal stress direction:

$$p_b^H = 3\sigma_V - \sigma_h - p_p + T_0 \tag{9.18}$$

Comparing Eq. (9.18) to Eq. (9.10), the horizontal well can have a lower or higher breakdown pressure than that in the vertical well depending on the magnitudes of the three in situ stresses.

It should be noted that the far-field minimum stress does not change with well azimuth and drilling direction. Therefore, if the minimum stress is used as fracture gradient, it should be a constant for the horizontal wells.

9.4 Temperature and depletion impacts on fracture gradient

9.4.1 Temperature impact on fracture gradient

Besides wellbore inclination and drilling direction, another important factor that impacts fracture gradient is the drilling mud temperature, which causes wellbore temperature change and consequently affects fracture gradient. Eq. (9.12) indicates that a lower mud temperature can reduce the formation breakdown pressure, namely, decrease fracture gradient. Borehole drilling and mud circulation cause the formation cooling and reheating. The formation cooling by drilling mud may cause the near-wellbore fracture gradient to be exceeded, inducing small fractures. Closure of these fractures on reheating is responsible for transient fracture pressure build up and back flow or wellbore ballooning (Maury and Idelovici, 1995). The rapid decrease in temperature at the wellbore wall leads to tensile stresses that cause cracks to initiate and propagate into the rock. The induced thermal stresses in a typical rock associated with a temperature change of only 50°F (10°C) can be of the order of 1−10 MPa. Cooling thus gives rise to tensile stress components and makes the formation to be more likely to generate hydraulic fractures (Stephens and Voight, 1982). Evidence from several ChevronTexaco deepwater wells suggests that reduction of fracture gradients owing to cooling around a wellbore may be a major contributor to lost circulation events, causing millions of dollars in additional well costs. A field test of the magnitude of the effect of temperature on fracture gradient was performed in a shallow sand and shale sequence in a South Texas well. The field tests showed that an increase in mud temperature of 61°F caused an increase in fracture gradient of 1.5 ppg at the depth of 3081 ft (Gonzalez et al., 2004; Pepin et al., 2004).

Using the finite element method (FEM) coupled with thermal and geomechanical effects, the temperature impacts are examined on wellbore stresses and fracture gradients. The boundary conditions of temperatures at

Table 9.1 In situ stresses and rock properties used in the FEM modeling

Parameter	Magnitude
Minimum horizontal stress, σ_h (psi)	5953
Maximum horizontal stress, σ_H (psi)	7053
Downhole mud pressure, p_w (psi)	6480
Young's modulus of the rock, E (psi)	1.09×10^6
Poisson's ratio of the rock, ν	0.225
Density of the rock, ρ (g/cm^3)	2.3
Hole diameter, d (in)	12
Heat capacity at constant pressure (J/kg·K)	1000
Thermal conductivity (W/m·K)	4.5
Coefficient of thermal expansion (1/K)	1.0×10^{-5}
Temperature at wellbore wall (°F)	146
Temperature at wellbore far-field (°F)	196

the wellbore wall (inner boundary) and the far-field (outer boundary) are added in the heat transfer model of solids and coupled to the geomechanical model. The in situ stresses, rock mechanical and thermal properties, and wellbore boundary temperatures are listed in Table 9.1, a similar case study reported in Zhang et al. (2016). Modeling results indicate that the wellbore cooling due to cooler mud than the formation original temperature decreases wellbore tangential stresses, hence reduces formation breakdown pressure. Fig. 9.6 compares the thermal effects on the tangential stresses using a cooler (50°F lower than the formation) mud to the one without considerations of temperatures. It indicates that cooling 50°F makes the tangential stress to decrease 9.26% in the maximum horizontal stress direction.

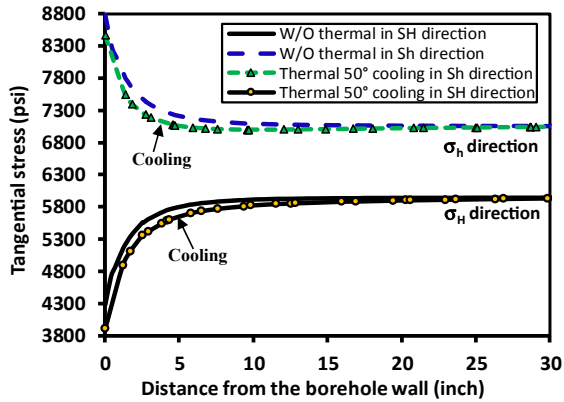

Figure 9.6 Tangential stresses along the minimum and maximum horizontal stress directions with thermal (cooling 50°F) and without thermal effects.

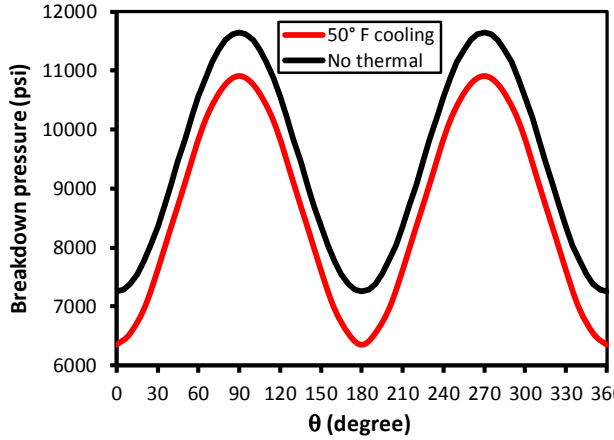

Figure 9.7 Formation breakdown pressures with and without thermal effects around a wellbore wall (pore pressure $p_p = 3535$ psi). $\theta = 0^\circ$ and 180° are the maximum horizontal stress direction, which is the tensile fracture initiation and formation breakdown direction.

The FEM model also shows that the breakdown pressure (the wellbore pressure when tensile failure occurs) decreases 905 psi or 12.5%, when the temperature difference between the formation and the drilling mud is 50°F (cooling), as shown in Fig. 9.7. It implies that cooling the wellbore reduces fracture gradient, and heating the wellbore through a heated mud can increase fracture gradient.

9.4.2 Pore pressure and depletion impacts on fracture gradient

Field measurements show that overpressures cause fracture gradient to increase, as shown in Figs. 9.5 and 7.22. Therefore, a higher pore pressure corresponds to a higher fracture gradient. However, pore pressure decrease (e.g., depletion, pressure regression) causes fracture gradient to decrease; consequently, this decreased fracture gradient may result in mud losses while drilling. Low fracture gradients or low LOT values caused by depletion have been found in many cases, e.g., in the Valhall field of the North Sea (Zoback and Zinke, 2002) and in the Bakken field of North Dakota (Dohman and Zhang et al., 2017). For the depleted reservoir, fracture gradient prediction can be conducted by using the aforementioned methods and replacing the pore pressure (p_p) by the reservoir pressure after depletion (p_d) (e.g., Lang et al., 2011).

9.5 Upper and lower bound fracture gradients

If neglecting temperature effect and assuming $\sigma_H - T_0$ is approximately equal to σ_h, Eq. (9.10) can be simplified to the following form for a vertical well (Zhang, 2011):

$$P_{FP\max} = 2\sigma_h - p_p \tag{9.19}$$

where

$$\sigma_h = \frac{\nu}{1-\nu}(\sigma_V - p_p) + p_p \tag{9.20}$$

Eq. (9.19) can be used to calculate the upper bound fracture pressure (or gradient), and the value obtained from Eaton's method (or the minimum stress method, Eq. 9.20) can be used as the lower bound fracture pressure (or gradient) (Zhang et al., 2008; Zhang, 2011). The average value of the lower bound and upper bound fracture pressures may be used as the most likely fracture pressure (Zhang, 2011)

$$p_{avg} = \frac{3\nu}{2(1-\nu)}(\sigma_V - p_p) + p_p \tag{9.21}$$

where p_{avg} is the average fracture pressure.

To illustrate the fracture gradient bounds, the measured LOT data in 14 wells in the Mississippi Canyon of the Gulf of Mexico are analyzed to examine the relationship of the measured LOT (fracture gradient) and the minimum stress (i.e., S_{min} in Fig. 9.8, calculated from Eq. (9.20)). Fig. 9.8 plots the lower and upper bound fracture gradients and the average fracture gradient calculated from Eq. (9.21), where Poisson's ratios are calculated from sonic logs (i.e., V_p and V_s). Fig. 9.8 shows that almost all data points are within the upper and lower bound fracture gradients and some data points are located close to the line of LOT = S_{min}. In this case study, several mud losses occurred even when mud weight or fracture gradient was less than the minimum stress, which might be caused by the preexisting natural fractures.

9.6 Fracture gradient in salt and subsalt formations

For subsalt wells in the Gulf of Mexico and other petroleum basins, drilling needs to penetrate thick salt formations to reach the hydrocarbon reservoirs. Salt creep in the subsalt well is a challenge for borehole stability (Zhang et al., 2008); therefore, a heavier mud weight (e.g., mud weight can be as

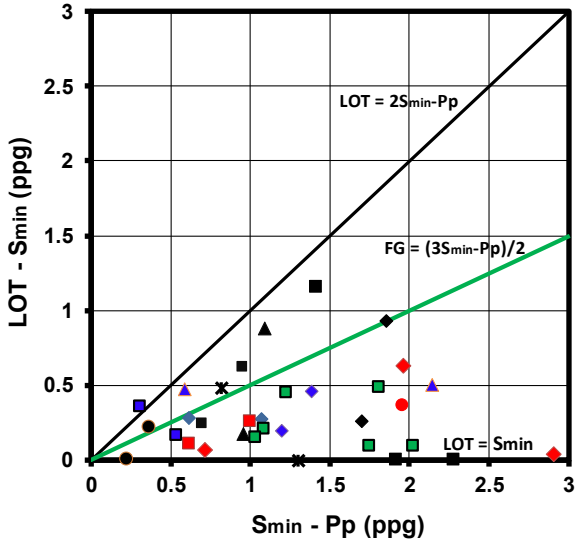

Figure 9.8 Measured LOT data in 14 deepwater wells plotted with the calculated minimum stress from Eaton's method (Eq. 9.20). The fracture gradients of upper and lower bounds and the average fracture gradient of upper and lower bounds (Eq. 9.21) are plotted for comparisons.

high as 80%–90% of the overburden stress) needs to be used to control salt creep. This heavy mud weight requires a high fracture gradient in the salt formation to avoid salt being fractured.

LOT and FIT data in salt formations in 15 wells in the Gulf of Mexico (10 in the Mississippi Canyon and 5 in the Green Canyon) are examined and presented in Fig. 9.9. It shows that the LOT and FIT pressures in most salt formations are higher than the overburden stress (σ_V) but less than $\sigma_V + 1000$ psi. Therefore, the following equation can be used to estimate fracture gradient in salt formations:

$$p_s = \sigma_V + C \tag{9.22}$$

where p_s is the fracture pressure in salt in psi; σ_V is the overburden stress in psi; C is a variable and varies from 0 to 1000 psi based on the data shown in Fig. 9.9, and for the most likely case, $C = 500$ psi.

It should be noted that Eq. (9.22) is an empirical equation only for salt formations. If rock inclusions and salt sutures exist in salt formations, fracture gradient should be lower and dependent on the fracture gradient of the involved rocks.

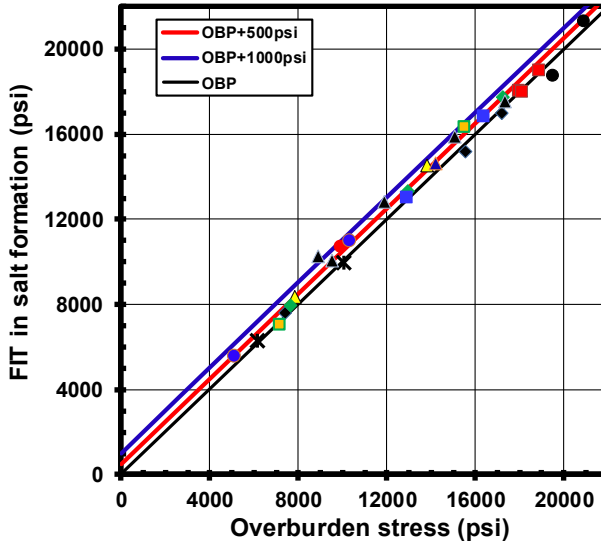

Figure 9.9 Measured FIT and LOT data points (the dots, triangles, squares, etc. in the figure) in salt formations plotted with the overburden stress (OBP) in 15 wells in the Gulf of Mexico.

A case study shown in Fig. 9.10 examines fracture gradients in salt, presalt, and subsalt formations. The salt fracture gradient is estimated from Eq. (9.22) with $C = 500$ psi, which matches the measured FIT data in the salt. In the subsalt formations, Eaton's method shown in Fig. 9.10 underestimates fracture gradient based on measured data, but the depth-dependent k_0 method (Eq. 9.5) gives a better estimate on fracture gradient. It should be mentioned that the pore pressure in pure salt should be zero, and the dashed pore pressure line in Fig. 9.10 is an imaginary line.

9.7 Reasons of leak-off test being greater than overburden stress gradient

It is often found that some LOT values in leak-off tests are greater than their overburden stress gradients (i.e., $LOT > OBG$); for example, in the Green Canyon area of the Gulf of Mexico and in some subsalt formations. These may be caused by the following reasons: (a) the measured LOT value is the formation breakdown pressure, and (b) the formation is in the tectonic stress regime.

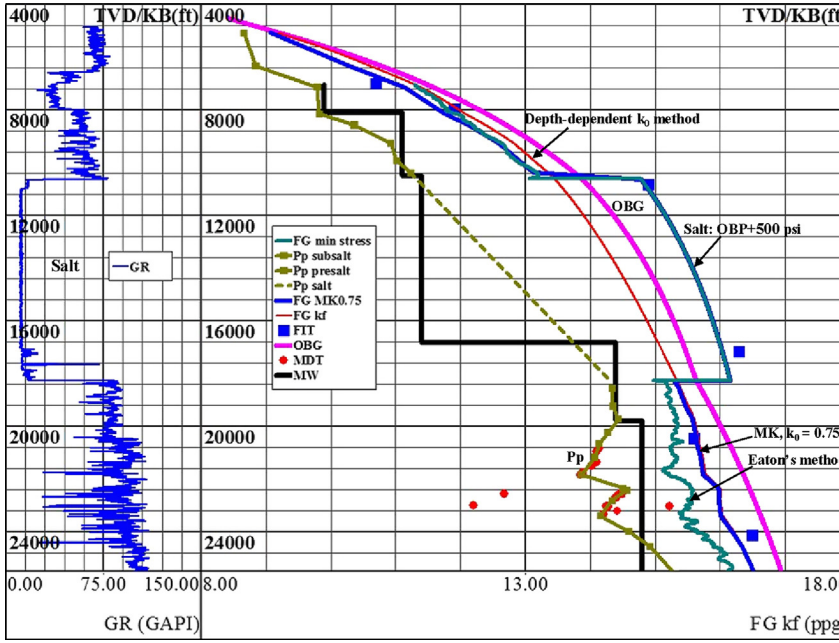

Figure 9.10 Salt fracture gradient estimated from Eq. (9.22) compared to measured FIT data in salt body in a subsalt well in the Gulf of Mexico. In the presalt and subsalt formations, the depth-dependent k_0 method (Eq. 9.5), Eaton's method, and Mathews and Kelly's method of $k_0 = 0.75$ are applied to estimate fracture gradients in rock formations.

9.7.1 Leak-off test value being the formation breakdown pressure

The LOT value reported from the leak-off test may be the formation breakdown pressure in which the rock has a high tensile strength. In this case, the breakdown pressure in a vertical well may be calculated from Eq. (9.10). An example is presented in Fig. 9.11 for illustration. At the depth of 10,800 ft, if the minimum horizontal stress gradient $\sigma_h = 12.8$ ppg, the maximum horizontal stress gradient $\sigma_H = 13.4$ ppg, pore pressure gradient $P_p = 11$ ppg, and tensile strength $T_0 = 100$ psi, then the breakdown pressure can be calculated from Eq. (9.10), i.e., the breakdown pressure gradient is 14.18 ppg. However, the overburden gradient at this depth is $OBG = 13.9$ ppg, as shown in Fig. 9.11. Therefore, the breakdown pressure gradient is greater than the overburden gradient (i.e., $LOT > OBG$). The measured LOT value in Fig. 9.11 at the depth of 10,800 ft is 14.1 ppg, similar to the calculated formation breakdown pressure gradient.

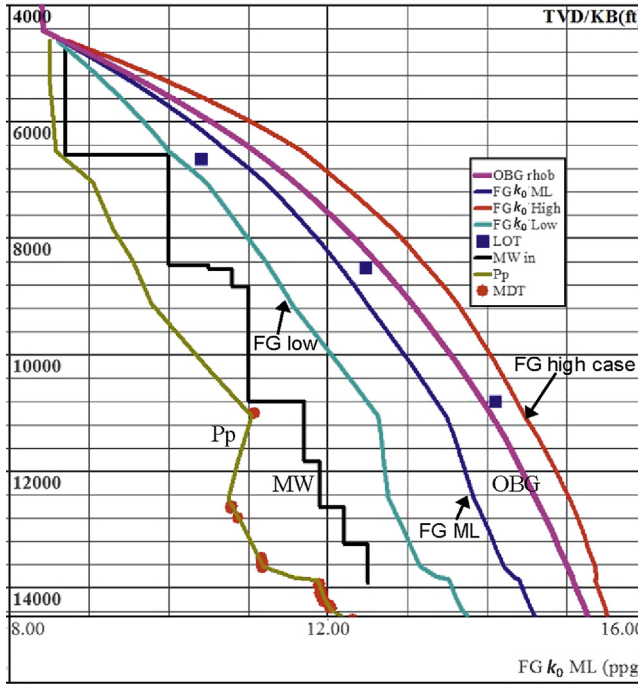

Figure 9.11 Measured LOT data plotted with depth versus the estimated high side, most likely and low side fracture gradients from Eq. (9.5) in a deepwater Gulf of Mexico well.

Fig. 9.11 plots the estimated and measured pore pressure gradient, surface mud weight, overburden gradient, and measured LOT values. It also plots the calculated fracture gradient bounds (high, most likely and low cases) from the depth-dependent k_0 method (Eq. 9.5). The figure also shows that one of measured LOTs is greater than the overburden gradient, and all LOT data are within the calculated fracture gradient range.

9.7.2 In tectonic stress regimes

When formations are in tectonic stress regimes or close to the base of salt, two horizontal stresses can be equal to or even greater than the overburden stress. For example, for the subsalt formations, not far from the base of salt, where three principal stresses are nearly equal ($\sigma_V \approx \sigma_H \approx \sigma_h$), the formation breakdown pressure can be calculated from Eq. (9.10) as follows:

$$LOT = P_b \approx 2\sigma_V - p_p + T_0 \tag{9.23}$$

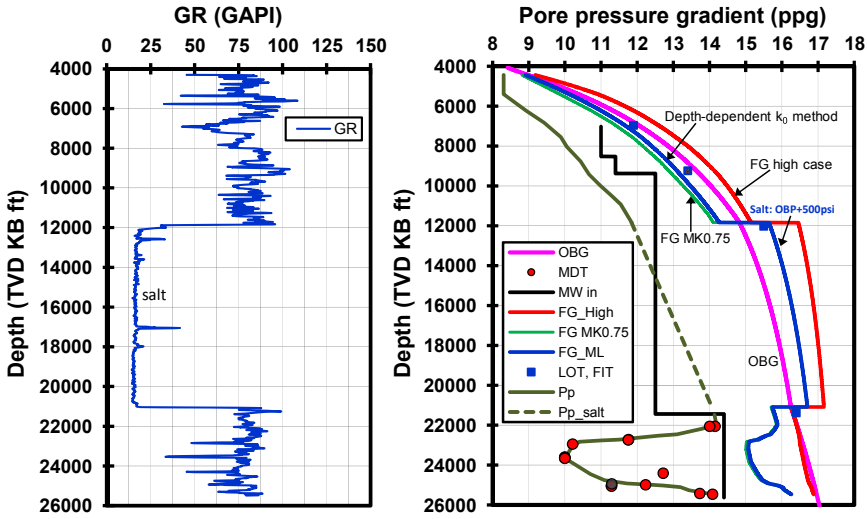

Figure 9.12 Measured LOT greater than the OBG in the subsalt formations. Fracture gradients (the most likely and high cases) are calculated from the depth-dependent k_0 method (Eq. 9.5) and compared to Matthews and Kelly's method with $k_0 = 0.75$ in a deepwater Gulf of Mexico well. The fracture gradients in salt are obtained from Eq. (9.22).

Because pore pressure is less than overburden stress ($p_p < \sigma_V$), from Eq. (9.23) it can be obtained that $P_b > \sigma_V$, i.e., the breakdown pressure gradient or LOT is greater than the overburden gradient (LOT > OBG). There are many cases where the measured peak values in LOTs are greater than their overburden stress values in subsalt formations, particularly when the formations are close to the base of salt. Fig. 9.12 shows a case that the measured LOT value is 16.4 ppg at 21,427 ft (342 ft below the base of salt), where the overburden stress gradient is 16.3 ppg, i.e., LOT > OBG.

Fig. 9.12 also plots the measured LOT values in the presalt and subsalt formations. There is also a measured FIT value in the salt formation. The high side and the most likely fracture gradients in shales calculated from the depth-dependent k_0 method (Eq. 9.5) are compared to Matthews and Kelly's method (with a constant $k_0 = 0.75$) in Fig. 9.12. It should be noted that the sandstone fracture gradient is not plotted in the figure. The most likely ($C = 500$ psi) and high case ($C = 1000$ psi) fracture gradients in salt formation are calculated from Eq. (9.22) and plotted in the same figure.

9.8 Wellbore strengthening to increase fracture gradient

9.8.1 Wellbore strengthening

Lost circulation is a major challenge in well construction operations, especially where drilling margins are narrow or in pressure-depleted reservoirs. Drilling-induced tensile fractures often occur in a low-pressure reservoir caused by pressure depletion or pore pressure regression, which induces a lower fracture gradient than the surrounding shale formations. This low fracture gradient presents significant drilling challenges. As a result, additional casing may be needed to isolate the risky zone. A lower mud weight may also be required to keep the wellbore pressure below the fracture gradient, which can then lead to wellbore instability or well control issues in higher pressure intervals within the same wellbore section (Zhang et al., 2016). Therefore, wellbore strengthening is required for increasing fracture gradient of the rock, widening the mud weight window, and consequently enhancing the well integrity and mitigating mud losses.

Various experts have proposed a variety of techniques to increase fracture gradient. Most of these techniques achieve an increase in fracture resistance by actually inducing a tensile fracture using a heavier mud density to increase tangential stresses and then arresting fracture growth by isolating wellbore pressure at some point between the mouth and tip of the fracture. Some techniques use fibers and other materials to cover the fracture mouth within the wellbore and thereby hydraulically isolate the fracture. The method proposed by Alberty and McLean (2004) uses large particles to plug and bridge the mouth of the fracture and then small particles to seal around the bridging particles to arrest fracture growth. Other methods use small particles to either build an immobile mass at some point along the fracture or to fill the fracture altogether from the tip to the mouth (Dupriest, 2005; Van Oort et al., 2009; Morita et al., 1990; Wang et al., 2009). Some methods also aim to isolate the very tip of the fracture with very small particles (Van Oort et al., 2009; Contreras et al., 2014). Wellbore strengthening techniques have been successfully used to increase formation fracture gradient, reduce mud losses, and access resources that may have been undrillable using conventional drilling methods.

The FEM modeling demonstrates that the stress cage methodology increases fracture resistance within a wellbore by increasing the tangential stresses around the wellbore wall in the vicinity of an induced fracture (Zhang et al., 2016, Feng et al., 2015). The FEM modeling indicates that after creating a bi-wing fracture in a wellbore the tangential stresses increase

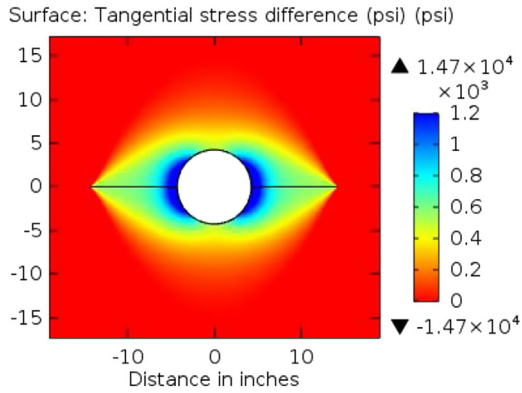

Figure 9.13 The increased tangential stress area induced by creating a bi-wing fracture in a wellbore modeled by the FEM (Zhang and Yin, 2019).

markedly around the fracture and the wellbore (Fig. 9.13). When the fracture is plugged, the wellbore is strengthened, which makes it difficult to create new fractures around the wellbore. Lab experiments verified that wellbore strengthening can greatly increase fracture gradient. For instance, experiments in the Roubidoux sandstone cores show that the formation breakdown pressures were increased by 39%–65%, and the fracture initiation pressures were increased by 15%–36% when the oil-based mud with the nanoparticles combined with graphite was used to seal the fractures (Contreras et al., 2014). Although several methods for wellbore strengthening and enhancing fracture gradients have been proposed, the drilling industry converges mainly on two methods, i.e., the stress cage method (Alberty and McLean, 2004) and tip resistance by developing an immobile mass (Dupriest, 2005). Dupriest (2005) pointed out that regardless of the type of treatment used, integrity is increased by widening the fracture to increase its closing stress (closure pressure). Wellbore strengthening method of the stress cage has been applied to several hundred wells (e.g., Aston et al., 2004, 2007), making those conventionally undrillable wells (because of their very narrow drilling margins) to be drilled successfully. For a successful wellbore strengthening application, the induced fracture width is one of the most important parameters because the particle concentration required for plugging the fracture is strongly dependent on the fracture width as lab experiments verified (Guo et al., 2014). Therefore, the geometry and width of the fracture are important inputs for wellbore strengthening treatment to increase fracture gradient.

9.8.2 Analytical solutions of the fracture width

A number of analytical and semianalytical solutions have been proposed to estimate the fracture width. The line crack solution proposed by Sneddon (1946) and Sneddon and Elliott (1946) can be used to determine the width of a 2-D plane strain fracture in an isotropic stress environment without the presence of a borehole. Perkins and Kern (1961) and Geertsma and de Klerk (1969) applied Sneddon's solutions to the oil and gas industry for hydraulic fracturing applications by representing the borehole as a crack with an internal pressure and isotropic horizontal stresses.

Sneddon and Elliott (1946) proposed a solution for fracture width as a function of internal constant pressure (p_0) with no confining stress and no borehole (the equivalent of a wellbore diameter of zero) in their Eq. 17 restated here in Eq. (9.24).

$$w(x) = \frac{4(1-\nu^2)}{E} p_o \sqrt{L^2 - x^2} \tag{9.24}$$

where $w(x)$ is the fracture width; E is Young's modulus; ν is Poisson's ratio; p_o is the internal pressure; L is the fracture half-length; x is the distance from the center of the fracture.

In planning wellbore strengthening applications the induced fractures are generally short; therefore, consideration of the borehole presence becomes critical in describing the behavior of the width and length of an induced fracture, especially near the mouth of the fracture. Alberty and McLean (2004) proposed the use of both numerical and analytical solutions for estimating the width of the mouth of an induced fracture for planning wellbore strengthening applications. Their analytical solution modified Eq. (9.24) to account for the presence of a wellbore and a minimum horizontal stress in the following form (as shown in Fig. 9.14):

$$w(x) = \frac{4(1-\nu^2)}{E} (p_w - \sigma_h) \sqrt{(L+R)^2 - x^2} \tag{9.25}$$

where σ_h is the minimum horizontal stress; p_w is the mud pressure in the wellbore; R is the wellbore radius; L is the fracture length in one side of the wellbore.

This solution works well as long as the in situ stresses are isotropic. As the difference between the minimum and maximum horizontal stresses increases, the aperture of the fracture will become larger and, in some cases, can even take on more of a funnel shape toward the mouth of the fracture.

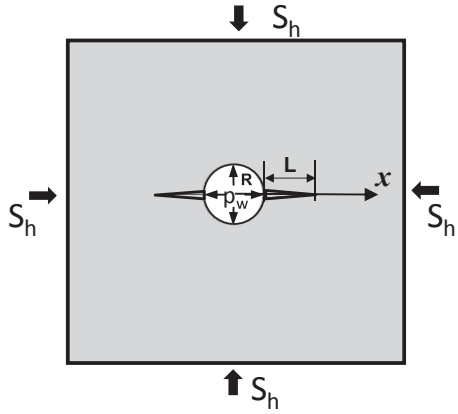

Figure 9.14 The schematic bi-wing fracture model in a wellbore ($S_h = \sigma_h$).

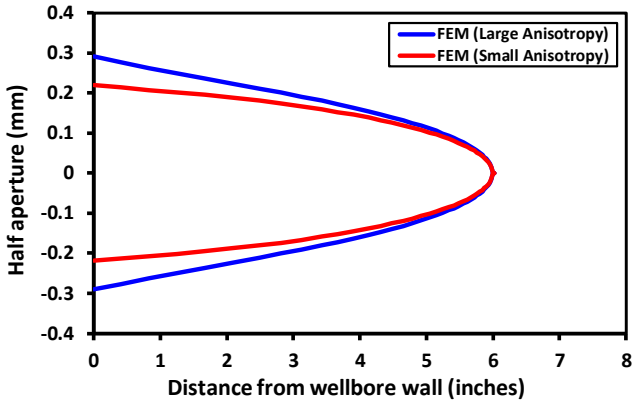

Figure 9.15 Comparison of fracture widths from the FEM numerical models with small (100 psi) and large (1000 psi) horizontal stress anisotropies.

This difference in the fracture widths can be critical in formulating mud additive concentrations when there is a need to quickly arrest fracture growth as is practiced in the stress cage methodology described by Alberty and McLean (2004). Fig. 9.15 displays a comparison of the fracture shape from the FEM model if the maximum horizontal stress is increased from 6053 psi to 6953 psi (the minimum horizontal stress is 5953 psi) while other inputs are held constant (Zhang et al., 2016). In this case, the width of the fracture mouth increases from 438 μm with 100 psi of horizontal stress anisotropy to 582 μm with 1000 psi of anisotropy. Although 1000 psi of stress anisotropy may seem large for an extensional basin, this amount of anisotropy is not unusual when a well is highly deviated.

9.8.3 Semianalytical solution of the fracture width accounting for stress anisotropy

Three in situ stress components are very different in most wells being drilled. For those wells, the analytical solution offered by Alberty and McLean (2004) in Eq. (9.25) would underestimate the fracture width due to the stress anisotropy. Therefore, a solution is needed to handle the stress anisotropy for calculating the fracture width. A number of studies have been conducted on fracture width analyses with considerations of the stress anisotropy (e.g., Guo et al., 2011; Morita and Fuh, 2012; Shahri et al., 2015; Mehrabian et al., 2015; Zhong et al., 2017). Applying superposition principle, Zhang et al. (2016) proposed a 2-D semianalytical solution for the fracture width calculation in a vertical borehole accounting for in situ stress anisotropy. They decomposed the problem into two parts, as shown in Fig. 9.16. In each part of the model, the fracture width can be obtained from Eq. (9.25); adding the two solutions together, the fracture width can be derived as the following form (Zhang et al., 2016):

$$w(x) = \frac{4(1-\nu^2)}{E}\left[p_w - \sigma_h + c(\sigma_H - \sigma_h)\right]\sqrt{(L+R)^2 - x^2} \qquad (9.26)$$

where $w(x)$ is the fracture width in the semianalytical solution; c is the stress anisotropy factor; σ_H is the maximum horizontal stress; E is Young's

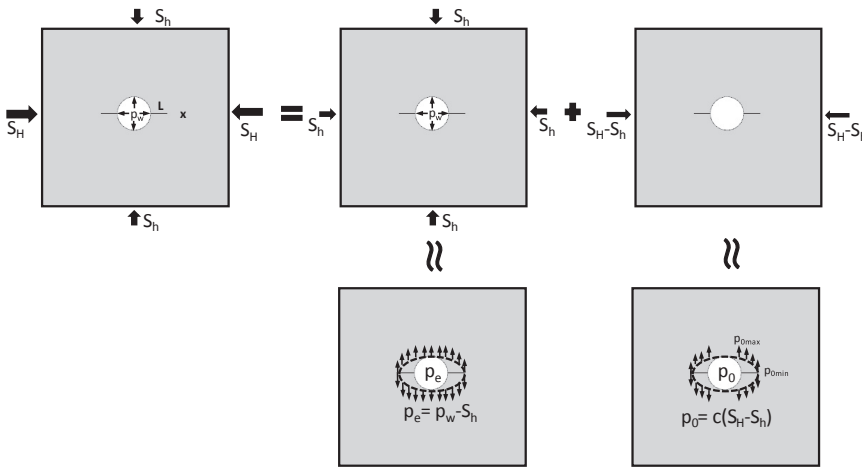

Figure 9.16 Schematic wellbore sections of a vertical borehole and fracture model under anisotropic far-field stresses, which can be decomposed and superposed in two separate models ($S_h = \sigma_h$, $S_H = \sigma_H$).

modulus of the rock; for field applications, the dynamic Young's modulus is used. This method has been applied to many cases to increase fracture gradients in the Gulf of Mexico and the North Sea.

The derivation of Eq. (9.26) can be found in the appendix of Zhang et al. (2016). A stress anisotropy factor (c) was considered in Eq. (9.26) to account for the impact of the difference of two horizontal stresses. The stress anisotropy factor was obtained from the FEM numerical modeling, which can be expressed in the following form, if the fracture length and radius are expressed in inches:

$$c = \frac{0.368R^{1/2}}{[L + 3(x - R)]^{1/1.3}} \tag{9.27}$$

where the units of R, L, and x are in inches.

In the metric units, if the radius and length (R, L, and x) are expressed in meters, the factor c can be rewritten as the following form:

$$c = \frac{0.137R^{1/2}}{[L + 3(x - R)]^{1/1.3}} \tag{9.28}$$

Fig. 9.17 shows the fracture shapes calculated from the semianalytical solution, Eq. (9.26), and from the 2-D FEM model for the small stress anisotropy case ($\sigma_H - \sigma_h = 100$ psi) and the large anisotropy case ($\sigma_H - \sigma_h = 1000$ psi). The results in two solutions match very well. Wide varieties of cases were analyzed, and the FEM and the semianalytical solutions were compared and shown to have an average difference of the width of the fracture mouth of 2.7% (Zhang et al., 2016).

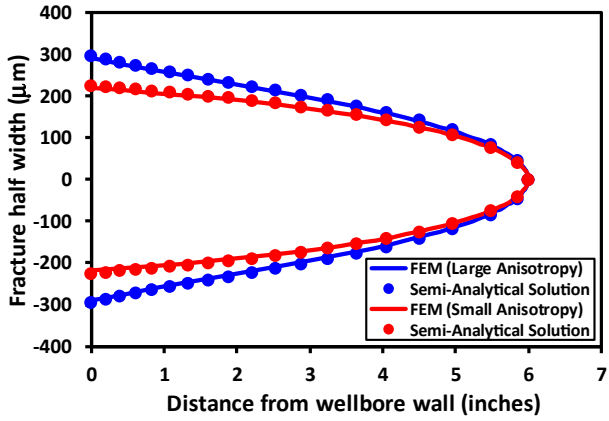

Figure 9.17 Comparisons of the semianalytical solution calculated from Eq. (9.26) and the 2-D FEM modeling for small and large horizontal stress anisotropies.

For an inclined borehole, in the wellbore cross section orthogonal to the borehole axis, the maximum and minimum far-field principal stresses ($\sigma_{\max}$, $\sigma_{\min}$) in the cross section can be calculated from the in situ stresses (σ_h, σ_H, and σ_V). Inserting $\sigma_{\max}$ and $\sigma_{\min}$ to Eq. (9.26), the fracture width can be obtained for an inclined well. In this case Eq. (9.26) becomes:

$$w(x) = \frac{4(1-\nu^2)}{E}\left[p_w - \sigma_{\min} + c(\sigma_{\max} - \sigma_{\min})\right]\sqrt{(L+R)^2 - x^2} \quad (9.29)$$

where $\sigma_{\max}$ and $\sigma_{\min}$ are the maximum and minimum far-field principal stresses in the wellbore cross section perpendicular to the borehole axis. In an inclined borehole, $\sigma_{\max}$ and $\sigma_{\min}$ can be approximately estimated from Eq. (9.13).

9.8.4 Fracture width impacted by inclinations and drilling directions

There are many factors affecting stress cage performance, e.g., mud pressure, in situ stresses, borehole deviation and drilling direction, hole size, and rock properties (i.e., Young's modulus, Poisson's ratio). For rock properties, it is straightforward to figure out their effects on the fracture widths through Eq. (9.29). For instance, a stiffer rock, i.e., a rock with a higher Young's modulus, is less deformable than a softer rock, thus having a smaller fracture width. In the following, the FEM modeling is applied to analyze the impacts of borehole deviations and drilling directions on the fracture widths. Table 9.2 lists the in situ stresses and rock properties used for modeling in a well in the North Sea. A six-inch long bi-wing fracture (the initial fracture

Table 9.2 In situ stresses and rock properties used in the FEM model.

Parameter	Magnitude
Minimum horizontal stress, σ_h (psi)	4620
Maximum horizontal stress, σ_H (psi)	4715
Overburden stress, σ_V (psi)	7085
Downhole mud pressure, p_w (psi)	5153
Young's modulus of the rock, E (psi)	5×10^5
Poisson's ratio of the rock, ν	0.23
Density of the rock, ρ (g/cm^3)	2.3
Hole diameter, d (in)	6.5
Fracture length, L(in)	6
Heat capacity at constant pressure, (J/kg·K)	1000
Thermal conductivity (W/m·K)	4.5
Coefficient of thermal expansion (1/K)	1.0×10^{-5}
Temperature at wellbore wall (°F)	146
Temperature at wellbore far-field (°F)	196

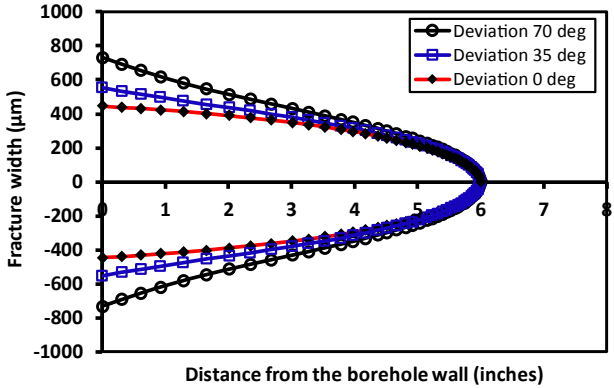

Figure 9.18 Fracture widths for a fixed fracture length of 6 inches in inclined boreholes drilled in the maximum horizontal stress direction with borehole deviations of 0, 35, and 70°.

aperture is very small, 0.0254 mm) is modeled in the borehole cross section using the COMSOL finite element software. The reason for selecting the fracture length of 6 inches is that the fracture is better to be blocked and sealed before its propagation length exceeds to 6 inches. In the first case of the modeling, the borehole drilling direction is parallel to the maximum horizontal stress direction. Fig. 9.18 displays the modeling results of fracture width variations as the inclination changes. It shows that the fracture width increases 39% for a change of inclination from 0 to 70°. Therefore, borehole inclinations affect the fracture widths very much, i.e., a higher inclination, a wider fracture for the borehole drilled in the maximum horizontal stress direction.

If inclined boreholes are drilled in different directions, the fracture widths induced by drilling are very different because the stress configurations are different around the wellbore. Two inclined boreholes with the same inclination of 35° but different directions are modeled: one is drilled in the maximum horizontal stress direction and the other is drilled in the minimum horizontal stress direction. Comparison of the two cases demonstrates that the fracture width for the borehole drilled in the maximum horizontal stress direction increases 17.8% compared to the one drilled in the minimum horizontal stress direction (Fig. 9.19).

9.8.5 Fracture widths in the stress cage with consideration of temperature

Normally the mud temperature is lower than the formation temperature, and this affects fracture width growth, particularly when the fracture is long.

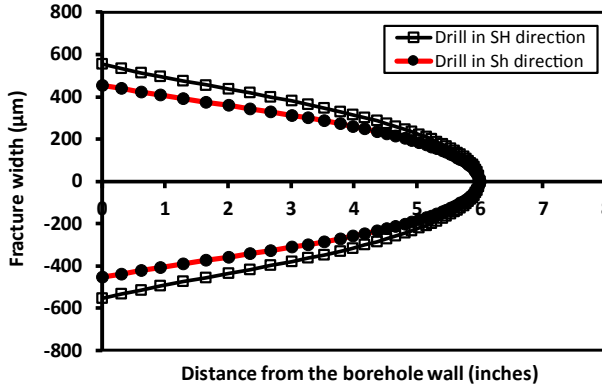

Figure 9.19 Comparison of fracture widths for boreholes drilled in the maximum and minimum horizontal stress directions for the hole inclination of 35°.

A low-temperature drilling mud cools more formation area in a longer fracture than that in a shorter fracture, because more cooling mud contacts the formation. A case in the North Sea is analyzed to examine temperature effect on the fracture width. A highly inclined borehole (deviation of 70°) is examined and the in situ stresses, mud pressure, rock properties, and temperature parameters are listed in Table 9.2. The FEM modeling shows that the temperature difference between the formation and the mud (50°F cooling) causes the fracture width to increase 7% compared to the isothermal case (Fig. 9.20) for a borehole drilled in the minimum horizontal stress direction. The increase in the fracture width leads to a requirement of

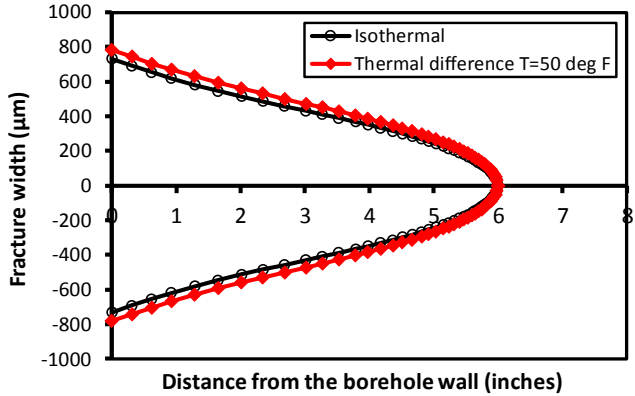

Figure 9.20 Fracture widths without thermal effect and the one when a 50°F cooler mud than the formation temperature pumped in an inclined wellbore. Cooler mud causes a wider fracture.

larger particles of mud additives to arrest the fracture growth. The decrease of the borehole temperature owing to a low mud temperature also causes the decreases of the tangential stresses (implying a decrease in fracture gradient, refer to Figs. 9.6–9.7).

9.8.6 3-D semianalytical solution of the fracture width

In the 2-D plane strain solution the fracture is assumed to be very long in one direction compared to other directions. This assumption may be appropriate for a long fracture, but it is not suitable for a near-wellbore fracture or a fracture in its early propagating stage. It is commonly assumed when a hydraulic fracture is in its early propagation stage, it propagates almost uniformly to the two major principal stress directions (e.g., the vertical and maximum horizontal directions for a vertical hydraulic fracture). In this case, the 2-D plane strain solution may not work properly. Therefore, a 3-D solution is needed for a better description of near-wellbore fractures. Fifteen application cases of 3-D FEM near-wellbore vertical fractures are modeled, and the fracture widths with different L/H (ratio of fracture half-length to fracture height) values are calculated in each case (Zhang and Yin, 2019). The corresponding 2-D FEM plane strain solution is also obtained for each case. The fracture widths and L/H in 2-D and 3-D conditions are plotted in Fig. 9.21. It can be found that the fracture widths from the 2-D to 3-D solutions are strongly dependent on the ratio of

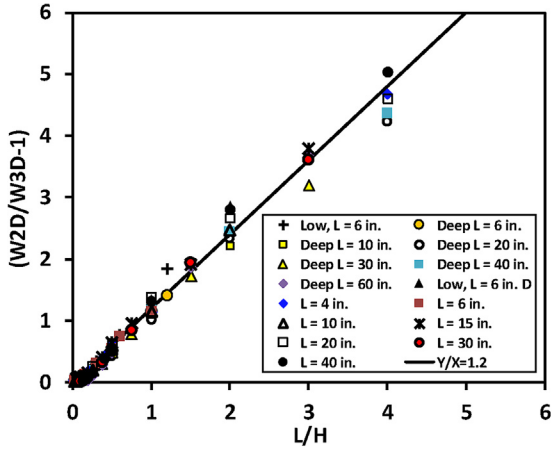

Figure 9.21 Fracture widths in 2-D and 3-D FEM models related to the ratios of fracture half-length and fracture height for 15 application cases.

fracture half-length to fracture height. The following relation between 2-D and 3-D solutions exists from the FEM modeling results:

$$\frac{w_{2D}}{w_{3D}} = 1 + \frac{1.2L}{H} \tag{9.30}$$

where w_{2D} and w_{3D} are the fracture widths in 2-D and 3-D conditions, respectively.

Assuming that the fracture propagates uniformly to the two major principal stress directions, for a vertical hydraulic fracture it has $H = 2L$. Therefore, Eq. (9.30) becomes:

$$\frac{w_{2D}}{w_{3D}} = 1.6 \tag{9.31}$$

If Eq. (9.29) is used as the 2-D solution (w_{2D}), then, from Eqs. (9.29) and (9.31) the 3-D semianalytical solution of the fracture width can be expressed in the following form:

$$w_{3D}(x) = \frac{4(1-\nu^2)}{1.6E}[p_w - \sigma_{\min} + c(\sigma_{\max} - \sigma_{\min})]\sqrt{(L+R)^2 - x^2} \tag{9.32}$$

where w_{3D} (x) is the fracture width of the 3-D solution; E is Young's modulus of the formation. Compared to Eq. (9.29), the 3-D solution predicts a smaller fracture width than the one obtained from the 2-D solution. This implies that the 2-D-based old design for wellbore strengthening may overestimate the fracture width.

In fact, fracture propagation is dependent on the principal stress magnitudes exerted in the fracture propagation directions. For a vertical hydraulic fracture, the fracture propagating length and height in the horizontal and vertical directions in an isotropic and homogeneous formation should be proportional to the far-field stress magnitudes in the corresponding directions, i.e., $2L/H \propto \sigma_H/\sigma_V$. Therefore, if the fracture propagation is controlled by the principal far-field stress magnitudes, then for a vertical fracture Eq. (9.30) can be written in the following form:

$$\frac{w_{2D}}{w_{3D}} = 1 + \frac{0.6\sigma_H}{\sigma_V} \tag{9.33}$$

Therefore, for a vertical fracture in a vertical well, the 3-D semianalytical solution of the fracture width can be expressed in the following equation:

$$w_{3D}(x) = \frac{4(1-\nu^2)}{(1+0.6\sigma_H/\sigma_V)E}[p_w - \sigma_h + c(\sigma_H - \sigma_h)]\sqrt{(L+R)^2 - x^2} \tag{9.34}$$

From Eq. (9.34) it can be observed that in the stress cage implementation, in situ stress anisotropy, rock properties, and borehole inclination impact the fracture width significantly. For a complicated case of wellbore strengthening, a numerical method (e.g., the FEM) should be used, but analytical solutions are much easier to implement for a simpler case.

References

Aadnoy, B.S., Larson, K., 1989. Method for fracture-gradient prediction for vertical and inclined boreholes. SPE Drill. Eng. 4 (2), 99–103. SPE-16695.

Alberty, M., McLean, M., 2004. A physical model for stress cages. In: SPE Annual Technical Conference and Exhibition, 26–29 September, Houston, Texas. SPE-90493.

Althaus, V.E., 1997. A new model for fracture gradient. J. Can. Pet. Technol. 16 (2), 99–108.

Anderson, R.A., Ingram, D.S., Zanier, A.M., 1973. Determining fracture pressure gradients from well logs. SPE-4135.

Aston, M., Alberty, M., McLean, M., de Jong, H., Armagost, K., 2004. Drilling fluids for wellbore strengthening. SPE-87130.

Aston, M., Alberty, M., Duncum, S., Bruton, J., Friedheim, J., Sanders, M., 2007. A new treatment for wellbore strengthening in shale. SPE-110713.

Barker, J.W., Meeks, W.R., 2003. Estimating fracture gradient in Gulf of Mexico deepwater, shallow, massive salt sections. SPE-84552.

Breckels, I.M., van Eekelen, H.A.M., 1982. Relationship between horizontal stress and depth in sedimentary basins. SPE-10336.

Constant, W.D., Bourgoyne, A.T., 1988. Fracture-gradient prediction for offshore wells. SPE Drill. Eng. June, 136–140.

Contreras, O., Hareland, G., Husein, M., Nygaard, R., Alsaba, M., 2014. Wellbore strengthening in sandstones by means of nanoparticle-based drilling fluids. SPE-170263.

Daines, S.R., 1980. The prediction of fracture pressures for wildcat wells. SPE-9254.

Detournay, E., Cheng, A.H.-D., 1988. Poroelastic response of a borehole in a non-hydrostatic stress field. Int. J. Rock Mech. Min. Sci. Geomech. Abstr. 25, 171–182.

Dohmen, T., Zhang, J., Barker, L., Blangy, J.P., 2017. Microseismic magnitudes and b-values for delineating hydraulic fracturing and depletion. SPE J. 22 (5), 1624–1634. SPE-186096.

Dupriest, F.E., 2005. Fracture closure stress (FCS) and lost returns practices. In: SPE/IADC Drilling Conference. SPE-92192.

Eaton, B.A., 1969. Fracture gradient prediction and its application in oilfield operations. J. Petrol. Technol., 25–32. SPE-2163.

Edwards, S.T., Bratton, T.R., Standifird, W.B., 2002. Accidental geomechanics – capturing in-situ stress from mud losses encountered while drilling. SPE/ISRM-78205.

Feng, Y., Arlanoglu, C., Podnos, E., Becker, E., Gray, K.E., 2015. Finite-element studies of hoop-stress enhancement for wellbore strengthening. SPE Drill. Complet. March. SPE-168001.

Fredrich, J.T., Engler, B.P., Smith, J.A., Onyia, E.C., Tolman, D.N., 2007. Predrill estimation of subsalt fracture gradient: analysis of the Spa prospect to validate nonlinear finite element stress analyses. SPE-105763.

Geertsma, J., de Klerk, F., 1969. A rapid method of predicting width and extent of hydraulically induced fractures. J. Petrol. Technol. December. SPE2458.

Gonzalez, M., Bloys, J., Lofton, J., Pepin, G., Schmidt, J., Naquin, C., Ellis, S., Laursen, P., 2004. Increasing effective fracture gradients by managing wellbore temperatures. IADC/SPE-87217.

Guo, Q., Feng, Y.Z., Jin, Z.H., 2011. Fracture aperture for wellbore strengthening applications. ARMA-11-378.

Guo, Q., Cook, J., Way, P., Ji, L., Friedheim, L., 2014. A comprehensive experimental study on wellbore strengthening. IADC/SPE-167957.

Haimson, B.C., Fairhurst, C., 1967. Initiation and extension of hydraulic fractures in rocks. SPE J. 7, 310–318.

Hubbert, M.K., Willis, D.G., 1957. Mechanics of hydraulic fracturing. Pet. Trans. AIME 210, 153–163.

Keaney, G., Li, G., Williams, K., 2010. Improved fracture gradient methodology understanding the minimum stress in Gulf of Mexico. In: 44th U.S. Rock Mechanics Symposium, 27–30 June 2010, Salt Lake City, Utah. ARMA, pp. 10–177.

Lang, J., Li, S., Zhang, J., 2011. Wellbore stability modeling and real-time surveillance for deepwater drilling to weak bedding planes and depleted reservoirs. SPE/IADC-139708.

Mehrabian, A., Jamison, D.E., Teodorescu, S.G., 2015. Geomechanics of lost-circulation events and wellbore-strengthening operations. SPE-174088.

Matthews, W.R., Kelly, J., 1967. How to predict formation pressure and fracture gradient. Oil Gas J. 65, 92–106.

Maury, V., Idelovici, J., 1995. Safe drilling of HPHT wells: the role of the thermal regime in loss and gain phenomenon. SPE-29428.

Morita, N., Black, A.D., Fuh, G.-F., 1990. Theory of lost circulation pressure. In: SPE Annual Technical Conference and Exhibition, New Orleans, 23–26 September. SPE-20409.

Morita, N., Fuh, G.F., 2012. Parametric analysis of wellbore strengthening methods from basic rock mechanics. SPE-145765.

Oriji, A., Ogbonna, J., 2012. A new fracture gradient prediction technique that shows good results in Gulf of Guinea wells. In: Abu Dhabi International Petroleum Conference and Exhibition. SPE-161209.

Pepin, G., Gonzalez, M., Bloys, J., Lofton, J., Schmidt, J., Naquin, C., Ellis, S., 2004. Effect of drilling fluid temperature on fracture gradient: field measurements and model predictions. ARMA/NARMS-04-527.

Perkins, T.K., Kern, L.R., 1961. Widths of hydraulic fractures. In: SPE Annual Fall Meeting, Dallas, 8–11 October. SPE-89-PA.

Pilkington, P.E., 1978. Fracture gradient estimates in Tertiary basins. Petrol. Eng. Int. May 138–148.

Postler, D.P., 1997. Pressure integrity test interpretation. SPE/IADC-37589.

Rai, U.B., Ghodke, N., Schutjens, P., Shete, K., 2014. Fracture gradient from leakoff test: pitfalls of using LOT data from nonvertical wells. SPE-167963-MS.

Shahri, M.P., Oar, T.T., Safari, R., Karimi, M., Mutlu, U., 2015. Advanced semianalytical geomechanical model for wellbore-strengthening applications. SPE-167976.

Sneddon, I.N., 1946. The distribution of stress in the neighbourhood of a crack in an elastic solid. Proc. Roy. Soc. Lond. Math. Phys. Sci. 187, 229–260.

Sneddon, I.N., Elliott, H.A., 1946. The opening of a Griffith crack under internal pressure. Q. Appl. Math. 4, 262–266.

Stephens, G., Voight, B., 1982. Hydraulic fracturing theory for conditions of thermal stress. Int. J. Rock Mech. Min. Sci. Geomech. Abstr. 19, 279–284.

Van Oort, E., Friedheim, J., Pierce, T., et al., 2009. Avoiding losses in depleted and weak zones by constantly strengthening wellbores. In: SPE Annual Technical Conference and Exhibition, New Orleans, 4–7 October. SPE-125093.

Wang, H., Solimon, M., Towler, B., 2009. Investigation of factors for strengthening a wellbore by propping fractures. SPE Drill. Complet. Sept., 441–451.
Wessling, S., Pei, J., Dahl, T., Wendt, B., Marti, S., Stevens, J., 2009. Calibrating fracture gradients – an example demonstrating possibilities and limitations. IPTC-13831.
Wojtanowicz, A.K., Bourgoyne, A.T., Zhou, D., Bender, K., 2000. Strength and Fracture Gradients for Shallow Marine Sediments. Final report, U.S. MMS, Herndon.
Zhang, J., Standifird, W.B., Lenamond, C., 2008. Casing ultradeep, ultralong salt sections in deep water: a case study for failure diagnosis and risk mitigation in record-depth well. SPE-114273.
Zhang, J., Roegiers, J.-C., 2010. Discussion on "Integrating borehole-breakout dimensions, strength criteria, and leak-off test results, to constrain the state of stress across the Chelungpu Fault, Taiwan". Tectonophysics 492, 295–298.
Zhang, J., Wieseneck, J., 2011. Challenges and surprises of abnormal pore pressure in shale gas formations. SPE-145964.
Zhang, J., 2011. Pore pressure prediction from well logs: methods, modifications, and new approaches. Earth Sci. Rev. 108, 50–63.
Zhang, J., 2013. Borehole stability analysis accounting for anisotropies in drilling to weak bedding planes. Int. J. Rock Mech. Min. Sci. 60, 160–170.
Zhang, J., Alberty, M., Blangy, J.P., 2016. A semi-analytical solution for estimating the fracture width in wellbore strengthening applications. SPE-180296.
Zhang, Y., Zhang, J., 2017. Lithology-dependent minimum horizontal stress and in-situ stress estimate. Tectonophysics 703–704, 1–8.
Zhang, J., Yin, S., 2017. Fracture gradient prediction: an overview and an improved method. Petrol. Sci. 14, 720–730.
Zhang, J., Yin, S., 2019. A three-dimensional solution of the hydraulic fracture width for wellbore strengthening applications. Petrol. Sci. 16.
Zhong, R., Miska, S., Yu, M., 2017. Modeling of near-wellbore fracturing for wellbore strengthening. J. Nat. Gas Sci. Eng. 38, 475–484.
Zoback, M., Zinke, J., 2002. Production-induced normal faulting in the Valhall and Ekofisk oil fields. Pure Appl. Geophys. 159, 403–420.

CHAPTER 10

Borehole stability

Contents

Applied Petroleum Geomechanics
ISBN 978-0-12-814814-3
https://doi.org/10.1016/B978-0-12-814814-3.00010-1

Abstract

Borehole instabilities pose significant challenges to drilling and completion operations. In this chapter, borehole failure types and their identifying methods are introduced. Wellbore stresses in inclined boreholes are studied; elastic and poroelastic solutions are given for determining the minimum required mud weight for borehole stability. The impacts of bedding planes and rock anisotropy are also considered in the wellbore solutions to improve borehole stability modeling. This improved model enables to calculate borehole failures and minimum required mud weight along borehole trajectories with various drilling orientations versus bedding directions. The slip failure gradient in the weak planes is derived, which can be used to model wellbore shear failures in the planes of weakness. Time-dependent rock compressive strength is examined to analyze wellbore failure evolution with time. The mud weight applied to prevent salt creep and borehole closure in salt formation is also examined. Chemical reaction between shales and drilling fluids is considered in wellbore stability analysis to select right mud salinity.

Keywords: Borehole stability solution; Drilling-induced tensile failure; Poroelastic solution; Bedding planes; Slip shear failure; Time-dependent failure; Wellbore breakout; Collapse pressure.

10.1 Wellbore instability and mud weight window

Borehole instability is a major cause of wellbore failures and represents a serious challenge in the drilling industry. A lack of accurate wellbore stability analysis brings many problems, such as borehole washouts, breakouts,

collapses, pack-offs, stuck drill pipes and drill bits, and even losses of boreholes. Many oil and gas reservoirs in the world, including some major fields in the Gulf of Mexico, the Campos basin of offshore Brazil, the Bohai Bay of China, and the Gulf of Guinea, are located in formations involving geologically young weak shales and unconsolidated sands where grains are either poorly cemented or even unbonded (Monus et al., 1992). Main problems associated with these weak formations are wellbore instability and sand production. For example, in the Gulf of Mexico, operators have experienced immense borehole instability and sanding because of the presence of unconsolidated sands and reactive shales. The chemical effect of drilling fluid on reactive shales is another important factor affecting wellbore stability, particularly for the shales containing more smectite clay minerals. When the water-based drilling mud is used, chemical reactions between the shale and the mud cause shale swelling and wellbore collapse.

Some wellbore instabilities associated with complex geologic conditions, where the in-situ stress regime was controlled by active faults, were reported in the Cusiana field (Colombia), the Pedernales field (Venezuela), the Alberta Basin (Canada), the Tarim Basin and the Sichuan Basin (China), certain areas of the Norwegian Sea, and offshore Indonesia (Willson et al., 1999; Plumb et al., 1998; Wiprut and Zoback, 1998; Ramos et al., 1996). In the drilling stage, the main concerns are to determine the mud composition and density to maintain wellbore stability and avoid the loss of drilling fluids. Before full production, downhole tests include open-hole logging, fluid sampling, and injection tests are possible to induce wellbore failure and casing collapse (e.g., Peng et al., 2007). As hydrocarbons are produced and reservoir pressure gets depleted, the drained formations compact, which could induce solids production, casing damage, surface subsidence, and wellbore failure. In all these stages, integrated borehole stability analyses are important to ensure the reservoir production and minimize the costly problems induced by wellbore instabilities.

Borehole instabilities are the primary cause of drilling difficulties, make logging very difficult to perform and interpret, add to nonproductive time, increase costs, and sometimes lead to abandoning the well before it reaches its target. Cost estimation to these issues can reach 10% of total drilling time on average (Li et al., 2012). The relationship of mud weight and wellbore failures (Fig. 10.1) demonstrates that when the mud pressure is less than the pore pressure, the wellbore has splintering failures or washouts. When the mud weight is less than the shear failure gradient (SFG in Fig. 10.1), wellbore instability can result in breakouts or hole closure in case of

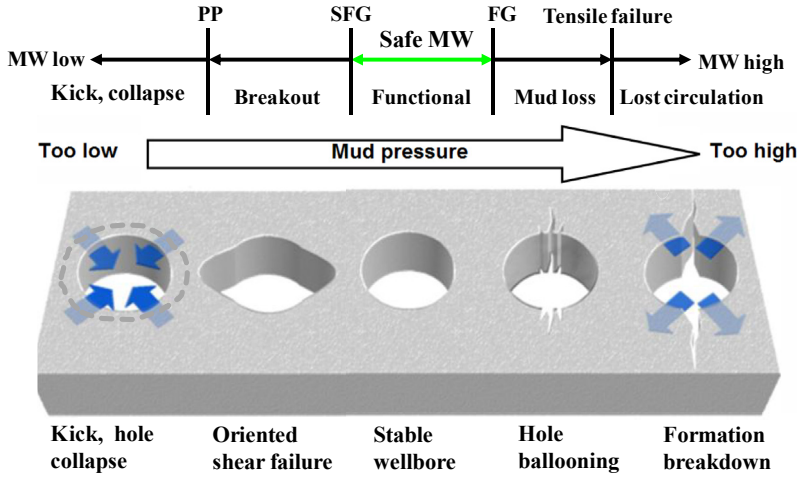

Figure 10.1 Schematic relationship of mud pressure (or downhole mud weight, MW) and borehole failures (Zhang, 2013).

compressive and shear failures. If applied mud weight is higher than the fracture gradient, drilling-induced hydraulic fractures are generated, causing drilling mud losses or even lost circulation. Therefore, to maintain borehole stability, the applied mud weight should be in an appropriate range. Borehole failures can primarily be classified into the following four categories as illustrated in Fig. 10.1:

(1) wellbore washouts or kicks due to underbalanced drilling, where the downhole mud weight is less than the pore pressure gradient (PP in Fig. 10.1);

(2) wellbore breakouts or shear failures caused by the induced stress concentrations because the downhole mud weight is lower than the required mud weight (or SFG);

(3) mud losses or lost circulation due to tensile failure (drilling-induced tensile fractures, DITF) caused by higher mud weight than the fracture gradient (FG in Fig. 10.1) and tensile failure gradient;

(4) rock failures or sliding related to preexisting fractures (Roegiers, 1990).

10.2 Borehole failure types and identification

10.2.1 Wellbore breakouts and drilling-induced tensile fractures

There are two major wellbore failures caused by inappropriate mud weight design during drilling, i.e., breakouts and drilling-induced hydraulic/tensile

fractures. When a borehole is drilled, the rocks removed from the subsurface are no longer supporting the surrounding rocks of the borehole, and drilling mud is used to support the wellbore. As a result, the stress concentration (increase in peak stresses) around the wellbore is formed. Wellbore breakouts or borehole enlargements occur when the stresses around the borehole exceed the ones required to cause compressive or shear failure of the borehole. Wellbore breakouts are mainly caused by the development of intersecting conjugate shear planes due to high compressive stresses that cause pieces of the borehole wall to spall off, as shown in Fig. 10.2. The stress concentration around a vertical borehole is greatest in the direction of the minimum horizontal stress. Hence, the long axes of borehole breakouts are oriented approximately parallel to the minimum horizontal stress orientation. Wellbore breakout causes borehole enlargement and borehole shape to be strongly modified giving an elongated hole in the minimum stress direction (Fig. 10.2A).

Breakouts nearly always form simultaneously on two opposite sides of the wellbore, which can be revealed from caliper logs (Fig. 10.2B). There are three parameters to describe wellbore breakout: breakout width, breakout depth, and breakout orientation. Breakout width or breakout angle is the angle subtended by the breakouts (θ_{BO}), as shown in Fig. 10.2B. Breakout depth is the distance from the original wellbore wall to the deepest part of the breakout. Breakout orientation is the orientation of the line that connects the center of the breakouts to each side of the wellbore.

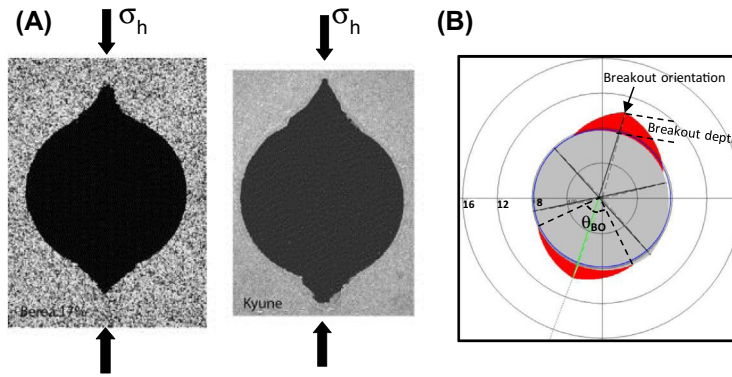

Figure 10.2 Wellbore breakouts in homogeneous rocks (A) Cross sections of drilled boreholes in medium- to high-porosity well-cemented Berea and Kyune sandstones from laboratory tests (Haimson, 2007). Breakouts are dog-eared. (B) Processed from downhole 6-arm caliper log measurement (the shaded area is the breakout and the unit is in inches).

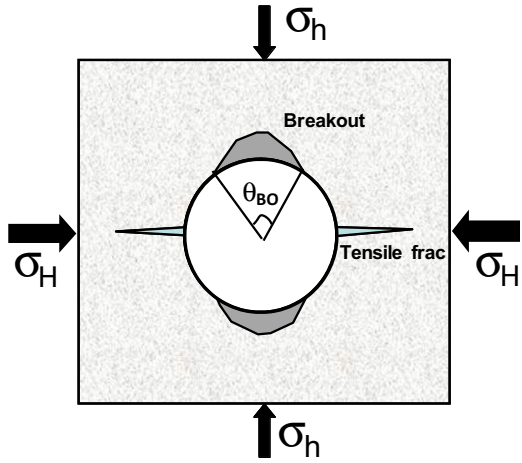

Figure 10.3 Schematic representation of stress-induced wellbore failures for a cross section in a vertical borehole—drilling-induced tensile fractures due to high mud weight and breakouts (shear failures) because of low mud weight.

Fig. 10.3 shows wellbore breakout, breakout width, and drilling-induced tensile fractures in a cross section of a vertical borehole. The drilling-induced tensile fracture is a tensile failure of the wellbore induced by a high mud weight. It is the result that the induced tensile stress in the wellbore exceeds rock tensile strength. Drilling-induced tensile fractures typically develop as narrow sharply defined features that are subparallel or slightly inclined to the borehole axis in a vertical well. These fractures are approximately parallel to the maximum horizontal stress orientation, perpendicular to the breakout direction in a vertical well, as shown in Fig. 10.3. They are thin fractures and may result in incidents of mud losses or lost circulation.

10.2.2 Borehole breakout diagnosis from caliper logs

Several methods can be used to identify borehole failures, e.g., from caliper and image logs and from drilling cuttings. The four-arm or six-arm caliper tool can be used to measure wellbore size to identify breakouts. Fig. 10.4 shows borehole enlargements measured from four-arm caliper logs and interpretations of the borehole geometry. Caliper 1—3 (C1) and Caliper 2—4 (C2) in the figure designate borehole diameters as measured between opposing dipmeter arms. The four-arm caliper tool will rotate as it is pulled up the borehole because of cable torque. However, the tool stops rotating

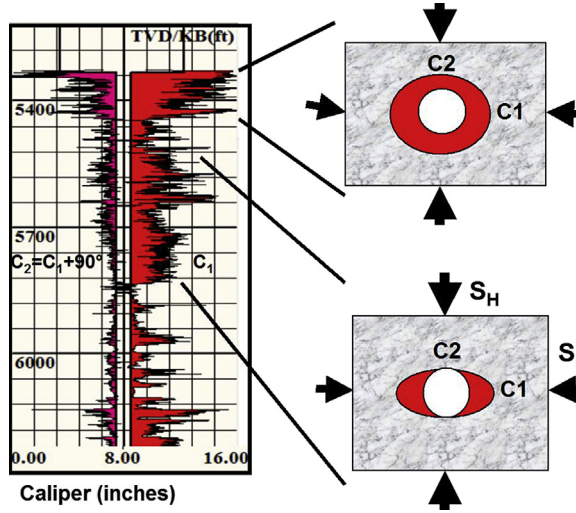

Figure 10.4 Wellbore washout (large breakout) and breakout from four-arm caliper measurements in downhole wireline log. Left figure: hole diameter variations in C1 and C2 direction with depth. The shaded areas are the hole diameter increment relative to the original hole size. The right diagrams are schematic borehole cross sections showing breakouts and horizontal stress directions.

in zones of borehole enlargement if one caliper pair becomes "stuck" in the enlargement direction (Plumb and Hickman, 1985). This enables the interpreter to distinguish zones of stress-induced breakouts from other borehole enlargements such as the key seats. A detailed method for interpreting borehole breakouts from four-arm caliper data can be found in Reinecker et al. (2003).

A more detailed breakout profile can be obtained from a six-arm caliper tool, as shown in Fig. 10.5, where wellbore breakout occurs in the shallower section, but the deeper section has a nearly in-gauged hole. The main advantage of six-arm caliper log is its ability to discriminate between asymmetrical "key seat" and symmetrical shear failure (breakout) more reliably than using four-arm caliper. However, for an off-centered six-arm caliper tool the breakout is difficult to analyze, and Jarosiński (1998) presented some examples to illustrate how to interpret borehole breakouts from off-centered six-arm caliper logs.

Breakout orientations rotate in inclined boreholes and may not always directly yield in the minimum horizontal stress orientations (Mastin, 1988; Peska and Zoback, 1995). Hence, the minimum horizontal stress

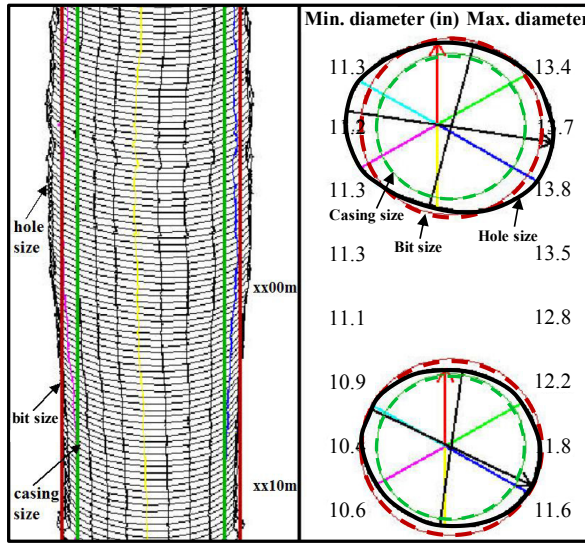

Figure 10.5 Measured borehole size by a six-arm caliper. The left track shows the profile of the borehole with depth; the right track plots borehole cross sections including tool centers, lengths of the arms, and the hole sizes. The bit and casing sizes are also displayed in the figure. Wellbore breakout is shown in the upper part of the borehole, and the maximum hole size reaches 13.8 inches compared to the bit size of 12 inches.

orientation can only be reliably estimated from breakouts in approximately vertical boreholes (less than 10 degrees deviation from vertical).

It should be noted that if mud pressure is much higher than pore pressure, drill pipe can become stuck against the borehole wall by the differential pressure between the mud pressure and pore pressure. This is called differential sticking, which is different from the struck pipe caused by low mud weight. Differential sticking requires dedicated skills to free it.

10.2.3 Breakouts and drilling-induced tensile fractures from image logs

Borehole imaging tools provide images of the borehole wall, which are typically based on physical property contrasts. There are currently a wide variety of imaging tools available, including resistivity, acoustic, optical, and density tools. For example, resistivity imaging logs can provide high-resolution images of the wellbore wall based on resistivity contrasts that allow for a direct observation of borehole breakouts. Borehole breakouts typically appear on resistivity image logs as broad, parallel, poorly resolved

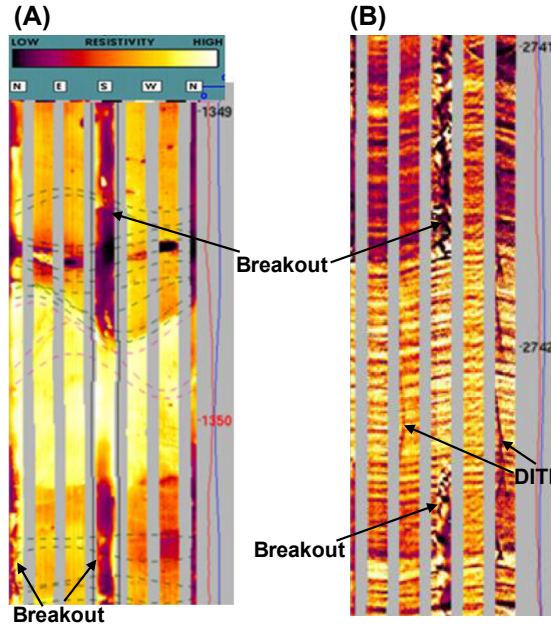

Figure 10.6 Wellbore breakouts (A) and drilling-induced tensile fractures (DITF in the figure) (B) measured from six-pad resistivity image log in the water-based mud. The breakouts are mainly formed in shale formations (darker color), and the drilling-induced tensile fractures are mainly created in the sandstones (lighter color). Depth is in meters.

conductive zones (for water-based mud) separated by 180° (i.e., observed on opposite sides of the borehole wall), as shown in Fig. 10.6A. Breakouts are typically conductive and poorly resolved because the wellbore failures associated with the breakouts result in poor contact between the tool pads and the wellbore wall, which in turn causes the tool to partially or fully measure the resistivity of the electrically conductive drilling mud rather than the formation. However, it is important to note that breakouts will appear as resistive, rather than conductive, zones in resistivity images run in the oil-based mud (Tingay et al., 2008) because the oil-based mud is more resistive.

Drilling-induced tensile fractures can be identified from mud losses or lost circulations, as described in Chapter 9. They can be observed on image logs, as shown in Fig. 10.6B. Drilling-induced tensile fractures typically become infiltrated by drilling mud and, thus, appear on resistivity image logs as pairs of narrow, well-defined conductive features (resistive in oil-based mud images) separated by 180° (Fig. 10.6B). Unlike natural

fractures that tend to cross-cut the wellbore, drilling-induced tensile fractures are usually aligned subparallel or slightly inclined to the borehole axis in a vertical well.

10.2.4 Borehole stability and lithology

Normally a sandstone has a higher compressive strength than that in a shale; therefore, compared to the sandstone the shale is more likely to develop breakouts under the same mud weight. A sandstone is usually more brittle and more prone to be fractured (with a lower fracture gradient) than a shale. This is the reason why the drilling-induced tensile fractures and mud losses are easily encountered in the sandstone. Fig. 10.7 presents borehole caliper

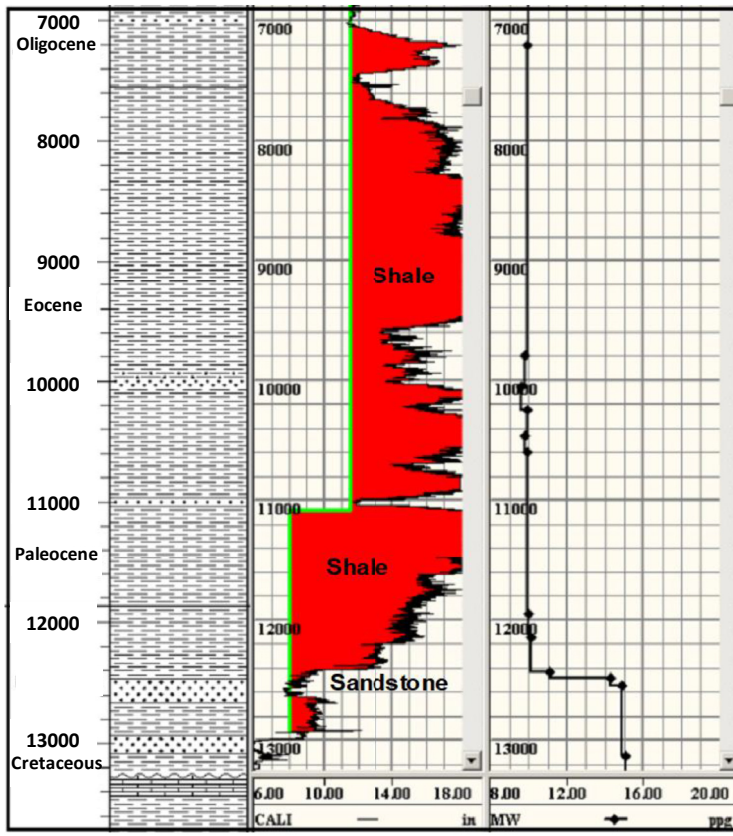

Figure 10.7 Caliper log showing major hole overgauges (breakouts, shaded areas in the caliper log) occurred in shales. The wellbores in sandstones are basically in-gauge or only with slight breakouts. The left track shows the lithology column; the middle track plots the caliper log; the right track displays mud weight (depth in feet and MW in ppg).

log, mud weight (water-based mud), and formation lithologies in a vertical well. The hole was highly overgauged, and the hole size at depth of 11,100–11,600 ft increased up to 18 inches compared to the bit size of 8 inches. The mud weight was too low in the shales, causing severe wellbore breakouts. However, wellbore breakouts in sandstones were much smaller than those in shales. In the deep section starting at 12,400 ft, mud weight was raised from 10 to 15 ppg, and wellbore enlargement reduced significantly. This indicates that mud weight is a key design parameter to minimize wellbore breakouts.

Fig. 10.8 shows another example of wellbore breakouts measured by caliper logs in a well drilled with the water-based mud in Rockies,

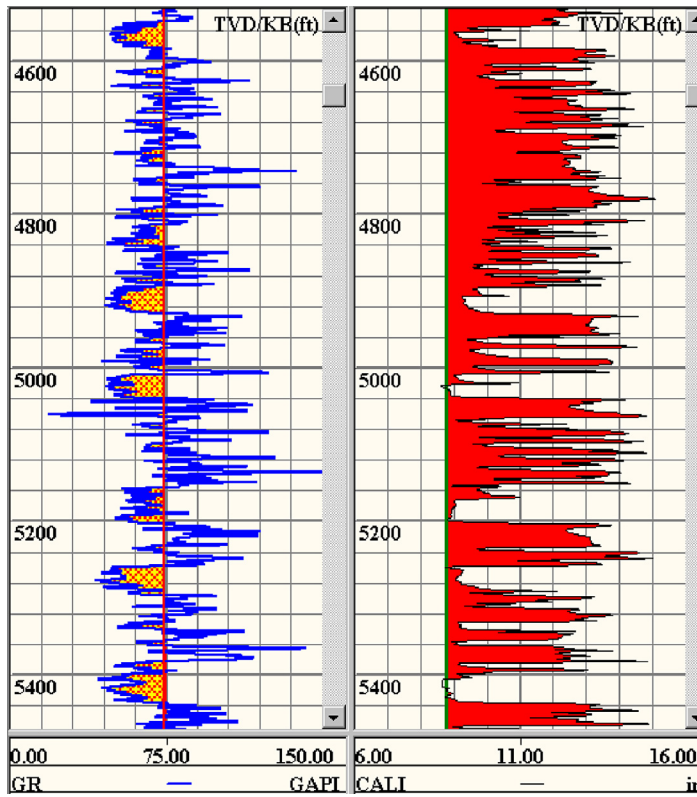

Figure 10.8 Borehole enlargements measured by caliper logs showing that most breakouts occur in shales. The left track displays the measured gamma ray with shale baseline (the shaded areas are sandstones) and the right track plots the bit size and caliper logs (the shaded areas are hole size enlargements).

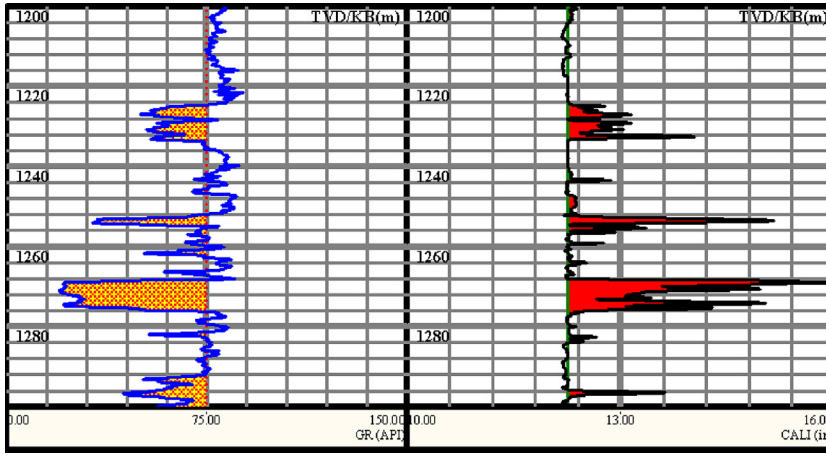

Figure 10.9 Wellbore breakouts measured from caliper logs showing that breakouts occur only in poorly- or un-consolidated sandstones in Neogene-aged formations of offshore West Africa. The left track plots the measured gamma ray with shale baseline (the shaded areas are sandstones), and the right track displays the bit size and caliper log (the shaded areas are hole size enlargement).

Wyoming. The caliper log indicates that most breakouts (hole enlargement) are in shales, and nearly no breakouts in sandstones. However, if sandstones are poorly- or un-consolidated in geologically young (e.g., in Neogene and Paleogene periods) formations, they may be very weak and have very low compressive strengths (Zhang et al., 2009). As a result, wellbore breakouts may be most likely to occur in the sandstones; instead, the shales are more stable, as shown in Fig. 10.9.

10.2.5 Borehole instability diagnosis from cuttings

Cuttings and cavings are often good indicators of wellbore instabilities as described in Chapter 8. When the applied mud weight is too low, wellbore instability events (e.g., breakouts) will occur and produce certain amount of large size cuttings or cavings. Analyzing caving morphology can help to diagnose wellbore failure types and adjust mud weight in real-time operations to maintain wellbore stability. There are generally four types of cuttings (cavings): normal cuttings, cavings from preexisting fractures, cavings owing to underbalanced drilling, and cavings owing to shear failures, as shown in Figs. 8.31–8.33. For the cavings induced by shear failures,

Figure 10.10 Large size cuttings from a gumbo shale at a depth of ~7300 ft TVD KB for drilling with a PDC bit in the Gulf of Mexico.

the general rule is that the borehole with lower than required mud weight produces more and larger cuttings (cavings). For example, splintering and angular cuttings are an indicator of shear failures, and the mud weight needs to be raised to cure it. Large size cuttings can also be generated from gumbo shales. Gumbo shale, or swelling shale, is a term for soft, sticky, swelling clay formations. It contains appreciable amounts of smectite clay and generally occurs at a shallower depth (e.g., < 10,000 ft) in the Gulf of Mexico. Gumbo shale may cause wellbore closure and bit balling while drilling, and it may also form mud rings and balls that can plug the annulus, flowline, and shale-shaker screens. Fig. 10.10 displays a picture of large size of cuttings from a gumbo shale in the Gulf of Mexico. Increasing mud weight, using oil-based mud and adjusting mud chemistry may help to mitigate swelling of the gumbo shale.

10.3 Wellbore stability—elastic solutions for inclined boreholes

Different analytical methods and numerical models have been used for wellbore stability analyses (e.g., Bradley, 1979; Zoback et al., 1985; Detournay and Fairhurst, 1987; Aadnøy and Chenevert, 1987; Roegiers and Detournay, 1988; Detournay and Cheng, 1988; Zheng et al., 1989; Roegiers, 1990; Woodland, 1990; McLean and Addis, 1990; Wang and Dusseault, 1991; Mody and Hale, 1993; Li et al., 1998; Willson et al., 1999;

Zhang and Roegiers, 2000; Van Oort, 2003; Zhang et al., 2003; Haimson and Lee, 2004; Papamichos et al., 2010; Dresen et al., 2010; Zhang, 2013; Liang et al., 2014; Gao et al., 2017; Chen and Abousleiman, 2017; Feng et al., 2018).

To predict wellbore stability, stress components and distributions near the wellbore due to drilling perturbation need to be analyzed. Applying rock failure criteria, wellbore stresses and rock strengths can, then, be compared to determine if the wellbore fails. Finally, a mud weight range can be determined to avoid wellbore shear, compressive, and tensile failures. This mud weight range can be used as the safe mud weight window for drilling.

10.3.1 Local far-field stresses in an inclined borehole

Borehole stability modeling for drilling operations is primarily to quantify a safe mud weight (mud pressure) window such that the designed mud density will be higher enough to ensure borehole stability and lower enough to not fracture the formation (i.e., avoid mud losses), as shown in Fig. 10.1. Therefore, the safe mud weight should be greater than the pore pressure gradient and shear failure gradient and less than the fracture gradient. To determine the shear failure gradient, the first step is to analyze near-wellbore stresses induced by drilling. It is commonly assumed that in situ or far-field stresses consist of three mutually orthogonal principal stresses: the vertical (overburden) stress (σ_V) and the minimum and maximum horizontal stresses (σ_h and σ_H). It is also assumed that the subsurface rocks are in the in situ stress state before drilling. When a borehole is excavated, the stress redistribution of the in situ stresses near wellbore occurs, causing stress changes around the wellbore. Fig. 10.11 shows in situ stresses and near-wellbore stresses induced by drilling. Borehole stability analysis is more complicated in an inclined borehole than a vertical one. The reason is that the local far-field stresses (i.e., the in situ stresses in the inclined borehole coordinate, as shown in Fig. 10.11B) are no longer in the principal stress state because shear stresses are introduced at the wellbore cross section in the deviated borehole. Therefore, in situ stresses in the borehole local coordinate system need to be established for the inclined borehole, as shown in Fig. 10.11; then, wellbore stresses induced by drilling can be obtained.

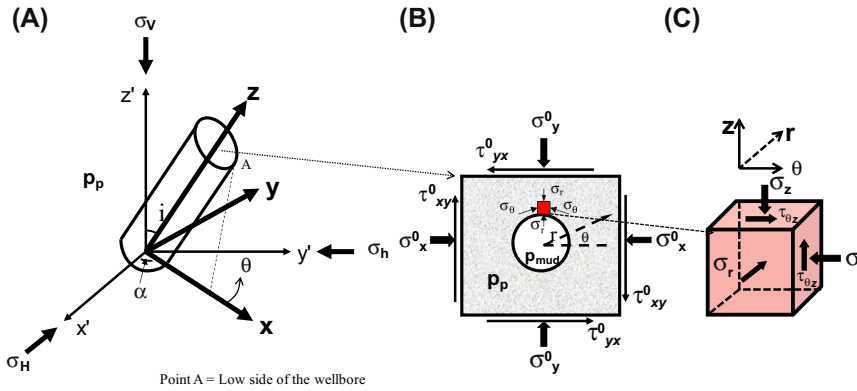

Figure 10.11 Coordinate transformation between in situ stresses (σ_V, σ_H, and σ_h) and local in situ stresses in an inclined borehole (σ^0_x, σ^0_y, σ^0_z, τ^0_{xy}, τ^0_{yz}, and τ^0_{xz}). (A). 3-D view of an inclined borehole; (B). Local in situ stresses and wellbore stresses in a cross section perpendicular to the axial direction of the inclined borehole; (C). A cubic element showing normal and shear stresses at the wellbore wall.

For an inclined borehole, the local in situ stresses in a cross section perpendicular to the wellbore axis (Fig. 10.11B) can be expressed as follows:

$$\begin{aligned}
\sigma^0_x &= (\sigma_H \cos^2\alpha + \sigma_h \sin^2\alpha)\cos^2 i + \sigma_V \sin^2 i \\
\sigma^0_y &= \sigma_H \sin^2\alpha + \sigma_h \cos^2\alpha \\
\sigma^0_z &= (\sigma_H \cos^2\alpha + \sigma_h \sin^2\alpha)\sin^2 i + \sigma_V \cos^2 i \\
\tau^0_{xy} &= \frac{\sigma_h - \sigma_H}{2}\sin 2\alpha \cos i \\
\tau^0_{yz} &= \frac{\sigma_h - \sigma_H}{2}\sin 2\alpha \sin i \\
\tau^0_{xz} &= \frac{1}{2}(\sigma_H \cos^2\alpha + \sigma_h \sin^2\alpha - \sigma_V)\sin 2i
\end{aligned} \tag{10.1}$$

where i is the borehole inclination, for a vertical well $i = 0°$ and for a horizontal well $i = 90°$; α is the angle of drilling direction with respect to σ_H direction of the borehole, as shown in Fig. 10.11A; σ^0_x, σ^0_y, σ^0_z, τ^0_{xy}, τ^0_{yz}, and τ^0_{xz} are the local in situ stresses in the cross section of the inclined borehole as shown in Fig. 10.11B.

10.3.2 Near-wellbore stresses in an inclined borehole

When a borehole is drilled, stress redistribution (near-field stresses) near wellbore wall occurs. This stress redistribution in the inclined borehole

cross section (Fig. 10.11B) in the polar system (r, θ, z) can be expressed in the following form, i.e., Kirsch's equation, or the elastic plane strain solution (Bradley, 1979; Fjær et al., 2008):

$$\begin{cases}
\sigma_r = \dfrac{\left(\sigma_x^0 + \sigma_y^0\right)}{2}\left(1 - \dfrac{R^2}{r^2}\right) + \dfrac{\left(\sigma_x^0 - \sigma_y^0\right)}{2}\left(1 - \dfrac{4R^2}{r^2} + \dfrac{3R^4}{r^4}\right)\cos 2\theta + \\
\tau_{xy}^0\left(1 - \dfrac{4R^2}{r^2} + \dfrac{3R^4}{r^4}\right)\sin 2\theta + p_m\dfrac{R^2}{r^2} \\
\sigma_\theta = \dfrac{\left(\sigma_x^0 + \sigma_y^0\right)}{2}\left(1 + \dfrac{R^2}{r^2}\right) - \dfrac{\left(\sigma_x^0 - \sigma_y^0\right)}{2}\left(1 + \dfrac{3R^4}{r^4}\right)\cos 2\theta - \\
\tau_{xy}^0\left(1 + \dfrac{3R^4}{r^4}\right)\sin 2\theta - p_m\dfrac{R^2}{r^2} \\
\sigma_z = \sigma_z^0 - 2\nu\left(\sigma_x^0 - \sigma_y^0\right)\dfrac{R^2}{r^2}\cos 2\theta - 4\nu\tau_{xy}^0\dfrac{R^2}{r^2}\sin 2\theta \\
\tau_{r\theta} = \left(-\dfrac{\sigma_x^0 - \sigma_y^0}{2}\sin 2\theta + \tau_{xy}^0\cos 2\theta\right)\left(1 + \dfrac{2R^2}{r^2} - \dfrac{3R^4}{r^4}\right) \\
\tau_{rz} = \left(\tau_{yz}^0\sin\theta + \tau_{xz}^0\cos\theta\right)\left(1 - \dfrac{R^2}{r^2}\right) \\
\tau_{\theta z} = \left(-\tau_{xz}^0\sin\theta + \tau_{yz}^0\cos\theta\right)\left(1 + \dfrac{R^2}{r^2}\right)
\end{cases} \tag{10.2}$$

where σ_r, σ_θ, σ_z, $\tau_{r\theta}$, τ_{rz}, and $\tau_{\theta z}$ are the radial, tangential, axial normal stresses, and shear stresses near the wellbore wall in the wellbore cross section (Fig. 10.11C), respectively; p_m is the mud pressure; θ is the angle indicating the orientation of the stresses around the wellbore circumference and measured from the x-axis (Fig. 10.11A, B).

The normal and shear stresses at the wellbore wall (when $r = R$, as shown in Fig. 10.11C) for an inclined borehole can be obtained from Eq. (10.2) in the following:

$$\sigma_r = p_m \tag{10.3}$$

$$\sigma_\theta = \sigma_x^0 + \sigma_y^0 - 2\left(\sigma_x^0 - \sigma_y^0\right)\cos 2\theta - 4\tau_{xy}^0 \sin 2\theta - p_m \tag{10.4}$$

$$\sigma_z = \sigma_z^0 - \nu\left[2\left(\sigma_x^0 - \sigma_y^0\right)\cos 2\theta + 4\tau_{xy}^0 \sin 2\theta\right] \tag{10.5}$$

$$\tau_{\theta z} = 2\left(\tau_{yz}^0 \cos\theta - \tau_{xz}^0 \sin\theta\right) \tag{10.6}$$

$$\tau_{r\theta} = \tau_{rz} = 0 \tag{10.7}$$

The effective stresses around the wellbore wall can be calculated from the stress components shown in the above equations by applying Biot's effective law, $\sigma' = \sigma - \alpha p_p$.

10.3.3 Principal effective stresses at the wellbore wall

The radial stress at the wellbore wall (σ_r) is always one of the three principal stresses, as shown in Fig. 10.11C. Therefore, only two principal stresses in (θ, z) plane need to be calculated at the wellbore wall of an inclined borehole. The following equations can be used to obtain the principal effective stresses at the wellbore wall (Zhang, 2013):

$$\sigma'_{\theta z1} = \frac{1}{2}\left(\sigma_\theta + \sigma_z + \sqrt{\left(\sigma_\theta - \sigma_z\right)^2 + 4\tau_{\theta z}^2}\right) - \alpha p_p \tag{10.8}$$

$$\sigma'_{\theta z3} = \frac{1}{2}\left(\sigma_\theta + \sigma_z - \sqrt{\left(\sigma_\theta - \sigma_z\right)^2 + 4\tau_{\theta z}^2}\right) - \alpha p_p \tag{10.9}$$

$$\sigma'_r = p_m - \alpha p_p \tag{10.10}$$

$$\tan 2\gamma = \frac{2\tau_{\theta z}}{\sigma_\theta - \sigma_z} \tag{10.11}$$

where $\sigma'_{\theta z1}$ and $\sigma'_{\theta z3}$ are the maximum and minimum effective principal stresses in (θ, z) plane; σ'_r is the effective principal radial stress in (r,θ) plane; γ is the angle between σ_1 and σ_θ; p_p is the pore pressure; α is Biot's coefficient.

10.3.4 Minimum mud weight calculation using the Mohr–Coulomb failure criterion

When induced stresses at the wellbore wall exceed rock strength, the wellbore starts to fail. The Mohr–Coulomb failure criterion (Eq. 3.38) can be used to determine wellbore shear failure. In shear failure condition, the applied mud weight is low and $\sigma_r = p_m$; therefore, σ'_r can be assumed as the

minimum effective stress, i.e., $\sigma'_3 = \sigma'_r$; therefore, $\sigma'_1 = \sigma'_{\theta z1}$, and this is true, particularly when θ is near 90 degrees (Fig. 10.11B), where the wellbore experiences high stresses of σ_θ and σ_z. Substituting Eqs. (10.8) and (10.10) to (3.38), the minimum mud pressure (shear failure pressure, p_m) to prevent shear failure around the wellbore wall for an inclined borehole can be obtained from the following equation:

$$\frac{1}{2}\left[\sigma_\theta + \sigma_z + \sqrt{(\sigma_\theta - \sigma_z)^2 + 4\tau_{\theta z}^2}\right] - \alpha p_p = UCS + q(p_m - \alpha p_p) \tag{10.12}$$

where UCS is the uniaxial compressive strength of the rock; $q = (1+\sin\varphi)/(1-\sin\varphi)$; and φ is the angle of internal friction of the rock.

From Eq. (10.12), the required minimum mud pressure (p_m) to prevent shear failure can be solved, but notice that σ_θ (can be obtained from Eq. 10.4) also includes p_m. Solving Eq. (10.12), the shear failure pressure (collapse pressure) can be obtained and used as the required minimum mud weight to prevent wellbore breakouts, and it has the following form:

$$p_m = \frac{b + \sqrt{b^2 - (k^2 - 1)c}}{k^2 - 1} \tag{10.13}$$

and

$$b = (k-1)\sigma_{\theta n} + (k+1)\sigma_z - dk \tag{10.14}$$

$$c = (2\sigma_z - d)(2\sigma_{\theta n} - d) - 4\tau_{\theta z}^2 \tag{10.15}$$

$$d = 2\left[UCS - \alpha p_p \frac{2\sin\varphi}{1-\sin\varphi}\right] \tag{10.16}$$

$$k = \frac{3+\sin\varphi}{1-\sin\varphi} \tag{10.17}$$

$$\sigma_{\theta n} = \sigma_x^0 + \sigma_y^0 - 2\left(\sigma_x^0 - \sigma_y^0\right)\cos 2\theta - 4\tau_{xy}^0 \sin 2\theta \tag{10.18}$$

where the axial stress σ_z can be obtained from Eq. (10.5); $\tau_{\theta z}$ can be obtained from Eq. (10.6); $\sigma^0{}_x$, $\sigma^0{}_y$, and $\tau^0{}_{xy}$ can be obtained from Eq. (10.1); Biot's coefficient can be assumed to be $\alpha = 1$, when the rock is in failure status.

The minimum mud pressure, p_m, is also called shear failure pressure or collapse pressure, which is the minimum mud pressure to prevent the

wellbore from shear failures. The minimum mud pressure gradient is also named the minimum mud weight, or shear failure gradient.

10.3.5 Minimum mud weight calculation using modified Lade failure criterion

Ewy (1999) employed the stresses at the wellbore wall predicted by linear elasticity and modified Lade failure criterion to calculate the minimum mud weight required to prevent borehole instability. He derived the following minimum mud pressure to prevent borehole instability (p_w) assuming no communication between the wellbore pressure and the formation pore pressure (i.e., impermeable wellbore wall):

$$p_w = (\mathrm{B} - \mathrm{C})/(2\mathrm{A}) \tag{10.19}$$

and

$$A = \sigma_z + S_1 - p_p \tag{10.20}$$

$$B = A\sigma_{\theta n} - \tau_{\theta z}^2 \tag{10.21}$$

$$C = B^2 - 4A\left\{D - (S_1 - p_p)\left[A(\sigma_{\theta n} + S_1 - p_p) - \tau_{\theta z}^2\right]\right\} \tag{10.22}$$

$$D = (\sigma_{\theta n} + \sigma_z + 3S_1 - 3p_p)^3/(27 + \eta) \tag{10.23}$$

$$S_1 = c/\tan\varphi \tag{10.24}$$

$$\eta = 4\tan^2\varphi(9 - 7\sin\varphi)/(1 - \sin\varphi) \tag{10.25}$$

where σ_z can be obtained from Eq. (10.5); $\tau_{\theta z}$ can be obtained from Eq. (10.6); $\sigma_{\theta z}$ can be obtained from Eq. (10.18); c is the cohesion of the rock.

Eq. (10.19) can be used to calculate the minimum wellbore pressure to prevent wellbore shear failure. However, this equation is not appropriate for situations in which there is communication between the wellbore pressure and the formation pore pressure, such as (1) underbalanced drilling, (2) overbalanced drilling without the presence of a filter cake on the wellbore wall, and (3) chemical effects in shales (Ewy, 1999).

Other failure criteria can also be used to calculate the minimum mud pressure to prevent wellbore shear failure, such as the Drucker–Prager criterion (e.g., Zhang et al., 2003) and the Mogi–Coulomb criterion (Al-Ajmi and Zimmerman, 2006).

10.4 Wellbore stability—elastic solutions for vertical boreholes

10.4.1 Near-wellbore stresses in a vertical borehole

In the cross section of a vertical borehole subjected to bi-axial far-field horizontal stresses (σ_H and σ_h) with no far-field shear stress (Fig. 10.12), Kirsch's wellbore solution can be used to obtain stress components around the wellbore. Assuming that the borehole wall is impermeable, the near-wellbore stress components can be written in the following form:

$$\begin{aligned}
\sigma_r &= \frac{(\sigma_H + \sigma_h)}{2}\left(1 - \frac{R^2}{r^2}\right) + \frac{(\sigma_H - \sigma_h)}{2}\left(1 - \frac{4R^2}{r^2} + \frac{3R^4}{r^4}\right)\cos 2\theta + p_m\frac{R^2}{r^2} \\
\sigma_\theta &= \frac{(\sigma_H + \sigma_h)}{2}\left(1 + \frac{R^2}{r^2}\right) - \frac{(\sigma_H - \sigma_h)}{2}\left(1 + \frac{3R^4}{r^4}\right)\cos 2\theta - p_m\frac{R^2}{r^2} + \sigma_T \\
\sigma_z &= \sigma_V - \nu\frac{4R^2}{r^2}\frac{(\sigma_H - \sigma_h)}{2}\cos 2\theta + \nu\sigma_T \\
\tau_{r\theta} &= -\frac{(\sigma_H - \sigma_h)}{2}\left(1 + \frac{2R^2}{r^2} - \frac{3R^4}{r^4}\right)\sin 2\theta \\
\tau_{z\theta} &= \tau_{rz} = 0
\end{aligned} \tag{10.26}$$

where σ_H and σ_h are the maximum and minimum far-field horizontal stresses; θ is defined in Fig. 10.12; σ_T is the thermal stress induced by the difference between the mud and the formation temperatures, and a cooler

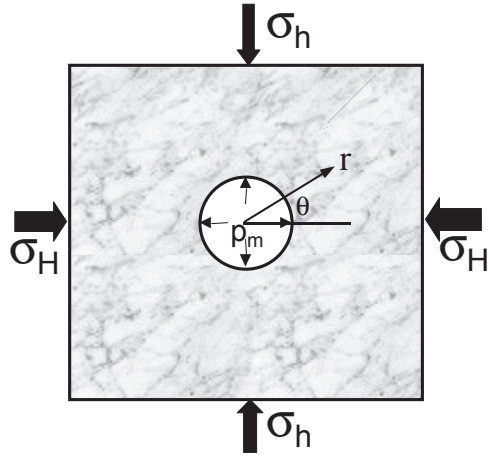

Figure 10.12 A cross section of a vertical borehole in an anisotropic stress field.

mud (cooling) reduces the thermal stress. The tangential thermal stress can be calculated by the following equation:

$$\sigma_T = \frac{\alpha_T E(T_m - T_f)}{1 - \nu} \tag{10.27}$$

where α_T is the thermal constant; E is Young's modulus; and ν is Poisson's ratio; T_m and T_f are the mud and formation temperatures, respectively.

At the borehole wall ($r = R$), the stress components can be obtained from Eq. (10.26) as follows:

$$\begin{cases} \sigma_r = p_m \\ \sigma_\theta = \sigma_H + \sigma_h - 2(\sigma_H - \sigma_h)\cos 2\theta - p_m + \sigma_T \\ \sigma_z = \sigma_V - 2\nu(\sigma_H - \sigma_h)\cos 2\theta + \nu\sigma_T \\ \tau_{\theta z} = \tau_{r\theta} = \tau_{rz} = 0 \end{cases} \tag{10.28}$$

There is no shear stress in Eq. (10.28); therefore, the stresses are principal stresses. The minimum and maximum tangential stresses at the wellbore wall in a vertical well can be obtained in the following form:

$$\begin{cases} \sigma_{\theta\min} = 3\sigma_h - \sigma_H - p_m + \sigma_T & \theta = 0^\circ \\ \sigma_{\theta\max} = 3\sigma_H - \sigma_h - p_m + \sigma_T & \theta = 90^\circ \end{cases} \tag{10.29}$$

It can be seen from Eq. (10.29) that the minimum tangential stress is in the maximum horizontal stress direction ($\theta = 0^\circ$), and the maximum tangential stress occurs in the minimum horizontal stress direction ($\theta = 90^\circ$), as shown in Fig. 10.12. This is the reason why the wellbore shear failures mainly occur in the minimum horizontal stress direction.

The minimum and maximum axial stresses at the wellbore wall can be obtained from Eq. (10.28) as follows:

$$\begin{cases} \sigma_{z\min} = \sigma_V - 2\nu(\sigma_H - \sigma_h) + \nu\sigma_T & \theta = 0^\circ \\ \sigma_{z\max} = \sigma_V + 2\nu(\sigma_H - \sigma_h) + \nu\sigma_T & \theta = 90^\circ \end{cases} \tag{10.30}$$

Using Eq. (10.28) and the in situ stress magnitudes listed in Table 10.1, the tangential, axial, and radial stresses along wellbore circumference (θ from 0 to 360 degrees) are calculated and plotted in Fig. 10.13 assuming $\sigma_T = 0$. It shows that tangential and axial stresses vary markedly with wellbore circumference. Both tangential and axial stresses reach the maximum values in the minimum horizontal stress direction ($\theta = 90^\circ$). However, radial stress keeps unchanged and is equal to the mud pressure.

Table 10.1 In situ stresses and rock property.

Parameter	Magnitude
Vertical stress, σ_V (MPa)	55.5
Minimum horizontal stress, σ_h (MPa)	41.1
Maximum horizontal stress, σ_H (MPa)	48.6
Downhole mud pressure, p_m (MPa)	40.6
Pore pressure, p_p (MPa)	24.5
Poisson's ratio of the rock, ν	0.3

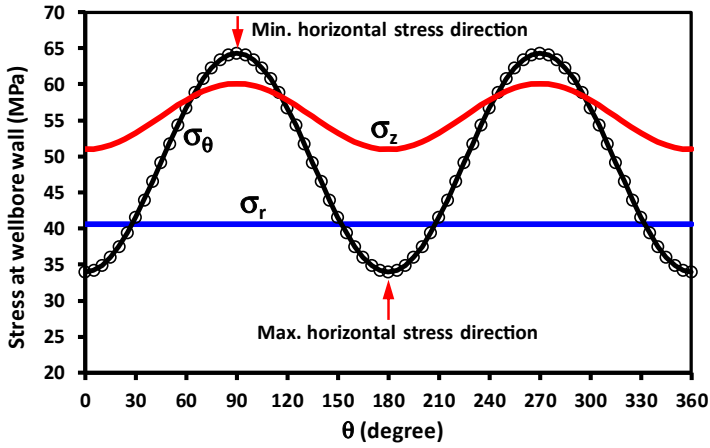

Figure 10.13 Variations of tangential, axial, and radial stresses along the wellbore circumference.

Fig. 10.14 displays the variations of two tangential stresses with the radial distance from the wellbore wall to the rock formation in the minimum and maximum horizontal stress directions ($\theta = 90°$ and $0°$). The two tangential stresses both decrease as the distance (r/R) increases. When r/R > 2, the changes of tangential stresses caused by stress concentrations due to drilling are very small. This means that the stress perturbation only occurs within a small distance from the wellbore wall. As r/R increases, the two tangential stresses approach gradually the two horizontal stresses.

10.4.2 Minimum mud weight calculation using the Mohr–Coulomb failure criterion

10.4.2.1 For the maximum tangential stress is the maximum principal stress

Assuming that the maximum tangential stress ($\sigma_{\theta\max}$) in Eq. (10.29) and radial stress (σ_r) in Eq. (10.28) are the maximum and minimum principal

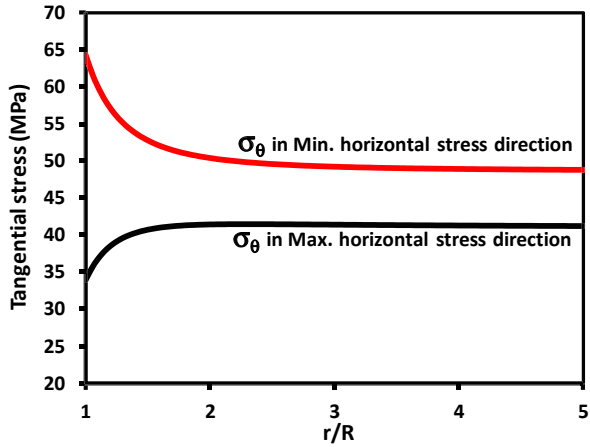

Figure 10.14 The maximum and minimum tangential stresses versus the distance from the wellbore wall (r/R) in two horizontal stress directions.

stresses (i.e., $\sigma_{\theta\max} > \sigma_{z\max}$), the Mohr–Coulomb failure criterion (Eq. 3.38) can be rewritten in the following form with consideration of effective stresses:

$$\sigma_{\theta\max} - \alpha p_p = UCS + q(\sigma_r - \alpha p_p) \tag{10.31}$$

Inserting $\sigma_{\theta\max}$ in Eq. (10.29) and σ_r in Eq. (10.28) into the above failure criterion, the required minimum mud pressure, p_m, can be obtained:

$$p_m = \frac{3\sigma_H - \sigma_h - UCS + \alpha(q-1)p_p + \sigma_T}{q+1} \tag{10.32}$$

where α can be assumed to be 1 at the failure status. The same assumption can be used in the following analysis.

Similarly, for a horizontal well drilled in the minimum horizontal stress direction in the normal stress regime, the required minimum mud pressure, p_{mH}, can be obtained in the following:

$$p_{mH} = \frac{3\sigma_V - \sigma_H - UCS + \alpha(q-1)p_p + \sigma_T}{q+1} \tag{10.32b}$$

Introducing $UCS = (2c\ cos\varphi)/(1-\sin\varphi)$, $q = (1+\sin\varphi)/(1-\sin\varphi)$, the minimum mud pressure, p_m, in a vertical well (i.e., Eq. 10.32) can be rewritten in the following form:

$$p_m = \frac{1}{2}(3\sigma_H - \sigma_h + \sigma_T)(1 - \sin\varphi) - c\cos\varphi + \alpha p_p \sin\varphi \tag{10.33}$$

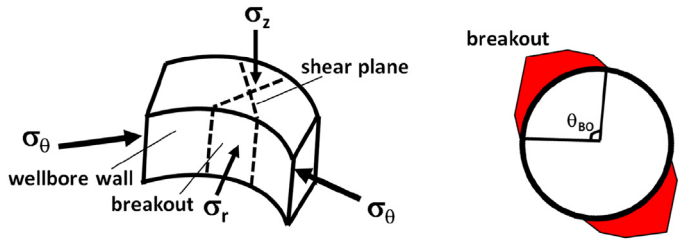

Figure 10.15 Schematic failure planes and breakouts caused by shear failures at the wellbore wall where the tangential stress is the maximum principal stress and the radial stress is the minimum principal stress (left). The right figure shows the breakouts in the cross section view.

where φ is the angle of internal friction; c is the cohesion.

It can be seen that the minimum mud weight depends highly on pore pressure. Therefore, accurate pore pressure prediction is of vital importance for determining the required mud weight in a prospect well. Other failure criteria can also be applied for obtaining the minimum mud weight in a vertical well. For example, for modified Lade failure criterion, Eq. (10.19) can be simplified by replacing all shear stresses by zero for a vertical borehole.

Fig. 10.15 displays a schematic diagram of wellbore breakouts (borehole elongation) along the intersecting conjugate shear planes caused by shear failures. The high tangential stress (σ_θ, the maximum principal stress) is the primary cause.

10.4.2.2 For the maximum axial stress is the maximum principal stress

If the maximum axial stress is greater than the maximum tangential stress ($\sigma_{z\max} > \sigma_{\theta\max}$) (refer to Eqs. 10.29 and 10.30), it needs to replace $\sigma_{\theta\max}$ by $\sigma_{z\max}$ in the Mohr–Coulomb failure criterion, Eq. (10.31). Then, combining Eq. (10.30), the minimum mud pressure, p_m, can be obtained in the following equation:

$$p_{mz} = \frac{\sigma_V + 2\nu(\sigma_H - \sigma_h) + \nu\sigma_T - UCS + \alpha(q-1)p_p}{q} \tag{10.34}$$

Fig. 10.16 plots a schematic diagram of wellbore shear failures for the case that the maximum axial stress is higher than the maximum tangential stress. The wellbore breakout shape is different from the one shown in Fig. 10.15.

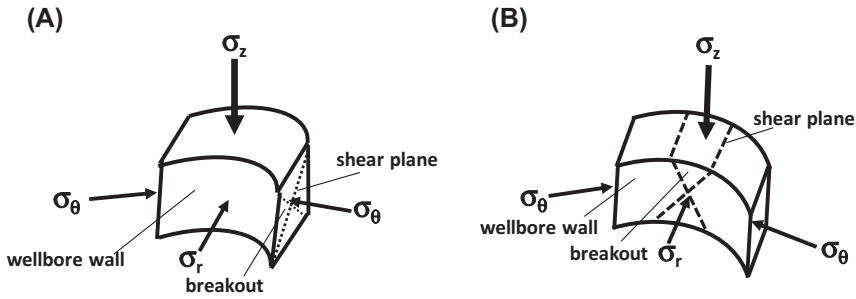

Figure 10.16 Schematic failure planes and breakouts caused by shear failures at the wellbore wall where the axial stress is the maximum principal stress. (A) Radial stress is the minimum principal stress. (B) Difference between radial and tangential stresses is small.

10.5 Required mud weight for borehole stability with allowable breakout width

A certain wellbore breakout width in drilling is allowable without affecting borehole stability. The breakout width is actually a breakout angle (θ_{BO}), as defined in Figs. 10.3 and 10.15. A rule of thumb of the allowable breakout width can be obtained from the following empirical equation:

$$\theta_{BO} = 90^\circ - 0.67i \tag{10.35}$$

where θ_{BO} is the allowable breakout angle in degrees; i is the borehole inclination in degrees. The allowable breakout angle should be calibrated by wellbore breakouts in the offset wells for new well planning. For a borehole in a complicated geological setting, θ_{BO} should be smaller or set to be zero.

To consider the allowed breakout in borehole stability modeling, a simplified assumption can be used, i.e., assuming that the wellbore azimuth at the wellbore breakout edge can be obtained from the following equation:

$$\theta = 90^\circ - \theta_{BO}/2 \tag{10.36}$$

Therefore, the equations accounting for allowable wellbore breakout width can be obtained by replacing θ by $90^\circ - \theta_{BO}/2$ in Eqs. (10.13) and (10.19) for the minimum mud weight calculations in the inclined boreholes. For a vertical borehole, when tangential stress (σ_θ) and radial stress (σ_r) are the maximum and minimum principal stresses, the required mud

weight in Eq. (10.32) with the allowable breakout can be written in the following form:

$$P_{mBO} = \frac{\sigma_H + \sigma_h + 2(\sigma_H - \sigma_h)\cos\theta_{BO} - UCS + \alpha(q-1)p_p + \sigma_T}{q+1} \tag{10.37}$$

When the maximum axial stress is greater than the maximum tangential stress ($\sigma_{z\max} > \sigma_{\theta\max}$), the required mud weight in Eq. (10.34) with consideration of the allowable breakout becomes:

$$P_{mzBO} = \frac{\sigma_V + 2\nu(\sigma_H - \sigma_h)\cos\theta_{BO} + \nu\sigma_T - UCS + \alpha(q-1)p_p}{q} \tag{10.38}$$

Eqs. (10.37) and (10.38) indicate that with allowable wellbore breakout widths, the required mud weight can be reduced compared to the case without allowable wellbore breakout.

The above analyses assume that the wellbore wall is impermeable, either for shales with very low permeability or for permeable rocks with mud cake at the wellbore wall. If the borehole wall is permeable, the pore pressure at the borehole wall is equal to the mud pressure. This means that mud pressure (p_m) rather than pore pressure (p_p) needs to be used when computing the effective stresses. Then the required mud weights of the permeable cases can be obtained by replacing p_p by p_m in the impermeable cases.

10.6 Wellbore breakout profiles

10.6.1 Rock strength effect on wellbore breakouts

The steady-state poroelastic finite element method (FEM) is applied to model wellbore stresses and breakouts. The main purpose of this section is to illustrate how in situ stresses, rock strength, and mud weight affect wellbore breakouts. A vertical borehole is modeled firstly, and Table 10.2 lists the parameters used in the modeling. In the first case, the horizontal stress difference is small, only 2 MPa. Although the difference in the horizontal stresses is small, the induced stress difference near the wellbore, particularly the tangential stress, is still very large, as shown in Fig. 10.17. Using the Mohr–Coulomb failure criterion, the wellbore shear failure zones (breakouts) are computed for different rock strengths. It can be observed from Fig. 10.18 that a higher uniaxial compressive strength

Table 10.2 In situ stresses and rock properties used in the FEM modeling.

Parameter	Magnitude
Vertical stress, σ_V (MPa)	68.2
Minimum horizontal stress, σ_h (MPa)	55
Maximum horizontal stress, σ_H (MPa)	57
Pore pressure, p_p (MPa)	46.8
Downhole mud pressure, p_m (MPa)	46.8
Young's modulus of the rock, E (GPa)	2.7
Poisson's ratio of the rock, ν	0.2
Density of the rock, ρ (g/cm^3)	2.3
Borehole diameter, d (m)	0.311

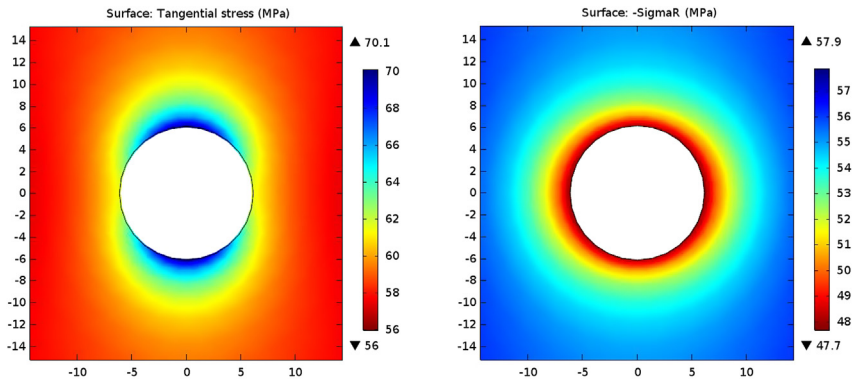

Figure 10.17 Tangential stress (left) and radial stress (right) around the wellbore modeled by COMSOL FEM software. The stress concentrations occur mainly near the wellbore wall.

corresponds to a smaller breakout. The difference of two horizontal stresses in this case study is small, thus the difference of the breakouts in the maximum and minimum horizontal stress directions is very small (Fig. 10.18).

10.6.2 Horizontal stress effect on wellbore breakouts

For modeling horizontal stress effect, the maximum horizontal stress (σ_H) is increased from 57 to 62 MPa; the other parameters remain the same as listed in Table 10.2. The FEM modeling results indicate that larger wellbore shear failure zones (breakouts) occur in the higher maximum horizontal stress condition (Fig. 10.19) than those in the smaller maximum horizontal

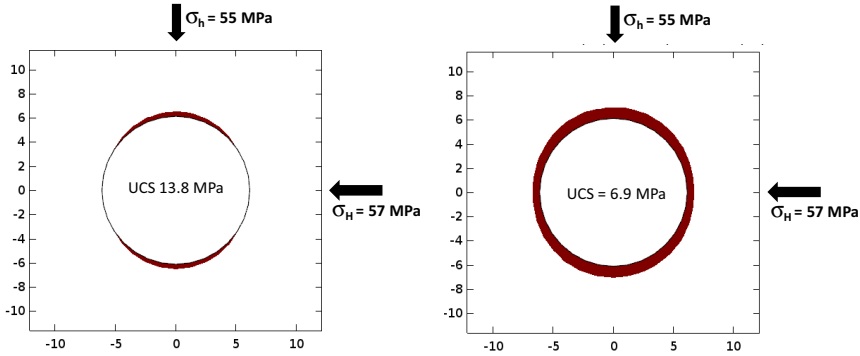

Figure 10.18 Wellbore shear failures for different rock strengths modeled by the FEM (shaded areas are the breakouts). Uniaxial compressive strength UCS = 13.8 MPa in the left plot and UCS = 6.9 MPa in the right plot.

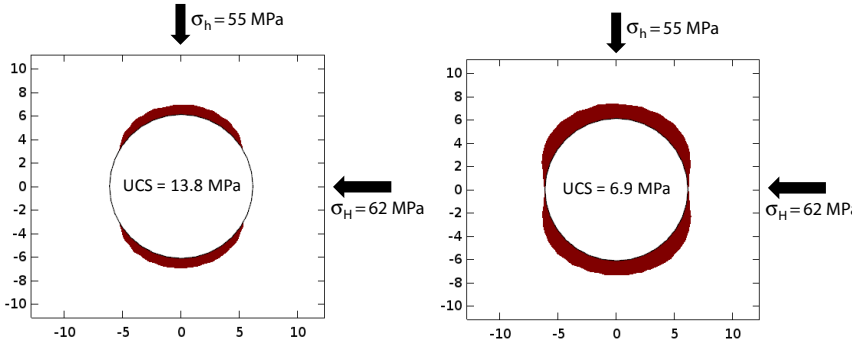

Figure 10.19 Larger wellbore breakouts occurred in the higher maximum horizontal stress case than those in Fig. 10.18.

stress condition (Fig. 10.18). A larger horizontal stress difference causes a larger wellbore breakout in the minimum horizontal stress direction (the borehole crown in Fig. 10.19).

10.6.3 Mud weight effect on wellbore breakouts

Raising mud weight can reduce wellbore breakouts. The case shown in the right figure of Fig.10.19 is used for the FEM modeling, but the mud weight is raised from $p_m = 46.8$ MPa to $p_m = 50$ MPa. The FEM modeling result shows that increasing mud weight can reduce the area of wellbore breakouts (Fig. 10.20).

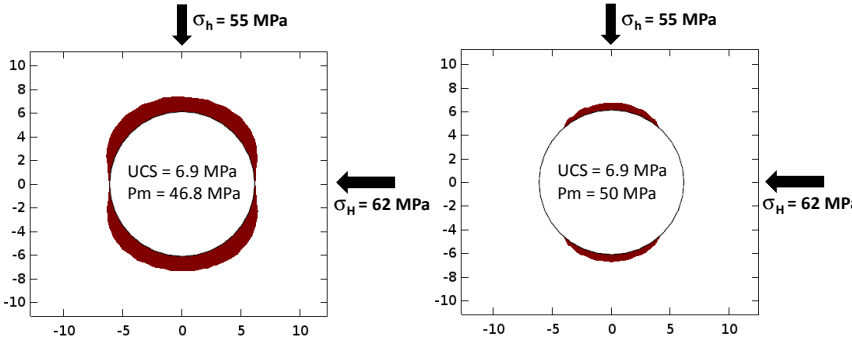

Figure 10.20 Wellbore breakouts with different mud weights. Higher mud weight reduces wellbore breakout area.

10.6.4 Breakouts in the horizontal well

In the normal faulting stress regime, a horizontal well has a larger shear failure (breakout) area than a vertical well. Fig. 10.21 models two horizontal wells drilled in the minimum horizontal stress direction with different rock strengths. In the horizontal well modeling, the same parameters are used as those in the vertical wells shown in Fig. 10.18 and with the same downhole mud pressure: $p_m = 46.8$ MPa. The FEM results demonstrate that the breakout area in the horizontal well is much larger (Fig. 10.21) than that in the vertical well (Fig. 10.18). It implies that in the normal faulting stress regime, a horizontal well needs a higher mud weight than that in a vertical well to maintain wellbore stability.

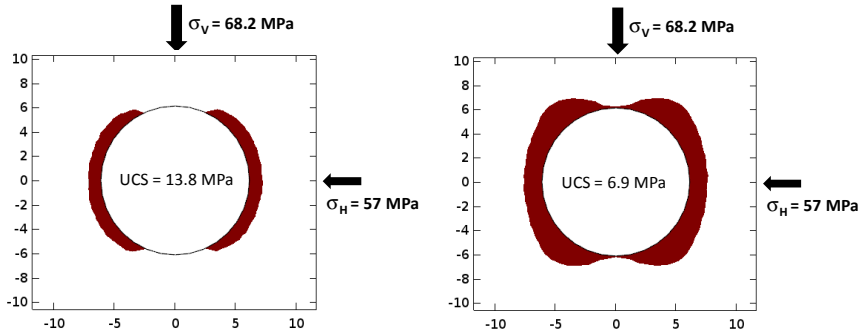

Figure 10.21 Wellbore breakouts in horizontal wells that have the same parameters to the ones in Fig. 10.18.

10.7 Single-porosity poroelastic wellbore stability solutions

10.7.1 Single-porosity poroelastic wellbore solution

Poroelastic solution for an anisotropic stress field was derived by Detournay and Cheng (1988). They considered a vertical borehole drilled in a porous rock formation characterized by a nonhydrostatic horizontal in situ stress field (Fig. 10.12). To facilitate the physical interpretation of this problem, the loading is decomposed into three fundamental modes: (1) a far-field isotropic stress; (2) a virgin pore pressure; and (3) a far-field stress deviator. Note that modes 1 and 2 are axisymmetric, whereas mode 3 is asymmetric. The poroelastic solution is time-dependent. For low values of time, the solution converges toward the following asymptotic expressions (Charlez, 1997):

$$\begin{aligned}
\frac{2p_p}{\sigma_H-\sigma_h} &= \frac{4}{3}B(1+\nu_u)\left[\sqrt{\frac{R}{r}}\,\mathrm{erfc}\left(\frac{r-R}{\sqrt{4ct}}\right)-\frac{R^2}{r^2}\right]\cos 2\theta \\
\frac{2\sigma_r}{\sigma_H-\sigma_h} &= \left[-4\frac{R^2}{r^2}+3\frac{R^4}{r^4}\right]\cos 2\theta \\
\frac{2\sigma_\theta}{\sigma_H-\sigma_h} &= \left[4\frac{\nu_u-\nu}{1-\nu}\sqrt{\frac{R}{r}}\,\mathrm{erfc}\left(\frac{r-R}{\sqrt{4ct}}\right)-3\frac{R^4}{r^4}\right]\cos 2\theta \\
\frac{4Gu_r}{R(\sigma_H-\sigma_h)} &= \left[4(1-\nu_u)\frac{R}{r}-\frac{R^3}{r^3}\right]\cos 2\theta
\end{aligned} \tag{10.39}$$

where erfc is the error function; ν and ν_u are the drained and undrained Poisson's ratios, respectively; B is Skempton's pore pressure coefficient; c is the diffusivity coefficient; G is the shear modulus; u_r is the displacement in the r-direction; t is the time starting from introduction of the borehole. When $t = 0^+$, Eq. (10.39) is the solution for dry materials.

10.7.2 Steady state poroelastic wellbore solution

In the poroelastic solution, time effect is very pronounced, particularly at a short time after the borehole excavation because of pore pressure diffusion. This time-dependent behavior needs to pick the right time step for the

poroelastic calculation. However, in some cases, a steady state solution is useful, e.g., for hydraulic fracturing modeling and sand production prediction. After a certain time, a steady state can be reached for fluid diffusion, and the following steady poroelastic solution can be used for an inclined wellbore when the wellbore wall is permeable:

$$
\begin{cases}
\sigma_r = \dfrac{\left(\sigma_x^0 + \sigma_y^0\right)}{2}\left(1 - \dfrac{R^2}{r^2}\right) + \dfrac{\left(\sigma_x^0 - \sigma_y^0\right)}{2}\left(1 - \dfrac{4R^2}{r^2} + \dfrac{3R^4}{r^4}\right)\cos 2\theta + \\
\tau_{xy}^0\left(1 - \dfrac{4R^2}{r^2} + \dfrac{3R^4}{r^4}\right)\sin 2\theta + p_m\dfrac{R^2}{r^2} + \dfrac{\alpha(1-2\nu)}{2(1-\nu)}(p_m - p_p)\left(1 - \dfrac{R^2}{r^2}\right) \\
\sigma_\theta = \dfrac{\left(\sigma_x^0 + \sigma_y^0\right)}{2}\left(1 + \dfrac{R^2}{r^2}\right) - \dfrac{\left(\sigma_x^0 - \sigma_y^0\right)}{2}\left(1 + \dfrac{3R^4}{r^4}\right)\cos 2\theta - \\
\tau_{xy}^0\left(1 + \dfrac{3R^4}{r^4}\right)\sin 2\theta - p_m\dfrac{R^2}{r^2} + \dfrac{\alpha(1-2\nu)}{2(1-\nu)}(p_m - p_p)\left(1 + \dfrac{R^2}{r^2}\right) \\
\sigma_z = \sigma_z^0 - 2\nu\left(\sigma_x^0 - \sigma_y^0\right)\dfrac{R^2}{r^2}\cos 2\theta - 4\nu\tau_{xy}^0\dfrac{R^2}{r^2}\sin 2\theta + \dfrac{\alpha(1-2\nu)}{(1-\nu)}(p_m - p_p) \\
\tau_{r\theta} = \left(-\dfrac{\sigma_x^0 - \sigma_y^0}{2}\sin 2\theta + \tau_{xy}^0\cos 2\theta\right)\left(1 + \dfrac{2R^2}{r^2} - \dfrac{3R^4}{r^4}\right) \\
\tau_{rz} = \left(\tau_{yz}^0\sin\theta + \tau_{xz}^0\cos\theta\right)\left(1 - \dfrac{R^2}{r^2}\right) \\
\tau_{\theta z} = \left(-\tau_{xz}^0\sin\theta + \tau_{yz}^0\cos\theta\right)\left(1 + \dfrac{R^2}{r^2}\right)
\end{cases}
\tag{10.40}
$$

For a vertical wellbore, the steady state poroelastic solution for the permeable wellbore wall can be written in the following:

$$\begin{aligned}
\sigma_r &= \frac{(\sigma_H+\sigma_h)}{2}\left(1-\frac{R^2}{r^2}\right)+\frac{(\sigma_H-\sigma_h)}{2}\left(1-\frac{4R^2}{r^2}+\frac{3R^4}{r^4}\right)\cos 2\theta \\
&\quad + p_m\frac{R^2}{r^2}+\frac{\alpha(1-2\nu)}{2(1-\nu)}(p_m-p_p)\left(1-\frac{R^2}{r^2}\right) \\
\sigma_\theta &= \frac{(\sigma_H+\sigma_h)}{2}\left(1+\frac{R^2}{r^2}\right)-\frac{(\sigma_H-\sigma_h)}{2}\left(1+\frac{3R^4}{r^4}\right)\cos 2\theta \\
&\quad - p_m\frac{R^2}{r^2}+\frac{\alpha(1-2\nu)}{2(1-\nu)}(p_m-p_p)\left(1+\frac{R^2}{r^2}\right) \\
\sigma_z &= \sigma_V-\nu\frac{4R^2}{r^2}\frac{(\sigma_H-\sigma_h)}{2}\cos 2\theta+\frac{\alpha(1-2\nu)}{(1-\nu)}(p_m-p_p) \\
\tau_{r\theta} &= -\frac{(\sigma_H-\sigma_h)}{2}\left(1+\frac{2R^2}{r^2}-\frac{3R^4}{r^4}\right)\sin 2\theta \\
\tau_{z\theta} &= \tau_{rz}=0
\end{aligned} \tag{10.41}$$

At the borehole wall ($r=R$), the stress components (principal stresses) can be obtained from Eq. (10.41) as follows:

$$\begin{aligned}
\sigma_r &= p_m \\
\sigma_\theta &= \sigma_H+\sigma_h-2(\sigma_H-\sigma_h)\cos 2\theta-p_m+\frac{\alpha(1-2\nu)}{1-\nu}(p_m-p_p) \\
\sigma_z &= \sigma_V-2\nu(\sigma_H-\sigma_h)\cos 2\theta+\frac{\alpha(1-2\nu)}{1-\nu}(p_m-p_p)
\end{aligned} \tag{10.42}$$

The minimum and maximum tangential stresses at the wellbore wall in a vertical well can be obtained from Eq. (10.42) as follows:

$$\begin{aligned}
\sigma_{\theta\min} &= 3\sigma_h-\sigma_H-p_m+\frac{\alpha(1-2\nu)}{1-\nu}(p_m-p_p) \\
\sigma_{\theta\max} &= 3\sigma_H-\sigma_h-p_m+\frac{\alpha(1-2\nu)}{1-\nu}(p_m-p_p)
\end{aligned} \tag{10.43}$$

If the wellbore wall is impermeable, then it needs to replace the item (p_m-p_p) by (p_i-p_p) in Eqs. (10.40–10.43), where p_i is the pore pressure at

the wellbore wall. If $p_i = p_p$, then the steady state poroelastic solution is reduced to the elastic solution.

10.8 Dual-porosity finite element wellbore stability solutions

For a naturally fractured formation, it may be treated as a double-porosity medium consisting of the primary rock matrix as well as the fractured systems, which are distinctly different in porosity and permeability. The double-porosity poromechanical model needs to couple matrix and fracture deformations as well as fluid flow aspects (Zhang et al., 2003). The double porosity and double permeability formulations can be solved by the FEM for any directional borehole (Zhang, 2002; Zhang and Roegiers, 2005).

10.8.1 Wellbore stresses in elastic, single-, and double-porosity media

An inclined borehole (inclination of 70 degrees) was examined to investigate the poroelastic effects. The borehole was located in the strike-slip faulting stress regime. The in situ stresses were $\sigma_H = 29$ MPa, $\sigma_h = 20$ MPa, $\sigma_V = 25$ MPa, and initial pore pressure in the rock matrices $p_p = 10$ MPa, pore pressure in the fractures $p_{fr} = 10$ MPa. The radius of the borehole is $R = 0.1$ m. It should be noted that borehole size has no effect on the induced stresses in the wellbore; therefore, a small hole size is used in this modeling, which does not affect final results. The rock properties for this case study are listed in Table 10.3. Fig. 10.22 shows the local far-field in situ stresses in the inclined wellbore calculated from the initial in situ stresses using Eq. (10.1). The FEM modeling was conducted to obtain the single-porosity and dual-porosity solutions. Fig. 10.23 compares the pore pressure distributions at time $t = 100$ s and $\theta = 90°$ for the elastic and single-porosity models as well as the one for the dual-porosity model (Zhang et al., 2003). The difference is evidenced by an increase in pore pressure in the matrix for the dual-porosity media due to the associated large fracture compliance, which induces a nonmonotonic pressure distribution. Fig. 10.24 displays effective radial stress response in the minimum stress direction ($t = 100$ s and $\theta = 90°$) without considering mud weight. It can be observed that for both single- and dual-porosity models, tensile stresses are induced at a small distance inside the borehole wall, which tends

Table 10.3 Rock properties for double-porosity poroelastic borehole analysis.

Parameter	Unit	Magnitude
Elastic modulus (E)	GPa	20.6
Poisson's ratio (ν)	–	0.19
Fracture stiffness (K_n, K_{sh})	MPa/m	4.82×10^5
Fluid bulk modulus (K_f)	MPa	419.17
Grain bulk modulus (K_s)	GPa	48.21
Matrix porosity (n_{ma})	–	0.02
Fracture porosity (n_{fr})	–	0.002
Matrix mobility (k_{ma}/μ)	m^4/MN s	10^{-10}
Fracture mobility (k_{fr}/μ)	m^4/MN s	10^{-9}
Fracture spacing (s)	m	0.1
Uniaxial compressive strength (UCS)	MPa	41
Internal friction angle (φ)	degree	30
Material strength parameter (α)	–	0.14
Material strength parameter (κ)	MPa	12
Tensile strength (T_0)	MPa	1.5

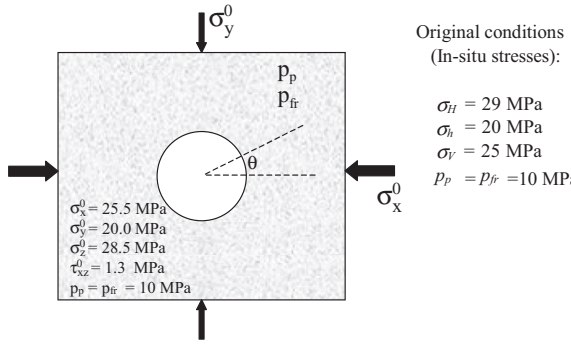

Figure 10.22 Far-field stresses in the borehole local coordinate for 70 degrees of borehole inclination.

to cause the wellbore spalling (tensile failure) because the rock has a very low tensile strength. This is a typical poroelastic effect.

The total tangential and radial stress distributions at $t = 100$ s and $\theta = 90°$ for the elastic and single-porosity models as well as the one for the dual-porosity model are compared in Fig. 10.25. Note that the elastic solution is obtained from Eq. (10.2) and has no time effects. Fig. 10.25 shows the tangential stress at near wellbore wall in the dual-porosity solution has the least magnitude compared to the elastic and single-porosity solutions. For the radial stress, the dual-porosity solution has the maximum value. The

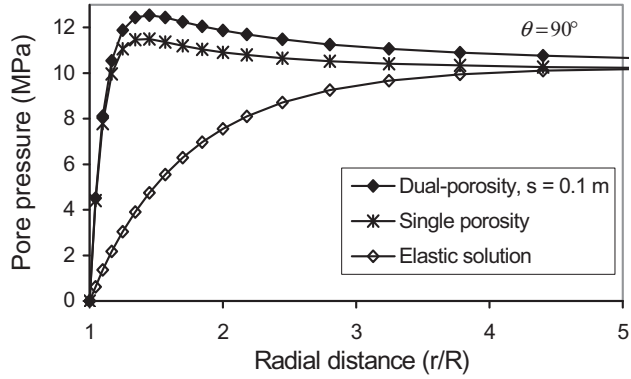

Figure 10.23 Comparison of pore pressures in elastic, single-, and dual-porosity solutions in the minimum stress direction ($\theta = 90°$) at time $t = 100$ s for the impermeable wellbore wall.

reason for this phenomenon is that the total deformation increases because of the introduction of a fracture elastic modulus in the dual-porosity governing equations, which leads to an increase in the total radial stress. Therefore, at and near wellbore wall (Fig. 10.25) the stress difference between the tangential and radial stresses is the minimum for the dual-porosity solution. The different results for the three solutions are primarily caused by pore pressure changes induced by borehole perturbation.

Poroelastic solutions have time-dependent effects, which are mainly caused by time-dependent behavior, as shown in Figs. 10.26 and 10.27.

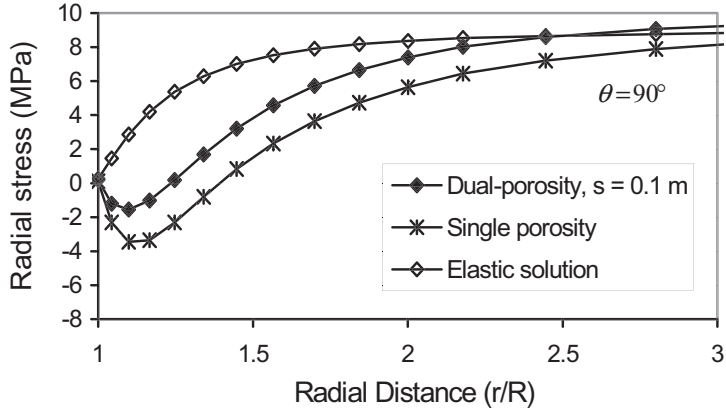

Figure 10.24 Comparison of effective radial stresses for single-porosity, dual-porosity, and elastic solutions in the minimum stress direction at time $t = 100$ s.

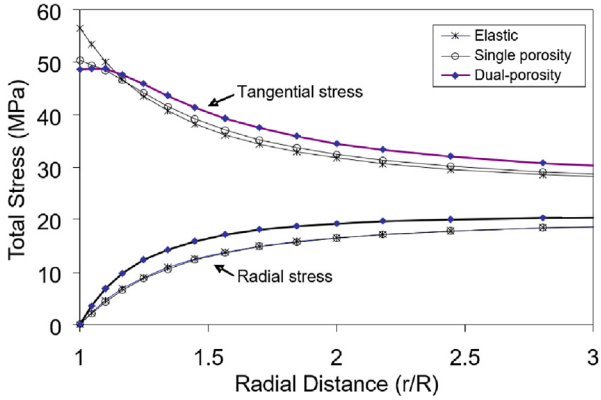

Figure 10.25 Total tangential and radial stresses around an inclined wellbore for elastic, single-porosity, and dual-porosity solutions in the minimum stress direction ($\theta = 90°$) at $t = 100$ s without considering the mud weight.

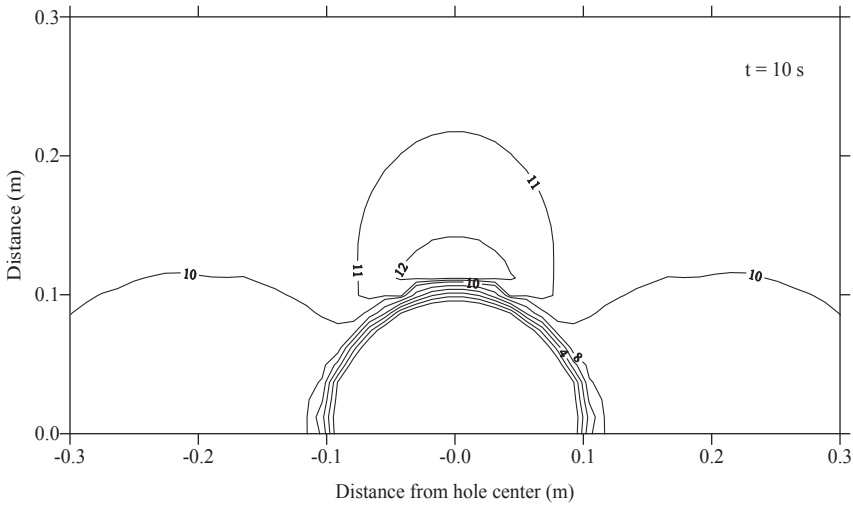

Figure 10.26 Pore pressure distribution around the wellbore at small time after drilling ($t = 10$ s), assuming an impermeable wellbore wall.

Pore pressure concentrations occur near the wellbore wall caused by drilling perturbation at smaller time (for $t = 10$ s in Fig. 10.26) around the minimum stress direction ($\theta = 90°$). Pore pressure concentrations decrease as time increases, as shown in Fig. 10.27 (Zhang and Roegiers, 2005). Note that nonmonotonic pressure distributions and pressure peaks are found at a

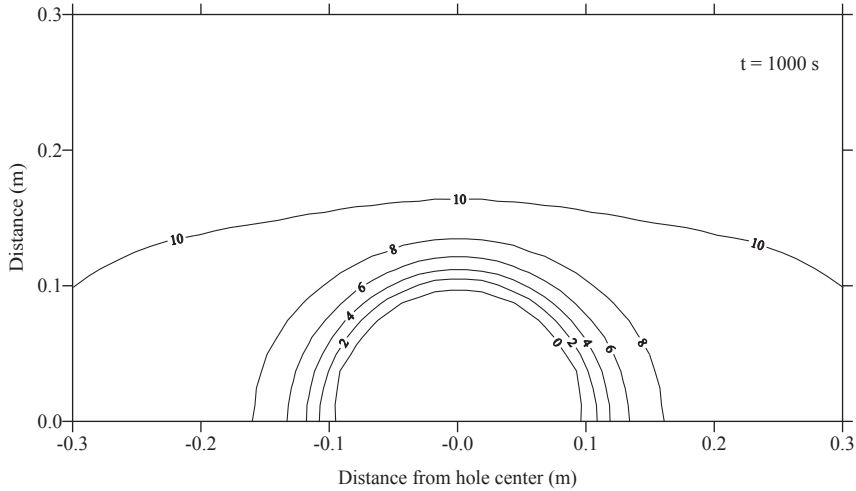

Figure 10.27 Pore pressure distribution around the wellbore at large time $t = 1000$ s, assuming an impermeable wellbore wall.

small distance inside the wall at a short time after drilling, which is attributed to the poroelastic effect. At larger time this effect disappears, i.e., as time increases the poroelastic effect becomes negligible. At large distances from the wellbore wall, the pore pressure approaches asymptotically the far-field pore pressure.

10.8.2 Wellbore failures in a strike-slip faulting stress regime

10.8.2.1 Inclined boreholes

In the following analysis, the in situ stresses and initial pore pressures are the same as shown in Fig. 10.22. Fig. 10.28 presents the Mohr–Coulomb shear failure around the cross section of a borehole with an inclination of 70 degrees at t = 100 s in a dual-porosity medium. The shear failure occurs mainly around the minimum stress direction because of low mud weight, whereas no failure occurs in the maximum stress direction. With sufficient mud pressure support, wellbore spalling and shear failure can usually be controlled. However, tensile failure or hydraulic fracturing may be induced in the wellbore when the mud pressure is too high. Fig. 10.29 shows the fracturing area for a hole inclination of 70 degrees at $t = 100$ s and for a mud pressure $p_m = 25$ MPa. It is observed that the fracturing takes place mainly around the maximum stress direction. It should be noted that both shear and tensile failure areas or safe mud weight window change with

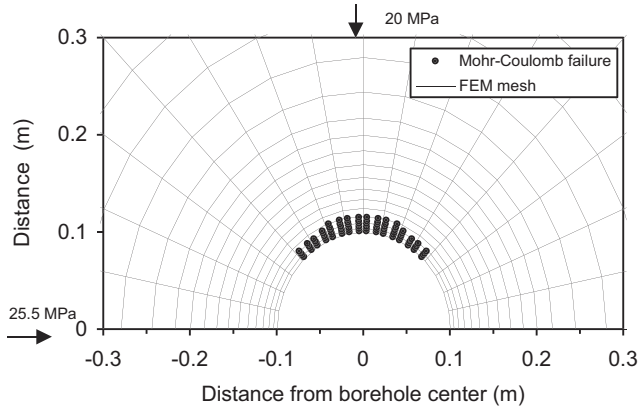

Figure 10.28 Shear failure area in the dual-porosity medium at time $t = 100$ s for a borehole inclination of 70 degrees.

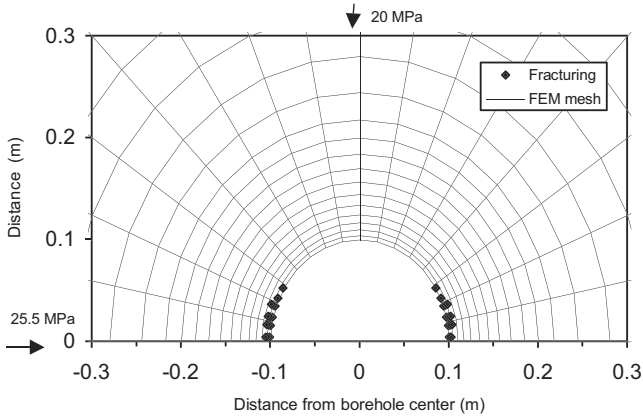

Figure 10.29 Tensile failure area in the dual-porosity medium at time $t = 100$ s and mud pressure $p_m = 25$ MPa for a borehole inclination of 70 degrees.

inclinations markedly. For example, the safe mud weight window decreases as borehole inclination increases in the normal faulting stress regime; however, in a strong tectonic stress regime, the mud weight window may increase as the inclination increases (Zhang et al., 2003).

10.8.2.2 Horizontal wells

Many oil companies provide horizontal drilling strategy guidelines that call for drilling in the direction of the minimum horizontal stress. Their

approach for best trajectory selections and drilling guidelines is to minimize the maximum value of stress concentration along the borehole wall. However, such an approach is mainly for drilling in the normal faulting stress regime. For drilling in a tectonic stress regime, wellbore stability behavior is different. The following analyses examine wellbore failures in a dual-porosity medium in the strike-slip faulting stress regime for the following two options: parallel and perpendicular to the maximum horizontal stress directions.

The Mohr–Coulomb shear failure areas are plotted in Figs. 10.30 and 10.31 for drilling parallel and perpendicular to the maximum horizontal

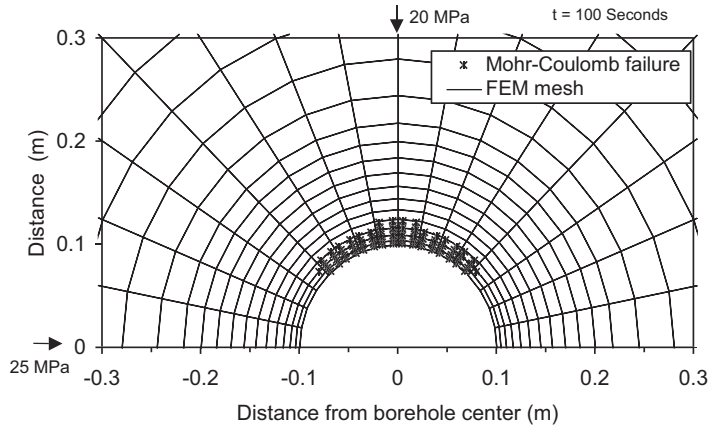

Figure 10.30 Shear failure area in the strike-slip stress regime at $t = 100$ s for a horizontal borehole drilled in the maximum horizontal stress direction.

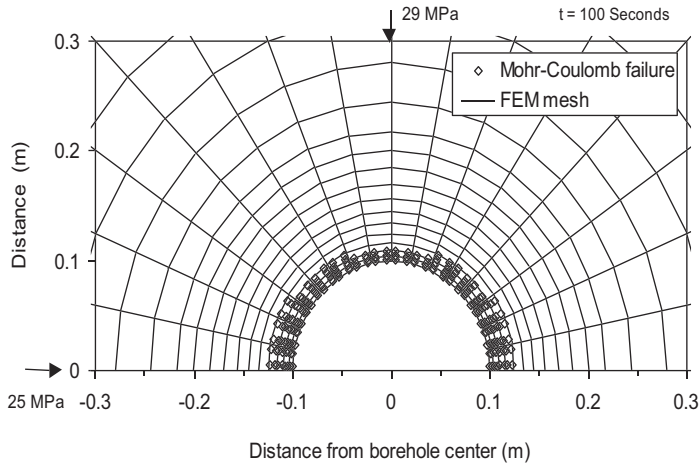

Figure 10.31 Shear failure area in the strike-slip stress regime at $t = 100$ s for a horizontal borehole drilled in the minimum horizontal stress direction.

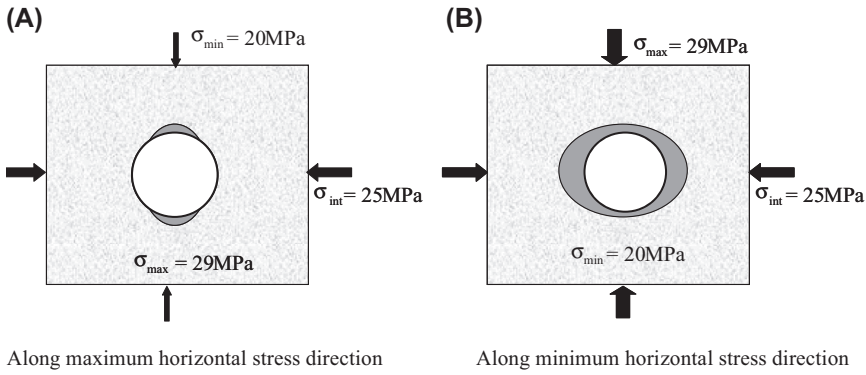

Figure 10.32 Schematic breakout areas in a strike-slip faulting stress regime for horizontal wells drilled in the maximum horizontal stress direction (A) and in the minimum horizontal stress direction (B).

stress direction. Comparing these two figures, it is obvious that there is a much larger failure area for the hole drilled in the minimum stress direction. Notice that the x-axis (direction of $\sigma_V = 25$ MPa) in Figs. 10.30 and 10.31 is the vertical stress direction. Therefore, in a tectonic stress regime a horizontal borehole drilled in the maximum stress direction has a smaller shear failure area, as shown in Fig. 10.32 (Zhang et al., 2006).

10.8.3 Wellbore failures in a normal faulting stress regime

The following specific geometry and material properties are used for wellbore stability analysis in a normal faulting stress regime. The radius of the borehole is $R = 0.1$ m. The rock is a Gulf of Mexico shale with the following properties: $G = 7.6 \times 10^2$ MPa, $\nu_u = 0.461$, $k = 1 \times 10^{-7}$ Darcy with $\mu = 0.001$ Pa·s. The poromechanical parameters used in the analysis can be found in Zhang et al. (2003). The far-field in situ stresses and pore pressure are in the following: $\sigma_H = 18$ MPa, $\sigma_h = 14$ MPa, $\sigma_V = 22.6$ MPa, $p_p = 10.4$ MPa (Bradley, 1979) at a true vertical depth of 1000 m.

Figs. 10.33 and 10.34 show the wellbore collapse (Drucker–Prager shear failure) areas around the borehole wall at $t = 100$ s for the hole inclinations of 50 degrees and 90 degrees. The collapse area increases with the borehole inclination in the normal faulting stress regime because the local

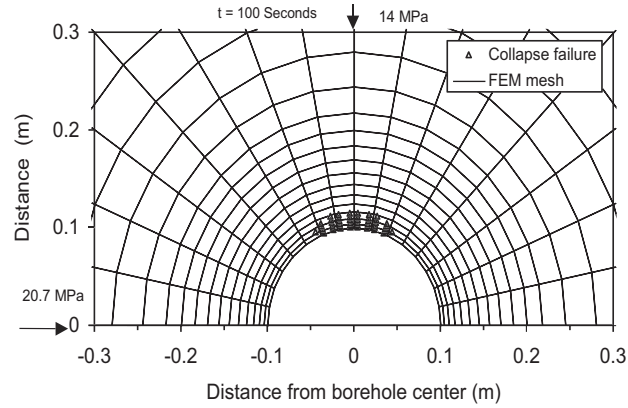

Figure 10.33 Collapse area in the normal faulting stress regime at $t = 100$ s for a hole inclination of 50 degrees.

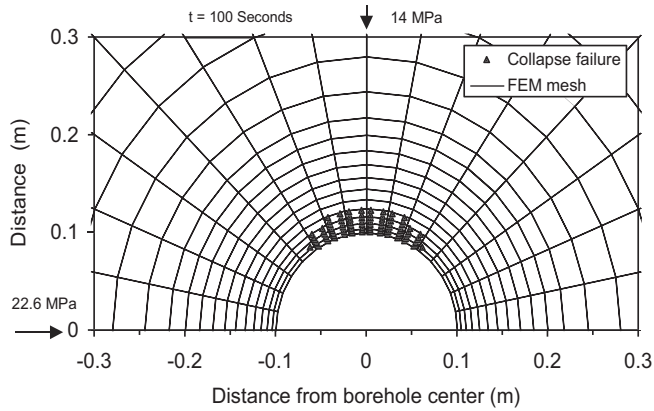

Figure 10.34 Collapse area in the normal faulting stress regime at $t = 100$ s for a hole inclination of 90 degrees.

far-field stresses and stress difference in the wellbore cross section increase as the inclination increases.

10.9 Wellbore tensile failures

10.9.1 Elastic solution of wellbore tensile failures

If applied mud pressure is too high, drilling-induced tensile fractures will be generated, which may cause drilling mud losses. Tensile failure will occur when the effective stress around the wellbore becomes tensile (negative)

and equals or exceeds the formation tensile strength. The tensile failure criterion, Eq. (3.77), can be used to compute wellbore tensile failure. Substituting the minimum effective principal stress Eq. (10.9) to (3.77), the maximum mud weight to generate tensile failure at the wellbore wall can be solved from the following equation:

$$\frac{1}{2}\left(\sigma_\theta + \sigma_z - \sqrt{(\sigma_\theta - \sigma_z)^2 + 4\tau_{\theta z}^2}\right) - \alpha p_p = -T_0 \tag{10.44}$$

where T_0 is the uniaxial tensile strength. Substituting σ_θ and σ_z in Eqs. (10.4), (10.5) and (10.6) to Eq. (10.44) and solving p_m in Eq. (10.44), the maximum mud weight or the fracture initiation pressure for the inclined borehole can be obtained.

For a vertical well, the maximum mud weight is much easier to be calculated. Substituting the first equation of Eq. (10.29) to Eq. (3.77), the following elastic solution can be obtained:

$$\sigma'_{\theta\min} = 3\sigma_h - \sigma_H - p_m + \sigma_T - \alpha p_p = -T_0 \tag{10.45}$$

Therefore, the maximum mud weight ($p_{\max}$) to generate tensile failures at the vertical borehole wall can be obtained from the following equation (considering Biot's coefficient $\alpha = 1$ when the tensile failure occurs):

$$p_{\max} = 3\sigma_h - \sigma_H + \sigma_T - p_p + T_0 \tag{10.46}$$

Therefore, drilling-induced tensile failures will occur when the applied mud weight is greater than $p_{\max}$ in a vertical well.

For a horizontal well drilled in the minimum horizontal stress direction in the normal faulting stress regime, the maximum mud weight to create tensile failures can be expressed as:

$$p_{\max}^H = 3\sigma_H - \sigma_V + \sigma_T - p_p + T_0 \tag{10.47}$$

In the reverse faulting stress regime, the vertical stress is the minimum in situ stress and horizontal tensile fractures may be created when the axial effective stress (the first equation in Eq. 10.30) exceeds the tensile strength. As shown in Eq. (6.61), horizontal tensile fractures are generated in a vertical well if the following relation holds:

$$\sigma_V - 2\nu(\sigma_H - \sigma_h) - p_p + T_V \le 0 \tag{10.48}$$

where T_V is the uniaxial tensile strength for the rock subjected to vertical tensile stress and is the strength for resistance to generate a horizontal tensile fracture and open it vertically.

For a horizontal well drilled in the minimum horizontal stress direction in the reverse and strike-slip faulting stress regimes, the maximum mud weight to create tensile failures (i.e. horizontal fractures in the maximum horizontal stress direction) can be obtained, similar as Eq. (6.66), in the following:

$$p_{\max}^{H} = 3\sigma_V - \sigma_H + \sigma_T - p_p + T_V \tag{10.49}$$

10.9.2 Poroelastic solution of wellbore tensile failures

Detournay and Cheng (1988) postulated that the wellbore tensile failure (formation breakdown) takes place when the Terzaghi effective tensile stress at the borehole wall is equal to the tensile strength of the rock, i.e.,

$$\sigma_\theta - p_p = -T_0 \tag{10.50}$$

In the permeable wellbore wall, it has $p_p = p_m$ and $\sigma_r = p_m$. Therefore, the above equation can be written in the following form (substituting $p_p = p_m$ to Eq. 10.50):

$$\sigma_\theta - p_m = -T_0 \tag{10.51}$$

The minimum tangential stress (tensile stress) at the vertical borehole wall in the steady-state poroelastic solution can be obtained from the first equation of Eq. (10.43):

Substituting Eq. (10.43) to (10.51) and solving p_m (denoted as p_{bl}), the breakdown pressure is given by the following expression:

$$p_{bl} = \frac{3\sigma_h - \sigma_H - 2\eta p_p + T_0}{2(1-\eta)} \tag{10.52}$$

where $\eta = \frac{\alpha(1-2\nu)}{2(1-\nu)}$.

When a rock starts to fail, the Terzaghi effective stress is normally considered (i.e., $\alpha = 1$). Therefore, when $\alpha = 1$, Eq. (10.52) is similar to the one obtained by Detournay and Cheng (1988). This expression, first derived by Haimson and Fairhurst (1967), represents a lower bound for the breakdown pressure.

Another case of interest is when the fracturing fluid cannot penetrate the rock (sleeve fracturing for example). Using the first equation of Eq. (10.43)

(replacing $p_m - p_p$ by $p_i - p_p$) and Eq. (10.50) (replacing p_p by p_i), the following breakdown pressure p_{bu}, can be obtained for impermeable case:

$$p_{bu} = 3\sigma_h - \sigma_H - 2\eta p_p - (1 - 2\eta)p_i + T_0 \tag{10.53}$$

where p_i is the pore pressure at the wellbore wall.

Assuming $p_i = p_p$, the Eq. (10.53) becomes the elastic solution of wellbore breakdown pressure for nonpenetrating fluid, i.e., Eq. (10.46) (without thermal effect). It yields a higher value for the breakdown pressure than the permeable case of Eq. (10.52).

In the reverse faulting stress regime, the condition to create horizontal tensile fractures is that the axial effective stress exceeds the tensile strength. The maximum axial stress in the poroelastic solution can be obtained from the third equation in Eq. (10.42) ($\theta = 0°$) for permeable case, then horizontal tensile fractures are generated if the effective axial stress becomes tensile and exceeds the tensile strength. Combining the third equation of Eq. (10.42) and tensile failure criterion ($\sigma_z - p_m \leq -T_V$), the following relation can be obtained for a vertical well:

$$\sigma_V - 2\nu(\sigma_H - \sigma_h) + (2\eta - 1)p_m - 2\eta p_p + T_V \leq 0 \tag{10.54}$$

10.10 Borehole stability analysis with consideration of weak bedding planes

10.10.1 Shear failure in weak bedding planes in vertical and horizontal wells

As described in the previous sections, different analytical methods and numerical models have been applied for borehole stability analyses. However, many borehole instabilities, particularly serious wellbore collapses, have occurred in difficult formations and conditions, such as unconsolidated formations, faulted and fractured rocks, weak planes, rubble zones, and subsalt formations. For instance, drilling through bedding planes and depleted reservoirs in the same hole section is very risky. When a well is drilled nonperpendicular to thinly bedded shales, it is often unstable. Rock failure can occur as a result of rock strength anisotropy caused by weak bedding planes. In these cases, increasing mud weight while drilling is required. However, when the reservoir immediately beneath the bedded shales is depleted, the increased mud weight can lead to lost circulation (Lang et al., 2011). Modeling of this geomechanical environment presents many challenges and requires coupling in situ stresses, pore pressure, mud

pressure, and anisotropic effects of rock strengths and stresses. Borehole stability modeling with considerations of rock anisotropy, preexisting fractures and planes of weakness in oil and gas wells has been reported, and different models have been proposed (e.g., Goodman, 1966; Aadnøy and Chenevert, 1987; Santarelli et al., 1992; Ong and Roegiers, 1993; Okland and Cook, 1998; Ekbote and Abousleiman, 2005; Willson et al., 2007; Lang et al., 2011; Gaede et al., 2012; Zhang, 2013).

In general, rocks or rock masses are more or less anisotropic, particularly, for example, the jointed rock masses or slates, shales, and schists. Experimental study of the stress states on failure behaviors in anisotropic rocks using the triaxial and polyaxial compression tests ($\sigma_1 > \sigma_2 \geq \sigma_3$) demonstrate that the strengths of anisotropic rocks vary significantly with directions of applied stresses and bedding planes (refer to Chapter 3, Sections 3.3 and 3.4.3). Experimental results demonstrate that the peak principal stress (σ_1) at rock shear failure is strongly dependent on the angle (β) between the maximum principal stress and the normal of the weak planes (Fig. 3.26). At different angle of β, the strength of the weak plane is very different (refer to Fig. 3.27), and the lowest strength occurs at $\beta_{\min} = 45^\circ + \varphi_w/2$ (φ_w is the angle of internal friction in the planes of weakness).

Jaeger and Cook (1979) proposed a weak plane shear failure criterion to correlate the maximum and minimum principal stresses associated with the weak plane sliding along preexisting planes of weakness for a rock mass having a set of parallel planes of weakness. This criterion can be applied to analyze wellbore stability with weak bedding planes, as shown in Fig.10.35. The principal effective stresses (σ'_1 and σ'_3) at the wellbore wall in each borehole section (e.g., Fig. 10.35) can be derived from the stress tensor at

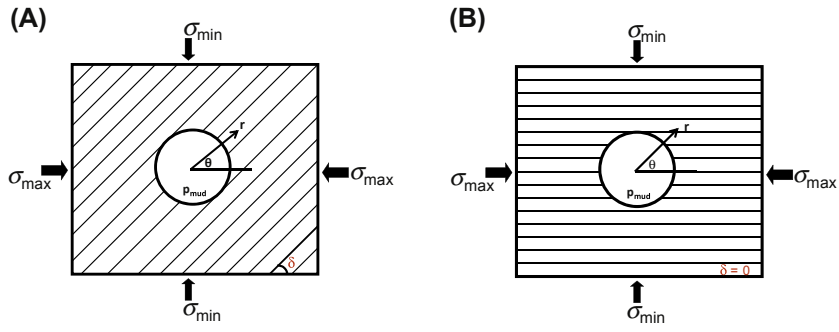

Figure 10.35 The cross sections (perpendicular to borehole axis direction) of two boreholes drilled in rocks with different orientations of the bedding planes (schematic representations of two cases) in anisotropic in situ stress field.

the wellbore wall from Eq. (10.2). From Eqs. (10.3–10.5), the principal effective stresses at the wellbore wall in a vertical or horizontal well can be written in the following form:

$$\begin{cases} \sigma'_r = p_m - \alpha p_p \\ \sigma'_\theta = \sigma_{\max} + \sigma_{\min} - \alpha p_p - p_m - 2(\sigma_{\max} - \sigma_{\min})\cos 2\theta \\ \sigma'_z = \sigma_{axis} - \alpha p_p - 2\nu(\sigma_{\max} - \sigma_{\min})\cos 2\theta \end{cases} \tag{10.55}$$

where σ'_r, σ'_θ, and σ'_z are the effective radial, tangential, and axial stresses at the wellbore wall, respectively; $\sigma_{\max}$ and $\sigma_{\min}$ are the in situ maximum and minimum principal stresses in the wellbore cross section, respectively. For a vertical well, $\sigma_{\max} = \sigma_H$, $\sigma_{\min} = \sigma_h$, and $\sigma_{axis} = \sigma_V$; for a horizontal well drilled in the minimum stress direction in the normal faulting stress regime, $\sigma_{\max} = \sigma_V$, $\sigma_{\min} = \sigma_H$, and $\sigma_{axis} = \sigma_h$; $\theta = 0°$ represents the direction of the maximum in situ stress ($\sigma_{\max}$) in the cross section of the borehole (Fig. 10.35).

Substituting the principal effective stresses (σ'_1 and σ'_3, or σ'_θ and σ'_r in Eq. 10.55) into the weak plane failure criterion, Eq. (3.50), the minimum mud weight for preventing wellbore sliding in the weak planes can be derived. For the shear failure with consideration of a set of parallel planes of weakness in a horizontal or vertical wellbore, the following equation can be obtained to calculate the minimum mud pressure for preventing wellbore sliding (shear failure) in the weak planes. This minimum mud pressure (p_w) is denoted to be the weak plane "slip failure pressure," and its gradient is "slip failure gradient" (Zhang, 2013):

$$p_w = \frac{[\sigma_{\max} + \sigma_{\min} - 2(\sigma_{\max} - \sigma_{\min})\cos 2\theta](1 - \mu_w \cot \beta_w)\sin 2\beta_w - 2c_w + 2\mu_w p_p}{2[\mu_w + (1 - \mu_w \cot \beta_w)\sin 2\beta_w]} \tag{10.56}$$

where θ is the angle defined in Fig. 10.35; c_w is the cohesion of the planes of weakness; μ_w is the coefficient of internal friction in the planes of weakness; $\mu_w = \tan \varphi_w$; φ_w is the angle of internal friction in the planes of weakness. For a horizontal well drilled in the minimum horizontal stress direction in the normal faulting stress regime, $\sigma_{\max} = \sigma_V$ and $\sigma_{\min} = \sigma_H$. For a vertical well, $\sigma_{\max} = \sigma_H$ and $\sigma_{\min} = \sigma_h$; β_w is the angle between the directions of

σ'_1 and the normal of the planes of weakness, $\varphi_w \le \beta_w \le 90°$. β_w varies with θ according to the following equations:

$$\beta_w = |\theta - \delta| \quad \text{for } 0 \le \theta \le \delta + 90^\circ \tag{10.57}$$

$$\beta_w = 180^\circ - |\theta - \delta| \quad \text{for } \delta + 90^\circ \le \theta \le 180^\circ \tag{10.58}$$

where δ is the angle of the bedding planes and $\sigma_{\max}$ direction as defined in Fig. 10.35.

It can be seen that the angle, β_w, varies around the wellbore cross section and with borehole trajectory, even the dip and strike of the weak planes kept unchanged. This means that β_w is a function of θ. When $\beta_w = 45° + \varphi_w/2$, the bedding planes have the lowest strength.

10.10.2 Shear failure of weak bedding planes in an inclined borehole

For the shear failure in the weak planes in an inclined borehole, by substituting Eqs. (10.8) and (10.10) to (3.50), the following equation can be obtained for calculating the minimum mud pressure (slip failure pressure, p^{incl}_w) to prevent wellbore sliding failure in the weak planes:

$$\frac{1}{2}\left(\sigma_\theta + \sigma_z + \sqrt{(\sigma_\theta - \sigma_z)^2 + 4\tau^2_{\theta z}}\right) - p^{incl}_w = \frac{2\left[c_w + \mu_w\left(p^{incl}_w - p_p\right)\right]}{(1 - \mu_w \cot\beta)\sin 2\beta} \tag{10.59}$$

The weak plane slip failure pressure p^{incl}_w can be solved from the above equation. It should be noted that σ_θ can be obtained from Eq. (10.4) by replacing p_m in the equation by p^{incl}_w.

10.10.3 Illustrative examples

A case study is examined to analyze borehole stability with impacts of weak bedding planes in a horizontal well drilled in the minimum horizontal stress direction. The following parameters are obtained from postdrill analysis: the maximum stress gradient of $\sigma_{\max} = \sigma_V = 13.8$ ppg, the minimum stress gradient at the borehole cross section of $\sigma_{\min} = \sigma_H = 13$ ppg, and pore pressure gradient of $p_p = 10.8$ ppg. The rock strength parameters are as follows: uniaxial compressive strength, UCS = 2995.2 psi; angle of internal friction, $\varphi = 30°$.

A set of weak planes, as shown in Fig. 10.35A, has an angle of $\delta = 40°$ to the maximum stress ($\sigma_{\max}$ or σ_V) direction at the wellbore section. The

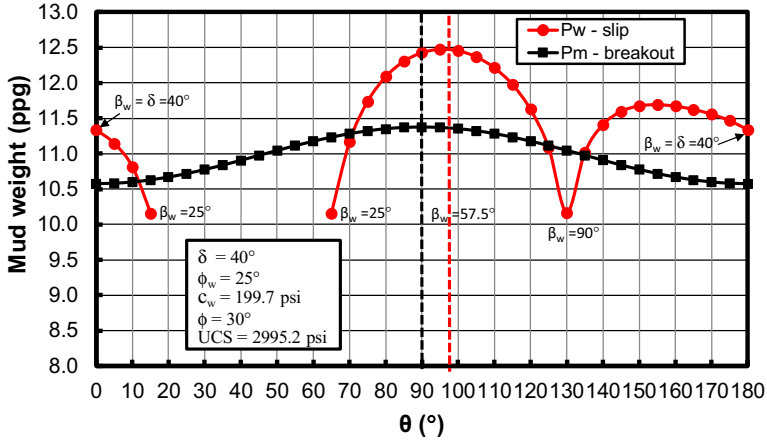

Figure 10.36 The slip failure gradient (p_w – slip) caused by weak planes calculated from Eq. (10.56) and the shear failure gradient (p_m – breakout) without the weak plane effects along a half circumference of the wellbore wall at $\delta = 40$ degrees (as shown in Fig. 10.35A). The slip failure is only calculated at $\varphi_w \leq \beta_w \leq 90°$; otherwise it is nonmeaningful because the failure will not occur in the weak planes.

weak planes have the following strength parameters: cohesion, $c_w = 199.7$ psi; angle of internal friction, $\varphi_w = 25°$. Using Eq. (10.56), the slip failure pressure around the wellbore wall can be calculated. It should be noted that β_w is a function of σ_1 and angles of δ and θ, as defined in Eqs. (10.57) and (10.58). Fig. 10.36 only presents the results in a half circumference of the wellbore wall (i.e., θ from 0 to 180 degrees) because of symmetry.

Fig. 10.36 displays the calculated slip failure gradient caused by weak bedding planes (presented as "p_w – slip" in the figure) from Eq. (10.56) and the shear failure gradient in the rock (calculated by Eq. (10.32b) without bedding plane effect, i.e., "p_m – breakout" in the figure). As expected the maximum shear failure gradient (p_m – breakout) appears in the minimum in situ stress direction ($\theta = 90°$, refer to Fig. 10.36). However, the slip failure gradient in the weak planes exhibits a rather distinct behavior. The maximum slip failure gradient occurs under the following two conditions: (1) when the bedding plane strength is near its minimum value (i.e., $\beta_{\min} = 45° + \varphi_w/2$) and (2) when the wellbore principal stress is close to its maximum value. Therefore, the location where the maximum slip failure gradient occurs is dependent on θ and δ. Thus, the slip failure locations and directions do not follow the conventional borehole breakout direction. The maximum slip failure in this case study occurs at $\theta = 98°$. Fig. 10.36 also indicates that the slip failure gradient varies markedly around the wellbore

in different locations owing to the fact that the peak strength of the weak planes varies significantly with the angle β_w. The slip failure in the weak planes only takes place if $\varphi_w < \beta_w < 90°$; otherwise, the failure occurs in the intact rock. For instance, when $\beta_w < 25° = \varphi_w$, the slip failure gradient is smaller than the shear failure gradient, as shown in Fig. 10.36; in this case, the wellbore should firstly have shear failure in the rock. When $\phi_w < \beta_w < 90°$, it is possible that the slip failure gradient is greater than the shear failure gradient; therefore, the wellbore creates slip failures in the weak planes (Fig. 10.36).

Fig. 10.37 shows another example for comparison of the slip failure gradient and shear failure gradient. In this case, only the angle of the weak planes changed, as shown in Fig. 10.35B with $\delta = 0°$. It again indicates that the wellbore slip failure is controlled strongly by the orientation of weak planes, δ, and the bedding plane angle, β_w.

Based on the above analyses, to avoid the slip failure in weak bedding planes it needs a higher mud weight than that in the intact rock. Fig. 10.38 plots an illustrative representation of wellbore slip failures caused by weak planes from the calculations in Figs. 10.36 and 10.37. If the applied mud weight (or ECD) is less than the calculated slip failure gradient, the slip failure will occur firstly in the weak planes. Notice that the maximum slip failure does not occur in the minimum stress direction (σ_{min} direction in Fig. 10.38). Instead, the maximum slip failures may occur in two directions, and the maximum slip failure direction has an angle with the minimum in situ stress direction (the conventional wellbore breakout direction), as

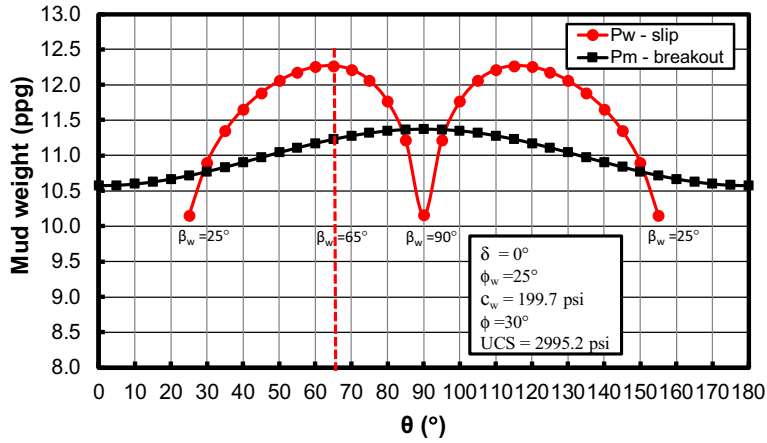

Figure 10.37 A similar case as Fig. 10.36 but for $\delta = 0°$ (as shown in Fig. 10.35B).

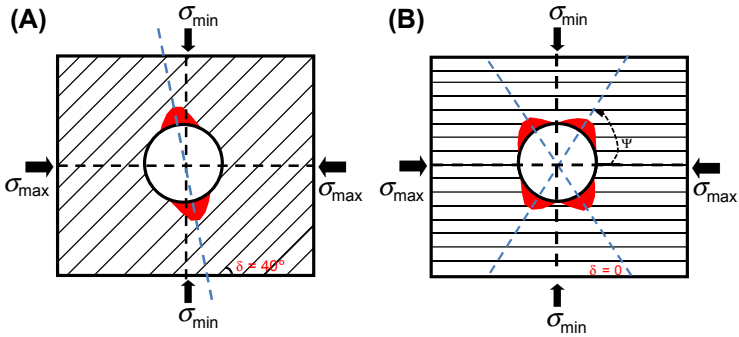

Figure 10.38 Schematic presentations of wellbore slip failures caused by the weak planes for two wellbores drilled in the weak bedding planes. The maximum slip failure direction is no longer in the minimum in situ stress (σ_{min}) direction, but with an angle to the minimum in situ stress direction. The shaded area represents the failures caused by the slip failures in the weak planes. (A) $\delta = 40°$. (B) $\delta = 0°$.

shown in Fig. 10.38. Borehole stability analysis needs to consider both effects of shear failures in the rock and the slip failure in the weak planes. When the slip failure and shear failure overlap, borehole stability becomes deteriorated.

In the drilling practice, the wellbore is more stable when drilling direction is perpendicular to the bedding planes or the borehole is drilled updip to the bedding direction. Otherwise, the wellbore is often unstable, and slip failures in the weak planes may occur. In this case, mud weight design needs to consider both wellbore breakouts in the rock and slip failures in the bedding planes.

10.11 Borehole stability in difficult conditions

10.11.1 Borehole stability in fractured formations

When boreholes are drilled in a naturally fractured formation, excessively high mud density allows the drilling fluid to penetrate into fractures, mobilizing the rock blocks and intensifying ovalization (Charlez, 1997). When this occurs, the fractured blocks can cave into the wellbore as a result of swabbing when tripping (mud pressure reduction due to pulling the drill string). When a borehole crosses a fault, drilling mud may invade the discontinuity planes. Apart from mud losses, penetration of the fluid reduces the normal stress and induces a displacement along the fracture planes or a fault that might shear the well, as shown in Fig. 10.39A. Resistivity

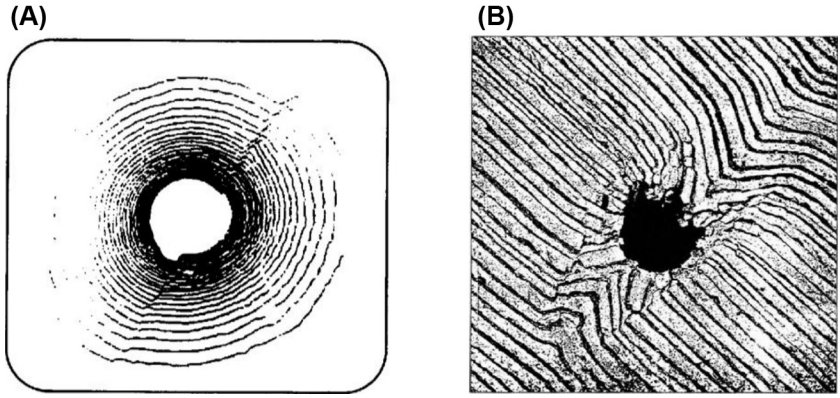

Figure 10.39 Wellbore failures caused by preexisting fractures. (A) Example of borehole shearing observed when crossing a fault mapped using a BHTV (from Maury and Zurdo, 1996); (B) A buckling mode of deformation and failure when penetrating thinly cycled beds (from Bandis, 2011).

image log shows that the presence of faults can cause breakout area to increase and breakout orientation to rotate (Moore et al., 2011). The consequences of fault impacts on wellbore breakout or mud losses can be dramatic and could lead to partial or even total loss of a well.

Fig. 10.39B presents a laboratory model of wellbore failure caused by bedding planes. It shows that a layered model, expertly fabricated by Bandis in 1987, consists of thinly bedded sandstones and micaceous interlayers. The steeply inclined beddings allow a buckling mode of deformations to develop, causing an elliptical failure zone. Such buckling mechanisms are common in thinly bedded rocks and presumably can compromise the integrity of horizontal wells (Barton, 2007). Laboratory tests in shales indicate that borehole instability is not a problem when drilling is perpendicular to bedding planes, but becomes very serious when the hole is parallel or very nearly parallel to bedding (Okland and Cook, 1998), a similar principle as described in the previous section.

Wellbore instability can easily occur when a borehole penetrates a preexisting fault or a natural fracture that has low or no cohesion. The finite element model can be used to model this problem by using different material parameters in different elements. A borehole in a formation cut by a fault zone was modeled in which the attitude of the fault is the same as the borehole drilling direction, as shown in Fig. 10.40. The in situ stresses are the same to the example given in Fig. 10.22. The material parameters in the rock and faulted area can be found in Zhang (2002). In the faulted area

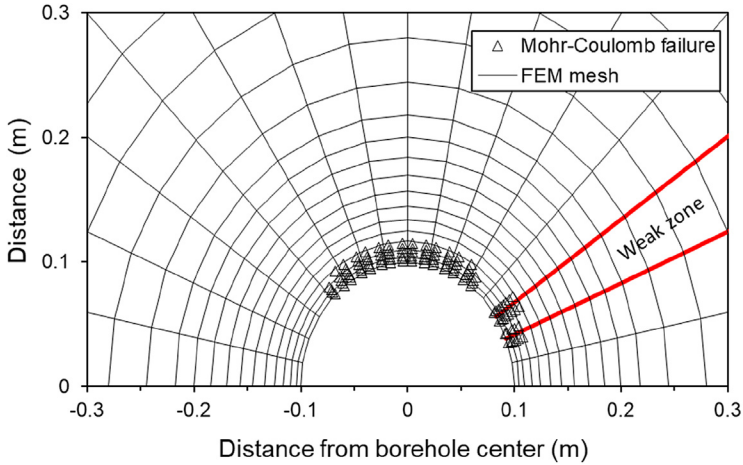

Figure 10.40 Shear failure area in the strike-slip faulting stress regime for an inclined borehole intersected by a weak zone with a low mud weight.

(weak zone), the rock has much lower compressive and tensile strengths, Young's modulus, and higher permeabilities than those in the surrounding rocks. The hole inclination is 70 degrees, and the true vertical depth of the hole is 1000 m. Fig. 10.40 presents the FEM-modeled shear failure areas for the inclined borehole intersected with a weak zone. The modeling result shows that shear failures occur not only along the local minimum stress direction (borehole crown in Fig. 10.40) but also in the weak rock zone. This is due to the fact that the weak rock has a much lower strength and, furthermore, there is a much larger stress concentration at the interface between the normal and weak rocks. Fig. 10.41 shows the tensile failure areas (fracturing in the figure) for an inclined borehole with a mud pressure of 24 MPa. It demonstrates that the tensile failures induced by high mud pressure appear mainly in the weak zone because it has a much lower tensile strength.

In the weak zone, the formation has low compressive strength, low tensile strength, and low fracture gradient. Therefore, mud weight management is needed while drilling: a good procedure would be to maintain the designed mud weight, making adjustments only when borehole breakouts or mud losses are observed.

10.11.2 Time effect on borehole stability

It is quite common that borehole breakouts occur after a certain time of drilling; even no wellbore instability problem has been encountered while

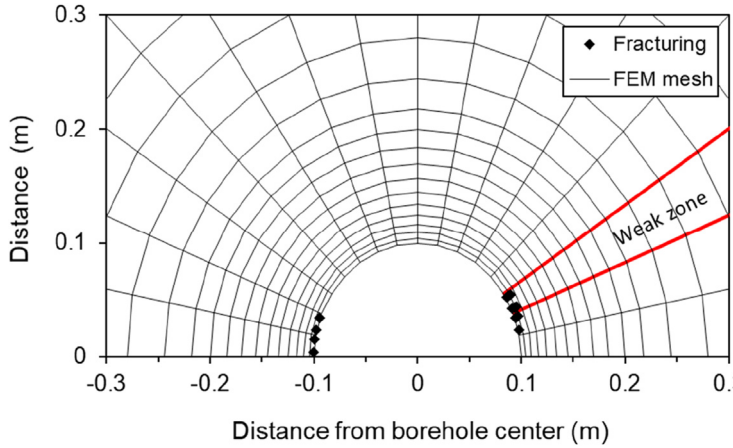

Figure 10.41 Tensile failure (fracturing in the figure) area in the strike-slip faulting stress regime for an inclined borehole intersected by a weak zone with a high mud weight.

drilling. Several reasons may cause this time-dependent wellbore failure, e.g., time-dependent rock strength reduction (Zhang, 2013), rock creep, seepage-induced stress changes (Li et al., 2017). Charlez (1997) considered that time-dependent diffusion through the porous medium profoundly modifies pore pressure and stresses and may affect wellbore stability. However, this diffusion may occur only in a very short time.

Laboratory experiments have demonstrated that rock compressive strength decreases as time lapses (Kranz, 1980; Kurita et al., 1983; Masuda, 2001). This is mainly caused by rock relaxation or creep, i.e., rock strain increases with time even under a constant loading stress. Therefore, when subjected to a constant stress even smaller than the rock strength, rock deforms and may eventually fail over time due to creep. The same phenomenon is observed in drilling, i.e., borehole deterioration with time. For example, wellbore breakouts increase greatly from the caliper logs performed a number of hours later compared to the caliper log run earlier in the same depth interval (Greenwood et al., 2006), as shown in Fig. 10.42A. Fig. 10.42B shows the caliper logs for two runs in the same borehole with a time difference of 12 days. In the first run, the borehole is only overgauged in some sections (red area) and the maximum breakout depth is 5 inches. However, in the second run after 12 days, all borehole sections are overgauged (red plus green areas), and the maximum breakout depth is greater

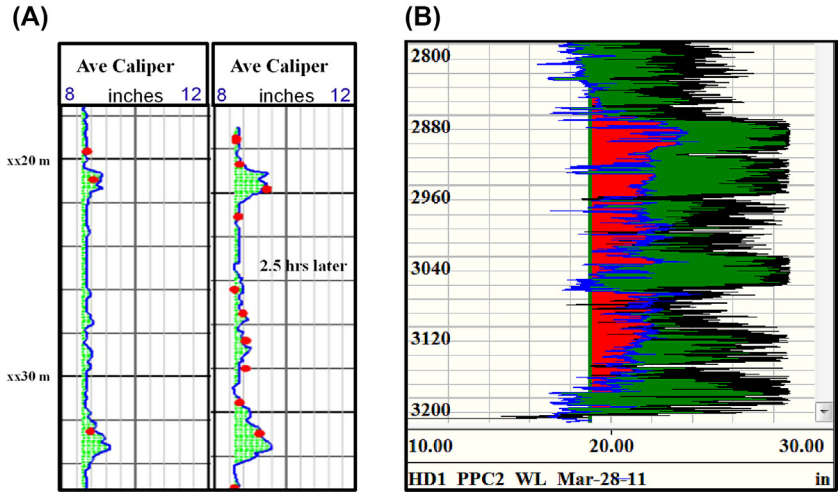

Figure 10.42 Caliper logs showing wellbore breakouts (shaded parts) increase with time. (A). Caliper logs in the same depth intervals observed between two logging runs with 2.5 h of elapsed time (based on the data from Greenwood et al., 2006). (B). Wireline caliper logs in a borehole: comparison of the first run and the second run after 12 days. The red area is the hole size increment (breakout) in the first run; the green area is the incremental wellbore breakout in the second run. The line represents the bit size, and the depth is in meters.

than 10 inches, i.e., as the borehole exposure time increases, wellbore breakout areas increase significantly.

Borehole image logs also show time-delayed wellbore breakouts. In the azimuthal density images, no breakout is found until 8 h after drilling; after 5 days of drilling, the borehole has obvious breakouts (the two bright bands along the borehole axis in Fig. 10.43). After 9 days of drilling, the breakout width increases significantly, and serious borehole breakouts occurs (Willson et al., 2007). Applying the LWD resistivity image logs, Moore et al. (2011) examined three examples to compare image logs a few minutes after drilling to the ones from about 30 min to 3 days after drilling (without changing the mud weight in each case). In all cases the borehole breakouts widen with time. These time-dependent failures could be a consequence of dilational deformation, decrease of pore fluid pressure, or decrease of rock strength with time.

One of primary reasons of the time-delayed wellbore failures is that the rock compressive strength decreases as the borehole exposure time increases. Based on experimental results (e.g., Masuda, 2001; Schmidtke and

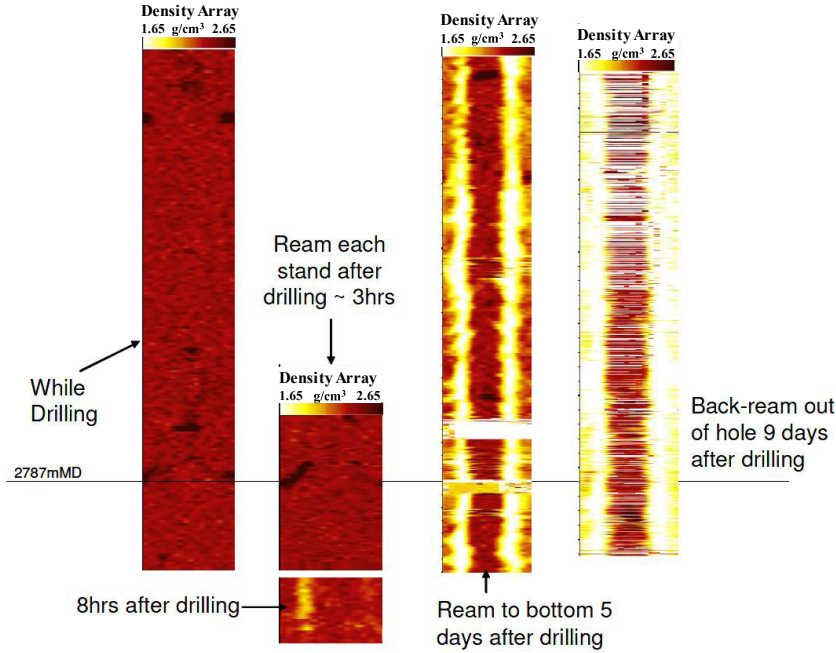

Figure 10.43 Time-delayed wellbore breakouts seen from azimuthal density images in a North Sea ERD well (Willson et al., 2007). The light color represents wellbore breakouts.

Lajtai, 1985), the following empirical equation can be used to determine rock uniaxial compressive strength reduction with time (Zhang, 2013):

$$UCS = UCS_0(1 - C\log t) \tag{10.60}$$

where UCS_0 is the original UCS without time effect; t is the rock exposure time in seconds ($t \geq 1$); C is a factor and can be obtained from lab experiments, e.g., $C = 0.24$ for granite (Masuda, 2001). For sedimentary rocks, parameter C can be measured from laboratory or obtained by calibrating borehole breakouts to borehole exposure time.

To reduce time-delayed wellbore failures, exposure time of an open hole should be decreased and the borehole should be cased soon after drilling. Otherwise, mud weight needs to be raised to reduce time-dependent failures.

10.11.3 Chemical effect on borehole stability

Chemical interaction of drilling fluid and shales (particularly smectite shales) is an important factor affecting wellbore stability. Some shales swell when

exposed to water-based mud or even oil-based mud, and this characteristic causes shales to be troublesome for drilling. One of the fundamental driving forces for the movement of water into or out of shale formations (osmotic diffusion) is the chemical-potential difference between shale formations and drilling fluids (Chenevert and Sharma, 1993; Mody and Hale, 1993). It is difficult to measure the chemical potential of a system; however, the chemical potential of the water phase can be estimated through its water activity. Water activity of shale formation is an excellent indicator of the shale state of hydration and its potential to absorb or lose water. Studies have shown that water absorption by shales due to the high activity (low salinity) drilling fluid makes the drilling fluid flow into the shale, causing pore pressure of the shale to increase. This alters stress distribution, reduces rock strength, and changes Young's modulus, therefore, potentially destabilize the wellbore (Zhang et al., 2008b). On the other hand, in the low-activity (high salinity) drilling fluid, water is drawn out of the shale, causing shale dehydration. The dehydration of shales results in near-wellbore pore pressure to decrease and shale compressive strength to increase, which sometimes is beneficial to wellbore stability, particularly in soft, high water content gumbo shales. However, overdehydration of shales causes tensile fractures in near wellbore formations and may disturb wellbore stability. Core test results show that overdehydration is detrimental to wellbore stability in naturally fractured formation (Rojas et al., 2006). Fig. 10.44 displays the effect of salinity of synthetic-based muds on the generation of tensile fractures in BP's shale samples cored from a depth of 17,055.1 to 17,055.9 ft in a Gulf of Mexico well. It is easily observed that tensile

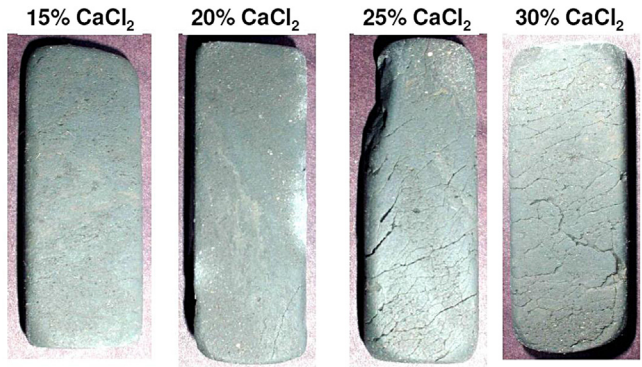

Figure 10.44 BP preserved core pieces immersed in synthetic-based drilling mud exhibit increasing shrinkage and tensile cracking as the mud activity is decreased (i.e., mud salinity increases, and water is drawn out from the shale cores) (Rojas et al., 2006).

fractures begin to occur as the shale is exposed to fluids with internal phase salinity above 15 wt%. Numerous cracks are generated after the mud salinity is increased to 25 wt% $CaCl_2$. As the salt concentration increases, water is removed from the shale because of osmotic effects and ions are added because of ionic diffusion, causing the shale fracturing.

Water activity difference in shale and drilling mud causes pore pressure change in the formation, which affects wellbore stability. Pore pressure changes caused by a given fluid activity contrast can be obtained from the following equation (Mody and Hale, 1993):

$$\Delta p = p - p_0 = -\alpha_m \frac{RT}{V} \ln\left(\frac{a_{w,shale}}{a_{w,mud}}\right) \tag{10.61}$$

where Δp is the differential pore pressure resulting from the water activity differences between the shale and the drilling fluid (osmotic pressure); p_0 and p are the far-field and near-wellbore pore pressures, respectively; α_m is the membrane efficiency, dimensionless; R is the gas constant, $R = 8.314$ kg m^2 s^{-2} g mol^{-1} K^{-1}; T is absolute temperature in Kelvin; V is the partial molar volume of the water, $V = 1.8 \times 10^{-5}$m^3/g/mol; $a_{w,shale}$ and $a_{w,mud}$ are the water activities for the shale and drilling mud, respectively, dimensionless.

It can be seen from Eq. (10.61) that if $a_{w,shale}$ (the shale pore fluid activity) is larger than $a_{w,mud}$ (the mud activity), water will be drawn out of the shale, causing near-wellbore shale pore pressure to decrease (thus Δp is negative). Therefore, appropriately decreasing the mud activity (increasing mud salinity) may ease shale swelling. However, it should avoid excessive decrease in mud activity; otherwise it may induce shale fracturing, as illustrated in Fig. 10.44. By contrast, if $a_{w,shale}$ (the pore fluid activity) is less than $a_{w,mud}$ (the mud activity), water will be drawn into the shale, causing near-wellbore pore pressure increase (Δp is positive) and making shale swelling.

As an example, consider a shale that has a water activity of $a_{w,shale} = 0.915$ in contact with a water-based fluid that has a water activity of $a_{w,mud} = 0.78$ and a membrane efficiency of 0.1. Assuming the rock temperature is 375.7 K, the osmotic pressure can be estimated from Eq. (10.61) as (Chen et al., 2003):

$$\Delta p = -0.1 \frac{8.314 \times 375.7}{1.8 \times 10^{-5}} \ln\left(\frac{0.915}{0.78}\right) = -2.77 \times 10^6 \text{Pa}$$

This would mean that there is a driving osmotic potential of 2.77 MPa trying to drive the water out of the shale.

The shale pore fluid activity $a_{w,shale}$ can be obtained from the following equation (Mody and Hale, 1993):

$$a_{w,shale} = \exp\left(\frac{V}{RT}\sigma'_m\right) \tag{10.62}$$

where σ'_m is the mean effective in situ stresses.

The mud activity $a_{w,mud}$ can be correlated to temperature in the following equation (Zhang et al., 2008b):

$$a_{w,mud} = C_1 \exp(C_2 T) \tag{10.63}$$

where T is the temperature in °C; C_1 and C_2 are constants and strongly dependent on the concentration of $CaCl_2$, which have the following relations (Chenevert and Strassner, 1975):

$$C_1 = -0.0153C + 1.1211 \tag{10.64}$$

$$C_2 = 8.451 \times 10^{-5} \exp(0.07114692C) \tag{10.65}$$

where C is the concentration of $CaCl_2$ solution in the internal phase of oil-based muds. Eqs. (10.64) and (10.65) are applicable only in a certain range of the concentrations of $CaCl_2$ solutions (10 wt% $< C <$ 40 wt%).

10.11.4 Borehole stability in salt and subsalt formations

Subsalt and near-salt formations are attractive exploration prospects in many operating areas including the Gulf of Mexico, offshore West Africa, Brazil, the Southern North Sea, Egypt, and the Middle East. One of the characteristic features of the Gulf of Mexico salt formation is that the salt bodies are highly mobile. This has two significant implications for wells drilled through salt: (1) creeping salt masses can exert catastrophic stresses on casing, and (2) unstable rubble zones created by the salt movement near the salt and rock interface and high overpressures in the subsalt formation, which can make drilling difficult or impossible.

One of the key challenges for well construction in salt is to maintain casing integrity. Salt-induced casing collapse has occurred in a number of the Gulf of Mexico wells. For example, a well was drilled through a salt body over 15,000 feet thick and eventually reached a total depth of more than 28,000 feet TVD. However, the casing collapsed near the base of the salt 3 months after the salt section was cased. The wellbore was abandoned.

Then, wellbore stability, salt creep, and casing failure were modeled (Zhang et al., 2008a). Based on the analysis, a bypass well successfully reached a great depth of 34,189 ft with a higher grade of casing than that in the original borehole.

10.11.4.1 Salt creep modeling

The ability of salt to deform under pressure and temperature changes makes it a good hydrocarbon trap generator over geological time. At the same time, the deformability and high creeping potential of salt make it a troublesome formation for borehole and casing stability. In typical sand and shale formations, in situ stress in the vertical direction is equal to the overburden stress, and the horizontal stresses are less than the vertical stress in the absence of tectonic activity. For a salt formation, the in situ stresses are generally assumed to be equal in all directions that are equal to the weight of the overburden formations. If mud pressure used to drill a well in the salt is less than the salt stress (i.e., horizontal stress), salt will creep into the wellbore. The closure rate of the borehole drilled in the salt grows with increasing temperature and differential pressure between the salt stress and the mud pressure. At shallow depths, temperature and differential pressure are small and the creep rate is slight. At greater depths, higher temperatures and higher differential pressures result in a more significant creep rate. In many cases, even a slight amount of salt creep can reduce the wellbore radius and impose the risks of stuck pipe and casing collapse.

The creep rate of salt depends on the burial depth, formation temperature, mineralogical composition, water contents, presence of impurities (such as clay), borehole diameter, and applied stress. Bischofite, carnallite, kieserite, and sylvite are the most mobile, even if present in small amounts. Halite is relatively slow-moving, and anhydrite and carbonates are essentially immobile (Willson et al., 2003). A review of the literature shows that casing loading problems were not reported in massive clean salts (Hackney, 1985). Extreme movements that have been reported (at rates of up to 1 in./hr) are limited to dirty salts with a high proportion of clay impurities or to salt intervals that are interbedded with shales.

The analytical results of salt samples in a studied borehole in the Green Canyon of the Gulf of Mexico show that more than 93% of minerals in the salt are halite (Zhang et al., 2008a). Minor amounts of sylvite (<1%) are reported in the lower salt section. This indicates that at deeper depths, the creep rate should be higher because of a larger salt stress and a higher level

of sylvite in the salt. Laboratory experiments show that sylvite has about 10 times creep rate of halite.

Barker et al. (1994) developed an analytical equation to allow engineering calculations at different stress, temperature, and closure rate combinations. This equation was based on steady-state creep of salt formations, and the steady state strain rate for salt was given in the following equation:

$$\frac{d\varepsilon}{dt} = Ae^{-B/[(T+459.67)/1.8]}(\sigma_H - p_m)^n \tag{10.66}$$

The hole size change caused by salt creep can be expressed as follows:

$$r = r_0\left[1 - Ae^{-B/[(T+459.67)/1.8]}(\sigma_H - p_m)^n t\right] \tag{10.67}$$

where $\frac{d\varepsilon}{dt}$ is the strain rate; r is the wellbore radius after creep, inches; r_0 is the original wellbore radius, inches; A is the salt constant $= (1.22 \pm 0.6) \times 10^{-8}$; B is the temperature exponent of salt, $B = 8000 \pm 2000$; T is the formation temperature, °F; n is the stress exponent of salt, $n = 4.5 \pm 1.3$; σ_H is the maximum horizontal stress (equal to the overburden stress), psi; p_m is the wellbore pressure (MW or ECD), psi; t is the time in days.

Because salt mineralogy is usually unknown in advance, a sensitivity analysis in salt creep rate needs to be conducted to estimate the high and low ranges, as shown in Fig. 10.45. This figure illustrates how hole size can be modified to maintain a sufficient clearance to allow casing to be run and cemented properly. In fast creep environments, hole reaming may be necessary. As salt creeps into the wellbore, it will eventually contact the casing and apply salt stress against the casing wall. Casing failure occurs

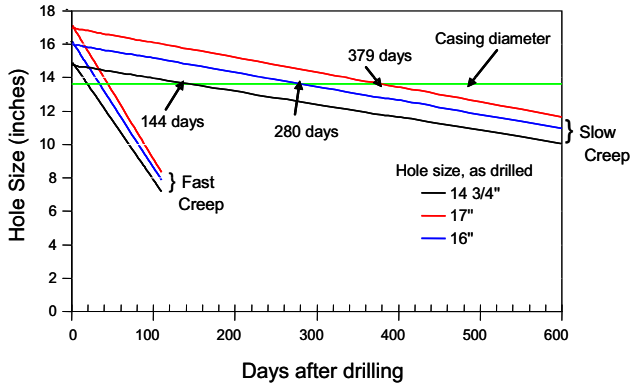

Figure 10.45 Hole size reductions caused by fast and slow rates of salt creep, with varying original borehole sizes modeled by Eq. (10.67).

when the salt-induced stress exceeds the casing strength. Case study in salt creep and casing failure indicates that nonuniform contact of salt and casing is the major reason to result in casing failures due to shear stresses (Zhang et al., 2008a).

10.11.4.2 Mud weight design in salt formation

The rule of thumb in estimating mud weight used for drilling through salt formation in the Gulf of Mexico is about 80%–90% of the overburden stress gradient. For an accurate determination of the mud weight, salt creep analysis is needed, and many studies have been carried out in this area (e.g., Fossum and Fredrich, 2002; Willson and Fredrich, 2005; Fredrich et al., 2007; Zhang et al., 2008a; Nikolinakou et al., 2014).

Based on salt creep rates and closure time of the borehole caused by the salt creep, the following empirical equation can be used to estimate mud pressure for drilling in salt in the Gulf of Mexico for the case of $\sigma_V > 2600$ psi:

$$p_S = \sigma_V + 6T - 3000 \tag{10.68}$$

where T is the formation temperature, in °F; σ_V is the overburden stress, psi; p_S is the mud pressure, psi. This empirical equation may need to be calibrated by drilling data and salt creep analysis for different cases.

At the exit of salt, highly overpressured formation and rubble zones may exist, and kicks or wellbore instability (e.g., hole collapses and mud losses) are the risks for subsalt drilling. Therefore, an exit salt strategy is needed.

10.11.4.3 Case study of borehole stability in subsalt formations

For subsalt formations, borehole instability is one of drilling risks because weak rocks sometimes exist in subsalt formations. A deepwater oil field with water depth of 3560 ft in the Gulf of Mexico is examined for post-well borehole stability (Zhang, 2013). The studied borehole is a subsalt vertical well, and the rocks in studied sections are weak shales and high-porosity sandstones with low compressive strength; therefore, wellbore breakouts took place in several sections. Using the Mohr-Coulomb failure criterion, the shear failure gradient is calculated by Eq. (10.32) based on the weak rock strength and sonic transit time correlation (Eq. 3.19). The calculated shear failure gradient is compared to the equivalent circulating density (ECD or downhole mud weight) while drilling, as shown in Fig. 10.46. The figure shows that the mud weight should be 13-14 ppg to avoid borehole breakouts from 28,000-28,360 ft, and a slightly higher mud

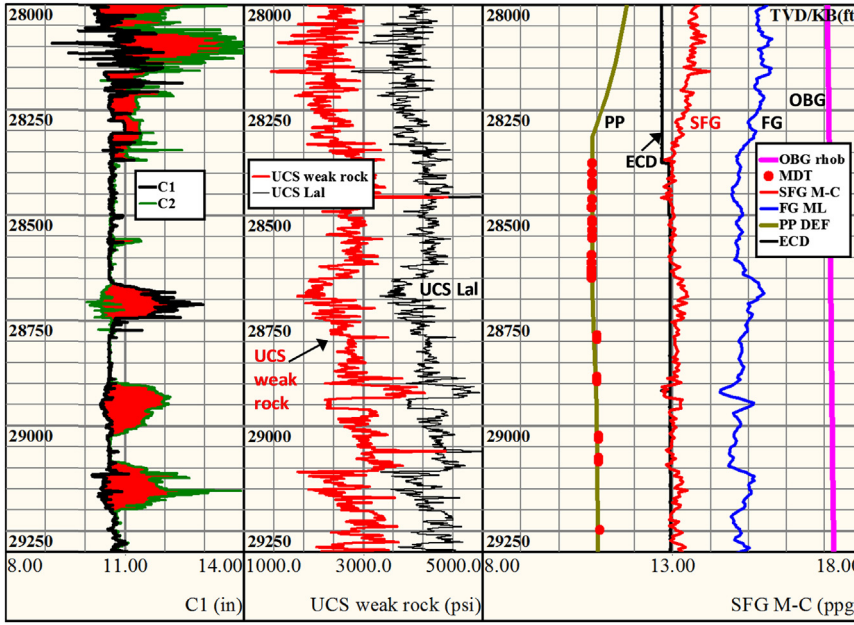

Figure 10.46 Post-well borehole stability analysis. The left track shows the 4-arm caliper log where the shaded parts are wellbore breakouts. The middle track presents uniaxial compressive strength (UCS) values calculated from sonic transit time. The right track shows pore pressures (PP) with measured formation pressure from MDT method, calculated shear failure gradient (SFG), the ECD, fracture gradient (FG), and overburden stress gradient (OBG).

weight (+0.2 ppg more) is needed to keep wellbore in-gauge from 28,650-29,220 ft. In the analysis, the weak rock strength correlation (Eq. 3.19) is used to calculate rock compressive strength and compared to the one obtained from Lal's correlation (Eq. 3.6), and the Lal's correlation overestimates rock strength in this case. Fig. 10.46 illustrates that the wellbore breakouts occur mainly in the sections where the UCS values are low.

References

Aadnoy, B., Chenevert, M.E., 1987. Stability of highly inclined boreholes. SPE Drill. Eng. 364–374.

Al-Ajmi, A.M., Zimmerman, R.W., 2006. Stability analysis of vertical boreholes using the Mogi–Coulomb failure criterion. Int. J. Rock Mech. Min. Sci. 43 (8), 1200–1211.

Bandis, S., 2011. Personal communication.

Barker, J.W., Feland, K.W., Tsao, Y.-H., 1994. Drilling long salt sections along the U.S. Gulf Coast. SPE Drill. Complet. 185–188.

Barton, N., 2007. Rock Quality, Seismic Velocity, Attenuation and Anisotropy. Taylor & Francis.
Bradley, W.B., 1979. Failure of inclined boreholes. Trans. ASME 101, 232–239.
Charlez, P.A., 1997. Rock Mechanics, Petroleum Application, vol. 2. Editions Technip, Paris.
Chen, S., Abousleiman, Y., 2017. Wellbore stability analysis using strain hardening and/or softening plasticity models. Int. J. Rock Mech. Min. Sci. 93, 260–268.
Chen, G., Chenevert, M.E., Sharma, M.M., Yu, M., 2003. A study of wellbore stability in shales including poroelastic, chemical, and thermal effects. J. Pet. Sci. Eng. 38, 167–176.
Chenevert, M.E., Sharma, A.K., 1993. Permeability and effective pore pressure of shales. SPE-21918-PA.
Chenevert, M.E., Strassner, J.E., 1975. Temperature effects on water activities of argillaceous shales and oil mud systems. Presented at the 15th Oil and Gas Conference, Balatonfured, Hungary, September 14–19.
Detournay, E., Cheng, A.H.D., 1988. Poroelastic response of a borehole in a non-hydrostatic stress field. Int. J. Rock Mech. Min. Sci. Geomech. Abstr. 25 (3), 171–182.
Detournay, E., Fairhurst, C., 1987. Two-dimensional elastoplastic analysis of a long cylindrical cavity under non-hydrostatic loading. Int. J. Rock Mech. Min. Sci. Geomech. Abstr. 24 (4), 197–211.
Dresen, G., Stanchits, S., Rybacki, E., 2010. Borehole breakout evolution through acoustic emission location analysis. Int. J. Rock Mech. Min. Sci. 47, 426–435.
Ekbote, S., Abousleiman, Y., 2005. Porochemothermoelastic solution for an inclined borehole in a transversely isotropic formation. J. Eng. Mech. 131 (5), 522–533.
Ewy, R.T., 1999. Wellbore-stability predictions by use of a modified Lade criterion. SPE Drill. Complet. 14 (2), 85–91. Paper SPE-56862.
Feng, Y., Li, X., Gray, K.E., 2018. An easy-to-implement numerical method for quantifying time-dependent mudcake effects on near-wellbore stresses. J. Pet. Sci. Eng. 164, 501–514.
Fjær, E., Holt, R.M., Horsrud, P., Raaen, A.M., 2008. Petroleum Related Rock Mechanics, second ed. Elsevier.
Fossum, A.F., Fredrich, J.T., 2002. Salt Mechanics Primer for Near-Salt and Sub-salt Deepwater Gulf of Mexico Field Developments. Sandia report. SAND2002–2063.
Fredrich, J.T., Fossum, A.F., Hickman, R.J., 2007. Mineralogy of deepwater Gulf of Mexico salt formations and implications for constitutive behaviour. J. Pet. Sci. Eng. 57, 354–374.
Gaede, O., Karpfinger, F., Jocker, J., Prioul, R., 2012. Comparison between analytical and 3D finite element solutions for borehole stresses in anisotropic elastic rock. Int. J. Rock Mech. Min. Sci. 51, 53–63.
Gao, J., Deng, J., Lan, K., Feng, Y., Zhang, W., 2017. Porothermoelastic effect on wellbore stability in transversely isotropic medium subjected to local thermal non-equilibrium. Int. J. Rock Mech. Min. Sci. 96, 66–84.
Goodman, R.E., 1966. On the distribution of stresses around circular tunnels in nonhomogeneous rocks. In: Proc. 1st Int. Congress. ISRM, Lisbon, pp. 249–255.
Greenwood, J., Bowler, P., Sarmiento, J.F., Wilson, S., Edwards, S., 2006. Evaluation and application of real-time image and caliper data as part of a wellbore stability monitoring provision. Paper IADC/SPE-99111 presented at IADC/SPE Drilling Conference, Miami, Florida, USA, 21–23 February.
Hackney, R.M., 1985. A new approach to casing design for salt formations. SPE/IADC-13431.
Haimson, B., 2007. Micromechanisms of borehole instability leading to breakouts in rocks. Int. J. Rock Mech. Min. Sci. 44 (2), 157–173.

Haimson, B.C., Fairhurst, C., 1967. Initiation and extension of hydraulic fractures in rocks. SPE J. 7, 310–318.
Haimson, B., Lee, H., 2004. Borehole breakouts and compaction bands in two high-porosity sandstones. Int. J. Rock Mech. Min. Sci. 41, 287–301.
Jaeger, J.C., Cook, N.G.W., 1979. Fundamentals of Rock Mechanics, third ed. Chapman & Hall.
Jarosiński, M., 1998. Contemporary stress field distortion in the Polish part of the Western Outer Carpathians and their basement. Tectonophysics 297, 91–119.
Kranz, R.L., 1980. The effects of confining pressure and stress difference on static fatigue of granite. J. Geophys. Res. 85 (B4), 1854–1866.
Kurita, K., Swanson, P.L., Getting, I.C., Spetzler, H., 1983. Surface deformation of westerly granite during creep. Geophys. Res. Lett. 10 (1), 75–78.
Lang, J., Li, S., Zhang, J., 2011. Wellbore stability modeling and real-time surveillance for deepwater drilling to weak bedding planes and depleted reservoirs. SPE/IADC-139708.
Li, X., Cui, L., Roegiers, J.-C., 1998. Thermoporoelastic analyses of inclined boreholes. SPE/ISRM-47296 presented at Eurock'98 Held in Trondheim, Norway.
Li, S., George, J., Purdy, C., 2012. Pore pressure and wellbore stability prediction to increase drilling efficiency. J. Pharm. Technol. 98–101. Paper SPE 144717.
Li, X., Mohtar, C., Gray, K., 2017. Investigation of wellbore breakouts in deviated wells – a 3D numerical modeling Approach. ARMA-2017-0826.
Liang, C., Chen, M., Jin, Y., Lu, Y., 2014. Wellbore stability model for shale gas reservoir considering the coupling of multi-weakness planes and porous flow. J. Nat. Gas Sci. Eng. 21, 364–378.
Mastin, L., 1988. Effect of borehole deviation on breakout orientations. J. Geophys. Res. 93, 9187–9195.
Masuda, K., 2001. Effects of water on rock strength in a brittle regime. J. Struct. Geol. 23 (11), 1653–1657.
Maury, V., Zurdo, C., 1996. Drilling-induced lateral shifts along pre-existing fractures: a common cause of drilling problems. SPE Drill. Complet. 11, 17–23.
Mclean, M.R., Addis, M.A., 1990. Wellbore stability analysis: a review of current methods analysis and their field application. In: SPE/IADC 19941, Drilling Conference, Houston, pp. 261–274.
Mody, F.K., Hale, A.H., 1993. A borehole stability model to couple the mechanics and chemistry of drilling fluid shale interaction. SPE/IADC 25728.
Monus, F.L., Broussard, F.W., Ayoub, J.A., Norman, W.D., 1992. Fracturing unconsolidated sand formations offshore Gulf of Mexico. SPE-24844.
Moore, J.C., Chang, C., McNeill, L., Thu, M.K., Yamada, Y., Huftile, G., 2011. Growth of borehole breakouts with time after drilling: implications for state of stress, Nan-TroSEIZE transect, SW Japan. Geochem. Geophys. Geosyst. 12, Q04D09.
Nikolinakou, M.A., Flemings, P.B., Hudec, M.R., 2014. Modeling stress evolution around a rising salt diapir. Mar. Petrol. Geol. 51, 230–238.
Okland, D., Cook, J.M., 1998. Bedding-related borehole instability in high-angle wells. SPE/lSRM 47285.
Ong, S.H., Roegiers, J.C., 1993. Influence of anisotropies in borehole stability. Int. J. Rock Mech. Min. Sci. 30 (7), 1069–1075.
Papamichos, E., Tronvoll, J., Skjærstein, A., Unander, T., 2010. Hole stability of Red Wildmoor sandstone under anisotropic stresses and sand production criterion. J. Pet. Sci. Eng. 72, 78–92.
Peng, S., Fu, J., Zhang, J., 2007. Borehole casing failure analysis in unconsolidated formation, a case study. J. Pet. Sci. Eng. 59, 226–238.
Peska, P., Zoback, M.D., 1995. Compressive and tensile failure of inclined well bores and determination of in situ and rock strength. J. Geophys. Res. 100, 12791–12811.

Plumb, R.A., Hickman, S.H., 1985. Stress-induced borehole elongation: a comparison between the four-arm dipmeter and the borehole televiewer in the Auburn geothermal well. J. Geophys. Res. 90, 5513–5521.
Plumb, R., Papanastasiou, P., Last, N.C., 1993. Constraining the state of stress in tectonically active settings. SPE/ISRM-47240.
Ramos, G.G., Wilton, B.S., Polillo, A.F., 1996. Usage and applicability of pseudo-3D stress analysis in borehole stability problems in petroleum drilling and production operations. In: Aubertin, Hassani, Mitri (Eds.), Rock Mechanics. Balkema, Rotterdam, pp. 1067–1073.
Reinecker, J., Tingay, M., Müller, B., 2003. Borehole breakout analysis from four-arm caliper logs. World Stress Map Project.
Roegiers, J.C., 1990. Stability and failure of circular openings. In: Rock at Great Depth, Maury & Fourmaintraux. Balkema, Rotterdam, pp. 1115–1121.
Roegiers, J.C., Detournay, E., 1988. Considerations on failures initiation in inclined boreholes. In: Proc. 29 U. S. Rock Symp. Balkema, Rotterdam.
Rojas, J., Clark, D., Greene, B., Zhang, J., 2006. Optimized salinity delivers improved drilling performance: AADE-06-DF-HO-11. In: AADE Drilling Fluids Technical Conference, Houston, Texas.
Santarelli, F.J., Dahen, D., Baroudi, H., Sliman, K.B., 1992. Mechanisms of borehole instability in heavily fractured rock media. Int. J. Rock Mech. Min. Sci. 29, 457–467.
Schmidtke, R.H., Lajtai, E.Z., 1985. The long-term strength of Lac du Bennet granite. Int. J. Rock Mech. Min. Sci. Geomech. Abstr. 22, 461–465.
Tingay, M., Reinecker, J., Müller, B., 2008. Borehole breakout and drilling-induced fracture analysis from image logs. World Stress Map Project Stress Analysis Guidelines. 1–18.
van Oort, E., 2003. On the physical and chemical stability of shales. J. Pet. Sci. Eng. 38, 213–235.
Wang, Y., Dusseault, M.B., 1991. Borehole yield and hydraulic fracture initiation in poorly consolidated rock media. Int. J. Rock Mech. Min. Sci. Geomech. Abstr. 28 (4), 247–260.
Willson, S.M., Fredrich, J.T., 2005. Geomechanics considerations for through- and near-salt well design. SPE-95621.
Willson, S.M., Last, N.C., Zoback, M.D., Moos, D., 1999. Drilling in South America: a wellbore stability approach for complex geologic conditions. Paper SPE 53940 presented at Latin America and Caribbean Petroleum Engineering Conference Held in Caracas, Venezuela.
Willson, S.M., Fossum, A.F., Fredrich, J.T., 2003. Assessment of salt loading on well casings. SPE Drill. Complet. 18, 13–21.
Willson, S.M., Edwards, S.T., Crook, A., Bere, A., Moos, D., Peska, P., 2007. Assuring stability in extended-reach wells – analyses, practice, and mitigations. SPE/IADC-105405.
Wiprut, D.J., Zoback, M.D., 1998. High horizontal stress in the Visund field, Norwegian North Sea: Consequences for Borehole Stability and Sand Production. SPE/ISRM-47244.
Woodland, D.C., 1990. Borehole instability in the Western Canadian overthrust belt. SPE Drill. Eng. 5, 23–33.
Zhang, J., Lang, J., Standifird, W., 2009. Stress, porosity, and failure dependent compressional and shear velocity ratio and its application to wellbore stability. J. Pet. Sci. Eng. 69, 193–202.
Zhang, J., 2002. Dual-Porosity Approach to Wellbore Stability in Naturally Fractured Reservoirs. PhD dissertation. Univ. of Oklahoma.

Zhang, J., 2013. Borehole stability analysis accounting for anisotropies in drilling to weak bedding planes. Int. J. Rock Mech. Min. Sci. 60, 160–170.
Zhang, J., Roegiers, J.-C., 2000. Horizontal borehole stability for naturally fractured reservoir. SPE-65513.
Zhang, J., Roegiers, J.-C., 2005. Double porosity finite element method for borehole modeling. Rock Mech. Rock Eng. 38 (3), 217–242.
Zhang, J., Bai, M., Roegiers, J.C., 2003. Dual-porosity poroelastic analyses of wellbore stability. Int. J. Rock Mech. Min. Sci. 40, 473–483.
Zhang, J., Bai, M., Roegiers, J.C., 2006. On drilling directions for optimizing horizontal well stability using dual-porosity poroelastic approach. J. Pet. Sci. Eng. 53, 61–76.
Zhang, J., Standifird, W., Lenamond, C., 2008. Casing ultradeep, ultralong salt sections in deep water: a case study for failure diagnosis and risk mitigation in record-depth well. SPE-114273.
Zhang, J., Rojas, J., Clark, D., 2008. Stressed-shale drilling strategy – water-activity. SPE Drill. Complet. 385–393. SPE-102498.
Zheng, Z., Kemeny, J., Cook, N.G.W., 1989. Analysis of borehole breakouts. JGR 94 (B6), 7171–7182.
Zoback, M.D., Moos, D., Mastin, L., 1985. Well bore breakouts and in situ stress. J. Geophys. Res. 90 (B7), 5523–5530.

CHAPTER 11

Geomechanics applications in hydraulic fracturing

Contents

Abstract

The impact of in situ stresses on hydraulic fracturing is investigated to enhance stimulation performance. The lithology-dependent stresses indicate that a shale formation has a higher minimum horizontal stress and acts as a barrier of hydraulic fracture propagation when hydraulic fracturing is performed in adjacent sandstones. However, when hydraulic fracturing is performed in a shale oil or gas formation, a stress barrier may not exist on the top or the bottom of the shale reservoir, and this will cause the hydraulic fractures to potentially grow out of the reservoir zone. Effects of the maximum and minimum horizontal stresses, shear stresses, and depletion on the

Applied Petroleum Geomechanics
ISBN 978-0-12-814814-3
https://doi.org/10.1016/B978-0-12-814814-3.00011-3

fracture initiation, breakdown, propagation, and containment are investigated. Shear stresses cause hydraulic fractures kinking, and in some cases the hydraulic fractures can eventually curve to the maximum stress direction. However, the curved fractures may create frictions for the proppant transport which affect productivity adversely. It finds that depletion reduces the minimum and maximum horizontal stresses and consequently changes hydraulic fracture propagation behavior when a new well is drilled and stimulated near a production well. Fracture interference and stress shadow are also discussed.

Keywords: Depletion; Formation breakdown pressure; Fracture curving; Hydraulic fracture; In situ stress impact; Stress containment; Stress shadow.

Hydraulic fracturing is the most important stimulation technology and has been used for several decades to enable operators to produce from tight and extremely low-permeable reservoirs. In the 1940s, Floyd Farris of Stanolind Oil proposed that fracturing a rock formation through hydraulic pressure might increase well productivity. This was followed in 1947 by the first application of the "Hydrafrac" process at the No. 1 Klepper well in the Hugoton Field, Kansas (Morton, 2013). Hubbert and Willis (1957) revealed that geomechanics played an important role in hydraulic fracturing. Through laboratory experiments on fracturing of solid blocks, they found that in situ stresses control hydraulic fracture initiation and propagation: the minimum stress depends primarily on where the fracture is initiated, and the maximum stress dominates which direction the fracture propagates to. Since then geomechanics has found more applications in hydraulic fracturing, such as hydraulic fracture design and operations, directions of horizontal well and perforations, fracture initiation, fracture propagation, fracturability and sweet spot, fracturing modeling, hydraulic fracture closure and proppant embedment, depletion effect, well and stage spacings, fracture hits, and fracture interferences. Some of these topics will be investigated in the following sections.

11.1 Fracture initiation and formation breakdown pressures

11.1.1 Fracture initiation pressure

To initiate a hydraulic fracture in a rock formation, high pressure fluid needs to be injected to the wellbore to break the rock and create tensile fractures. Haimson and Fairhurst (1967) assumed that the wellbore fracture

initiation occurs when the tangential stress reaches the tensile strength of the rock. They derived an equation to calculate the hydraulic fracture initiation pressure in a vertical well for a nonpenetrating injection fluid. The fracture initiation pressure as described in Eq. (9.10) can be restated in the following:

$$p_i = 3\sigma_h - \sigma_H - p_p + T_0 \tag{11.1}$$

where p_i is the fracture initiation pressure; T_0 is the tensile strength of the rock; σ_h and σ_H are the minimum and maximum horizontal stresses, respectively.

Haimson and Fairhurst (1967) stated that this fracture initiation pressure (Eq. 11.1) may predict the formation breakdown pressure. However, it may not work well in some cases. Some laboratory hydraulic fracturing experiments indicate that the breakdown pressure predicted from Eq. (11.1) is smaller than the one obtained from laboratory test results (e.g., Zoback et al., 1977; Guo et al., 1993; Morita et al., 1996). For example, more than 40 large rock samples ($76.2 \times 76.2 \times 76.2\ \text{cm}^3$) were hydraulically fractured to test the fracture initiation and propagation around a borehole (Morita et al., 1996). Their results showed that the borehole breakdown pressure was not only controlled by in situ stresses but also dependent on Young's modulus of the formation, wellbore size, and type of drilling fluids. The measured borehole breakdown pressures were higher than the magnitudes predicted from Eq. (11.1). The test results of Morita et al. (1996) also showed that the calculated tensile strength from Eq. (11.1) using measured breakdown pressure was higher than the measured rock tensile strength. This could be caused by using the fracture initiation pressure (Eq. 11.1) as the formation breakdown pressure.

11.1.2 Formation breakdown pressure

Formation breakdown pressure, closely related to in situ stresses, is a very important parameter for hydraulic fracturing planning and operations. However, to date, the industry still faces challenges to predict formation breakdown pressure with reasonable accuracy. Actually, Eq. (11.1) may not be the breakdown pressure because when a rock experiences a certain tensile failure, some tensile fractures will be generated, but this may not be the case when the rock is completely broken down. In a typical extended leak-off test, when the pump pressure starts to depart from the linearity, tensile fractures are initiated and the pump injection pressure is the fracture

initiation pressure (p_i). After the fracture initiation, additional injection is still needed to reach the breakdown pressure (p_b) to break the formation completely, except for very brittle rocks. For example, an extended leak-off test shows additional 0.3 bbls fluid needs to be injected after the fracture initiation to reach the formation breakdown (Zhang and Yin, 2017 and Fig. 9.2A in Chapter 9). This 0.3 bbls of injection fluid will cause a two-wing fracture (e.g., with an aperture of 0.2 in. and height of 12 in.) to extend ~37.8 ft away from the wellbore into the formation. In this case, Kirsch's borehole solution is no longer valid; therefore, the breakdown pressure should not be calculated from Kirsch's equation, except for a very brittle rock in which the fracture initiation and breakdown occur almost simultaneously.

Fig. 11.1 can be used to schematically represent fracture tensile failure process from fracture initiation to breakdown in a vertical well (Zhang et al., 2018a). The fracture initiation area in one side of the wellbore can be treated as a crack (i.e., initiation fracture), and the crack tip will experience tensile failure as the injection pressure reaches the breakdown pressure, causing the formation to be broken down. From fracture mechanics, the principal tensile stress in the vicinity of the tip in a Mode I crack (point A in Fig. 11.2) can be approximately obtained from Eq. (4.13), but here with a compression loading condition:

$$\sigma_{ts} = (\sigma_N - p_b)\sqrt{\frac{a}{2r}}\cos\frac{\beta}{2}\left(1 - \left|\sin\frac{\beta}{2}\right|\right) \tag{11.2}$$

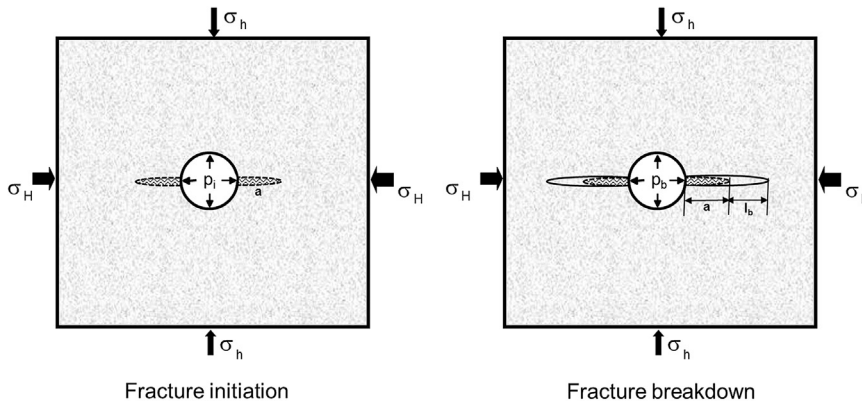

Figure 11.1 Schematic representation of a vertical borehole from the fracture initiation to breakdown.

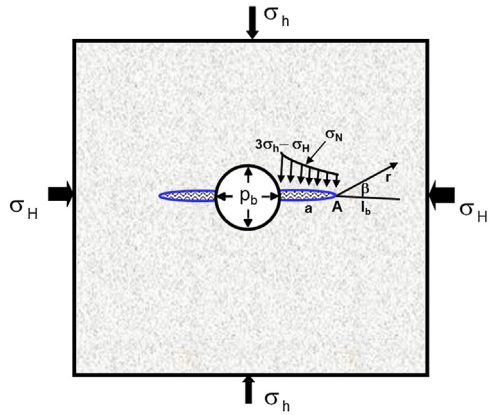

Figure 11.2 A simplified fracture mechanics model used for deriving the breakdown pressure.

where σ_{ts} is the tensile principal stress in the vicinity of the crack tip; σ_N is the far field stress applied on the fracture; p_b is the breakdown pressure; a is the crack length; r is the distance from the crack tip; β is an angle as shown in Fig. 11.2.

A tensile failure zone will be formed at the crack tip when formation breakdown pressure is reached. In this case, the minimum effective principal stress at the tip should be equal to or greater than the tensile strength (T_0). Notice that the compressive stress is positive; therefore, the following equation exists:

$$\sigma'_{ts} = \left(\sigma'_N - p'_b\right)\sqrt{\frac{a}{2r}}\cos\frac{\beta}{2}\left(1 - \left|\sin\frac{\beta}{2}\right|\right) = -T_0 \tag{11.3}$$

For simplification, assume that the fracture propagates in σ_H direction and only consider the case of $\beta = 0$. Substituting $\beta = 0$ to Eq. (11.3) and assuming that the length of the tensile failure zone in σ_H direction is $r = l_b$, the formation breakdown pressure can be obtained in the following form:

$$p_b = \sigma'_N + \alpha p_p + T_0\sqrt{\frac{2l_b}{a}} \tag{11.4}$$

The stress (σ_N), perpendicular to the initiation fracture in Fig. 11.2, is difficult to be determined analytically. However, it can be approximately obtained from Kirsch's equation (e.g., Zhang, 2013), i.e.,

$$\sigma'_N(x) = \frac{\sigma_H + \sigma_h - 2\alpha p_p}{2}\left(1 + \frac{R^2}{x^2}\right) - \frac{\sigma_H - \sigma_h}{2}\left(1 + \frac{3R^4}{x^4}\right) \tag{11.5}$$

where R is the wellbore radius; x is the length in the maximum stress direction, starting from the wellbore center and $x = R + a$ (refer to Fig. 11.2).

When the fracture initiation length (a) is very small (i.e., $x \approx R$), σ'_N reaches the maximum value; therefore, from Eq. (11.5) the following equation can be obtained:

$$\sigma'_{N\max} = 3\sigma_h - \sigma_H - 2\alpha p_p \tag{11.6}$$

Substituting Eq. (11.6) to Eq. (11.4) and assuming $\alpha = 1$, the maximum breakdown pressure ($p_{b\max}$) can be obtained:

$$p_{b\max} = 3\sigma_h - \sigma_H - p_p + kT_0 \tag{11.7}$$

where $k = \sqrt{\frac{2l_b}{a}}$. If assume $l_b = a$, then $k = \sqrt{2}$; therefore:

$$p_{b\max} = 3\sigma_h - \sigma_H - p_p + \sqrt{2}T_0 \tag{11.8}$$

This can also be used as the breakdown pressure for a vertical perforation in a horizontal well if the effect of horizontal borehole stress concentration on the perforation is small. Comparing Eq. (11.8) to Eq. (11.1), this new equation predicts a higher breakdown pressure value than the conventional method, and the predicted tensile strength from Eq. (11.8) is $1/\sqrt{2}$ times of that calculated from the old method, Eq. (11.1). It can be seen from Eq. (11.7) that if the formation has a higher minimum stress, it has a much higher breakdown pressure or the formation is difficult to be fractured.

For a horizontal well drilled in the minimum horizontal stress direction, the maximum breakdown pressure in the borehole (p_{bH}) can be derived in the following forms (similar to Eq. 11.7):

$$p_{bH} = 3\sigma_H - \sigma_V - p_p + kT_0, \quad \text{if} \quad \sigma_V > \sigma_H \tag{11.9}$$

$$p_{bH} = 3\sigma_V - \sigma_H - p_p + kT_0, \quad \text{if} \quad \sigma_V \le \sigma_H \tag{11.10}$$

It should be noted that simplifications are used for the derivation of the above equations; therefore, for field applications the diagnostic fracture injection tests (DFIT) or other tests (e.g., XLOT) are suggested to use for calibrating and determining k value. If the fracture initiation and breakdown occurs simultaneously, then, $k = 1$; otherwise $k > 1$. The default value is $k = \sqrt{2}$.

11.1.3 Fracture propagation pressure

After the formation breakdown, the internal fluid pressure of the fracture must be large enough to overcome the magnitude of the minimum compressive stress and to increase the driving stress of the initial fracture to generate tensile stress to the point where it begins to propagate (as shown in Fig. 11.3). This pressure is the fracture propagation pressure. Hubbert and Willis (1957) proposed that injection pressure needs to be equal to or greater than the minimum stress to hold open and extend a fracture, i.e., $p_{\min} = \sigma_h$. In this equation, rock tensile strength is neglected.

From Eq. (11.4), when the fracture initiation length (a) is quite large, σ_N reaches the minimum stress, i.e., $\sigma_N = \sigma_h$. This is the case that the fracture is far away from the wellbore, and wellbore stresses have little impact on the fracture tip. In this case, the pressure to break the rock should be the fracture propagation pressure ($p_{b\min}$), which can be obtained from Eq. (11.4) by substituting $\sigma'_N = \sigma_h - \alpha p_p$, i.e.,

$$p_{b\min} = \sigma_h + kT_0 \tag{11.11}$$

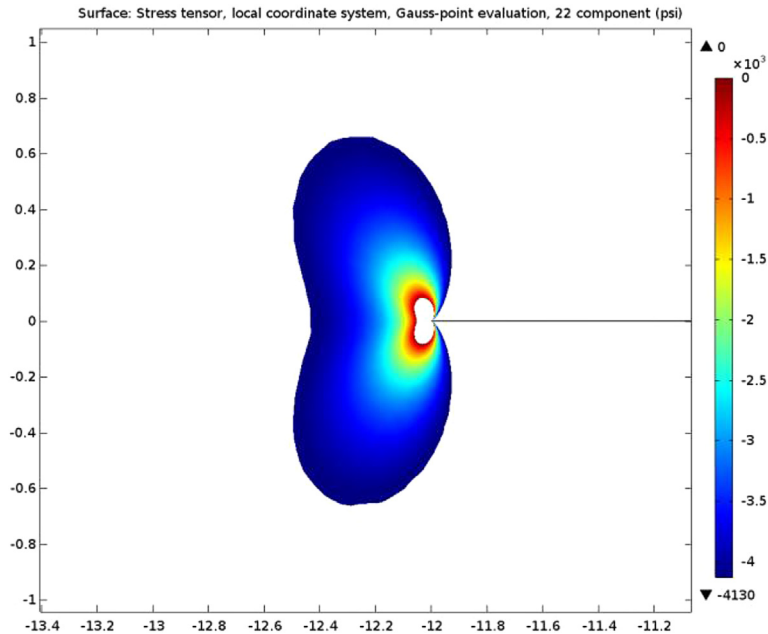

Figure 11.3 The FEM modeled fracture propagation after a hydraulic fracture is generated. The white area at the fracture tip is the zone of tensile stress in y-direction (σ_y) induced by injection pressure. The stress is in psi.

Eq. (11.11) indicates that the fluid pressure needs to overcome both the minimum stress and the tensile strength for fracture propagation.

For a fracture with a length of 2a, Broek (1986) proposed a similar equation to calculate fracture propagation pressure (p_g) for Mode I fracture:

$$p_g = \sigma_h + \frac{K_{IC}}{\sqrt{\pi a}} \tag{11.12}$$

where K_{IC} is the toughness of Mode I fracture.

11.2 In situ stresses controlling fracture propagation

11.2.1 In situ stress regimes and hydraulic fracture propagation

Hydraulic fracture propagation is highly dependent on the in situ stress state. Hydraulically induced fractures should be formed approximately perpendicular to the minimum stress direction (Hubbert and Willis, 1957). Therefore, in tectonically relaxed areas (the normal and strike-slip faulting stress regimes), hydraulic fractures should be vertical and propagate in the vertical and the maximum horizontal stress directions, as shown in Fig.11.4A. However, in tectonically compressed areas (reverse faulting stress regime) hydraulic fractures should be horizontal and propagate in two horizontal stress directions, as shown in Fig.11.4B. Downhole ultrasonic borehole image log after hydraulic fracturing test and observation of the hydraulic fracture after mining back in the URL, France, show the vertical hydraulic fracture propagating in the maximum horizontal stress direction (Fig. 11.5). Other hydraulic fracture mined back results have come to the same conclusion (e.g., Warpinski et al., 1982).

Hydraulic fracture propagation is also controlled by the direction of the minimum horizontal stress and horizontal well orientation (Abass et al.,

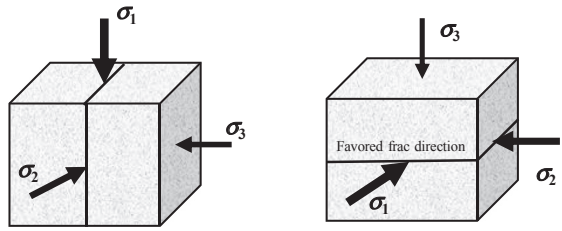

Figure 11.4 Vertical hydraulic fracture created in normal or strike-slip faulting stress regime (left) and horizontal fracture generated in reverse faulting stress regime (right). In situ stresses $\sigma_1 > \sigma_2 > \sigma_3$.

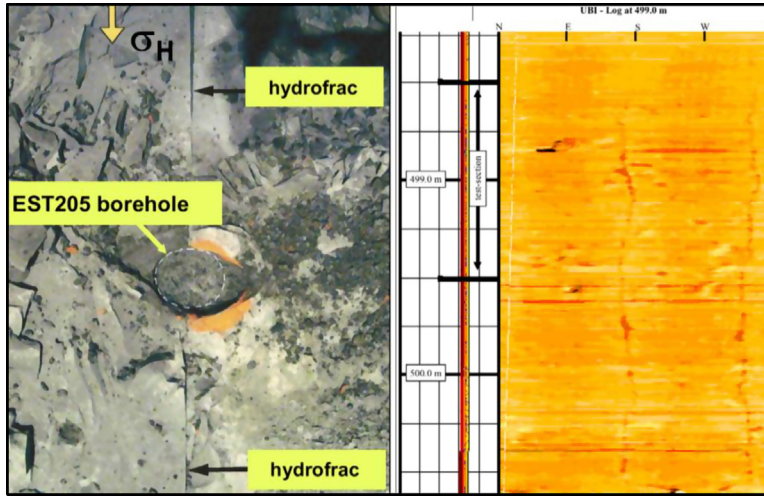

Figure 11.5 Top-view of the vertical hydraulic fracture at depth of 499 m after excavating the fractures (left) and ultrasonic borehole image after hydraulic fracturing test at depth of 499 m (right) in the URL, France (Wileveau et al., 2007).

1992). Fig. 11.6 shows the hydraulic fracture propagation directions versus drilling directions in normal and strike-slip stress faulting regimes. If a horizontal well is drilled in the minimum horizontal stress direction, hydraulic fractures may be optimal for contacting more reservoir rocks. If a horizontal well is not drilled in one of the principal stress directions, then shear stresses will be generated in the wellbore and in the perforation tunnels, causing hydraulic fractures kinking. Therefore, fully understanding

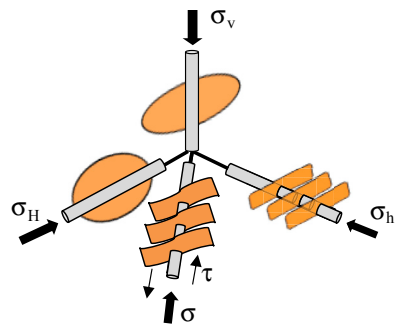

Figure 11.6 Propagation directions of hydraulic fractures versus drilling directions in normal and strike-slip faulting stress regimes.

in situ stresses and stress regimes can help to optimize horizontal well drilling and completion.

11.2.2 Stress barrier and hydraulic fracture containment

Hydraulic fractures are most likely to be contained within a reservoir if the reservoir formation has a markedly smaller minimum horizontal stress than those in its upper and lower formations (Simonson et al., 1978; Fung et al., 1987). When a stress contrast is present in the formations, hydraulic fractures are mostly developed in a formation with a smaller minimum stress; the reason is that the formation with a higher minimum stress has a much higher breakdown pressure (as indicated in Eq. 11.7) and can act as a stress barrier to block hydraulic fractures for developing, as shown in Figs. 11.7 and 11.8. This is the case normally for a sandstone reservoir interbedded within two shale formations (Fig. 11.9A). However, in the unconventional play, a shale reservoir normally has a higher minimum horizontal stress and does not have obvious stress barriers in the overburden and underburden formations (Zhang and Zhang, 2017). This will cause hydraulic fractures to develop out of the reservoir zone and create much taller fractures than the planned, as shown in Fig. 11.9B.

It has become widely accepted that the stress contrast between the reservoir and its bounding layers is the most important factor for determining facture height growth (Warpinski and Teufel, 1987). The variation of the minimum in situ stress is the predominant factor controlling fracture growth, and the hydraulic fractures terminate at the layer with a high minimum stress (Warpinski et al., 1982). The following example illustrates

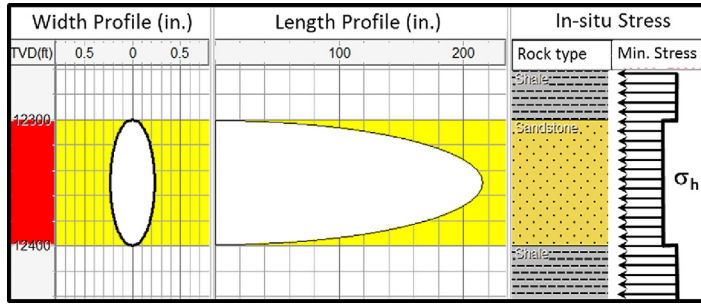

Figure 11.7 The minimum horizontal stress barriers (higher σ_h) on the top and bottom formations of the reservoir containing the hydraulic fractures within the lower minimum stress zone (the reservoir). The hydraulic fracture profiles were modeled by FracPro software.

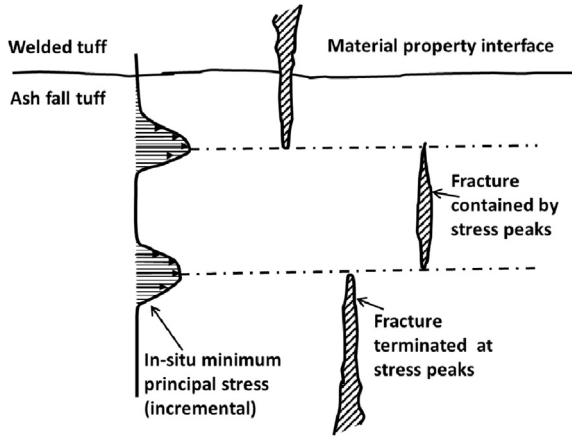

Figure 11.8 Schematic plot of the minimum stress profile and the hydraulic fracture propagation from in situ mined back observations. *(Modified from Warpinski, N.R., Schmidt, R.A., Northrop, D.A. 1982. In situ stresses: the predominant influence on hydraulic fracture containment. J. Petrol. Technol. 34, 653–664.)*

that the shale gas reservoir has a higher minimum stress than those in its overburden formations, and hydraulic fractures develop beyond the reservoir zone.

Based on well logging data (MSEEL, 2015) in the Marcellus shale play in West Virginia, Fig. 11.10 displays Poisson's ratio calculated from compressional and shear sonic logs, the minimum horizontal stress calculated from Poisson's ratio, and static Young's modulus calculated from well

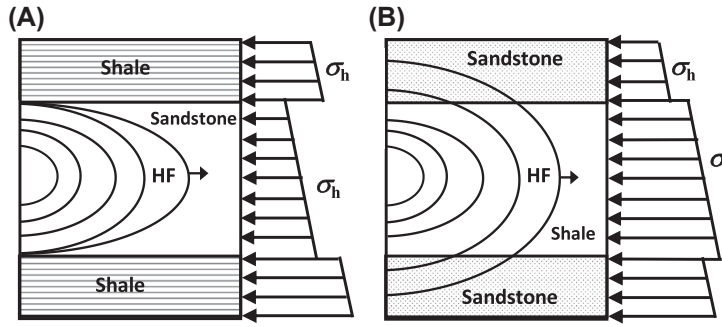

Figure 11.9 Schematic diagram of hydraulic fracture propagations related to the minimum horizontal stress profiles. (A) hydraulic fracture (HF) propagation in a sandstone interbedded with shales; (B) hydraulic fracture propagation in a shale interbedded with sandstones.

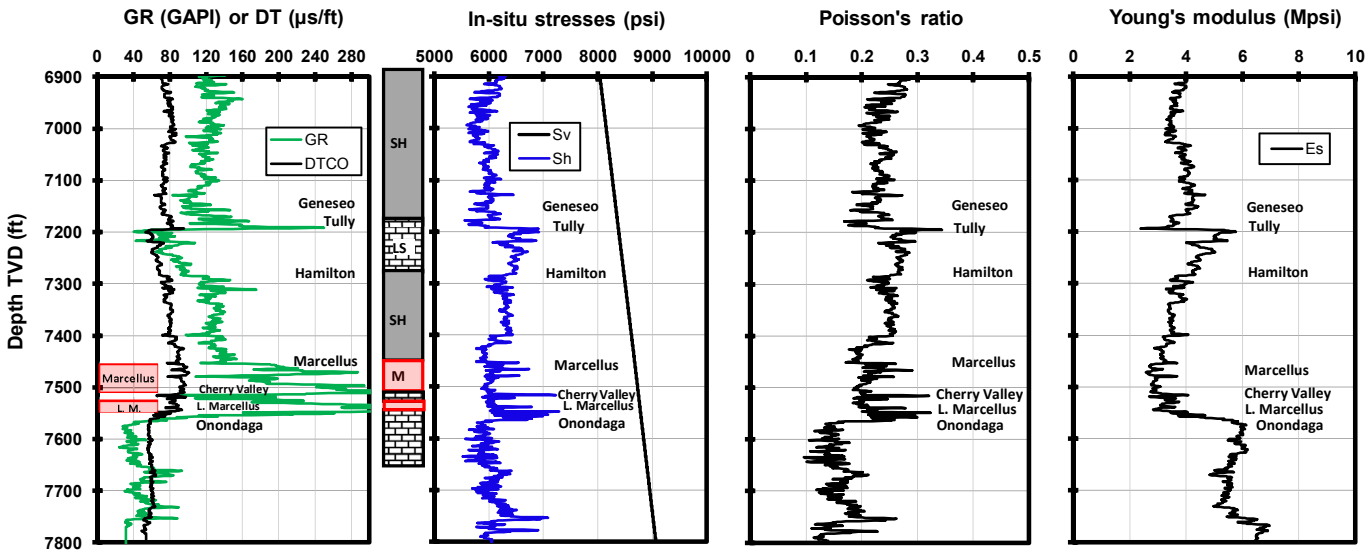

Figure 11.10 The minimum horizontal stress and rock properties calculated from well log data in well MIP-3H of the MSEEL site. The first track plots gamma ray (GR) and sonic compressional transit time (DTCO); the second track displays the minimum horizontal stress (Sh) and overburden stress (Sv); the third track shows Poisson's ratio calculated from sonic logs; the fourth track plots the static Young's modulus calculated from well log data. The annotations in each plot are the formation tops. In the geologic column, SH, LS, M, and L.M. represent shale, limestone, Upper Marcellus and Lower Marcellus, respectively.

log data. From the direct overburden formation to the Hamilton shale, the minimum horizontal stress is lower than that in the Marcellus reservoir. This means that the overburden shales (before reaching the Tully limestone) are lack of the stress barrier, because they have low minimum horizontal stresses. Therefore, when fracturing the Marcellus reservoir, most hydraulic fractures will propagate out of the reservoir zone to the Hamilton shale. Notice that although the Tully limestone has a very high Young's modulus, it can still act as a hydraulic fracture barrier because it has a higher minimum stress. However, below the Lower Marcellus reservoir, there is a thin formation with much higher minimum horizontal stress, which acts as a stress barrier to partially block hydraulic fractures propagating to the low minimum stress formation (i.e., the Onondaga limestone).

Microseismic monitoring was conducted in a horizontal well, in which geology and rock properties are similar to the well shown in Fig. 11.10, in the Marcellus reservoir in central Pennsylvania. The results indicate that hydraulic fractures extend a long distance above the treatment well (Fig. 11.11). That is, the hydraulic fractures propagate upward into the Hamilton shale formation and terminate at the Tully limestone (high minimum stress formation). Some hydraulic fractures also propagate downward into the limestone formation in the underburden.

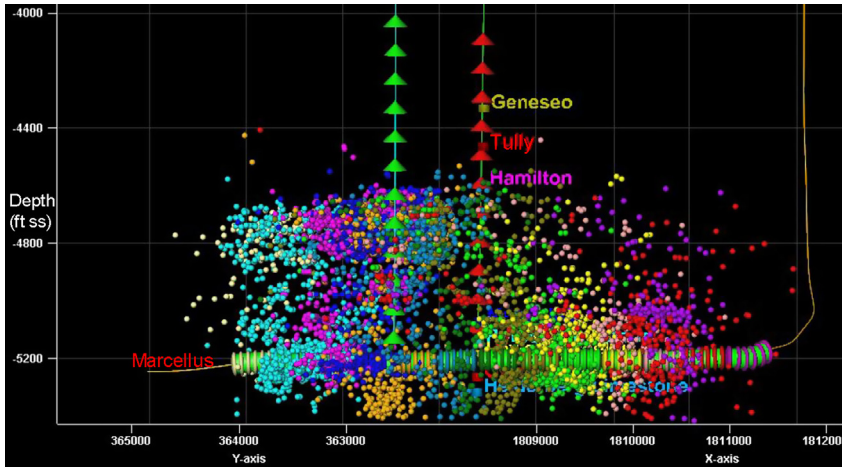

Figure 11.11 Vertical distribution of microseismic events located during hydraulic fracturing of a horizontal shale gas well in the Marcellus at the Clearfield County Site in central Pennsylvania (Hakala and Guthrie, 2013).

11.2.3 Rock properties and heterogeneities on hydraulic fracture propagation

It should be noted that the stress barrier is not the only condition to terminate hydraulic fracture propagation. Other factors also affect the height growth (Bunger and Lecampion, 2017). The hydraulic fracture mined back results show that a small rock property difference (e.g., Young's modulus) in the formations cross the interface is incapable of containing hydraulic fractures (see Fig. 11.8). However, a large rock property difference cross the interface may contain hydraulic fractures. For example, a very tight rock formation with a high tensile strength could stop the fracture development because it is difficult for hydraulic fractures to be generated or propagated (e.g., a very tight limestone formation underlying or overlying the reservoir) because hydraulic fracture propagation is also dependent on formation breakdown and propagation pressures. If formation breakdown and propagation pressures are higher, fracture propagations become more difficult. Certainly, formation breakdown and propagation pressures are controlled by in situ stress magnitudes and stress regimes. Therefore, in-situ stress magnitudes and regimes also control the fracture propagation. Observations of hydraulic fractures from in situ mined back in coal seams indicate that hydraulic fractures arrested at relatively stiff/strong roof and floor layers, branched a horizontal component along the contact between the coal seam and a relatively strong roof rock (Diamond and Oyler, 1987).

Coring was conducted in some horizontal monitor wells in the Eagle Ford shale play after hydraulic fracturing (Raterman et al., 2017). The coring results show that hydraulic fracture branching occurred in bedding surfaces, which was probably caused by the mechanical property difference in different rocks or interfaces. It was also observed both in cores and image logs that multiple, usually two or three, hydraulic fractures often developed in close association (Fig. 11.12). The common occurrence of these doublets and triplets along the length of the well indicates that hydraulic fracture branching might be widespread. Branching along with the observed influence of bedding surfaces on hydraulic fracture propagation leads to the postulation that the mechanical stratigraphy resulting from interbedded organic marl and stiffer limey beds is in part responsible for much of the observed fracture complexity and the large number of fractures encountered. Other natural heterogeneities in the formation may also impact fracture complexity.

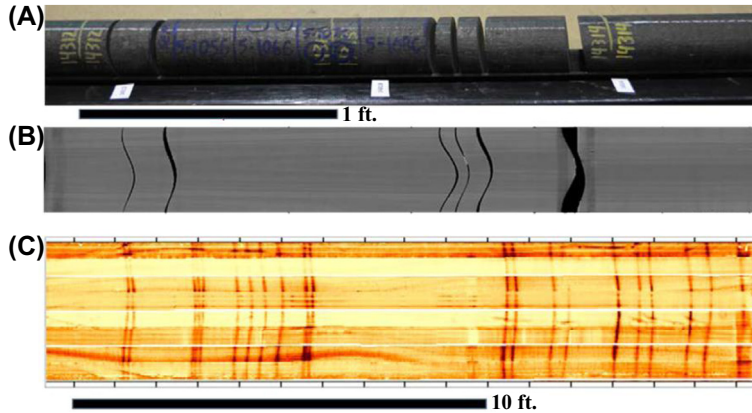

Figure 11.12 Cores with hydraulic fractures cored in the horizontal monitor well S3 in the Eagle Ford shale. (A) dipping hydraulic fractures in cores. (B) CT image as an unwrapped circumferential image in the same section of (A). (C) 18 ft section of FMI-HD image log containing several fracture doublets and triplets showing up as dark sinusoids across image. *(From Raterman et al., 2018.)*

From coring observations, the distribution of hydraulic fractures along the wellbores was nonuniform (Raterman et al., 2017). In the post-stimulation cores, the hydraulic fractures formed swarms, in which many fractures were spaced a few inches apart and were separated by lengths of core with several feet between fractures (Fig. 11.12). The number of hydraulic fractures interpreted in the image logs far exceeds one per perforation cluster. This might be caused by natural heterogeneities in the formation, which induced fracture complexity.

From the coring results the hydraulic fracture strike was consistent with the maximum horizontal stress direction. However, the hydraulic fractures were dipping 75–80° SE, i.e., the fractures were not true vertical fractures as anticipated from geomechanical theory. Therefore, either these fractures were not pure opening mode but hybrid (with shear stresses) or the in situ principal stresses were rotated away from vertical and horizontal directions.

11.2.4 Stress difference and hydraulic fracture propagation

The difference of two horizontal stresses is an important factor to affect hydraulic fracture propagation. The general rule is that the formation with large horizontal stress difference creates longer and more planar hydraulic fractures, e.g., in the Middle Bakken reservoir, the minimum horizontal stress gradient is 0.786 psi/ft and the difference of two horizontal stress gradients is more than 0.15 psi/ft before depletion (Dohmen et al., 2017).

However, the formation with small horizontal stress difference generates shorter and more complex hydraulic fractures. For example, the Barnett shale formation displays different in situ stresses in different regions. Generally, the horizontal stress difference is small, but it varies even in a single horizontal well. This heterogeneous nature makes standardization of the completion process problematic (Daniels et al., 2007). Fig. 11.13 displays microseismic events observed during the hydraulic fracturing of a horizontal Barnett shale gas well (Well #2) located within the Fort Worth basin. In Stage 1 and Stage 2, the horizontal stress difference is relatively larger ($\sigma_H - \sigma_h = 0.07$ psi/ft and $\sigma_H - \sigma_h = 0.1$ psi/ft) than these in stage 3 ($\sigma_H - \sigma_h = 0.04$ psi/ft) and stage 4 ($\sigma_H - \sigma_h = 0.03$ psi/ft). From microseismic measurements in Fig. 11.13, directional and planar hydraulic fractures are generated in Stage 1 and Stage 2. However, irregular and complex fractures are created in Stage 3 and Stage 4 because they have smaller stress differences than those in Stage 1 and Stage 2.

The following analysis can illustrate the effect of stress difference on hydraulic fracture propagation. When a hydraulic fracture is initiated, any imperfection (e.g., heterogeneity, natural fracture) or shear stress in the

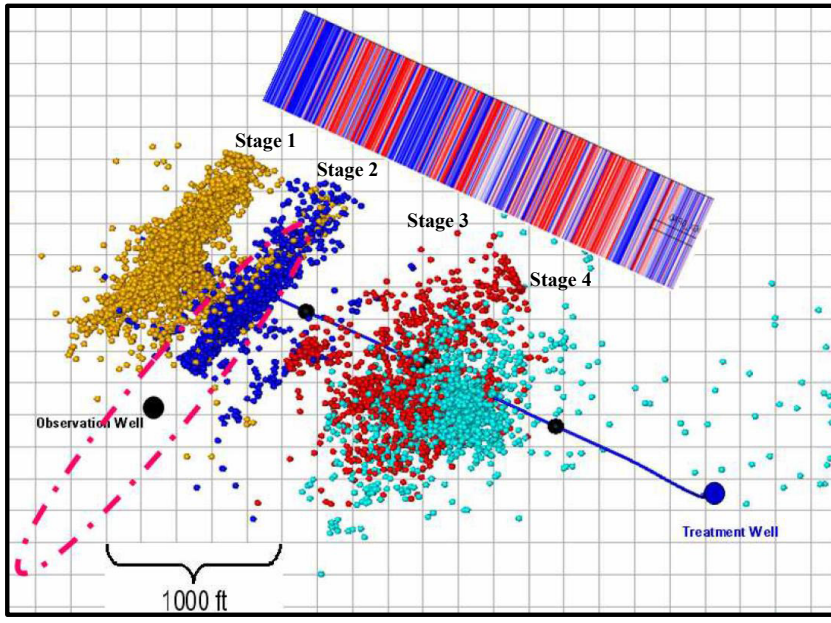

Figure 11.13 An overhead view of Well #2 with the microseismic events shown. The large black dots separate the sections of the bridge plugs set between each fracturing stage (Daniels et al., 2007).

formation may cause the fracture propagating path to deviate from its initial direction. The tendency whether or not for straight propagation can be quantified by the ratio R for Mode I fracture (Cruikshank et al., 1991), which is related to stress difference $(\sigma_H - \sigma_h)$ and net pressure $(p_t - \sigma_h)$:

$$R = \frac{\sigma_H - \sigma_h}{p_t - \sigma_h} \tag{11.13}$$

where p_t is the internal pressure of the fracture or the treatment pressure for hydraulic fracturing operations.

For an isolated fracture with a length of 2a, the magnitude of p_t at propagation must satisfy Eq. (11.12), i.e., $p_t \geq \sigma_h + K_{IC}/(\pi a)^{1/2}$. Inserting Eq. (11.12) to Eq. (11.13), the ratio R can be expressed in the following equation (Renshaw and Pollard, 1994):

$$R = \frac{\sigma_H - \sigma_h}{K_{Ic}/\sqrt{\pi a}} \tag{11.14}$$

If inserting Eq. (11.11) to Eq. (11.13), the ratio R can be rewritten in the following form:

$$R = \frac{\sigma_H - \sigma_h}{kT_0} \tag{11.15}$$

When R or horizontal stress difference $(\sigma_H - \sigma_h)$ is small, or rock tensile strength is high, hydraulic fracture will curve to adjacent natural fractures and form complex fractures. Otherwise, planar (straight) hydraulic fracture will be created. Renshaw and Pollard (1994) concluded that some fractures have roughly planar geometries due to the occurrence of large differential stresses, which limit the development of fracture curvature. Otherwise, fractures that develop under relatively small differential stresses may be quite curvaceous, as shown in Fig. 11.14. Therefore, parameter R can be used to identify how hydraulic fractures propagate: straight (planar) or curved (complex).

11.3 Impact of shear stresses on fracture propagations

11.3.1 Shear stress and fracture kinking

If a wellbore (perforation tunnel) is not parallel (perpendicular) to the minimum stress direction (refer to Fig. 11.6), shear stresses will be induced in the wellbore or perforation tunnel (e.g., Zhang and Chen, 2010; Zhang et al., 2011; Waters and Weng, 2016; Zhu et al., 2015). The shear stresses

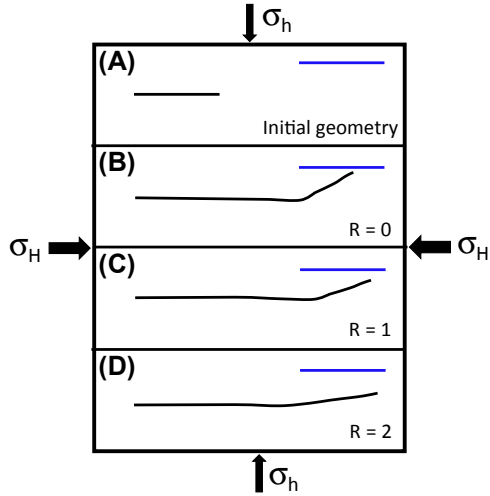

Figure 11.14 Schematic representation of the relationship of fracture paths and the stress ratio *R*. Two initial fractures were of equal length and arranged as shown in (A). Only the inner right fracture tip of the lower fracture was allowed to propagate in (B), (C), and (D). *(Modified from Renshaw Pollard, 1994.)*

tend to make the two fracture surfaces slide, causing propagating path of the hydraulic fracture to deviate from straight, as shown in Fig. 11.15. Whether a hydraulic fracture is straight propagating or curving is quantified by the shear and normal displacements in the fracture. Cruikshank et al. (1991) use a ratio R_s to define the hydraulic fracture kinking for Mode I fracture. The ratio of shear displacement (U) and normal displacement (W) or $R_s = U/W = \tau_{xy}/(p_t - \sigma_y)$ in the fracture controls the degree of the fracture

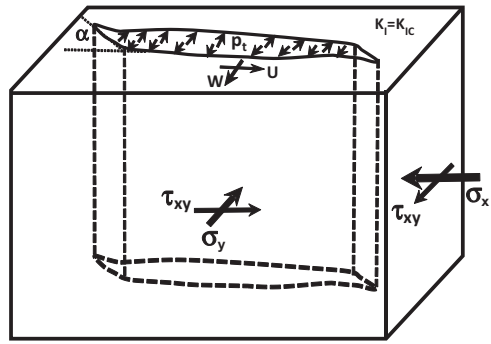

Figure 11.15 Schematic representation of a kinked fracture due to the internal pressure and far-field shear and normal stresses.

propagation direction. Based on Cottrell and Rice (1980), Cruikshank et al. (1991) proposed the following equation to calculate the kinking angle:

$$\frac{\tau_{xy}}{p_t - \sigma_y} = \frac{\sin(\alpha/2) + \sin(3\alpha/2)}{\cos(\alpha/2) + 3\cos(3\alpha/2)} \tag{11.16}$$

where α is the kinking angle from the original fracture (see Fig. 11.15); σ_y is the far-field normal stress in the direction perpendicular to the original fracture orientation and the compressive stress is positive; τ_{xy} is the far-field shear stress.

Based on Eq. (11.16), the relationship of the kinking angle and the fracture kinking stress ratio, $\tau_{xy}/(p_t - \sigma_y)$, is plotted in Fig. 11.16. It shows that the kinking angle increases as the shear stress increases. However, as the treatment pressure p_t increases (refer to Eq. 11.16), the kinking angle decreases. It implies that high treatment pressure can reduce hydraulic fracturing curving.

11.3.2 Shear stress and hydraulic fracture propagation

Assuming that a horizontal well is drilled with an angle (β) to the minimum horizontal stress direction and the perforation tunnel is perpendicular to the horizontal well axis, as shown in Fig. 11.17, the shear and normal stresses around the horizontal well can be obtained from the following equations:

$$\begin{aligned} \tau_{xy} &= \frac{1}{2}(\sigma_H - \sigma_h)\sin 2\beta \\ \sigma_y &= \sigma_H \cos^2\beta + \sigma_h \sin^2\beta \end{aligned} \tag{11.17}$$

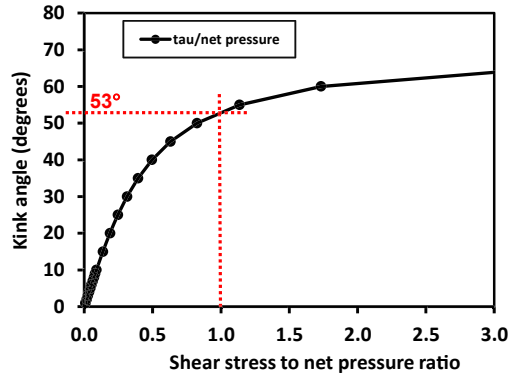

Figure 11.16 Fracture kinking angle versus the ratio of the shear stress to the net pressure, $\tau_{xy}/(p_t - \sigma_y)$.

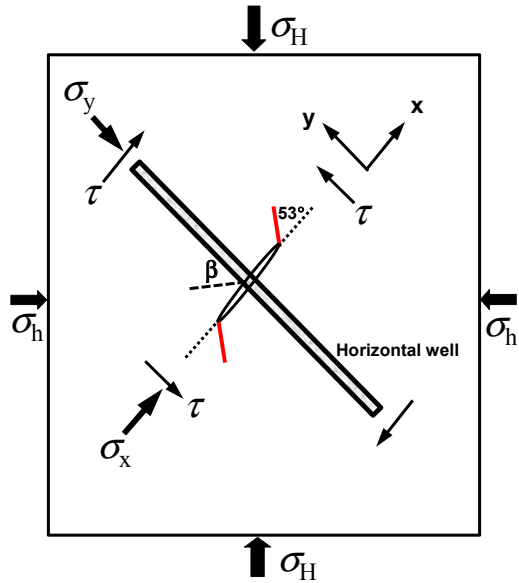

Figure 11.17 Hydraulic fracture kinking to the maximum horizontal stress direction. It shows the calculated kinking angle from Eq. (11.18) in a horizontal well drilled with an angle ($\beta = 45°$) to the minimum horizontal stress direction.

Inserting Eq. (11.17) to Eq. (11.16), the following equation can be obtained:

$$\frac{\tau_{xy}}{p_t - \sigma_y} = \frac{(\sigma_H - \sigma_h)\sin 2\,\beta}{2[p_t - (\sigma_H \cos^2\beta + \sigma_h \sin^2\beta)]} = \frac{\sin(\alpha/2) + \sin(3\alpha/2)}{\cos(\alpha/2) + 3\cos(3\alpha/2)} \tag{11.18}$$

Eq. (11.18) indicates that as the difference of in situ horizontal stresses decreases, the kinking angle decreases. If the two horizontal stresses are equal ($\sigma_h = \sigma_H$), then $\tau_{xy} = 0$, and there will be no kinking; this means that the hydraulic fractures will propagate along the perforation direction. If the two horizontal stresses are not equal, the treatment pressure $p_t = \sigma_H$, and $\beta = 45°$, then,

$$\frac{\tau_{xy}}{p_t - \sigma_y} = \frac{(\sigma_H - \sigma_h)/2}{p_t - (\sigma_H + \sigma_h)/2} = 1$$

Substituting the above equation to Eq. (11.18) and solving it, the kinking angle from the parent fracture (i.e., the perforation) can be obtained (i.e., $\alpha = \sim 53°$), as shown in Fig. 11.17. This figure indicates that when a horizontal well is not drilled in the minimum horizontal stress direction, the induced shear stresses cause hydraulic fracture kinking, i.e.,

the fracture propagating path deviates from the perforation direction. This kinking makes the fracture curve to the maximum horizontal stress direction, as shown in Fig. 11.17. It implies that a horizontal well can be drilled with a certain angle to the minimum horizontal stress direction because this does not have much impact on the final direction of the hydraulic fracture propagation, if the difference of two horizontal stresses is not very small. However, these curved fractures may increase fracture tortuosity, causing frictions in proppant transport, which may affect productivity.

11.3.3 Off-azimuth and on-azimuth horizontal wells

Noncontiguous acreage positions commonly lead to drilling azimuths parallel to section boundaries. Analysis of well performance with drilling azimuth across plays in North America reveals that on-azimuth wells (parallel to the minimum horizontal stress direction) are typically better than off-azimuth wells (with certain angle to the minimum horizontal stress direction). A microseismic trial was conducted in two wells on the same pad (one was on-azimuth and the other was 45° off-azimuth) in the Duvernay shale oil play in Canada (Stephenson et al., 2018). Microseismic observation from the hydraulic fracture treatments in the two wells showed a large contrast in microseismic event density: the on-azimuth well had far fewer microseismic events, but its productivity was doubled. More microseismic events occurred in the off-azimuth well might be due to more shear fractures (kinked fractures) generated. There was a small difference in treatment fluid; the total injected volumes were equivalent in the two wells. Therefore, horizontal well azimuths control the mechanics and the productivity of the two wells.

Using the publicly available data in 475 wells in the Marcellus shale gas play in Pennsylvania and West Virginia, Zinn et al. (2011) calculated the normalized estimated ultimate recovery (EUR) against an estimated azimuth of horizontal well direction and the minimum horizontal stress direction. The result shows a definite correlation between drilling azimuth and productivity (Fig. 11.18). For each degree that the wellbore is oriented away from the minimum horizontal stress direction, the EUR is adversely affected by 7.25 MCF/ft, and 90 degree off-azimuth well is the worst case. In the Eagle Ford shale play, a similar conclusion was obtained, i.e., when the angle of the horizontal well direction and the minimum horizontal stress direction is greater than 30−40 degrees, well productivity drops off dramatically.

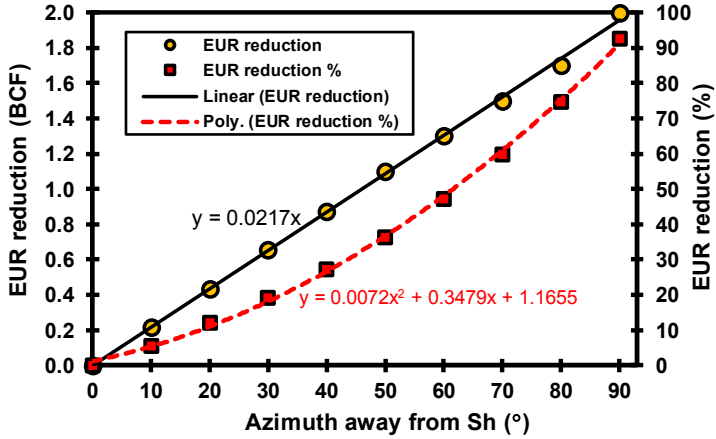

Figure 11.18 The EUR reduction amount and percentage caused by the wellbore azimuth oriented away from the minimum horizontal stress (S_h) direction. *(Plotted from the data presented by Zinn et al., 2011)*

Several hypotheses exist to explain the poorer well performance in the off-azimuth well:

(1) The perforation tunnels in the off-azimuth well are not parallel to the maximum horizontal stress direction, which introduces near wellbore shear stresses. The shear stresses generate more shear fractures and make hydraulic fractures curve to the maximum stress direction, as shown in Fig. 11.19A. These curved fractures cause hydraulic fracture

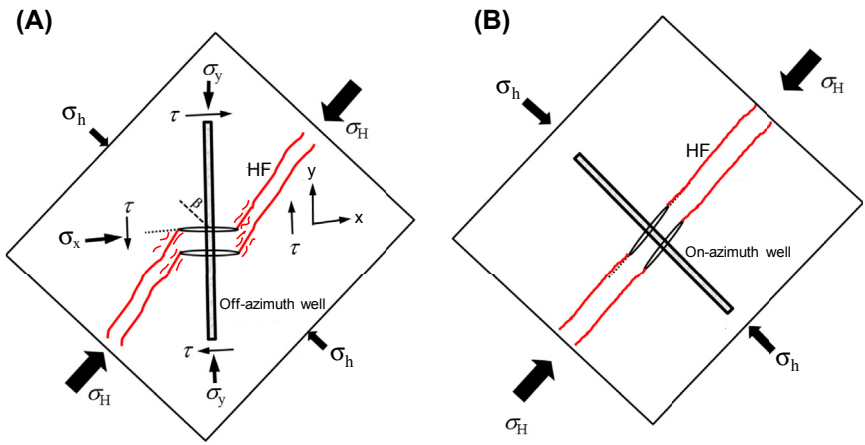

Figure 11.19 Schematic diagrams showing the effect of shear stresses on hydraulic fracture propagation. (A) in an off-azimuth well, shear stresses cause hydraulic fracture kinking and complexity, which increase the tortuosity. (B) in an on-azimuth well, simple hydraulic fractures are generated.

complexity and increase the tortuosity, introducing more friction for proppant transport than that in the on-azimuth well (Fig. 11.19B).

(2) Out-of-stage restimulation causes inefficient treatments and potential overflushing with a loss in near wellbore conductivity supported by generally lower breakdown pressures in off-azimuth well (Stephenson et al., 2018), and

(3) Pinching out of the planes of shear failures results in areas of stranded connectivity.

Therefore, understanding the minimum horizontal stress magnitude and direction is critically important for hydraulic fracturing planning and operations.

11.4 Impact of depletion on hydraulic fracturing propagation

Microseismic measurements during hydraulic fracture operations indicate that depletion reduces horizontal stresses and impacts hydraulic fracture propagation (Dohmen et al., 2013, 2014a). The DFIT measurements show that the minimum horizontal stress decreases as the reservoir pressure decreases. The reduction of the minimum horizontal stress causes both the breakdown and propagation pressures to decrease (Dohmen et al., 2017); therefore, new fractures are much easier to be generated in the depleted reservoir. Understanding the depletion surrounding a produced well is important for efficiently developing unconventional plays, particularly for optimizing infill well spacing, because more than 60% of the US land wells drilled in 2017 are infill wells (Vidma et al., 2018).

Microseismic measurements show that when an infill well is close to a production well, depletion effect on hydraulic fracturing in the infill well is pronounced. Fig. 11.20 displays an example of microseismic measurements recorded during hydraulic fracturing in one of the infill wells (H4), close to an existing production well (H1) in the Middle Bakken reservoir (Dohmen et al., 2017). It can be observed that the fracture trend defined by microseismic events in each stage is most likely parallel to the maximum horizontal stress direction (approximately N56°E, as shown in Fig. 11.20). However, from measured microseismic events in Fig. 11.20, it is evident that when depletion exists, the new fractures are highly influenced by the depletion of the produced well and grow asymmetrically toward the production well H1 (i.e., depletion area). Therefore, one-wing fractures are generated in the direction of the production well. This is due to that the

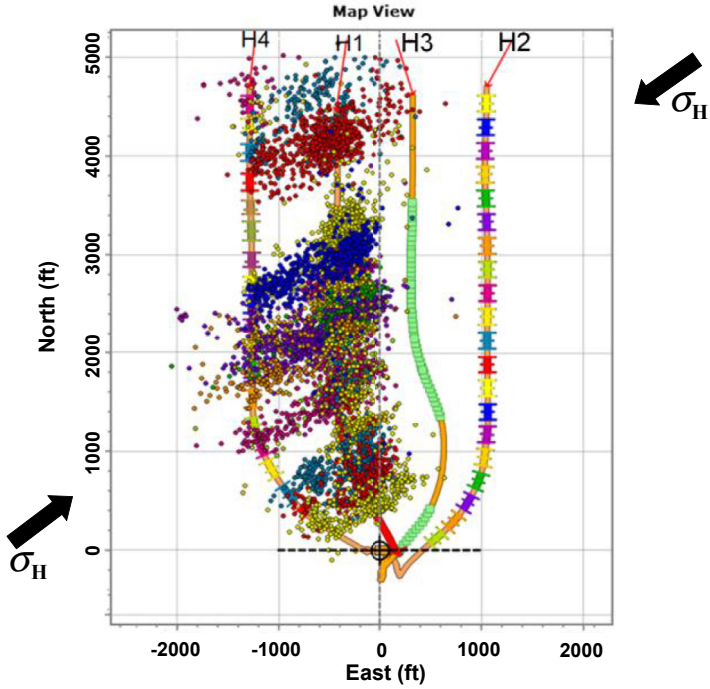

Figure 11.20 Microseismic measurements recorded during hydraulic fracturing of an offset well (H4). Hydraulic fractures grow asymmetrically toward the existing production well H1. The microseismic events are color-coded by stages (Dohmen et al., 2017).

depletion-induced minimum stress reduction cause the produced area to have a much smaller breakdown pressure and to be more prone to generate new hydraulic fractures. The depletion may also cause well interference and frac hits. After the three infill wells completion and production, the original production well H1 resumed production and then its production increased three times compared to the production before the well shut-in (Cipolla et al., 2018). This indicates that some hydraulic fractures in the infill wells might have propagated to the production well, as shown from microseismic measurements in Fig. 11.20.

Repressuring (preloads), refracturing the depleted reservoir, or using far-field diverters may improve hydraulic fracturing performance to create two-wing symmetrical fractures. Water injection to repressure a production well (preloads) can provide a significant, temporary increase in fracture pressure (and the minimum stress) in the depleted area, which can reduce frac hits. Production performance in the Eagle Ford field shows that oil production in average preload well has an improvement of 25% compared to the production before the infill well fracturing (Whitfield et al., 2018).

11.5 Stress shadow and fracture interference

11.5.1 Stress shadow and spacing of stages

Placing multiple hydraulic fractures in a horizontal well is a highly effective method to increase per well production. However, production performance is dependent not only on the hydraulic fracturing process but also on the spacing of the horizontal wells and the spacing of multiple hydraulic fracture stages. Industry experience in unconventional plays shows that production performance does not scale up in simple increments when adding hydraulic fracture stages in closely spaced completions. Instead, closer stage spacing incrementally adds less hydrocarbon production per stage (Dohmen et al., 2014b), although the total productivity of the whole well increases. Therefore, determining the appropriate stage spacing is an important step in well performance optimization.

To properly simulate multiple fracture propagations for a completion stage in a horizontal well, the fracture model needs to take into account the interaction between adjacent hydraulic fractures, often referred to as the "stress shadow" effect. Stress shadow is a term often used to describe the increase of stresses in the direct vicinity of an existing hydraulic fracture. That is, when a hydraulic fracture is opened under a finite fluid net pressure, it induces stress changes in the surrounding rocks, which will affect other fractures in the vicinity.

Sneddon (1946) proposed an analytical solution for the stress distribution in the neighborhood of a long 2-D crack of plane strain condition in a homogeneous isotropic elastic solid under an internal pressure. His solution can be used to illustrate the stress variations caused by a hydraulic fracture (as shown in Fig. 11.21) under an internal treatment pressure. Warpinski

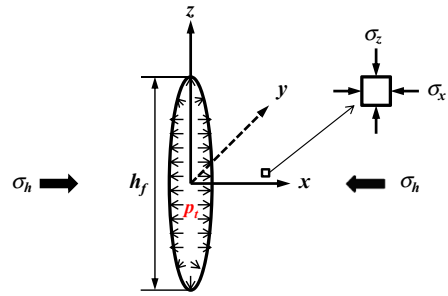

Figure 11.21 Schematic cross section cut in the minimum horizontal stress direction of a long hydraulic fracture propagated in the maximum horizontal stress direction (perpendicular to the page).

and Teufel (1987) assumed that the induced stresses near the center of a fracture (at $z = 0$) are representative of the stresses over a large area. Therefore, a simplified solution to explain the effect of stress shadow in closely spaced hydraulic fractures can be obtained. From Sneddon's solution and according to Warpinski and Teufel (1987), the induced stress increments in the minimum horizontal stress direction (x-direction) and vertical stress direction (z-direction) at $z = 0$ can be written in the following forms:

$$\Delta\sigma_x = p_n\left[1 - \frac{x^3}{\left(h_f^2/4 + x^2\right)^{3/2}}\right] \tag{11.19}$$

$$\Delta\sigma_z = p_n\left[1 - \frac{xh_f^2/2 + x^3}{\left(h_f^2/4 + x^2\right)^{3/2}}\right] \tag{11.20}$$

where $\Delta\sigma_x$ and $\Delta\sigma_z$ are the induced incremental stresses in the directions of the minimum horizontal stress and the vertical stress, respectively; p_n is the net pressure in the fracture and approximately equal to the difference of the treatment pressure (p_t) and the minimum horizontal stress (σ_h), $p_n = p_t - \sigma_h$; h_f is the fracture height; x is the distance away from the center of the fracture.

If the hydraulic fracture is markedly long compared to its height, then the condition of 2-D plane strain can be used to obtain the induced stress in the maximum horizontal direction, i.e.,

$$\Delta\sigma_y = \nu(\Delta\sigma_x + \Delta\sigma_z) \tag{11.21}$$

where $\Delta\sigma_y$ is the induced incremental stresses in the direction of the maximum horizontal stress; ν is Poisson's ratio of the rock.

Assuming that the superposition principle is applicable for the stress changes in the perturbed area, the stress shadow causes the minimum horizontal stress to increase to $\sigma_h + \Delta\sigma_x$, the maximum horizontal stress to increase to $\sigma_H + \Delta\sigma_y$, and the vertical stress to increase to $\sigma_V + \Delta\sigma_z$.

Based on hydraulic fracturing data in the Bakken formation (e.g., the treatment pressure $p_t = 11{,}500$ psi, the minimum horizontal stress of 7860 psi; hence, net pressure $p_n = p_t - \sigma_h = 3640$ psi), the induced stresses versus the distance away from the center of a fracture are calculated by Eq. (11.19) in two cases of fracture heights ($h_f = 300$ ft and $h_f = 100$ ft, as shown in Fig. 11.22, Dohmen et al., 2014b). It demonstrates that the treatment pressure exerts a compressive stress to the fracture on top of the minimum

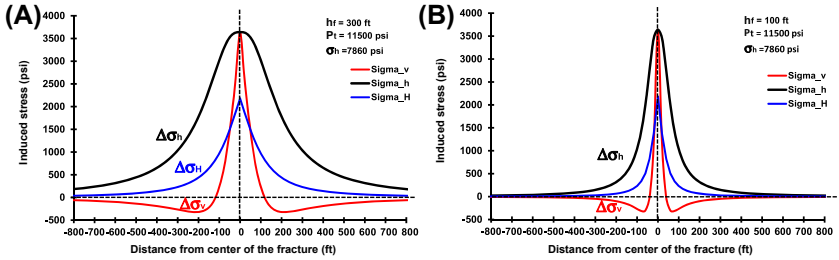

Figure 11.22 Induced stresses in surrounding area along the fracture cross section direction of a hydraulic fracture. (A) fracture height of 300 ft; (B) fracture height of 100 ft.

horizontal stress, which is equal to the net pressure at the fracture face, but quickly falls off with the distance from the fracture. At a distance beyond one fracture height, the induced stress (stress shadow) is only a small fraction of the net pressure. If a second hydraulic fracture (or second stage) is created parallel to the existing open fracture, and if the second fracture falls within the stress shadow, then the fracture will have a horizontal stress greater than the original horizontal stress. This implies that the second fracture will have a higher fracture initiation pressure. The induced stresses may also change the in situ stress directions and stress regimes in the interference area, causing subsequent fractures to grow in a nonplanar fashion or alter propagation direction. Comparing Fig. 11.22A and B, it can be observed that a greater fracture height has a larger impacted area of the induced stresses. Fig. 11.23 shows that a smaller fracture stage creates a stronger stress

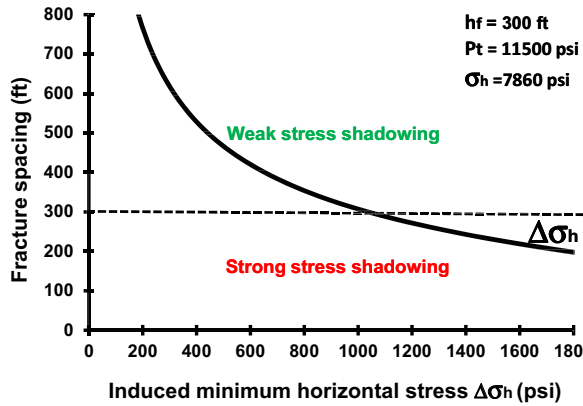

Figure 11.23 Induced minimum horizontal stress versus the spacing of the hydraulic fractures for a fracture height of 300 ft and an injection pressure of 11500 psi.

shadow. It should be noted that if the treatment pressure is lower, then the stress shadow effect will be smaller.

In recent years, numerical models involving 2-D and 3-D finite element, finite difference, and boundary element methods have been applied to simulate interactions of multiple hydraulic fractures in horizontal wells to optimize the spacing of fracture stages (e.g., Roussel and Sharma, 2011; Wu and Olson, 2013). The finite element method (FEM) verifies that when the spacing of hydraulic fractures is too small, it will cause stress increase and induce fracture interference. Fig. 11.24 presents the minimum horizontal stress distributions after three hydraulic fractures are simultaneously created with different fracture spacings in the Middle Bakken formation. The parameters used in this case are the same as the inputs used in Fig. 11.22. It can be observed that the horizontal stress increases markedly as the fracture spacing decreases. Therefore, a smaller fracture spacing causes a stronger stress shadow (Figs. 11.24 and 11.25). Although stress shadow affects hydraulic fracture performance when fractures are closely spaced, the current industry practice is to put more hydraulic fractures per stage; e.g., cluster spacing has been reduced to 10-20 ft. By doing so, the total production can increase although stress shadows are generated in those closely spaced hydraulic fractures. Therefore, it needs an optimized design to compromise stress shadow effect and total productivity of the well.

11.5.2 3-D conceptual model of stress shadow impact

To examine stage spacing and stress shadow effect, microseismic measurements were performed during hydraulic fracturing in three horizontal

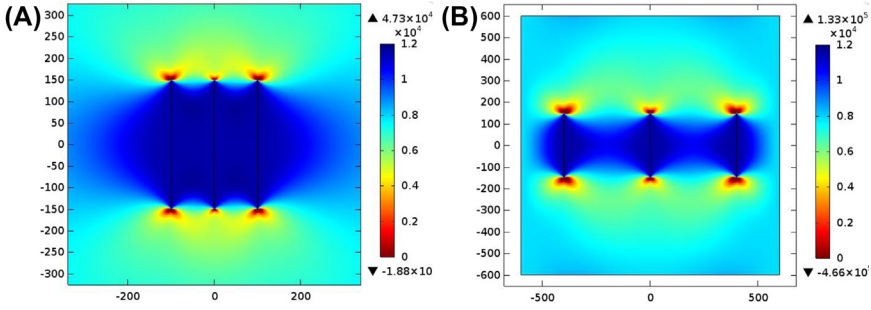

Figure 11.24 Stress distribution in x-direction (σ_x) after three fractures are simultaneously generated. (A) Fracture spacing of 100 ft; (B) fracture spacing of 400 ft. The geometry is in inches, and stresses are in psi. The blue and dark-red colors represent compressive and tensile stresses, respectively.

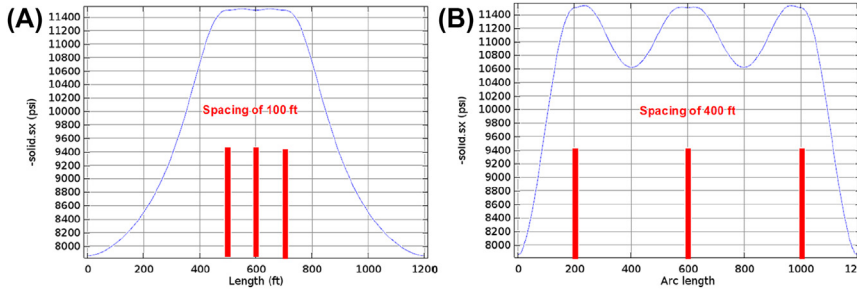

Figure 11.25 The minimum stress magnitudes (σ_x) after three fractures are simultaneously generated. (A) fracture spacing of 100 ft; (B) fracture spacing of 400 ft.

wells stimulated with different stage spacing in the Middle Bakken and the Utica reservoirs (Dohmen et al., 2014b). The microseismic measurements from those wells show that hydraulic fractures in closely spaced stages (clusters) interfere with each other by cyclically bouncing out-of-zone, i.e., the stress shadow exhibits a 3-D behavior. When hydraulic fractures develop in-zone (i.e., in the reservoir zone), as planned, the fractures sequentially elevate the minimum stress causing stress accumulation at the reservoir, i.e., the stress shadow. This elevated stress forces subsequent fractures preferentially upward, out-of-zone. As the stress accumulates in the zone above (causing the minimum stress increase), the following fractures reform and are back in-zone in a repetitive cycle, as shown in Fig. 11.26. Microseismic observation and analysis show periodic "bounces"

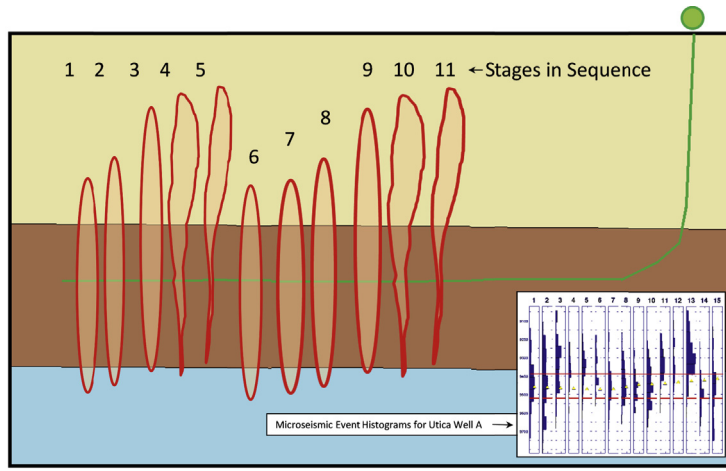

Figure 11.26 Schematic representation of fractures caused by closely spaced hydraulic fractures in Well A. If initial fractures interact and send successive fractures up, then the following fractures may once again develop in-zone (Dohmen et al., 2014b).

of the microseismic activity by approximately 50–200 ft vertically (Dohmen et al., 2014b). This is enough distance to significantly affect the amount of fracture contact within the producing intervals. The physics controlling incremental hydrocarbon production per stage may be related to this observed cyclical reduction of the in-zone fracture area.

11.6 Interaction of hydraulic fractures and natural fractures

Gu et al. (2012) summarized several cases of a hydraulic fracture to cross or open a natural fracture. The interaction of hydraulic and natural fractures can be classified as (a) hydraulic fracture propagating along the natural fracture, (b) hydraulic fracture crossing the natural fracture and the natural fracture staying close, and (c) hydraulic fracture both branching into and crossing the natural fracture (Fig. 11.27). Whether a hydraulic fracture opens a natural fracture is dependent not only on the properties of the natural fracture but also on the in situ stresses and treatment pressure. There are several approaches to determine if the hydraulic fracture enables to open or cross the natural fractures.

Nolte and Smith (1981) presented an elastic plane strain model to determine if the hydraulic fracture can open a natural fracture. They found that a natural fracture at any angle to a PKN hydraulic fracture will open when a critical net pressure (P_{nf}) is reached (i.e., $p_n \geq P_{nf}$):

$$P_{nf} = \frac{(\sigma_H - \sigma_h)}{(1 - 2\nu)} \tag{11.22}$$

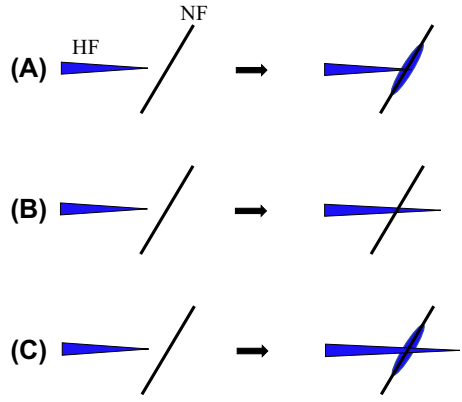

Figure 11.27 Hydraulic fracture (HF) propagation in the presence of a natural fracture (NF): (A) along natural fracture, (B) crossing natural fracture and natural fracture staying close, (C) branching into and crossing natural fracture.

It implies if the treatment pressure is high, it is easier to open natural fractures. At the same treatment pressure, when the difference of two horizontal stresses is smaller, it is easier to open natural fractures to form complex hydraulic fractures. From Eq. (11.22), if Poisson's ratio is 0.25, then the net pressure needs to be 2 times of the horizontal stress difference to open natural fractures. This equation may be oversimplified, because it does not consider the strength effects of the natural fractures.

From Eq. (11.22), for a hydraulic fracture to cross (not open) a natural fracture, the treatment pressure (p_t) needs to satisfy the following condition:

$$p_t < \frac{(\sigma_H - \sigma_h)}{(1-2\nu)} + \sigma_h \tag{11.23}$$

Assuming a natural fracture or an interface is perpendicular to the hydraulic fracture and using fracture mechanics theory, Renshaw and Pollard (1995) proposed a hydraulic fracture crossing criterion by considering that the fractures are in 2-D tensional in situ stress condition without internal pressure. If 2-D compressive in situ stress condition with effect of the treatment pressure is considered, the solution of Renshaw and Pollard (1995) can be modified as the following equations:

(1) For a horizontal hydraulic fracture to cross a vertical natural fracture (slip will not occur along the natural fracture as shown in Fig. 11.28), it needs to satisfy the following condition:

$$\frac{\sigma_H - p_t}{\sigma_h - p_t + T_0} > \frac{0.35 + 0.35/\mu}{1.06} \tag{11.24}$$

where μ is the friction coefficient of the natural fracture; T_0 is the tensile strength of the rock. If μ and σ_H are larger, it is easier for the hydraulic fracture to cross a vertical natural fracture or interface.

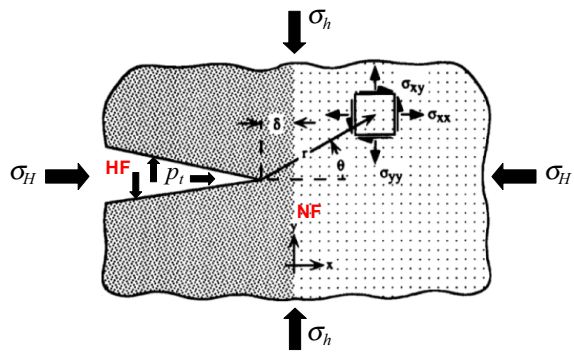

Figure 11.28 Interface geometry and coordinate system used to describe the stresses near a fracture tip that is almost impinging on a frictional interface. *(Modified from Renshaw and Pollard, 1995.)*

(2) For a vertical hydraulic fracture to cross a horizontal interface or other natural fracture, it needs to satisfy the following condition:

$$\frac{\sigma_V - p_t}{\sigma_h - p_t + T_0} > \frac{0.35 + 0.35/\mu}{1.06} \tag{11.25}$$

It can be seen from Eq. (11.25) that if μ and σ_V are larger, it is easier for a vertical hydraulic fracture to cross the horizontal interface. However, it is not applicable to the open fractures. It is obvious that for an open natural fracture, the hydraulic fracture will propagate or branch into the natural fracture. If the formation is in the reverse faulting stress regime: σ_V is smaller than σ_h and σ_H, then a vertical hydraulic fracture is much easier to open a horizontal interface according to Eq. (11.25). This may cause the vertical hydraulic fracture to propagate into a horizontal interface. This is also one of the reasons why horizontal fractures are more likely to be generated in a strong tectonic stress regime.

For an inclined natural fracture, the Mohr–Coulomb failure criterion can be used to analyze shear failures at the fracture tip to determine whether the tip develops shear sliding to open the natural fracture (Gu et al., 2012).

11.7 Rock brittleness

Fracturing ability of a rock is not only dependent on in situ stresses but also controlled by rock mechanical properties (e.g., tensile strength, Young's modulus, Poisson's ratio), rock physical properties, and mineral contents. The general rule for the effect of rock mechanical properties on hydraulic fracturing is that high Young's modulus and low Poisson's ratio correspond to a brittle rock, which is easier for hydraulic fracture propagating. Certainly, a rock with low tensile strength makes it easier to be broken (refer to Eq. 11.1). Rickman et al. (2008) used the brittleness index to evaluate rock brittleness to assist in locating the preferred stimulation intervals. This brittleness index combines the effect of Young's modulus and Poisson's ratio of the rock and can be expressed in the following equation:

$$B = 50\left(\frac{E - E_{\min}}{E_{\max} - E_{\min}} + \frac{\nu - \nu_{\max}}{\nu_{\min} - \nu_{\max}}\right) \tag{11.26}$$

where B is the brittleness index (%); E is the static Young's modulus of the rock; $E_{\max}$ and $E_{\min}$ are the maximum and minimum Young's moduli, respectively (constants); ν is Poisson's ratio of the rock; $\nu_{\max}$ and $\nu_{\min}$ are

the maximum and minimum Poisson's ratio, respectively; $\nu_{max} = 0.4$, $\nu_{min} = 0.15$. In the US unit system, E is in Mpsi, and $E_{max} = 8$ Mpsi, $E_{min} = 1$ Mpsi (Rickman et al., 2008). In the metric unit system, E is in GPa, and $E_{max} = 55.2$ GPa, $E_{min} = 6.9$ GPa.

Eq. (11.26) shows that a high brittleness index (e.g., $B \geq 60$), i.e., high Young's modulus and low Poisson's ratio, corresponds to a brittle rock, and a low brittleness index corresponds to a ductile rock. The brittleness index combining with formation closure and breakdown pressures can be used to help hydraulic fracturing design. It should be noted that the brittleness of a rock is not only controlled by rock mechanical properties but also related to rock physical properties (e.g., bulk density, porosity, the mineral contents). Additionally, a high Young's modulus may correspond to a high brittleness, but it may also relate to a low porosity and low TOC. In this case the shale reservoir may not be highly productive. Alzate and Devegowda (2013) proposed a method accounting for both brittleness of the shale and reservoir quality. This method is the $\lambda\rho$-$\mu\rho$ cross-plot, which is a reservoir rock quality classification template to integrate seismically inverted rock properties such as Lamé parameter (λ), shear modulus (μ or G), bulk density (ρ), Young's modulus, and Poisson's ratio. It was applied to the Lower Barnett shale play to describe rock brittleness (based on Poisson's ratio) and reservoir quality (based on Young's modulus, an indicator of porosity). This method considers that the best reservoir is the shale play in Group 0 or classified as "Brittle and Rich", which has low values of Poisson's ratios (brittle) and low values of Young's moduli (high porosity, hence large hydrocarbon volume). The worst reservoir is the shale play in Group 3 or "Ductile and Poor" with high Poisson's ratios and high Young's moduli. Group 1 or "Rich and Ductile" is those regions of the shale play characterized by high values of Poisson's ratios and low values of Young's moduli; Group 2 or "Brittle and Poor" is for the shale play exhibiting low values of Poisson's ratios and high values of Young's moduli.

11.8 PKN and GDK models of hydraulic fracturing

2-D hydraulic fracture models have been used for decades with reasonable success. In this section, only 2-D analytical models and principles are introduced. With high-performance computers available to most engineers, pseudo-three-dimensional (P3D) and 3-D numerical models can be applied for hydraulic fracture design.

11.8.1 PKN model and calculation of fracture dimensions

11.8.1.1 PKN model and its modification

For hydraulic fracturing design, the hydraulic fracture volume needs to be calculated. The PKN fracture solution (Perkins and Kern, 1961; Nordgren, 1972) has been applied in calculating induced hydraulic fracture width. The PKN solution is a 2-D analytical solution with assumption of plane strain deformation in the vertical plane. In the model of Perkins and Kern, each vertical cross section is assumed to act independently, i.e., the fracture height is fixed and independent to the fracture length (or length - >> height). In practice, this is true if the fracture length is much greater than the height.

Numerical modeling technique has been extensively applied to model hydraulic fractures; however, different numerical methods give very different results even when using the same input parameters and for the same case study as investigated by Warpinski et al. (1994) and by the American Rock Mechanics Association in 2017 (Han, 2017). Owing to the uncertainties in numerical models, the traditional PKN model is still applicable, e.g., for the planar hydraulic fractures and especially for validating numerical solutions. Perkins and Kern (1961) applied Sneddon and Elliott's solution (Sneddon and Elliott, 1946) to the oil and gas industry for hydraulic fracturing applications. They assumed that the hydraulic fracture was mostly kept in the pay zone or restricted at the top and bottom. This means when the hydraulic fracture height reaches the thickness of the pay zone, the hydraulic fracture is no longer to develop in the vertical direction and then mainly propagate in one of the horizontal directions, as shown in Fig. 11.29. Based on this assumption, the following 2-D plane strain solution can be used to calculate the maximum fracture width:

$$w_{\max} = \frac{2(1-\nu^2)}{E}(p_t - \sigma_h)H \tag{11.27}$$

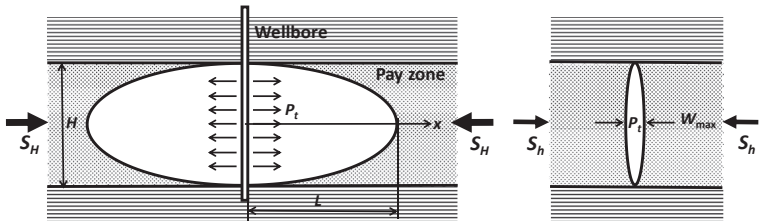

Figure 11.29 The PKN fracture growth model in two horizontal directions in a vertical well.

where w_{max} is the maximum fracture width; H is the fracture height (the maximum H is the thickness of the pay zone).

The PKN model assumes that the fracture is much longer in one direction than other two directions. This assumption is appropriate for a long fracture. However, it may not be suitable when the fracture height is very large or the ratio of the fracture length to height is small. For instance, the prolific Wolfcamp shale oil formations in West Taxes are very thick, and very tall hydraulic fractures are created during well stimulation operations. Microseismic measurements in six Wolfcamp wells (Friedrich and Milliken, 2013) show that the ratios of the hydraulic fracture length to height are quite small, from 1.1 to 2.4. In this case the PKN model may not be applicable. Using the FEM modeling, Zhang et al. (2018b) examined the applicability of the PKN solution in 3-D condition and obtained a modified solution. To compare 3-D FEM to 2-D plane strain (PKN) solutions, they modeled fracture width variations with varied fracture lengths for a fixed fracture height (the reservoir thickness). The purpose of doing so is to verify whether the 2-D PKN solution is applicable to the 3-D condition. In the 3-D FEM modeling, Table 11.1 was used as the input parameters. Fig. 11.30 shows the fracture widths calculated from the 3-D FEM versus the fracture lengths for the Bakken reservoir with a thickness of 1200 in. (i.e., the fracture maximum height is $H = 120$ ft) in the central horizontal plane of a vertical borehole in the reservoir zone. The 3-D FEM modeling shows that the fracture width increases as the fracture length increases before the fracture half length reaches 1.5 times of the maximum reservoir thickness (1.5×1200 in.). When $L/H = 2$, the fracture width reaches the maximum width or the PKN solution (the two dots in Fig. 11.30).

Table 11.1 In situ stresses and rock properties of the Bakken field used in the FEM modeling.

Parameter	Magnitude
Minimum horizontal stress, σ_h (psi)	7860
Maximum horizontal stress, σ_H (psi)	9432
Vertical stress, σ_V (psi)	10,480
Downhole treatment pressure, p_t (psi)	11,500
Young's modulus of the rock, E (psi)	3.8×10^6
Poisson's ratio of the rock, ν	0.25
Density of the rock, ρ (g/cm^3)	2.3
Hole radius, R (in.)	4.25
Reservoir depth, D (ft.)	10,000
Reservoir thickness H (ft.)	100

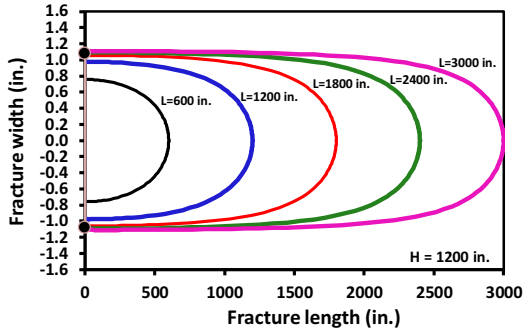

Figure 11.30 Fracture widths versus the fracture half lengths from 3-D FEM modeling. The two black dots are the maximum fracture width calculated from the PKN solution (Eq. 11.27).

By examining 2-D and 3-D FEM models, Zhang et al. (2018b) found that the fracture width increases as the fracture length or L/H (the ratio of the fracture half length to fracture height) increases. When the fracture length is relatively large ($L/H > 1.5$), the fracture width from the 3-D FEM model increases very slowly and approaches the 2-D plane strain FEM solution. That is, the 2-D FEM solution is the asymptote of the 3-D result. The fracture widths in 2-D and 3-D conditions have the following empirical relation (as shown in Fig. 11.31):

$$\frac{w_{2D}}{w_{3D}} = 1 + H/L^{1.22} \tag{11.28}$$

where w_{2D} and w_{3D} are the fracture widths in the 2-D and 3-D cases, respectively; L is the fracture half length.

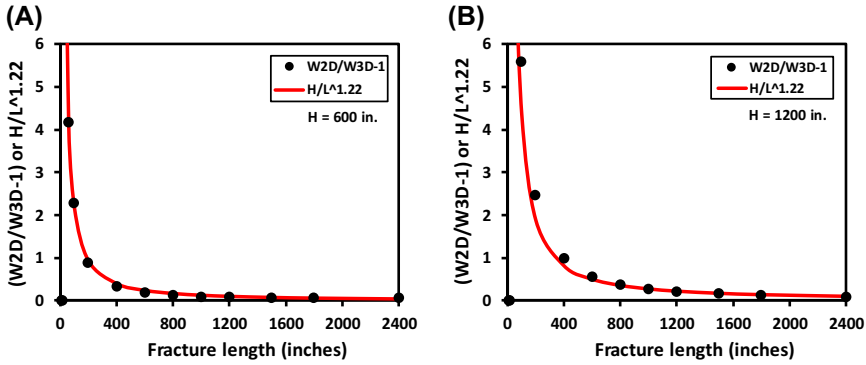

Figure 11.31 The fracture widths obtained from 3-D and 2-D FEM models and $H/L^{1.22}$ versus the fracture length. (A) $H = 600$ in.; (B) $H = 1200$ in.

Using Eq. (11.27) to replace w_{2D} in Eq. (11.28) and solving w_{3D}, the 3-D empirical solution of the maximum fracture width for the PKN fracture can be expressed in the following form (Zhang et al., 2018b):

$$w_{3D\_\max} = \frac{2(1-\nu^2)}{(1+H/L^{1.22})E}(p_t - \sigma_h)H \tag{11.29}$$

where $w_{3D\_\max}$ is the maximum fracture width of the PKN model in the 3-D condition.

11.8.1.2 Simple calculation of hydraulic fracture dimensions

From the mass balance equation, the volume of the injection fluid and proppants should be equal to the volume of the hydraulic fractures, i.e.,

$$aV = L_{tot}HW_{avg} \tag{11.30}$$

where V is the total injected fluid and proppant volume; a is the fluid efficiency, fraction; L_{tot} is the total length of the fractures; H is the fracture height; W_{avg} is the average fracture width; $W_{avg} \approx 0.628w_{\max}$; $w_{\max}$ can be obtained from Eqs. (11.27) or (11.29).

For a fracture stage, if the injected volume and the numbers of clusters are known, then, the fracture half length can be estimated from the following approximate equation:

$$L = \frac{aV_S}{2nHW_{avg}} \tag{11.31}$$

where V_S is the total injected fluid and proppant volume in one stage; n is the cluster numbers in the studied stage.

Eq. (11.31) assumes that each cluster only creates one bi-wing planar fracture. For complex fractures, numerical methods should be used for determining the fracture size.

11.8.2 KGD model

Geertsma and de Klerk (1969) presented another 2-D analytical solution (KGD model) for a linearly propagating fracture by assuming that the fracture height is much greater than the fracture length (height >> length). The KGD model was initially developed by Khristianovitch and Zheltov (1955) assuming the plane strain to be in the horizontal direction, i.e., all horizontal cross sections act independently or equivalently (Mack and Warpinski, 2000). This holds true only if fracture height is much greater

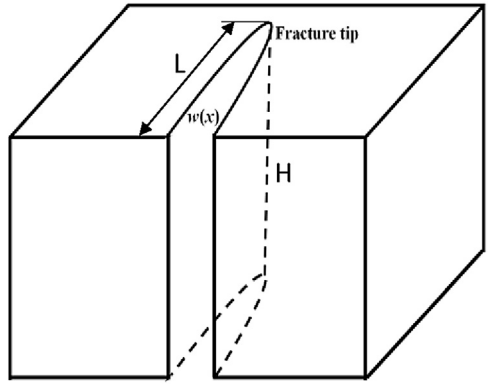

Figure 11.32 The KGD model (only half fracture is shown because of symmetry). The fracture height is much greater than the fracture length.

than the fracture length. The assumptions of the KGD model are listed in the the following:

(1) elliptical cross section in the horizontal plane, as shown in Fig. 11.32;
(2) each horizontal plane deforms independently;
(3) fracture height is a constant; and
(4) cross sections in the vertical plane are rectangular (fracture width is constant along its height).

The maximum fracture width in KGD model was obtained from the solution of Sneddon (1946) in the following equation:

$$W_{\max} = \frac{4(1-\nu^2)}{E} L(p_t - \sigma_h) \tag{11.32}$$

References

Abass, H.H., Hedayati, S., Meadows, D.L., 1992. Nonplanar fracture propagation from a horizontal wellbore: experimental study. In: SPE Ann. Tech. Conf. & Exh., Washington, DC, October 4–7. SPE-24823.

Alzate, J., Devegowda, D., 2013. Integration of surface seismic, microseismic, and production logs for shale gas characterization. Interpretation, 1(2), SB37-49.

Brock, D., 1986. Elementary Engineering Fracture Mechanics. Martinus Nijhoff, Boston.

Bunger, A.P., Lecampion, B., 2017. Four critical issues for successful hydraulic fracturing applications. In: Feng, X.-T. (Ed.), Rock Mechanics and Engineering, Surface and Underground Projects, vol. 5. CRC Press/Balkema (Chapter 16).

Cipolla, C., Motiee, M., Kechemir, A., 2018. Integrating microseismic, geomechanics, hydraulic fracture modeling, and reservoir simulation to characterize parent well depletion and infill well performance in the Bakken. URTEC-2899721.

Cottrell, B., Rice, J.R., 1980. Slightly curved or kinked cracks. Int. J. Fract. 16, 155–169.

Cruikshank, K., Zhao, G., Johnson, A., 1991. Analysis of minor fractures associated with joints and faulted joints. J. Struct. Geol. 13 (8), 865–886.
Daniels, J., Waters, G., LeCalvez, J., Lassek, J., Bentley, D., 2007. Contacting more of the Barnett Shale through and integration of real-time microseismic monitoring, petrophysics, and hydraulic fracture design. SPE 110562 presented at SPE Annual Technical Conference and Exhibition, Anaheim, California.
Diamond, W.P., Oyler, D.C., 1987. Effects of Stimulation Treatments on Coalbeds and Surrounding Strata. Technical Report. Report of Investigations 9083. United States Bureau of Mines.
Dohmen, T., Zhang, J., Li, C., Blangy, J.P., Simon, K.M., Valleau, D.N., Ewles, J.D., Morton, S., Checkles, S., 2013. A new surveillance method for delineation of depletion using microseismic and its application to development of unconventional reservoirs. Paper SPE 166274 presented at the SPE Annual Technology Conference in New Orleans, Louisiana.
Dohmen, T., Blangy, J.P., Zhang, J., 2014a. Microseismic depletion delineation. Interpretation 2 (3).
Dohmen, T., Zhang, J., Blangy, J.P., 2014b. Measurement and analysis of 3D stress shadowing related to the spacing of hydraulic fracturing in unconventional reservoirs. SPE 170924.
Dohmen, T., Zhang, J., Barker, L., Blangy, J.P., 2017. Microseismic magnitudes and b-values for delineating hydraulic fracturing and depletion. SPE J. 22 (5), 1624–1634.
Friedrich, M., Milliken, M., 2013. Determining the contributing reservoir volume from hydraulically fractured horizontal wells in the Wolfcamp formation in the Midland Basin. URTEC-1582170. https://doi.org/10.1190/URTEC2013-149.
Fung, R.L., Vilayakumar, S., Cormack, D.E., 1987. Calculation of vertical fracture containment in layered formations. SPE Form. Eval. 2 (4), 518–523. SPE 14707.
Geertsma, J., de Klerk, F., 1969. A rapid method of predicting width and extent of hydraulically induced fractures. J. Pet. Technol. 21 (12), 1571–1581. SPE-2458.
Gu, H., Weng, X., Lund, J., et al., 2012. Hydraulic fracture crossing natural fracture at nonorthogonal angles: a criterion and its validation. SPE Prod. Oper. 27 (1), 20–26. SPE-139984.
Guo, F., Morgenstern, N.R., Scott, J.D., 1993. An experimental investigation into hydraulic fracture propagation – Part 2. Single well tests. Int. J. Rock Mech. Min. Sci. 30, 189–202.
Haimson, B.C., Fairhurst, C., 1967. Initiation and extension of hydraulic fractures in rocks. SPE J. 7, 310–318.
Hakala, A., Guthrie, G., 2013. Unconventional Resources Portfolio Annual Report. NETL-TRS-UCR-2013, NETL Technical Report Series. U.S. Department of Energy, National Energy Technology Laboratory, Pittsburgh, PA, p. 84.
Han, G., Nov 2017. Hydraulic fracturing simulation: physics and models. Presented at SPE Completions & Production Study Group. SPE Gulf Coast Section.
Hubbert, M.K., Willis, D.G., 1957. Mechanics of hydraulic fracturing. Pet. Trans. AIME 210, 153–168.
Khristianovich, S.A., Zheltov, Y.P., 1955. Formation of vertical fractures by means of highly viscous liquid. In: Proc 4th World Petroleum Congress, Rome, Italy, pp. 579–586.
Mack, M.G., Warpinski, N.R., 2000. Mechanics of hydraulic fracturing. In: Economides, M.J., Nolte, K.G. (Eds.), Reservoir Stimulation, third ed. (Chapter 6).
Morita, N., Black, A.D., Fuh, G.-F., 1996. Borehole breakdown pressure with drilling fluids—I. Empirical results. Int. J. Rock Mech. Min. Sci. 33, 39–51.
Morton, M., 2013. Unlocking the earth – a short history of hydraulic fracturing. GeoExPro 10 (6).

MSEEL, 2015. MIP-3H Well Log Data and Mechanical Properties Processed by Schlumberger.
Nolte, K.G., Smith, M.B., 1981. Interpretation of fracturing pressures. J. Pet. Technol. 33, 1767–1775. SPE-8297-PA.
Nordgren, R.P., 1972. Propagation of vertical hydraulic fractures. J. Pharm. Technol. 253, 306–314.
Perkins, T.K., Kern, L.R., 1961. Widths of hydraulic fractures. In: SPE Annual Fall Meeting, Dallas, October 8–11. SPE-89-PA.
Raterman, K.T., Farrell, H.E., Mora, O.S., Janssen, A.L., Gomez, G.A., Busetti, S., McEwen, J., Davidson, M., Friehauf, K., Rutherford, J., Reid, R., Ge, J., Roy, B., Warren, M., 2017. Sampling a stimulated rock volume: An Eagle Ford example. URTeC-2670034.
Raterman, K.T., Farrell, H.E., Mora, O.S., Janssen, A.L., Gomez, G.A., Busetti, S., McEwen, J., Davidson, M., Friehauf, K., Rutherford, J., Reid, R., J., Ge., Roy, B., Warren, M., 2018. Sampling a Stimulated Rock Volume: An Eagle Ford Example. SPE Reservoir Evaluation & Eng. SPE-191375.
Renshaw, C.E., Pollard, D.D., 1994. Are large differential stresses required for straight fracture propagation paths? J. Struct. Geol. 16, 817–822.
Renshaw, C.E., Pollard, D.D., 1995. An experimentally verified criterion for propagation across unbounded frictional interfaces in brittle, linear elastic materials. Int. J. Rock Mech. Min. Sci. 32, 237–249.
Rickman, R., Mullen, M., Petre, E., Grieser, B., Kundert, D., 2008. A practical use of shale petrophysics for stimulation design optimization: all shale plays are not clones of the Barnett Shale. Paper SPE-115258 presented at the 2008 Annual Technical Conference and Exhibition.
Roussel, N.P., Sharma, M.M., 2011. Optimizing fracture spacing and sequencing in horizontal well fracturing. SPE Prod. Oper. 26 (2), 173–184. SPE-127986.
Simonson, E.R., Abou-Sayed, A.S., Clifton, R.J., 1978. Containment of massive hydraulic fractures. SPE J. 18 (1), 27–32. SPE-6089.
Sneddon, I.N., 1946. The distribution of stress in the neighbourhood of a crack in an elastic solid. Proc. Roy. Soc. Lond. Math. Phys. Sci. 187, 229–260.
Sneddon, I.N., Elliott, H.A., 1946. The opening of a Griffith crack under internal pressure. Q. Appl. Math. 4, 262–266.
Stephenson, B., Galan, E., Williams, W., MacDonald, J., Azad, A., Carduner, R., Zimmer, U., 2018. Geometry and failure mechanisms from microseismic in the Duvernay Shale to explain changes in well performance with drilling azimuth. SPE-189863.
Vidma, K., Abivin, P., Dunaeva, A., Panga, M., Nikolaev, M., Usoltsev, D., Mayo, J., 2018. Far-field diversion technology to prevent fracture hits in tightly spaced horizontal wells. SPE-191722-MS.
Warpinski, N.R., Teufel, L.W., 1987. Influence of geologic discontinuities on hydraulic fracture propagation. Soc. Petrol. Eng. J. 39 (2), 209–220.
Warpinski, N.R., Schmidt, R.A., Northrop, D.A., 1982. In situ stresses: the predominant influence on hydraulic fracture containment. J. Pharm. Technol. 34, 653–664.
Warpinski, N.R., Moschovidis, Z.A., Parker, C., Abou-Sayed, I.S., 1994. Comparison study of hydraulic fracturing models – test case: GRI staged field experiment no. 3. SPE Prod. Facil. 9 (1), 7–16. SPE-25890.
Waters, G., Weng, X., 2016. The impact of geomechanics and perforations on hydraulic fracture initiation and complexity in horizontal well completions. SPE-181684.
Whitfield, T., Watkins, M., Dickinson, L., 2018. Pre-loads: successful mitigation of damaging frac hits in the Eagle Ford. SPE-191712.

Wileveau, Y., Cornet, F.H., Desroches, J., Plumling, P., 2007. Complete in situ stress determination in an argillite sedimentary formation. Phys. Chem. Earth 32, 866–878.
Wu, K., Olson, J.E., 2013. Investigation of the impact of fracture spacing and fluid properties for interfering simultaneously or sequentially generated hydraulic fractures. SPE Prod. Oper. Nov. 427–436.
Zhang, J., 2013. Borehole stability analysis accounting for anisotropies in drilling to weak bedding planes. Int. J. Rock Mech. Min. Sci. 60, 160–170.
Zhang, G., Chen, M., 2010. Dynamic fracture propagation in hydraulic re-fracturing. J. Pet. Sci. Eng. 70 (3–4), 266–272.
Zhang, J., Yin, S., 2017. Fracture gradient prediction: an overview and an improved method. Petrol. Sci. 14, 720.
Zhang, Y., Zhang, J., 2017. Lithology-dependent minimum horizontal stress and in-situ stress estimate. Tectonophysics 703–704, 1–8.
Zhang, X., Jeffrey, R.G., Bunger, A.P., Thiercelin, M., 2011. Initiation and growth of a hydraulic fracture from a circular wellbore. Int. J. Rock Mech. Min. Sci. 48, 984–995.
Zhang, Y., Zhang, J., Yuan, B., Yin, S., 2018. In-situ stresses controlling hydraulic fracture propagation and fracture breakdown pressure. J. Pet. Sci. Eng. 164, 164–173.
Zhang, J., Zhang, Y., Yin, S., 2018. PKN solution revisit: 3-D hydraulic fracture size and stress anisotropy effects. Rock Mech. Rock Eng. 51 (2), 653–660.
Zhu, H.Y., Deng, J.G., Jin, X.H., Hu, L.B., Luo, B., 2015. Hydraulic fracture initiation and propagation from wellbore with oriented perforation. Rock Mech. Rock Eng. 48, 585–601.
Zinn, C., Blood, D., Morath, P., 2011. Evaluating the impact of wellbore azimuth in the Marcellus Shale. SPE-149468.
Zoback, M.D., Rummel, F., Jung, R., Raleigh, C.B., 1977. Laboratory hydraulic fracturing experiments in intact and pre-fractured rock. Int. J. Rock Mech. Min. Sci. 14, 49–58.

CHAPTER 12

Sanding prediction

Contents

Abstract

Sand production prediction can help identify the most economical way of sand control methods with the desired production rate. This chapter examines some methods to model perforation failures for sanding prediction. Wellbore geometry, reservoir properties, depletion, and drawdown are addressed to analyze sand production, with particular attention focused on stress redistributions and sand failures in perforations and wellbores. Sanding failure criteria are very different from the conventional ones, and some criteria and rock strength correlations are discussed for sanding prediction. The critical bottomhole flowing pressure and critical drawdown are given to optimize production rate for reducing sand production. The relationships of perforation orientation, rock strength, in situ stresses and sanding potentials are analyzed to provide optimal perforation direction for mitigating sand production.

Keywords: Critical drawdown; Optimal perforation orientation; Poroelastic solution; Sand production; Sanding failure criterion; Sanding prediction.

Sand production is a critical issue impacting well production and casing stability. The major cause of sand production is wellbore instability and perforation tunnel failure in poorly-consolidated and unconsolidated formations. Classical sand control techniques are primarily based on installing gravel pack, frac-and-pack, and sand screen. It is desirable to predict perforation stability and sanding potential before completion engineers make a decision on which sand control procedures are required. Because

Applied Petroleum Geomechanics
ISBN 978-0-12-814814-3
https://doi.org/10.1016/B978-0-12-814814-3.00012-5

sand production usually takes place in unconsolidated porous formations, sanding prediction models, to be more effective, need to address elasto-plastic behavior and accommodate the transient behaviors of the stresses and fluid pressure around the borehole and perforation tunnels during production. Both analytical solutions and numerical models can be employed to model perforation and hole stability and predict sanding potentials.

12.1 Elastic solutions for sanding prediction

Sanding prediction is generally based on the following three categories: sand arch stability, perforation tunnel stability, and open hole wellbore stability.

12.1.1 Sand arch stability

Laboratory experiments show that a sand arch is formed when sand is produced in a sandstone reservoir. The arch serves to support a load by resolving vertical stress into horizontal stress. When the arch fails, sand production will begin. Fig. 12.1 shows a numerical model of a sand arch failure causing sand production (Peng et al., 2007). An early model for sand arch stability assumed an idealized production cavity with full spherical symmetry of stress field, and the following sand arch stability criterion was derived by Bratli et al. (1981):

$$\frac{\mu q}{2\pi k r_1} < 2UCS \tag{12.1}$$

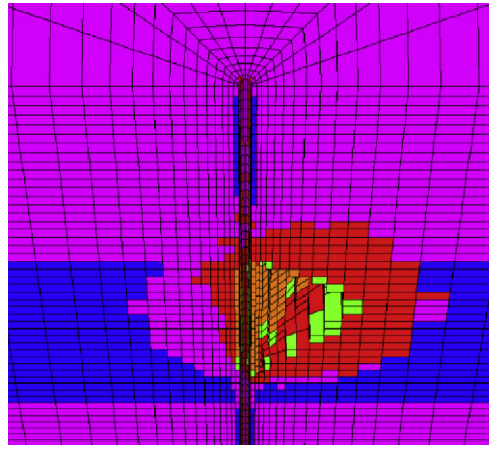

Figure 12.1 Sand cavity in an unconsolidated reservoir from a numerical simulation. Sand production in the reservoir depends on sand arch stability.

where *UCS* is the uniaxial compressive strength of the formation; q is the flow rate of the cavity; k is the formation permeability; r_1 is the cavity radius; and μ is the fluid viscosity.

12.1.2 Open hole wellbore stability

For open hole production, sand production may occur if the wellbore fails in poorly-consolidated and unconsolidated reservoirs. A stable wellbore is the minimum requirement for keeping safe production and preventing sanding. For wellbore stability analysis, readers can refer to Chapter 10.

12.1.3 Elastic solution on perforation tunnel stability

Instability of the perforation tunnel may cause sand production. Perforation tunnel stability is dependent on in situ stresses, reservoir and wellbore pressures, rock strength, and perforation geometry. If wellbore pressure is too low, shear failure may occur; however, if well pressure is too high, tensile failure may occur. It has been found that the increase of effective stresses due to reservoir pressure depletion results in the rock approaching shear failure envelope, making shear failure more likely to occur (refer to Fig. 5.13). Therefore, depletion-triggered tensile failure is less likely, but a shear-induced sanding problem is dominant. Earlier study for sanding prediction was based on elastic solutions to examine stress concentration around perforations and shear failures induced by the stress concentration.

Once the production borehole has been drilled, cased, and cemented, the reservoir can be perforated at regular intervals for production. Production is begun by imposing on the well a pressure p_{wf} (bottomhole flowing pressure) lower than the virgin reservoir pressure, p_R. According to Darcy's law, a flow rate converges toward the well, as shown in Fig. 12.2. To increase production, flowing pressure must be kept as low as possible. However, the low flowing pressure may trigger sand production. Therefore, the minimum flowing pressure needs to be determined. The minimum flowing pressure in the bottomhole without sand production is the critical flowing pressure (p_{cwf}). The critical total drawdown pressure (p_{CDP}) is defined as the difference of the reservoir pressure and the critical flowing pressure. It is also defined as the critical drawdown from the reservoir pressure to cause failure (sand production) of the reservoir formation, as shown in the following equation:

$$p_{CDP} = p_R - p_{cwf} \tag{12.2}$$

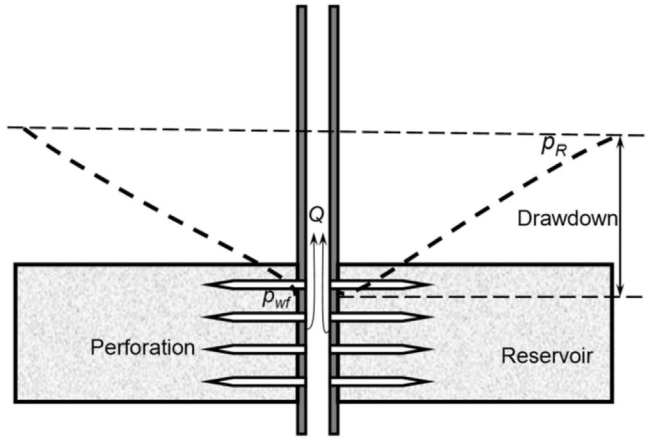

Figure 12.2 Schematic representation of the reservoir pressure and the bottomhole flowing pressure in a reservoir.

where p_{CDP} is the critical total drawdown pressure; p_R is the virgin reservoir pressure; p_{cwf} is the critical flowing pressure.

Charlez (1997) considered a circular drainage area produced at a constant flow rate Q in a vertical open hole with isotropic horizontal stress ($\sigma_H = \sigma_h$). For an elastic plane stress condition and using the Mohr–Coulomb failure criterion, the critical total drawdown pressure was proposed in the following equation:

$$p_{CDP} = \frac{1}{1-\alpha}\left[\frac{UCS}{2} - (\sigma_h - p_R)\right] \tag{12.3}$$

where α is Biot's effective stress coefficient. Charlez (1997) noted that the critical total drawdown is almost insensitive to flow rate.

In general, in situ stresses are not isotropic (the maximum and minimum horizontal stresses are not equal), and different in situ stress regimes exist in different basins. Therefore, Eq. (12.3) is oversimplified and more advanced models are needed to predict the critical drawdown.

12.2 Poroelastic solutions for sanding prediction

12.2.1 Critical drawdown in an open hole or perforation tunnel

Willson et al. (2002) proposed a formulation used for the onset of sanding calculations, i.e., the calculation of the critical bottomhole flowing pressure

(CBHFP) resulting in sand production. It is based on a simple apparent strength criterion, together with assumed linear-elastic behavior, applied to a formation element next to the wall of a circular hole. The hole could be a wellbore (for open hole completion) or a perforation (for cased hole completion). The orientation of the wellbore or the perforation is reflected in the calculation of the principal stresses perpendicular to the hole in terms of suitably transformed in situ principal stresses.

Given the far-field total stresses (in situ stresses) on a plane perpendicular to the axis of a hole, the maximum tangential stresses on the wall of the hole (Fig. 12.3) for permeable case can be obtained from the second equation of Eq. (10.43) (steady state poroelastic solution), which occurs in the minimum in situ stress direction:

$$S_{t2} = 3\sigma_{\max} - \sigma_{\min} - p_w(1 - A) - Ap_R \tag{12.4}$$

where S_{t2} is the maximum tangential stresses at the wall of the hole cross section, as shown in Fig. 12.3; $\sigma_{\max}$ and $\sigma_{\min}$ are the maximum and minimum in situ stresses, respectively; p_w is the wellbore pressure; A is a poroelastic constant, and $A = \frac{\alpha(1-2\nu)}{1-\nu}$.

To avoid sand production the maximum effective tangential stress ($S_{t2} - p_w$) should be smaller than the effective strength of the formation (U) next to the hole (Willson et al., 2002), i.e.,

$$S_{t2} - p_w \leq U \tag{12.5}$$

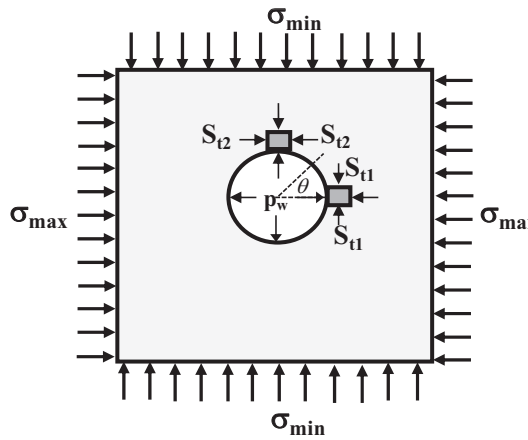

Figure 12.3 In situ stresses and tangential stresses at the wall of a hole (wellbore or perforation).

Inserting Eq. (12.4) into Eq. (12.5) and solving for p_w and the CBHFP without sanding can be derived as the following equation (BP sand onset model, Willson et al., 2002):

$$p_w \geq p_{cwf} = \frac{3\sigma_{\max} - \sigma_{\min} - U}{2 - A} - p_R \frac{A}{2 - A} \tag{12.6}$$

Combining Eqs. (12.2) and (12.6), the critical total drawdown pressure (p_{CDP}) can be obtained:

$$p_{CDP} = \frac{1}{2 - A}[2p_R - (3\sigma_{\max} - \sigma_{\min} - U)] \tag{12.7}$$

The effective strength of the formation (U) can be obtained from the thick-walled cylinder (TWC) test, which is used as the fundamental strength measurement for unsupported boreholes and perforations (Willson et al., 2002; Palmer et al., 2003):

$$U = 3.1TWC \tag{12.8}$$

where TWC is the strength as determined in the TWC test. The factor 3.1 includes the scale transformation from laboratory (OD:ID = 3) to field (OD:ID = infinity).

Based on global data on laboratory tests of the TWC and unconfined compressive strength (UCS) conducted on sandstones (e.g., Ewy et al., 1999; Tronvoll et al., 1997; Wu and Tan, 2000), the following correlation is obtained:

$$TWC = 11.46UCS^{0.53} \tag{12.9}$$

where the UCS and TWC are in MPa.

Combining Eq. (12.8) and the correlation of Eq. (12.9), the effective strength can be written as the following form:

$$U = 35.526UCS^{0.53} \tag{12.10}$$

Using the poroelastic solution and the Mohr–Coulomb failure criterion to analyze shear failure in the perforation tunnel, the following equation is derived to predict the CBHFP (p_{cwf}) for keeping perforation tunnel stability (Zhang et al., 2007):

$$p_{cwf} = k_0(1 - \nu)\left[3\sigma_{\max} - \sigma_{\min} - \alpha\frac{(1 - 2\nu)}{1 - \nu}p_R - UCS\right] \tag{12.11}$$

where k_0 is a calibration factor; ν is Poisson's ratio; σ_{max} and σ_{min} are the maximum and minimum in situ stresses applied in the cross section perpendicular to the perforation tunnel axis. If the bottom hole flowing pressure is smaller than the critical pressure, i.e., $p_{wf} < p_{cwf}$, then sanding will occur.

When shear failures occur in the perforation tunnel, it is not necessary to have sand production. Therefore, parameter k_0 is considered in Eq. (12.11) as a calibration factor, which can be obtained from sanding case study in offset wells.

12.2.2 Case application for sanding prediction

Marsala et al. (1994) and Moricca et al. (1994) presented a detailed case study of sand production in the Northern Adriatic Basin in Italy. The pay zone situated at depths of between 3280 and 14760 ft in this basin was a sandstone reservoir with a low cohesion. The vertical lithology was made of regular alternations of sands and shales. The sand reservoir had a porosity of between 10% and 40% and a permeability of between 10 and 100 mD. Increasingly, frequent sanding events occurred because of reservoir depletion. It was observed that the critical total drawdown was clearly related to the formation cohesion according to a logarithmic-type law. For cohesion of less than 1 MPa (145 psi), sand production occurred immediately after the well was put on stream. However, as soon as cohesion reached a few MPa, sand production becomes increasingly improbable.

Zhang et al. (2007) analyzed Well #3 in the Northern Adriatic Basin to predict CBHFP and to examine the influence of perforation directions on sand production by using Eq. (12.11). This well was cased and perforated from 8453 to 8458 ft. The average reservoir pressure was $p_R = 5508$ psi. Field data indicated that sand production occurred at a bottomhole flowing pressure of 5486 psi. Rock mechanical properties are available for the analysis from Marsala et al. (1994).

Fig. 12.4 represents the calculated CBHFP and sanding prediction using Eq. (12.11). The zone of sanding risk is also given. The field production point plotted in the figure was a case of having sand production because of the bottomhole flowing pressure being too low. The prediction shows that this case lies in a sanding risk zone (the square in Fig. 12.4). Fig. 12.4 shows that at a higher bottomhole flowing pressure, the reservoir depletion can be kept sand free ("No sanding" area in the figure).

Fig. 12.5 displays the calculated CBHFP versus rock strength and perforation directions. It shows that the CBHFP is closely related to rock strength, i.e., if the rock is stronger, then the CBHFP is smaller and it is less

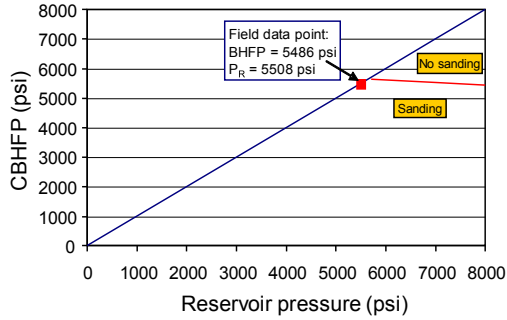

Figure 12.4 Critical bottomhole flowing pressure (CBHFP) versus sand production predicted by Eq. (12.11). The BHFP represents the bottomhole flowing pressure.

risky for sand production. Fig. 12.5 also displays that perforation orientations have profound effects on the CBHFP in this well. If the perforation tunnels are shot in the direction of the maximum horizontal stress, the reservoir allows smaller bottomhole flowing pressure. It demonstrates that perforating in this direction reduces the risk of sanding. The field-measured

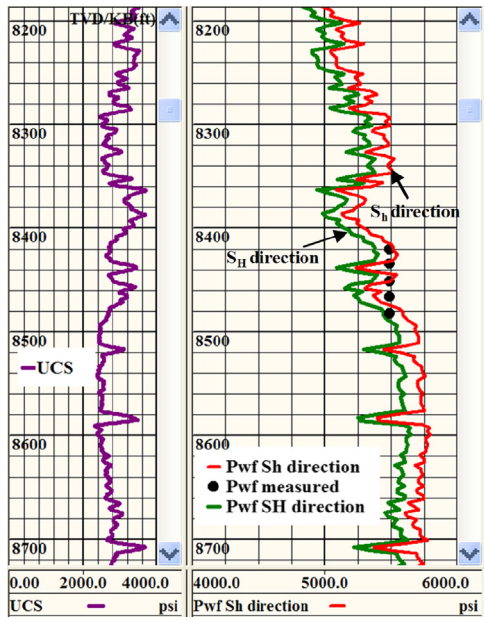

Figure 12.5 Comparison of critical bottomhole flowing pressures (with depth in feet) in two perforation directions of the maximum and minimum horizontal stresses. The left track displays the rock strength (UCS in psi), and the right track plots the critical bottomhole flowing pressures in the maximum horizontal direction (P_{wf} SH direction), the minimum horizontal stress direction (P_{wf} Sh direction), and the field-measured critical bottomhole flowing pressures (dots).

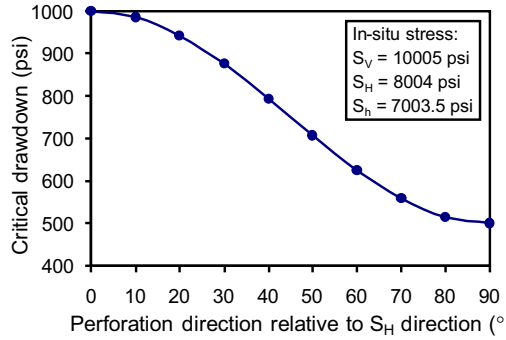

Figure 12.6 Perforation direction effect on critical drawdown indicating that an appropriate perforation direction increases reservoir drawdown.

bottomhole flowing pressures are also plotted in Fig. 12.5. Compared to the calculated result, the predicted flowing pressure from Eq. (12.11) matches the measured flowing pressure.

Fig. 12.6 presents the perforation direction effect on critical drawdown. It demonstrates that appropriate perforation direction (i.e., 0 degree or the maximum horizontal stress direction in the figure), depending on the in situ stress state, can increase reservoir drawdown and reduce the risk of sand production.

12.3 Sanding failure criteria and sanding prediction

12.3.1 Sanding failure criteria

Many models were developed to predict sand production (e.g., Nouri et al., 2006; Vaziri et al., 2006). Most sand production onset models for field applications have been derived from the hollow cylinder hole failure models based on the assumption that wellbore failure corresponds to onset of sand production. The stress expressions for the open hole wellbore can be applied to the perforated completions by considering the perforations as open holes of small diameters. In such a case, it is assumed that the wellbore does not influence the stress field around the perforations. The hole failure criteria have been expressed through an equivalent cavity stress σ_C that is compared with the hole failure strength σ_S of the formation such that (Papamichos and Furui, 2019):

$$\sigma_C - \eta^p \sigma_S < 0 \quad \text{no failure, no sanding} \tag{12.12}$$

$$\sigma_C - \eta^p \sigma_S = 0 \quad \text{Hole failure, sanding onset} \tag{12.13}$$

$$\sigma_C - \eta^p \sigma_S > 0 \quad \text{Sand production} \tag{12.14}$$

where η^p is a field calibration factor to scale σ_S such that field or laboratory data can be reproduced satisfactorily, and the default value is $\eta^p = 1$. This fit factor can be used to the field to calibrate the sanding onset predictions, set a higher or lower threshold for sand tolerance, etc.

The equivalent cavity stress σ_C in different criteria is given as follows (Papamichos and Furui, 2019):

1. Simplified Mohr–Coulomb sanding criterion

$$\sigma_C = \frac{\sigma'_{\theta i}}{2} \tag{12.15}$$

Combining Eqs. (12.13–12.15), the simplified Mohr–Coulomb sanding criterion can be rewritten as Eq. (12.16), i.e., when the following equation satisfies, it has sand production:

$$\sigma'_{\theta i} \geq 2\eta^p \sigma_S \tag{12.16}$$

where $\sigma'_{\theta i}$ is the effective tangential stress at the hole wall; σ_S is the hole failure strength of the formation and can be related to the uniaxial compressive strength of the rock.

In Eq. (12.16) it is assumed that if the effective tangential stress is equal to or greater than two times of the hole failure strength (σ_S), then sand production occurs. This implies that the strength for sanding in Eq. (12.16) is two times the conventional strength (e.g., the strength used for wellbore stability evaluation).

2. The Mohr–Coulomb sanding criterion

$$\sigma_C = \frac{1}{4}\left[\sigma'_{\theta i} + \sigma'_{zi} + \sqrt{\left(\sigma'_{\theta i} - \sigma'_{zi}\right)^2 + 4\tau^2_{\theta zi}}\right] \tag{12.17}$$

where σ'_{zi} is the effective axial stress at the hole wall; $\tau_{\theta zi}$ is the shear stress at the hole wall.

Using Eqs. (12.13) and (12.14), the Mohr–Coulomb sanding criterion Eq. (12.17) can be rewritten as Eq. (12.18), i.e., when the following equation satisfies, it has sand production:

$$\left[\sigma'_{\theta i} + \sigma'_{zi} + \sqrt{\left(\sigma'_{\theta i} - \sigma'_{zi}\right)^2 + 4\tau^2_{\theta zi}}\right] \geq 4\eta^p \sigma_S \tag{12.18}$$

Compared to the conventional shear failure, such as wellbore breakout, the strength for sanding in Eq. (12.18) is two times of the conventional strength. The other failure criteria can also be applied for sanding analysis, such as the Drucker–Prager criterion.

12.3.2 Sanding strength and critical drawdown

A scaling law for σ_S must also be employed if necessary to account for the strengthening of a hole with decreasing hole diameter. A scaling law proposed based on experiments on sandstones is written as (Papamichos et al., 2010):

$$\sigma_S = \left(\frac{1}{3} + \frac{2}{3}\frac{D_{ref}}{D}\right)\sigma_{Sref} \tag{12.19}$$

where σ_S is the sanding onset (hole failure) strength of a hole with diameter D and σ_{Sref} is the sanding onset strength of a reference hole with diameter $D_{ref} = 2$ cm. The isotropic sanding onset strength σ_{Sref} can be related to the uniaxial compressive strength of the rock (UCS).

The hollow cylinder hole failure strength σ_{Sref} can be obtained either through a hollow cylinder failure test or through a correction with the UCS. Papamichos (2002) obtained the following correlation from experimental test data in the sand production process for both reservoir and outcrop sandstones:

$$\sigma_{Sref} = 6.0841 UCS^{0.6346} \tag{12.20}$$

Now the right parts of Eqs. (12.16) and (12.18) are known, and the effective stresses in the left parts of the equations need to be obtained. In the case of a deviated wellbore with fluid pressure p_w, the effective stresses σ'_{mni} at the hole wall ($r = r_i$) are obtained from the following equations and setting radial stress $\sigma_{ri} = p_w$ (Papamichos and Furui, 2013, 2019):

$$\begin{aligned}
\sigma'_{\theta i} =& \sigma_X + \sigma_Y - 2(\sigma_X - \sigma_Y)\cos 2\,\theta - 4\sigma_{XY}\sin 2\,\theta - 2p_{reso} + 2\Delta p_{dep} \\
&+ \left(2 - 2\eta_B - \frac{\eta_B}{\ln r_i/r_e}\right)\Delta p_{dd} \\
\sigma'_{zi} =& \sigma_Z - 2\nu(\sigma_X - \sigma_Y)\cos 2\,\theta - 4\nu\sigma_{XY}\sin 2\,\theta - p_{reso} + \Delta p_{dep} \\
&+ \left(1 - \eta_B - \frac{\nu\eta_B}{\ln r_i/r_e}\right)\Delta p_{dd} \\
\sigma'_{\theta zi} =& 2(\sigma_{YZ}\cos\theta - \sigma_{ZX}\sin\theta)
\end{aligned} \tag{12.21}$$

where σ_{IJ} are the formation stresses in the (x, y, z) coordinate system of the wellbore; p_{res} is the reservoir pore pressure; r_i is the hole radius; r_e is the reservoir external radius; θ is the angle starting from the maximum

far-field stress direction, as shown in Fig. 12.3; and $\eta_B = \frac{\alpha(1-2\nu)}{2(1-\nu)}$. For failure, Biot's coefficient of 1 has been used in Eq. (12.21) for the calculation of effective stresses; and the drawdown Δp_{dd} and the depletion Δp_{dep} are defined as follows:

$$\begin{aligned} \Delta p_{dep} &= p_{reso} - p_{res} \\ \Delta p_{dd} &= p_{res} - p_w = p_{reso} - \Delta p_{dep} - p_w \end{aligned} \tag{12.22}$$

where p_{reso} are the original reservoir pore pressure; p_{res} is the reservoir pore pressure after depletion Δp_{dep}; p_w is the pressure at the wellbore.

The stresses σ_{IJ} can be expressed through the original in situ stresses σ_H, σ_h, and σ_V after depletion Δp_{dep} through the coordinate system transformation for the inclined hole. The conversion is similar to Eq. (10.1), but with consideration of depletion effect of $2\eta_B \cdot \Delta p_{dep}$ (i.e., stress decrease in two horizontal stresses due to depletion). Therefore, for an inclined hole the local in situ stresses in a cross section perpendicular to the hole axis can be expressed as follows:

$$\begin{aligned} \sigma_X &= [(\sigma_H - 2\eta_B\Delta p_{dep})\cos^2\alpha + (\sigma_h - 2\eta_B\Delta p_{dep})\sin^2\alpha]\cos^2 i + \sigma_V \sin^2 i \\ \sigma_Y &= (\sigma_H - 2\eta_B\Delta p_{dep})\sin^2\alpha + (\sigma_h - 2\eta_B\Delta p_{dep})\cos^2\alpha \\ \sigma_Z &= [(\sigma_H - 2\eta_B\Delta p_{dep})\cos^2\alpha + (\sigma_h - 2\eta_B\Delta p_{dep})\sin^2\alpha]\sin^2 i + \sigma_V \cos^2 i \\ \sigma_{XY} &= \frac{\sigma_h - \sigma_H}{2}\sin 2\alpha \cos i \\ \sigma_{YZ} &= \frac{\sigma_h - \sigma_H}{2}\sin 2\alpha \sin i \\ \sigma_{XZ} &= \frac{(\sigma_H - 2\eta_B\Delta p_{dep})\cos^2\alpha + (\sigma_h - 2\eta_B\Delta p_{dep})\sin^2\alpha - \sigma_V}{2}\sin 2i \end{aligned} \tag{12.23}$$

where i is the hole inclination, for a vertical hole $i = 0°$ and for a horizontal hole $i = 90°$; α is the angle of the hole direction with respect to the σ_H direction, as shown in Fig. 10.11a; σ_{IJ} are the in situ stresses after depletion in the cross section of the inclined hole as shown in Fig. 10.11b.

The critical drawdown for sand production initiation can be calculated by substituting the effective stresses at the wellbore wall, Eq. (12.21), into the simplified Mohr–Coulomb sand failure criterion (Eq. 12.16) or the Mohr–Coulomb sand failure criterion (Eq. 12.18) and solving the drawdown Δp_{dd} to yield the critical drawdown for sand production. For the

simplified Mohr–Coulomb criterion, the critical drawdown for sand production can be obtained from the following equation:

$$\sigma_X + \sigma_Y - 2(\sigma_X - \sigma_Y)\cos 2\,\theta - 4\sigma_{XY}\sin 2\,\theta - 2p_{reso} + 2\Delta p_{dep} + \left(2 - 2\eta_B - \frac{\eta_B}{\ln r_i/r_e}\right)\Delta p_{dd}^{cr} = 2\eta^p \sigma_S \tag{12.24}$$

For a vertical hole or perforation and $\alpha = 0°$, Eq. (12.23) becomes:

$$\begin{aligned} \sigma_X &= \sigma_H - 2\eta_B \Delta p_{dep} \\ \sigma_Y &= \sigma_h - 2\eta_B \Delta p_{dep} \\ \sigma_{XY} &= 0 \end{aligned} \tag{12.25}$$

When $\theta = 90°$, the left part of Eq. (12.24) reaches the maximum value. Substituting Eq. (12.25) and $\theta = 90°$ to Eq. (12.24), the critical drawdown for sand production in a vertical wellbore or perforation can be obtained:

$$\Delta p_{dd}^{cr} = \frac{1}{\left(2 - 2\eta_B - \frac{\eta_B}{\ln r_i/r_e}\right)}[2\eta^p \sigma_S - 3\sigma_H + \sigma_h + 2(2\eta_B - 1)\Delta p_{dep} + 2p_{reso}] \tag{12.26}$$

For a horizontal perforation ($i = 90°$) and the perforation direction parallel to σ_H direction, ($\alpha = 0°$), Eq. (10.23) becomes:

$$\begin{aligned} \sigma_X &= \sigma_V \\ \sigma_Y &= \sigma_h - 2\eta_B \Delta p_{dep} \\ \sigma_{XY} &= 0 \end{aligned} \tag{12.27}$$

Substituting Eq. (12.27) and $\theta = 90°$ to Eq. (12.24), the critical drawdown for sand production in a horizontal wellbore or perforation tunnel perforated in the σ_H direction can be obtained in the following:

$$\Delta p_{dd}^{cr} = \frac{1}{\left(2 - 2\eta_B - \frac{\eta_B}{\ln r_i/r_e}\right)}[2\eta^p \sigma_S - 3\sigma_V + \sigma_h - 2(\eta_B + 1)\Delta p_{dep} + 2p_{reso}] \tag{12.28}$$

Notice that all the closed-form sanding onset predictive models presented above are based on the idealization that the reservoir rocks are

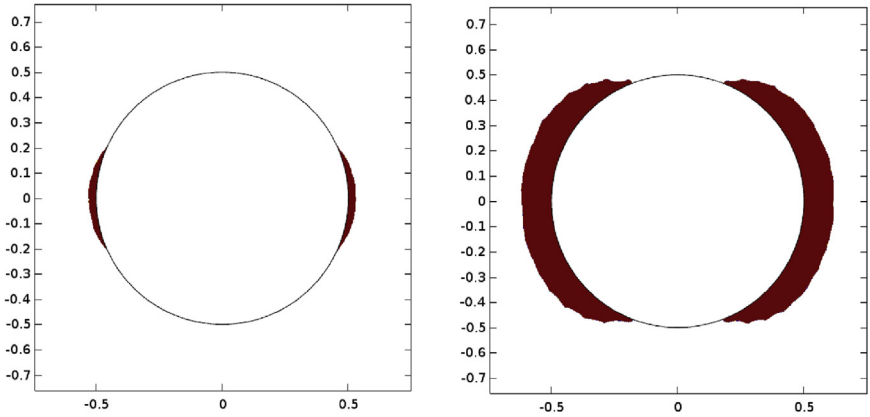

Figure 12.7 The FEM modeled sanding failure (left) using the failure criterion Eq. (12.18) and the wellbore failure (right) using the conventional Mohr–Coulomb failure criterion with the same depletion and drawdown in the two cases.

isotropic, linear-elastic materials before running into plastic yielding. In the situations where these assumptions do not hold, the analytical solutions may not be able to give reliable prediction; therefore, numerical modeling may be required. Many numerical models have been developed and used to simulate sand production (e.g., Detournay et al., 2006; Han and Cundall, 2013). The finite element method (FEM) can be applied to model sanding failure and determine optimized drawdown. A 3-D FEM is applied to model shear failures caused by sand production in an inclined borehole. The sanding failure criterion (Eq. 12.18) and conventional Mohr–Coulomb failure criterion are used to analyze a perforation tunnel perpendicular to the axis of a deviated wellbore with inclination of 38 degrees. The modeling results show that the sanding failure area is much smaller than the conventional Mohr–Coulomb failure area, as shown in Fig. 12.7. This implies that the conventional wellbore failure is not equivalent to sand production, and the sand production failure area is much smaller.

References

Bratli, R.K., Risnes, R., 1981. Stability and Failure of Sand Arches 21 (02), 236–248. SPE-8427.

Charlez, P.A., 1997. Rock Mechanics. In: Petroleum Application, vol. 2. Editions Technip.

Detournay, C., Tan, C., Wu, B., 2006. Modeling the mechanism and rate of sand production using FLAC. In: Hart, R., Varona, P. (Eds.), Numerical Modeling in Geomechanics . Paper No. 08-10. Itasca, Minneapolis, Minnesota.

Ewy, R.T., Ray, P., Bovber, C.A., Norman, P.D., Goodman, H.E., 1999. Openhole stability and sanding predictions by 3D extrapolation from hole collapse tests. SPE-56592.

Han, Y., Cundall, P.A., 2013. LBM–DEM modeling of fluid–solid interaction in porous media. Int. J. Numer. Anal. Methods Geomech. 37, 1391–1407.

Marsala, A.F., Ragazzini, G., Meazza, O., Brignoli, M., Santarelli, F.J., 1994. Basin scale rock mechanics: logs and core measurements. SPE-28034.

Moricca, G., Ripa, G., Sanfilippo, F., Santarelli, F.J., 1994. Basin scale rock mechanics: field observations of sand production. SPE-28066.

Nouri, A., Vaziri, H., Kuru, E., Islam, R., 2006. A comparison of two sanding criteria in a physical and numerical modeling of sand production. J. Pet. Sci. Eng. 50 (1), 55–70.

Palmer, I., Vaziri, H., Willson, S., Moschovidis, Z., Cameron, J., Ispas, I., 2003. Prediction and managing sand production, a new strategy. Paper SPE 84499.

Papamichos, E., 2002. Sand mass prediction in a North Sea reservoir. SPE/ISRM-78166, OilRock 2002. Irving, Texas.

Papamichos, E., Tronvoll, J., Skjærstein, A., Unander, T.E., 2010. Hole stability of Red Wildmoor sandstone under anisotropic stresses and sand production criterion. J. Pet. Sci. Eng. 72, 78–92.

Papamichos, E., Furui, K., 2002. Sand production initiation criteria and their calibration. ARMA 13-304, 47th US Rock Mechanics/Geomechanics Symp.

Papamichos, E., Furui, K., 2019. Analytical models for sand onset under field conditions. J. Pet. Sci. Eng. 172, 171–189.

Peng, S., Fu, J., Zhang, J., 2007. Borehole casing failure analysis in unconsolidated formations: a case study. J. Pet. Sci. Eng. 59, 226–238.

Tronvoll, J., Papamichos, E., Sanfilippo, F., 1997. Sand production in ultra-weak sandstones: is sand control absolutely necessary? SPE-39042.

Vaziri, H., Allam, R., Kidd, G., Bennett, C., Grose, T., Robinson, P., Malyn, J., 2006. Sanding: a rigorous examination of the interplay between drawdown, depletion, start-up frequency and water cut. SPEPO 21 (4), 430–440. SPE-89895-PA.

Willson, S.M., Moschovidis, Z.A., Cameron, J.R., Palmer, I.D., 2002. New model for predicting the rate of sand production. SPE/ISRM-78168.

Wu, B., Tan, P., 2000. Relationship between thick-walled cylinder and unconfined compressive strength for application in sanding prediction. In: Girard, Liebman, Breeds, Doe (Eds.), Pacific Rocks 2000. Balkema, Rotterdam.

Zhang, J., et al., 2007. Optimized perforation tunnel geometry, density and orientation to control sand production. In: European Formation Damage Conference. SPE-107785.

Index

'*Note:* Page numbers followed by "f" indicate figures and "t" indicate tables.'

C

D

G

H

I

K

L

M

N

O

P

R

S

T

U

V

W

X

Y

Applied Petroleum Geomechanics

Jon Jincai Zhang Geoscience Advisor-Geomechanics, USA

Answers to real-world challenges in petroleum geomechanics including pore pressure and fracture gradient predictions with this practical reference

Petroleum engineers have a difficult time making the leap between theory of rock mechanics and practical applications surrounding petroleum geomechanics especially in more complex operations such as hydraulic fracturing. *Applied Petroleum Geomechanics* delivers the bridge between theory and practice as a daily reference with direct industry applications. Going beyond the basic fundamentals of rock properties and mechanical behaviors, this guide covers critical field and lab tests along with interpretations that follow within actual drilling and completion operations and worldwide case studies, including abnormal formation pressures from many major petroleum basins. Rounding out with borehole stability solutions and the geomechanics surrounding hydraulic fracturing and unconventional reservoirs, *Applied Petroleum Geomechanics* gives petroleum engineers and geologists a much-needed resource to tackle today's advanced oil and gas operations.

Key Features:

- Explores a great wealth of methods in formation evaluation, geomechanics and the most recent advancements in the area including tools, techniques, and success stories
- Bridges the gap between theory of rock mechanics and practical oil and gas applications
- Explains pore pressure calculations and predictions critical to deepwater drilling, shale reservoirs and hydraulic fracturing activity

Related Titles:

- *Petroleum Related Rock Mechanics*, 2nd Edition by Fjar, Holt, Raaen, Risnes, and Horsrud, 978-0-44-450260-5
- *Hydraulic Fracturing in Unconventional Reservoirs,* 2nd Edition by Belyadi, Fathi, and Belyadi, 978-0-12-817665-8
- *Petroleum Rock Mechanics*, 2nd Edition by Aadnoy and Looyeh, 978-0-12-815903-3
- *Unconventional Oil and Gas Resources Handbook* by Ma and Holditch, 978-0-12-802238-2

TECHNOLOGY AND ENGINEERING / PETROLEUM

ISBN 978-0-12-814814-3

9 780128 148143

ELSEVIER

G P P

Gulf Professional Publishing

An imprint of Elsevier

elsevier.com/books-and-journals